404

CONF-760539

MASTER

PROCEEDINGS OF ERDA SYMPOSIUM ON X- AND GAMMA-RAY SOURCES AND APPLICATIONS

May 19-21, 1976

Ann Arbor, Michigan

NOTICE

CONF-760539
Distribution Category UC-23

PROCEEDINGS OF ERDA SYMPOSIUM ON X- AND GAMMA-RAY SOURCES AND APPLICATIONS

Held at
The University of Michigan
Ann Arbor, Michigan

May 19-21, 1976

HENRY C. GRIFFIN, Chairman, Editorial Committee

SYMPOSIUM SPONSORS

United States Energy Research and Development Administration
Edsel B. Ford Institute for Medical Research
Michigan Memorial - Phoenix Project of The University of Michigan
Ford Motor Company, Scientific Research Laboratories
General Motors Research Laboratories

SYMPOSIUM ORGANIZING COMMITTEE

L. E. Preuss - Chairman	Edsel B. Ford Institute for Medical Research
H. J. Lum - Secretary	The University of Michigan
R. F. Hill - Treasurer	General Motors Research Laboratories
G. J. Rotariu	US Energy Research and Development Administration
M. F. Elgart	Ford Motor Company
H. C. Griffin	The University of Michigan
J. D. Jones	The University of Michigan
G. F. Knoll	The University of Michigan
J. McIlroy	The University of Michigan
M. A. Short	Ford Motor Company
D. H. Vincent	The University of Michigan

SUPPORTING COMMITTEES

Scientific Program
- G. F. Knoll - Chairman
- H. C. Griffin - Assistant Chairman
- H. J. Lum - Secretary
- M. F. Elgart
- R. F. Hill
- J. D. Jones
- L. E. Preuss
- M. A. Short
- D. H. Vincent

Publicity
- H. J. Lum - Chairman

Poster Papers
- D. H. Vincent - Chairman
- J. D. Jones

Local Arrangements
- J. D. Jones - Chairman
- J. McIlroy

Editorial
- H. C. Griffin - Chairman
- H. J. Lum
- M. F. Elgart
- R. F. Hill
- G. F. Knoll
- L. E. Preuss

Commercial Exhibits
- M. F. Elgart - Co-Chairman
- M. A. Short - Co-Chairman

Guest Speaker
- G. F. Knoll - Chairman
- H. C. Griffin

Liaison, USERDA
- G. J. Rotariu

Liaison, U. of M. Extension Service
- J. McIlroy

PREFACE

This symposium was the fourth in a series of meetings which have emphasized sources and applications of electromagnetic radiation in the domain of x rays, bremsstrahlung, and low energy gamma rays. The series began with the 1964 meeting in Chicago at the IIT Research Institute[1], subsequent meetings were held at the University of Texas, Austin[2] (1967) and at Boston College[3] (1970). Although the U.S. Atomic Energy Commission (now ERDA) has been a sponsor of all of these meetings, each was organized by a local group and to some extent reflected their particular interests. Perhaps the local flavor is diminishing, the Ann Arbor symposium approached an international scope with over ten per cent of the papers given by authors from Europe and Japan.

Not surprisingly the emphases of the meetings have shifted from the relatively specific concerns of the first meeting to a broad spectrum of techniques and applications. The spectrum is sufficiently continous that organization of the scientific program into topical sessions present at some difficulties. Of the 75 papers in the program, the largest number (17) concerned detectors per se, with particular emphasis on high resolution spectroscopy with semiconductor detectors. Of course detectors played a crucial role in many applications to life sciences (13 papers), environmental studies (16 papers), and industrial analysis (16 papers). Interest in sources (16 papers) ranged from "traditional" radioisotopes to high current accelerators to synchrotron radiation. The three papers concerning Mossbauer spectroscopy included new techniques and new applications.

The sessions of invited and contributed papers were held in the Horace H. Rackham building on the campus of the University of Michigan. In addition to the oral presentations in 6 sequential sessions, 18 papers were given in two poster sessions held on the second day of the symposium. Although the poster format requires a substantial amount of space for each paper, it proved valuable in overcoming limits on discussion imposed by the more rigid schedule of oral sessions. Concurrent with the technical sessions, manufacturers' exhibits[4] and demonstrations of the ERDA Simulator by S. Wood were open to the symposium participants.

The organizers of the "symposium" did not ignore the origin of the word - a convivial gathering with drinking, music, and conversation - even if the order of events was not strictly correct. Early registrants took part in a wine and cheese tasting during the evening before the formal opening of the meeting, and a social hour and banquet were an integral part of the symposium. Of course, a banquet requires a speaker, and Professor B. L. Cohen met that requirement with a report on his studies of techniques for disposal of nuclear reactor wastes.

Informal contacts are an important mechanism for exchange of information at any sucessful meeting. These contacts are necessarily and desirably off the record. Perhaps floor discussion following individual papers could be considered part of the record, but we have chosen to treat this exchange in the same manner as that arising more informally - off the record. The papers which are main body of this volume are direct reproductions of manuscripts supplied by the authors. Because the editorial committee constrained the length of these manuscripts, in some cases the oral presentations were more detailed than is the record. The omission of discussion removes the distinction between oral and poster presentations; both types of papers are grouped into the somewhat arbitrary categories of the technical sessions.

The organizing committee acknowledges the support of the U.S. Energy Research and Development Administration in underwriting initial expenses and publishing these proceedings. We thank the session chairmen, R. Jenkins, M. Kato, A.B. Brill, J.W. Winchester, G. Rotariu, and D. Vincent, for keeping the meeting lively, C. Wysocki for maintaining the schedule, and C. Artman for tending the session signs.

Henry C. Griffin
Chairman, Editorial Committee

1. Proc. Symp. on Low Energy X- and Gamma Sources and Applications, Chicago, Ill., 1964, Eds., P.S. Baker and M. Gerrard, ORNL-IIC-5, 1965.
2. Proc. 2nd Symp. on Low-Energy X- and Gamma Sources and Applications, Austin, Tex., 1967, Eds., P.S. Baker and M. Gerrard, ORNL-IIC-10, 1967.
3. Applications of Low Energy X- and Gamma Rays, Ed. C.A. Ziegler, Gordon and Breach, New York, 1971.
4. Exhibitors at the Symposium were: Amersham-Searle Corp., Bicron Corp., Canberra Ind., The Harshaw Chemical Comp., Isotope Products Laboratories, Kevex Corp., LND, Inc., New England Nuclear Corp., Nuclear Data Inc., ORTEC, Inc., Tracor Northern, Inc., U. S. Energy Research and Development Administration

TABLE OF CONTENTS

SOURCES

DETECTORS

LIFE SCIENCE, DIOMEDICAL APPLICATIONS

ENVIRONMENTAL, GEOLOGICAL APPLICATIONS

INDUSTRIAL APPLICATIONS

MOSSBAUER SPECTROSCOPY

Proceedings, ERDA X-and Gamma-Ray Symp Ann Arbor, MI, May 19-21 1976 (Conf 760539)

EXCITATION METHODS FOR ENERGY DISPERSIVE ANALYSIS*

Joseph M. Jaklevic

Lawrence Berkeley Laboratory
University of California
Electronics Engineering Department
Berkeley, California 94720 U.S.A.

ABSTRACT

The rapid development in recent years of energy dispersive X-ray fluorescence analysis has been based primarily on improvements in semiconductor detector X-ray spectrometers. However, the whole analysis system performance is critically dependent on the availability of optimum methods of excitation for the characteristic X-ray, in specimens. A number of analysis facilities based on various methods of excitation have been developed over the past few years. This paper discusses the features of various excitation methods including charged particles, monochromatic photons, and broad-energy band photons. The effects of the excitation mode that on background and sensitivity will be illustrated from both the optical and experimental viewpoints. Recent developments such as pulsed excitation and polarized photons will also be discussed.

INTRODUCTION

Over the past several years, the level of activity in the area of energy-dispersive analysis has increased dramatically. Much of this work has involved applications in environmental research and monitoring where the capabilities of the energy dispersive methods closely match the analytical requirements.[1] These capabilities include the accurate multiple-element, non-destructive analysis of large volumes of samples at a reasonable cost.

Modern energy-dispersive analysis using semiconductor detector spectrometers is made possible by the improvements in electronic energy resolution,[2] detector background characteristics,[3] and system counting rate performance[4] which occurred in the years before and immediately following the previous 1970 conference in this series.[5] More recently, however, development in these areas have been less dramatic and only minor improvements in energy resolution have been reported in the past few years. On the other hand, there has been a considerable amount of recent research into the design of complete analytic systems including the optimization of the excitation method for particular types of applications. These methods now include heavy charged particles,[6-8] continuous photon sources,[9] and discrete energy photon sources.[10,11] These radiations can be derived either from radioisotope sources or from particle accelerators and X-ray tubes. In many applications where a high sensitivity or large sample throughput are required, the latter methods are preferred over radioisotope sources due to the higher counting rates which can typically be achieved.

To apply these various techniques to a given problem it is important to understand the basic difference between the spectral data obtained in each case. The goal of the present paper is to present a quantitative description of the basic physical processes operating in each of the excitation methods and to relate this to the spectral response in each case. Estimates for the sensitivity and limits of detection can subsequently be calculated.

Spectra will be calculated using simple theoretical models and empirical data where necessary. Although the calculations are of necessity approximate, it is hoped that the description of the interactions and their effect upon the final spectrum will serve to elucidate the basic differences in the methods and provide a basis for comparison between them in a given application. Experience has shown that even relatively simple calculations can provide accurate representations of the experimental response of the complete analytical system.

CALCULATIONS

The calculations assume a simplified sample form as shown in Fig. 1. It consists of a 25 mg/cm^2 carbon substrate on which has been deposited 250 ng/cm^2 of the elements Al, Si, Ca, Fe, Cu and Br. This corresponds to the type of sample obtained by deposition on a typical cellulose fiber filter and is of the same areal density as a very thin biological specimen. If the elemental deposits were uniformly distributed through the substrate the concentrations would correspond to 10 ppm by weight.

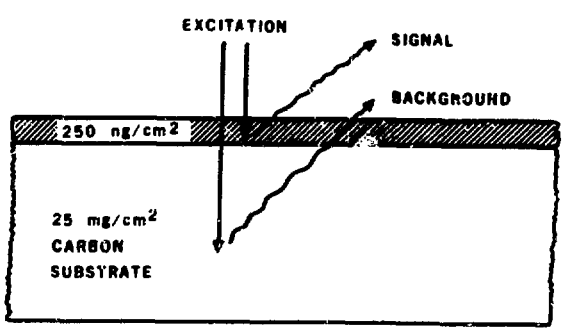

Fig. 1. Schematic of the idealized sample form used in the calculations.

* This report was done in part with support from the United States Environmental Protection Agency under interagency agreement with the United States Energy Research and Development Administration. Any conclusions or opinions expressed in this report represent solely those of the author and not necessarily those of The Regents of the University of California, the Lawrence Berkeley Laboratory or the United States Energy Research and Development Administration.

This form of sample was chosen for consideration since the trace element type of measurement represents a more challenging problem from the point of view of sensitivity and detectability. It more closely approximates the typical samples encountered in air pollution and biological analysis. Finally, the sample form in Fig. 1 represents the most easily calculable since one can validly make a number of simplifying approximations.

The calculations assume that the signal originates from interactions in the surface layer only and that energy loss or attenuation effects in this layer are negligible. The background radiation observed in the detector is caused by the interaction of the exciting radiation in the 25 mg/cm^2 substrate. Enhancement effects between the two layers and absorption within a layer are neglected.

Four types of fluorescence excitation will be considered: a) direct electron bombardment, b) charged particle excitation with 3 MeV protons, c) monoenergetic photon excitation, and d) continuous photon irradiation. The spectral data are calculated assuming an energy resolution of 200 eV full width at half maximum (FWHM) independent of X-ray energy.

Direct Electron Excitation

Although it is not readily used for routine X-ray fluorescence analysis of large samples, direct electron excitation is included in the comparison because of its importance in electron-probe devices. The dominant feature of electron excited spectra is the continuous Bremsstrahlung background generated by the electrons as they are slowed down in the electrostatic field of the atoms in the substrate. Fluorescent X rays result from the direct vacancy production in the atoms in the surface layer.

Although very detailed calculations of these effects are available in the electron probe literature, the results shown in Fig. 2 are based on an earlier X-ray production model.[12] It is assumed that the 20 and 40 keV electrons are completely stopped in the substrate and produce a continuous spectrum described by:[12]

$$N(E) = 2.76 \times 10^{-7} \, Z \, \frac{(E_o - E)}{E} \, \Delta E \qquad (1)$$

where $N(E)$ is the number of quanta of energy E in the interval ΔE, E_o is the energy of the electron beam, and Z is the atomic number of the target. The ionization cross sections are calculated assuming a full energy electron beam with no corrections for energy loss in the thin deposited layer. The low-energy X-ray spectrum is attenuated by a 50 μm Be window. This accounts for the steeply sloped background at low energies and the subsequent difficulty in detecting the Al signal. A more rigorous treatment would include the effect of X-ray absorption in the substrate resulting in a reduction in background at very low energies.

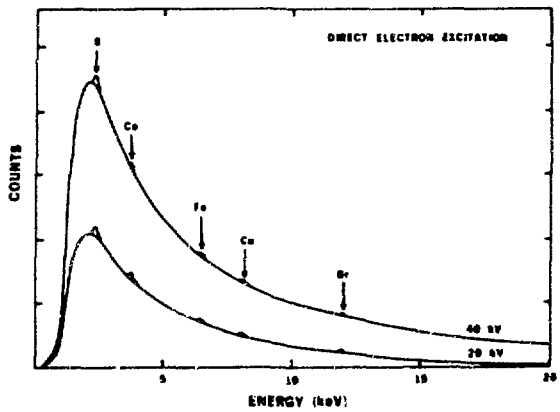

Fig. 2. Calculated spectra assuming 20 keV and 40 keV electron excitation.

Charged Particle Excitation

Fluorescence measurements using heavy-charged particles such as protons or alpha particles are expected to be much more sensitive than electron excitation. The cross section for Bremsstrahlung production is reduced by several orders of magnitude due to the increased mass of the particles.[13] The dominant spectral background no longer results from direct Bremsstrahlung production but is due to continuum radiation emitted in the slowing down of secondary electrons produced in the sample. Heavy particles are very efficient at producing ionization in light elements resulting in a sizeable number of energetic electrons which have been ejected from the inner atomic shells in the substrate. These produce a continuum photon distribution whose endpoint energy is determined by the maximum energy transfer to the electrons by the heavy ionizing particles. The energy of the charged particle beams are normally limited to 3 MeV for protons and 16 MeV for alpha particles in order to achieve optimum sensitivity.

Very successful models have been developed to describe ionization by heavy-charged particles including expressions for the energy distributions of the ejected inner shell electrons. These results have been combined with the appropriate Bremsstrahlung calculations in order to predict the background spectra for charged-particle analysis.[14] These calculations together with the associated X-ray production cross sections have been used to calculate the spectrum for 3 MeV proton excitation shown in Fig. 3. The model assumes the sample form of Fig. 1 with a slight modification due to the reduced range of the protons. An 8 mg/cm^2 substrate is assumed to approximately compensate for the energy loss of the protons in the substrate. The solid line is derived from the theoretical calculations of Ref. 14 whereas the dashed lines are adapted from measurements on very thin substrates.

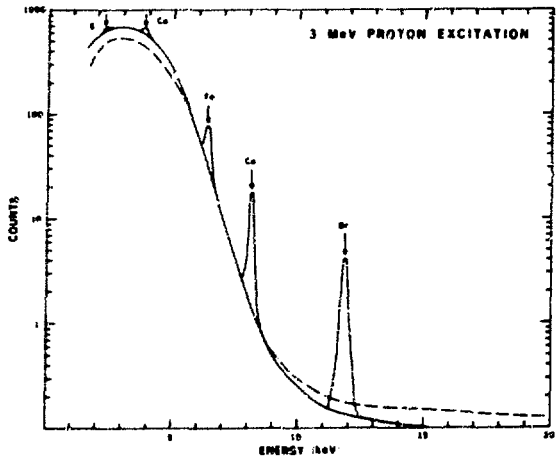

Fig. 3. Calculated spectrum assuming 3 MeV proton excitation. Smooth curve is theoretical background; dashed curve is based on thin film measurements. A 375 μm Be absorber is assumed.

The dominant feature of charged-particle excited spectra is the background intensity at very low energies as indicated in the logarithmic plot of Fig. 3. This is mostly due to secondary-electron Bremsstrahlung. The continuum background due to direct production by the protons would be about three orders of magnitude below the level plotted. The calculated spectrum assumes a low-energy detection efficiency dominated by absorption in a 375 μm Be window. This type of absorption profile has been deliberately chosen to enhance the relative sensitivity for the heavier elements at the expense of the very light ones. A thinner window would enhance the light element sensitivity but the drastic increase in background counts at low energies would reduce the relative counting rate for the higher energy X rays. A compromise solution adopted by some workers is to use a variable attenuation filter consisting of a thick absorber in which a very small hole has been drilled. A normal background reduction is thus maintained over most of the detector area with the exception of a 10% hole through which the low energy spectrum can pass unattenuated.

The theoretical background calculations neglect the effects of electronic pile-up of the low-energy continuum and additional background due to nuclear reactions induced in the sample. These would result in an increased background at the higher energies. On the other hand, a higher peak-to-background ratio is normally achieved in charged-particle analysis through the use of thinner substrates and small area deposits.

Monoenergetic Photon Excitation

The use of photons for fluorescence excitation has the advantage that the radiation is easily available either from radioisotope sources or in conventional X-ray tubes. The fluorescence is induced in the sample by the photoelectric interaction of the incident photons in the inner atomic shells of the elements of interest. An important feature of this interaction is the strong dependence of the cross section on the energy of the incident photon. The maximum value occurs immediately above the binding energy of a particular shell and decreases approximately as E^{-3} as the photon energy is increased. Optimum sensitivity for a given element is therefore achieved using incident energies near the absorption limit.

The background in the spectrum is the result of the elastic and inelastic scattering of the incident radiation in the sample substrate. Elastic scattering results in a change in direction of the scattering photons with no loss in energy. Inelastic scattering causes a loss in energy governed by the kinematic relationship expressed in the Compton equation. For typical X-ray photons, this loss in energy is a few hundred eV or less for each scattering collision.

The simplest case to calculate is monoenergetic photon excitation. This idealized concept is normally approximated in practice by using the characteristic X rays of a particular element as the exciting source. These can be generated either by the direct output from an X-ray source or by a secondary target which is fluoresced by a primary radiation source.

The advantage of monoenergetic or discrete energy photon sources is their ability to optimally excite elements whose absorption edge is slightly lower in energy. Fluorescent peak-to-background ratios can be maximized by confining the scattering of the incident X-ray lines to an energy region of the spectrum where no fluorescent X ray of interest are expected. The disadvantage of the technique results from the loss of sensitivity for those elements whose absorption edges are at a much lower energy. In order to measure these elements efficiently a second fluorescent energy is normally used.

According to the simplified model used in these calculations the spectrum should consist of an elastic scatter peak at the energy of the exciting radiation, an elastic scattering peak at a slightly lower energy, and the fluorescent X rays at their appropriate energies. The area of the scattered peaks is proportional to the appropriate cross section for interaction in the substrate as obtained from the literature.[15] The fluorescent X-ray lines are proportional to the photoelectric cross section in the deposited layers.

Figure 4 shows a calculated spectrum for the case of 17 keV monoenergetic photons incident on the test sample. The dashed line below the inelastic peak represents the background as calculated assuming the simplified model discussed above. The lack of background at lower energies is clearly unrealistic in view of the experimental results. Observed spectra shows a continuous distribution whose intensity is proportional to the high-energy scatter peaks.

Assuming that appropriate measures such as collimation or guard-ring rejection have been used to reduce detector background to a minimum,[9] then it is difficult to attribute the continuous background to any obvious physical processes. Earlier published calculations have estimated the background contributions due to photoelectron induced Bremsstrahlung in the sample and resulting from escape of energetic electrons and their associated Bremsstrahlung from the detector.[16] These effects failed to account for the total observed background.

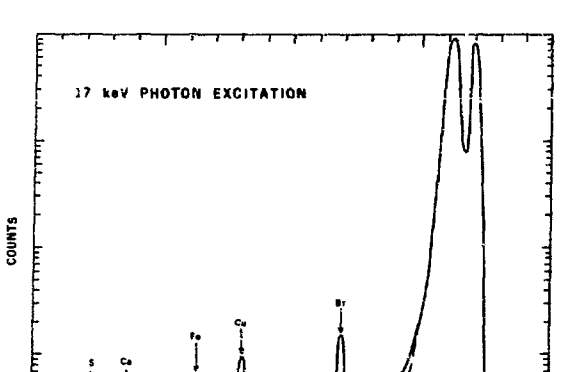

Fig. 4. Calculated spectrum assuming 17 keV photon excitation. The continuous background is based upon a fraction of the total continuous background to scatter peak equal to 2%.

In order to obtain a realistic value for spectral background to use in the calculation, an empirical value for the background level was chosen based on measurements of a low-background guard-ring rejection detector. In the calculated spectrum of Fig. 4 it is assumed that 2% of the scattered intensity is uniformly distributed over the energy range from 0 to 15 keV.

Since the detection sensitivity for the very light elements is greatly reduced due to the energy dependence of the photoelectric cross section, a second measurement is typically performed. Figure 5 shows the calculated spectrums for 4.5 keV photon excitation. It is assumed that 4% of the total scattered intensity is distributed uniformly over the spectrum and that the low-energy X rays are attenuated by a 25 μm Be window. The greatly enhanced sensitivity for Al and S is apparent.

Continuous Photon Excitation

A method for reducing the effects due to the energy dependence of the photoelectric yield is to employ a continuous photon distribution for fluorescence excitation. A continuous distribution guarantees that there will be a portion of the exciting radiation in the energy region most favorable for efficient X-ray production. On the other hand there will also be a portion of the radiation which can be scattered into the region of the spectrum where the fluorescent X rays are to be measured. The net effect is a slower variation of sensitivity with atomic number but with some loss in detectability relative to monoenergetic excitation.

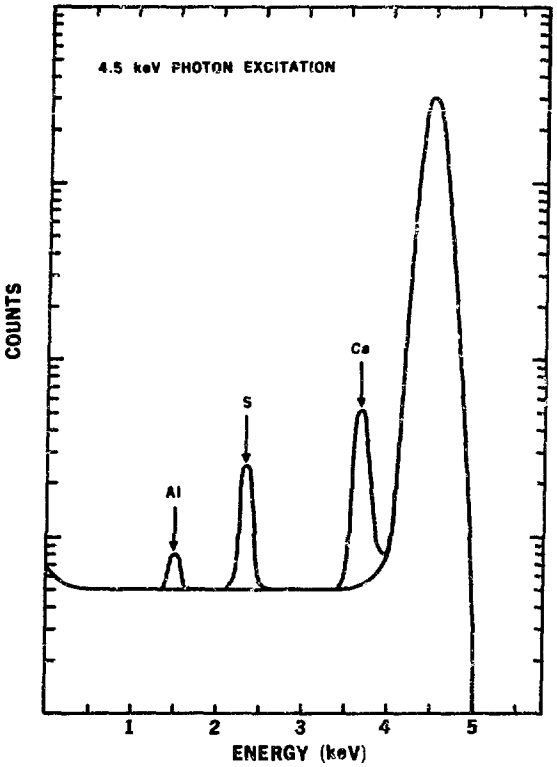

Fig. 5. Calculated spectrum assuming 4.5 keV photon excitation. The background-to-peak ratio is assumed to be 4%.

The present calculations assume a flat energy distribution of incident radiation. The fluorescence intensity is obtained by integrating the photoelectric cross section over this distribution in the region above the K absorption edges of the elements. Two separate cases of background are calculated. A pessimistic estimate is calculated assuming that coherent and incoherent scattering contribute equally to the continuous background. Since at low energies the forward peaked elastic scattering constitutes the major portion of the cross section, it is reasonable to assume that a reasonably designed geometry could reduce this component. A lower limit for the scattered background is calculated assuming that only the incoherent process is present. The actual background would lie somewhere between these two extremes.

Figure 6 shows the calculated spectral responses. A 25 μm Be window is assumed. As expected the peak to background varies more slowly with energy than with discrete excitation. The low-energy background is shown to approach zero at very low energies although in a more realistic calculation the effect of the continuous background due to the detection of high energy events should be included.

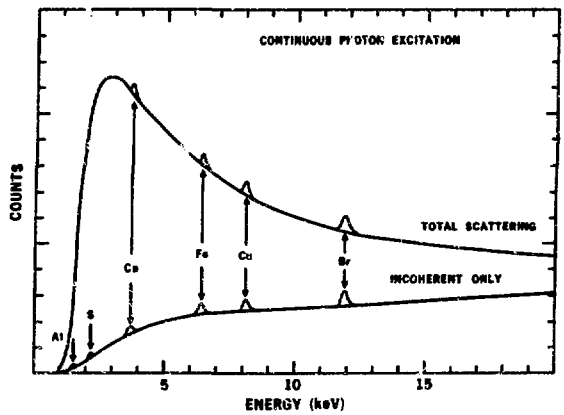

Fig. 6. Calculated spectra assuming a continuous flat photon distribution. The two background spectra represent possible extreme values. More accurate calculations would lie somewhere between these.

COMPARISON OF RESULTS

In order to summarize quantitatively the results of the calculations, the detectable limits for each of the methods have been derived from the model. This limit assumes a value of 3σ where σ is the root mean square deviation equal to the square root of the background under the peak. The comparison is normalized to a total counting rate of 10^4 counts/second for each method consistent with a maximum counting rate limit determined by the pulse processing electronics. The total analysis time is 300 seconds for each.

These conditions are appropriate for high intensity sources such as accelerators or X-ray tubes. The results will probably require scaling to lower counting rates and longer intervals if radioisotope sources are used.

Table 1 is a summary of calculated detectabilities for each of the methods considered. The results appear to agree reasonably well with the trends observed experimentally and in some instances the agreement is better than might be expected on the basis of the simplified calculations. It should be emphasized that these results represent optimistic approximations of what might be achieved under idealized conditions.

The values for Al and S quoted for the 3 MeV protons were calculated assuming a much thinner window (0.025 μm Be) relative to the other elements in the column. A thinner window has the effect of improving the detectabilities for low atomic number elements at the expense of the heavier element values. This follows from the assumption that the counting rate is limited to 10^4 counts/second. Since the low-energy background is such a dominant feature of the spectrum, a large counting rate in this region reduces the relative counting rate at the higher energies. Thus, the absorption of the lower energy portion of the spectrum plays an important role in determining the sensitivity of charged particles.

In the case of photon excitation, the monoenergetic source achieves a better sensitivity in cases where the energies are close to optimal. The detectabilities for continuous excitation exhibit a smoother behavior with energy and are comparable to those for monoenergetic excitation for the very light elements.

TABLE 1

CALCULATED DETECTABILITIES[a)]

	PROTONS 3 MeV	PHOTONS 17 keV	PHOTONS 4.5 keV	CONTINUOUS PHOTONS (Total Scatter)	CONTINUOUS PHOTONS (Incoherent Only)	ELECTRONS 40 keV
Al	.018[b)]		.162	.277	.048	.342
S	.046[b)]	.178	.034	.116	.017	.196
Ca	.018	.062	.010	.068	.015	.164
Fe	.0058	.014		.036	.011	.160
Cu	.0028	.0076		.028	.010	.195
Br	.014	.0038		.021	.009	.277

a) Expressed as $\mu g/cm^2$ referred to a 25 mg/cm^2 substrate. Results are based upon simplified theoretical models described in the text assuming 10^4 cts/sec and 300 sec intervals.

b) Results for Al and S were calculated assuming a 25 μm Be window. The remaining elements were calculated assuming 375 μm Be.

Although one is tempted to pursue these comparisons into greater detail, it is probably best to limit the discussion to these few observations in view of the approximate nature of the calculations. However, the calculations do give one the assurance that the models represent a reasonable interpretation of the actual processes involved in each excitation method. In all but the case of monoenergetic excitation, the calculations are based upon fundamental physical interactions inherent in the irradiation process. For monoenergetic excitation, a semiempirical approach was required to quantify the effect of continuous spectral background.

TECHNIQUES FOR IMPROVEMENT

Some improvement in the capabilities of each method relative to the calculated values is possible. The use of thinner substrates and variable attenuation absorbers have already been discussed with reference to charged-particle excitation.

The detectability of photon excited analysis could be improved if the magnitude of the scattered radiation could be reduced. Several authors have attempted to employ linearily polarized photons for excitation in order to take advantage of the minimum scattering in the direction of the polarization.[17-19] Although a relative reduction in background to fluorescence signal has been observed, it has not proved practical to construct high intensity polarized sources by conventional techniques.

All of the methods can profit by the ability to handle higher counting rates in the pulse processing system. The technique of pulsed excitation has been employed successfully in each case with the accompanying increase in output counting rate.[20-22] The method of pulsed excitation also has a number of secondary advantages such as the reduced target heating which benefits charged-particle techniques.

The question of the continuous background induced by the high-energy scattered photons is an important area for improvement in the case of monoenergetic excitation. Insofar as this effect cannot be attributed at present to any fundamental interactions involved in the irradiation and detection processes, it is hoped that future developments might reduce this background contribution considerably.

CONCLUSION

The observed energy dispersive X-ray fluorescence spectra obtained with various forms of fluorescence excitation can be described using simplified physical models. Theoretical and semiempirical calculations based on these models give reasonable agreement with experimental values for sensitivity and detectability.

REFERENCES

1. T. Dzubay, Ed. "X-ray Fluorescence Analysis of Environmental Samples", Ann Arbor Science Publishers, Inc., Ann Arbor, Michigan, to be printed 1976.

2. F. S. Goulding, J. T. Walton and R. H. Pehl, IEEE Trans. Nucl. Sci NS-17, No. 1, 218 (1970).

3. F. S. Goulding, J. M. Jaklevic, B. V. Jarrett and D. A. Landis, Adv. X-ray Anal. 15, 470 (1972).

4. D. A. Landis, F. S. Goulding and R. H. Pehl, IEEE Trans. Nucl. Sci. NS-18, No. 1, 115 (1971).

5. C. A. Zeigler, Ed. "Applications of Low Energy X- and Gamma-Rays", Gordon and Breach Science Publishers, Inc., New York (1971).

6. T. A. Cahill and P. I. Feeney, University of California, Davis report UCD-CNL-169 (1973).

7. R. Akselsson, C. Orsini, P. L. Meinert, T. B. Johansson, R. E. Van Grieken, H. C. Kaufmann, K. R. Chapman, J. W. Nelson and J. W. Winchester, Adv. X-ray Anal. 18, 588 (1975).

8. R. L. Walter, R. D. Willis, W. F. Gutknecht and J. M. Joyce, Anal. Chem. 46, 843 (1974).

9. J. C. Russ, A. O. Sandborg, M. W. Barnhart, C. E. Sonderquist, R. W. Lichtinger and C. J. Walsh, Adv. X-ray Anal. 16, 284 (1973).

10. J. M. Jaklevic, F. S. Goulding, B. V. Jarrett and J. D. Meng, in "Analytical Methods Applied To Air Pollution Measurements", R. K. Stevens and W. F. Herget Eds., Ann Arbor Science Publishers, Chap. 7, 123 (1974).

11. R. D. Giauque, R. B. Garrett, L. Y. Goda, J. M. Jaklevic and D. F. Malone, Adv. X-ray Anal. 19, 305 (1976).

12. M. Green and V. E. Cosslett. Proc. Phys. Soc. (London) 78, 1206 (1961).

13. T. B. Johansson, R. Akselsson and S. A. E. Johansson, Nucl. Instr. and Methods 84, 141 (1970).

14. F. Folkmann, C. Gaarde, T. Huus and K. Kemp, Nucl. Instr. and Methods 116, 487 (1974).

15. W. H. McMaster, N. Kerr Del Grande, J. H. Mallet and J. H. Hubbell, Lawrence Livermore Laboratory report UCRL-50174 (1970).

16. J. M. Jaklevic and F. S. Goulding, Ann. Rev. Nucl. Sci., Vol 23, 45 (1973).

17. T. G. Dzubay, B. V. Jarrett and J. M. Jaklevic, Nucl. Instr. and Methods 115, 297 (1974).

18. L. Kaufman and D. C. Camp, Adv. X-ray Anal. 18, 247 (1975).

19. R. H. Howell, W. L. Pickles and J. L. Cate, Jr., Adv. X-ray Anal. 18, 265 (1975).

20. J. M. Jaklevic, D. A. Landis and F. S. Goulding, Adv. X-ray Anal. 19 253 (1976).

21. H. Thiebeau, J. Stadel, W. Cline and T. A. Cahill, Nucl. Instr. and Methods 111, 615 (1973).

22. P. J. Statham, G. White, J. V. P. Long and K. Kandiah, X-Ray Spec. 3, 153 (1974).

Proceedings, ERDA X-and Gamma-Ray Symp Ann Arbor, MI, May 19-21, 1976 (Conf 760539)

A COMPARISON OF SENSITIVITIES AND DETECTION LIMITS BETWEEN DIRECT EXCITATION AND SECONDARY EXCITATION MODES IN ENERGY DISPERSIVE X-RAY FLUORESCENCE ANALYSIS

Bruce E. Artz and M. A. Short
Engineering and Research Staff - Research
Ford Motor Company
Dearborn, Michigan 48121

Summary

A comparison has been made between the direct tube excitation mode and the secondary target excitation mode using a Kevex 0810 energy dispersive X-ray fluorescence system. Relative sensitivities and detection limits have been determined with two system configurations. The first configuration used a standard, high power, X-ray fluorescence tube to directly excite the specimen. Several X-ray tubes, including chromium, molybdenum, and tungsten, both filtered and not filtered, were employed. The second configuration consisted of using the X-ray tube to excite a secondary target which in turn excited the specimen. Appropriate targets were compared to the direct excitation results. Relative sensitivities and detection limits have been determined for K-series lines for elements from magnesium to barium contained in a low atomic number matrix and in a high atomic number matrix.

Introduction

In conventional, wavelength dispersive, X-ray fluorescence analysis the source of primary excitation can be changed only by changing the X-ray tube and a selection of tubes including chromium, molybdenum, rhodium, tungsten, and gold is usually available. In some X-ray fluorescence spectrometers, the intensity-energy distribution of the primary radiation can be modified by inserting a filter between the tube and sample. The advent of energy dispersive spectrometry has been accompanied by a proliferation of X-ray sources used to excite a sample. In addition to the use of X-ray tubes, with and without filters, there are also transmission target tubes, pulsed output tubes, and secondary target sources in which an X-ray tube excites a secondary target and this in turn excites the sample. Additional filters may be placed between the tube and secondary target and/or between the secondary target and sample. A suitable radioactive isotope can also be used as a source of X-rays either directly or in a secondary excitation mode. With the availability of such a wide choice of X-ray sources it is necessary to study the relative efficiencies of the different sources so that an optimum or near optimum selection can be made for use in an analysis. The present study is concerned with a comparison of sensitivities and detection limits for elements in light and heavy materials in direct excitation and secondary excitation modes in energy dispersive fluorescence analysis. A Kevex 0810 excitation system, with Siemens X-ray tubes, an 80 sq. mm Kevex Si(Li) detector, collimated to 3 sq. mm with a resolution of 175 eV, and amplifier (with Lowes' live time correction), and a Tracor Northern NS 880 analyzer were used. The study encompasses chromium, molybdenum, and tungsten X-ray tubes, and titanium, copper, yttrium, zirconium, tin, and gadolinium secondary targets.

Sensitivities and Detection Limits

In X-ray fluorescence analysis, as in any form of chemical analysis, it is desirable to obtain the best precision within the available time. When analyses for trace elements are being considered, the lowest amount detectable should be known. Detection limits, precision, and time of analysis are all related and it is often possible to adjust the configuration of the X-ray equipment to optimize the results. The precision of a result is usually increased by increasing the counting time and by obtaining the highest system sensitivity for the measurement. The system sensitivity is defined here as the measured intensity (peak minus background) per unit concentration, for example, counts per second per weight percent. On the other hand, when trace elements are analyzed the system may be configured to produce the minimum detection limit. The detection limit is influenced by the sensitivity, the background intensity and the counting time. The detection limit is defined here as that concentration which gives a measured signal that is three times the standard deviation of the background. This relationship is given in Equation 1:

$$\text{Detection limit} = \frac{3 \times \sqrt{\text{background count rate} \times \text{time}}}{\text{sensitivity} \times \text{time}} \qquad (1)$$

From Equation 1 it is evident that the detection limit can be minimized by any of three factors: increasing the time, increasing the sensitivity, and decreasing the background.

Consider the effect of time in general on the determination of both precision and detection limit. When solid state detectors are used, the processing of

TABLE I Source Configurations

Excitation Mode	X-Ray Tube (Wattage)		
	Cr (2400)	Mo (2800)	W (2800)
1. Direct	Cr	Mo	W
2. Direct/Filter	Cr/0.02 mm Cr	Mo/0.025 mm Mo	W/0.025 mm W
3. Direct/Filter	Cr/0.025 mm VO_2	Mo/0.05 mm Mo	-
4. Secondary Target	Ti	Ti	Ti
5. Secondary/Filter	Cu/0.04 mm Cu	Cu/0.04 mm Cu	Cu/0.04 mm Cu
6. Secondary/Filter	Zr/0.05 mm Zr	Y/0.05 mm Zr	Zr/0.05 mm Zr
7. Secondary Filter	Graphite	Graphite	Graphite
8. Secondary/Filter	Graphite/0.025 mm VO_2	Graphite/0.05 mm Mo	Graphite/0.025 mm W
9. Secondary/Filter	Sn/0.05 mm Sn	Sn/0.05 mm Sn	Sn/0.05 mm Sn
10. Secondary/Filter	Gd/1 mm Al	Gd/1 mm Al	Gd/1 mm Al

the pulses within the amplifier, ADC, and MCA results in an increasing system dead time as the input counting rate increases. This dead time must be considered when computing the total analysis time, which is equal to the live time plus dead time. To process the most counts in a given analysis time, a system is usually adjusted to between 50% and 70% dead time. For the system used in this study, the input count rate of about 8000 cps gave the largest number of counts per second of analysis time. A live time of 100 seconds took about five minutes of analysis time. Adjusting the count rate as described gives the best sensitivity value for any particular X-ray source configuration.

Procedure

To investigate the various X-ray source configurations, two series of samples were produced. One series consisted of low levels (less than 2 weight percent) of elements from magnesium to barium in a light element matrix (lithium tetraborate). Samples were prepared from finely ground powders mixed into the lithium tetraborate with the addition of 10% resin. Pellets were pressed at about 20,000 psi and then placed in an oven for 20 minutes at 140°C. A second set of samples was prepared using a heavy element matrix (tungstic acid). This set of samples included 10% of Somar Mix as a binder and was pressed at 50,000 psi. No heating was necessary. In order to minimize errors in sample preparation each element was used at different levels in at least two samples. Where possible these samples were prepared from different compounds. Each sample was mixed in a mixer mill for 20 minutes and two pellets were made to check for homogeneity. Interelement effects were considered negligible since the total weight of non-matrix elements was kept to less than five weight percent. In addition to these samples, several standards on Whatman 541 filter paper were purchased from Columbia Scientific.

The source configurations used in this study are given in Table I and data were collected from the prepared samples for all of these configurations. The X-ray tube voltage was maintained at 55 kV and the tube current was adjusted to give ≈ 8000 cps from the pure matrix material for each configuration. Several configurations (Gd secondary target for light and heavy matricies, and all secondary targets for filter papers) would not five 8000 cps and for these cases the X-ray tube was run at close to the maximum power.

The net integrated counts for kα (kα plus kβ for light elements) were used. The integration limits were set to include the entire peak using an algorithm that adjusted the integration width to three times the full width at half maximum for elements above titanium and to six times the full width for elements below titanium. All data were collected for 100 seconds live time and all detection limits are given for 100 seconds live time.

Results

Consider first the effect of filtering the source radiation. Figures 1 and 2 show how the sensitivities and detection limits are affected by filtering. These results are for a molybdenum target X-ray tube in the direct excitation mode. The effect of filtering is beneficial, giving higher sensitivities and lower detection limits for most elements except those with low atomic numbers. This effect was seen independent of X-ray tube, secondary target, or matrix. The effect of filtering becomes more pronounced as the atomic number of the exciting source increases.

Figures 3 and 4 show the results for different X-ray tubes being used for direct excitation of elements in a light matrix. Examination of Figure 3 shows that the chromium X-ray tube gives a much greater sensitivity for light elements than the others while keeping a low background. This is the ideal case and results in a vastly superior detection limit for light elements. For heavier elements, the molybdenum and tungsten tubes prove superior with the tungsten tube being best for elements from strontium to barium. As with any form of excitation, a major problem is encountered in the energy region near the characteristic lines of the X-ray source. In direct excitation the tube must be filtered to eliminate the characteristic lines when measuring a line in these regions. This filtering results in greatly decreased sensitivity and increased detection limits in this region. It is important to consider these regions when choosing an X-ray tube for direct excitation.

The problem of characteristic lines can be somewhat alleviated by using a secondary target system that has selectable secondary targets. This allows the operator to choose the secondary target that provides the most information in the range of interest. In addition, the entire energy range from 0 to 40 keV can be covered quite well by as few as three secondary targets. Figures 5 and 6 show the sensitivities, backgrounds, and detection limits for titanium, tin, and gadolinium secondary targets being excited by chromium, molybdenum, and tungsten tubes for elements in a light element matrix. The choice of which X-ray tube to use depends on the energy-range of interest but the superiority of the chromium X-ray tube and titanium secondary target combination for light elements usually offsets the relatively smaller losses at higher atomic numbers. It is of interest to note that the result for the intermediate atomic number targets such as zirconium and tin are affected little by the choice of the X-ray tube. The largest effect is seen when the characteristic line of the X-ray tube is very efficient at exciting the secondary target. Examples of this are chromium tube/titanium secondary target and molybdenum tube/yttrium secondary target. For higher atomic numbers in the range 50-60, continuum radiation becomes dominant in the excitation of a high atomic number target such as gadolinium and consequently the tungsten tube proves superior in this range.

Figure 7 compares the detection limits for the secondary target system and direct excitation for elements in a light element matrix. As can be seen, the secondary target system is superior in all cases except very high energies. This superiority is most significant with the chromium target X-ray tube and in general the secondary target system gives higher sensitivities and lower detection limits. This generality seems to hold providing the secondary target system can produce the optimal 8000 cps at the detector. The failure of the gadolinium target to surpass the direct excited mode is primarily because this target produced significantly less than 8000 cps. This effect is also significant when comparing detection limits and sensitivities on Whatman 541 filter papers. The direct excitation mode gave much higher sensitivities as well as higher backgrounds and gave detection limits comparable to secondary targets. With the present 2 mm collimator, the secondary targets did not produce 8000 cps when filter papers were used. It is expected that there may be a better system arrangement when measuring filter papers and further work is being done.

Matrix effects can be seen in Figure 8 where detection limits in light and heavy element matricies are compared. The increase in detection limit is caused primarily by absorption in the matrix and the

fact that the characteristic lines from the matrix form a large fraction of the measured intensity. Table II summarizes the effects seen.

TABLE II

Summary of Configurations That Give High Sensitivities and Low Detection Limits

Light Element Matrix

Atomic Number		
<	20	Cr-Ti (Secondary)
	21-46	W-Secondary Targets
	46-60	W-Direct/Filter

Heavy Element Matrix

Atomic Number		
	35-60	W-Direct/Filtered

Whatman 541

Atomic Number		
<	20	Cr-Ti (Secondary) or Cr Direct
	21-35	W-Secondary Targets
	35-60	W-Direct/Filtered

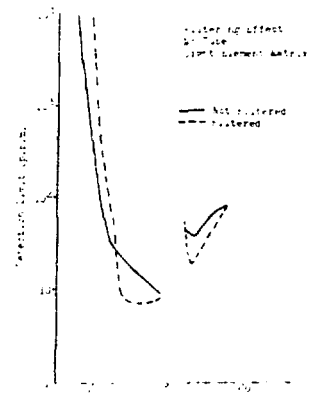

Figure 2. Effect of filtering on detection limit. 55 kV, 8000 cps input, 100 seconds live time.

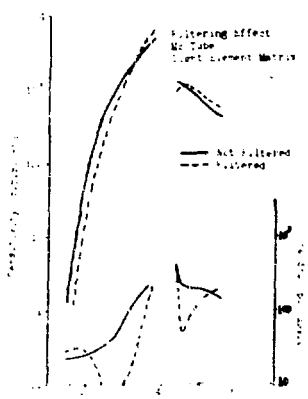

Figure 1. Effect of filtering on sensitivity and background using a Mo X-ray tube with and without a 0.05 mm Mo filter. Data collected for elements in lithium tetraborate matrix at 55 kV with tube current adjusted as described in text.

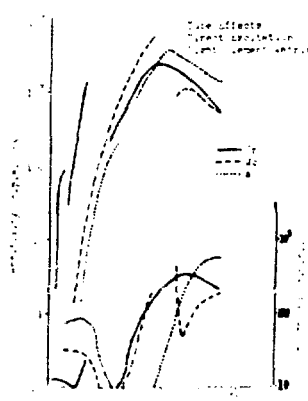

Figure 3. Sensitivities and backgrounds in light element matrix using Cr, Mo, and W target tubes. 55 kV, 8000 cps input.

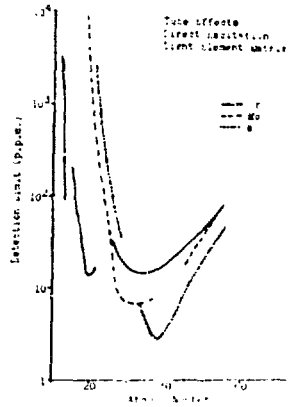

Figure 4. Detection limits in light element matrix for Cr, Mo, and W target X-ray tubes in direct excitation. 55 kV, 8000 cps input, 100 seconds live time.

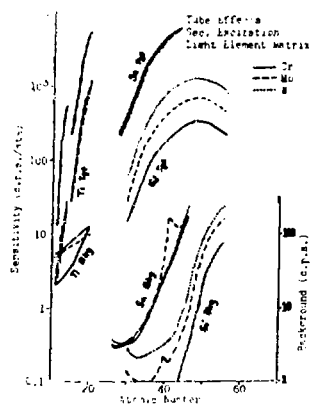

Figure 5. Sensitivities and backgrounds for Ti, Sn, and Gd secondary targets using Cr, Mo, and W X-ray tubes. 55 kV, 8000 cps input.

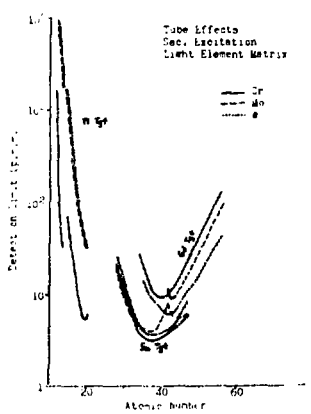

Figure 6. Detection limits for Ti, Sn, and Gd secondary targets using Cr, Mo, and W X-ray tubes. 55 kV, 8000 cps input, 100 seconds live time.

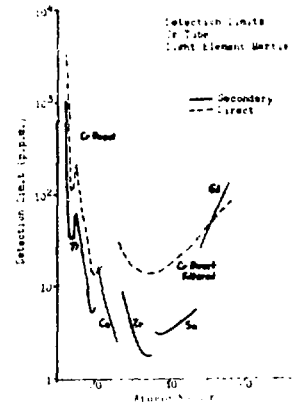

Figure 7. Comparison of detection limits for direct excitation and secondary target excitation. 55 kV, 8000 cps input, 100 seconds live time.

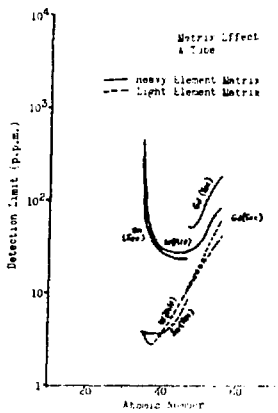

Figure 8. Comparison of detection limits in lithium tetraborate and tungstic acid. 55 kV, 8000 cps input, and 100 seconds live time.

Proceedings, ERDA X-and Gamma Ray Symp. Ann Arbor, MI, May 19-21, 1976 (Conf 760539)

SYNCHROTRON RADIATION: PROPERTIES, SOURCES AND RESEARCH APPLICATIONS

I. Lindau and H. Winick
Stanford Synchrotron Radiation Project
Stanford University
Stanford, CA 94305

The development of modern electron storage rings for high energy physics research has provided other disciplines within physics, chemistry and biology with a new unique radiation source, namely synchrotron radiation. In this paper we describe the general properties of synchrotron radiation and its characteristic features as an X-ray source. The Stanford Synchrotron Radiation Project (SSRP) was established as a national facility for synchrotron radiation research in 1973 and will be described in some detail. Finally we will give a short summary of the scientific research program at SSRP, demonstrating the capability of synchrotron radiation as compared to standard X-ray sources.

Properties of Synchrotron Radiation

From elementary physics it is well-known that an accelerating dipole emits electromagnetic radiation with a radiation pattern of sine-squared angular distribution. For relativistic particles this radiation pattern is changed drastically to be confined to the forward direction of the dipole's motion and also given other unique properties. During recent years high-energy physics research has developed storage rings,[1] where electrons (and positrons) travel in circular motion with velocities very close to that of light and with several giga electron volt (GeV) energy. These new machines are the basis for the exploitation of the radiation (synchrotron radiation) from these relativistic electrons as a new X-ray and ultraviolet source. The theory of synchrotron radiation is now well developed and goes back to the pioneering work by Schwinger,[2] who devised the equations for both the wavelength and angular distribution of the radiation. Before giving a short description of salient features in Schwinger's[2] equations it may be appropriate to present a summary of the most important properties of synchrotron radiation: a) an intense, continuous spectral distribution from infrared to X-ray wavelengths; b) highly collimated radiation confined near the orbital plane of the circulating electrons; c) highly polarized radiation with the electric field vector in the orbital plane; d) the absolute intensity and spectral distribution can be accurately calculated from well-defined parameters; e) a pulsed light-source with time structure on the nanosecond scale; f) a stable, low-noise source operating in ultrahigh vacuum environment. There are several comprehensive review articles describing the properties of synchrotron radiation and its research applications within different fields.[3-13]

Following closely the treatment by Schwinger[2] and Godwin[12] the instantaneous power radiation from a monoenergetic electron in circular motion is given by:

$$I(\psi,\lambda) \sim \frac{R}{\lambda_4}\left(\frac{m_0c^2}{E}\right)^4 (1+X^2)^2 \times \left(K^2_{2/3}(\xi) + \frac{X^2}{1+X^2} K^2_{1/3}(\xi)\right), \qquad (1)$$

with

$$X = (E/m_0c^2)\psi$$

and

$$\xi = (2\pi R/3\lambda)(m_0c^2/E)(1 + X^2)^{3/2},$$

where ψ is the azimuthal angle of observation and is defined as the angle between the line of observation and its projection on the orbital plane; λ is the wavelength; E is the electron energy; R is the orbital radius; and $K_{1/3}$, $K_{2/3}$ are modified Bessel functions of the second kind. Equation (1) is the basis for the description of synchrotron radiation and from it all the properties a) - f) listed above can be deduced.

By integrating the above equation over all angles ψ we can obtain the total instantaneous power as a function of wavelength:

$$I(\lambda) \sim (E^7/R^3)\ G(y) \qquad (2)$$

where

$$G(y) = y^3 \int_0^\infty K_{5/3}(\eta)d\eta$$

with

$$y = (4\pi R/3\lambda)(m_0c^2/E)^3 = \lambda_c/\lambda$$

and

$$\lambda_c = (4\pi R/3)(m_0c^2/E)^3 \sim R/E^3 \qquad (3)$$

is the critical wavelength. The critical wavelength is proportional to the orbital radius and inversely proportional to the cube of the electron energy, clearly showing the high electron energies push the radiation maxima towards harder X-rays. G(y) is a universal spectral distribution function similar in shape to the blackbody radiation curve with a long tail extending to long wavelengths and a sharp cutoff at short wavlengths.

By performing one further integration the total power into all angles and wavelengths can be determined:

$$I \sim E^4/R^2$$

and hence the energy radiation per revolution is $\sim E^4/R$. The energy losses due to synchrotron radiation is thus a strong function of electron energy and, in fact, is a severe limitation in design of high-energy storage rings and synchrotrons for electrons.

The synchrotron light is elliptically polarized and the intensities of the two polarization components, parallel and perpendicular to the electron orbit, are given by the two terms in Eq. (1). It appears that the synchrotron light is completely polarized in the plane of the electron orbit. Integration of the two components (see Eq. 1) over all angles and all wavelengths gives 75% degree of polarization, independent of orbital radius R and electron energy E. Furthermore, the polarization remains high at all wavelengths since the intensity of radiation emitted into a certain angle falls off about as fast as the polarization does for increasing angle ψ. The degree of collimation of the synchrotron radiation can be estimated (valid near the peak of the synchrotron spectrum) from m_0c^2/E, showing the importance of high electron beam energies for good collimation. Other properties of synchrotron radiation, more specifically connected to the Stanford Synchrotron Radiation Project, will be discussed in a following section.

The discussion above has been carried out for one electron with constant orbital velocity. In reality the situation is more complicated due to synchrotron and betatron oscillations of the electron beam and other beam dynamical effects.[1] Despite this, it can be stated the the properties of synchrotron radiation are

well understood from the expressions discussed above or from a further elaboration of these equations.

Synchrotron Radiation Facilities

Historically research using synchrotron radiation began with the work of Tomboulian[8] and others at the 300 MeV Cornell synchrotron in 1955 and was continued by a team at the National Bureau of Standards 180 MeV synchrotron.[9] Internationally the most extensive synchrotron radiation research work was started by Haensel and co-workers[10] at DESY in Hamburg, Germany, as a secondary operation on a high energy physics machine. For the moment synchrotron radiation research is going on at a large number of laboratories all over the world. A summary of existing facilities is given in the paper by Winick.[14] In the following we will concentrate our discussion on the Stanford Synchrotron Radiation Project (SSRP), which now is used extensively for X-ray and UV research.

The Stanford Synchrotron Radiation Project (SSRP)

The Stanford Synchrotron Radiation Project (SSRP)[15-18] was funded in June 1973 by the National Science Foundation as a national facility for UV and X-ray research using synchrotron radiation from the storage ring SPEAR at the Stanford Linear Accelerator Center. SSRP started operation in May 1974 and is open to all qualified users. SPEAR[19,20] operates normally in the electron-positron colliding-beam mode with stored beam energy E varying from 1.5 to 4.0 GeV and with up to 35 mA in each beam (May 1976). In operation as a single-beam synchrotron radiation source much higher currents can be obtained. Thus for 225 mA has been accumulated[22] and more is clearly possible. It typically takes 15-30 min to fill SPEAR with electron and positron beams, after which the beams are stored and made to collide for several hours, the lifetime being 3-5 hrs. Extended periods of time are thus available for synchrotron radiation experiments even when SSRP is operating in a symbiotic mode on the high energy physics program. Looking into the future conceptual designs have been developed to use SPEAR exclusively for synchrotron radiation research,[21] in which case considerable more synchrotron radiation can be produced in a single-beam mode of operation.

So far SSRP has been operating around a single beam port on the SPEAR vacuum system accepting 11.5 mrad of synchrotron radiation in the horizontal plane. For the moment (May 1976) a major expansion of the facility is under way at SSRP, including a second tangential beam line accepting 20 mrad of radiation and providing accommodation for at least 4 additional X-ray experiments. The potential exists for future expansion of additional beam lines, each with the same capacity of the second beam line.[21]

SSRP is an experimenter-operated facility designed for maximum access to and utilization of the radiation within the limitations set by the radiation shielding and personal protection systems, and the protection of the ultrahigh vacuum system. Shielding and a personnel-protection interlock system are designed to permit close access to experimental equipment during all phases of SPEAR operation (filling, storing, and dumping of beam). The experimental area is divided into so called hutches, one for each experiment. The hutch concept means that each experimenter is permitted access to his experiment by means of his own control and interlock panel without requiring further permission from outside operators and independently of the condition of other synchrotron beam runs or of the SPEAR ring status. The hutch system is interlocked into the SPEAR operation in terms of radiation and vacuum safety.

SPEAR has a radius curvature of 12.7 m. The spectral distribution of synchrotron radiation from SPEAR, given as photons s^{-1} $mrad^{-1}$ mA^{-1} (10% bandwidth)$^{-1}$, is shown in Fig. 1 with the electron-beam energy E as the

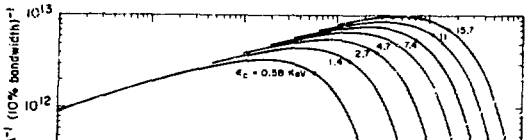

Fig. 1--Spectral distribution of the synchrotron light from the SPEAR storage ring.

parameter from 1.5 - 4.5 GeV. As seen, it is an intense, continuous distribution extending from the ir to the X-ray region. The critical energy E_c related to the critical wavelength described above is also shown for each beam energy. The extreme importance of high electron-beam energies for extending the spectral distribution into the X-ray region is clearly demonstrated by this plot, the critical energy increasing from 0.58 keV (21 Å) at E=1.5 GeV to 11 keV at E=4.0 GeV. The $mrad^{-1}$ refers to the collection angle in the horizontal plane. In the vertical plane the beam is naturally collimated and has a divergence of about ± 0.2 mrad (typical at 2.5 GeV), i.e., the height of the beam 20 m from the source point is about 4 mm. The source size (electron-beam size) is typically 1.6 - mm (FWHM) high and 3.' (FWHM) wide at 2.5 GeV during colliding beam runs. As was discussed in a previous section the synchrotron radiation losses are a strong function of the electron-beam energy. In the case of SPEAR, typical values are 4 kW (2.5 GeV, 15 mA) and 45 kW (4.0 GeV, 25 mA).[16] Normally SPEAR is operating in the single-bunch colliding-beam mode, i.e., there is one bunch of electrons and one of positrons circulating the ring with orbital frequency 1.28 MHz. The SPEAR radiofrequency is 358 MHz, which is thus the 280th harmonic of the orbital frequency. The one-bunch mode of operation offers unique timing capabilities of using the synchrotron light as a pulsed source, since the pulse duration if 0.3-0.4 ns and repeats at 1.28 MHz. It is thus possible to perform experiments requiring fast time correlations.

Orbit monitoring and control are important since a small vertical electron-beam orbit distortion can result in a displacement of several millimeters at the location of the experiment (20 m from the source point) due to the angles associated with orbit motion. Thus it has been found necessary to reproduce the position of the synchrotron radiation source point to ± 0.2 mm. This is accomplished by powering a pair of trim coils, which provide horizontal dipole fields, positioned approximately 180° apart in the phase of the vertical betatron oscillation. Position monitors produce an electrical signal proportional to the vertical beam displacement, and a feedback system on the power supply controlling the beam bump keeps the beam centered automatically, giving the synchrotron

radiation beam an accurate and reproducible position at all times.

An artist's view of the SSRP facility is shown in Fig. 2. The 11.5 mrad of synchrotron radiation, corresponding to 15 cm of curved path in a spear bending

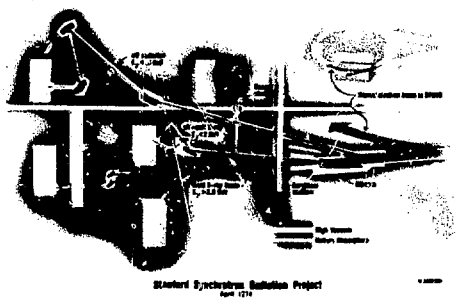

Fig. 2--A schematic drawing of the different beam-lines at the Stanford Synchrotron Radiation Project.

magnet, emerges tangentially into a UHV pipe. Part of the horizontal fan of radiation is split away from the tangential direction by reflection at grazing incidence on two ultrasmooth (rms surface roughness 30-70 Å) Pt-coated Cu mirrors placed 6.5 m from the source point.[23] One of the mirrors intercepts the outer 2 mrad of the radiation fan at 2° horizontal grazing angle of incidence, resulting in a horizontally focussed 4° deflected beam. A plane mirror intercepts the inner 3-5 mrad of the fan at 4° vertical grazing angle of incidence. The mirrors can be remotely inserted and adjusted and are cooled thermoelectrically to enable operation with up to 25 W of synchrotron radiation per mrad. The vacuum system is an all-metal, bakable UHV system. The central beam pipe extends to 10.5 m from the source terminating at the Be window assembly (see above). The 4° and 8° beamlines continue in the vacuum, without any window material, into the experimental areas 16 and 23 m, respectively, from the source point. The different beam lines can be isolated from each other and from SPEAR by gate values. Water-cooled masks define the synchrotron light path through the vacuum system.

The central part of the beam contains 4-10 mrad of radiation (depending on insertion of mirrors) which proceeds down the UHV pipe and passes through a pair of 5-μm-thick water-cooled pyrolitic graphite foils, which absorb the UV and soft X-ray part of the white radiation. The radiation then leaves the vacuum system 10.5 m from the source point through a pair of 250-μm water-cooled beryllium windows. The foil and window system begins to transmit radiation at about 3.5 keV and reaches 50% transmission at 4.5 keV. After emerging from the SPEAR vacuum system the X-rays travel in a helium atmosphere into a shielded area in wich several monochromators are installed.

Scientific Research Program

During the two years SSRP has been in operation a variety of experiments have been performed from photon energies of 5 eV up to 30,000 eV involving research programs in physics, chemistry and biology. About 130 scientists from 30 different experimental groups have participated in the program. Here we can only summarize briefly these different research projects.[24]

We will concentrate on the X-ray research and only mention briefly the activities in the ultraviolet and soft X-ray regions. The 8° beam line[25] is equipped with a Seya-Namioka monochromator[26] which provides monochromatic radiation up to 30 eV. The design of the optical system enhances the degree of polarization to about 98% in the spectral range 6-30 eV. Research programs including scattering,[24] reflectivity,[24] absorption, fluorescence and photoemission[27,28] have been established. The 4° beam line[29] is equipped with a grazing incidence monochromator[30] with fixed entrance and exit slits (modified version of the Vodar-type) and with a resolution of 0.1 Å in the photon energy range 30-600 eV. Research on this beam-line has included soft X-ray absorption[31], reflectance, photoemission[27,28,32-35] and grating calibration as well as time-of-flight spectroscopy[36-37] utilizing the unique time structure of the pulsed synchrotron light.

Several different crystal monochromators are installed on the central beam line for use in the X-ray region: 3-25 keV (4-0.5 Å). A double-crystal monochromator in the non-dispersive mode is installed for X-ray photoelectron spectroscopy measurements[38,39] with high resolution (0.3 eV at 8.0 keV) on the second floor in the building (see Fig. 2). It has also been used for small-angle scattering of X-rays to determine the morphology of macromolecules in solution.[24]

A tunable focusing X-ray monochromator has been made operational at SSRP since May 1975.[40] The focusing geometry is shown in Fig. 3. Both the elliptically

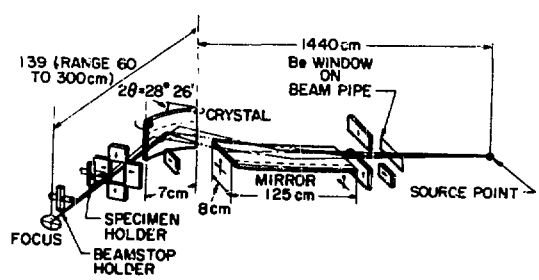

Fig. 3--Schematic of the tunable, focusing X-ray monochromator (from ref. 41).

curved glass mirror and the logarithmically spiraled silicon crystal provide variable focus and monochromatization from 0.5 to 3.0 Å.[41-43] It has been applied to low-angle X-ray diffraction studies of biological structure problems, e.g. frog sciatic nerve myelin, retinal tissue and muscle.[24] The same experimental set-up has also been used for protein crystallography studies[44] of e.g. rubredoxin, azurin, nerve growth factor and L-glutaminase-asparaginese.

The third X-ray monochromator[45] (shown to the right in Fig. 2) consists of a channel-cut Si (220) single crystal, which provides monochromatic radiation of a bandwidth of approximately 1 eV over the photon energy range 5-25 keV.[46-49] This monochromator has been used extensively by several groups[24] for X-ray absorption studies and also for resonant Raman

scattering[50,51] and fluorescence experiments. The technique known as Extended X-ray Absorption Fine Structure (EXAFS[52]) has been developed extensively at SSRP with this instrument and has been applied to a large category of samples: gases,[46,47] liquids,[53] crystals,[48] glasses,[24] catalysts,[24] enzymes and proteins.[54-55] The power of the EXAFS technique lies in its ability to determine the local atomic environment. Spectra of this type can be obtained 10^4-10^5 faster than with a standard X-ray source.

REFERENCES

*Work supported by the NSF (DMR 73-07692 A02) in cooperation with the Stanford Linear Accelerator Center and the Energy Research and Development Administration.

1. C. Pellegrini, Annual Review of Nuclear Science (ed. E. Segre'), Vol. 22, p. 1 (1972).
2. J. Schwinger, Phys. Rev. 75, 1912 (1949).
3. W. Hayes, Contemp. Phys. 13, 441 (1972).
4. K. Codling, Rep. Prog. Phys. 36, 541 (1973).
5. R. E. Watson and M. Perlman, Research Applications of Synchrotron Radiation, (eds.) Brookhaven National Laboratory Report BNL 50381, (unpublished).
6. F. C. Brown, Solid State Phys. 29, 1 (1974).
7. E. E. Koch, R. Haensel, and C. Kunz (eds.) Vacuum Ultraviolet Physics, (Pergamon, NY 1974).
8. D.H. Tomboulian and P.L. Hartman, Phys. Rev. 102, 1423 (1965).
9. R.P. Madden and K. Codling, J. Appl. Phys. 36, 830 (1965).
10. R. Haensel and C. Kunz, Z. Angew. Phys. 23, 276 (1967).
11. A.A. Sokolov and I.M. Ternev, Synchrotron Radiation (Berlin Akademic-Verlag, Berlin, 1968).
12. R.P. Godwin, in Springer Tracts in Modern Physics, Vol. 51 (Springer-Verlag, Berlin and New York, 1968).
13. C. Gahwiller, F. C. Brown, and H. Fujita, Rev. Sci. Instrum. 41, 1275 (1970).
14. H. Winick, in McGraw-Hill Encycl. of Sci. and Tech., 1976.
15. S. Doniach, I. Lindau, W. E. Spicer and H. Winick, J. Vac. Sci. Technol. 12, 1123 (1975).
16. H. Winick, in Proc. IX International Accelerator Conf., SLAC 2-7 May 1974, p. 685. Also, SLAC Pub. -1439 (1974).
17. A.D. Baer, et al., IEEE Trans. Nucl. Sci. NS-22, 1974 (1975).
18. H. Winick, in ref. 7, p. 776.
19. J.M. Paterson, in Proc. IX International Accelerator Conference, SLAC 2-7 May 1974, p. 37 (1974).
20. J.M. Paterson, IEEE Trans. Nucl. Sci. NS-22, 1366 (1975).
21. H. Winick, SSRP Report No. 75/06. Avail. from SSRP on request.
22. G. Fischer, SPEAR Report 192, April 1976 (unpublished).
23. J.L. Stanford, V. Rehn, D.S. Kyser, V.O. Jones, and A. Klugman, in ref. 7, p. 783.
24. A comprehensive listing of all published abstracts and papers based on research at SSRP can be found in SSRP Report No. 75/01 and 75/05 (avail. from SSRP on request)
25. In addition to NSF funding this beam was implemented by financial support from the Office of Naval Research through Michelson Laboratory, China Lake.
26. V. Rehn, A.D. Baer, J. L. Stanford, D. S. Kyser and V.O. Jones, in ref. 7, p. 780.
27. I. Lindau, P. Pianetta, K. Y. Yu and W. E. Spicer, J. Vac. Sci. Technol. 13, 269 (1976).
28. W.E. Spicer, I. Lindau, P. E. Gregory, C. M. Garner, P. Pianetta and P. W. Chye, J. Vac. Sci. Technol. 13, xxx (1976).
29. In addition to NSF funding, this beam line was implemented by financial support from Xerox Corp.
30. F.C. Brown, R.Z. Bachrach, S.B.M. Hagstrom, N. Lien, and C.H. Pruett, in ref. 7, p. 785.
31. F.C. Brown, R.Z. Bachrach, and M. Skibowski, Phys. Rev. B 13, 2633 (1976).
32. I. Lindau, P. Pianetta, K. Y. Yu and W. E. Spicer, Phys. Lett. 54A, 47 (1975).
33. I. Lindau, P. Pianetta, K. Y. Yu and W. E. Spicer, Phys. Rev. B 13, 492 (1976).
34. P. Pianetta, I. Lindau, C. M. Garner and W. E. Spicer, Phys. Rev. Letters 35, 1356 (1975).
35. I. Lindau, P. Pianetta, K.Y. Yu and W.E. Spicer, J. Electron Spectrosc. 8, xxx (1976).
36. R. Z. Bachrach, S. B. M. Hagstrom, and F.C. Brown, in ref. 7, p. 795.
37. R. Z. Bachrach, F.C. Brown, and S.B.M. Hagstrom, J. Vac. Sci. Technol. 12, 309 (1975).
38. I. Lindau, P. Pianetta, S. Doniach, and W.E. Spicer, Nature 250, 214 (1974).
39. I. Lindau, P. Pianetta, S. Doniach, and W.E. Spicer, in ref. 7, p. 805.
40. In addition to NSF funding this beam line was implemented by financial support from California Institute of Technology.
41. N.G. Webb, S. Samson, R.M. Stroud, R.C. Gamble and J.D. Baldeschwieler, J. Appl. Cryst. (to be published 1976).
42. N. G. Webb, Rev. Sci. Instr. 47, xxx (1976).
43. N.G. Webb, S. Samson, R.M. Stroud, R.C. Gamble and J.D. Baldeschwieler, Rev. Sci. Instr. 47, xxx (1976).
44. J.C. Phillips, A. Wlodawer, M.M. Yevitz and K.O. Hodgson, Proc. Nat. Acad. Sci. 73, 128 (1976).
45. In addition to NSF funding this beam line was implemented by financial support from Bell Telephone Labs. and Univ. of Washington, Seattle.
46. B.M. Kincaid, Doctoral Thesis, Stanford University May 1975; also SSRP Report No. 75/03.
47. B.M. Kincaid and P. Eisenberger, Phys. Rev. Letters 34, 1361 (1975).
48. B.M. Kincaid, P. Eisenberger and D. Sayers, Phys. Rev. B 13, xxx (1976).
49. P. Eisenberger, B. Kincaid, S. Hunter, D. Sayers, E. A. Stern, and F. Lytle, in ref. 7, p. 801.
50. P. Eisenberger, P.M. Platzman and H. Winick, Phys. Rev. Letters 36, 623 (1976).
51. P. Eisenberger, P.M. Platzmann and H. Winick, Phys. Rev. B 13, 2377 (1976).
52. D.E. Sayers, E.A. Stern, and F.W. Lytle, Phys. Rev. Lett. 27, 1204 (1971).
53. P. Eisenberger, P.M. Platzman and H. Winick, Phys. Rev. B 13, 2377 (1976).
54. B.M. Kincaid, P. Eisenberger, K.O. Hodgson and S. Doniach, Proc. Nat. Acad. Sci. 72, 2340 (1975).
55. R.G. Shulman, P. Eisenberger, W.E. Blumberg and N.A. Stombaugh, Proc. Nat. Acad. Sci. 72, 4003 (1975).

Proceedings, ERDA X-and Gamma-Ray Symp. Ann Arbor, MI, May 19-21, 1976 (Conf 760539)

A HIGH-INTENSITY, SUBKILOVOLT X-RAY CALIBRATION FACILITY*

R. W. Kuckuck, J. L. Gaines, and R. D. Ernst
Lawrence Livermore Laboratory, University of California
Livermore, California, 94550

Summary

A high-intensity subkilovolt x-ray calibration source utilizing proton-induced inner-shell atomic fluorescence of low-Z elements is described. The high photon yields and low brensstrahlung background associated with this phenomenon are ideally suited to provide intense, nearly monoenergetic x-ray beams. The proton accelerator is a 3 mA, 300 kV Cockroft-Walton using a conventional rf hydrogen ion source. Seven remotely-selectable targets capable of heat dissipation of 5 kW/cm^2 are used to provide characteristic x-rays with energies between 100 and 1000 eV. Source strengths are of the order of 10^{13}-10^{14} photons/sec. Methods of reducing spectral contamination due to hydrocarbon build-up on the target is discussed. Typical x-ray spectra (Cu-L, C-K and B-K) are shown.

Introduction

Considerable need has arisen for the development of well-calibrated x-ray detectors capable of detecting photons with energies between 100 and 1000 electron-volts. This energy region is of significant interest since the x-ray emission from high-temperature (kT $\sim$ 0.5 keV), laser produced plasmas is predominantly in this range. For this application interest is mainly on fast, current-mode detectors capable of responding linearly to the intense x-ray bursts produced by these sources. These bursts are characterized by durations of approximately 100 ps and peak photon intensities of $\sim 10^{25}$ photons/ster-sec. Typical detectors used in these measurements include semiconductor detectors, scintillator photodiode detectors and photoelectric diodes.[1] Since these detectors have sensitivities of the order of 10^{-17}-10^{-20} coul/keV, it is clear that, in order to be accurately calibrated in the current mode, intense sources of monoenergetic x-rays must be available.

One obvious source of monoenergetic subkilovolt x-rays is the characteristic line emission from inner-shell atomic fluorescence of low-Z elements. This fluorescence can be induced by various types of exciting radiations, i.e., photons, electrons, or ions. However, the fluorescence yield for low-Z elements is quite low and intense ionization sources are needed to obtain useful x-ray yields. While photon or electron excitation methods are common x-ray generation techniques, both approaches exhibit a serious disadvantage, namely lack of spectral purity due to photon scattering and/or bremsstrahlung continuum backgrounds superimposed on the characteristic line emissions. To avoid this particular difficulty, x-ray production via ion bombardment has become a phenomenon of significant recent interest. The high yields and low bremsstrahlung backgrounds associated with this process are ideally suited to the above detector calibration objectives.

Numerous investigators have reported x-ray yields from charged particle bombardment for many different species of target and projectile ions and over a wide range of incident particle energies.[2] Consequently, much of the physical principles of the excitation and emission processes are well understood. In view of this understanding, and with the above-stated detector-calibration objectives in mind we have developed a calibration facility at LLL utilizing characteristic x-ray production in elemental targets via Coulomb excitation from proton bombardment. While heavier ions may provide greater photon yields for specific cases in which the energy levels of the projectile and target atoms overlap, proton excitation provides a consistently high yield for general excitation of a wide variety of target materials. Also, in considering the dependence of x-ray yield and of secondary electron bremsstrahlung production upon the incident proton energy it appeared practical to base the facility around a low-energy (300 kV) accelerator.

Facility Description

The LLL calibration facility consists of a charged particle accelerator, x-ray target chamber, photon monitoring system, experimental detector chamber and crystal diffractometer (Figure 1). Figure 2 shows a schematic layout of the x-ray generation and detection portion of the system. The accelerator power supply is based on conventional Cockcroft-Walton voltage multiplying principles and was designed and fabricated at LLL.[3] It has an oscillation frequency of 100 kHz and maximum load capability of 5 mA and 300 kV. The voltage is applied across a conventional accelerating column and the proton beam is magnetically analyzed and delivered to the x-ray target through electrostatic quadrupole focusing elements. The accelerating column and beam drift tubes are maintained at a pressure of $\sim 2 \times 10^{-6}$ Torr during full beam loading by two 1500 ℓ/sec oil-diffusion pumps. Vacuum integrity throughout this section is achieved using Viton O-ring seals.

Fig. 1. Photograph of the LLL extreme low-energy x-ray facility. Vacuum chamber in foreground is the x-ray chamber. Accelerator beam tube is seen to the upper left. The two chambers in the upper right are the experimental detector chamber and the crystal diffractometer chamber, respectively.

*Work performed under the auspices of the U.S. Energy Research and Development Administration under contract No. W-7405-Eng-48.

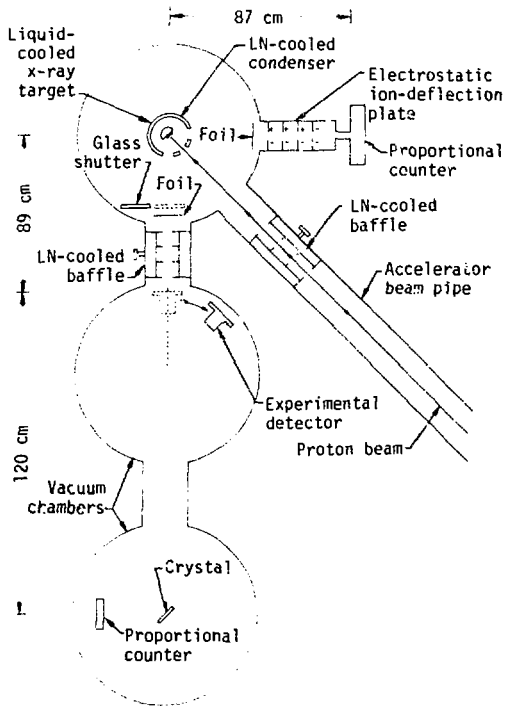

Fig. 2. Schematic illustration of the x-ray production and detection portion of the facility.

The proton beam is provided by a standard rf ionization source and beam currents of ~ 2.5 mA have been delivered on target in a spot size of less than 5 mm diameter. Smaller spot sizes are possible but under such conditions target heat loads are excessive. The accelerator is also capable of accelerating heavier ions or electrons with only minor system modifications.

Three high-vacuum stainless steel experimental chambers are mounted in series at the end of the accelerator drift tube (Figures 1 and 2). These chambers have metal vacuum seals and are evacuated to pressures of 10^{-7}-10^{-8} Torr using 250 ℓ/sec sputter-ion pumps. Isolation of these chambers from the poorer vacuum environment of the accelerator beam tube is achieved by a low-conductance (6 ℓ/s), double-walled, LN-cooled cold trap mounted in the beam pipe at the entrance to the target chamber. This trap is designed to reduce hydrocarbon buildup on the x-ray target which, as will be discussed later, is a serious detriment to spectral purity in subkilovolt x-ray generators.

The x-ray target has two primary features: a) heat dissipation of 5 kW/cm^2, and b) capability of remote selection of one of several different target materials, and hence, characteristic photon energies. Seven target materials (Cu, Fe, Cr, Ti, C, B, Be) are deposited on the flat machined surface of a high-purity Cu cylinder to thicknesses ranging from 3 to 5 mg/cm^2 (Figure 3).

A 50 percent mixture of ethylene glycol and water is flowed through the cylinder past the back of the targets for temperature control. The flow system is designed not only to dissipate up to 5 kW/cm^2 of

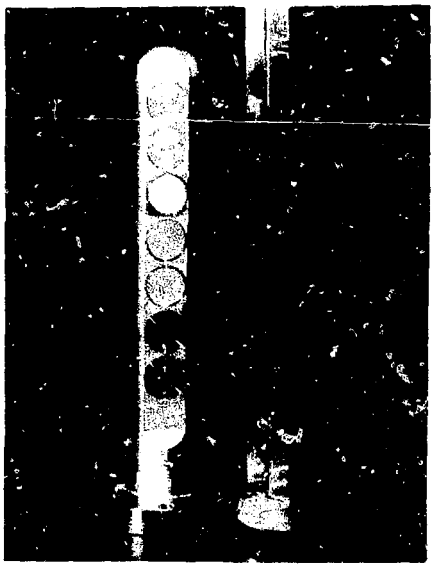

Fig. 3. X-ray targets plated on high-purity Cu cooling probe.

target heat during beam loading conditions but also to maintain the target temperature at 115° C during beam-off conditions. The latter is achieved by heating the liquid and is an attempt to further reduce condensation of hydrocarbon contaminants on the target face. The liquid is flowed at 6 ℓ/min, through a closed-loop pump and heat exchanger system and is nozzled to pass the back of the targets with a turbulent velocity of 7.5 m/sec.

As a final step in minimizing carbon buildup a double-walled, LN-filled cylinder is mounted around the targets to serve as a hydrocarbon condenser. The target and condenser are electrically isolated to permit beam current measurements and to allow bias voltage suppression of secondary electron emission from the target. The target assembly is vertically driven by a remotely-controlled stepping motor and will automatically position any pre-selected target in the proton beam. Figures 4 and 5 show the target assembly mounted to the chamber lid.

The target chamber geometry is designed to allow continuous monitoring of the x-ray flux with a proportional counter during calibration of an experimental detector. Both the experimental detector and the proportional counter monitor are mounted symmetrically at an angle of 135° with respect to the incident proton beam direction (Figure 2). The x-ray emission is found to be isotropic only for very smooth targets (polished so that average peak-to-valley surface roughness is less than 0.05 μm). Targets with rougher surfaces, e.g., 8 μm, exhibit highly nonisotropic emission and preclude use of the monitor detector output to derive the flux level incident on the experimental detector. Consequently, since target surface damage and roughness can readily occur at high current loads, it is necessary to frequently recheck isotropy using a second proportional counter in place of the experimental detector.

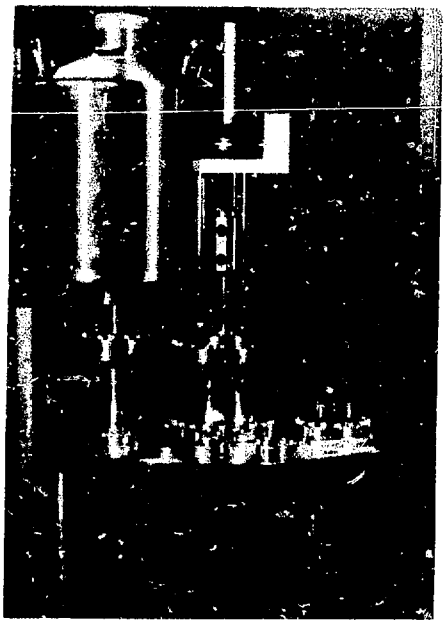

Fig. 4. Photograph of remotely switchable target assembly mounted on vacuum chamber lid.

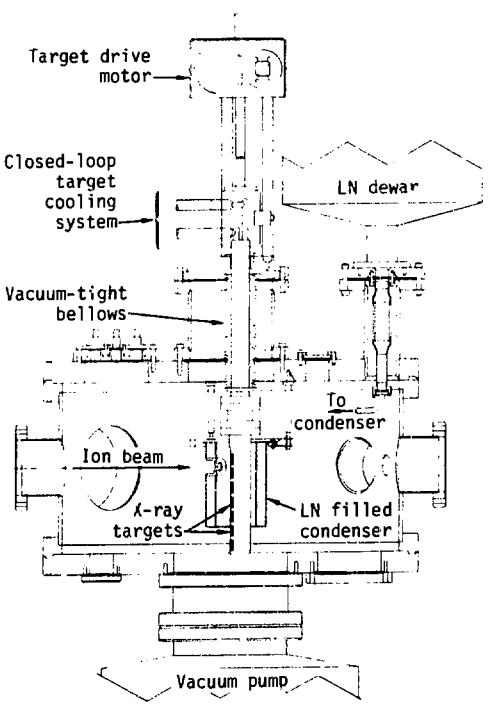

Fig. 5. Schematic illustration of remotely switchable target assembly mounted on vacuum chamber lid.

The proportional counters are side-window, cylindrical, gas-flow counters with 2.5 cm inside diameters, 0.25 μm diameter tungsten anode wires and 0.25 mm diameter, 85 μg/cm^2 Formvar entrance windows. Their operating characteristics for detecting Cu-L (930 eV) and C-K (280 eV) x-rays are shown in Table I.

	Cu-L (930 eV)	C-K (280 eV)
Counter gas:	P-10	He-isobutane
Gas pressure:	760 Torr	760 Torr
Anode voltage:	1600 V	1150 V
Window transmission: (measured)	0.75	0.76
Counting efficiency: (calculated)	1.0	0.76
Energy resolution: (measured)	325 eV	112 eV

Table I. Operating characteristics of the gas-flow proportional counters.

The counter window transmissions are measured for each photon energy of interest and the counter efficiencies are calculated using published mass absorption coefficients for P-10 and helium-isobutane gases.[4] The output pulses of the proportional counter are amplified and analyzed using conventional techniques.

The experimental detectors are mounted on a rotary table in a second vacuum chamber connected to the target chamber and can be remotely rotated onto the 135° x-ray beam axis symmetrical with the monitor detector (Figure 2). Various thin foils are placed in front of both detectors, experimental and monitor, and serve several purposes. First, in some cases, they are opaque and shield the detectors from visible and infrared fluorescent and incandescent radiation emitted from the hot target. Optical pyrometer measurements have shown a carbon target to stabilize at approximately 1900° C during loading with a 2 mA proton beam. Second, they are thick enough to stop backscattered protons and hydrogen atoms. Buck et. al.[5] have shown that for these proton energies (≈ 300 keV) a large fraction of the backscattered projectiles are neutralized. Consequently, any attempt to remove recoil particles from the x-ray flux by electrostatic deflection techniques would only be partially successful. Hence, absorbing foils are necessary. Finally, in some cases the foils selectively absorb photons characteristic of carbon contamination on the target surface. This requires matching the x-ray absorption cross-section of the foil with the characteristic photon energies of carbon and of the target material to maximize the x-ray flux at the detector. All three functions are considered in selection of the proper foil-target combinations. For example, 600 μm/cm^2, opaque, carbon foils are used with a carbon target and 700 μg/cm^2, opaque Be foils are used with a copper target.

A third vacuum chamber mounted behind the experimental detector chamber (Figure 2) will house a crystal diffractometer and gas-flow proportional counter for high-resolution spectrum analysis.

Facility Performance

The facility is designed for nominal operation at 3 mA beam current and 300 kV accelerating potential.

Table II lists the x-ray source strengths anticipated for these operating parameters. To date, however, the accelerator has been routinely operated at only 1 mA and 200 kV and has been used to generate characteristic x-rays in solid B, C and Cu targets. Results have been encouraging. Figures 6 and 7 show pulse-height spectra obtained from the monitor proportional counter for Cu-L and C-K rays, respectively. Although filtered from the spectrum shown in Figure 6 by a thin Be foil in front of the detector, x-rays due to carbon contamination of the Cu target have been apparent. However, no special precautions were taken to reduce this contamination and significant improvement is anticipated with the incorporation of continuously heated targets and the LN-cooled condenser associated with the multiple target assembly. This assembly will be installed on the system shortly. The spectrum shown in Figure 8 was obtained by subtracting the C-K component from a composite carbon-boron spectrum emitted by a carbon-contaminated boron target.

Target	Photon Energy (eV)	Approximate Source Strength (Photons/sec)
Be-K	110	4×10^{14}
B-K	185	4×10^{14}
C-K	280	4×10^{14}
Ti-L	450	1×10^{14}
Cr-L	570	1×10^{14}
Fe-L	704	1×10^{14}
Cu-L	930	2×10^{13}

Table II. X-ray source strengths for 3 mA proton beam current and 300 kV accelerating potential.

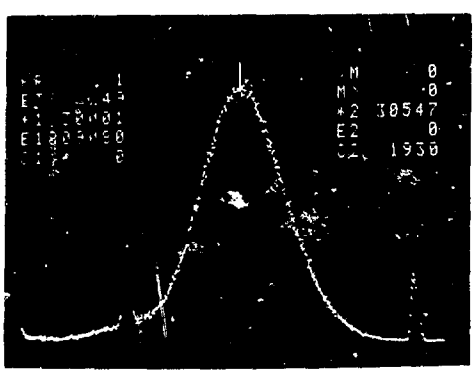

Fig. 6. Pulse height spectrum due to Cu-L (930 eV) x-rays detected by thin-window proportional counter. See Table I for counter operating characteristics.

Table III lists the x-ray source intensities and thick-target photon yields obtained from the present single-target (1 mA, 200 kV) data. These are in excellent agreement with published results.[6] It should be noted that for a given target material, the L-shell photon yield is many orders of magnitude greater than the K-shell yield[6] and hence, the latter may be ignored with respect to the spectral purity of the x-ray source. Note that these source strengths will increase by a factor of ten when the accelerator is operated at its design level of 3 mA and 300 kV.

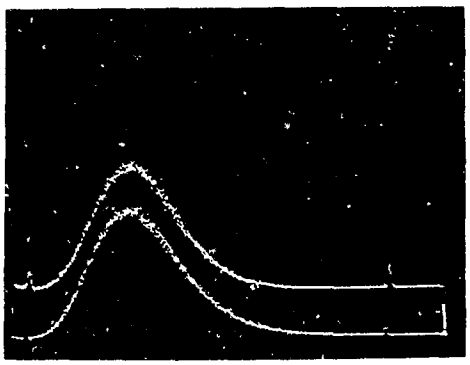

Fig. 7. Pulse height spectra due to C-K (280 eV) x-rays detected by two thin-window proportional counters Counters were mounted simultaneously in the monitor and experimental detector positions (see Figure 2) to demonstrate isotropy of the x-ray emission. See Table I for counter operating characteristics.

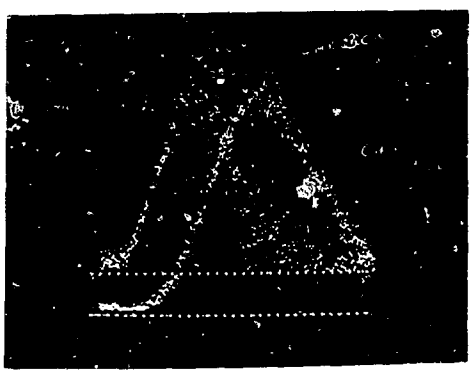

Fig. 8. Pulse height spectrum due to B-K (185 eV) x-rays detected by thin-window proportional counter. Carbon contamination of the target was significant and Boron spectrum was obtained by subtracting C-K component from composite spectrum.

	Cu-L (930 eV)	C-K (280 eV)
Source strength (photons/sec)	1.9×10^{12}	6.5×10^{13}
Thick-target yield (photons/proton)	3×10^{-4}	1×10^{-2}

Table III. Source strengths and proton-induced thick-target x-ray yields obtained from experimental data (proton beam current: 1 mA, accelerating voltage: 200 kV). See Table II for anticipated source strengths when accelerator is operated at full design level of 3 mA and 300 kV.

Acknowledgements

We would like to acknowledge the contributions of M. E. Smith, R. Steele and R. Ullman for designing the accelerator power supply, accelerator control systems and multiple-target assembly, respectively. Also we wish to thank D. Nelson, M. Griffin and J. Arguello for their efforts in fabricating and assembling the apparatus.

(cont. on p. 283)

Proceedings, ERDA X-and Gamma-Ray Symp. Ann Arbor, MI, May 19-21, 1976 (Conf 760539)

COMPACT ALPHA-EXCITED SOURCES OF LOW ENERGY X-RAYS

Karl Amlauer, ISOTOPE PRODUCTS LABORATORIES
Burbank, California

and

Ian Tuohy, Department of Physics, CALIFORNIA INSTITUTE OF TECHNOLOGY
Pasadena, California

Introduction and Theory

For the purpose of this article we define the low energy X-ray region as lying below 5.9 keV, which corresponds to the K_α energy of manganese associated with the decay of Fe-55. While the scope of our discussion is limited to X-ray production by alpha particle excitation, we shall briefly summarize X-ray sources in this region from some commercially available electron capture nuclides. (Table 1).

TABLE 1

Nuclide	$T_{\frac{1}{2}}$	Weighted K_α Energy	Fluorescence Yield
A -37	35.1 D	2.957	0.086
Ca-41	8×10^4 Y	3.690	0.129
Ti-44	48 Y	4.508	0.174
V-49	330 D	4.949	0.200
Fe-55	2.7 Y	5.895	0.282

Because of the lack of availability of emitters in the region below 3 keV we must look to another mode of production. Alpha excitation of characteristic lines was demonstrated by Chadwick in 1912, but it is only within the last ten years that the needs of X-ray astronomers for compact monoenergetic energy markers for ground test and in-flight calibration of X-ray detectors has created renewed interest in this phenomenon. Although compact X-ray tubes are available, their size, reliability and power requirements restrict their use for flight applications. Laboratory evaluations have been made of the alpha excitation technique to determine the feasibility of mineral analysis in lunar exploration (Trombka, et al., 1966). A prototype portable analyser for general geological use has also been built (Sellers, et al., 1968).

Characteristic lines of all the elements can be generated by bombardment of a suitable target with alpha particles, with the purest monoenergetic emissions arising from K_α lines of the low Z elements. The cross section for the production of K-shell X-rays is given by:

$$\sigma(E) \propto \frac{\omega_Z E^4}{Z^{12}}$$

where E is the energy of the alpha particle, Z is the atomic number of the target and ω_Z is the corresponding fluorescent yield. The X-ray production increases with decreasing Z, but the increase is partly offset due to lower fluorescent yields. The theory of this process is treated in detail by Sellers et al (1968).

A number of alpha emitting isotopes are available for X-ray production such as Am-241, Cm-242, Po-210, Ra-226 and Th-228. The two most useful are Po-210 and Cm-244 because of their relative freedom from undesirable radiations. (See Table 2). Polonium has a short half-life and a somewhat volatile nature, and is therefore recommended only for the most demanding spectral purity requirements.

TABLE 2

	Po-210	Cm-244
$T_{\frac{1}{2}}$	138 D	17.6 Y
ALPHA	5.305 meV (100%)	5.81, 5.77 meV
GAMMA	0.803 meV (0.0011%)	0.043 MeV (0.02%) 0.100 MeV (0.0015%) 0.150 MeV (0.0013%) 0.262 MeV (1.4×10^{-3}%) 0.59 MeV (2.5×10^{-3}%) 0.82 MeV (7×10^{-3}%)
X-RAYS	Pb L&M (Trace)	Pu L&M

DESCRIPTION OF SOURCES

Several practical combinations of alpha source and target material are available to give X-ray sources of high integrity. The simplest and most compact of these consists of the alpha emitter sandwiched between two pieces of the target foil and sealed in an outer capsule. (Fig. 1a). Units can be made as small as 3 mm diameter X 3 mm long, but the technique is restricted to energies greater than about 1 keV due partially to lack of suitable window materials below Z=12 (Mg), and also to the difficulty of adjusting window thicknesses to allow reasonable transmission of the desired X-rays while at the same time completely attenuating the alpha particles.

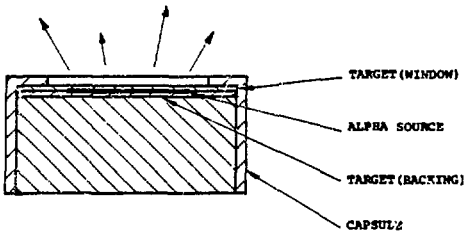

Fig. 1a

Another limitation of this configuration involves the use of Cm-244, whose L X-rays easily penetrate the thin foil window and may swamp the detector electronics. Intensities may actually exceed those of the desired Kα line by a large factor. Po-210, decaying directly to the ground state, is substantially free of this type of emission although traces of lead L and M X-rays can be detected.

A different approach, shown in Fig. 1b utilizes a sealed alpha source placed in opposition to the target material a few mm away. The X-ray beam emerges in a broad cone, but with the center portion occulted by the alpha capsule. In a commercial version of this device, the "X-KIT" produced by ISOTOPE PRODUCTS LABORATORIES, the alpha source is placed at

the side of the target to obtain a larger effective aperture. (Fig. 1c). A serendipitous benefit from this arrangement is a larger than-expected X-ray yield, which appears to be caused by the alpha particles striking the target at shallow incidence. In this case X-ray excitation occurs closer to the surface of the target, and self absorption is less pronounced. The X-KIT provides for replaceable targets down to Z=4 (beryllium) and is designed primarily for laboratory use.

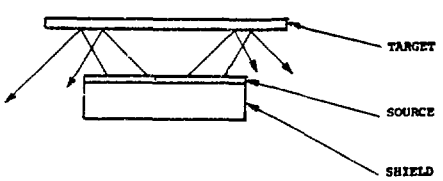

Fig. 1b

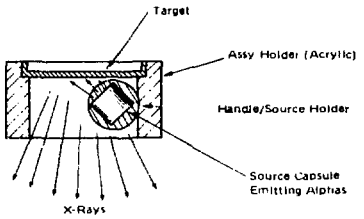

Fig. 1c

A more compact design based on this principle has been developed for rocket application at the suggestion of the Mullard Space Science Laboratory (Tuohy 1975). A thin annular sealed source of Cm-244 is placed about 1 mm from a disc of the desired target material so that the excited X-rays exit through the center hole (Fig. 1d). The source-target distance is important and optimum spacing is a function of Z. Fluxes of at least 2×10^4 photons/sec-steradian per mCi of contained Cm-244 are typical and the complete unit is only 12.5 mm diam. by 6 mm thick. For targets of Z=12 (Mg) or more the aperture is fitted with a thin beryllium window to absorb backscattered alpha particles. By substituting a gas tight chamber for the target it is possible to obtain characteristic X-rays of neon and argon as well as gaseous compounds of sulfur, phosphorus and chlorine.

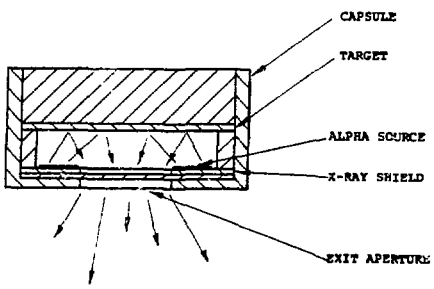

Fig. 1d

The alpha source is a self-contained sealed unit consisting of a thin layer of curium coated with 300-500 ug/cm^2 of gold. An additional backing of nickel in combination with the platinum support helps to minimize interference by the L X-rays associated with the curium decay. For critical applications, the source can be packaged in a tungsten alloy shield assembly to attenuate higher energy Cm-244 emissions.

MEASUREMENT OF PHOTON OUTPUT

The X-ray emission from a 2 millicurie Cm-244 source has been measured for several different targets using the source configuration shown in Fig. 1d. The instrumentation comprised a proportional counter fitted with a one micron carbon-coated polypropylene window and filled with 0.00426 gcm^{-2} of argon-methane gas. Window support was provided by an 80% transmission mesh which covered a circular aperture of 1.27 cm diameter. The solid angle for X-ray detection was set by positioning the curium source above the counter aperture with a precision spacer. A removable vacuum shroud was fitted to the detector to evacuate the region above the window. Standard NIM electronics modules were used for single channel analysis of the various target spectra Threshold levels were set to include only the X-ray peak under measurement in order to minimize the contribution from curium L X-rays and back-scattered alpha particles.

The X-ray fluxes observed from various target materials are summarized in Table 3 for solid angles of 0.5 and 1.0 steradian. The data have been corrected for the detector efficiency. In particular, the X-ray transmission of the detector window was accurately calibrated for energies below silicon-K by measuring the beam attenuation produced by identical samples of window material. Systematic errors in the absolute photon fluxes are estimated to be 10% (statistical errors are negligible).

Figure 2

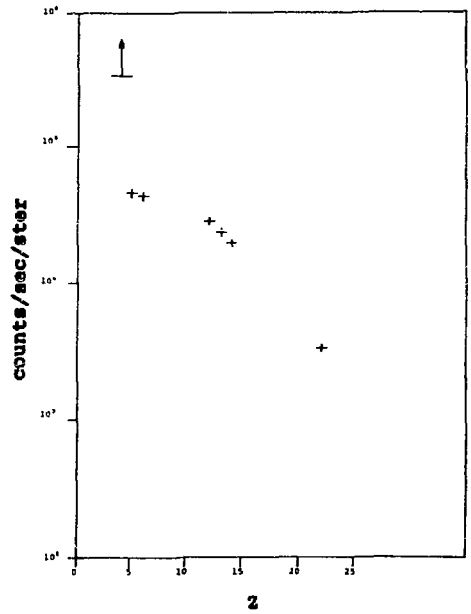

X-RAY INTENSITIES # (PHOTONS/SEC)

Target	Form	Energy (keV)	Z	Ω = 1.0	Ω = 0.5
Beryllium	Metal	0.109	4	> 3.4×10^5	> 1.9×10^5
Boron	Elemental	0.184	5	4.6×10^4	2.9×10^4
Carbon	Graphite	0.279	6	4.4×10^4	2.8×10^4
Magnesium	Metal	1.255	12	2.9×10^4	1.8×10^4
Aluminum	Metal	1.487	13	2.4×10^4	1.5×10^4
Silicon	Elemental	1.742	14	2.0×10^4	1.3×10^4
Titanium	Metal	4.550	22	* 3.1×10^3	* 1.7×10^3
Carbon	Teflon R	0.279	6	~ 6.1×10^3	~ 4.2×10^3
Fluorine		0.675	9	~ 2.6×10^4	~ 1.6×10^3
Silver	Metal	3.1 (L)	47	* 4.1×10^3	* 2.3×10^3

Intensities are corrected for detector efficiency.

* With 0.0051 cm beryllium.

Table 3

The photon outputs for the single elements in Table 3 are plotted in Figure 2 with an additional correction for Z>16 to allow for attenuation by the beryllium filter. The X-ray emission shows a marked increase with decreasing Z, as expected from the cross-section formula given previously. However, the emissions from boron and carbon appear to be lower than expected. This effect could be related to the target preparation, and is being further investigated.

The X-ray output of the source was also determined as a function of solid angle using carbon and aluminum targets. Both targets showed an essentially linear decrease in X-ray intensity as the solid angle was reduced from 0.5 to 0.01 steradian. Finally, some typical proportional counter spectra are shown in Figure 3 for targets of beryllium, carbon, silicon and teflon.

Figure 3

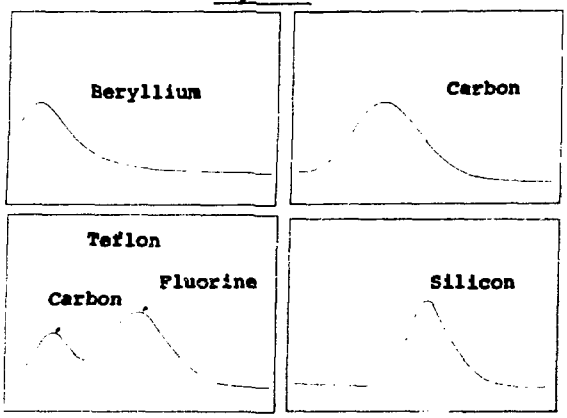

Figure 4

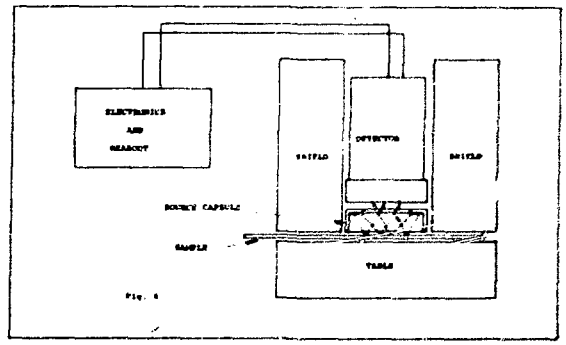

Commercial Applications Of The Alpha Excitation Technique

Until the present time the primary application of this technique has been almost exclusively in X-ray astronomy and for the calibration of thin films by the transmission technique. Some fusion research groups have found calibrated low energy standards useful in the determination of X-ray flux densities in plasma. It is now possible to construct a ruggedized version of the annular type source which will make it convenient for many types of laboratories to possess and use these devices for routine calibration purposes. Contained activities of 10-100 μCi corresponding to 200-2000 photons/sec, should suffice for many applications.

The annular source with its high efficiency can be adapted for analytical use by removal of the target and mounting the source assembly in a platen in such a manner that the distance is about one mm. (Fig. 4). With the addition of a permanently mounted proportional or solid state detector and protective cover combined with appropriate readout instrumentation, a compact bench-top instrument could be constructed capable of the surface analysis of a number of low Z sheet materials, such as paper, minerals, glass and plastic. By utilizing higher activity levels (10-100 mCi) and strip configurations, it may also be feasible to perform on-line quality control of certain materials produced in sheet or roll form as well as to monitor organic coating thicknesses. The possibility also exists of using this concept for the on-line monitoring of gaseous process streams for sulfur and chlorine, as well as other elements.

BIBLIOGRAPHY

1. B. Sellers, F. A. Hanser, H. H. Wilson, "Measurement of The K-Shell Ionization Cross Sections of Al and Mg for 1- to 5-Mev α Particles," Physical Review, Vol. 182, No. 1, June 5, 1969.

2. I. Tuohy, private communication , 1975.

3. J. I. Trombka, I. Adler, R. Schmadebeck, R. Lamothe, "Non-Dispersive X-ray Emission Analysis For Lunar Surface Geochemical Exploration," Goddard Space Flight Center, Greenbelt, Maryland, Vol. X-641-66-344, August 1966.

4. B. Sellers, H. Wilson, F. A. Hanser, "Generation and Practical Use of Monoenergetic X-rays From Alpha Emitting Isotopes," U. S. Atomic Energy Commission, Vol. NYO-3491-3, 1968.

Proceedings, ERDA Second Conference Ray Synop. Ann Arbor, MI, May 19-21, 1976 (Conf-760530)

THE PREPARATION OF VERY SMALL POINT SOURCES FOR HIGH RESOLUTION RADIOGRAPHY

F. N. Case

Oak Ridge National Laboratory*
Post Office Box X
Oak Ridge, Tennessee 37830

Summary

The need for very small point sources of high specific activity ^{192}Ir, ^{169}Yb, ^{170}Tm, and ^{60}Co in non-destructive testing has motivated the development of techniques for the fabrication of these sources.

To prepare ^{192}Ir point sources for use in examination of tube sheet welds of LMFBR heat exchangers, ^{191}Ir enriched to ~90% was melted in a helium blanketed arc to form spheres as small as 0.38 mm in diameter. Methods were developed to form the roughly spherical shaped arc product into nearly symmetrical spheres that could be used for high resolution radiography. The specific activity of these sources was ~5000 Ci/g. Because of the small size, special graphite holders were developed to permit hot cell handling after irradiation and to position the source in the radiographic camera pigtail capsule.

Similar methods were used for spherical shaped sources of ^{169}Yb and ^{170}Tm. The oxides were arc melted to form rough spheres followed by grinding to precise dimensions, neutron irradiation of the spheres at a flux of 2 to 3 × 10^{15} n/cm²-sec, and use of enriched ^{168}Yb to provide the maximum specific activity.

Cobalt-60 with a specific activity of ~1100 Ci/g was prepared by processing ^{59}Co that had been neutron irradiated to nearly complete burnup of the ^{59}Co target to produce ^{60}Co, ^{59}Ni, and ^{63}Ni. After separation of the nickel isotopes, a nearly theoretical specific activity ^{60}Co was obtained, which was reformed into right cylinder pellets for radiography.

Ion exchange methods were used to separate the cobalt from the nickel. The cobalt was reduced to metal by plating either onto aluminum foil which was dissolved away from the cobalt plate, or by plating onto mercury to prepare an amalgam that could be easily formed into a pellet of cobalt with exclusion of the mercury. Both methods are discussed.

To prepare very high specific activity ^{192}Ir we have used three methods, each of which has provided alternatives for the fabrication of spherical point sources. One preparation involves the irradiation of 2-mil-thick iridium ribbon wrapped around an aluminum pin to prevent shadowing during neutron irradiation for optimum yield. The use of very thin ribbon overcomes the problem of the high neutron cross section of ^{191}Ir which reduces the neutrons available to the interior of pellets that are normally used in the preparation of ^{192}Ir radiographic sources. After irradiation the ribbons are melted by feeding them into an oxygen propane flame to form spheres up to 1/8-in. diameter, thus providing sources for use in conventional radiography.

*Operated by Union Carbide Corporation, Nuclear Division for the Energy Research and Development Administration.

A second method developed to overcome the problem of high neutron loss to the interior of massive ^{192}Ir targets involves the use of iridium sponge. To prepare the sponge a solution of iridium chloride in alcohol is saturated in ashless filter paper, dried, and ignited. The iridium is reduced to the elemental form and replicates the paper fibers, leaving a highly extended surface that provides optimum irradiation conditions. After irradiation, the sponge is pressed into pellets in the form of right cylinders or it may be melted to form small spheres using a Heli-arc welding torch and a graphite boat. Some vaporization of the iridium occurs during this melting operation; therefore, a small disposable enclosure made with a wire frame and aluminum foil is used in the hot cell where the fabrication is carried out. This enclosure is connected directly to the cell hot off-gas system and protects the interior of the hot cell from serious contamination. During the melting operation the graphite boat serves as one electrode and a graphite electrode in the Heli-arc torch the other. The sphere thus produced provides optimum geometry and density. When right cylinders are pressed, a density of only about 80% can be achieved. The following table shows a comparison of specific activity obtainable under various conditions of irradiation and fabrication.

Table 1

Iridium Target	Flux, n/cm²-sec	Irradiation Time	^{192}Ir, curies/g*
1/16 × 1/16 pellets	3 × 10^{15}	6 weeks	260
2-mil thick ribbon	3 × 10^{15}	6 weeks	630
sponge	3 × 10^{15}	6 weeks	680
1/16 × 1/16 pellet	2 × 10^{15}	10 days	600
sponge	2 × 10^{15}	5 days	1023

*Measured 10 days after removal from reactor.

One problem encountered in the melting of iridium to form spheres following neutron irradiation is the difficulty in maintaining size control. While approximate sizes can be prepared, whenever precise control is necessary the spheres must be fabricated prior to irradiation. Although pre-irradiation fabrication offers the advantage of size control, a compromise must be made concerning the optimization of surface area per unit weight during neutron irradiation. To partially overcome this problem, calutron separated ^{191}Ir enriched to greater than 90% as contrasted with a natural occurring 37.3%, is prepared into spheres of the desired size by Heli-arc melting and grinding between rotating plates. To facilitate remote handling the spheres are placed in graphite holders that also serve to center and fix their position in the radiographic camera. Sources as small as 0.38 mm in diameter having a specific activity of 5,000 Ci/g were prepared in this manner and were used to verify welds in heat exchanger tube sheets as shown in Fig. 1 (ORNL-Dwg. 75-4511). The source contained 0.5 Ci of ^{192}Ir. Weld defects approximately 0.025-in. in diameter were easily visualized using this source.

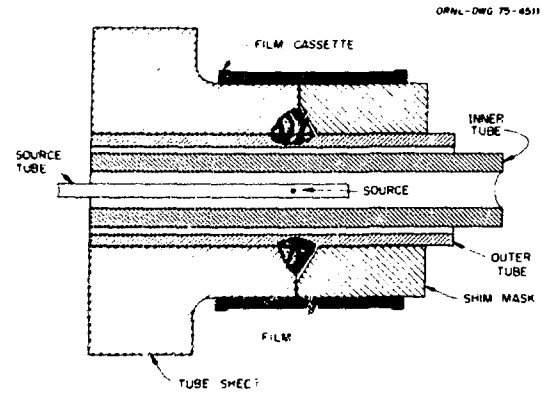

Fig. 1. Cross-Sectional View of Source Tube in Position for Radiography

Ytterbium-169 and ^{170}Tm sources were prepared in a similar manner. For these sources ytterbium or thulium oxide was arc melted into spheres using a tungsten boat instead of graphite to prevent the formation of carbides. Irregularities in the spheres were corrected by grinding between two plates covered with carborundum paper. As with the iridium, the spheres were placed in graphite holders prior to irradiation to facilitate remote handling and to position the active source in the radiographic camera.

The small very high specific activity sources are not commercially available since for most radiographic inspection the 1/16 by 1/16 or 1/8 by 1/8 sources are adequate for such applications as pipe line welds, normal foundry quality control and fabrication weld inspection procedures. However, under conditions of very rigid welding specifications, the very small sources are frequently required.

Very high specific activity ^{60}Co has been shown to be advantageous in radiographic inspection of thick material sections. We have developed methods in which greater than 1100 Ci/g cobalt can be prepared and formed into right cylinders for radiographic use. This is an important development since radiographers have been limited to 250-400 Ci/g ^{60}Co and for a number of applications the source must be either collimated with much loss of output or placed at considerable distance from the object being radiographed. In one case we prepared a 10,000 Ci source of 1100 Ci/g ^{60}Co that provided inspection capability nearly equal to an accelerator for inspection of very massive components. We are currently preparing a 30,000 Ci high specific activity ^{60}Co source for ERDA project use as a point source for instrument calibration.

Since the bar to production of very high specific activity ^{60}Co by simple neutron irradiation of ^{59}Co is the production of ^{60}Ni and ^{61}Ni, the maximum concentration obtainable by ordinary irradiation is ~720 Ci/g. However, by removal of the nickel from ^{59}Co that has undergone complete neutron burnup it is possible to approach the theoretical specific activity of 1140 Ci/g. Furthermore, once theoretical specific activity has been obtained it can be reprocessed to remove decay produced nickel, restoring it to its original theoretical specific activity.

In the process, high burnup ^{60}Co is dissolved in nitric acid and converted to the chloride and the solution adjusted to 9 N HCl for separation of the nickel on a Dowex 1 ion exchange column. The cobalt remaining on the column is washed with 9 N HCl for removal of final traces of nickel and stripped in <1 N HCl. Batches as large as 10,000 Ci of ^{60}Co have been adsorbed on the column without serious decomposition of the resin. While some gassing of the column occurs, the separation is relatively easy and complete nickel separation is achieved. Following nickel separation the cobalt is electroplated either into mercury to form an amalgam or onto aluminum foil in the form of a thick plate. The advantage of the amalgam process is that it protects the cobalt from oxidation during forming operations and it has desirable physical properties for pressing into a final pellet form. By placing the amalgam into a die and pressing at 30,000 psi most of the mercury is removed and a cobalt compact is provided that can be sintered at 800°C under hydrogen to provide a final product with greater than 90% theoretical density.

The second method avoids high temperature sintering at a small sacrifice in density. In this process the nickel for cobalt is complexed with ammonium hydroxide and electroplated onto aluminum foil at a current density of 6 amps at ~5 volts. After >95% of the cobalt is electroplated from the solution, the aluminum foil containing the plate is washed with water, after which the aluminum is dissolved in sodium hydroxide solution. The thin cobalt foil remaining is washed with water to remove sodium aluminate and sodium hydroxide after which it is placed in a blender with water and broken into flakes with approximately 1/16-in. maximum dimensions. These flakes are washed with alcohol and protected from oxygen under a blanket of argon. The dry flakes are loaded by weight into a die and pressed at 300,000 psi to yield a density in the final pellet of 87% of theoretical.

A number of sources have been prepared by this method and in addition to radiographic uses we currently have a cooperative program with Duke University Medical Center to evaluate very high specific activity ^{60}Co in teletherapy. With high specific activity material, very intense and highly collimated gamma ray beams make it possible to direct the beam onto special areas without excessive exposure of healthy tissue.

Proceedings, ERDA X-and Gamma Ray Symp. Ann Arbor, MI, May 19-21, 1976 (Conf 760539)

DEVELOPMENT OF THE NATIONAL BUREAU OF STANDARDS LOW-ENERGY-PHOTON-EMISSION-RATE RADIOACTIVITY STANDARDS*

J.M.R. Hutchinson W. B. Mann, and P. A. Mullen
National Bureau of Standards
Washington, D. C. 20234

Summary

The National Bureau of Standards has recently developed point source low-energy-photon-emission-rate standards of ^{55}Fe, ^{85}Sr, ^{109}Cd and ^{125}I. The standardizations were performed using a defined solid angle, NaI(Tl) spectrometer that can be operated with gas fillings at atmospheric and reduced pressure. The corrections applicable to such a spectrometer have been discussed by W. B. Bambynek.[1/]

Defined-Solid-Angle, NaI(Tl) Spectrometer

Figure 1 shows a picture of the spectrometer. The NaI(Tl) detector is a 1-in diameter by 1/16-in thick cleaved crystal. It has a 0.005-in Be window, and an XP1010 photo tube, especially selected for low noise. A diaphragm, made from 0.015-cm thick platinum, with an aperture diameter of 0.9505 (±0.0020) cm, is used to define the solid angle subtended by the detector to the source. The ±0.0020-cm uncertainty in the aperture diameter results in an uncertainty of ±0.5 percent in the geometrical efficiency.

Figure 1. NBS defined solid angle X-ray spectrometer

A source mount is taped across a lip protruding from the bottom of a pure aluminum holder, which slides into channels cut in the aluminum side walls. The holder is then pressed into position against the top of the channels, which are at accurately measured distances from the diaphragm.

Initially, the source holder was designed with a spring-loaded hammer to hold the source in place. However the hammer was discarded in favor of taping the sources when it was found that γ rays backscattered from it into the detector. The results of a series of measurements on 22 keV K x rays of silver are shown in Table I. The percentage differences between the count rates with and those without a thick hammer in place are listed for different "hammer" materials. These results appear to disagree with W. B Bambynek[2/] who reported that no significant backscattering occurs for γ rays of low energies.

Hammer Material	Percent Increase with Hammer in Place	Hammer Material	Percent Increase with Hammer in Place
Boron nitride	9.0	Monel	0.7
Lucite	7.7	Brass	0.9
Glass	3.8	Copper	1.0
Aluminum	2.8	Silver	1.0
Titanium	1.1	Cadmium	1.2
Stainless steel	2.2	Tungsten	1.6
Nickel	0.7	Platinum	1.2
		Gold	1.4
		Lead	1.2

TABLE I

A cylindrical lucite sheath can be raised to enclose the counter so that it can then be operated in a hydrogen atmosphere or evacuated if desired.

Detector Efficiency Measurements and Calculations

Extrapolated Values to $h^{-2} = 0$

The geometrical efficiency for a point source (see Figure 2), as mentioned by Bambynek,[1/] is

$$\epsilon = 0.5 - \frac{h}{2r}$$

where h is the source-to-diaphragm distance and r is the hypotenuse of the right triangle in which the aperture radius and h are the other two sides. Although the distances between the upper edges of the various channels are very accurately known, uncertainties of a few thousandths of a centimeter exist in the vertical positioning of the diaphragm. In addition, finite source diameter, typically 3 to 5 mm, must be taken into account.

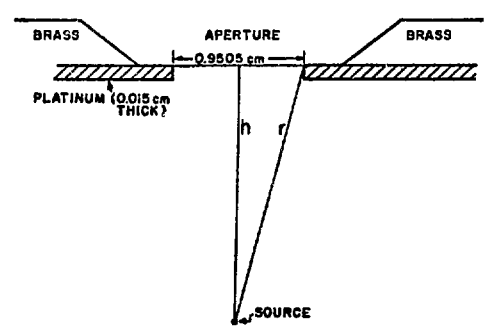

Figure 2. Schematic diagram of diaphragm and source

* Contribution of NBS, not subject to copyright.

Small uncertainties due to these effects and, for example, penetration of the platinum diaphragm become negligible at large values of h for which also the geometrical efficiency must approach an h^{-2} dependence. Therefore, the emission rates were determined from a plot of $\frac{N}{\varepsilon}$ vs h^{-2} where N is the count rate at a given (but uncertain) value of h. An extrapolation, which appears to be closely linear as shown in Figure 3, is made to $h^{-2} = 0$, thus determining the corrected value of the emission rate.

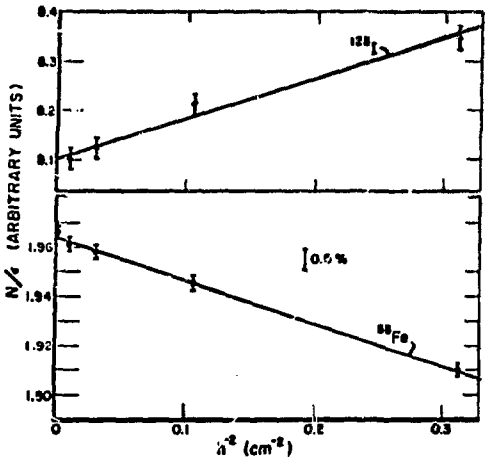

Figure 3. Plot of N/ε vs h^{-2} for ^{55}Fe and ^{125}I

In this figure, positive and negative slopes were obtained, corresponding to a change in estimated h of 0.01 cm. The results obtained in both cases agreed to within 0.1 percent with values in which carefully calculated corrections were made for longitudinal and lateral displacements.

Absorption Corrections

Absorption of photons by the air, source mount and beryllium window were measured and corrected for. The absorption by the air was found from measurements with first air then hydrogen in the intervening space; the absorption of the mylar source cover was found from measurements with and without added layers of mylar tape. These measurements agreed within ±5 percent with the calculated values using tabulated narrow-beam, linear-attenuation coefficients.[3] The calculated absorption in the beryllium window was checked by measurements on an ^{55}Fe source which had previously been calibrated by high-pressure 4π proportional x-ray counting. The ^{55}Fe measurements are discussed in a later section.

Other Corrections

A number of photon interaction processes lead to pulses that are unresolved in the pulse-height spectrum from those caused by the total absorption by the NaI(Tl) of the photons of interest. These processes each contribute less, and in most cases, much less than one percent of the total count rate. The processes are listed below and are further discussed in the next section.

(i) Production of platinum L x rays due to interaction of photons in the diaphragm;

(ii) Scattering from the NaI(Tl) crystal of high-energy gamma rays which accompany the photons being measured. (For example, in the case of ^{109}Cd, approximately 20 keV is deposited in the crystal when 88-keV gamma rays are backscattered through 180 degrees. The 22-keV K-x-ray pulses are unresolved from these "backscattering" pulses);

(iii) Interaction of conversion electrons with the NaI(Tl);

(iv) Scattering of photons from the aluminum sides and source mount into the detector. (This effect is of the order of 1% of the total count rate based on measurements made with and without a baffle placed between the source and detector);

(v) Production of copper and zinc K x rays from the scattering of high energy γ rays in the brass backing of the platinum diaphragm. (This effect is measured from a spectrum taken with low-energy photons removed from the beam with an absorber);

(vi) "Photoelectron escape," in which a photoelectron originates near the edge of the NaI(Tl) and leaves without depositing all its energy in the crystal. The pulse-height spectrum of such pulses has been shown to be constant from zero energy up to close to the photon energy.[4] The contribution of such pulses will be added to the total count rate, therefore, by making a linear extrapolation down to zero energy of the integrated count rate;

(vii) Iodine K x rays excaping from the NaI(Tl) detector (This effect was significant in the measurements described here only for the 35-keV gamma rays in the decay of ^{125}I).

Preparation and Measurement of the Standard Samples

The decay schemes of the radionuclides used are shown in Figure 4[5] and the radiations of interest in this paper are listed in Table II.[6]

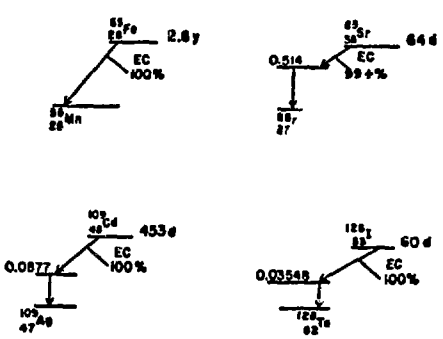

Figure 4. Decay schemes of ^{55}Fe, ^{85}Sr, ^{109}Cd and ^{125}I

Iron-55

Each iron-55 sample is a dried deposit of iron chloride on a stainless-steel disc which had been covered by a layer of lacquer. Another layer of lacquer was applied after the source was dry. Photon interaction with the backing is totally by the photoelectric process, thus there is no significant backscattering.

Photon-emission rates obtained using the procedure outlined in the previous section agree with

those determined by comparison with sources calibrated by 4πx high-pressure proportional counting[7,8] to 0.6 percent.

Radiation Type	Energy (keV)	Intensity (%)
^{55}Fe EC DECAY (2.7 Y 1)		
X-ray L	0.65	0.02 10
X-ray $K\alpha_2$	5.88765	8.2 7
X-ray $K\alpha_1$	5.89875	16.3 12
X-ray Kβ	6.49	3.3 3
^{109}Cd EC DECAY (453 D 2)		
X-ray L	3	11 4
X-ray $K\alpha_2$	21.9903 3	29.1 10
X-ray $K\alpha_1$	22.15290 1	55.1 18
X-ray Kβ	24.9	17.8 7
γ 1	88.037 5	3.72 11
^{85}Sr EC DECAY (64.85 D 3)		
X-ray L	1.69	1.5 6
X-ray $K\alpha_2$	13.33560 2	17.1 6
X-ray $K\alpha_1$	13.39530 2	33.0 7
X-ray Kβ	15	8.67 24
γ 1	513.990 10	93.0 10
^{125}I EC DECAY (60.14 D 11)		
X-ray L	3.77	15 6
X-ray $K\alpha_2$	27.20178 2	39.8 16
X-ray $K\alpha_1$	27.47220 2	76.2 25
X-ray Kβ	31	25.8 10
γ 1	35.46 3	6.67 22

TABLE II

An extrapolation, which corrects for "photoelectron escape" events, of the integrated count rate to zero energy is shown in Figure 5.

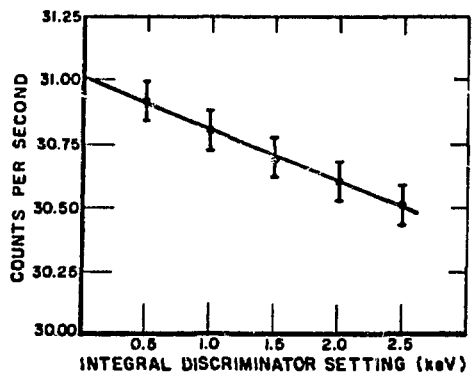

Figure 5. Count rate vs integral discrimination level for an ^{55}Fe source.

From the agreement between the results from the 4π and defined solid angle counting, it is clear that calculated Be absorption corrections are also adequate for the photons of higher energies emitted in the decay of ^{85}Sr, ^{109}Cd and ^{125}I.

Strontium-85

Dried, quantitatively deposited radioactive strontium chloride is sealed between 0.006-cm mylar tape. The solution from which the sources are made was standardized at NBS for activity by means of x-γ coincidence counting and agreed with similar measurements[9] made at IAEA, Seibersdorf to 0.1%.

Figure 6 shows a spectrum of the strontium-85 sources in the region of the Rb K-x-ray peak which is riding on the Compton continuum of the 514-keV gamma rays. The count rate of the 514-keV gamma rays was obtained using an absorber to screen out the K x rays.

The K-x-ray emission rate determined by the method described here, agreed to 0.3 percent with that obtained by x-γ coincidence counting using a previously published K-x-ray abundance of 0.588.[6]

Cadmium-109

Cadmium-109 emits K x rays with energies between 22 and 24 keV, 88-keV gamma rays, and L, M.. x rays as well as conversion and Auger electrons which are screened out by the Be window. The pulse-

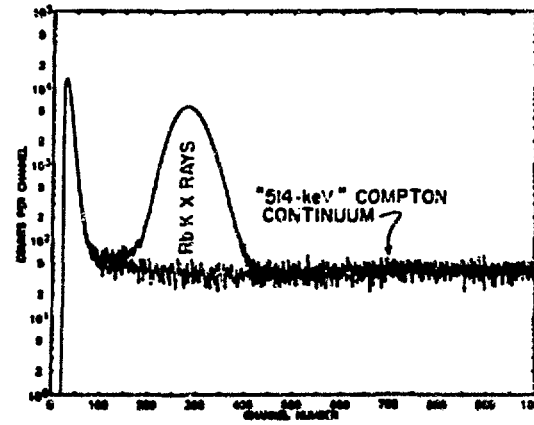

Figure 6. ^{85}Sr spectrum in the region of the Rb K x ray. The Compton continuum under the peak is superimposed.

height spectrum in the NaI(Tl) detector is shown in Figure 7. The "tail" of the 88-keV gamma ray response is assumed to be flat from above the 24-keV x rays down to zero energy.[4]

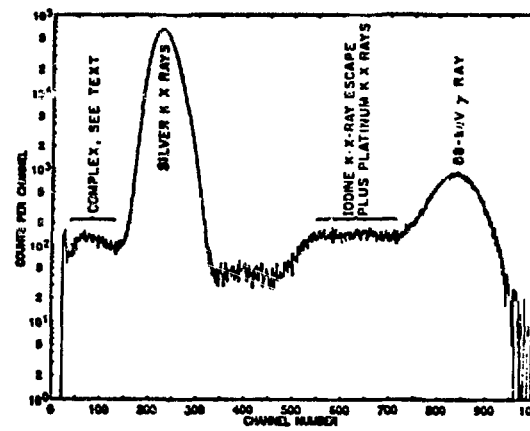

Figure 7. ^{109}Cd pulse height spectrum

The sum of pulses in the low-energy "tail" of the K x rays, after subtraction of the 88-keV contribution constitutes less than 0.3% of the total counts. This "tail" is probably quite complex, containing pulses due to "photoelectron escape," Pt x rays, and Cu K x rays generated in the brass backing of the diaphragm. Since it was not possible to distinguish between these different groups of pulses, one half of the count rate under the "tail" was added to the number under the total energy peak and an uncertainty of this small additional rate was assumed.

Iodine-125

The decay scheme of iodine-125 is shown in Figure 4. Using the compiled values of M. J. Martin et al,[6] there are 146.5 ± 5.1 % x rays plus 35-keV gamma rays per 100 ^{125}I disintegrations. The 27 to 31 keV K x rays originating both in K capture and internal conversion are unresolved in the NaI(Tl) spectrum from the gamma rays.

Because iodine in the chemically unattached state volatilizes, sources were prepared by first depositing weighed aliquots of a solution of iodine in 1N HCL onto mylar source mounts and then precipitating the

iodine as AgI using $AgNO_3$. After drying, another layer of tape was placed over the top to hold the material in place. In the first sources prepared the number of fluorescent silver K x rays produced by tellurium photons was unacceptably large. This problem was overcome, however, by drastically reducing the amount of inactive iodine carrier and, hence, also the two-times stoichiometric amount of $AgNO_3$ used to precipitate the AgI. Each source had an activity of approximately 3×10^5 s^{-1}, contained less than one microgram of silver and had an inactive to active ratio of 10. Upon examination with the Si(Li) and pure Ge detectors (see Figure 8), it was found that less than 2 silver K x rays per 1000 tellurium photons were emitted by the sources.

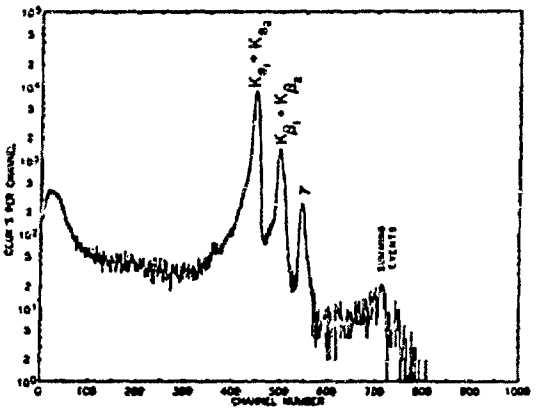

Figure 8. ^{125}I photon spectrum in Si(Li) detector

Iodine K-x-ray escape events are seen as a peak at approximately 8 keV in a pulse-height spectrum obtained with an absorber covering the source to cut out L x rays. The number of iodine K-x-ray escapes per Te K x ray plus gamma ray is 0.9%, which is obtained by dividing the total counts under this peak by the summed counts in the total spectrum. This value means that 21% of 35-keV gamma rays that were detected result in an iodine K-x-ray escape, which agrees with Heath's value[10] for a 3-in x 3-in detector.

Summing of K x rays from the electron-capture transition with K x rays or γ rays in decay from the 35 keV energy level in tellurium was taken into account by counting each summed event, at roughly 60 keV, twice.

The value of N obtained in these measurements agreed, to less than 1 percent, with the value obtained from NBS sum-peak measurements and using 146.5 K x ray plus gamma rays per 100 disintegrations.

Conclusion

A defined-solid-angle spectrometer for the measurement of the emission rates of photon emitters with energies from 5 keV to 40 keV has been developed. The detector, which employs a thin NaI(Tl) crystal was tested using ^{55}Fe sources (K x ray energies of approximately 5.9 keV) which had been calibrated by 4π high-pressure proportional counting. The results show that there are no surface effects or "dead spots" in the crystal which cause these low-energy photons to go undetected. Scattering from the air and beryllium window can be calculated to sufficient accuracy with narrow beam linear attenuation coefficients.

Although backscattering of photons from ^{55}Fe sources from the source mount was negligible, as discussed by Bambynek,[1] there was as much as 8 percent backscattering for the 22 keV photons emitted in the decay of ^{109}Cd. "Photoelectron escape" is taken into account by an extrapolation of integral count rate to zero energy. Iodine K x ray escape for the NaI(Tl) crystal using ^{125}I sources was determined from the photon spectrum with a 20 mg/cm^2 absorber over the source to cut out the L x rays. The K x ray escape peak is well resolved for this condition. Using the spectrometer, standards of ^{55}Fe, ^{85}Sr, ^{109}Cd, and ^{125}I have been developed and issued as SRM's thus reducing to 5.9 keV the lower limit of the photon energy range, 88 keV to 1.86 MeV, of the NBS "kit" of point-source photon standards. Additional corroborative measurements on ^{85}Sr, ^{109}Cd and ^{125}I have been performed using published abundances and Kx/γ ratios.

It was necessary to reduce the amount of silver per ^{125}I source to 1 μg or less because for greater amounts, the silver atoms are activated to an unacceptably large amount by the ^{126}Te photons.

Acknowledgement

The authors wish to express gratitude to Miss L. M. Cavallo, Dr. B. M. Coursey, and Dr. J. R. Noyce for preparing the radioactive sources used in the measurements described in this paper.

References

1. Bambynek, W. B., Standardization of Radionuclides, IAEA Symposium on the Standardization of Radionuclides, Vienna, 373 (1967).
2. Bambynek, W., Lerch, O. and Spernol, A., Nucl. Inst. Meth., 39, 104 (1966).
3. Hubbell, J. H., NSRDS, NBS 29 (1969).
4. Hutchinson, J.M.R. and Garfinkel, S. B., Int. J. Appl. Rad. Isotopes, 22, 405 (1971).
5. Lederer, C. M., Hollander, J. M. and Perlman, I., Table of Isotopes (Sixth Edition), John Wiley, New York (1967).
6. Martin, M. J. (Editor) ORNL-5114, March (1976).
7. Allen, R. A., Int. J. Appl. Rad. Isotopes, 1, 289 (1957).
8. Garfinkel, S. B. and Hutchinson, J.M.R., Int. J. Appl. Rad. Isotopes 13, 629 (1962).
9. Private communication
10. Heath, R. L., A.E.C. Research and Development Report IDO-16880-1. Physics TID-4500 (31st Ed.) August (1964).

Proceedings 1FIDA X and Gamma Ray Symp Ann Arbor, MI, May 19-21, 1976 (Conf 760539)

DEVELOPMENTS IN THE DESIGN AND APPLICATION OF γ AND X-RAY SOURCES INCORPORATING TRANSURANIC NUCLIDES

P E Fletcher and P A Lorch

The Radiochemical Centre Limited

Amersham, England

Summary

The increasing application and use of radioisotope X and γ-ray sources based on transuranic nuclides has been accompanied by significant improvements in source designs and production methods. At the same time, considerable progress has been made in both prototype and long term testing. This critical approach to design and testing has emphasized that due to inevitable ageing effects such as radiation damage, sources cannot be expected to retain their initial high performance standards indefinitely but should be regarded as having a limited working life not related to the long half-life of the nuclide.

Introduction

Radioisotope sources of low energy gamma and X-radiation continue to find increasing application in many diverse fields of industry, medicine and research. Significant developments in instrumental techniques are extending and improving these applications particularly in the fields of thickness gauging and X-ray fluorescence analysis.

Among sources commonly used are those incorporating the transuranic nuclides ^{241}Am, ^{238}Pu and ^{244}Cm, which enable useful sources to be prepared with emitted radiation in the energy region 10 to 60 KeV. Although these nuclides also emit α-particles and are thus of high radiotoxicity, they do combine the advantages of high specific activity, long half-life and relative cheapness not found in other low energy radioisotope sources.

However, it is essential that the design of sources based on these nuclides should not only allow efficient emission of the required radiation but should ensure continuous safe containment during the working life of the source.

Design Considerations

Primary Containment

In order to achieve acceptable safety standards attention at the Radiochemical Centre has concentrated on the incorporation of the radioisotope in a ceramic matrix which is usually fired onto a metal insert and then further contained in a welded metal capsule.

The aim is to produce inserts which are relatively free from contamination and in which the nuclide is in an insoluble material with good thermal and radiation resistance, high mechanical strength and which, in the event of accidental damage to the outer capsule, minimizes the possibility of released aerosol particulates. A similar rationale has led to the development of special ceramics for nuclear waste fixation.[1]

The development reported earlier by Ansell and Hall[2] for ^{241}Am gamma [59.5 KeV] sources has been extended to enable sources emitting X-rays to be prepared in both disc and annular configurations. Examples of inserts are shown in Fig 1.

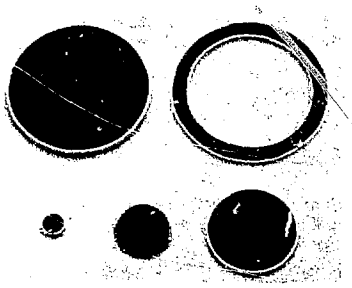

Fig 1 Typical disc and annular source inserts.

Stainless steel or tungsten are the favoured backing materials for the ceramics, the choice depending on the degree of back shielding required.

Emission efficiency curves for typical inserts are given in Figs 2 and 3 and illustrate how the effects of self absorption limit the output intensity as the activity per unit area increases.

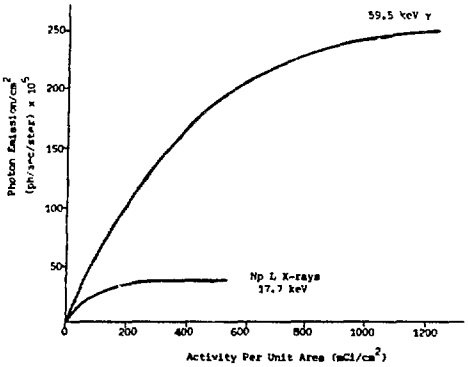

Fig 2 Gamma and X-ray emission for ^{241}Am as a function of activity

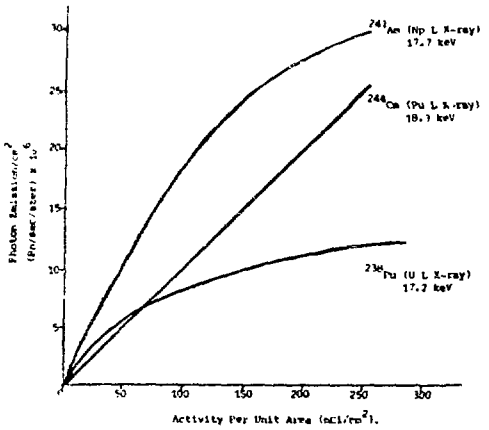

Fig 3 X-ray emissions for ^{241}Am, ^{238}Pu and ^{244}Cm as a function of activity per unit area.

For ^{241}Am gamma [59.5 KeV] sources the maximum practical loading is reached at about 800 mCi/cm^2. However, a new ceramic system which enables loadings of up to 1200 mCi/cm^2 to be prepared is currently under development.

Final Encapsulation

For ^{241}Am gamma [59.5 KeV] sources stainless steel capsules are normally employed. In order to minimise absorption losses windows must necessarily be thin, usually 0.25 mm; it is therefore important to use high grade material, preferably vacuum cast, which has been carefully tested for mechanical and chemical properties and certified defect free. Examples of disc and annular source capsules are shown in Fig 4.

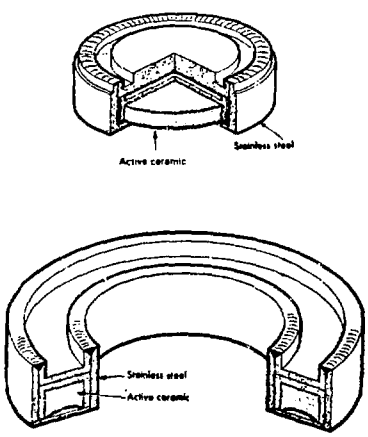

Fig 4 Typical annular and disc source designs

For disc sources using ^{241}Am, ^{238}Pu and ^{244}Cm where X-radiation in the range 10 - 25 KeV is required, it is no longer possible to use a stainless steel window and capsules with 1 mm thick beryllium windows have been developed. The window is bonded to a monel capsule body by use of a high temperature braze material. After loading of the insert the capsule is finally sealed by argon arc welding. A typical design is shown in Fig 5.

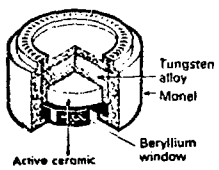

Fig 5 Monel capsule with brazed beryllium window for ^{241}Am, ^{238}Pu and ^{244}Cm X-ray sources.

Annular sources are the preferred configuration for many applications and designs based on this construction are currently under development.

Prototype and Long Term Testing

Since their introduction about fifteen years ago it is estimated that many thousands of low energy gamma and X-ray sources based on these transuranics have been supplied world-wide and remain in use today, with a commendable record of safety in terms of containment. However, because the range of applications and environments for use is so diverse and increasing, source manufacturers must continually be conscious of the safety requirements for each design.

Ideally each source type should be tested according to the actual conditions likely to prevail during use. Since this is clearly impracticable for all cases the normal practice is to test prototypes according to the International Standard for sealed radioactive sources.[3] This establishes a source classification based on radiotoxicity, maximum activity and the performance in a series of tests of graded severity. The resulting classification is then compared with source performance standards which are suggested for particular applications. The tests comprise temperature, external pressure, impact, vibration and puncture tests.

Details of the test classes are given in APPENDIX 1.

Some testing facilities in current use at The Radiochemical Centre are shown in Fig 6 and 7.

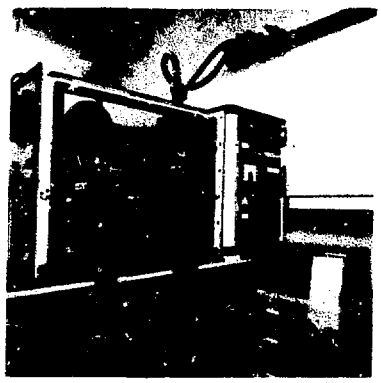

Fig 6 Vibration Testing Facility

Fig 7 Facility for Impact and Puncture Testing

Sealed Source Usage	Performance Requirement Class				
	Temp	Ext Pressure	Impact	Vibration	Puncture
Sources for low energy gamma gauge or XRF analysis	3	3	2	2	2

Source Construction	Performance Achieved by Testing				
	Temp	Ext Pressure	Impact	Vibration	Puncture
Disc Source.All stainless steel capsule.Welded.	6	4	3	4	4
Disc Source.Monel capsule (welded)with brazed Be window	6	4	3	4	4

TABLE 1

The performance ratings determined by testing for typical TRC source designs are shown in TABLE 1 and are well above the suggested minimum requirements for typical uses.

The standard also clearly stresses the need for both the manufacturer and the user to assess any special hazards. With sources based on nuclides which emit alpha particles two particular hazards need consideration at the design stage:

1) helium gas build up
2) radiation damage, particularly of the source insert material.

For ceramics the problems are inter-related in that at normal temperatures the amount of gas released depends on the degree of lattice disturbance due to radiation damage. In the extreme case all the gas produced will be evolved from the ceramic and accumulate within the capsule. Source designs must therefore include sufficient void space to accommodate this gas and prevent bursting of the capsule window even in the event of accidental exposure to high temperature. Since the bursting pressures are difficult to predict accurately by calculation, they have been determined by testing at normal and elevated temperatures for many TRC capsule types.

Fig 8 shows a stainless steel capsule used for sources containing up to 5 Ci ^{241}Am after internal pressure testing. Rupture of the window occurred at 1600 p.s.i.

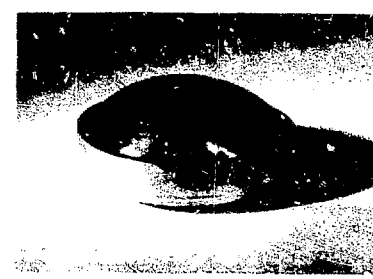

Fig 8 Stainless steel source capsule after internal pressure testing to destruction

This illustrates how for this type of capsule the problem is self-relieving to some extent since as the internal pressure rises the thin window bulges and thereby increases the available void space.

The effects of radiation damage in the insert are also difficult to predict theoretically. For alpha emitting nuclides it is likely that most effects result from the displacement of atoms by the recoiling decayed nucleus. Although the threshold energies for this process in ceramic systems are not well known, it can be expected that for sources of high loading [Ci/cc] a large fraction of the lattice atoms will have been displaced from their original sites within a few years.

A programme of long term testing and inspection is currently in progress to study the effect of this damage on the physical properties of the ceramic.

Fig 9 shows a 5-year old sample containing 2.5 Ci ^{241}Am/cc of ceramic. Despite the massive internal radiation dose received, the ceramic layer remains hard and smooth, firmly bonded to the metal backing and shows no evidence of swelling or cracking at this stage.

Fig 9 2.5 Ci ^{241}Am source insert

Discussion

The continuous programme of development and testing at TRC whilst leading to improved source designs has also emphasized that a radiation source is a dynamic system in which ageing effects occur and accumulate and, moreover, that such effects can only be minimized not eliminated by good design practice. Sources of this type should not therefore be expected to retain their initially high performance standards indefinitely but should be regarded as having a limited working life not related to the long half-life of the nuclide but determined by the particular source design and the environment in which it is intended to be used. This should not prove to be a great disadvantage since for the typical source designs described in this paper recommended lifetimes are likely to be at least 15 - 20 years in normal conditions and to exceed the life of any associated instrumentation.

This attitude is now becoming customary in countries which require licensing of each source type, and where the authorities frequently request a statement of the estimated maximum working life for each design.

It is considered that this approach and the further development of improved source designs will result in the continuing safe use of sources based on these potentially hazardous materials, despite the widespread and varying range of applications.

REFERENCES

1. K D B Johnson, J R Glover and W H Hardwick "Work in the United Kingdom on Fixation of Highly Radioactive Waste in Glass". 3rd United Nations Conference on the Peaceful Uses of Atomic Energy. 1964, 14 244.

2. K H Ansell and E G Hall, "Recent Developments in Low Energy Photon Sources". Applications of Low Energy X and Gamma Rays. Ed C A Ziegler Gordon and Breach 1971

3. "Sealed Radioactive Sources - Classification" ISO/DIS 2919. 2.

APPENDIX 1

CLASSIFICATION OF SEALED SOURCE PERFORMANCE STANDARDS

Test	Class 1	2	3	4	5	6	X
Temperature	No test	-40 °C (20 min) -80 °C (1 h)	-40 °C (20 min) -180 °C (1 h)	-40 °C (20 min) -400 °C (1 h) and thermal shock 400 °C to 20 °C	-40 °C (20 min) -600 °C (1 h) and thermal shock 600 °C to 20 °C	-40 °C (20 min) -800 °C (1 h) and thermal shock 800 °C to 20 °C	Special test
External pressure	No test	25 kPa absolute to atmospheric pressure	25 kPa absolute to 2 MPa absolute	25 kPa absolute to 7 MPa absolute	25 kPa absolute to 70 MPa absolute	25 kPa absolute to 170 MPa absolute	Special test
Impact	No test	50 g from 1 m	200 g from 1 m	2 kg from 1 m	5 kg from 1 m	20 kg from 1 m	Special test
Vibration	No test	30 min 25 Hz to 500 Hz at 5 g_n peak amplitude	30 min 25 Hz to 50 Hz at 5 g_n peak amplitude and 50 Hz to 90 Hz at 0.635 mm amplitude peak to peak and 90 Hz to 500 Hz at 10 g_n	90 min 25 Hz to 80 Hz at 1.5 mm amplitude peak to peak and 80 Hz to 2000 Hz at 20 g_n	—	—	Special test
Puncture	No test	1 g from 1 m	10 g from 1 m	50 g from 1 m	300 g from 1 m	1 kg from 1 m	Special test

Proceedings, ERDA X-and Gamma-Ray Symp. Ann Arbor, MI, May 19-21, 1976 (Conf 760539)

THE NUCLEAR DATA PROJECT DATA BANK*

M. R. Schmorak and M. J. Martin
Oak Ridge National Laboratory, Oak Ridge, Tennessee 37830

Introduction

The Nuclear Data Project, part of the Physics Division of the Oak Ridge National Laboratory, has as its main responsibility the collection, evaluation, and dissemination of nuclear structure information for the basic research community. This information is published in the Nuclear Data Sheets.[1]

Prior to 1971 the Nuclear Data Sheets[1] were produced manually. The tables of experimental nuclear data, as well as the compilers' comments, were typed, and the drawings summarizing the nuclear level schemes were drawn by draftsmen (only the reference lists were computer readable). By 1971 parts of the drawings were being produced by computer, and now (1976) the bulk of the drawings, tables, and comments is produced essentially automatically from the Nuclear Data Project data bank (also referred to as ENSDF, Evaluated Nuclear Structure Data File). This automation process has improved the efficiency of production, increased the reliability of the product, and enabled retrieval of information on request. In particular, the evaluated data can be of use in applied programs which require an authoritative base of radioactive decay information

I. Input to the Data Bank

A. Physics

The physical quantities can be divided (somewhat arbitrarily) into 1) nuclear level properties such as energy relative to the ground state, half-life, spin and parity, static electromagnetic moments, probability of radioactive decay branches and 2) radiation properties such as α-, β-, γ-radiation energies, intensities, time-coincidence relationships, multipole orders, association with other related radiations (e.g., conversion electrons, X-rays, neutrinos). Uncertainties are given where available.

B. Organization

The details of the organization of information are given in ORNL-5054.[2] A brief description is given below. The information is keypunched on standard IBM equipment. Separate punched cards, called records, are used for each level and radiation; α-, β-, and ϵ-radiation cards follow physically the level card they feed, and γ-radiation cards follow the level card they deexcite. The punched cards are grouped into "data sets".

The ENSDF standard formats, from which data sets are built up, are shown in Fig. 1. The nucleus label appears in columns 1-5. Column 8 contains the record type: L for level, G for gamma (γ), B for negatron (β^-), E for positron (β^+), and/or electron capture (ϵ), A for alpha (α), Q for Q-value, N for normalization, and P for parent. For level records are given the level energy (E), spin and parity (J^π), and half-live (T), among other quantities. For gamma records are given the energy (E), relative intensity (RI), multipolarity (M), mixing ratio (MR), total conversion coefficient (CC), and (occasionally) the total intensity of photons + conversion electrons (TI). B-records contain the endpoint energy (E), intensity (IB), and log ft. E-records contain the total transition energy (E), positron intensity (IB), electron capture intensity (IE), log ft, and (occasionally) the total transition intensity IB + IE (TI). For alpha records are given the energy (E), intensity (IA), and hindrance factor (HF). The parent record contains the level energy [0.0 for the ground state (E), J^π, half-life (T), and ground-state Q-value. The normalization record contains data required to convert the relative photon intensities to photons per 100 decays of the parent. Uncertainties in the above quantities are denoted by "D", as DE, DRI, etc.

Data types other than those mentioned above can be included on continuation cards. In particular, average β^+- and β^--energies, K-, L-, etc., conversion coefficients, and K-, L-, etc., electron capture fractions are needed for the output program, MEDLIST, to be discussed below. Comments can be made relating to any of the data types. These are denoted by a "C" in column "7".

NUCLEAR DATA SET-ORNL NUCLEAR DATA PROJECT

STANDARD FORMATS

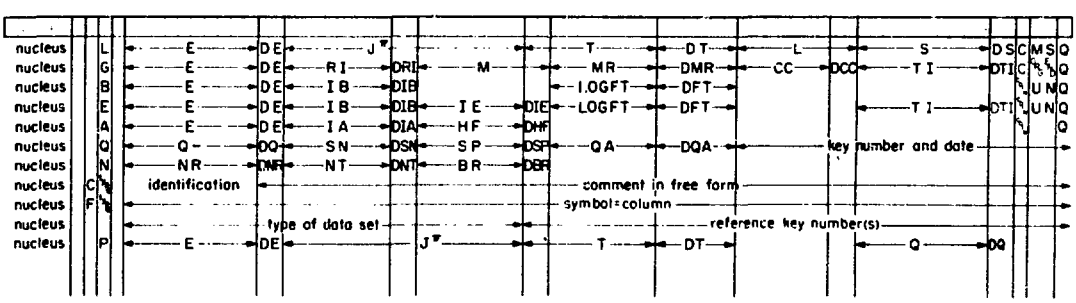

Figure 1

Figure 2 shows a sample data set.

88SR 88Y EC DECAY

is the "name" of the data set that contains all "adopted" information on β^+-radiations and γ-rays following ^{88}Y EC-decay and on levels in ^{88}Sr fed in this decay. Similarly,

88SR 86KR(A, 2NG)

is the name of a data set (not shown) that contains all "adopted" information on levels and γ-rays in ^{88}Sr observed in a ^{86}Kr(α, 2nγ) reaction.

The best and most complete information on nuclear levels, based on all available decay and reaction studies, is given in "Adopted Levels" data sets, together with nuclear mass differences (Q-values). Finally, the data sets are grouped into "A-chains" containing information relevant to all nuclides with mass number A. Each A-chain has a stated literature cutoff date and is the responsibility of one or more compilers.

C. Status Report

The number of evaluated data sets grows rapidly; at the present time (April 1976), there are 1230 radioactive decay, 1800 nuclear reaction, and 1540 "Adopted Levels" data sets.

II. Output from the Data Bank

The major output up till now has been the Nuclear Data Sheets.[1] The drawings show, to scale, some relationships of the nuclear levels and radiations; the vertical scale is energy (in keV). Information pertaining to levels of each nucleus can be shown side by side for ease of comparison. The tables include 1) adopted levels listed in order of increasing energy (ground-state and long-lived isomer properties usually include the radioactive decay branching probabilities in % of decay for the unstable nuclides; 2) tables of radiations grouped by type of radiation and listed in order of increasing energy; 3) tables of levels seen in nuclear reactions; and 4) literature references listed in chronological order. Figure 3 shows the ^{88}Y EC-decay data set as it would appear in the Nuclear Data Sheets. Figure 4 shows the decay scheme.

III. Gamma Rays and X-Rays

This being the topic of this symposium, I will mention in more detail our treatment of these topics. Gamma rays comprise a significant fraction of the bulk of information in the data bank.

The placement of a γ-ray in a decay scheme or nuclear reaction level scheme is established by physical location of the punched card (see Sec. 1.B and Fig. 2). Unplaced γ's are inserted before the first level card, and will appear in any γ-ray listing. The energy is given (usually) in keV with its uncertainty (in the last one or two digits). The annihilation radiation and tungsten $K_{\alpha 1}$ X-ray are considered as primary energy standards (the best measurements are accurate to 0.2 eV relative to the tungsten X-ray standard). As a rule, only a few of the very best data are corrected by compilers for changes in the γ-calibration standards (this being a time-consuming and uncertain procedure). The internal consistency of the decay scheme, as well as the degree of realism of the uncertainties in γ-energies, is checked routinely by a least-squares adjustment program; energies inconsistent by more than the standard deviation are flagged by the program, and the resulting adjusted level energies and uncertainties are used for the adopted levels data sets. (Systematic errors which are linear in the γ-energy cannot be discovered by this program.)

The γ-ray photon intensities are usually given relative to the intensity of one (usually among the more intense) γ-ray in the data set. The normalization record is then used to convert the relative intensity to other units. The computer program allows different choices of units for the data bank output (for example, γ-intensity in photons per 100 β^--decays, photons in % per decay, total intensity of photons + conversion electrons, etc.). A γ-intensity balance is calculated routinely for each level, and the deduced β^--, ϵ-, or α-decay branch is usually given and compared to direct experimental information when available. Note that the extent to which such deduced quantities are correct depends upon the correctness of the decay scheme and the intensity of any unplaced gammas.

The time and angular-correlation relationships among γ-rays can be deduced from the level scheme, provided the level half-lives, the relevant level spins, and γ-multipolarities are known. Conversely, experimental information on angular correlations and distributions is used to infer level spins and γ-ray multipolarities.

The large number and variety of calculations and other operations performed on one unique data set improve the reliability of that data set. This general observation is, hopefully, true also for γ-rays included in each data set.

An additional output format in which decay data sets can be provided is shown in Fig. 5. This output is generated by the program MEDLIST. Based on the data sets in ENSDF described above, and computerized tabulations of relevant Z-dependent constants (fluorescence yields, X-ray energies, etc.), MEDLIST calculates the energies and intensities of the atomic radiations (X-ray and Auger-electron transitions and conversion electrons). The program then combines these radiations with the nuclear radiations, sorts them according to radiation type, and within each type arranges and numerically labels them in order of increasing energy. A report[3] containing data on ≈190 nuclei in the format of Fig. 5 has recently been published by the Nuclear Data Project.

Specific information retrieval on request is becoming more common. This may involve information which was not published in the Nuclear Data Sheets (for lack of space) or information from several A-chains listed in a specific order (for example, a list of γ-rays in the actinide region listed in order of increasing energy or a list of γ-rays observed following a (d,p) reaction on any Sn (tin) nucleus. The information may be provided in computer-readable form (punched cards, magnetic tapes). The nature of further development of information retrieval capabilities will probably depend on user interests.

```
88SR    88Y EC DECAY
88SR  N 0.9935     3
88SR CN NR         FROM RI(1836+2734+3220G)=100
88Y   P 0.0          4-                107 D      1              3619      4
88SR  L 0.0          0+                STABLE
88SR  L 1836.06    2 2+
88SR  E 1783       4 0.20    1 5.8     6 9.76    5              6.0       7 10
88SR2 E K=0.840  $ L=0.101  $ M+=0.022  $ EAV=358 2$
88SR CE IB         FROM 63EH01 (0.20% 1), 04BA26 (0.203% 16)
88SR  G 1836.04    2 100
88SR  L 2734.08    3 3-
88SR  E 885        4            94.6    7 6.849   7
88SR2 E K=0.873  $ L=0.105  $ M+=0.023  $
88SR  G 898.02     2 94.0     7
88SR  G 2734.03    7 0.64     3
88SR  L 3218.47    5 2+
88SR  E 401        4            0.032   5 9.37    7                         10
88SR2 E K=0.852  $
88SR  G 1382.39    5 0.024    5
88SR  G 3218.48    8 0.0078  17
88SR  L 3584.7     8
88SR  E 34         4            0.066  13 6.8     2
88SR2 E K=0.69  5$
88SR  G 850.6      8 0.066   13
```

Figure 2

$\gamma(^{88}Sr)$ from ^{88}Y ε decay
γ-norm. from Iγ(1836+2734+3220γ)=100

Eγ	Iγ†
850.6 8	0.066 13
898.02 2	94.0 7
1382.39 5	0.024 5
1836.04 2	100
2734.03 7	0.64 3
3218.48 8	0.0078 17

† for absolute intensity per 100 decays multiply by 0.9935

Figure 3

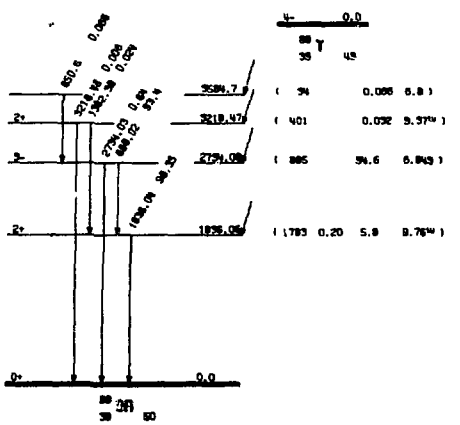

Figure 4

88Y EC DECAY (107 D 1) I(min)=0.10%

Radiation Type	Energy (keV)	Intensity (%)	Δ(g-rad/μCi-h)
Auger-L	1.79	105 6	0.0080
Auger-K	12	27.1 23	0.0070
β+ 1 max	761 4		
avg	358.0 20	0.200 10	0.0915
X-ray L	1.8	1.7 6	≈0
X-ray $K\alpha_2$	14.09790 2	17.6 8	0.0053
X-ray $K\alpha_1$	14.16500 2	33.9 14	0.0102
X-ray Kβ	15.8	9.1 4	0.0031
γ 2	898.020 20	93.4 7	1.79
γ 4	1836.040 20	99.35 3	3.89
γ 5	2734.03 7	0.64 3	0.0370

3 weak γ's omitted (ΣIγ = 0.10%)
Maximum γ-intensity = 0.40%

Figure 5

References

*Research sponsored by the U. S. Energy Research and Development Administration under contract with Union Carbide Corporation.

1. Nucl. Data Sheets (1959-1965), Nucl. Data B1-B2 (1966-1968), Nucl. Data Sheets B (1968-1972), Nucl. Data Sheets (1973-present), Nuclear Level Schemes, A = 45 through A = 257 (1973), Academic Press, Inc., New York and London.
2. W. B. Ewbank, M. R. Schmorak, F. E. Bertrand, M. Feliciano, and D. J. Horen, Nuclear Structure Data File — A Manual for Preparation of Data Sets, ORNL-5054 (June 1975).
3. Nuclear Decay Data for Selected Radionuclides, edited by M. J. Martin, ORNL-5114 (March 1976).

Proceedings, ERDA X-and Gamma-Ray Symp, Ann Arbor, MI, May 19-21, 1976 (Conf 760539)

X-RAY CALIBRATION SOURCES FOR THE 100-1000 eV REGION

Burton L. Henke

University of Hawaii
Department of Physics and Astronomy
Honolulu, Hawaii 96822

In order to calibrate windows, detectors and dispersive analyzers for low energy x-ray spectroscopy, certain characteristic line sources have been found to be particularly useful. These are obtained directly from an appropriate anode of a two-kilowatt demountable x-ray source, or from a fluorescent secondary radiator that is coupled closely to the x-ray source as shown in Fig. 1. Often the characteristic lines may be effectively isolated by filter and/or by pulse height discrimination with a proportional counter.[1] This is possible in the low energy x-ray region because the spectral line series are simpler and the line intensity relative to the associated continuum background is considerably higher than that for the ordinary x-ray region. This is illustrated in the spectra presented in Figs. 2 through 13 of fluorescent line sources in the 100 to 1000 eV region (10 to 100 A region). Also presented are typical absolute intensities as measured off a crystal analyzer and directly from the fluorescent radiator. The absolute characteristic radiation output intensities from three often-used anode sources for the excitation of the fluorescent lines are listed in Fig. 1. All intensities were measured with a calibrated proportional counter and with the window set to accept the full pulse height distribution. The measured intensities were divided by the appropriate x-ray tube window transmission. (Typical window transmissions are 50 to 80%.) The demountable x-ray source that is used in this laboratory is described in Fig. 14.

DIRECT SOURCE INTENSITY - I

PHOTONS / SEC - STEARADIAN - KILOWATT

(FOR CHARACTERISTIC RADIATION)

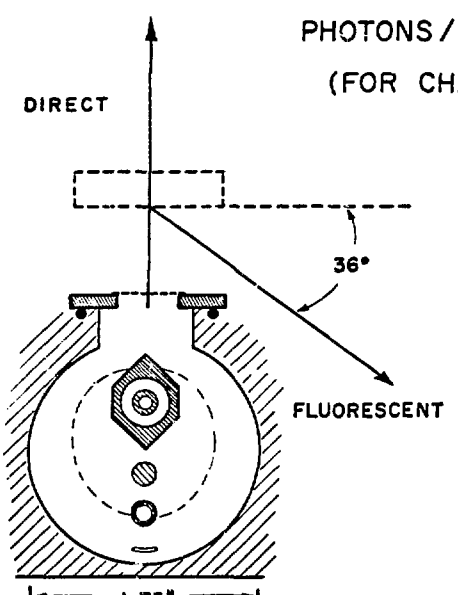

ANODE	RADIATION	I
ALUMINUM	Al-K_α (8.34 Å/1490 eV)	6×10^{13}
COPPER	Cu-L_α (13.3 Å/930 eV)	6×10^{13}
GRAPHITED COPPER	C-K_α (44.7 Å/277 eV)	2×10^{14}

Fig. 1. Showing the direct and fluorescent x-ray source geometries. Also listed are typical, absolute characteristic radiation output intensities from aluminum, copper and graphited anodes as used in the excitation of the fluorescent spectra shown in Figs. 2 through 13.

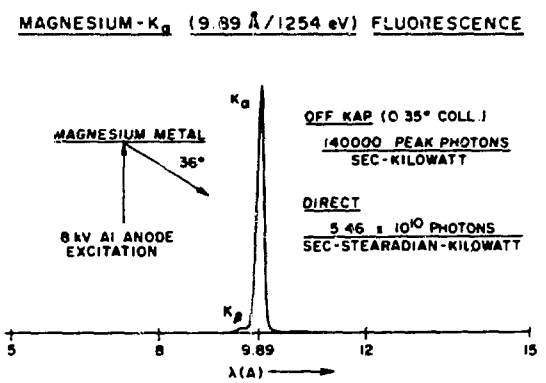

Figure 2

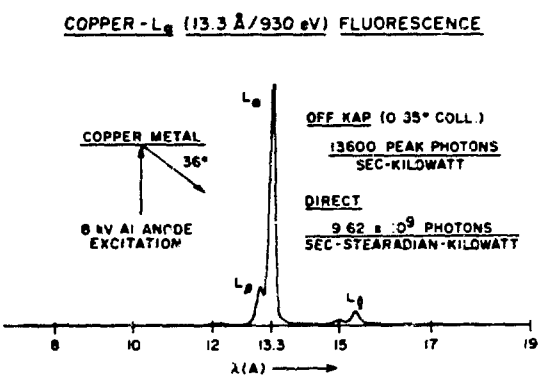

Figure 3

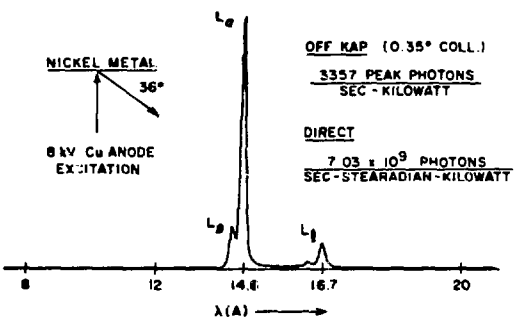

Figure 4

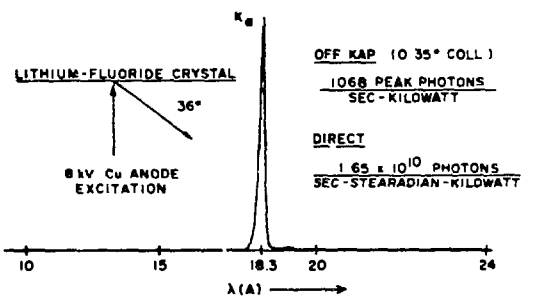

Figure 5

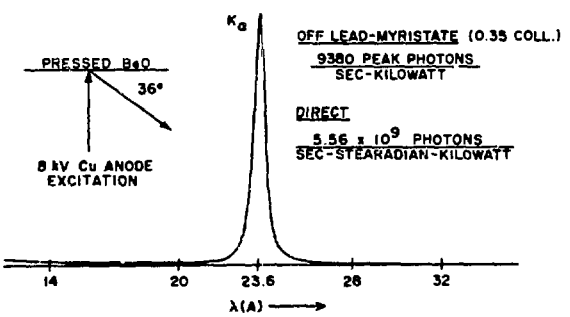

Figure 6

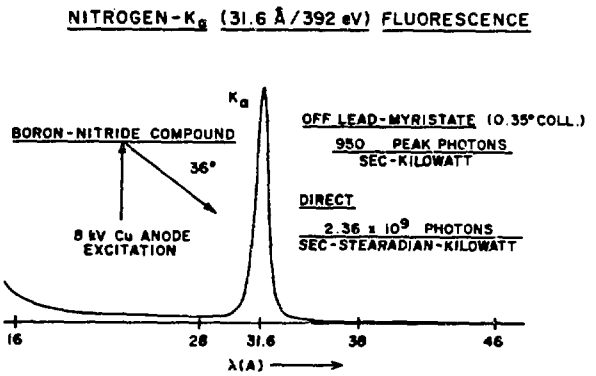

Figure 7

CARBON - K_α (44.7 Å/277 eV) FLUORESCENCE

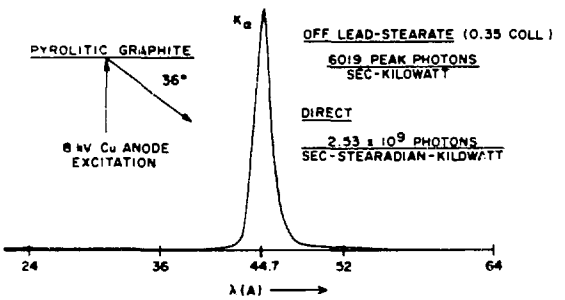

Figure 8

MOLYBDENUM - M_ζ (64.3 Å/193 eV) FLUORESCENCE

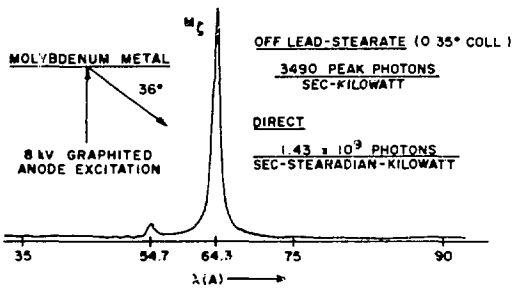

Figure 9

BORON - K_α (67.5 Å/163 eV) FLUORESCENCE

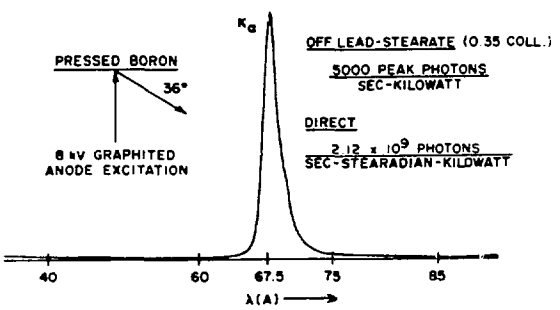

Figure 10

NIOBIUM - M_ζ (72.0 Å/172 eV) FLUORESCENCE

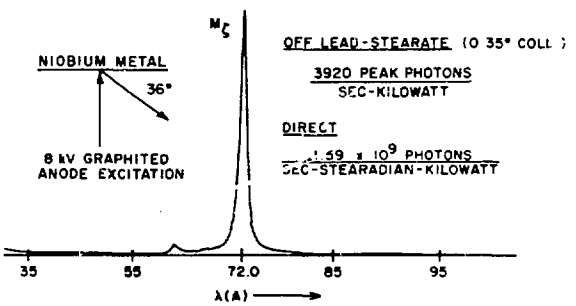

Figure 11

ZIRCONIUM - M_ζ (81.9 Å/151 eV) FLUORESCENCE

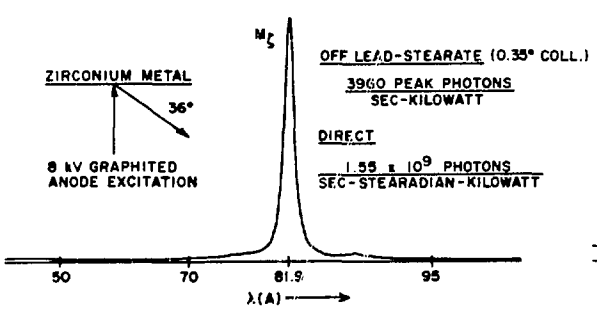

Figure 12

YTTRIUM - M_ζ (93.2 Å/133 eV) FLUORESCENCE

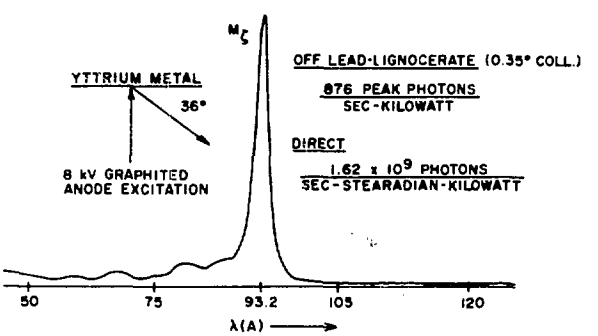

Figure 13

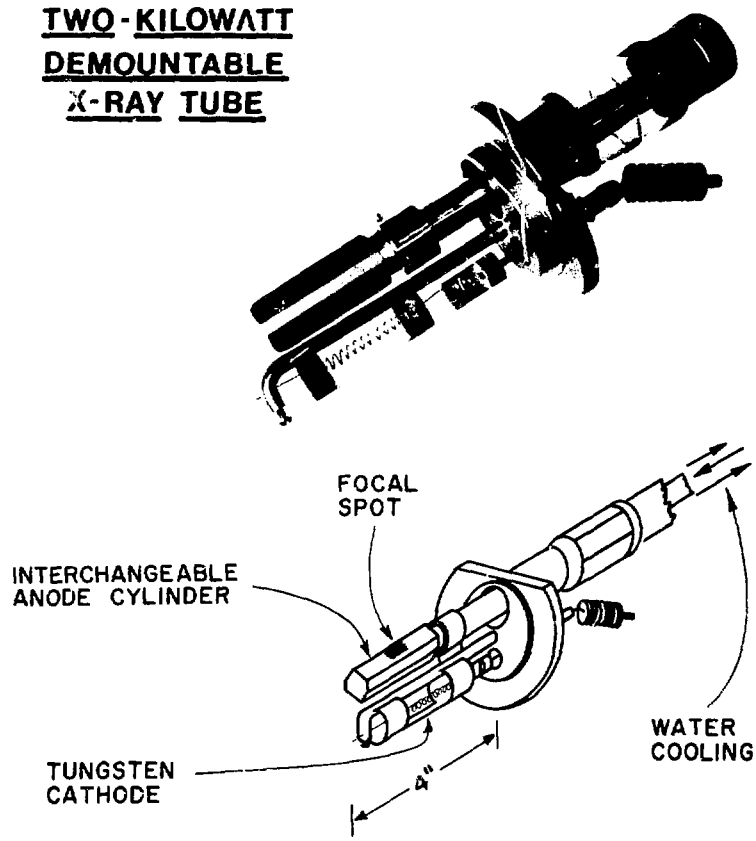

Figure 14

In Fig. 14 is shown the demountable structure of the x-ray source. The constructional details are available from the author. This tube design places about 1.5 square centimeters of effective anode area very close to a two centimeter diameter port over which a thin window may be introduced by a sliding vacuum isolation gate when the spectrometer has been evacuated. Because only the anode is at a positive potential, above housing and cathode ground potential, electrons reflected from the anode to the thin window arrive at essentially zero energy. This simple geometry allows the focusing of electrons from the tungsten filament into the effective anode region with sufficient intensity (at typical anode voltage of about 6 to 8 kV) to melt a heavily water cooled anode structure. By "hiding" the tungsten cathode below the anode structure, essentially no tungsten contamination of the effective anode area occurs. This tube is pumped by a parallel, closely coupled combination of a sputter-ion pump and a Zeolite molecular sieve trap both at about 10^{-7} Torr. These approaches assure that the target remains effectively clean through weeks of operation and thereby yields a constant output of useful line radiation that is characteristic of the target material. In the particular design illustrated here, the anodes are interchangeable (machined from ½" material and simply inserted into the water-cooling structure with a Viton O-ring seal).

Acknowledgements

I gratefully acknowledge the invaluable assistance in this work of Murray Tester and Priscilla Piano. This research program is supported by the Air Force Office of Scientific Research Grant No. 75-2762.

References

1. "Techniques of Low Energy X-Ray Spectroscopy (0.1 to 2 keV Region)," B. L. Henke and M. A. Tester, Advances in X-Ray Analysis (Plenum Press, New York, 1975), Vol. 18.

Proceedings, ERDA X-and Gamma-Ray Symp. Ann Arbor, MI, May 19-21, 1976 (Conf 760539)

CURRENT RESEARCH RELEVANT TO THE IMPROVEMENT OF γ-RAY SPECTROSCOPY AS AN ANALYTICAL TOOL

R. A. Meyer

Lawrence Livermore Laboratory,* University of California Livermore, CA 94550
and
International Committee for Radionuclide Metrology†

K. G. Tirsell and G. A. Armantrout
Lawrence Livermore Laboratory,* University of California, Livermore, CA 94550

Summary. We consider four areas of research that will have significant impact on the further development of γ-ray spectroscopy as an accurate analytical tool. The areas considered are: 1) Automation 2) Accurate multigamma ray sources, 3) Accuracy of the current and future γ-ray energy scale, and 4) New solid state X and γ-ray detectors.

Introduction

Several constraints become quite apparent when one considers what the scope of a presentation on γ-spectroscopy ought to be at this symposium. First, the past problems and current status are very well presented in the Herceg Novi International Summer School on Radionuclide Metrology.[1-9] Second, current research is aptly chronicled in the IEEE proceedings of its annual Nuclear Science Symposium[10-13] In addition, presentations at this symposium deal with some of the current problems and their solutions in far better detail than can be justly done in a single lecture. These facts and this symposium committee's guidance, that they wished us to explore the issues involved in the future of the field, lead one to ask what areas of current work will have the biggest impact on expansion of γ-ray spectroscopy as a common and accurate analytical tool? A review of the current literature shows that present and future work on automization, accuracy of measurement, and advanced design detectors certainly are three prime areas where significant developments can give a major impact. Indeed, these areas make up the majority of general problems to be considered as first priority by the International Committee for Radionuclide Metrology's (ICRM) Working Group on α, β and γ-ray Spectrometry. As pointed out by the chairman, Dr. Debretin,[14] we should explore "general problems related to:

- construction and type of detectors
- set-up of spectrometers (shielding, geometry, electronics, . . .
- calibration procedures
- sources and standards used for calibration
- data acquisition and analysis."

Here, we propose to 1) discuss an example of a highly automated γ-ray spectroscopy facility 2) present the results of some current research efforts at increasing the accuracy and simplicity for calibration of γ-ray intensities and, hence, detector efficiencies 3) discuss some aspects of precise γ-ray energy measurements and 4) discuss what areas of research in solid state detectors present the most promising prospects.

1. Automation of γ-ray Spectroscopy

As an example of a highly automated γ-ray spectroscopy facility, I have picked the facility of which I have the greatest familiarity. This facility, housed in LLL's Radiochemistry Division, processed in excess of 6,000 samples last year yet is staffed with a group of five workers headed by Dr. Ray Gunnink. The versatility of the system is illustrated by considering what variety of sample sizes and level of activities must be processed. Large, low-level samples from environmental research must be counted along with small high-level sources used in the diagnostics of underground nuclear explosions. In addition, various sizes and activity levels from activation analysis samples from the Livermore Pool Type Reactor and the LLL intense 14 MeV neutron source must be accommodated.

A significant factor in providing the high through put of samples is the presence of five automated sample changers. These 16 position changers feed a selected sample to a ram that positions the sample to be counted below a Ge(Li) detector at a preselected distance. The Ge(Li) spectrometers and the entire system is controlled by a central small computer. Entry of commands allows coded identification along with the selection of counting duration, source-to-detector distance or count rate and sequence of counting on one of the changers. During the counting period events in excess of 10^6 ("overflow")are automatically recorded. A central decimal day clock records start and stop counting times. The measured spectra are recorded on a disc and latter transferred, via magnetic tape to the LLL computations center for processing on CDC-7600 computers.

At this point, it is instructive to consider the actual analysis of spectra by large computer. "Spectral analyses can generally be divided into two parts; first, the reduction of the spectral features into understandable entities such as photopeak energies and intensities, and secondly, the quantitative interpretation of these items as disintegration rates, atoms or grams of specific nuclides or materials. Some of the spectral features we will now discuss are: 1) The proper form of the bacground continuum under a peak or peak multiplet, 2) The components of the observed peak shape, 3) Methods for fitting peak multiplets, and 4) Schemes for interpretating the observed peaks. Much of this material originates directly from R. Gunnink et.al's,[15] publications on GAMANAL and its applications.

If one were to consider a hypothetical detector system exhibiting no instrumental noise or line dispersions, all of the full-energy pulses corresponding to a given γ-ray would appear in one channel rather than as a broadened distribution. The background just before the peak presumably consists of degraded full-energy events resulting from such effects as "trapping" in the detector and low angle scattering by the source or materials surrounding it. It would appear that these produce events that would continue right up to the full peak energy; the result being a discontinuity or step in the level of the "background". If this is so, any processes that disperse the original narrow γ-ray line width will also smooth the background discontinuity. In GAMANAL, a procedure which closely represents the detector process initially interpolates a step function with the discontinuities occurring at the peak positions and with step heights proportioned according to the approximate peak heights. The region is subsequently smoothed with two or three cycles of linear smoothing.

There are at least three distinct components in the observed line shape of a gamma-ray photopeak. These are illustrated in Fig. 1. Additional structure may result from improper usage or alignment of the electronic components of the system. The major portion of the peak can be described by a Gaussian equation. However,

accurate data interpretation requires that the "short-term" tailing in particular not be ignored. The "long-term" tailing may be important in the analysis of some complex multiplets. Otherwise it can frequently be treated as part of the "background" as is done in GAMANAL. Gunnink has found an algorithm adequately fits the observed peak shapes.[15,16] Techniques have been found[15] whereby all of the peak shape parameters can be determined from two widely separated peaks in a spectrum.

The simultaneous fitting of several peaks in a multiplet is generally accomplished by some iterative method. For example, GAMANAL linearizes the equations by using the first terms of a Taylor's expansion about the trial values and then use a Newton-Raphson or Gauss iterative technique. Very complicated unfoldings can be made using this approach.[15]

If Ge(Li) detectors are to be used for quantitative measurements, they must be calibrated using appropriate sources. The counting efficiency at any particular gamma energy is dependent on a number of factors. Most of these are associated with the interaction process within the detector, the source-detector geometry, or with gamma-ray attenuations within the source or from surrounding materials. If the samples to be analyzed all have the same size, shape, set of radioactive components, and activity level, then it is possible to carry out a specific calibration for this sample type such that gamma-peak intensities can subsequently be directly converted to the desired units. This condition does not generally prevail in our case. As a consequence, Gunnink has developed a more flexible approach where he separates the overall efficiency into two components as follows: Efficiency = $\varepsilon \times G$, where ε = intrinsic efficiency G = a geometry factor (includes attenuation factors). This scheme requires only one efficiency curve, which can be used for all samples without regard for their shape, size, or activity level. A rather elaborate model has been developed to compute the geometry term and is discussed by Gunnink later in this session.

A popular method of interpreting a spectrum is to hand pick one or more gamma-ray peaks for each nuclide represented and to compute nuclide abundances assuming that no interference exists. Although this is very practical for some situations, it generally means that much useful data is discarded and furthermore, unanticipated interference may cause errors.

A more generally applicable approach is to assume that the observed intensity of each peak is a linear addition of intensities from one or more components, i.e., $Y_i = \sum_{j=1}^{J} A_j \cdot X_{ij}$, where Y_i is the intensity of the i^{th} peak in gammas/min, X_{ij} is the branching intensity of the j^{th} component at the i^{th} peak energy and A_j is the disintegration rate of the j^{th} component (a number that is to be determined). The calculational method is to write the equations in matrix form to find those sets of equations that are interdependent and then to solve them by the method of lease squares. This approach becomes almost imperative for complex spectra, such as mixed-fission-product and some activation-analysis spectra, because of the large number of unresolved peak interferences.[11-15]

2. Intensities

The large number of issues that ought to be discussed in relation to the measurement, standarization and utilization of γ-ray intensities could well take up the entire conference. Indeed, some of the major review papers and a full session of the First International Summer School on Radionuclide Metrology at Herceg Novi covered this topic. Those covered by Grinberg,[3] Spernol,[4] Campion,[5] Müller,[6] Cavallo et.al[7], Legrand[8] and Fink et.al.[9] state the issues very well. Hence, it would be only repetitious to explore the metrology problems discussed there. In addition, several talks in this conference are addressed to current efforts in the γ-ray intensity and efficiency calibration sphere. We have tried to avoid duplication of those subjects as well. Indeed, when one asks: "As far as the question of γ-ray intensities, what facet may have a major impact on the future of γ ray spectroscopy?" The availability of accurate, detailed multigamma ray sources of single long-lived nuclides emerges as a current "front runner". Automization of γ-ray spectrometers, such as we have discussed, certainly will open up new analytic uses. However, for large systems with high usage factors detailed calibration with many single γ-ray sources is not going to be possible or cost effective. Further, the fundamental aim of any metrologist is to improve the accuracy of his measurements. Le Gallic[17] as well as Mann[19] have pointed out that efforts are under way through the aegis of the Bureau International des poids et Mesures to improve the accuracies of their radioactive standards to the order of 0.1 percent. On the analytic usage side of the coin, the ability to identify and quantitatively measure radioactive constituents is limited, in some crucial cases, by the accuracy in the knowledge of both major and minor γ-ray components of a radionuclide's spectra. Let me cite an example from the field of environmental chemistry and its utilization of activation analysis. W. H. Zoller, G. E. Gordon and W. B. Walters[20] of the University of Maryland have pointed to two classic examples. In their work, zinc and mercury are two important elements that must be identified. However, zinc is identified only by the 1115 keV γ-ray of ^{65}Zn and mercury by the 279-keV γ-ray of ^{203}Hg. A number of other workers have been mislead in attributing Zn to a low abundant impurity. Once rare earth terbium is present, neutron capture in ^{159}Tb produces significant amount of ^{160}Tb and it has a low abundance 1115 keV γ-ray that can give false identification of Zn. To add to this ^{154}Eu, ^{110}Ag and ^{46}Sc have 1115 keV γ rays that can interfer. Similarly, mercury can be mistakenly identified when ^{75}Se, ^{192}I or ^{129}Te are present. Again, the latter two have low amount γ rays of identical energy, hence, are not obvious as the ^{75}Se interference. Hence, efforts aimed at delination of accurate values of both high and low intensity γ-rays will allow the γ ray spectroscopy field to extend its utility.

Here, we wish to point to some technological problems associated with multi-gamma sources, then present some cross evaluated multi-gamma sources that have emerged as a result of the LLL-Radiochemistry Division's nuclear structure research effort.

The major technological problems concern dead time effects, summing, and an accurate knowledge and description of large volume Ge(Li) detector efficiences below 200 keV. A discussion of dead time and pile up problems is a vast subject in itself and I refer to the fine Herceg Novi Summer School article by J. W. Müller[6] for that subject. The paucity of accurate γ rays in the range up to 200 keV has hindered accurate description of the Ge(Li) efficiency curve in this critical region. Here a number of workers, including NBS and LLL have adopted a procedure of matching two analytic functions in order to describe the efficiency curve, one to cover the region up to 200 to 300 keV and one for the region above (at least to 3 to 4 MeV). Both calibration and analytic uses are hampered by the summing nemesis. For most multi-gamma sources accurate calibration ought to be performed at a minimum of 10 cm if not 20 to 30 cm. Examples of the summing problem in analytic work comes from applications where low intensity samples, must be counted at small distances to gain any results. Activity such as ^{152}Eu can have a 30 percent error introduced by not recognizing summing effects. Even at 3 cm some lines of ^{75}Se can be off by 16 percent. The literature values for ^{131}Ba γ-rays vary as much as 20 percent. Our work on this decay has been able to duplicate almost

every value . . . if we vary the source to detector distance. The final results, given later, were obtained by counting at distances of 20 cm or greater.

As a result of our research effort, which explores nuclear structure through systematic studies of the electromagnetic interaction in related nuclei, we have developed a set of long-lived multi γ-ray nuclides which are internally consistent. That is, they have been measured on the stable of cross calibrated spectrometers in existence at LLL. In Table 1, we present a selected list of those that may be useful as multi-gamma standards and shall use them to illustrate a few potentially interesting cases of multi-gamma standards of the future. To do so, we will break the discussion into two areas: Those multi-gamma sources below 2 MeV and those above 2 MeV. These two categories reflect the fact that a majority of the analytic natural and induced radioactivity measurements can be performed with spectrometer settings of 0-2 MeV while in-beam and research disciplines are more interested in the above 2 MeV region. Before continuing we wish to pause to stress a pragmatic point. A number of the researchers and standards laboratory workers are being forced to the conclusion that for high percision and accurate work, gain settings of less than 0.25 keV per channel are mandatory. Hence, for future analytic purposes, it would be useful to witness the availability and use of more 8096 channel analyses to allow 0-2 MeV measurements at 0.25 keV/channel.

For the region below two meV, we have already discussed the problems of efficiency shape and fitting up to 200 keV. The correct description of this region is still not resolved. Our best value for the ^{75}Se of exactly equal intensity for the for the two most intense γ-rays is quite different than that in the published literature. However, it is in agreement with preliminary results from the international standards laboratories. For the higher energies, two nuclides that have had increased attention are $^{110}Ag^{m}$ and ^{152}Eu. These two nuclides have much to speak for them as they can be produced easily (have large neutron capture formation cross sections and can be prepared relatively pure e.g., ^{151}Eu enriched isotope is inexpensive and high purity Ag-foil is readily available.) Our γ-ray list for $^{110}Ag^{m}$ is more extensive than in published literature and is a result of studies using the LLL Ge(Li) systems and the new LLL intrinsic Ge anti-Compton spectrometer described by Dave Camp in this session of the symposium. The ^{152}Eu has been studied by many workers, however, the relative intensity values in the literature again vary by large amounts e.g., normalized to 100.0 for the 344-keV γ-ray the 121 keV γ ray has relative intensities of 125, 110, 117, 103 and 105. These values presumably vary because of a combination of problems in the past, the main two of which are summing and knowledge of the low-energy efficiency curve. In Table 2. we compare the major lines measured at 30, 43, 67, and 100 cm on various LLL Ge(Li) detectors as well as the result values of Debritin,[21 22] Barrette et.al.[23] and Legrande.[24]

We have explored the question of how well we can fit a region of the efficiency curve above 300 keV but below 2000 keV. This was done as part of our recent studies on ^{134}Cs decay where special attention was given to the determination of the relative γ-ray intensities as precisely as possible. The errors shown for the intensities in Table 1 are a result of the measurements described in Ref. 88.

Is there a way one can test the relative efficiency curves that are in use today by using sources that have an inherent accuracy better than the known detector efficiences? The answer we contend is yes. However, there are very few instances where a concerted effort has been made and is an area where some research is much needed. First, we wish to recall some pertinent nuclear decay features. If a parent nucleus has a progeny (does the term "daughter" violate the equal rights ammendment?) which differs by a large spin charge then no decay can occur to the ground state. In this case it may cascade through several levels where maximum angular momentum charge occurs. In the ideal case, a γ-ray cascade will result with several γ rays of equally differing energy. We have encountered at least three cases $^{93}Mo^{m}$, ^{48}V and ^{46}Sc. In these three, their low Z does not allow significant electron conversion to occur. Our measurements can easily reproduce the required results within 2 percent. However, to reach the statistical accuracy possible of 0.3 percent special attention has to be given not only to recalibration of the detector but to the peak shape fit of each photopeak.

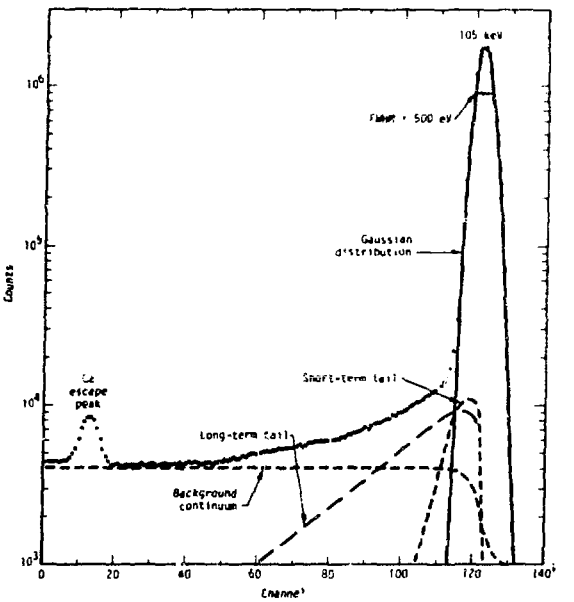

Fig. 1

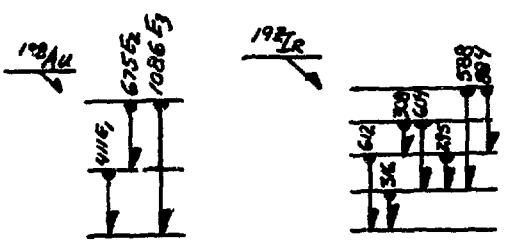

Fig. 2

3. Energy Standards

Although the current general usage of analytical γ-ray spectroscopy does not demand the full precision with which γ-ray energies can be determined some techniques are sensitive enough that errors of 1- or 2-eV in the energy of a peak can effect the final result. Applications which do require a precise knowledge of the γ-ray energies, we are led to ask: What limits our current knowledge of accurate γray energies? The continuing question of an absolute energy scale, determination of primary energy standards and their errors are the most limiting at the moment. We recall that using Ge(Li) detector systems, the relative energies of γ-rays can be measured with precisions of better than 10 ppm (10 eV/MeV). To achieve this precision, the inherent nonlinearity and poorly-defined zero characteristic of these spectrometers can be overcome by measuring the difference in energy between closely spaced lines, one of which has a "known" energy. Therefore, convenient energy calibration standards must be known with adequate accuracy. Moreover, since Ge(Li) spectrometer nonlinearities are normally measured with calibration lines, it is important that the distribution and number of lines be adequate.

Basic Reference Values: Some authors[30,31] have based their energy calibrations on two energy standards; the W $K\alpha_1$ - x-ray[32] line and the 412 keV line of ^{198}Au which is usually considered to be the working definition of the m_0c^2 (electron rest mass) scale. There are problems in using these scales. Besides being relatively wide, x-ray line shapes recorded using high precision, crystal diffraction spectrometers, for example, tend to be unsymmetric. Precise determination of x-ray centroids is therefore compromised.[33] Moreover, it has been suggested that x-rays emitted after ^{182}Ta β-decay, a source used in many earlier basic measurements, are shifted by 1.8 ± 0.5 eV relative to "normal" W $K\alpha_1$ x-rays,[34] a question which still remains to be resolved.[35] The second energy scale is based on the rest mass of the electron, m_0c^2, with a value known to within 3.3 ppm according to the Taylor 1973 adjustment.[36] The line from annihilation of a positron-electron pair, however, is not useful for energy measurements. The observed line is a few keV wide and shifted to a slightly lower value (by an amount which is material dependent) due to the annihilation of positrons with bound electrons. Therefore, most experimenters have used the 412 keV line of ^{198}Hg decay as a primary standard. The value for this line is based on a careful series of experiments by Murray, et. al.,[37,38] in which one of the externally converted lines of ^{198}Au are compared with the narrow component of the annihilation radiation using a high resolution electron spectrometer. The resulting uncertainty in this scale is 19 ppm which, incidently is equivalent to 68 eV at a γ-ray energy of 3500 keV. Until recently, the only confirmation of this 412 value involved a comparison with the 412 value based on the W $K\alpha_1$ scale.

In comparing 411 values based on the two primary scales, one must revise Murray's m_0c^2 comparison results to incorporate new information (recall Taylor's revision) being careful not to introduce any x-ray scale dependence. The best value for 411 based on the W Kα, scale is obtained from a weighted average of three direct comparisons using crystal-diffraction spectrometers and a fourth value by Greenwood et.al. who summed low energy lines in ^{183}Ta to obtain a 406-keV crossover γ-ray and then measuring the 406-411 energy difference. The low energy ^{183}Ta lines were compared directly with W Kα, using crystal diffraction methods. Averaging the four results yields a value based on W Kα of 411.794 ± 0.007 keV in exact agreement with the value based on m_0c^2. Combining direct measurements and measurements through 411 keV we obtain 1 ± 11 eV for the m_0c^2 energy increase needed to bring the scales into agreement.[39,40]

The accurate measurement of γ-ray energies will soon benefit from a series of extremely precise 412 keV calibration measurements being conducted by Deslattes, Kessler, et.al, at NBS.[41,42] They are bypassing the problems inherent in the two basic standards by relating the ^{198}Au 412 wavelength to that of a visible iodine line near 633 nm which is known to within ± .0009 ppm. The three stages of their measurement include: (1) establishing the lattice spacing in one or more Si crystals using the visible standard, (2) determining the lattice spacing of several Ge crystals by comparison with that of the Si, (3) measuring the diffraction angles of the γ-ray wavelength, very precisely using a two crystal transmission spectrometry. An accuracy better than 1 ppm (0.4 eV) is expected; this is equivalent to only 3.5 eV at an energy of 3500 keV.

Secondary Standards: In order to extend γ-ray energy measurements to higher energies, it is necessary to establish an appropriate set of secondary standards which have been referenced with precision against the primary absolute scale. In their respective reviews Marion[1] and Kern[2] both rejected a large number of precise crystal spectrometer measurements and chose to use results obtained using iron-free magnetic spectrometers (mainly that at Chalk River) in order to establish secondary standards. In using this procedure the density of secondary standards is not very great, there is a serious gap between 600 and 1200 keV, and little advantage is taken of the cascade method. Moreover since we have observed good agreement between 412 values measured using both types of measurements, its not clear that the crystal spectrometer results should be rejected.

Cascade-Crossover Method: A fundamentally sound method for "bootstrapping" to higher energies involves summing the energies of cascade transitions to obtain that of the crossover after correcting for recoil energy differences. Some cascades in the decay of ^{192}Ir are being used by Deslattes, et.al, example, to investigate small systematic energy-dependent uncertainties in their very precise series of measurements.

In their work Greenwood, Helmer, and Gehrke (GHG),[43,44] used the two different set of cascades shown in Fig.2 . as a basis for substantially increasing the number of standards below 1300 keV. The measured energy differences were obtained using Ge(Li) spectrometer techniques. The values obtained for energy differences are relatively insensitive to changes in the calibration energies. Explicit energy differences enable easier future revision in case more accurate primary standards become available. The authors have also done a more careful error analysis than one finds in much of the previous work. They explicitly identified the systematic error component of the fundamental energy value defining their energy scale. This reference error is clearly common to all γ-ray energies measured on this scale and must be identified in order that errors may be properly combined. It is perhaps their lack of rigor in obtaining weighted averages and in using a basic scale intermediately between the two energy sets which resulted in their work being rejected by Kern.

Ge(Li) γ-ray Energy Measurement Technique -- Error Components: In a precision Ge(Li) γ-ray-energy measurement, data from an "unknown" source (source to be measured) and from a set of standard sources are accumulated simultaneously. Energy values for lines in the unknown are then obtained by comparison with standard lines in the spectrum.

System Nonlinearity: To limit the uncertainty due to system nonlinearity, the unknown full energy peak should be relatively close to the standard to which it is being compared. A sufficient number of adequately well-known standards should cover the region to permit

the nonlinearity relation to be determined. Since the electric field effect produces nonlinearity,[16] the sources should enter the detector at the same range of angles as the standards and preferably in a perpendicular direction with respect to the source.

Good technique must be used in developing the nonlinearity curve and handling the associated errors. In order to take into account the combined system nonlinearity, we least-squares fit the standards in each spectrum with a power series polynomial of the form:

$$E_i = \sum_{n=0}^{N} a_n D_i^n$$

where E_i is the energy corresponding to the channel C_i. For each of the standards, peak energies and centroids along with corresponding standard deviations were input to a computer code. The appropriate standard deviation of the energies includes only measurement errors, not the reference component to the total error. (Reference errors bear a common relationship to all of the standards and, hence, should not affect the weighting.) The code generates an error matrix which gives the total measurement error for any peak energy under consideration. This includes contributions due to the measurement error of the standards, the peak fitting errors and an error associated with interpolating between standards, that is, the size of the error envelope at a given energy depends on its proximity to the standards. For most spectra, a polynomial of order 4 or 5 proved to be adequate to fit the standards with an average deviation of less than that of the average statistical deviation of the standards. No apparent integral nonlinearity remained and the deviations from the fit suggest that differential nonlinearities are small.

Addition of Errors in the Cascade Method: A problem in using the cascade method which is not fully appreciated is the complexity in the error analysis. Because of the interdependence of errors, a rigorous γ-ray energy error analysis, particularly when several cascades are involved, is very difficult. Consider the decay scheme shown in Fig.2 for which we wish to determine the energy and uncertainty of the crossover line ($E_{\gamma_3} - G_{\gamma_3}$) by measuring the energies of two cascade γ-rays (γ^1 and γ^2) with total uncertainties σ_{γ^1} and σ_{γ^2} respectively. Clearly

$$E_{\gamma_3} = E_{\gamma_1} + E_{\gamma_2} (+ \text{recoil corrections})$$

If the uncertainties in E_{γ_1} and E_{γ_2} are independent then

$$\sigma_{\gamma_3} = [\sigma_{\gamma_1}{}^2 + \sigma_{\gamma_2}{}^2]^{1/2}$$

Using a 25 eV scale error combined with 10 eV measurement errors for γ_1 and γ_2 (i.e., $E_{\gamma_1} \simeq E_{\gamma_2} \simeq 1$ MeV):

$$\sigma_{\gamma_3} = [(29)^2 + (29)^2]^{1/2} = 41 \text{ eV}$$

But can we assume that σ_{γ_1} and σ_{γ_2} are independent? Consider two cases:

Case 1. E_{γ_1} and E_{γ_2} are both determined by comparison with the same standard line -- then clearly the scale error σ_s is a systematic error component which must be separated out and added directly. Hence,

$$\sigma_{S_3} = \sigma_{S_1} + \sigma_{S_2} = 2\,\sigma_{S_1}$$

$$\sigma_{M_3} = [\sigma_{M_1}{}^2 + \sigma_{M_2}{}^2]^{1/2}$$

$$\sigma_{\gamma_3} = [\sigma_{M_3}{}^2 + \sigma_S{}^2]^{1/2}.$$

where σ_{mi} is the i^{th} measurement error. And for example:

$$\sigma_{\gamma_3} = [(10)^2 + (10)^2 + (50)^2]^{1/2} = 52 \text{ eV},$$

an increase of 21% over the result obtained by disregarding systematic components. If, however, γ_1 and γ_2 were compared to different standard lines, the effect would be less serious.

Case 2. Consider the same cascade with γ_1 and γ_2 each lying close to a different standard line.-- Can we now treat the errors in the two standards as being independent, giving

$$\sigma_{S_3} = [\sigma_{S_1}{}^2 + \sigma_{S_2}{}^2]^{1/2} ?$$

We can only if σ_{S_1} and σ_{S_2} have no common elements. But this is not usually the case. If the two calibrated γ-rays have a common "ancestor" (a standard line) from which their energies were obtained, then the uncertainty in the ancestor is common to both and is therefore a systematic component. Once this common element is identified, then the uncertainty in each standard is obtained from $\sigma_S = [\sigma_\delta^2 + \sigma_i^2]^{1/2}$

where $\sigma_\delta \equiv$ the systematic component of the uncertainty in the primary or secondary standard,

$\sigma_i \equiv$ the independent component of the uncertainty in the standard.

The total error due to the standards becomes

$$\sigma_{S_3} = [\sigma_{i_1}{}^2 + \sigma_{i_2}{}^2 + (\sigma_{\delta_1} + \sigma_{\delta_2})^2]^{1/2}$$

Based on Helmer et. al.,[44] it is reasonable to assume that of the 25 eV error in the standards, the systematic component is at least 21 eV. Using this along with other components used in Case 1 gives

$$\sigma_{S_3} = [(14)^2 + (14)^2 + (42)^2]^{1/2} = 46 \text{ eV},$$

and for the total error

$$\sigma_{\gamma_3} = [(20)^2 + (46)^2]^{1/2} = 51 \text{ eV}$$

which is still substantially higher than the 41 eV obtained when systematic components were disregarded. Of course, the effect of incorrectly handling systematic components decreases rapidly with increasing measurement errors. But it also increases with γ-ray energy since the error in the standards is dominated by the systematic component above about 1 MeV.

The frequently used procedure of obtaining level adjusted energies by means of a least-squares fitting scheme must be critically examined. Because of the interdependence of the errors involved, it is not clear how valid are the weights used for the averages. The error in the average level energy is too small because the assumptions concerning the input errors are not valid. What is needed and certainly does not now exist, is a similar procedure for obtaining level energies in which the errors are handled rigorously.

Gamma Rays in the 1.2 to 1.8 MeV Energy Range: As an example of the use of the cascade method to calibrate higher energy γ-ray lines, we will discuss the measurements made in the 1.2 to 1.8 MeV energy range. The isotopes ^{72}Ga, ^{82}Sr, ^{110m}Ag, and ^{124}Sb were used simultaneously for this region because they provide many cascade crossover combinations. As can be seen from Table 3 , there is a good distribution of crossover energies with which to define the nonlinearity curve. Note that we have tabulated the uncertainties due to the standards 412, and 675 separately to aid in the handling of errors. These intermediate energy crossovers will serve as secondary standards for the direct comparison of ^{72}Ga, ^{56}Co, and ^{56}Mn cascade lines which will enable us to extend the calibration work to 3.5 MeV.

Gamma Ray Standards up to 3.5 MeV:

Because the impact of the NBS calibration work will be very significant, particularly at these energies, we feel it is premature to present our results.

4. Basic Considerations and Future Prospects of Solid State Detectors

A semiconductor γ-ray spectrometer operates as a solid state ionization chamber. Their performance and ultimate resolution depend on a number of factors including charge generation statistics, signal "size", a multitude of charge collection effects, and the electronic characteristics of the amplifying system. Consideration of new detector types and comparison with present detectors requires understanding of these factors. In general, a large, fluctuation free signal is desired from the detector. The signal size, which is important in reducing electronic noise, depends on the average energy needed to produce an ion-pair. In general, this parameter does not vary significantly for different materials, ranging from 2.9 eV/ion pair for Ge to 4.33 eV/ion-pair for HgI_2.[47] Translated into electronic effects, this means that an electronics system which has 1 keV FWHM resolution for Ge would have 1.49 keV for HgI_2 - a material with nearly 3 times the bandgap. The value of the eV/ion-pair for other semiconductor materials of interest generally fall within this range.[48]

Another factor which becomes increasingly important at higher energies are the charge generation statistics. Due to a quantifying effect in the energy partition, true randomness is not observed so that observed statistical fluctuations during charge generation are reduced by a constant called the Fano factor, F, which takes on values from 0 to 1.[49] The signal-to-noise ratio is $\sim N/\sqrt{FN} = \sqrt{N/F}$ where N is the average number of ion-pairs produced in a given event. Quite small measured Fano factors have been found for Ge (0.06) and Si (0.08).[50] Larger Fano factors have been observed for other semiconductors, but these are probably not true values due to the increased importance of trapping effects.

The effect of the electronic noise depends on the detector size and geometry, detector technological excellence, and the detector energy bandgap. The latter is extremely important due to the exponential dependence of noise on the band gap energy (Eg) where noise ~ exp(- Eg/kT). For low energy γ-ray and x-ray applications, this noise is extremely important.

Up until now, we have considered only the effects on resolution of basic properties of materials. A very important line broadening effect is that due to "trapping". "Trapping" refers to the temporary or permanent loss of charge from the ionized state during collection of the charge in the crystal with a resulting loss in signal amplitude. A measure of trapping severity is the mean time before trapping, τ. Generally, the larger values of τ correspond to better spectrometer performance. In considering detector effects, a parameter termed mean trapping length, $L = \mu\tau\varepsilon$, is used where μ is the carrier mobility and ε is the electric field. In general, if the detector thickness, d, equals or exceeds L, then extremely large statistical spreads due to trapping can be expected. However, if $L >> d$, then resolution effects due to trapping are minimized. In most real-world detectors, it is not the value of L with relation to d which is most important - rather, it is the fluctuation in the value of L in different regions of the detector which is important. These fluctuations produce different amplitude responses from different portions of the detector which in turn result in significant line broadening, especially at higher γ-ray energies.[51,53] Since $L=\mu\tau\varepsilon$, localized fluctuations in the magnitude of the electric field, ε, represent one source of variation in pulse amplitude which adversely affects the resolution. These variations in ε can occur due to dopant fluctuations (as can occur as a result of partial loss of compensation in a Ge(Li) detector) or due to surface state charging effects. The other very important source of fluctuation in L is the variation in the trapping time, τ. These variations are caused by localized regions of high trap density. Such traps are caused by both deep level impurities and crystal defects and their control is extremely important for a high resolution spectrometer.

In summary, the parameters of importance for spectrometer performance are high mobility (μ), small Fano factor (F), small energy per ion pair (ε), minimal detector noise, excellent detector fabrication technology, negligible charge trapping. The parameters μ, F, and ε are optimized for a small bandgap material. Detector technology and trapping are optimum for elemental semiconductors and the detector noise is minimized by cryogenic cooling. Based on these collective considerations, Ge and Si will remain detector materials of choice for high resolution spectroscopy. For x-rays, Silicon has the advantage of lower detector noise and relative freedom from K-edge fluorescent x-ray escape artifacts. Germanium has the advantage at higher energies due to its smaller bandgap, higher atomic number and density. All other semiconductor materials are and will be of inferior spectrometer quality in the foreseeable future providing other factors such as the desire to operate the detector at room temperature are not of prime importance.[54] The only realistic alternate choices available at present for semiconductor detectors are the Group III-V and Group II-VI compounds and HgI_2.[55] However, the carrier diffusion length, L, for these materials is smaller by a factor of at least 10^4 as compared to that obtainable for Ge and Si so that the detector thickness, d, is greater than L for reasonable detector dimensions.[56] The result is relatively poor spectrometer performance for these materials.

Virtually all Si x-ray detectors are lithium compensated. Lithium compensation presents no stability problem and results in relatively uniform electric fields with a minimum applied detector bias. Trapping is an ever-present problem but its effect is minimal at lower energies. Electric field nonuniformities, especially near the edges, can result in "background" in the x-ray energy range. Various geometries and electronic means have been employed to reduce the contribution of these slow pulses so that significant background reductions have been achieved.[57] At present, the main limitations on resolution are electronic noise and the spread due to charge generation statistics with the result that attainment of the ultimate resolution is approaching an asymptotic value.

Germanium detectors, which are made either by lithium compensating P-type germanium (Ge(Li)) or by using high purity "intrinsic" germanium, are normally used for γ-ray spectroscopy where the ultimate energy resolution is required. Historically, it was relatively easy to compensate germanium by the lithium drift process and high quality spectrometers with active volumes in excess of 100 cm^3 were relatively easily made. Basic difficulties in fabricating these detectors have been overcome through years of research which included minimizing oxygen content, controlling dislocations and quenched-in point defects in the crystal during growth.[58,59] The main sources of trapping,[51,53,60,61] which included lithium precipitates, thermally-induced point defects, transition element impurities, and SiO_2 inclusions, are now well controlled and Ge(Li) detectors with active volumes > 50 cm^3 and resolutions < 1.8 keV FWHM @ 1.33 MeV are readily available.

While Ge(Li) detectors at present are less expensive and are available in larger volumes with excellent energy resolution than detectors made from high purity germanium (HP Ge), they do suffer from stability problems due to loss of compensation if accidentally brought to ambient temperature. Also, Ge(Li)

detectors which are subjected to radiation damage cannot be easily annealed but must be redrifted.[62] To overcome the stability problem, high purity germanium was grown by R. N. Hall[63] wherein the electrically active impurity concentration in the Ge was low enough such that a reasonable volume of detector material could be depleted with realistic bias levels in a PN junction. To achieve this, net impurity levels on the order of 2 x 10^{10}/cm^3 are needed before 1 cm of Ge can be depleted by 1000 volts bias in a P-N junction. This corresponds to an electrically active purity level of about 1 part in 10^{12}.

HP Ge detectors have a number of advantages. Since they are not formed by the lithium drift process, they are stable at room temperature. In addition: the fabrication time is hours rather than weeks since only a P-N junction need be formed, a wide variety of junction geometries are possible limited only by the depletion characteristics of the material, very thin P-regions are possible as opposed to the Ge(Li) detectors which normally contain undepleted P-type material which adversely affects spectra performance,[64] the N contact can be made much thinner since excess lithium is not needed for the drift process,[65] and the HP Ge detectors are relatively easy to anneal following radiation damage.[66] The present drawbacks of HP Ge detectors are their smaller available size and the relatively higher cost of the high purity germanium. These are being overcome as the technology and acceptance of HP Ge detectors advances.[67-69]

The actual spectrometer performance is for all practical purposes, the same for HP Ge and Ge(Li) detectors.[70] The main sources of trapping are crystal point defects such as vacancies and the SiO_2 inclusions.[61,71] Since these are some of the same traps of concern as in Ge(Li) detectors, similar trapping effects are expected. Some difference, however, is seen since electric field uniformity is more difficult to obtain in HP Ge due to the higher net ionized impurity density (~ 10^{10}/cm^3 for HP Ge versus ~ 10^8/cm^3 for Ge(Li)) and the apparent greater surface sensitivity of HP Ge detectors.[72-76] The actual ability to cycle HP Ge detectors between room temperature and 77°K is variable due to this surface sensitivity and generally requires the use of a clean vacuum cryostat where the thermal design is such that the detector is the last part to cool down.

Future detector developments using detector materials other than Ge and Si are being undertaken to gain specific advantages in terms of operating temperature or higher specific sensitivity per unit volume. Detector materials which have received significant attention in this regard include GaAs, CdTe, and HgI_2.[9] GaAs has the advantage of larger bandgap with reasonable mobility so that it can be used as an x-ray or γ-ray spectrometer at room temperature. Successful detectors have been made using epitaxial growth but they tend to be relatively thin.[77-79] Since the atomic number of GaAs is about the same as Ge, significant losses in efficiency will occur for such thin detectors used as γ-ray detectors.

CdTe has a higher atomic number and a large energy bandgap so that it can be used as a room temperature γ-ray spectrometer with reasonable efficiency.[80-83] However, CdTe has a relatively small hole mobility so L < d for the hole and trapping becomes a severe problem. Geometry changes have been employed to overcome the single carrier collection problem but this also introduces energy-dependent distortion effects on the spectrum. An additional problem with CdTe is the difficulty in forming effective blocking contacts. The result is a conductivity type of counter with relatively large leakage currents and an appreciable detector noise contribution to resolution.

HgI_2 is a large bandgap, high-z semiconductor which has shown some recent promise as an x-ray spectrometer.[47,84] While the detector noise is quite low and the specific efficiency is relatively high, HgI_2 has a very low hole mobility coupled with a low electron mobility. The result is that L < d for both carriers in all but very thin detectors. The successful detectors that have been used for x-ray spectroscopy are thinner than 1 mm and rely on only electron collection since all the x-rays are absorbed on one detector surface. Serious technological problems remain in growth, handling, and with trapping effects so that it is unlikely that HgI_2 detectors will make any serious contributions to γ-ray spectroscopy though there may be specific x-ray spectroscopy applications where they will be quite useful.

Any prospects for other room-temperature γ-ray spectrometers revolve around the availability of semiconductors with 1) band gap energy greater than 1.5 eV, 2) at least one high-z element in the matrix, and 3) good charge collection parameters in terms of carrier mobility and minority carrier lifetime. The most promising unexploited material is AlSb which, on the basis of computer simulated spectra, appears to be a good candidate for γ-ray spectroscopy.[85] However, AlSb is still in its technological infancy and significant developmental work is required.

*Work performed under the auspices of the U.S. Energy Research & Development Administration, contract No. W-7405-Eng-48.

†Member, Working Group on α,β, and γ-ray spectroscopy.

References

1. Proc. 1st Internat'l Summer School on Radionuclide Metrology, Nucl. Instr & Meth (NIM) 112 (Nr 1 & 2) (1973).
2. L.M.Cavallo, B.M.Coursey,, S.B.Garfinkel, J.M.R. Hutchinson and W.B.Mann, N.I.M. 112, 5, (1973).
3. B.Grinberg, NIM 112, 19 (1973).
4. A. Spernol, NIM 112, 23 (1973).
5. P.J. Campion, NIM 112, 41 (1973).
6. J.W. Muller, NIM 47, (1973).
7. G. Bertolini et.al., NIM 112, 219 (1973).
8. J. Legrand, NIM 112, 229 (1973).
9. R.W. Fink, NIM 112, 243 (1973).
10. Proc. IEEE NS-22,(1975).
11. Proc. IEEE NS-21,(1974).
12. Proc. IEEE NS-20,(1973).
13. Proc. IEEE NS-19,(1972).
14. K. Debertin (Private Communication 1976).
15. R. Gunnink & J. B. Niday, UCRL-76699 (1975).
16. W. M. Sanders & D. M. Holm, LASL Rpt. LA-4030(1969).
17. Y. LeGallic, NIM 112, 18 (1973).
18. W. B. Walters, Private Confession (1976).
19. W. B. Mann, NIM 112, 18 (1973).
20. W. H. Zoller, G.E. Gordon & W. B. Walters, Univ. of Maryland, College Park, MD (private communication 1976).
21. K. Debertin, U. Schotzig, K.F. Walz and H.M. Weiss, Proc. this Conf. (1976).
22. K. Debertin, U. Schotzig & H. M. Weiss, PTB - Mitteilungen 85, 187 (1975).
23. J. Barrette et.al., Can. J. Phys. 49 2462 (1971).
24. J. Legrand, J. Morel, & A. Traverse, Bull. d'Inf. B.N.M. 19 (Jan 1975).
25. L. Jonsson and R. Hardell, Proc. Internat'l Symp. on n-Capt γ-Spec, Studsvik, Sweden p199 (1969).
26. D.C. Camp & G. L. Meredith, Nucl. Phys. A166, 349 (1971).
27. M.E. Phelps, D.G. Sarantites & W. G. Winn, Nucl. Phys. A149 647 (1970).
28. T. Katou, NIM 124 257 (1975).
29. G. J. McCallum & G.E. Coote, NIM 124, 309 (1975).
30. J. B. Marion, Nucl. Data B4, 301 (1968).
31. J.Kern, Proc. Panel on CHG'D-particle Induced Radiative Capture, Vienna, IAEA, p.345 (1974).

32. J.A. Bearden, Rev. Mod. Phys. 39, 78 (1976).
33. e.g. see disc Ref. 45.
34. W. Beer and J. Kern Phys. Letters 47B, 345 (1973)
35. R.G. Helmer et.al., sub. to NIM 1976.
36. E. R. Cohen & B. N. Taylor, J. Phys. Chem. Ref. Data 2, 663 (1973).
37. G. Murray, R. Graham & J. S. Geiger, Nucl. Phys. 45,177 (1963).
38. ibid 63 353 (1965).
39. J. W. Knowles, Can. J. Phys. 40, 257 (1962).
40. P. H. M. Van Assche et.al., NBS Publication Nr 343, 271 (1971).
41. R.P. Deslattes, Proc. Conf. Gaithersberg, p.265 (1970).
42. E.G. Kessler, R.D. Deslattes, A. Henins and W. C. Sander, Bull. Am. Phys. Soc. 21, 621 (1976)
43. R.G. Greenwood et.al., NIM 77, 141 (1970).
44. R. G. Helmer et.al., NIM 96, 173 (1971).
45. R. Gunnink & J.B. Niday, LLL Rpt.UCRL 51061(1972).
46. R. Gunnink, R.A. Meyer, J.B. Niday & R.P.Anderson Nim 65 26 (1968).
47. S.P. Swierkowski et.al.IEEE Trans.on Nucl. Sci. NS-21,302 (1974).
48. R. Stuck et.al., ibid NS-22, 160 (1975).
49. C.A. Klein, ibid NS-15, 214 (1968).
50. H.R. Zulliger & D.W. Aitken, ibid NS-17,187(1970).
51. G.A. Armantrout & H.W. Thompson Jr.,ibid NS-17, 165 (1970).
52. J.W. Mayer et.al.,ibid NS-17, 221 (1970).
53. A.H. Sher, ibid NS-18, 175 (1971).
54. S.P. Swierkowski & G.A. Armantrout,ibid NS-22, 205 (1975).
55. G.L. Miller,ibid NS-19 251 (1972).
56. G. Ottaviani et.al.,ibid,NS-22 192 (1975).
57. J.M. Jaklevic & F.S. Goulding ibid NS-19 384(1972).
58. L.P. Adda et.al. ibid,NS-15, 347 (1978).
59. G. Lopes da Silva et.al., ibid, NS-15,448(1968).
60. R. Henck et.al. ibid NS-19, 229 (1972).
61. R.N. Hall ibid, NS-21,260 (1974).
62. F.S. Goulding & R.H. Pehl,ibid NS-19,91(1972).
63. R.N.Hall & J.J. Soltys,ibid NS-18,160(1971).
64. E. Sakai, ibid NS-18,208(1971).
65. R.H. Pehl & R.C. Cordi ibid NS-22,177(1975).
66. H.W. Kraner et.al., ibid NS-22, 149(1975).
67. R.O. Baertsch & R.N. Hall,ibid NS-17,235(1970).
68. R.N. Hall,ibid NS-19, 266 (1972).
69. W.L. Hansen & E.E. Haller,ibid NS-21,251(1974).
70. R.H. Pehl, et.al.,ibid NS-19, 265(1972).
71. P.A. Glasow & E.E. Haller, ibid NS-23,92(1976).
72. R.D. Baertsch,ibid NS-20,488(1973).
73. R.D. Baertsch,ibid NS-21, 347(1974).
74. V.L. Geleyunes, ibid NS-21,360 (1974).
75. R.J. Dinger,ibid NS-22,135 (1975).
76. H.L. Malm & R.J. Dinger ibid NS-23,76(1976)
77. A.J. Tavendale & E.M. Lawson,ibid NS-19,318(1972).
78. T. Kobayashi et.al., ibid NS-19,324(1972).
79. P.E. Gibbons & J.H. Howes,ibid NS-19,353(1972)
80. R.O. Bell & F.V. Wald, ibid NS-19, 334(1972).
81. K. Zano et.al.,ibid NS-21,315(1974).
82. H.B. Serreyl et.al.,ibid NS-21,404 (1974).
83. P.S. Siffert et.al., ibid NS-22,211(1975).
84. J.P. Ponpon et.al., ibid NS-22 182(1975).
85. J.H. Lee et.al., UCRL-77748 (1976).
86. R.Greenwood (private communication 1975).
87. L.G. Multhauf & K.G. Tirsell(private communication 1972).
88. J.R. VanHise, D.C. Camp & R.A. Meyer Zeit. für Physik 247 322 (1975).
89. The energies quoted in these tables were obtained using a set of γ-ray energies that we have adopted based on the value of 411.793 ± 0.005 for the ^{198}Au base line. These values must be altered by the scaling factor when Deslattes new value is adopted. Our adopted standards are an average of Greenwood[86] and coworkers and the unpublished work of L.G. Multhauf and K.G. Tirsell.[87]
90. R.A. Meyer (to be published 1976).
91. R.A. Meyer & D.Nethaway(to be published 1976).
92. R.A. Meyer & R. Yaffe (to be published 1977).
93. O.G. Lein III&R.A. Meyer(to be published 1977).
94. D.Brenner&R.A. Meyer(sub.to Phys.Rev 1976).
95. M.Lindner&R.A. Meyer (to be published 1977).
96. R.A. Meyer,W.B. Walters&F.F. Momyer,Z.Phys. 268 387 (1975).
97. S.V. Jackson&R.A. Meyer JINC(in Press)(1976).
98. W.R. Myers&R.A. Meyer(to be published 1977).
99. R.A. Meyer,R.G. Lanier&J.T.Larsen Phys.Rev. C13 339 (1976).
100. W.B. Walters&R.A. Meyer(sub. to Phys.Rev.C13,1976).
101. H. Easterday&R.A. Meyer(to be pub.) 1977).
102. D.S. Brenner&R.A. Meyer,Phys.Rev.C13 1125(1976).

Table 3 Gamma Ray Cascade and Crossover Transitions Used in the 1,2 to 1,8 MeV

			Error Components (in eV)			
Isotope	Crossover*	Measure.	675	411	Total	
Br-82	1317.440	5	8	16	19	619+698 827+1043-544
Ag-110m	1384.270	8	8	17	20	677+706 620+763 446+937
Ga-72	1464.047	11	8	18	23	629+834
Ag-110m	1505.001	8	16	18	25	620+884 686+818
Ag-110m	1562.266	11	16	19	27	744+818 677+884
Ga-72	1596.704	11	16	19	27	786+810
Sb-124	1690.949	10	16	20	27	645+1045 722+968

*based on the 411.794 keV Au scale. It must be recognized that these values will change by a scale factor that depends upon the 412-keV value currently being finalized by Deslattes.

Table 1 Intensity Values of Long-Lived Radionuclides that could Serve as Multigamma-ray Standards

$E_\gamma(\Delta E_\gamma)$	$I_\gamma(\Delta I_\gamma)$
$^{110}Ag^m$ (Rel)	[90]
116.482(46)	0.085(4)
120.223(26)	0.19 (1)
133.330(15)	0.77 (3)
219.342(15)	0.70 (2)
221.073(15)	0.72 (2)
229.417(23)	0.128(8)
264.247(58)	0.059(5)
266.906(12)	0.43 (1)
341.19 (19)	0.02 (2)
356.42(100)	0.045(5)
360.219(75)	0.035(7)
365.441(12)	1.02 (8)
387.065(12)	0.55 (2)
396.887(23)	0.43 (2)
409.320(45)	0.068(7)
446.797(15)	38.9 (9)
467.017(36)	0.26(5)
493.420(91)	0.11 (1)
544.541(45)	0.22 (1)
573.00 (40)	0.13 (1)
603.050(90)	0.042(9)
620.346(12)	29.4 (5)
626.246(12)	2.48 (4)
630.610(55)	0.40 (2)
657.749(12)	1000 (*)
676.560(100)	1.5 (2)
677.606(12)	112 (3)
686.988(12)	68.3(1.4)
706.670(13)	173 (2)
708.115(25)	2.9 (2)
744.260(15)	49.3 (8)
763.928(14)	236 (6)
774.77 (20)	0.2 (1)
818.016(15)	77.1(1.5)
884.667(14)	771 (15)
937.478(14)	363 (9)
957.344(85)	0.08 (1)
997.233(19)	1.32 (4)
1018.867(50)	0.15 (2)
1085.435(25)	0.71 (2)
1117.446(29)	0.52 (2)
1125.686(25)	0.30 (2)
1163.130(75)	0.79 (7)
1164.930(85)	0.50 (5)
1186.68(20)	0.015(5)
1251.025(42)	0.26 (1)
1300.00 (12)	0.[illegible] (1)
1334.307(19)	1.49 (5)
1384.270(21)	261 (8)
1421.045(50)	0.24 (2)
1475.759(25)	42.4 (8)
1505.001(25)	140 (4)
1562.266(25)	12.6 (7)
1572.31 (20)	0.012(3)
1592.632(95)	0.22 (1)
1629.651(65)	0.046(5)
1775.377(39)	0.063(4)
1783.435(30)	0.092(6)
1930.482(35)	0.16 (1)
2004.69 (10)	0.011(2)
[88]	
— 134 - CS —	
— See Text —	
242.89 (5)	0.0210(8)
326.45 (10)	0.0144(6)
475.35 (5)	1.465(40)
563.26 (5)	8.38 (5)
569.29 (3)	15.43 (11)
604.66 (2)	97.56 (32)
795.76 (2)	85.44 (38)

$E_\gamma(\Delta)$	$I_\gamma(\Delta)$
801.84(3)	8.73 (4)
847.0 (2)	0.0003(1)
1038.50(5)	1.00 (1)
1167.86(6)	1.805(26)
1365.13(10)	3.04 (4)
[91]	
— 150 Eu —	
(35 Year)	
78.775(28)	0.86 (8)
135.05 (17)	0.12 (3)
205.142(79)	0.31 (4)
251.590(25)	1.80 (9)
272.778(87)	0.40 (5)
284.988(26)	1.74 (8)
286.286(15)	2.35 (8)
298.053(14)	6.71 (9)
305.688(75)	0.35 (6)
310.811(82)	0.31 (6)
314.98 (18)	0.18 (6)
333.963(12)	1000 (*)
340.369(35)	1.63 (15)
342.553(35)	1.77 (15)
345.947(19)	4.15 (15)
370.712(25)	1.12 (9)
372.719(25)	2.49 (9)
377.718(27)	1.18 (8)
381.980(26)	1.17 (8)
402.142(12)	8.13 (8)
403.35 (10)	2.50 (10)
406.508(50)	1.46 (15)
420.54 (22)	0.14 (6)
439.390(15)	837 (17)
448.778(12)	2.7 (1)
453.367(99)	0.27 (5)
458.363(61)	0.46 (5)
461.749(15)	8.60 (19)
464.102(72)	1.6 (3)
464.748(34)	3.5 (3)
474.486(25)	1.51 (7)
476.88 (13)	0.19 (5)
485.919(20)	1.72 (7)
505.508(25)	50 (1)
509.830(48)	1.3 (1)
515.779(5)	10.3 (2)
520.072(19)	4.8 (1)
540.531(59)	0.90 (7)
542.958(25)	1.40 (7)
553.184(97)	0.34 (7)
571.245(15)	4.3 (1)
575.499(75)	0.32 (8)
584.259(12)	548 (15)
590.69 (11)	0.33 (5)
596.514(38)	0.77 (7)
607.309(29)	1.74 (5)
612.678(28)	0.97 (6)
615.149(33)	0.84 (4)
625.552(20)	3.23 (7)
637.81 (24)	0.15 (7)
658.263(55)	0.55 (5)
662.64 (15)	0.16 (4)
667.033(25)	2.7 (1)
675.839(25)	5.3 (1)
699.52 (29)	0.06 (4)
712.187(15)	11.3 (3)
731.202(24)	3.5 (1)
737.436(15)	100 (2)
744.448(26)	8.9 (1)
748.038(12)	54 (1)
749.778(28)	7.0 (1)

$E_\gamma(\Delta)$	$I_\gamma(\Delta)$
751.049(14)	22.3 (5)
756.493(26)	1.18(7)
759.547(85)	0.30(7)
762.015(85)	0.29(5)
773.263(15)	6.3 (1)
816.420(75)	0.51(5)
828.541(14)	6.09(18)
830.795(21)	5.54(12)
831.92 (25)	0.7 (2)
836.557(31)	3.2 (1)
838.381(79)	0.6 (1)
859.845(18)	6.1 (1)
869.234(14)	19.3 (2)
899.048(15)	9.8 (1)
910.859(41)	0.9 (1)
915.26 (2)	0.17(7)
923.244(19)	3.2 (1)
953.178(83)	0.47(7)
978.445(49)	0.21(5)
1046.150(55)	4.1 (5)
1046.708(55)	6.3 (5)
1049.016(25)	56 (2)
1070.975(25)	1.5 (1)
1081.433(48)	0.3 (1)
1083.314(31)	1.7 (1)
1115.32 (26)	0.16(6)
1122.827(15)	3.5 (1)
1165.710(27)	1.1 (1)
1170.557(24)	13.9 (2)
1193.796(24)	8.3 (2)
1197.078(24)	11.8 (4)
1246.936(24)	19.9 (5)
1251.216(28)	1.7 (1)
1261.946(27)	4.8 (1)
1308.642(23)	9.3(2)
1321.879(27)	1.8 (1)
1334.026(29)	4.3 (1)
1334.743(22)	27.0 (7)
1346.363(69)	0.30(7)
1350.255(31)	1.8 (1)
1379.083(55)	0.41(5)
1485.450(31)	19.8 (8)
1499.31 (10)	0.41(2)
1636.489(31)	7.5 (1)
1690.625(17)	1.6 (5)
1783.145(46)	1.07(3)
1818.471(75)	0.040(5)
1833.25 (15)	0.027(5)
[102]	
— 187 W —	
— (1 day) —	
16.61(2)	0.07 (1)
29.23(3)	0.044(10)
(36.38)	≤0.25
40.92(5)	0.02 (1)
43.66(6)	0.02 (1)
72.46(1)	129 (4)
77.37(5)	0.08 (2)
93.22(5)	0.07 (1)
100.14(2)	0.104(15)
106.59(1)	0.295(7)
113.75(2)	0.89 (2)
123.79(11)	0.03 (1)
134.22(1)	102 (2)
138.50(6)	0.05 (2)
165.67(40)	0.010(4)
168.50(40)	0.030(11)
198.34(12)	0.020(5)
206.29(3)	1.65 (4)
208.29(16)	0.008(3)

$E_\gamma(\Delta)$	$I_\gamma(\Delta)$
239.03(3)	1.00 (4)
246.18(1)	1.38 (4)
275.61(12)	0.024(7)
352.86(17)	0.018(7)
374.31(14)	0.03 (1)
375.93(13)	0.04 (1)
454.92(2)	0.34 (2)
479.53(1)	253 (4)
484.15(3)	0.20 (1)
492.80(20)	0.3 (1)
511.76(1)	7.47 (8)
551.55(1)	59 (1)
564.62(19)	0.14 (5)
573.71(14)	0.006(2)
576.31(8)	0.077(11)
578.72(11)	0.011(4)
589.09(3)	1.41 (3)
612.92(42)	0.024(12)
618.37(1)	73 (1)
625.52(1)	12.6 (3)
638.65(13)	0.037(11)
647.30(25)	0.009(4)
682.34(20)	0.08 (8)
685.81(1)	316 (8)
693.06(22)	0.015(9)
745.21(2)	3.45 (8)
767.37(75)	0.018(7)
772.87(2)	48 (1)
816.56(2)	0.114(8)
825.95(25)	0.0027(4)
826.55(25)	0.0027(4)
844.70(50)	0.0028(16)
864.55(1)	3.89 (8)
879.43(5)	1.64 (3)
960.17(5)	0.0153(8)
1056.24(5)	0.0026(7)
1190.38(12)	0.0025(3)
1220.80(25)	0.00020(6)
1230.10(4)	0.0153(17)
[95]	
— 183 Re —	
40.976(*)	8(2)
46.484(*)	2520(140)
52.596(4)	699(35)
82.919(4)	80(2)
84.712(4)	275(16)
99.080(4)	850(35)
101.933(37)	4(1)
102.481(85)	0.8(4)
103.10 (10)	1.3(6)
107.933(5)	687(30)
109.731(5)	915(30)
120.372(90)	1.0(2)
144.125(1)	37(1)
160.532(8)	186(7)
161.342(24)	114(15)
192.646(15)	81(2)
203.269(15)	14(1)
205.081(15)	35(1)
208.812(14)	939(20)
209.890(17)	70(1)
210.30 (10)	3(2)
244.267(17)	130(3)
245.250(17)	81(12)
246.062(15)	417(12)
291.723(14)	1000(*)
313.021(15)	131(3)
353.998(15)	169(4)
365.614(19)	21(1)
406.593 (16)	7.9 (5)

Table 1 (continued)

$E_\gamma(\Delta E_\gamma)$	$I_\gamma(\Delta I_\gamma)$
^{99}Mo (141)	
— γ per 10,000 Decays	
40.586(15)	103 (5)
89.40 (20)	0.28(18)
140.462(15)	9062(181)
142.671(25)	2.27(7)
158.778(15)	1.67(8)
162.366(15)	1.16(5)
181.052(15)	604 (12)
242.280(76)	0.14(2)
249.024(27)	0.29(3)
366.412(15)	119 (3)
380.123(79)	0.90(3)
410.264(95)	0.19(4)
411.481(15)	1.44(6)
455.83 (13)	0.13(6)
457.591(29)	0.67(5)
469.617(70)	0.26(5)
490.52 (15)	0.11(4)
528.775(15)	5.36(11)
537.78 (15)	0.16(6)
580.490(65)	0.43(5)
581.28 (12)	0.10(5)
620.010(35)	0.23(8)
621.755(24)	2.56(8)
739.481(17)	1200(33)
761.755(76)	0.11(1)
777.901(20)	424 (9)
822.951(15)	12.7(4)
960.730(20)	9.1(2)
986.418(35)	0.13(1)
1001.318(18)	0.40(1)
1056.170(49)	0.10(1)
^{75}Se (90)	
24.390(55)	0.46(4)
66.059(15)	18.7 (1)
80.935(30)	0.19(4)
96.732(5)	57.2 (2)
121.118(7)	298.3 (7)
135.996(9)	1000 (7)
198.591(8)	25.4 (2)
264.651(3)	1000 (5)
279.528(5)	422 (4)
303.915(5)	22.3 (2)
400.647(9)	194.5 (8)
419.291(45)	0.18(3)
572.710(20)	0.60(3)
617.880(35)	0.077(4)
821.895(35)	0.0022(2)
^{125}Sb (100)	
110.892(12)	0.009(1)
116.952(11)	2.55 (4)
146.08 (10)	0.0062(4)
172.615(15)	1.82 (3)
176.334(11)	67.9 (2)
178.78 (5)	0.27 (4)
198.65 (6)	0.13 (3)
204.129(25)	3.23 (4)
208.088(25)	2.36 (4)
227.911(35)	1.32 (4)
314.94 (11)	0.042(4)
321.03 (4)	4.10 (4)
380.435(20)	15.2 (1)
408.01 (4)	1.83 (6)
427.889(15)	294.4 (9)
443.497(35)	3.03 (7)
463.383(15)	104.5 (2)
491.28 (-)	<0.0004
497.36 (12)	0.036 (4)
600.557(18)	177.8 (3)
606.641(19)	50.2 (1)
635.895(18)	113.2 (2)
671.409(20)	18.0 (4)
121 Tem+g (99)	
37.138(2)	13.3 (13)
65.548(8)	3.23(9)
81.788(15)	0.61(3)
103.850(78)	0.011(4)
212.189(27)	1039(12)
470.472(8)	17.5 (1)
507.591(5)	220 (1)
511.00	0.052(21)
573.139(4)	1000 (5)
909.847(15)	0.881(8)
946.989(15)	0.103(2)
998.291(5)	0.997(9)
1024.000(250)	0.0010(5)
1035.400(95)	0.0072(27)
1102.149(15)	31.8 (1)
1107.600(175)	0.005 (2)
1144.650(35)	0.0135(5)
131-Ba (93)	
54.876(25)	2.8 (9)
78.759(18)	24 (1)
82.479(35)	0.5 (2)
92.285(15)	20.8 (7)
123.828(12)	1000 (*)
133.635(12)	76.3(1.5)
137.383(18)	1.3 (1)
157.183(15)	6.9 (2)
216.113(12)	689 (20)
239.629(13)	93 (9)
246.913(15)	21 (1)
249.426(15)	98 (4)
294.482(15)	5.5 (7)
351.202(17)	3.4 (5)
373.236(15)	478(25)
404.033(15)	46 (2)
461.254(19)	4.0 (2)
480.404(14)	11.7 (5)
486.511(15)	73 (1)
496.317(15)	1612(35)
534.14 (10)	0.26(5)
572.706(15)	10.5 (8)
585.043(14)	45 (3)
620.149(18)	51 (3)
674.462(25)	4.7 (4)
696.534(15)	6.0 (4)
703.40 (10)	0.3 (1)
831.594(35)	8.5 (5)
914.096(25)	1.9 (1)
919.33 (19)	0.23(4)
923.877(15)	25 (1)
1047.705(25)	48 (2)
83 Rb (90)	
9.39 (9)	131 (80)
K x-ray	1300 (280)
32.18 (5)	0.8(1)
119.32 (9)	0.32(5)
128.55 (12)	0.030(5)
237.19 (-)	< 0.011
520.41 (3)	1000 (50)
529.64 (1)	656 (30)
552.65 (2)	357 (15)
562.16 (7)	0.19(2)
648.96 (5)	1.9 (1)
681.17 (7)	0.7 (1)
790.14 (5)	14.7 (4)
799.36 (5)	5.3 (2)
67 Ga (98)	
— 3.261(1) days —	
91.235(35)	30 (2)
93.289(30)	366 (14)
184.564(30)	217 (9)
208.965(30)	24 (1)
300.222(25)	166 (4)
393.529(25)	45 (1)
494.120(30)	0.7 (1)
703.060(50)	0.10(1)
794.358(50)	0.53(3)
887.642(40)	1.49(5)
67 Cu (98)	
— 2.6 days —	
91.235(25)	6.8 (1)
93.289(21)	16.1 (3)
184.564(25)	49 (1)
208.965(25)	0.115(5)
300.222(25)	0.80 (1)
393.529(25)	0.22 (1)
93 Mo (92)	
114.024(9)	6.8 (1)
155.841(90)	0.10 (3)
263.062(5)	569 (8)
385.375(85)	0.6 (1)
541.220(65)	0.6 (1)
572.760(63)	0.5 (1)
684.672(9)	1000 (3)
689.070(49)	0.7 (1)
844.900(200)	0.2 (1)
949.817(30)	1.2 (1)
1363.023(32)	7.9 (1)
1417.900(200)	0.3 (1)
1477.113(20)	994 (15)
48 V (97)	
803.23 (8)	1.5 (2)
928.32 (4)	7.7 (5)
944.101(7)	77.6 (9)
983.501(2)	1000 (2)
1063.88 (-)	0.05
1312.087(3)	975 (2)
1437.31 (7)	1.2 (2)
2240.341(17)	24.1 (4)
2375.0 (5)	0.10 (5)
2421.7 (5)	0.10 (5)
^{24}Na 1368.608(20)	
2753.964(38)	
^{56}Co 846.751(13)	
1037.815(15)	
1175.071(16)	
1238.253(17)	
1360.173(19)	
1771.305(26)	
1963.676(32)	
2015.135(28)	
2034.708(29)	
2598.394(33)	
3009.514(42)	
3201.895(46)	
3253.340(45)	
3272.909(45)	
3451.065(47)	
3547.835(61)	
^{60}Co 1173.208(15)	
48 Sc (97)	
175.357(5)	74.7 (7)
983.501(2)	1000 (3)
1037.496(2)	975 (3)
1212.849(7)	23.8 (2)
1312.087(3)	1000 (3)
131 I (96)	
80.183(2)	26.0 (3)
85.920(150)	0.0009 (5)
177.210(2)	2.63 (2)
232.17 (15)	0.014(8)
272.491(17)	0.56 (1)
284.298(5)	60.1 (1)
295.833(150)	0.007(4)
302.411(150)	0.045(9)
318.080(16)	0.79 (3)
324.643(25)	0.22 (4)
325.781(4)	2.49 (4)
358.380(150)	0.091(2)
364.480(5)	806
404.804(4)	0.56 (2)
449.570(170)	0.07 (2)
502.991(4)	3.58 (3)
636.973(2)	72.1 (2)
642.703(5)	2.18 (2)
722.893(2)	17.9 (1)
133 Ba (90)	
53.155(5)	34.8 (7)
79.621(5)	37.7 (9)
80.997(4)	512 (4)
160.605(25)	10.5 (3)
223.110(35)	7.1 (2)
276.397(7)	113 (2)
302.850(5)	292 (3)
356.005(9)	1000 (-)
383.849(9)	145 (2)
^{207}Bi 569.690(10)	
1063.637(14)	
1770.185(26)	
^{228}Th 583.179(10)	
2614.473(35)	
^{46}Sc 889.259(12)	
1120.518(14)	
^{65}Zn 1115.520	
^{95}Tc^{m} 204.117(6)	
252.950(15)	
582.069(14)	
786.183(15)	
820.607(15)	
835.133(15)	
1039.25 (2)	
^{137}Cs 661.645	
^{88}Y 898.022(13)	
1836.016(27)	

ADOPTED FIDUCIAL GAMMA RAY ENERGIES

See Footnote 89

Table 2. Comparison of γ-Ray Intensities in the Decay of ^{152}Eu

E_γ[a]	LLL[b,c,90] ($I_\gamma(\Delta I_\gamma)$)				Legrande[c]	Barrette et al.[c]	Debritin[c]
	d=30 cm (det X)	d=43 cm (det Y)	d=67 cm (det T)	d=100 cm (det K)[e]			
121	1064 (20)	1051 (23)	1042 (29)	1040 (3)	1068 (19)	1037 (45)	1072 (17)
244	284 (18)	284 (11)	287 (5)	277 (3)	280 (5)	281 (22)	279 (5)
295	16.8 (4)	16.7 (4)	16.8 (4)	16.4 (4)	16.0 (5)	16.1 (1.9)	-
344	1000 (-)[d]	1000 (-)[d]	1000 (-)[d]	1000 (-)[d]	1000 (-)[d]	1000 (-)[d]	1000 (-)[d]
367	31.9 (5)	32.4 (3)	32.6 (4)	32.0 (4)	31.8(11)	32.2 (2.6)	-
411	83.9 (7)	84.9 (3)	84.4 (9)	84.8 (6)	83.7(15)	83.9(71)	84.1 (1.3)
415	3.8 (4)	4.2 (1)	3.9 (2)	4.2 (3)	3.4 (6)	4.1 (8)	-
443	117 (1)	118.5 (1.2)	117.6 (1.3)	118.5 (9)	116.5(19)	119 (2)	116 (1.2)
488	15.5 (5)	15.8 (3)	15.2 (4)	15.7 (4)	15.2 (9)	15.4(19)	-
503	6.0 (5)	5.7 (2)	5.6 (3)	5.9 (5)	5.7 (5)	5.6 (8)	-
563	18.6 (5)	19.0 (8)	18.4 (4)	18.8 (4)	18.4 (8)	19.1(23)	-
566	5.0 (4)	5.2 (2)	5.0 (3)	5.0 (2)	4.8 (5)	4.5(11)	-
586	17.9 (4)	17.6 (5)	17.4 (4)	17.5 (7)	17.2 (9)	17.6(19)	-
656	5.6 (6)	5.7 (3)	5.4 (3)	5.5 (4)	5.1 (6)	5.6 (8)	-
674	6.6 (5)	7.1 (3)	6.6 (4)	7.1 (4)	6.6 (9)	6.7(11)	-
678	17.4 (5)	17.7 (2)	17.1 (5)	17.6 (5)	17.4 (8)	18.0(19)	-
688	33 (1)	32.9 (6)	32.4 (5)	32.9 (7)	32.1(10)	32.2 (7)	-
719	12.5 (8)	12.7 (3)	12.9 (5)	13.1 (6)	12.2 (7)	12.8(15)	-
764	6.4 (6)	6.8 (4)	6.0 (4)	6.9 (4)	5.4 (7)	7.1(11)	-
778	491 (7)	490 (4)	485 (5)	492 (4)	492 (8)	487 (34)	483 (4)
810	11.7 (7)	12.3 (8)	11.9 (5)	12.2 (6)	12.1 (9)	12.4(15)	-
867	160 (2)	161 (2)	160.4 (1.1)	161.2 (1.2)	158 (2)	157 (11)	-
919	15.7 (7)	16.1 (3)	16.1 (5)	16.5 (5)	15.5 (8)	16.1(26)	-
926	10.0 (7)	10.1 (2)	10.0 (4)	10.5 (5)	9.6 (8)	10.1(15)	-
964	553 (5)	551 (5)	549 (4)	554 (4)	548 (9)	544 (4)	546 (4)
1005	24.1 (7)	24.6 (3)	24.5 (5)	24.7 (6)	22.4(11)	24.3(38)	-
1086	373 (10)	385 (8)	382 (2)	369 (6)	384 (6)	393 (30)	374 (6)
1089	65 (2)	68 (1)	66.0 (6)	65 (1)	64 (3)	67 (7)	-
1112	515 (5)	514 (5)	515 (3)	516 (5)	513 (8)	506 (37)	505 (5)
1212	54 (1)	537 (8)	52.7 (6)	53.5 (9)	52.7(11)	55.1(44)	-
1249	7.0 (4)	7.3 (3)	7.0 (3)	6.8 (4)	6.8 (6)	6.7 (8)	-
1261	1.3 (1)	1.4 (1)	1.7 (3)	1.2 (2)	1.3 (6)	1.3 (4)	-
1292	3.9 (4)	3.7 (1)	3.7 (3)	4.2 (3)	4.3 (9)	3.8 (8)	-
1289	63.0 (7)	61.9 (5)	61.5 (5)	62.8 (4)	61.7 (1.1)	64.0(64)	-
1348	0.6 (2)	0.67(8)	0.6 (1)	0.6 (2)	0.7 (2)	0.7 (1)	-
1363	0.9 (3)	1.03(9)	1.0 (2)	1.2 (2)	1.0 (2)	1.0 (2)	-
1407	790 (8)	792 (6)	788 (5)	795 (6)	784 (11)	809 (22)	779 (6)
1457	18.9 (5)	18.8 (3)	18.6 (3)	18.5 (3)	18.5 (6)	19.1(22)	-
1528	10.0 (3)	10.1 (2)	9.8 (1)	10.0 (2)	10.1 (6)	10.1(11)	-
1768	0.3 (1)	0.35(3)	0.33(5)	0.3 (1)	0.3 (1)	0.3 (1)	-

[a] The E_γ values are currently being finalized. For values contact R. A. Meyer, LLL.

[b] Approximately twice the number of γ-rays as listed here have been identified using the new LLL intrinsic Ge Compton suppression spectrometer.

[c] Fiducial, the γ-ray intensities are quoted as relative intensities.

[d] The precise values of these γ-rays are being recalculated.

[e] Detector K efficiency curve: 93 Mo-m decay test: a relative efficiency curve is correct to < 1% (see text).

Proceedings, ERDA X-and Gamma-Ray Symp. Ann Arbor, MI, May 19-21, 1976 (Conf 760539)

APPLICATION OF STATE-OF-THE-ART MONTE CARLO METHODS TO GAMMA-RAY (AND ELECTRON) SOURCES AND DETECTORS

N. Vagelatos, N. A. Lurie, and J. P. Wondra

IRT Corporation
P. O. Box 80817
San Diego, California 92138

Introduction

Advances made in recent years make it possible — and more importantly, practical — to perform photon and electron transport in complex three-dimensional geometries. The purpose of this work is to acquaint the user community — experimenters and applied scientists — with the kind of calculational information which can be generated with present codes and computers. The central discussion involves the solution of coupled photon-electron problems using Monte Carlo methods in general, and the code SANDYL[1] in particular. The examples we present are results of such calculations obtained with this code. The emphasis on SANDYL is not intended to imply superiority over other codes, but is simply due to our greater familiarity with this code which we use routinely in our laboratory. It should be viewed as representative of currently available codes.

The Monte Carlo Method

Systematic development of Monte Carlo methods began in about 1944 with the work of Fermi, von Neumann, and Ulam on neutron transport.[2] Since then, as large, high-speed computers developed, Monte Carlo methods have been used to solve an increasingly larger number of complex problems. Indeed, many of these problems cannot be solved by any other means.

A general description of Monte Carlo methods is clearly beyond the scope of the present work. However, there are a number of good reviews of this subject which adequately fill this need and provide generous references to the literature.[2-5] Rather, we intend to illustrate the use of Monte Carlo methods for problems involving the detection and measurement of radiation from electron and gamma-ray sources.

There have been many photon and electron transport codes written with varying degrees of sophistication. Space limitations prevent us from describing the operation of the various codes. Instead, we will concentrate on SANDYL which is one of the most complete, general codes. Like many of the transport codes, SANDYL uses the physical approach which consists of random sampling and simulation of individual histories which are used to construct the solution to the physical problem. A transport equation is never explicitly written and solved. The only information needed to simulate a history is the probabilistic description of all events which may occur at each point in the history. The random, probabilistic nature of particle/radiation interaction with matter renders Monte Carlo methods particularly well suited to problems of particle/radiation transport. The necessary information in this case includes a description of the geometrical boundaries of the different regions through which transport occurs, the material composition of each region, and the cross sections (differential in energy and direction) of the constituent isotopes.

A simulation consists of generating a large number of particle histories one at a time, with primary particles starting at the source, and secondaries starting at their generation points along the trajectories. As the particles traverse the different regions of the system, the contributions to the quantities of interest are tallied following each collision to generate the desired information. The average of these quantities for a number of primary, and their induced secondary, particle histories represents a statistical approximation of the solution.

Photon histories are generated by tracing their trajectories from collision to collision. At each point of photon-medium interaction the type of interactions, secondaries and the new photon energy, direction, and distance to the next collision are determined on the basis of probability distributions characteristic of the medium composition. Photon collisions can result in photoelectric absorption, Compton scattering, or pair production. Secondary photons include bremsstrahlung, fluorescence, and annihilation radiation.

Electrons are treated in a slightly different manner because, as a result of being electrically charged, they suffer a much larger number of collisions. The method used for electron transport is known as condensed-history Monte Carlo.[6] Accordingly, an electron history is generated by following the trajectory in spatial steps of pre-computed length, so that the electron energy and direction at each point may depend on a number of different collisions which may have occurred in the previous step. Therefore, electron energies and directions are determined on the basis of multiple scattering distributions. Within a step, secondary photons and electrons are generated according to the corresponding probability distributions. Electron interactions include electron-electron collisions, bremsstrahlung radiation, and medium polarization. Secondary electrons which are followed include knock-on, pair, Auger, Compton, and photoelectric electrons.

Three-dimensional geometries with a high degree of complexity can be treated. The problem geometry is divided into zones of homogeneous atomic composition bounded by planes and quadrics. Options are available for splitting or biasing to improve the statistical uncertainty in certain problems. The code calculates flux or energy deposition (dose or spectrum) in any desired zones.

Photon and electron transport are followed in an energy range from 1 keV to 1 GeV or higher. The lower energy limit is a result of inadequate cross-section information for electrons below 1 keV. For most gamma-ray problems, a 1 keV lower cutoff is not a severe limitation.

In addition to SANDYL, there are a number of good codes which are similar; comparisons between the different codes are difficult to make with any generality. Potential users should consult the code centers at Oak Ridge National Laboratory and Argonne National Laboratory for information on available codes and their properties.

Examples of Results

The most sensitive test of gamma-ray transport calculations is comparison with measured pulse-height spectra. The first example is a calculation of the spectral energy response of an NE-213 organic liquid scintillation detector.[7] The liquid is contained in a pyrex glass cylinder and surrounded by an iron-nickel alloy magnetic shield. The purpose of these

calculations was to obtain a gamma-ray response matrix for this detector to be used for spectral unfolding.[8] The lack of monoenergetic gamma-ray sources with energies in a range sufficiently wide to determine the response matrix accurately, convinced us that the only practical means to generate this matrix was by calculation. However, in order to verify that our model of the detector and the computer code were satisfactory, measurements were made using available sources. A comparison of the measured pulse-height distribution for a ^{137}Cs source with the SANDYL calculated spectrum is shown in Fig. 1. Calculations were made of the energy deposited in the active region of the detector which is proportional to the light output and, hence, to the measured signal. The results were resolution broadened by folding the energy deposition spectrum with a gaussian resolution function. The low energy cutoff of this spectrum is approximately 100 keV, imposed by the noise of the detector electronics; the agreement is remarkably good. Similar results were obtained for other laboratory sources such as ^{60}Co and ^{22}Na; the former is shown in Fig. 2.

In most cases we found a minor discrepancy at the lowest energies where the experimental problems (background subtraction, noise, etc.) are most severe. Part of that discrepancy may be due to the energy degradation of the source radiation. It is rarely possible to obtain monoenergetic gamma rays from standard laboratory sources without some secondary or degraded primary radiation present. Fortunately, our Monte Carlo methods can also examine this problem. An example is presented in Fig. 3, which shows a rather crude calculation of the leakage spectra of a weak ^{60}Co source. Although

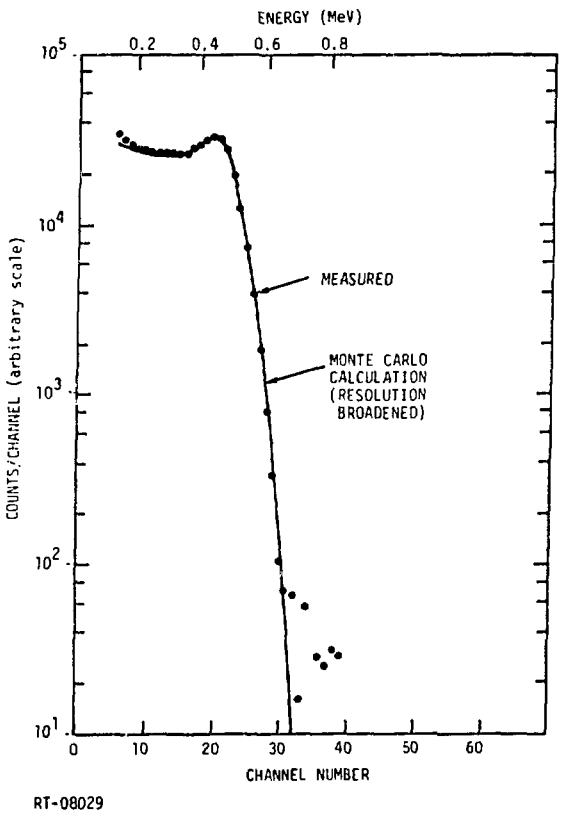

Figure 1. Comparison of measured and calculated pulse-height spectra for a ^{137}Cs source

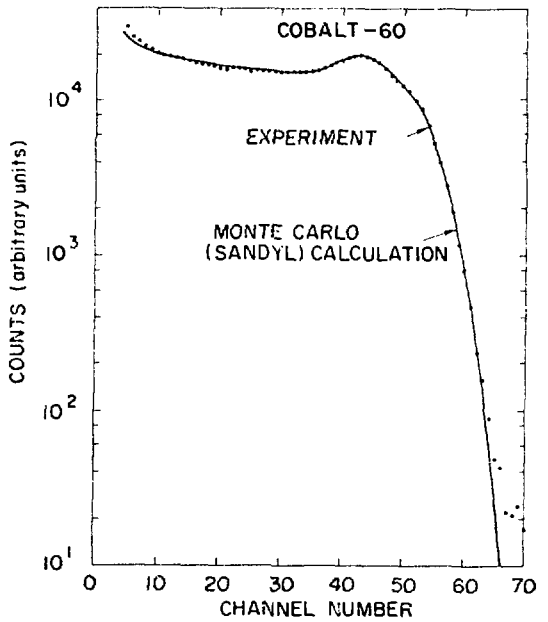

Figure 2. Comparison of measured and calculated pulse-height spectra from a ^{60}Co source. Complete source spectra (shown in Fig. 3) were used in the calculations.

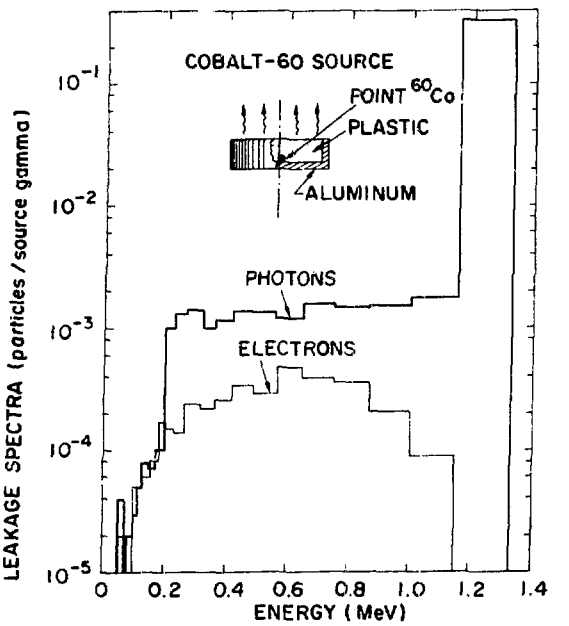

Figure 3. ^{60}Co source leakage spectra showing both photons and secondary electrons emitted from the top of the source

this was considered to be a very small, thin source, the energy-degraded or secondary radiation still represents about 5% of the total number of gamma rays. The effect is amplified by the fact that the lower energy part of the source spectrum is detected with higher efficiency than the primary source radiation. The ^{60}Co spectrum shown in Fig. 2 included the contribution of source secondaries. More detailed discussion of these results is given in Ref. 8. For large (kilocurie) gamma-ray sources, the problem can be much more significant. For a 5000 Ci ^{60}Co source at the Salk Institute, we found that approximately 35% of the source photons are energy degraded. Similar results can be obtained for electron sources.

Another comparison of calculated and measured pulse-height spectra using a different radiation detector is shown in Fig. 4. The detector in this case is a fully depleted silicon surface barrier detector which is surrounded by 1 cm of silicon;[9] the source was ^{137}Cs. As before, the energy deposition spectrum was broadened by a gaussian resolution function. Again, the agreement is quite remarkable. In formulating a model for this detector we learned a great deal about its principle of operation, especially the spatial variation of the charge collection efficiency in the sensitive region of the detector. The interested reader is referred to Ref. 9 for additional details.

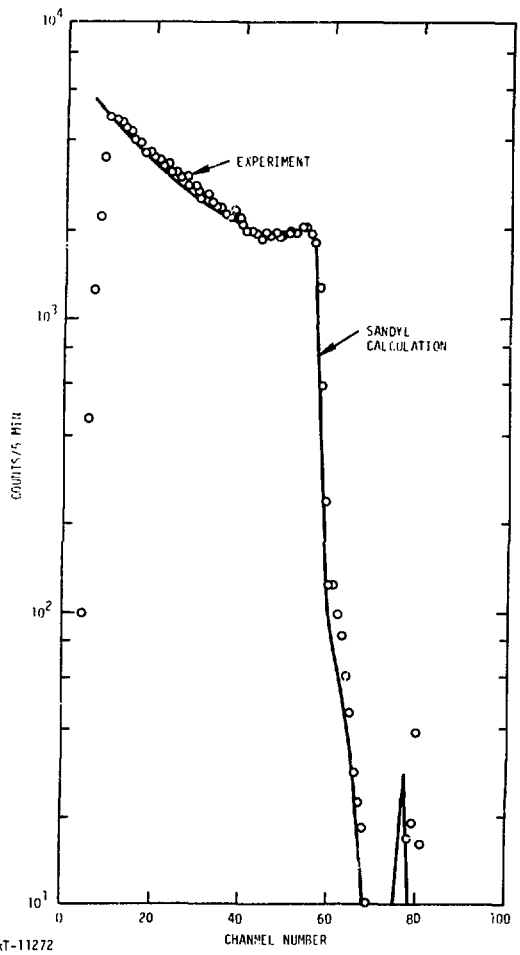

Figure 4. Measured and calculated pulse-height distributions for a ^{137}Cs source on the silicon surface barrier dosimeter

The purpose of showing comparisons for the two rather different detectors is twofold: (1) to display the remarkable quality of the calculated responses achievable by careful modeling and with presently available codes; and (2) to demonstrate the general nature of the calculations.

An example of a detector response to an electron source is shown in Fig. 5. The measurements were made by Berger et al.,[10] who also performed a calculation using the one-dimensional code ETRAN.[11] In this experiment, a 1-MeV electron beam, produced by a d.c. accelerator and collimated to 3-mm diameter, impinged on a 10-mm-diameter by 0.53-mm-thick diffused silicon detector. The experimental conditions constituted a good approximation to a one-dimensional slab. The results for both the ETRAN and SANDYL calculations are in excellent agreement with measurements. Similar agreement was found for the other detector thicknesses and source electron energies investigated by Berger et al.

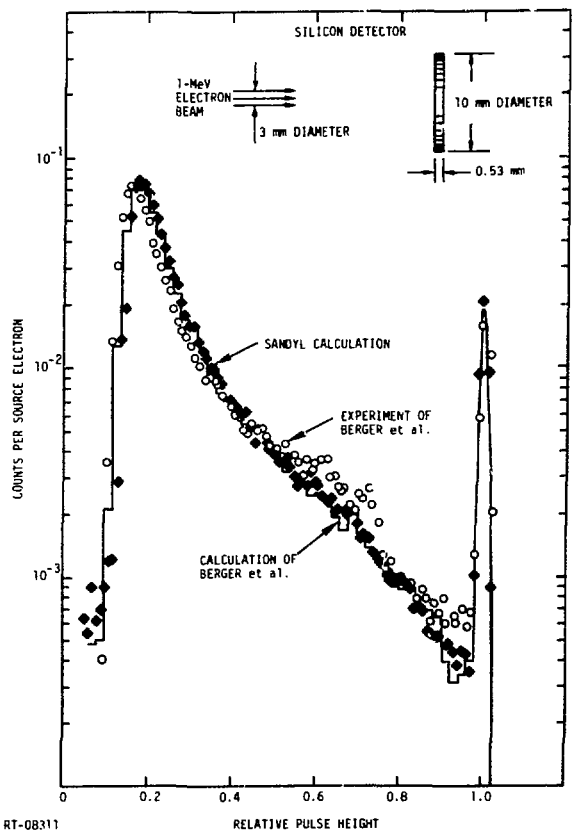

Figure 5. Pulse-height spectra for a 1-MeV electron beam on a silicon detector. Circles are measurements of Berger et al.,[10] and solid line histogram is their ETRAN calculation. Black points are SANDYL calculation.

The examples discussed so far have been comparisons between calculated and measured pulse-height spectra for photon and electron detectors. These provide the most sensitive tests of the calculations. There are, however, many other applications for which it is not possible or necessary to obtain energy spectra. These include the whole class of dose-measuring devices. The final example we wish to show is an application of thermoluminescent dosimeters (TLDs) in a device known as a depth-dose spectrometer.[12] It was constructed for the purpose of measuring bremsstrahlung spectra consisting of short, intense bursts of photons in the energy range of 30 to 1000 keV. The device consists of 13 layers of TLDs separated by metallic foils graded in Z and thickness, so that the responses provided a unique measure of photon energy.

A response function for the spectrometer was calculated using SANDYL. The response in this case consisted of the total dose in each of the 13 TLDs. As a check on the calculations, measurements were made for four monoenergetic gamma-ray sources; the results are shown in Fig. 6. As with the other examples, we find excellent agreement.

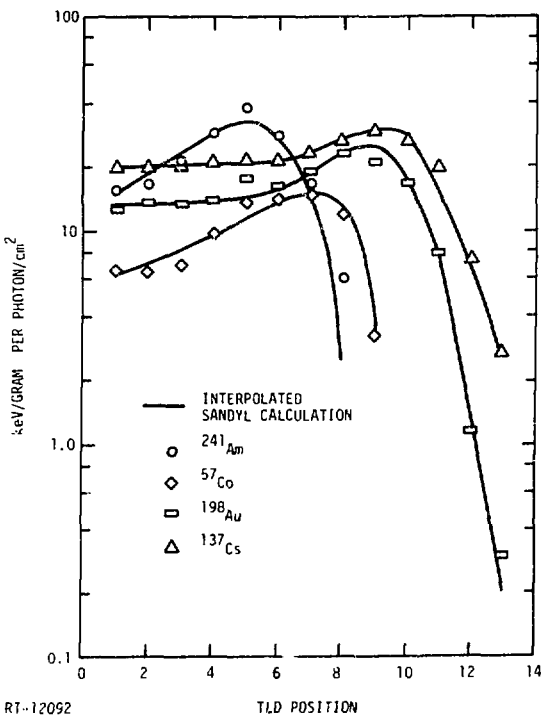

Figure 6. Responses of TLD-based depth-dose spectrometer for four gamma-ray lines[12]

Additional Applications

The examples shown above are just a few of the many applications we have found for these powerful calculational tools. The results demonstrate the generality of the Monte Carlo methods, and the remarkable accuracy with which they simulate experimental situations. The degree of precision and the range of reliability having been demonstrated, additional applications become apparent. An obvious, but extremely useful application, is the simulation of experiments, or parts of experiments, intended to detect or measure radiation spectra or doses. The results of such simulations can be useful in optimizing the design of the experiment, thus possibly saving time and redesign expenses. A second application is the calculation of detector response to a source or different sources for actual source-detector configurations. This information can be useful in new detector development, and as an aid in selecting the best detector for a measurement in order to extract the most useful data. Another very important application is the prediction of dose enhancement phenomena which occur at the interface of materials with different atomic numbers.[13-15] Doses very close to the interface can be many orders of magnitude larger than the bulk dose. This effect is very important in studies of radiation damage in electronic devices. Other applications include design of gamma-ray shielding and bremsstrahlung converters, and prediction of doses in structures, devices, and systems.

There are likely many other applications of Monte Carlo photon-electron transport calculations. On the basis of the examples presented in the previous sections, and many others which we have not been able to include, we are convinced that SANDYL, or any similar transport code, is a highly versatile and reliable experimental/analytical tool.

References

1. H. M. Colbert, Sandia Livermore Laboratories Report SLL-74-0012 (1974).
2. For an early history of Monte Carlo methods, see M. J. Hammersley and D. C. Handscomb, Monte Carlo Methods (John Wiley & Sons Inc., New York, 1964).
3. A recent review and bibliography is given by L. L. Carter and E. D. Cashwell, Particle-Transport Simulation with the Monte Carlo Method (U. S. Energy Research & Development Administration, TLD-26607, 1975).
4. Y. A. Shreider, ed., The Monte Carlo Method (Pergamon Press, Inc., New York, 1966).
5. E. D. Cashwell and C. J. Everett, A Practical Manual on the Monte Carlo Method for Random Walk Problems (Pergamon Press, Inc., New York, 1959).
6. M. J. Berger, in Methods of Computational Physics, eds. B. Alder, S. Fernbach, and M. Rotenberg (Academic Press, New York, 1963), Vol. 1, p. 135; M. J. Berger and S. M. Seltzer, NBS-9836, 9837.
7. The NE-213 detector is manufactured by Nuclear Enterprises, Ltd., and consists of xylene, naptnalene, activators, and POPOP wave shifter.
8. N. A. Lurie, L. Harris, Jr., and J. C. Young, Nucl. Instr. and Meth. 129, 543 (1975).
9. N. A. Lurie, D. K. Steinman, L. Harris, Jr., and J. P. Wondra, IEEE Trans. Nucl. Sci. NS-22, 2582 (1975).
10. M. J. Berger, S. M. Seltzer, S. E. Chappell, J. C. Humphreys, and J. W. Matz, Nucl. Instr. and Meth. 69, 181 (1969).
11. M. J. Berger and S. M. Seltzer, "Electron and Photon Transport Programs," National Bureau of Standards Report 9837 (June 10, 1968).
12. V. V. Verbinski, J. C. Young, and F. J. Sazama, to be published.
13. J. A. Wall and E. A. Burke, IEEE Trans. Nucl. Sci. NS-17, 305 (1970).
14. J. C. Garth, W. L. Chadsey, and R. L. Sheppard, Jr., IEEE Trans. Nucl. Sci. NS-22, 2562 (1975).
15. R. A. Berger and J. L. Azarewicz, IEEE Trans. Nucl. Sci. NS-22, 2568 (1975).

Proceedings, ERDA X-and Gamma-Ray Symp. Ann Arbor, MI, May 19-21, 1976 (Conf 760539)

A WORKING MODEL FOR Ge(Li) DETECTOR COUNTING EFFICIENCIES*

R. Gunnink and J. B. Niday
Lawrence Livermore Laboratory, University of California
Livermore, California 94550

Summary

A practical model has been developed that is capable of describing the overall Ge(Li) detection efficiency as a function of several known or measurable parameters such as gamma-ray energy, source-to-detector distance, detector dimensions, source extension (area and volume), source composition, and external absorbers. The algorithms of this model permit the evaluation of a large variety of sample shapes, sizes, material compositions, and source strengths with a single initial detector calibration. Sources of small volume generally can be measured to within 1 to 2% regardless of energy or source-to-detector distance. Even large volume sources placed at close-in geometries give results within 10% of the correct values.

Introduction

Absolute gamma emission rates and quantitative analyses by Ge(Li) gamma-ray spectrometry can be obtained only with detectors that have been calibrated for photopeak detection efficiency. A common approach is to make such a determination for each counting configuration used. However, this procedure is very restrictive and the effects of small uncontrollable variations in the source cannot be compensated for easily and errors result. To handle the many and varied samples routinely analyzed, we have developed a model that adequately describes the detection efficiency as a function of energy as well as a function of source and detector parameters.

Some of the principal source parameters taken into account are source-to-detector distance, source extension in area and volume, self-attenuation by the various materials of a volume source, and attenuations by external absorbers that may be interposed between the sample and the detector. The attenuation of low-energy radiations by the Ge(Li) dead layer is also considered.

Description of the Model

A basic premise of the model is that the overall efficiency can be treated as the product of two components: the intrinsic efficiency of the detector (defined in Eq. 1), and the source-to-detector geometry. Calculation of two hypothetical points in space, one at which the detector is said to reside and another at which all of the sample is said to be concentrated, determines the latter component. When this is accomplished, a basic rule of physics is invoked; namely, that the detection efficiency is inversely proportional to the square of the source-to-detector distance. The fundamental equation used by the model is

$$\varepsilon_E = \frac{C_E}{\gamma_E} \times d^2, \qquad (1)$$

where

ε_E = counting efficiency for gamma ray of energy E, normalized to 1 cm

C_E = net counts per unit time in peak

γ_E = source emission rate of gamma energy E

d = source-to-detector distance.

Once a calibration curve (ε vs E) has been determined, the equation can be transposed to yield photon emission ratios, γ_E, for sources of unknown intensity.

A typical configuration for a cylindrical detector and a point source is shown in Fig. 1. To use Eq. (1), the parameter d must be assessed by using measured or calculated values for:

x = distance from source to window

w = distance from window to active detector surface

p = effective penetration of gamma ray into detector

r = effective interaction radius in the detector

r_o = limiting value of r at low energy

d = distance from source to effective zone of interaction

T = detector thickness

R = detector radius

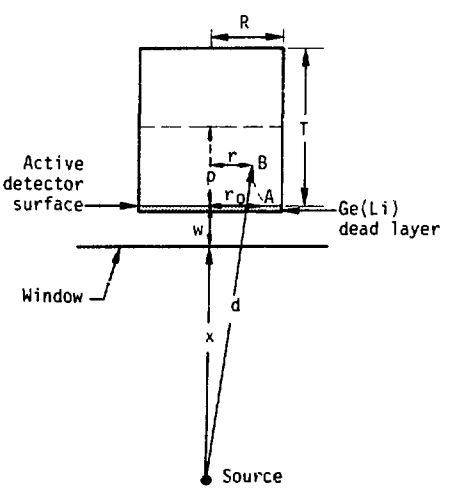

Fig. 1. Point source and cylindrical detector used in the model.

*This work was performed under the auspices of the U.S. Energy Research & Development Administration, under contract No. W-7405-Eng-48.

From simple geometry we have

$$d^2 = (x + w + p)^2 + r^2. \quad (2)$$

Of these, x is the only easily measured parameter. The others must be empirically determined. Our studies of these parameters were made on a variety of detectors ranging from small x-ray detectors to detectors as large as 70 cc. Obviously, the model is tested most severely in the case of large detectors.

The first parameter we consider is the penetration value, p. It is dependent on the gamma-ray energy and has limiting values of zero at low energy and one-half the detector thickness, T, at very high energy. The following equation[1] describes the penetration

$$p = \frac{1}{\mu}\left[1 - \frac{\mu T \exp(-\mu T)}{1 - \exp(-\mu T)}\right], \quad (3)$$

where μ is an appropriate energy-dependent absorption coefficient. This relationship is depicted in Fig. 2.

Although the form of Eq. (3) appears reasonable, we must decide on appropriate absorption coefficients. Quite precise values can be found for the photoelectric, Compton, and total attenuation coefficients.[2] However, it is not clear which, if any, of these should be used in the above equation because we are concerned only with the interactions that eventually result in full energy deposition in the detector, whether by photoelectric or multiple Compton scattering processes. Since the latter process is complex, no rigorous meaning should be assigned to the penetration parameter, p, or to the absorption coefficient, μ. However, we have found an empirical function that adequately describes the total absorption:

$$\ln \mu = -2.316 + 4.2 \exp[-0.478 \ln E - 1.434]. \quad (4)$$

It is important to consider the dependence of gamma-ray penetration on energy even when establishing relative efficiency curves. These variations in penetration result in efficiency curves of different shapes for different detector geometries. This effect becomes very pronounced at close-in counting geometries.

The effective interaction radius, r, is more difficult to characterize. A rigorous meaning can be attached to it only for low energies, when the interaction is primarily photoelectric and occurs at the surface of the detector. In this case, r and r_o are equivalent and can be used interchangeably in the following discussion. This case can be used for normalizing purposes since the exact detector efficiency and the effective radius can be computed from simple geometry (see Fig. 1). That is,

$$\text{Physical geometry} = 1/2\left[1 - \ell/\sqrt{\ell^2 + R^2}\right], \quad (5)$$

where $\ell = x + w$. However, in our model, the geometry, G, is described by:

$$G = \frac{k}{\ell^2 + r_o^2}. \quad (6)$$

A value of $k = R^2/4$ is determined by normalizing the two expressions as ℓ goes to infinity. The relationship between the effective interaction radius, r, and the detector radius, R, can now be given by

$$r_o^2 = (1 - C\ell^2)/C, \quad (7)$$

where

$$C = 1\left(- \ell/\sqrt{\ell^2 + R^2}\right)\frac{2}{R^2}. \quad (8)$$

However, a study of experimental data indicates that the effective interaction radius decreases from the initial value of r as the gamma-ray energy increases. Although the determination of the radius parameter is very sensitive to statistical and other sources of error, a definite trend of r with energy is demonstrated in Table 1.

This trend may be qualitatively explained by the increased importance of multiple Compton scattering within the detector producing full-energy pulses from the higher energy gamma rays. Compton gamma rays escape from the detector more easily after interaction near the outer surface than after interaction near the center of the detector. Thus, the effective radius of interaction for production of photopeaks decreases as the penetration depth increases. This is shown in Table 1 and as curve A-B in Fig. 1. The magnitude of the trend indicates that other surface and edge effects also modify r. The empirical algorithm we have found to describe this trend is

$$r = r_o(1.2 - p/\sqrt{T}). \quad (9)$$

The distance from the window to the active detector surface, w, is the final parameter to be discussed. Since detector design specifications do not describe w accurately enough, its determination is always the first requirement in calibrating the total detector efficiency. This is accomplished by counting

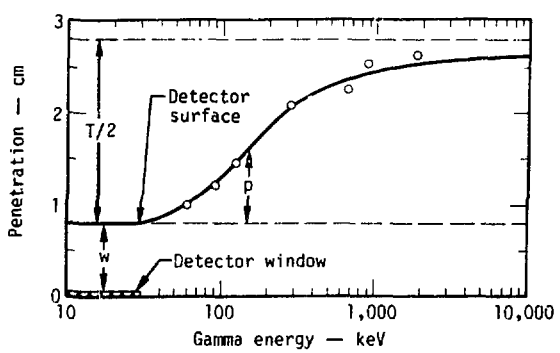

Fig. 2. Measured effective penetration of various energy gamma rays into a 38 cc coaxial detector.

Table 1. Data from a 38 cc coaxial detector showing an inverse relationship between energy and radius parameter, r.

Source	Energy (ke V)	r
^{241}Am	60	1.49
^{147}Nd	91	1.38
^{57}Co	122	1.28
^{203}Hg	279	0.61
^{137}Cs	661	0.35

sources of different energy at several distances. The sets of data at each energy are used to calculate (w + p) values, which are plotted as shown in Fig. 2. The idealized curve derived from Eq. (3) is fitted to these data points and the y axis intercept is taken to be the window-to-active detector surface distance.

There is a lack of standardization of Ge(Li) detector sizes or shapes and thus, care must be taken in applying this model to each detector. At times, estimations or adjustments of the model parameters must be made to obtain a better fit with the observed data. For example, slight adjustments may have to be made in the thickness, T, for coaxial detectors, depending on the size and position of the inactive core.

For most larger Ge(Li) detectors, an additional correction related to the dead layer must be made for low-energy gamma emissions. Although the efficiency curve accounts for the attenuation of gamma rays entering the detector in a direction perpendicular to the detector surface, many gamma rays from sources counted at close-in geometries enter the detector at oblique angles. Low-energy gamma rays especially will suffer greater attenuation than indicated by the efficiency curve. If there were no attenuation (i.e., no dead layer), a detector's efficiency would not vary with energy and its efficiency at low energies would be determined solely by its area. Thus, the dead layer thickness can be estimated by using the slope of the efficiency curve in such a low-energy region. Once this thickness has been calculated, a correction can be applied that will approximately account for the additional attenuation suffered by gamma rays entering the detector obliquely.

A typical test of the model using a point source is shown in Fig. 3. Our experience indicates that the geometry contribution to the counting efficiency can be described to within ±1 to 2% of correct values for all energies and usable source-to-detector distances.

Measurement of the Intrinsic Efficiency Curve

The intrinsic efficiencies as defined in Eq. (1) are determined by counting absolute standards at relatively large distances and normalizing these efficiencies to a 1-cm distance. These values may be described by a fifth- or sixth-order polynomial equation of the form

$$\ln \varepsilon_i = \sum_{j=1}^{N} a_j (\ln E_i)^{(j-1)} , \qquad (10)$$

where

ε_i = efficiency at the ith energy

E_i = gamma energy

a_j = coefficients of the polynomial.

We found this single function to be inadequate over the full range of interest (0.05 to 4.0 MeV). Thus, we used two polynomial equations that overlap in the 100 to 200 keV energy region. After the data were fitted by a least squares analysis, the resulting curves were examined in the region of overlap and a crossover energy which gave the same efficiency by either equation was chosen. In this way, the efficiency data can be fitted to within ±1 to 2% of the correct values.

Correcting for Sample Extension

In the discussion thus far, we have assumed that the sample activity resided at a point. In practice,

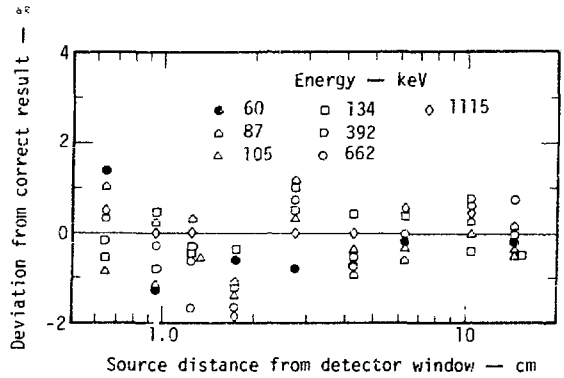

Fig. 3. Deviation from correct results using a point source and a 50 cc detector.

however, most samples extend in two or three dimensions. Not only must the change in geometry be considered, self-attenuation in volume sources also must be properly calculated.

Our approach was to use approximate formulas to reduce the sample to an equivalent point in space. The location of this point depends on the energy of the gamma ray and on the physical dimensions and composition of the sample. To avoid the extreme complexity of volume-volume geometry calculations, we have assumed that the detector is adequately represented by an equivalent point (Fig. 4).

It can be shown that for disk sources placed on axis at distances that are large compared to the source radius, the counting efficiency decreases by the ratio

$$G_d/G_p = \frac{a^2 \ln\left(\frac{a^2 + R^2}{a^2}\right)}{R^2} , \qquad (11)$$

where

G_d = disk geometry,

G_p = point-source geometry,

a = source-to-detector distance,

R = source radius.

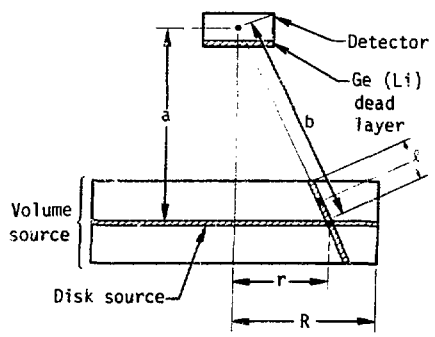

Fig. 4. Detector and volume or disk source. Here, a = source-to-detector distance, b = distance from detector to mid-point of source, ℓ = one-half the effective sample thickness, r = effective source interaction radius, and R = source radius.

This equation can be used to correct the point source calculations. Tests of the model were made using sources up to 50 cm^2 in area. Some anomalous behavior was noted at low energies, as Fig. 5 shows, but otherwise, this description appeared to be quite adequate for most applications.

Volume sources can be thought of as multilayered disk sources. Gamma ray attenuation in passing through the upper layer of the source poses an additional complication. The effect on the counting rate, n/n_o, for a linear element of 2 ℓdx dimensions is expressed by

$$n/n_o = \left(e^{-\mu\ell}/2\ell\right) \int_{-\ell}^{\ell} e^{\mu x} \times (1 - x/b)^{-2}\, dx, \qquad (12)$$

where

ℓ = one-half sample thickness,

μ = absorption coefficient,

b = distance from detector to midpoint of source.

When this integrand is expanded and integrated term by term, we obtain:

$$n/n_o = e^{-\mu\ell}\left[\left(\frac{b^2}{b^2 - \ell^2}\right) + \frac{\mu^2\ell^2}{3!} + \frac{\mu^4\ell^4}{5!} + \ldots + \frac{2\ell}{b}\left(\frac{\mu\ell}{2(1!)} + \frac{\mu^3\ell^3}{5(3!)} + \ldots\right) + \ldots\right]. \qquad (13)$$

If either μ or ℓ/b are small when compared with 1.0, the higher-order terms can be disregarded. The average sample thickness that gamma rays must penetrate to reach the detector is calculated at an effective sample radius approximately $R/\sqrt{2}$. (See Ref. 3 for a more complete discussion.)

Figure 6 illustrates the application of these corrections for sample extension in which a large volume sample was counted in several positions.

Corrections for External Absorption

It is also necessary to correct for gamma-ray attenuation by external absorbers. These absorbers may be an unavoidable part of the sample container or environment or deliberately used to attenuate the lower-energy gamma rays.

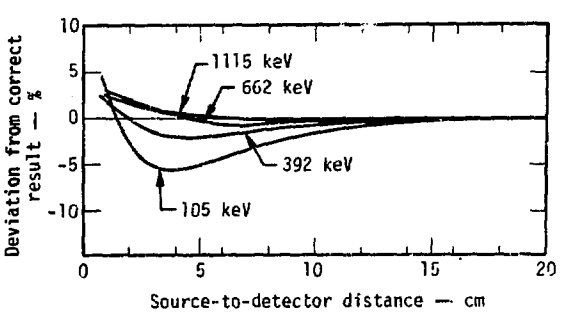

Fig. 5. Deviation from correct results using a 50 cm^2 disk source.

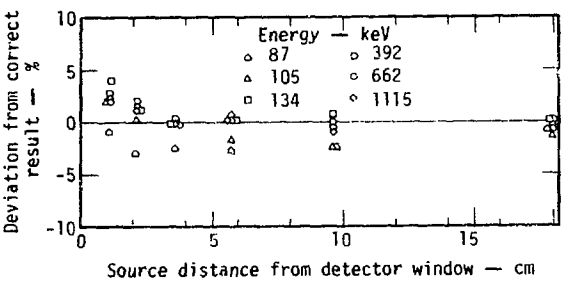

Fig. 6. Deviation from correct results using a 240 ml aqueous sample of 62 cm^2 area.

For these calculations, as well as for those discussed in the previous section, it is necessary to know the composition of the absorbing materials and to determine the absorption coefficient at each energy. Values corresponding to the logarithms of the cross section[2] and energy can be fitted to a seventh-order polynomial. The resulting coefficients can be used in subsequent analyses to compute absorption coefficients at any given energy.

A problem arises with a discontinuity in the absorption curve at the K-shell binding energy. We have found that the magnitude of the discontinuity can be represented empirically by

$$\mu_\ell/\mu_\mu = 0.1027 + 0.0068\sqrt{E_K} + 0.000654\ E_K, \qquad (14)$$

where μ_ℓ and μ_μ are the respective mass absorption coefficients just below and above the absorption edge, and E_K is the K-shell binding energy. The slope of the absorption curve is assumed to be the same just below and just above the absorption edge and Eq. (14) is used, together with the polynomial equation, to describe the absorption coefficient below the absorption edge.

Application

The above description of detector efficiency has become an integral part of our GAMANAL code which is the general-purpose program used to reduce and interpret over 5000 spectra yearly. Admittedly, many approximations are being made, but fortunately, in most cases where high accuracy is required, the corrections are small and results within a few percent of the correct values can be achieved.

References

1. R. Gunnink and J. B. Niday, Computerized Quantitative Analysis by Gamma-Ray Spectrometer, Vol. I., Lawrence Livermore Laboratory Rept. UCRL-51061, 1972.
2. E. Storm and H. I. Israel, Nucl. Data Tables, U. S. Atomic Energy Comm. A7, 565 (1970).
3. R. D. Evans and R. O. Evans, Rev. Mod. Phys. 20, 305 (1948).

Proceedings, ERDA X-and Gamma-Ray Symp. Ann Arbor, MI, May 19-21, 1976 (Conf 760539)

EFFICIENCY CALIBRATION OF SEMICONDUCTOR SPECTROMETERS - TECHNIQUES AND ACCURACIES

K.Debertin, U.Schötzig, K.F.Walz and H.M.Weiß
Physikalisch-Technische Bundesanstalt, Braunschweig,
Federal Republic of Germany

Summary

In this paper we discuss the accuracies which may be attained in the efficiency calibration of semiconductor detectors in the energy range from 13 to 2800 keV. Peak efficiency curves for two coaxial Ge(Li)- and a planar high purity Ge-detector were established using standard sources of about 20 radionuclides, the activity of which was determined absolutely by sophisticated $4\pi\beta(X)$-γ coincidence methods. An uncertainty of 0.5 to 2%+, depending on energy, was obtained.

Fast though less accurate calibrations can be performed by using multigamma sources. For some suitable radionuclides relative γ-ray emission probabilities have been determined.

The reduction in calibration accuracy for measurements at low source-detector distances and at high counting rates is discussed.

Calibration with High Accuracy

In this paragraph we report on efficiency calibration measurements in the energy range from 13 to 2800 keV performed with three semiconductor spectrometers.

Detectors

G1 Ge(Li), 30 cm^3, resolution 2.9 keV at 1.33 MeV
G2 Ge(Li), 70 cm^3, resolution 2.2 keV at 1.33 MeV
G3 high purity Ge, 16 mm diameter, 5 mm thick, resolution 1.7 keV at 1.33 MeV and 220 eV at 6.4 keV

Standard Sources

Nearly all sources used in the calibration were prepared in our laboratory. The radioactive substance was deposited between two 0.25 mm thick polyethylene foils. The activity has been determined absolutely by simple and more sophisticated $4\pi\beta$-γ- coincidence methods[2,3] for sources which were prepared from the original one by gravimetric dilution. These methods have been checked over the last ten years within the framework of international and bilateral intercomparisons.

Radionuclides from which standard sources have been produced are given in Table 1, along with the decay data and uncertainties $\Delta A/A$ of the activity determination. Half-lives $T_{1/2}$, energies E and photon emission probabilities (intensities) I are either PTB-recommended values, or taken from the Nuclear Data Sheets and more recent original publications. Only those energies are listed and used for which the uncertainty $\Delta I/I$ of the emission probability is less than or equal to 2 %.

Table 1. Decay data of radionuclides and activity uncertainty of the standards used in the efficiency calibration

Nuclide	$T_{1/2}$	E [keV]	I [%]	$\Delta I/I$ [%]	$\Delta A/A$ [%]
^{22}Na	2.60a	1274.5	99.95	0.0	0.3
^{24}Na	15.0 h	1368.5	100.0	0.0	0.5
		2754.0	99.85	0.0	
^{46}Sc	83.7 d	889.2	99.98	0.0	0.3
		1120.5	99.99	0.0	
^{54}Mn	312.5 d	834.8	99.98	0.0	0.5
^{57}Co	272 d	14.4	9.6	1.0	0.5
		122.1	85.6	0.3	
^{60}Co	5.27a	1173.2	99.88	0.0	0.3
		1332.5	99.98	0.0	
^{85}Sr	64.8 d	13.4	50.7	1.5	0.6
		514.0	99.28	0.0	
^{88}Y	106.6 d	14.2	52.5	1.5	0.5
		1836.1	99.4	0.2	
^{95}Nb	35.15d	765.8	99.80	0.0	0.5
^{113}Sn	115.2 d	24.1	79.5	2.0	0.7
^{131}J	8.02d	364.5	82.4	0.5	0.3
^{134}Cs	2.06a	604.6	97.5	0.2	0.3
^{137}Cs	30.0 a	31.8/32.2	5.64	2.0	0.7
		661.6	85.3	0.4	
^{139}Ce	137.6 d	33.0/33.4	64.1	2.0	0.3
		165.8	80.0	0.4	
^{141}Ce	32.5 d	35.6/36.0	12.6	2.0	0.3
		145.5	48.4	0.9	
^{140}La	40.27h	1596.6	95.6	0.3	0.5
^{198}Au	2.696d	411.8	95.53	0.1	0.3
^{203}Hg	46.6 d	70.8/72.9	10.1	1.5	0.5
		279.2	81.3	0.2	
^{241}Am	432 a	59.5	36.0	1.0	0.5

A few sources by other suppliers have been used in addition. Discrepancies in the ratio counting rate/nominal activity was largest for ^{203}Hg (3 %) but this was found to be due to continuous activity losses by diffusion and sublimation. No losses were observed for our ^{203}Hg-source.

For low energies (<30 keV) self-absorption in the radioactive substance may lead to errors in the efficiency calibration as was pointed out just recently by Campbell et al.[4]. For our sources errors due to self-absorption are assumed to be less than 1 % for energies above 13 keV.

+ Throughout this paper uncertainties are always given at the 68 % confidence level. Estimated maximum systematic uncertainties δ_i and random uncertainties σ_i at the 68 % confidence level are combined, following a suggestion by Wagner[1], to a total uncertainty

$$u = \sqrt{\Sigma\sigma_i^2 + \frac{1}{3}\Sigma\delta_i^2}$$

which has a confidence level of about 68 %.

Measuring Conditions

Measuring conditions were chosen such that any corrections for real and random summing effects were low, and that they did not contribute to the uncertainty of the calibration points. Total counting rates were less than 1000 s^{-1}. The pulse generator method was applied for deadtime and pile-up corrections. Uncertainties due to variations in source positioning were less than 0.1 %. The stability of the complete spectrometer set-up was ensured by regularly checking for efficiency constancy with a ^{152}Eu source. Numerous spectra were taken for each calibration point, in part with two or three sources of different activity. The uncertainty due to counting statistics has always been less than 0.3 %.

For measurements with the Ge-detector G3 and energies below 100 keV, lead diaphragms of 2 mm thickness and 10 mm hole diameter were mounted in front of the detector and just behind the source. Thus, peak-shape distorting contributions from the detector edges and contributions of scattered radiation to the recorded spectra are reduced[5].

Peak analysis

Peak areas were obtained both by fitting analytical functions and simply summing up the counts in a well-defined region around the peak. In the latter case background was subtracted by extrapolation of the spectrum above the peak. Of course, the efficiency curve depends on the type of peak analysis since, due to the asymmetric peak shape, several definitions of peak area are conceivable. But if the calibration and all later emission rate measurements are evaluated in the same manner, it is unimportant which method is applied, so long as isolated peaks are considered. The attainable accuracy does not depend upon it. Only when multiple peaks have to be resolved, peak fitting procedures should be used.

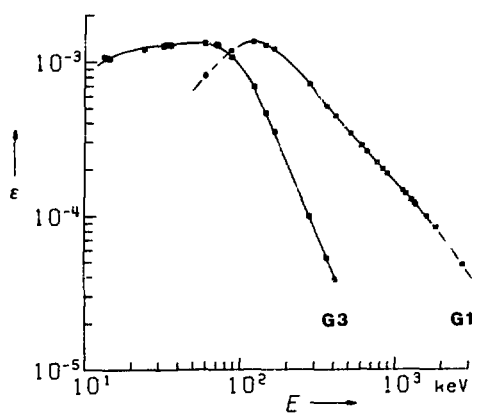

Fig. 1. Efficiency curves for detectors G1 and G3.

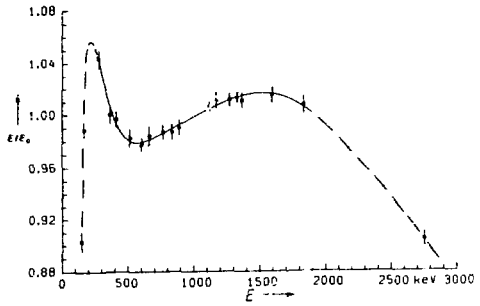

Fig. 2. "Reduced" efficiency curve for detector G1 (cf. text).

Efficiency Curves

In Fig.1 the efficiency curves of detectors G1 and G3 are given in a double logarithmic plot. The curve for G1 is almost a straight line in the energy region from [illegible] to 2000 keV, i.e. $\varepsilon(E) \approx \varepsilon_o(E) = aE^{-b}$ with

ε efficiency,
ε_o approximate value of efficiency,
E energy,
a,b constants.

The double logarithmic representation does not allow clear judgement of calibration accuracy. Hence, in Fig.2 we give the ratio $\varepsilon(E)/\varepsilon_o(E)$ on a rather large scale, where one unit on the ordinate corresponds to 1 % deviation of ε from ε_o. The solid line was obtained by fitting an analytical function, similar to that used by McNelles and Campbell[6], to the calibration points. For detector G3 the double logarithmic efficiency plot is almost linear down to 120 keV.

For the energy region below 120 keV we give in Fig.3 an efficiency ε^* which is deduced from ε by correcting for absorption losses in the source foil and in air, and by adding the escape peak to the full energy peak areas. The detector is almost black for photons with energies below 60 keV. The observed drop at low energies is due to absorption losses in the thin beryllium window, in the gold contact layer and possibly, in a

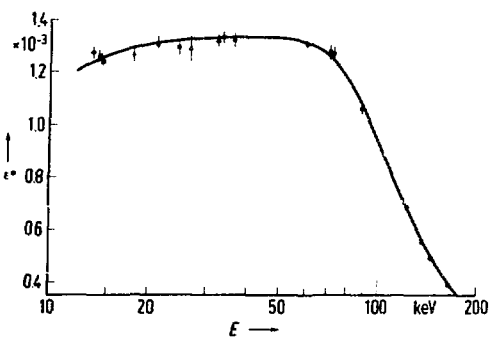

Fig. 3. Efficiency curve for detector G3;
• primary calibration points
Δ secondary ^{241}Am calibration points
□ commercial emission rate standard

thin germanium dead layer on the effective volume of the crystal. The solid line is a physically established function[7] with four free parameters fitted to the calibration points.

Calibration Accuracy

In the energy region between 550 and 1600 keV, where the density of calibration points is high, we estimate the calibration accuracy to 0.3 to 0.5 %. The small scatter of nearby points obtained from different independent standard sources encourages us to give such low figures. The interpolation between 1836 and 2754 keV is believed uncertain to 1.5 %. Below 30 keV the interpolated line deviates from the calibration points by up to 2 %. This may be due to the uncertainties of the X-ray emission probabilities, but it cannot be ruled out that particularly the scatter of the triplet at 14 keV is partly caused by variations in self-absorption. In Table 2 we have given estimated accuracies in specified energy regions. The figures taken as valid at the 68 % confidence level, are considered to be pessimistic estimates.

In order to maintain this accuracy in emission rate measurements based on the efficiency calibration, it is important that the sources under study, and the calibration sources, are similar in construction. This is particularly true for low energies where thick backings, for example, give rise to considerable contributions of scattered radiation to the full energy peak[5] and render the results incorrect.

Table 2. Calibration accuracy obtained in the energy range 13 to 2800 keV

Detector	Energy region [keV]	Accuracy [%]
G3	13 - 30	2
	30 - 70	1
	70 - 110	2
	110 - 180	0.7
	180 - 250	1
G1, G2	110 - 180	1
	180 - 250	1.5
	250 - 550	0.7
	550 - 1600	0.5
	1600 - 1900	0.8
	1900 - 2800	1.5

Calibration with Sets of Standard Sources

Commercially available sets of standard sources for the energy region above 60 keV usually consist of ^{241}Am, ^{57}Co, ^{203}Hg, ^{22}Na, ^{137}Cs, ^{54}Mn, ^{60}Co and ^{88}Y. One may achieve similar efficiency calibration accuracies as quoted in Table 2 in the immediate neighbourhood of the calibration points. On account of the larger interpolation ranges, however, accuracy will be less by at least a factor of about 2 in the intervals between the points.

Care should also be exercised in using so-called "emission rate standards". Here the emission rate may have been calibrated with scintillation or gas detectors of low energy resolution. Since scattering events are more likely to fall into the broad peak region obtained with these detectors than into the narrow peaks of semiconductor detectors, errors can occur in the efficiency calibration of the latter. These will be small, but not negligible, for sources on thin plastic foils.

Calibration with Multigamma Sources

Fast efficiency calibrations can be performed by using sources of radionuclides emitting γ-radiation with different energies spread over the energy region of interest. Several nuclides have been proposed in the literature. With regard to half-life, number, distribution and relative abundance of photons, ^{152}Eu is particularly suited for the energy region from 100 to 1500 keV. The uncertainty of interpolation is largest between 122 and 245 keV and between 444 and 779 keV. The details of this nuclide have been published elsewhere[8]. We reproduce here in Table 3 the relative γ-ray emission probabilities of ^{152}Eu which we have determined.

Table 3. Relative γ-ray emission probabilities of ^{152}Eu taken from reference[8].

E [keV]	I_r	ΔI/I [%]
121.8	137.5	1.6
244.7	35.8	1.7
344.3	128.3	1.0
411.1	10.79	1.5
444.0	14.90	1.0
778.9	62.0	0.8
964.0	70.0	0.8
1085.8	48.0	1.5
1112.1	64.8	0.9
1408.1	100.0	0.7

One of the main disadvantages of multigamma sources is the enhanced background under the lines of low energy which gives rise to additional statistical and, in some cases, systematical uncertainties. Moreover, it often happens that the calibration lines are not sufficiently isolated from neighbouring small lines, thus leading to further uncertainties. Nevertheless, the attainable accuracy of efficiency calibration with a ^{152}Eu standard source is estimated to be less than the figures given in Table 2 by no more than a factor of two.

In some fields of application, e.g. burn-up determination, extended sources are needed which can easily be produced by neutron activation of silver foils. In the energy region from 600 to 1500 keV a calibration accuracy of 1 % can be achieved by using a $^{110}Ag^m$-Source. The relative emission probabilities we determined are given in Table 4.

Sources of ^{133}Ba, ^{182}Ta and ^{75}Se are suitable secondary calibration standards in the energy region below 400 keV. The accuracy attainable is slightly poorer than that given in Table 2. Results on emission probabilities of ^{133}Ba and ^{182}Ta with uncertainties of the order of 1 % are or will be published elsewhere[9,10].

For energies above 1500 keV ^{56}Co or ^{226}Ra may be used as multigamma sources. Owing to the lack of primary calibration

Table 4: Relative γ-ray emission probabilities of $^{110}Ag^m$.

E [keV]	I_r	ΔI/I [%]
657.7	100.0	0.7
706.7	17.5	0.8
763.9	23.7	0.8
884.7	77.5	0.7
937.5	36.6	0.8
1384.3	26.1	0.9
1505.0	13.9	1.0

points, γ-ray emission probabilities cannot be determined to better than ± 2 to 3 %.

Calibration at low source-detector distances

In many practical applications source-detector distances cannot be chosen as large as has been assumed in the preceding paragraphs. For low-level measurements for example where the source is placed directly on top of the detector summation corrections for radionuclides emitting two or more coincident photons (e.g. ^{60}Co, ^{88}Y, ^{152}Eu) are no longer small but may reach values of 20 to 30 %. This is very often not realized by workers in application fields of γ-ray spectrometry. An "inexplicable" scattering of calibration points can frequently be traced back to such summation effects. In principle, the corrections, may be calculated[11] from the decay scheme, angular correlation coefficients and the total efficiency. The determination of the latter as a function of energy, however, is a new problem. An uncertainty of 5 to 10 % for the correction factors is regarded as typical. This introduces an additional uncertainty of 1 to 3 % in the efficiency calibration.

For the calibration of Ge(Li)-detectors in the energy region between 100 and 1200 keV one may find some radionuclides emitting photons which are either not accompanied by any other quanta or where the detection probability of these quanta is negligibly small (e.g. ^{54}Mn, ^{57}Co, ^{65}Zn, ^{85}Sr, ^{95}Nb, ^{137}Cs, ^{139}Ce, ^{198}Au, ^{203}Hg). For these radionuclides no, or only small, summation correction factors have to be applied and the calibration accuracy may reach that given in Table 2. This is, however, of limited value if the source under study emits coincident photons. In that case high accuracy can only be obtained if a source of the same radionuclide is used for calibration. In addition, differences in source dimensions have to be avoided.

We caution against the use of multigamma sources such as ^{152}Eu or $^{110}Ag^m$ in calibration at low source-detector distances. On account of the complex decay scheme and incomplete knowledge of the angular correlations of the photons, any calculated summation correction factors are of low confidence.

Measurements at high counting rates

Up to now all statements on the attainable accuracy were valid for low counting rates. It was tacitly assumed that corrections due to dead time and pile-up losses were small, and did not give rise to additional uncertainties in the efficiency calibration.

One often comes across the opinion that a multichannel analyzer, operated in the live time mode, suitably accounts for any counting losses. This is particularly untrue for pile-up losses which may amount to one or more percent, depending on the shaping time constant τ of the amplifier, even at counting rates as low as 1000 s^{-1}. For counting rates up to 3000 s^{-1} (τ=2μs) the pulser timing method[12] is considered the most reliable to correct for each kind of counting losses. It should be applied regularly in all measurements aiming at high accuracy. The limitations of this method were pointed out by Bolotin et al.[13], for example. We have observed that the method also fails for asymmetrical peaks at counting rates above 3000 s^{-1} if inadequate peak evaluation routines are applied[14]. Additional uncertainties of 1 to 5 % may arise for counting rates between 3000 and 10000 s^{-1}.

References

1. Wagner S.: PTB-Mitteilungen 79, 343 (1969)
2. Debertin K., Schötzig U., Walz K.F., Weiß H.M.: Ann. Nucl. Energy 2, 37 (1975)
3. Baerg A.P.: Metrologia 2, 23 (1966)
4. Campbell J.L., Thompson J.A., Jorch H.H.: to be published in Nucl. Instr. and Meth.
5. Peßara W., Physikalisch-Technische Bundesanstalt: to be published
6. McNelles L.A., Campbell J.L.: Nucl. Instr. and Meth. 109, 241 (1973)
7. Gallagher W.J., Cipolla S.J.: Nucl. Instr. and Meth. 122, 405 (1974)
8. Debertin K., Schötzig U., Weiß H.M.: PTB-Mitteilungen 85, 187 (1975)
9. Schötzig U., Debertin K., Walz K.F.: to be published
10. Debertin K., Peßara W., Walz K.F.: Verhandl. DPG(VI) 11, 879 (1976)
11. McCallum G.J., Coote G.E.: Nucl. Instr. and Meth. 130, 189 (1975)
12. Strauss M.G., Sifter L.L., Lenkszus F.R., Bremer R.: IEEE Trans. Nucl. Sci. NS 15, Nr.3, p.518 (1968)
13. Bolotin H.H., Strauss M.G., McClure D.A.: Nucl. Instr. and Meth. 83, 1 (1970)
14. Debertin K., Schötzig U.: to be published

Proceedings, ERDA X-and Gamma-Ray Symp. Ann Arbor, MI, May 19-21, 1976 (Conf 760539)

HIGH RESOLUTION X- AND GAMMA-RAY COINCIDENCE SPECTROMETRY*

F. P. Brauer, J. E. Fager and R. W. Goles
Battelle
Pacific Northwest Laboratories
Richland, Washington 99352

Summary

A data acquisition and analysis system has been developed for high resolution coincidence spectrometry. The system hardware and software are described together with the system capabilities. The sensitivity and selectivity of NaI(Tl)-NaI(Tl), NaI(Tl)-Ge(Li) and Ge(Li)-Ge(Li) coincidence detector systems have been experimentally evaluated. The NaI(Tl)-Ge(Li) system was found to have about the same sensitivity, based on a 5000 minute count, as the all-NaI(Tl) system with improved selectivity. The applications of Ge(Li)-Ge(Li) detectors are limited by their low efficiency. The utilization of time as a third parameter was investigated by correlation studies of the coincidence event energies and the time interval between signals from the two detectors.

Introduction

X- and gamma-ray spectrometric methods are being used to investigate and regulate the impact of nuclear and conventional power generating facilities upon the environment. Both radioactive effluents and non-radioactive effluents are measured by nuclear detection techniques. Currently high resolution diode detector systems and two-parameter NaI(Tl) coincidence systems are being used for high-sensitivity measurements.[1-8] The NaI(Tl) coincidence systems are useful for some measurements of those trace radionuclides whose emissions tend to be obscured by other radioactive compounds in the sample matrix or by natural background levels. However, more sensitive, selective, and versatile methods are required for the instrumental measurement of trace radionuclides in complex mixtures encountered in activation and environmental analyses.

Abundant short-lived radionuclides can often interfere with the detection and measurement of significant longer-lived activities. The natural and fallout radioactivity in soil, silt, and other environmental samples interferes with normal gamma-ray spectrometric analyses for nuclear industry produced effluents. Highly selective detection for many radionuclides can be achieved by exploiting unique and extremely specific correlations between decay emissions. Multidimensional spectrometric analysis methods utilizing x-rays, gamma-rays, particles and time relationships between coincident emissions are being developed for radionuclide measurements.[9-13] The high resolution of diode detectors requires the use of large arrays for data storage if full advantage of the detector resolution is to be utilized.

A megachannel, multiparameter analyzer system coupled with two or more detectors permits simultaneous high resolution measurements in many coincidence modes.[13] This is especially advantageous for low radioactivity-level samples when it is not known beforehand what nuclides to expect.

This paper discusses the hardware and software used for data acquisition and analysis of megachannel, multiparameter coincidence spectra. The capabilities of several high-resolution coincidence spectrometry systems are compared with the more conventional NaI(Tl) coincidence spectrometers.

Data Acquisition and Analysis System

Hardware

The data acquisition and analysis system used in these studies is illustrated in Figure 1. The system consists of a commercial, computer interfaced data acquisition system with added peripheral components. One of the several possible detector arragements is also shown in this figure.

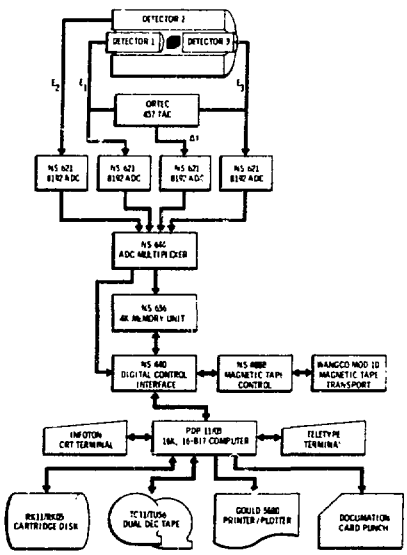

FIGURE 1. Diagram of 4-Parameter Data Acquisition and Analysis System

The system allows the accumulation of event descriptions (ADC addresses) on magnetic tape at low count rates. After acquisition, selected data may be read at maximum tape reading speed by the computer.

List mode data storage on magnetic tape is used for coincidence spectrometry data acquisition. The ADC multiplexer accepts data from up to four ADC's. The multiplexer then generates sequential 16-bit words corresponding to data from each ADC. Thirteen bits (8192 channels) are used for data from each ADC. Two bits are used to identify the ADC being stored and one bit indicates whether ADC rejection of a conversion occurred (as opposed to address zero due to no input). Data can be acquired in several different modes including: 1) a four-parameter coincidence configuration, 2) a three-parameter coincidence configuration and one independent ADC, 3) two dual-parameter coincidence configurations and 4) various other combinations of coincidence and independent configurations. Provision for

* Work performed under ERDA, Contract E(45-1)-1830.

rejection of noncoincident (singles) events is provided. This reduces data storage requirements when only coincidence events are of interest.

Either hardware or software list-mode operation is possible. The multichannel analyzer memory is used for buffer storage of the data in hardware list-mode. Data accumulation is interrupted and the data recorded on magnetic tape when the 4096-word buffer is filled. The computer is completely available for other uses during hardware list-mode data acquisition. This feature is especially valuable, since week-long counts may be taken and the computer is only required for short intervals for analysis of the acquired data.

In software list-mode the multichannel analyzer memory is used for accumulation of preselected portions of any of the ADC outputs as a function of any other ADC coincident events while the computer memory is used for buffer storage of all the raw data. When filled the computer memory buffer is written to magnetic tape along with a four decimal digit experiment identification tag. The pulse-height analyzer and the data acquisition are controlled from the computer teletype in software list-mode. A total of 6.4×10^6, 16 bit words can be stored on a 2400 foot reel of magnetic tape.

Software

Software supplied by the multichannel analyzer manufacturer has been previously described.[13] These routines required considerable operator interaction and were not written for use with the added peripheral equipment such as the disk system and the printer/plotter. Additional programs which operate under the RT-11 (DEC) operating system have been written to fit our experimental needs.

Detailed analysis of the list mode, megachannel data stored on magnetic tape is accomplished by reading the magnetic tape data file under computer control and constructing spectra in computer memory or on disk files. Portions of the spectra may be viewed on the pulse height analyzer display for rapid data scanning or the data may be listed or plotted with the printer/plotter. Several data selection modes are available depending on the experiment requirements and how the data was accumulated. The system allows analysis of up to four-parameter data. The data can be examined by reading the list mode data file and accumulating spectra from one ADC gated by a channel or range of channels from the other ADC's. Since the list mode data file contains all of the coincidence data from a particular experiment, the data can be examined for different coincidences after all the experimental data has been accumulated. As many spectra coincident with any combination of ADC gates may be examined as are required to completely analyze the data. The spectra can be further processed using peak location, energy computation, area computation, nuclide identification and nuclide estimation programs. These computer routines greatly reduce the man-hours required for data analysis.

Specific programs which can be used in various sequences as required are described below:

XYLP Constructs a spectrum on the disk file from list mode data of all events from a specified ADC in coincidence with any events from a second ADC.

XYLP3 Constructs a spectrum on a disk file of all events from a specified ADC in coincidence with any events from a second ADC and in coincidence with a specified range of channels from a third ADC.

XYPLOT Plots and lists spectrum constructed on disk files by XYLP and XYLP3, locates peaks in spectrum, lists peak energies on plot, and prepares table of peak energies.

NSSORT Constructs spectra on a disk file from list mode data from a specified ADC in coincidence with events of specified energy ranges from a second ADC.

NSSORT3 Constructs spectra on a disk file from list mode data from a specified ADC in coincidence with events of specified energy ranges from second and third ADC's.

NSPLOT Locates peaks in spectra constructed on disk files by NSSORT, prepares table of peak energies located in each spectrum, lists and plots each spectrum with peaks labeled with energies.

NSTABL Lists by channel number, energy and peak area each peak found in each spectrum constructed by NSSORT, also prints out two-dimensional summary table containing the energies and area of each coincidence peak.

LODK2 Constructs from list mode data a compressed two-parameter coincidence spectrum and produces printed output.

LOOK3 Constructs from list mode data a compressed two-parameter coincidence spectrum in coincidence with events of a specified range of channels from a third ADC and produces printed output.

XYLIST Constructs from list mode data a specified 50x20 channel region of a two-parameter coincidence spectrum and produces printed output.

XYGEM Sorts list mode data, performs specified summing and prepares punch card output for further processing.

NS6P Prepares a plot of data displayed on pulse height analyzer display.

Experimental

Detector System Comparison

Data from two parameter NaI(Tl) coincidence spectra are normally reduced to radionuclide analytical results by use of weighted least squares computer programs.[14-16] These programs require calibration information obtained using the same counting geometry for each nuclide present in the sample. The method gives good quantitative results when proper calibrations are available but can yield spurious results when unsuspected components or differences between the sample and the calibration standards exist. The coincidence photopeaks resulting from minor constituents in the sample are often obscured by radiations from other sample components. The analyst must then depend on the quantitative weighted least squares data analysis. The improved resolution obtained by using one or more diode detectors in a coincidence system improves the coincidence spectrometer's nuclide identification capabilities. The effect on the spectrometer's detection sensitivity has been investigated.

The detection limits for the major long-lived, coincidence-detectable radionuclides present in environmental river sediment samples have been compared for three detector configurations. The radionuclides used in this investigation were ^{60}Co, ^{106}Ru, ^{134}Cs, ^{152}Eu, ^{154}Eu, ^{226}Ra plus daughters and ^{232}Th plus daughters. The coincidence photopeak detection efficiencies for the nuclides studied are listed in Table I. The detector configurations consisted of the following three systems:

1. A pair of opposed 15-cm diameter by 13-cm thick NaI(Tl) detectors with NaI light pipes and an anticoincidence shield.
2. A 28-cm diameter by 15-cm thick NaI(Tl) detector opposed with a 120-cm^3 Ge(Li) detector.
3. A pair of opposed 60-cm^3 Ge(Li) detectors.

TABLE I

COINCIDENCE PHOTOPEAK DETECTION EFFICIENCIES

DETECTION SYSTEM	COUNTS PER DISINTEGRATION						
	^{60}Co	^{106}Ru	^{134}Cs	^{152}Eu	^{154}Eu	^{226}Ra	^{232}Th
NaI(Tl) + NaI(Tl)	.023	.008	.045	.019	.012	.0096	.0059
NaI(Tl) + Ge(Li)	.0029	.0008	.0099	.010	.0050	.0015	.0015
Ge(Li) + Ge(Li)	.00012	.00008	.0005	.0007	.0003	.00006	.00012

The detection sensitivities of the three detector configurations were calculated from data obtained by counting pure radionuclide sources mounted to simulate a 5-cm diameter by 1.3-cm thick sample geometry. The calculations were performed for an inactive sample matrix and a sample matrix containing only the natural radioactivity from a typical silt sample. The GEM program[14] was used to calculate the 1σ level detection limits for a 5000 minute counting period. The results of this investigation are presented in Table II. The data shows that the measurement sensitivity of the NaI(Tl)-Ge(Li) coincidence spectrometer is at least as good as the NaI(Tl)-NaI(Tl) coincidence spectrometer. The detection limits for the Ge(Li)-Ge(Li) system were about a factor of ten higher than the other systems. The NaI(Tl)-NaI(Tl) detector background levels limit the improved sensitivity which can be obtained with longer than 5000 minute counts while the detector backgrounds for systems containing one or more diode detectors are sufficiently low that improved detection sensitivities would be expected with longer counting times.

TABLE II

DETECTION LIMIT (1σ) AS A FUNCTION OF DETECTOR SYSTEM AND SAMPLE MATRIX FOR A 5000 MINUTE COUNT

(dpm/sample)

NUCLIDE	NO SAMPLE BACKGROUND ACTIVITY			SILT SAMPLE		
	NaI + NaI	NaI + Ge	Ge + Ge	NaI + NaI	NaI + Ge	Ge + Ge
^{60}Co	.14	.16	2.	.2	.16	2.
^{106}Ru	.8	1.0	7.	2.	3.	9.
^{134}Cs	.2	.09	.6	.9	.18	1.
^{152}Eu	.8	.2	.9	4.	.3	1.
^{154}Eu	.8	.16	1.0	2.	.3	2.
^{226}Ra	.8	.7	6.	NATURAL RADIOACTIVITY IN SAMPLE		
^{232}Th	1.5	1.8	5.	"	"	"

The radionuclide estimates calculated from a gamma-ray spectrum are correlated with each other due to the overlap of portions of the spectrum of individual nuclides. The correlations between pairs of nuclide estimates as calculated by the GEM program[14] are listed in Table III. An absolute correlation value of 1. is the maximum and values close to 0 are low correlations. A considerable reduction in correlations between nuclides was found for the detector systems which used one or more high resolution detectors. Also the positive correlations which indicate a possible over estimation of a pair of nuclides were reduced. Negative correlations indicate over estimation of one nuclide and underestimate of the other nuclide in a pair.

TABLE III

CORRELATION BETWEEN PAIRS OF NUCLIDES AS A FUNCTION OF DETECTOR SYSTEM AND SAMPLE MATRIX

NUCLIDE PAIR		NO SAMPLE BACKGROUND ACTIVITY			SILT SAMPLE		
		NaI + NaI	NaI + Ge	Ge + Ge	NaI + NaI	NaI + Ge	Ge + Ge
^{60}Co	^{226}Ra	-.04	-.006	-.009	-.06	-.004	-.007
^{60}Co	^{232}Th	-.02	-.004	-.015	-.02	-.008	-.02
^{106}Ru	^{226}Ra	-.02	-.004	-.017	-.03	-.016	-.03
^{106}Ru	^{232}Th	-.3	-.08	-.04	-.4	-.08	-.06
^{134}Cs	^{226}Ra	-.3	-.02	-.15	-.5	-.07	-.13
^{134}Cs	^{232}Th	-.13	-.04	-.04	-.05	-.04	-.17
^{152}Eu	^{226}Ra	.06	-.02	-.07	.2	-.08	-.08
^{152}Eu	^{232}Th	-.9	-.11	-.06	-.8	-.12	-.07
^{154}Eu	^{226}Ra	-.08	-.014	-.03	.02	-.05	-.03
^{154}Eu	^{232}Th	-.6	-.03	-.07	-.7	-.09	-.11
^{106}Ru	^{152}Eu	.2	-.005	-.008	.3	-.0001	-.006
^{106}Ru	^{154}Eu	.2	.0004	-.007	.3	.0017	-.017
^{152}Eu	^{154}Eu	.4	-.16	-.24	.5	-.17	-.26

The detector calibrations and data analysis methods were evaluated by analyzing a standard river sediment sample (NBS-SRM-4350). The results of these analyses are listed in Table IV for the nuclides measured by coincidence spectrometry. A comparison with the values reported by NBS was found to be generally within the range of the NBS certified and uncertified (other measurement results reported by NBS) values.

TABLE IV

RESULTS OF A COINCIDENCE SPECTROMETRIC ANALYSIS OF NBS STANDARD REFERENCE MATERIAL 4350

(NUCLEAR TRANSFORMATIONS PER SECOND PER GRAM OF MATERIAL)

NUCLIDE	NBS		COINCIDENCE DETECTOR SYSTEM		
	CERTIFIED	UNCERTIFIED	NaI + NaI	NaI + Ge	Ge + Ge
^{60}Co	.15 ± .01	.14	.15 ± .01	.15 ± .01	.17 ± .02
^{152}Eu	.24 ± .01	.16	.16 ± .01	.18 ± .01	.17 ± .01
^{154}Eu	.052 ± .004	.044	.040 ± .003	.042 ± .002	.049 ± .005

Delayed Coincidence

Radionuclides which decay through an intermediate isomeric state can be selectively detected by means of delayed coincidence methods. The megachannel analyzer can be used to record the energy of each gamma event and the time interval between events with the arrangement shown in Figure 1. The data can then be simultaneously analyzed for the presence of both prompt and delayed gamma-ray emitters. An example of the application of this technique is the determination of ^{57}Co in the presence of ^{152}Eu. The 122 keV gamma-ray from ^{152}Eu interferes with the measurement of ^{57}Co especially when the less abundant ^{57}Co 136 keV gamma-ray is not detectable due to the presence of other radioactivity. A source consisting of a mixture of ^{57}Co and ^{152}Eu was counted between a 60-cm^3 closed coaxial Ge(Li) detector and a 500-mm^2 planar Ge(Li) low-energy photon detector. The energy and time data were recorded with the megachannel analyzer. Figure 2 shows the coaxial Ge(Li) spectra observed both in prompt and delayed coincidence with the low energy photon detector. By gating off the prompt time peaks one can totally discriminate against all prompt events. Moreover, another degree of discrimination, although not needed in this case, can be obtained through conventional energy gating techniques.

Conclusion

High-resolution coincidence spectrometry has applications to a variety of radiochemical analysis problems including low-level environmental sample analysis. Sensitivities equivalent to all-NaI(Tl) detection systems can be obtained with increased selectivity by use of high-resolution coincidence spectrometric techniques. Data acquisition and analysis of the large arrays associated with high-resolution detectors can be accomplished with relatively modest equipment investments. Software has been developed to aid in the examination and reduction of the spectral data. The use of time as well as radiation energy in coincidence spectrometry has been shown to provide a further means for radionuclide measurement selectivity. It merits further investigation and development.

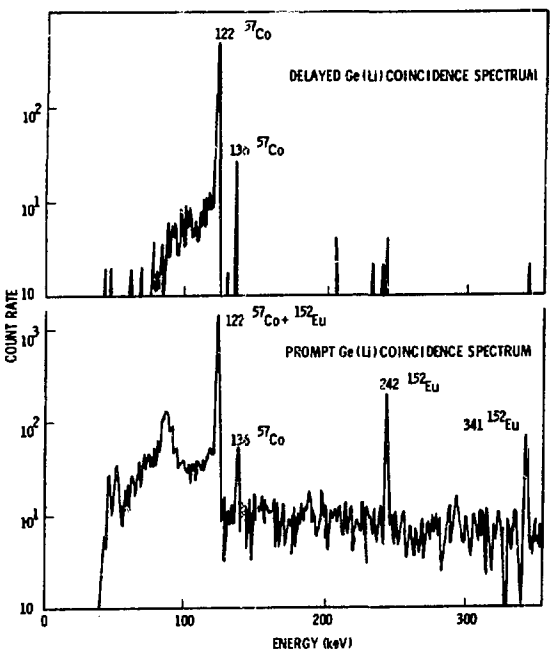

FIGURE 2. Ge(Li) Spectra of a Mixture of ^{57}Co and ^{152}Eu in Prompt and Delayed Coincidence Modes with a Coaxial Ge(Li) Detector and a Planar Ge(Li) Detector.

References

1. N. A. Wogman, "Comparison of Ge(Li) and Anti-Compton Systems for Measurements of Environmental Samples," IEEE Trans. on Nucl. Sci. NS-21 (1974) 526.
2. F. P. Brauer, J. H. Kaye, R. E. Connally, "X-ray and β-γ Coincidence Spectrometry Applied to Radiochemical Analysis of Environmental Samples," Radionuclides in the Environment, Am. Chem. Soc., Washington, DC (1970) 231.
3. R. E. Connally, W. A. Mitzlaff, F. P. Brauer, "Four Input Multiplexer for Two-dimensional Gamma-ray Spectrometry," IEEE Trans. Nucl. Sci. NS-17 (1970) 440.
4. F P. Brauer, J. E. Fager, W. A. Mitzlaff, "Evaluation of a Larger Ge(Li) Detector for Low-Level Radionuclide Analysis," IEEE Trans. Nucl. Sci. NS-20 (1973) 57.
5. J. H. Kaye, F. P. Brauer, R. E. Connally, H. G. Rieck, Jr., "Background Reduction Obtained with Gamma Detector by Use of Massive Cosmic-Ray Shielding," Nucl. Instr. and Meth. 100 (1972) 333.
6. J. H. Kaye, F. P. Brauer, R. E. Connally, H. G. Rieck, Jr., "Background Reduction of High-efficiency Ge(Li) Detector," Nucl. Instr. and Meth. 113 (1973) 5.
7. N. A. Wogman, R. W. Perkins, J. H. Kaye, "An All Sodium Iodide Anticoincidence Shielded Multi-dimensional Gamma-ray Spectrometer for Low-Activity Samples," Nucl. Instr. and Meth. 74 (1969)197.
8. J. A. Cooper, L. A. Rancitelli, R. W. Perkins, "An Anti-coincidence-shielded Ge(Li) Gamma-ray Spectrometer and Its Application to Radioanalytical Chemistry Problems," J. Radioanal, Chem 6 (1970) 147.
9. F. P. Brauer, J. H. Kaye, J. E. Fager, W. A. Mitzlaff, H. G. Rieck, Jr., "A Dual Ge(Li)-Dual NaI-(Tl) Gamma-ray Spectrometer," Nucl. Instr. and Meth. 102 (1972) 223.
10. J. A. Cooper, R. W. Perkins, "An Anticoincidence-Shielded Dual Ge(Li) Gamma-Ray Spectrometer for Low-Level Environmental Radionuclide Analysis and Gamma Coincidence Studies," Nucl. Instr. and Meth. 94 (1971) 1.
11. J. A. Cooper, R. W. Perkins, "A Versatile Ge(Li) Coincidence-Anticoincidence Gamma-Ray Spectrometer for Environmental and Biological Problem," Nucl. Instr. and Meth. 99 (1972) 1.
12. F. P. Brauer, R. E. Connally, H. G. Rieck, Jr., "Anticoincidence-Shielded Multiple-Coincidence Gamma-Ray Scintillation Spectrometer," Trans. Am. Nucl. Soc. 15 (1972) 153.
13. F. P. Brauer, J. H. Kaye, J. E. Fager, "NaI(Tl)-Ge(Li) Coincidence Gamma-Ray Spectrometry for Radionuclide Analysis of Environmental Samples," IEEE Trans. on Nucl. Sci. NS-22, (1975) 661-670.
14. W. L. Nicholson, J. E. Schlosser, F. P. Brauer, "The Quantitative Analysis of Sets of Multicomponent Time Dependent Spectra from Decay of Radionuclides," Nucl. Instr. and Meth. 25 (1963) 45-66.
15. F. P. Brauer, J. E. Schlosser, "Spectral Data Handling Systems," Modern Trends in Activation Analysis, National Bureau of Standards, Washington DC, (1969) 1102.
16. F. P. Brauer, J. E. Fager, "A Computer System for Environmental Sample Analysis and Data Storage and Analysis," IEEE Trans. on Nucl. Sci. NS-23, (1976) 743-747.

Proceedings, ERDA X-and Gamma-Ray Symp. Ann Arbor, MI, May 19-21, 1976 (Conf 760539)

A HPGe COMPTON-SUPPRESSION AND PAIR SPECTROMETER*

David C. Camp
Lawrence Livermore Laboratory, University of California
Livermore, California 94550

Summary

A HPGe detector incorporated into a Compton-suppression and pair spectrometer yields a continuum suppression factor of over 30. Cryostat housing requirements to obtain such suppression are discussed, sample spectra are presented, and several experiments making use of the HPGe dual system are discussed.

Introduction

Early Ge(Li) detectors were small. Consequently, the signal-to-noise or peak-to-Compton-continuum values were poor, and ways to improve peak identifiability were sought. Pulse-shape discrimination, Compton scattering-summing spectrometers, Compton-suppression spectrometers, and three-crystal pair spectrometers were all tried. The first two methods proved unsatisfactory, but the latter two have been more successful. These methods are more fully discussed and referenced in an earlier review.[1]

Compton-suppression and pair spectrometers are useful in measuring gamma-ray spectra. They improve upon the peak-to-continuum ratio of a Ge detector alone. Also, they simplify the spectrum, remove interferences, and lead to improved accuracies in determining transition intensities. Compton continuum suppression factors have varied from 4 to 12 depending on the geometry employed. Pair spectrometers can lead to dramatically simplified spectra, but generally they require longer data accumulation times.

Over the past five years, the efficiency of Ge(Li) detectors has increased from 10% to almost 50% relative to a 7.6 cm × 7.6 cm NaI(Tℓ) at 1.33 MeV. Excellent energy resolution (∿ 2.0 keV @ 1.33 meV) has been maintained. Thus, the necessity or desire for continuum reduction appears to have lessened. This is unfortunate because suppression and pair spectrometers can always improve the signal-to-noise ratio regardless of the Ge(Li) detector size. The use of Ge(Li) detectors of 15% to 45% relative efficiency in combination with appropriate anticoincidence geometries can result in Co-60 peak-to-minimum ratios of from 100/1 to perhaps 500/1. Unfortunately, these larger Ge(Li) detectors no longer function effectively as three-crystal pair spectrometers because of the reduced amount of annihilation radiation that escapes. However, if careful attention is paid to the experimental arrangement, it is possible to achieve excellent continuum suppression and use the spectrometer simultaneously as a three-crystal pair spectrometer. This paper describes the use of a high-purity-germanium (HPGe) detector and large anticoincidence NaI(Tℓ) detectors in combinations which lead to simultaneous use of the system as a Compton-suppression and pair spectrometer.

Principles of Operation

The two most common anticoincidence geometries used for Compton-suppression spectrometers are illustrated in Fig. 1. Another geometry is discussed by Konijn, et al.[2] Generally, a Ge(Li) detector within its own vacuum housing is placed within a scintillation detector (usually NaI(Tℓ) or plastic scintillators with a split-annulus or split-halves enclosing geometry). Gamma rays from a source positioned outside are collimated to strike the central Ge(Li) detector. Those gamma rays scattering between Θ-min and Θ-max have a finite probability of interacting with the surrounding scintillator. If these scattered gamma rays can be detected above the scintillator noise level, they can be used as anticoincidence gates for the corresponding central Ge(Li) detector events. In principle, then, only full-energy events should remain in the Ge(Li) detector spectrum.

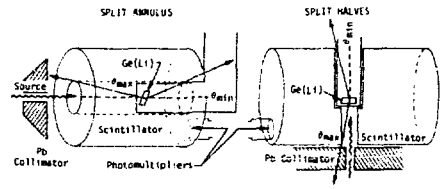

Fig. 1. The two most common geometries used in Compton-suppression spectrometers.

In practice, however, the Compton continuum is not eliminated, but only partially suppressed. Those gamma rays having scattering angles less than Θ-min will not be suppressed, while those having backscattering angles greater than Θ-max escape detection. The latter contribute high-energy photoelectrons to the Ge(Li) spectrum concentrated near the Compton edge. Contributions to the Compton continuum also come from gamma rays that scatter from inactive Ge, the cryostat housing, or the collimator walls and then interact completely with the Ge(Li) detector and from gamma rays that scatter out of the Ge(Li) detector and are totally absorbed in inactive Ge, cryostat walls, or the scintillator housing. Therefore, the extent of continuum suppression will depend on the completeness of enclosure by the anticoincidence detectors, the active to total volume of the Ge detector, and the materials enclosing and surrounding the central detector.

In three-crystal pair spectrometers, source gamma rays are collimated to strike only the central Ge detector. Those interacting with Ge via the pair production process produce electron-positron pairs, most of which lose their kinetic energy within the central detector. If the two oppositely directed 511-keV annihilation quanta escape the Ge detector and deposit their full energy in the surrounding scintillators, a triple coincidence will allow recording of only the double escape or pair peaks. As the central detector volume increases, the probability of both 511-keV quanta escaping decreases rapidly. Thus, large-volume Ge detectors make poor central detectors for pair spectrometers, but excellent detectors for Compton- suppression spectrometers. A more detailed discussion can be found in Ref. 1.

The HPGe Central Detector

The availability of HPGe offers the possibility that both the n- and p-junctions required to make a detector can be made vanishingly thin (0.1-100 μm); thus the active to total volume ratio can approach 1.0. With inactive Ge reduced to a minimum, the next requirement is to reduce the amount of total mass surrounding the detector. Figure 2 is a schematic drawing of the detector-holding arrangement. The detector is 31 mm

* This work was performed under the auspices of the U.S. Energy Research & Development Administration, under contract No. W-7405-Eng-48.

(cont. on p. 285)

Proceedings, ERDA X-and Gamma-Ray Symp. Ann Arbor, MI, May 19-21, 1976 (Conf 760539)

NUCLEAR APPLICATIONS OF CdTe DETECTORS

Gerald Entine
Radiation Monitoring Devices, Inc.
6 Silver Lake Avenue
Newton, Massachusetts 02158

Introduction

During the past year, CdTe detectors have been used by diverse groups needing compact, sensitive, room temperature instrumentation for nuclear measurement.

These applications are interesting both in themselves and as a means of understanding more about CdTe detector behavior. The applications which will be discussed include nuclear medicine, communications, satellite spectroscopy, heat shield ablation and reactor monitoring.

CdTe detectors are usually made from chlorine-doped or indium doped crystals with metallic or aquadag (carbon) contacts. Despite differences in the operating parameters of the two types of devices (such as bias voltage, and leakage current), both types of detectors perform comparably well. As I am more familiar with detectors from chlorine-doped material, I shall focus predominantly on uses of that detector.

A typical chlorine-doped detector consists of a 1 cm dia. crystal, 2 mm thick, with symmetrical platinum disc contacts of 7.5 to 8.0 mm dia. Bias voltages run from 10 to 100 volts with leakage currents of 10 to 400 nA. While the wide band gap (1.44 eV) reduces the signal pulse height slightly with respect to silicon, it reduces the noise even more, so that the signal to noise ratio of a CdTe detector at room temperature usually exceeds that of a comparable Si device. In addition, the high atomic number provides excellent stopping power. A 2 mm thick CdTe detector stops 85% of the 100 keV rays hitting it and 8.5% of the 661 keV rays. Of particular importance is the fact that below 150 keV, over 80% of the absorbed rays can be in the photopeak.[1]

One of the nicest features of the detectors is the ease with which they can be handled. They can be stored indefinitely, handled by tweezer without clean room precautions, and can be used in non-hermetic packages if the humidity is kept low enough to avoid the formation of a temporary conductive moisture film. They cannot be permanently damaged by overvoltages or changes in temperature between -30°C and +70°C. Strong lead attachment is straightforward because the platinum is chemically bonded to the crystal.

In addition, it is possible to epoxy bond the detectors to a printed circuit board to form very compact arrays. Some problems have been encountered, however, when epoxies were used to totally encapsulate the sensors.[2] Apparently the epoxies will occasionally create a surface film on the detector which can alter its leakage current and noise characteristics. Control experiments have indicated that the effects do not arise from the heating of the detector during the curing cycle. Rather, it is the chemistry of the epoxies that is most suspect. In general, the overall handling aspects of the CdTe detector have proven quite nice.

Nuclear Medicine

The first use of CdTe detectors for nuclear medicine involved the development of subminiature detectors small enough to fit into hypodermic needles. These have been used for both brain research and intracavitary exploration.[3] More recently, larger sensors have been used for instruments which rely on external sensing for non-invasive detection of disease.

One clinical application of CdTe detectors is now under test at the V.A. Hospital in West Roxbury, Massachusetts.[4] A recognized screening procedure to identify patients with a high predisposition to pulmonary embolism is based on the early detection of venous thrombosis of the legs. I-125 labeled fibinogen, injected into the patient will collect at the clot over the course of several days and create a hot spot which can be detected externally.

The detection equipment standardly used consists of a NaI probe over 3 cm in diameter and almost 23 cm long. This large probe is particularly inconvenient for bedridden patients of limited mobility, especially since one of the most common clot sites is high between the thighs. A CdTe probe consisting of a 1 cm dia. crystal and a miniaturized preamplifier was developed with overall dimensions of less than 5 cm. This small size not only provides greater comfort for the patient, but also allows the sensor to be positioned more precisely over the index marks which are put on the patient to aid in placement reproducibility.

At this time all patients in the study are being measured with both the NaI and the CdTe probes in order that a direct comparison can be done. The procedure consists of measuring the count rate over several points along the leg and comparing those rates to that measured above the heart which serves as the nomalization site. A clotted site shows a significant increase in count rate over 3 days while an unclotted site shows little change. In all, over 200 patients will be studied. The initial results show that the CdTe probe is performing as expected - namely that it provides convenience, comfort and precision with at least as good and possibly better clinical sensitivity as the NaI probe. This convenience is essential if the fibrinogen screening procedure is to be widely used.

Another nuclear medicine instrument using CdTe detectors is being developed by the U. of Cal. S. F. Med. Center.[5] The instrument will be capable of measuring the absolute density of a patient's lung as an aid in detecting pulmonary edema. The system consists of a collimated Gd-153 source and two CdTe detectors separated by a small fixed angle. The source is first placed opposite detector 1 which measures the transmitted beam while detector 2 measures the scattered beam. The source is then placed opposite detector 2 and the measurement is repeated. Finally the instrument is moved to different positions to scan various parts of the lung. The use of CdTe detectors allows the system to be quite compact. In particular the tight shielding of the detectors which is necessary because of the low intensity of the scattered beam is made much easier by the elimination of the phototube associated with NaI detectors.

The development of such a non-invasive clinically useful instrument for measuring lung density will permit significant advances in the evaluation of pulmonary edema. The simplifications of the mechanical and electrical aspects of the system through the use of CdTe should help to make the system cost effective and convenient to operate. This particular application will be described in detail at tomorrow's session.

Current Mode Communication System

While most detector applications are presently based on the pulsed mode of operation, the current mode will surely be used in many future applications. One such development effort by the Navy is now underway. An x-ray communications system is being designed based on a pulsed x-ray source and a CdTe sensor. The x-ray source has a peak voltage of 40 kV, an average energy of 25 keV, and a pulse width of 5 microseconds. The CdTe detector is required to operate at temperatures of up to 70°C with as little noise as possible. An interesting approach to the problem of reducing the leakage current at the higher temperatures is being used, namely to run the detectors at only 10 V bias. The reduction in signal level is more than compensated for by the reduction in noise and leakage currents. In addition, this voltage is extremely compatible with the requirements of the solid state electronics so that the system is greatly simplified.

Present Navy results indicate that the quiescent leakage current of the detectors can be taken into account by subtraction, reduction with low bias voltage, or by source modulation, and that CdTe detectors will perform well in this mode.

Satellite Spectroscopy

Nowhere is detector size and efficiency of more central importance than in space satellites where each cubic centimeter is worth thousands of dollars. It is therefore not surprising that work is under way to use CdTe sensors for gamma ray spectroscopy above the atmosphere. In this application, both long term stability and resistance to radiation damage are a necessity. Because of the polarization effects which occured before the development of the modern platinum contact, several long term studies were done on recent detectors to measure the change of signal pulse height with time. In one of these, a platinum contacted, chlorine-doped detector was operated continuously for over 100 days with no measurable change in peak position.[7] This particular detector had energy resolution of 7 keV at 122 keV.

In a program undertaken to measure the effects of proton bombardment, detectors were subjected to fluxes of between 10^8 and 10^{11} 33 MeV protons per cm^2.[8] No significant degradation was observed until a flux of 10^9 per cm^2 was reached, at which dose the energy resolution degraded rapidly with further irradiation.

The main focus of these programs at present is to provide relatively large - 10 cm^2 - assemblies of detectors for launches in the next two years. In particular, valuable information about the performance of the detectors at temperatures near -15°C is resulting. Here, the leakage current and noise are reduced enough to allow large areas to be practical while the carrier mobilities are still quite good. It is expected that this cooling approach may be applicable in other areas as well, where the small added bulk of thermoelectric coolers can be accepted in exchange for improved performance.

Heat Shield Ablation Studies

At present, the largest use of CdTe detectors in the world is in an Air Force program which studies the ablation of spacecraft heatshields during their passage through the atmosphere. Heat shield materials are difficult to test because the extremely high temperatures and frictional forces of reentry are impossible to duplicate on the ground. Thus, new materials are tested on very small rockets with measurements taken of tip recession during flight. The shield material is impregnated with radioactivity and a sensor, located far enough behind the tip to stay at room temperature, measures the decrease in count rate as a function of time. This decrease can be directly correlated to the ablation of the tip while the velocity and height of the rocket can be used to estimate the forces of the atmosphere.

Very stringent instrumentation difficulties arise here because of the small time interval over which the measurements must be made (seconds). The sensor package has to be as sensitive as possible so that sufficient counts are received to provide the required statistical accuracy. In addition, as the top of the shield sees much different conditions than the bottom, the package must be as small as possible so that several sensors can be put in one rocket tip. To do this, the previously used bulky scintillator-photomultiplier tube detectors were replaced with the CdTe sensors. As a result, a great deal has been learned, not only about heat shields, but about the performance of the detectors and how they behave under conditions of rugged environments.[2,9]

One finding concerns the sensitivity of detectors to vibration. CdTe detectors are microphonic but do not generate spurious signals under ordinary laboratory or field use. However, the extremely high shock and vibration levels of the test flights requires that the detectors be packaged in a highly sophisticated isolator of foam and rubber. One of the packages for this Air Force program which isolates the crystal from vibrations as high as 10,000 g's at 24 kHz is less than 6 cm long by 2 cm dia. Included in the package with the detector is a complete preamplifier. Another of the preamplifiers developed under this program has noise of below 6 keV and is a hybrid circuit of postage stamp size. These circuits could be very useful if they were made generally available.

Over 100 detectors have been used in the Air Force program. All were used in the counting mode with bias voltages between 35 and 67 volts. Variations among the sensors in sensitivity were small enough that it was not difficult to exchange one for another with only minor changes in calibration. Leakage currents were variable but always below the design maximum of 250 nA.

At this time CdTe sensor packages have been used successfully on several flights and have resulted in significant improvement in measurement precision. The instrumentation packages are becoming more perfected and should provide engineering data which will allow other CdTe users to progress at a rapid rate.

Techniques To Improve Energy Resolution

The major limitation to the energy resolution of CdTe detectors at present involves the difficulty of applying large bias voltages to the detector. While a few detectors have been made which can operate at several hundred volts, the typical bias is about 60 volts. Significant efforts are being directed into this area, both in the United States and Europe, which should result in detectors operating at up to 1000 V. In the meantime, two electronic techniques have been developed to circumvent this problem.

One of these techniques involves the use of an MIS-type contact.[10] The uncontacted crystal is sandwiched between two thin, metallized mylar films with the metallic side outward. An electronic timing circuit applies one to two thousand volts of bias to the sandwich for tens of seconds, and then short circuits

the device for about one second. Because the device is thermoelectrically cooled to -20°C, its internal impedance is high enough that it will not self-discharge during the on time; thus, excellent charge collection is achieved. During the off period, a pulse of light from an LED discharges the detector so that no long term charge buildup occurs. The spectrometer head which contains the detector sandwich, the thermoelectric cooler and the preamp is only 11 cm long by 7 cm in dia. Resolution of 3.0 keV at 30 keV and 6.0 keV at 122 keV with the large fraction of the counts in the photopeak were obtained with crystals 2 mm thick. The system is now being developed for use in several areas of application.

A totally different electronic approach to improving the resolution of the detectors has been developed in conjunction with work on reactor monitoring.[11] Here pulse shape discrimination is used to select those pulses which arise near the negative contact of the detector. This results in the rejection of pulses which do not have 100% charge collection efficiency, and is effective if the corresponding decrease in count rate can be tolerated. For example, using Radium 226, resolution of 13 keV at 295 keV and 17 keV at 1765 keV were obtained at room temperature with a 1 mm thick detector operating at 200 volts. Cooling the detector to -20°C further improved the results. For Cs^{137}, the 661 keV peak was resolved to 14 keV at room temperature and to 8 keV at -20°C with a peak to compton ratio of 6 to 1.

This resolution, even at room temperature, is sufficient to readily distinguish the isotopes and fusion products relevent to reactor monitoring. The small physical size of the detectors will allow the measurements to be made in situ despite the narrow constrictions dictated by reactor design, thus overcoming one of the major drawbacks of the cryogenically cooled solid state detectors.

Future of CdTe Detector Applications

It has always been difficult to predict the most probable applications for CdTe detectors. The detectors were initially developed for reactor monitoring and fuel analysis. For reasons as yet unclear, this area for CdTe has developed extremely slowly, while the field of heat shield ablation measurement, which was entirely unknown to almost everyone in the CdTe field a few years ago, is now the largest by far.

At present the users who are displaying the most interest are those in nuclear medicine. Clinical instruments such as the lung densitometer and blood clot detector appear to be stimulating researchers to consider using CdTe in other medical instruments. In particular, there are several instruments being contemplated which will use fairly long linear arrays of CdTe sensors in order to reduce measurement time in present scanning systems.

Research groups in reactor monitoring, process control and safeguard surveillence are also beginning to show interest in CdTe. Although many industrial development engineers are reluctant to make a major commitment to usage until they can be assured that there will be an inexpensive version of the CdTe detector suitable for counting applications. This should be forthcoming in the near future.

The rate at which CdTe detectors become widely used will depend upon several factors, only some of which are in the hands of the producers of these devices. The producers must necessarily develop detectors, which are either larger, have better resolution, have lower leakage current, or are much cheaper and in a short enough time that the momentum built up over the past year is not lost. This requires that Government funding agencies continue to provide development money so that the technology gets to the point that it is commercially viable. Finally, application groups must strive to keep continuous direct contact with the producers so that their short term development efforts can be interfaced with needed long term research emphases. With the cooperation of these three segments of the field, CdTe detectors should become the basis for a large number of useful instruments in the nuclear instrumentation field.

During the coming two years, the place of CdTe detectors in the nuclear instrumentation field should become clear. Detectors will be available in a large enough quantity and at a low enough price that engineers will be able to consider them on their technical merits and on their cost effectiveness rather than on their promise for the future. Already prototypes for large linear arrays, small clinical instruments, and new flight packages for both satellites and ablation studies are being tested. Operating parameters are being pinned down, and compatible microcircuits are well along in development. As a result of the intensive activity now being carried out both by detector development groups and by application groups, CdTe detectors should produce a significant, beneficial impact on the field of nuclear instrumentation.

References

1. Serreze HB, Entine G, Bell RO, 1974 IEEE Trans Nuc Sci 21, 404

2. Droms CR, Langdon WR, Robison AG, Entine G, 1976 IEEE Trans Nuc Sci 23 - 1, 493

3. Martini M, Walford GV, 1972 3rd Int Conf on Medical Phys. Gothenburg Sweden

4. Entine G, Serreze HB, Garcia DA, 1974 IEEE Trans Nuc Sci 21, 726, 1976 IEEE Trans Nuc Sci 23-1, 594

5. Kaufman L, et al, 1976 IEEE Trans Nuc Sci 23-1, 498, also private communication

6. Ward PT, Carver GP, Naval Surface Weapons Center, White Oak Lab. priv. comm

7. Nakano GH, Imhof WL, Kilner JR, 1976 IEEE Trans Nuc Sci 23-1, 599

8. Ibid

9. Baxter R, 1976 IEEE Trans Nuc Sci 23-1, 498, also priv. comm

10. Eichinger P, Halder N, Kemmer J, 1974 Nuc Instr & Methods 117, 305; priv. comm

11. Jones LT, Woollam PB, 1975 Nuc Instr & Methods, priv comm

Note: The most comprehensive recent source of papers on CdTe nuclear detectors is the IEEE Trans Nuc Sci Vol 23-1 which contains 11 papers. The 2nd International Symposium on Cadmium Telluride: Physical Properties and Applications will be held in Strasbourg, France in June, 1976 with a published proceedings.

Proceedings, ERDA X-and Gamma-Ray Symp. Ann Arbor, MI, May 19-21, 1976 (Conf 760539)

ADVANCES IN MERCURIC IODIDE SINGLE CRYSTAL NUCLEAR DETECTORS*

P.T. Randtke, C. Cirtale, R.C. Whited, and L. van den Berg
EG&G, Santa Barbara Operations

Abstract

The preparation of crystalline detector material of high perfection, the methods used for its characterization, and the fabrication of individual detectors are described. Major progress has been made in the uniformity of large-area (1 cm × 1 cm × 0.5 mm) detectors manufactured from crystals having a low dislocation density. An array of nine individual matched detectors has been built and evaluated.

Introduction

During the past several years mercuric iodide has been studied as a potential room temperature, high-Z semiconductor, gamma spectrometer detector material. It has been reported[1] that thin (0.1-0.4 mm) small area (~10 mm^2) HgI_2 detectors work very well for low energy (<60 keV) gamma-rays. Efficient high energy (0.4-1.0 MeV) gamma-ray detectors, however, require thicker, larger volume devices. An integrated effort, starting from commercially available HgI_2 powder and extending through to packaged detectors, is being made at this laboratory to produce such detectors.

In this report, preparation and selection of the crystalline material and the consistent manufacture of 1 cm × 1 cm × 1 mm detectors with 20 mm^2 active contact area are described. With continual improvements in the quality of the crystals, the uncollimated gamma-ray spectra now obtained are equal to those previously obtained on significantly smaller detectors. Nine individual detectors have been combined into a 3 by 3 array, and the resulting spectra are reported.

Material Selection

The use of thick detectors with a large area requires that the detector material is uniform, and that the mobility-trapping time ($\mu\tau$) product of the charge carriers is sufficiently large. Crystalline uniformity is reflected in the resolution of uncollimated nuclear spectra, and $\mu\tau$ determines the trapping occurring for a given thickness and electric field. The crystals used for detector fabrication are selected and tested by five procedures.

Etch Pit Count

A single crystal is cut in half perpendicular to the c axis. One of the sawed surfaces is etched in either methanol for 1 to 6 minutes or in 10% KI solution for 1 to 3 minutes, in order to reveal dislocations across the surface as evidence by etch pits. Earlier crystals were nonuniform, containing growth rings generally perpendicular to the direction of growth. Density of dislocations in the growth rings was usually about 10^6 cm^{-2} and between the rings about 10^5 cm^{-2}. The presence of the growth rings has been correlated with changes in the ambient temperature in the crystal growing room, which was also observed independently by Scholz.[2] Correction of temperature variations during crystal growth have largely eliminated this type of nonuniformity. Figure 1 shows three crystals with severe, medium, and minimal growth ring structure, and Figure 2 shows uncollimated ^{241}Am gamma-ray spectra from three identical size detectors fabricated from these crystals. The FWHM of the 60-keV peak decreases with increasing dislocation homogeneity. In addition to being more homogeneous, recently grown crystals also have a lower average dislocation density of about 10^4 cm^{-2}.

Fig. 1. Three crystals with (left to right) severe, medium, and minimal growth ring structures.

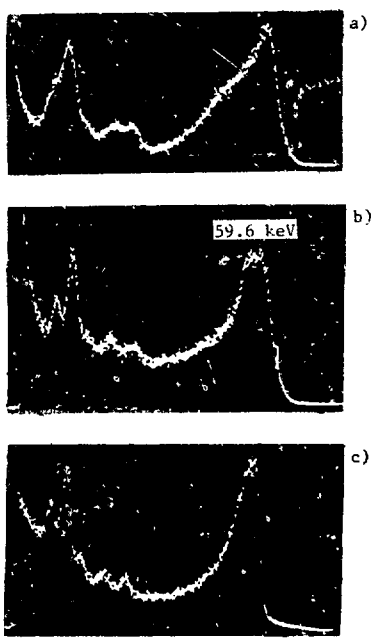

Fig. 2. Uncollimated ^{241}Am gamma-ray spectra for a) severe, b) medium, and c) minimal growth ring structures; FWHM are 22 keV, 9 keV, and 5 keV, respectively; pulser FWHM 2.6 keV.

*This work was performed under the auspices of the U.S. Energy Research and Development Administration.

Optical Homogeneity Check

A raster pattern light scanner has been used to look for inhomogeneities in HgI_2 using both He-Ne (6328Å) and He-Cd (4416Å) lasers. Such scans should reveal inhomogeneities not visible on the surface by etch pit densities. Details of the measurements will be published later.

μτ Product

The μτ products are determined from changes in the pulse height of an ^{55}Fe gamma-ray spectrum (5.9 keV) as a function of the bias voltage.[3] Since HgI_2 detectors have low noise at low gamma-ray energies, ^{55}Fe with its 2-micron penetration depth can be used, which permits separation of $\mu_e\tau_e$ and $\mu_h\tau_h$ while avoiding the plasma effect associated with alpha particles. To insure stability of the detector response, 12 to 24 hours are generally allowed to elapse after the bias is applied before a measurement is made. Table 1 lists the products measured on several recent large single crystals.

Table 1. μτ products for several HgI_2 crystals

Crystal Batches	$\mu_e\tau_e$ (cm^2/V)	$\mu_h\tau_h$ (cm^2/V)
S1-6	1.5×10^{-4}	2.0×10^{-6}
S5-4	2.0×10^{-4}	1.5×10^{-5}
S5-8	2.0×10^{-4}	3.0×10^{-6}
S5-9	1.5×10^{-4}	5.0×10^{-6}
S6-8	0.8×10^{-4}	2.0×10^{-6}

Experimental[4] and theoretical[5] studies indicate that the values of the mobility for electrons, μ_e, and holes, μ_h, are lattice scattering limited. Therefore, increasing the μτ product necessitates increasing the trapping time, which is directly related to the cross section and density of the traps. Since μτ is measured using an electronic shaping time of 10^{-6} seconds, shallow traps with a detrapping time much less than 10^{-6} seconds do not affect the measured trapping time (unless a high density of shallow traps results in a multiple trapping-detrapping process).

Polarization Effects

The presence of polarization effects is checked by measuring the count rate as a function of time at low bias. Figure 3 shows a recently grown crystal (S6-8) with minimal polarization, while an earlier crystal (S5-2) has substantial polarization effects. The data were taken with a source count rate of 700 counts/sec. The time to reach stable conditions depends on the count rate. Polarization effects are present in recent cryatals only at low fields and therefore do not affect detector performance under usual conditions.

TSC Measurements

To increase the trapping time it is necessary to understand in detail the nature of the traps involved. The most straightforward method to obtain information about the shallower traps is provided by thermally stimulated conductivity (TSC) measurements. In TSC measurements on recent crystals, major hole traps have been observed at 165°K and 180°K; other traps are present at 81°K, 98°K (electron trap), 102°K (hole trap), 116°K and 138°K. The energy level of the 165°K trap as determined by the Garlick-Gibson initial rise method[6] was 0.32 eV. Details will be published later.

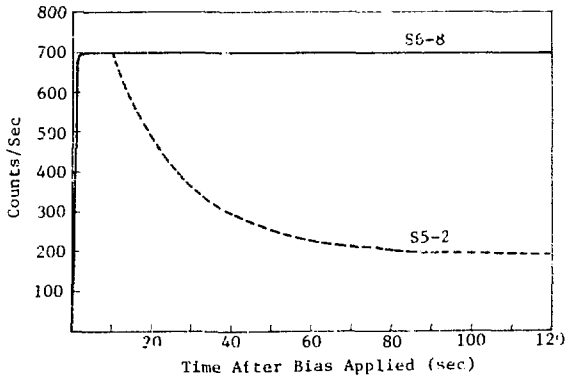

Fig. 3. Count rate as a function of time for Crystals S6-8 and S5-2.

Detector Preparation

One half of a crystal is cut into approximately 1 cm^2 blocks. One block is mounted on a jig and the top face is polished and etched with 10% KI solution. A 200Å thick palladium contact is evaporated onto this surface and a platinum lead wire is attached. The top area is then covered with Humiseal, and a glass cover plate is attached to the Humiseal with epoxy. The upper part of the block is then cut off to about 1 mm greater than the final thickness, and the surface is again polished and etched. The thickness is periodically checked with a non-contact gauge which monitors absorption of the 59.5-keV photopeak of a ^{241}Am source. The contacting procedure is repeated, and the entire detector is finally encapsulated in Humiseal (Fig. 4).

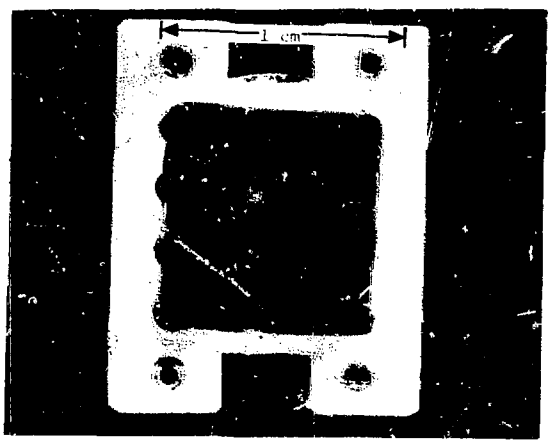

Fig. 4. Photograph of a finished detector.

Detector and Array Performance

Figures 5a, b, and c show the uncollimated gamma-ray response for ^{241}Am, ^{57}Co, and ^{137}Cs, respectively. The detector, 1 cm × 1 cm × 1 mm with a 20 mm^2 area and 200Å thick palladium contact, was biased with 2500 V, and the amplifier shaping time was 3 μsec. Table 2 lists the peak to valley ratios for detectors from different crystals. These values show an improvement compared to previous large-area detectors.

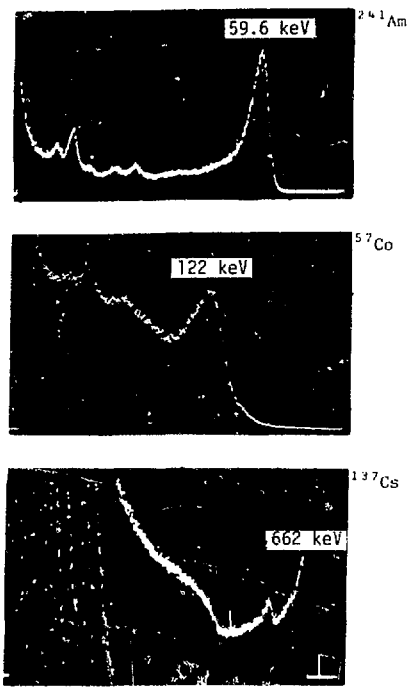

Fig. 5. Uncollimated gamma ray spectra of ^{241}Am, ^{57}Co, and ^{137}Cs.

Table 2. Peak-to-valley ratio of several detectors

Detector Number	Peak-to-Valley Ratio (^{137}Cs)
S1-6-4-2	1.8:1
S1-6-3-2	2.1:1
S3-8-5-1	1.9:1
S3-8-5-4	2.5:1
S3-8-7-1	2.4:1
S5-8-3-1	1.9:1
S5-8-3-2	1.7:1

Twelve planar detectors were fabricated from crystals S1-6 and S3-8 as described above. The detectors were 1 cm × 1 cm × 1 mm with a 20 mm^2 Temporel contact. Three detectors were wired to a Tennelec 161A preamplifier with three preamplifiers used to form a 3 by 3 array.

The preamplifier outputs were summed by a linear amplifier and passed to an Ortec 450 shaping amplifier. Figure 6 shows the array setup. Figure 7a is the total array output for uncollimated ^{241}Am, and Figs. 7b-d are the outputs of each preamplifier. The FWHM of the 60 keV photopeak in Fig. 7a is 11 keV. Figures 8a and b show the uncollimated ^{137}Cs and ^{239}Pu spectra (log scale) for the 3 by 3 array.

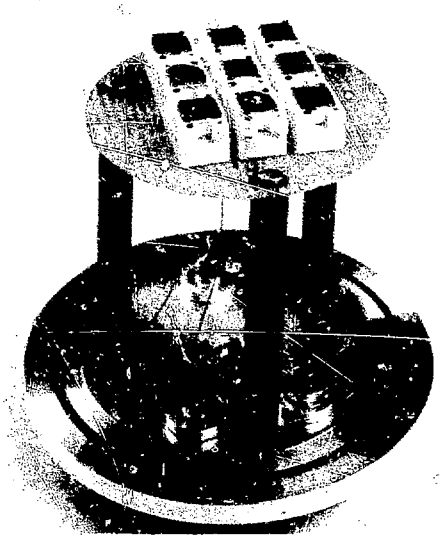

Fig. 6. Photograph of array arrangement.

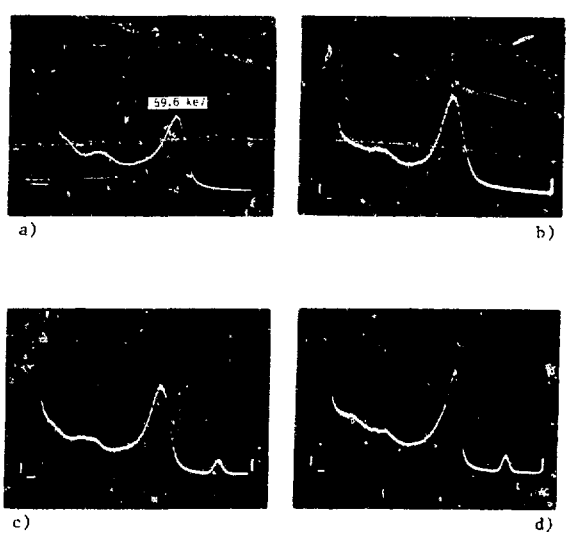

Fig. 7. Uncollimated gamma-ray spectra of ^{241}Am for a) array output, b-d) three individual preamplifiers.

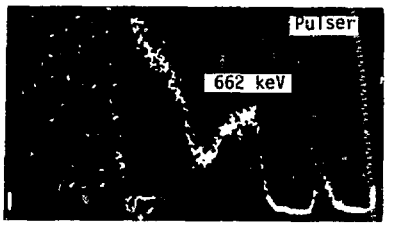

a) ^{137}Cs

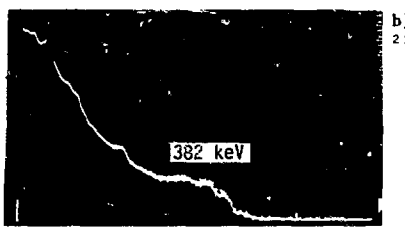

b) ^{239}Pu

Fig. 8. Uncollimated spectra from array for
a) ^{137}Cs (linear scale) and
b) ^{239}Pu (log scale)

Summary and Conclusion

Recent improvements in crystalline homogeneity allow better resolution for large area HgI_2 detectors. A FWHM of 5 keV for an uncollimated ^{241}Am spectrum has been achieved with a 20 mm^2 by 0.5 mm detector at room temperature. A prototype array which increased the active volume to approximately 0.1 cm^3 had a FWHM of 11 keV for ^{241}Am, which is comparable to the resolution of a NaI detector.

Further improvements in μτ products and crystalline uniformity will allow larger active detector volumes with resulting increases in detector efficiency and resolution.

Acknowledgment

The authors wish to acknowledge M. Slapa and W. Seibt of UCLA for helpful discussions and use of special equipment.

References

1. M. Slapa, G.C. Huth, W. Seibt, M. Schieber, and P.T. Randtke, *IEEE Trans. Nucl. Sci., NS-23*, No. 1, 102 (1976).

2. H. Scholz, private communication.

3. H.B. Serreze and G. Entine, *IEEE Trans. Nucl. Sci., NS-22*, No. 4, 1995 (1975).

4. R. Minder, G. Majni, C. Canali, G. Ottaviani, R. Stuck, J.P. Ponpon, C. Schwab, and P. Siffert, *J. Appl. Phys., 45*, 5074 (1974).

5. J.H. Yee, J.W. Sherohman, and G.A. Armantrout, *IEEE Trans. Nucl. Sci., NS-23*, No. 1, 117 (1976).

6. G.F. Garlick and A.F. Gibson, *Proc. Phys. Soc., (London), 60*, 574 (1948).

Proceedings, ERDA X-and Gamma-Ray Symp. Ann Arbor, MI, May 19-21, 1976 (Conf 760539)

X-RAY DETECTOR CALIBRATIONS IN THE 280-eV TO 100-keV ENERGY RANGE*

J. L. Gaines, R. W. Kuckuck, and R. D. Ernst
Lawrence Livermore Laboratory, University of California
Livermore, California 94550

Summary

The absolute sensitivity for several different types of radiation detectors has been measured using x-rays in the energy range of 280 eV to 100 keV. The photons in this energy range are produced using three separate x-ray-generating facilities. The detectors include a silicon semiconductor, two photoelectric diode detectors employing aluminum and gold photocathodes, and three detectors incorporating plastic scintillators and photodiodes. The plastic scintillators were MEL-150C, Pilot B, and NE102.†

Introduction

The measurement of intense, low-energy x-ray pulses has received a significant degree of attention in the last few years, primarily because these measurements are important for laser-plasma interaction studies. To perform these measurements requires a detector whose time response and whose sensitivity as a function of photon energy are both well known.

The detector sensitivity is generally determined using x-ray flux levels, where a small steady-state output current can be accurately measured and where counting techniques can be used to determine the incident x-ray flux absolutely. Thus, for the measured sensitivity to be meaningful when measuring much larger x-ray fluxes, the linearity of the detector must also be considered. It is important therefore that the detectors be operated only in those ranges of incident flux where the output current is directly proportional to the incident flux, i.e. where the sensitivity is constant. Since previous studies[1,2] have examined both the time response and the linearity of detectors similar to the type used in the present work, we were concerned only with the sensitivity as a function of photon energy. The absolute sensitivity S of an x-ray detector is here defined by the expression, $S = I/h\nu\phi A$, where I is the detector output current, ϕ is the incident photon flux of energy $h\nu$, and A is the area of the x-ray beam incident on the detector. To determine the sensitivity, the detector is placed behind a collimator of known area in a known x-ray flux of energy $h\nu$, and the output current is measured. A correction is usually made to the measured current to account for the presence of contaminant x-rays in the calibration spectrum. This is achieved with the aid of computer codes[3,4] able to account properly for these contaminants. The absolute sensitivity as defined above was measured for the following detectors: a silicon semiconductor, three plastic scintillator-photodiode detectors, and two photoelectric diode detectors.

Experiment

Apparatus

Detectors. The silicon semiconductor detector, an R series ruggedized surface barrier detector with a 500-μm depletion depth, had a nominal 40 $\mu g/cm^2$ aluminum front electrode thickness and was obtained from Ortec. The active area was 25 mm^2, and during the calibration a 0.51-cm-diameter collimator was used. This detector is illustrated in Fig. 1.

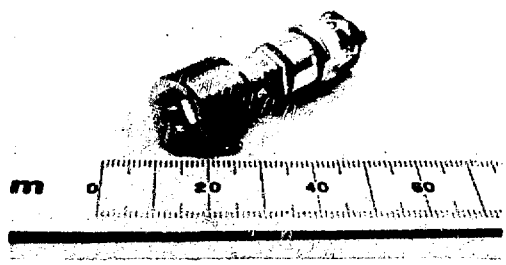

Fig. 1. Silicon semiconductor detector.

The plastic scintillators, MEL-150C, Pilot B, and NE102, were coupled to an FW-128 photodiode using Dow Corning 20-057 optical coupling compound. For MEL-150C and the Pilot B, the photodiodes used had S-20 responses, while for the NE102, the photodiode used had an S-4 response. The MEL-150C and the Pilot B were 2.5 cm in diameter by 2.54 cm thick. The NE102 was 2.54 cm in diameter by 0.519 cm thick and was coupled to the photodiode via a 2.54-cm-diameter by 0.476-cm-thick Lucite light pipe. All the scintillators were collimated with a 1.27-cm-diameter collimator. Figure 2 illustrates one of these detectors.

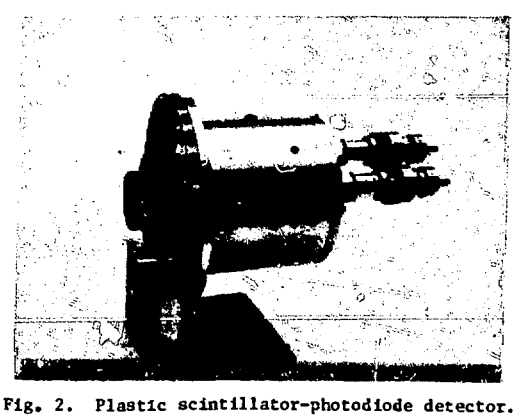

Fig. 2. Plastic scintillator-photodiode detector.

*Work performed under the auspices of the U.S. Energy Research & Development Administration, under contract No. W-7405-Eng-48.

†Reference to a company or product name does not imply approval or recommendation of the product by the University of California or the U.S. Energy Research and Development Administration to the exclusion of others that may be suitable.

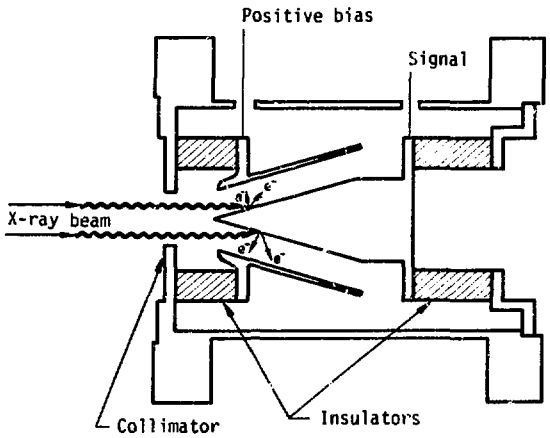

Fig. 3. Schematic view of conical aluminum cathode windowless photoelectric diode detector.

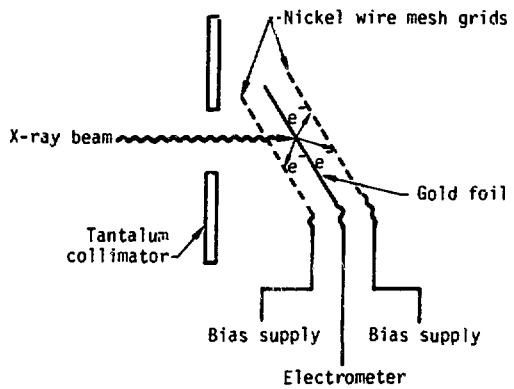

Fig. 4. Schematic view of gold foil cathode windowless photoelectric diode detector.

The photoelectric diodes were both windowless detectors. The first of these had a conically shaped aluminum cathode with a truncated conical shell surrounding it acting as the anode. X-rays enter the detector through the truncated end after passing through a 1.59-cm collimator as shown schematically in Fig. 3. The other detector consisted of a thin gold foil, 0.95 mg/cm^2 thick, spaced between two wire-mesh grids having optical transmissions of 96%. The x-ray beam enters the detector through a 0.95-cm-diameter collimator, passes through the front grid, and interacts with the gold foil, producing electrons that are collected by the grids as shown schematically in Fig. 4.

X-ray Generators. Three separate x-ray generators were used for the calibrations reported in this paper, and all have been described in greater detail elsewhere.[5-8] For the sub-kilovolt energy region, the x-rays were produced using an ion accelerator that generates fluorescent x-rays via proton bombardment of the target materials. An overall view of this facility is shown in Fig. 5. Figure 6 is an overall view of the x-ray generator used in the 1.5- to 8-keV energy range. In this machine, an electron beam is

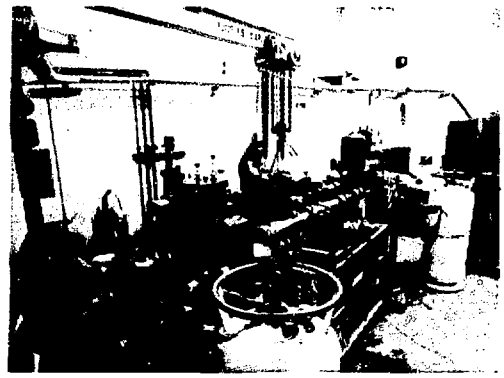

Fig. 5. The sub-kilovolt x-ray calibration facility.

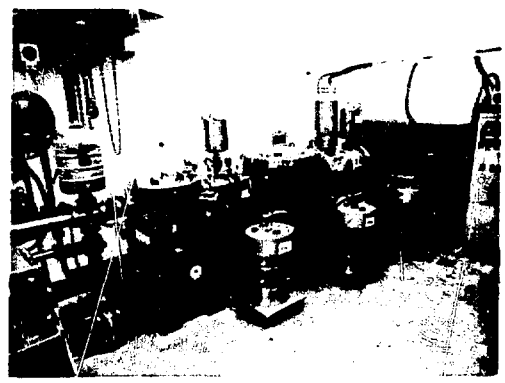

Fig. 6. The 1.5- to 8-keV x-ray calibration facility.

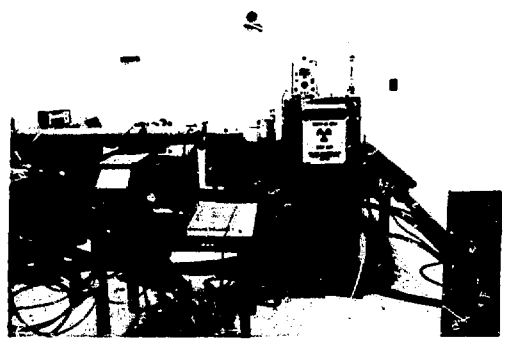

Fig. 7. The 8-keV to 100-keV x-ray calibration facility.

used to excite the target materials, producing fluorescent x-rays, which are absorption-edge-filtered for additional beam purity. In both of the above x-ray facilities, the calibrations are carried out in evacuated chambers. The x-ray generator used for calibrations from 8 keV to 98 keV uses photon bombardment of the target materials to produce fluorescent x-rays. The spectral purity is further improved by using k-edge absorption filters. Calibrations on this machine are carried out in air. An overall view of this calibration facility is shown in Fig. 7.

Electronics. The current from the detectors was measured using an electrometer in conjunction with a digital voltmeter and a chart recorder. A phase lock amplifier was also used in some of the semiconductor calibrations where the x-ray source was modulated at 1080 Hz with a 50% duty cycle using a mechanical beam chopper. The bias voltages were obtained from a variable supply incorporating a series of dry cells and exhibiting a very low leakage current.

Procedure

The calibration procedure was very straightforward. The detectors were placed behind a collimator of known area and irradiated with x-rays of known energy and intensity in a manner similar to that shown schematically in Fig. 8 for the sub-kilovolt x-ray facility. It was necessary to place a 600-μg/cm^2-thick, calibrated carbon foil over the collimator on the scintillation detectors while they were being calibrated using the subkilovolt x-ray facility. This was to eliminate the light produced at the target from entering the detector and creating a large background signal. This was not necessary on the 1.5- to 8-keV x-ray generator, since the calibration chamber could be completely darkened. While using the 8-keV to 100-keV x-ray machine, a 0.00127-cm-thick beryllium window was used on the scintillation detectors to eliminate the effects of the room light. To calibrate the windowless photoelectric diode detector on this latter facility required that a 0.0254-cm-thick beryllium window be added and the detector evacuated, since the calibrations on this machine are carried out in air. The x-ray transmission of all the various windows used were accounted for by the computer code used in reducing the data.

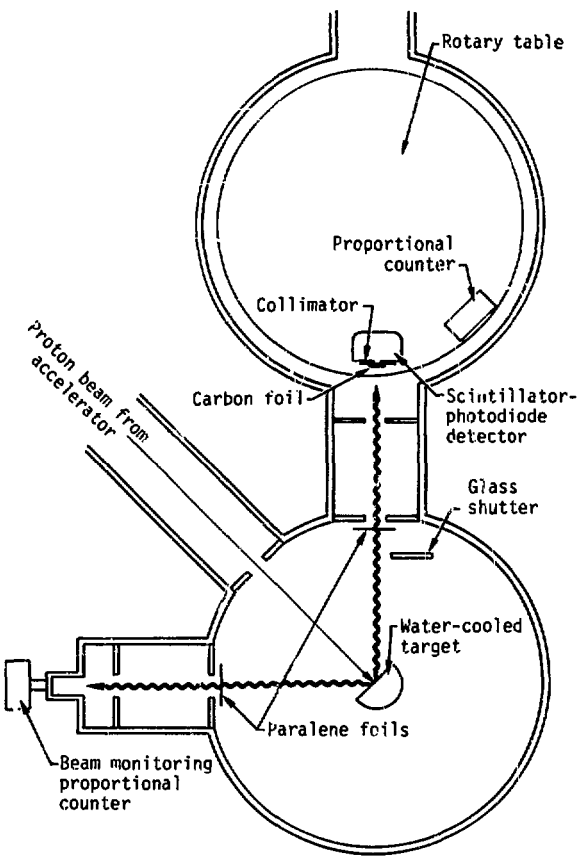

Fig. 8. Schematic view of calibration geometry on the sub-kilovolt x-ray generator.

Results and Discussion

Semiconductor Detector

The absolute sensitivity of the silicon semiconductor detector described above is shown in Fig. 9.

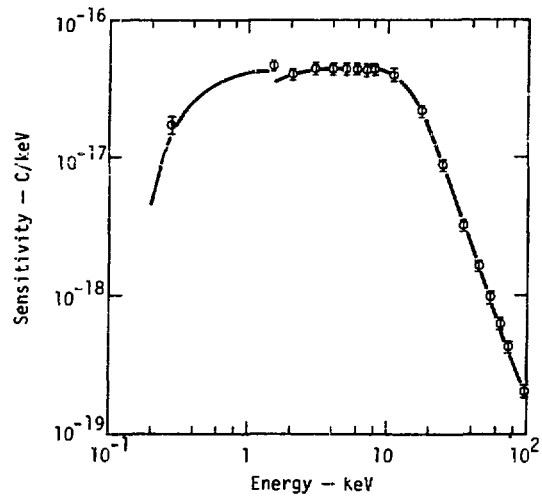

Fig. 9. Sensitivity versus energy for a silicon semiconductor detector with a 500-μm depletion depth.

The solid line is a calculated value[9] for a detector with a 500-μm depletion depth and a 40-μg/cm^2 aluminum front electrode. For the calibrations from 280 eV to 8 keV, we were able to calibrate this detector in a dc mode. For any particular calibration run, the dark current of 10^{-7} A varied only by 10^{-11} A. The signal was in the 10^{-9} -A range and also varied by only 10^{-11} A. The measurements were repeatable to within 2%. The digital voltmeter connected to the electrometer output allowed these small changes in current to be precisely measured. Although the signal-to-noise ratio was only 0.02 to 0.04, the uncertainty in the measurements is estimated to be within the error bars shown in Fig. 9, due to the stability of the signal and the noise. A phase look amplifier was used for the calibrations on the 8- to 98-keV x-ray generator due to the smaller signals. The agreement between the calculation and the experimental points is quite good, with the exception of the lower-energy points. Here, the difference might be attributed to the low-energy secondary electrons from the aluminum being collected.

Photoelectric Diode Detector

Figure 10 shows the absolute sensitivities as a function of x-ray energy for the gold and aluminum cathode photoelectric diode detectors. The gold cathode detector was only calibrated on the two lower-energy x-ray machines, where it could be placed in a vacuum. There was no convenient way to evacuate it for calibration on the 8- to 100 keV machine. The aluminum cathode photoelectric diode detector was designed so that beryllium windows could be attached

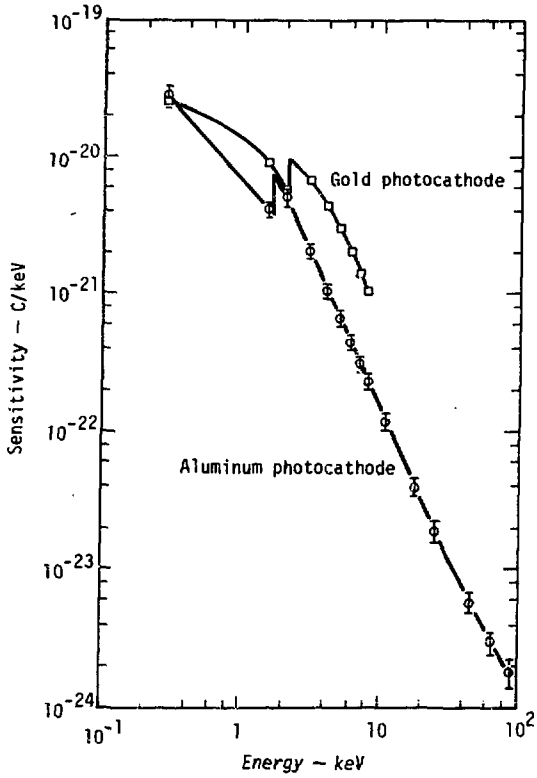

Fig. 10. Sensitivity versus energy for the gold and aluminum cathode photoelectric diode detectors.

and the detector evacuated for calibration on the 8- to 100-keV x-ray machine. Thus, the calibration shown in Fig. 10 for this detector goes from 280 eV to 98 keV. The dark currents for these detectors were very low ($<2 \times 10^{-15}$ A) while the signals varied from 10^{-11} to 10^{-14} A. The uncertainties in the calibrations come primarily from the uncertainties in determining the x-ray flux and the output current, and the error bars shown are believed to be for the worst possible situation.

Plastic Scintillator-Photodiode Detectors

The absolute sensitivities of the photodiodes used together with the MEL-150C, Pilot B, and NE102 plastic scintillators are shown in Fig. 11. The uncertainties in the measurements are indicated by the error bars shown on the graphs. The error bars at 282 eV represent an uncertainty of 25%. This uncertainty results from taking the estimated uncertainty of each of the variables that enter into the calibration in quadrature. For the calibrations from 1.5 to 98 keV, this uncertainty is within 10%, being determined in a similar manner.

The MEL-150C and Pilot B scintillators are thick enough to be 100% absorbing below about 10 keV, while the NE102 is totally absorbing only below about 4 keV.

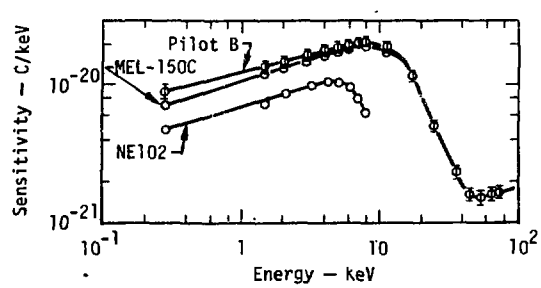

Fig. 11. Sensitivity versus energy for the scintillator photodiode detectors.

The difference in absolute sensitivity between the NE102 and the other two scintillators shown in Fig. 11 is due primarily to the difference in sensitivity of the S-4 response and S-20 response of the photodiodes. At the lower energies, the shapes of all of the curves are very similar, which is what might be expected.

References

1. Churchill, W., "Photodiode Linearity System," Lawrence Livermore Laboratory, Detector Handbook, UCRL-50176, p. 1-1 (1967).

2. Ebert, P. J., and Lauzon, A. F., "Vacuum Diode Detector for Measuring High Intensity Gamma Ray Flux," Rev. Sci. Inst. 38, No. 12, pp. 1747-1752 (1967).

3. Lyons, P. B., "Computer Analysis of X-Ray Detector Responses," Los Alamos Scientific Laboratory, Internal Document J-14 (1971).

4. Gaines, J. L., "Unfolding the Effects of Spectral Contaminants in X-Ray Calibrations," Lawrence Livermore Laboratory, Internal Document UOPE 73-10 (1973).

5. Kuckuck, R. W., Gaines, J. L., and Ernst, R. D., "A High Intensity, Subkilovolt X-Ray Calibration Facility," presented at ERDA Symposium on X- and Gamma-Ray Sources and Applications, University of Michigan, 1976.

6. Ebert, P. J., Gaines, J. L., and Leipelt, G. R., "Production of Monoenergetic X-Ray Sources of Known Absolute Intensity," Nuclear Instruments and Methods 99, pp. 29-34 (1972).

7. Gaines, J. L., "A Generator for Producing Monoenergetic, High Intensity, Soft X-Rays," Nuclear Instruments and Methods 102, pp. 7-12 (1972).

8. Gaines, J. L. and Hansen, R. A., "An Improved Annular-Shaped Electron Gun for an X-Ray Generator," Nuclear Instruments and Methods 126, pp. 99-101 (1975).

9. Ebert, P. J. and Kornblum, H. N., "Sensitivity of Silicon Detectors," Lawrence Livermore Laboratory, Internal Document UOPAD 67-80 (1967).

Proceedings, ERDA X-and Gamma-Ray Symp. Ann Arbor, MI, May 19-21, 1976 (Conf 760539)

SUB-KEV X-RAY CALIBRATION OF PLASTIC SCINTILLATORS

P. B. Lyons, R. H. Day, D. W. Lier, T. L. Elsberry

Los Alamos Scientific Laboratory

Los Alamos, NM

INTRODUCTION

Several types of x-ray detectors have found widespread use for plasma diagnostic applications in the energy range below a few keV. Silicon diodes, photoelectric diodes, and plastic scintillators have been used to obtain diagnostic information in this region. In this paper we will report sub-keV calibration data for plastic scintillator detectors and contrast the advantages and limitations of these three detectors in diagnostic measurements.

In a previous paper[1] we presented calibration data for plastic scintillators from 1.5 to 20 keV. In this paper the data are extended to the C-K_α line (277 eV). These data represent one application of a new sub-keV x-ray calibration facility at the Los Alamos Scientific Laboratory.

CALIBRATION SYSTEM

The system is shown schematically in Fig. 1. The detectors view the x-ray tube anode[2] through a filter window that also acts as a vacuum isolation window between the high vacuum tube ($<2\times10^{-7}$ Torr) and the low vacuum detector region ($\sim1\mu$).

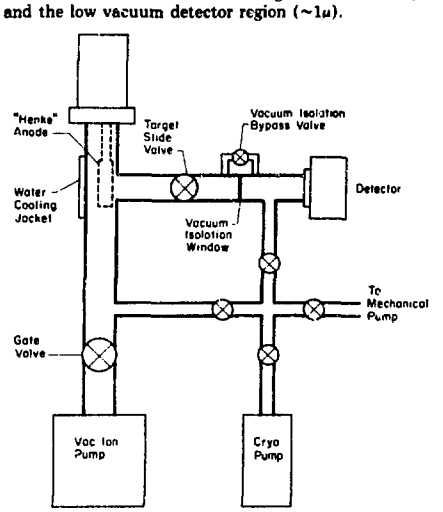

Fig. 1. Schematic of the ultrasoft system.

The x-ray tube is shown in Figs. 2 and 3. The demountable anodes are either machined from the bulk metal of interest or vacuum deposited on Cu anodes. The filter windows are thin metallic or metal coated plastic. Beam purity is controlled by limiting the tube high voltage to about twice the absorption edge of each anode material. The filter is used to provide additional optimization of beam purity.

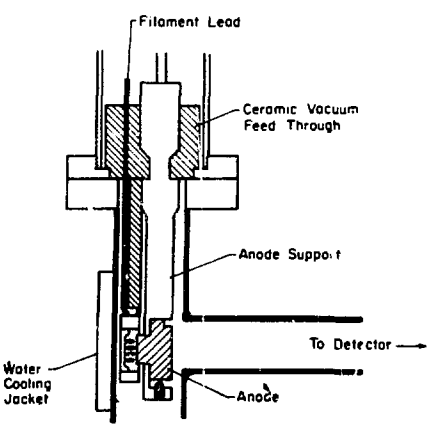

Fig. 2. Schematic of "Henke" x-ray tube.

Of particular importance in these filters is the limitation of C-K radiation that is evident despite the low system pressure. The source of this contamination is still under investigation.

Additional calibration data were acquired with two conventional calibration systems similar to that described in Ref. 1. The systems used Cu and Al anodes, respectively, to fluoresce secondary targets. Filters were used to enhance spectral purity. The anodes utilized in the present study are listed in Table I. Also listed are beam filters, tube high voltage, and tube emission current. Currents were kept below the onset of space charge limitation. In some cases (the oxygen anode using vacuum deposited Li_2O), the current was limited by anode deterioration.

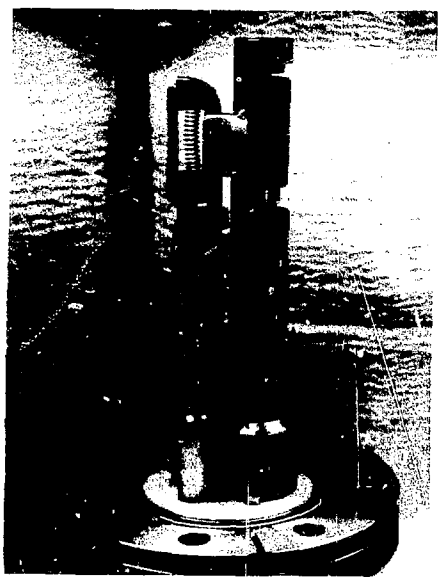

Fig. 3. The "Henke" x-ray tube, showing the demountable anode.

DETECTOR FABRICATION

Thin plastic films were placed directly on the faceplate of an ITT FW114 diode behind a light-tight entrance window of either aluminized polycarbonate film (Kimfoil[3]) , or 150 $\mu g/cm^2$ magnesium foil . NE111[4] plastic films of 0.57 and 11.51 mg/cm^2 were used. An entrance collimator of 1.59 cm was used.

In previous work[1], the importance of diode faceplate response was stressed in cases where the fraction of energy absorbed in the plastic film was very low and a special glass substrate was used to limit this response. However, since most of the beam energy is absorbed in the plastic for the energies and plastic thicknesses used in this report, a glass substrate was not used; most practical applications of the plastic films should utilize the special substrate.

DETECTOR CALIBRATION

A Cary model 401 electrometer was used to record the photodiode current (>$2x10^{-15}$ A). An in-line, 30 volt, battery provided bias to the photodiode. The overall calibration of the current measuring system utilized a Keithly model 261 precision current source.

Beam normalization was done with a thin window flow proportional counter with a 0.5 mm entrance aperture. The gas path length was 2.5 cm. Fill gases were propane, methane or P-10 at atmospheric pressure. The entrance window was either 80 $\mu g/cm^2$ polypropylene (with 50 Å Nichrome overcoat) or 150 $\mu g/cm^2$ magnesium foils. At most energies, the transmission of both the counter and scintillator windows was measured.

TABLE I

X-RAY SOURCE PARAMETERS

Element	Line Energy	Anode	Filter	High Voltage	Emission Current
C	277 eV	C on Cu	250 $\mu g/cm^2$ Kimfoil[3] + 38 $\mu g/cm^2$ Al	600 V	10 mA
Ti	452	solid Ti	600 $\mu g/cm^2$ Ti + 150 $\mu g/cm^2$ Mg	1000	35
O	525	Li_2O on Cu	370 $\mu g/cm^2$ Cr	1000	10
F*	679	Al	600 $\mu g/cm^2$ Ni or 590 $\mu g/cm^2$ CF_2	2600 2400	350 350
Ni	852	Ni on Cu	1.15 mg/cm^2 Ni	1600	50
Ni*	852	Al	600 $\mu g/cm^2$ Ni	2800	350
Mg*	1041	Al	2.7 mg/cm^2 Mg	2800	350
Mg*	1253	Al, Cu	2.7 mg/cm^2 Mg	2400	350
Al*	1487	Cu	1.7 mg/cm^2 Al	3000	600
Si*	1741	Cu	370 $\mu g/cm^2$ Nb	3400	600

*Secondary fluorescence mode

DATA ANALYSIS

From current and fluence data, the response R(E) of the detector (photodiode current per incident MW of x-ray energy) was determined. The plastic conversion efficiency C(E) (photodiode current per MW of absorbed x-ray energy) is defined by

$$R(E) = \epsilon(E)\ C(E)\ T(E)$$

where $\epsilon(E)$ is the plastic absorption efficiency $(1 - \exp(-\mu x))$, T(E) is the measured window transmission. X is the plastic thickness and μ is the absorption coefficient for NE111[5,6].

The four configurations, two windows and two plastic foil thicknesses, all lead to different values of the conversion efficiency, due to differences in foil optical quality and window reflectivity. To obtain data on a common scale, a normalizing factor was applied to all conversion efficiencies measured in a given configuration to bring the value of C(E) at E=Mg-K into agreement with the value obtained with the Mg window and the thin plastic. Thus, for example, C(E) values measured with the highly reflective Kimfoil window were scaled by 0.76 to agree with the less reflective Mg window data.

For cases where data from all configurations were available, agreement (after the above scaling) was excellent. The resulting conversion efficiencies are tabulated in Fig. 4. In Fig. 4, distinction is made only between the direct and secondary fluorescer data; the various configurations are not shown separately. It should be noted that the agreement of the data at Ni-L(where both system types were used) is excellent.

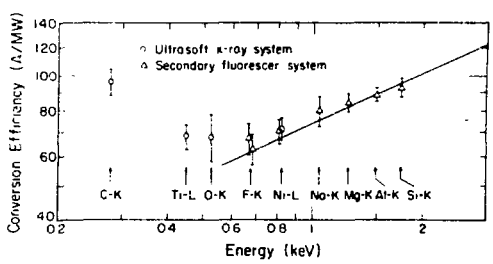

Fig. 4. NE111 conversion efficiency. The solid line is an extrapolation of the data from 1.5 to 10 keV (Ref. 1).

Corrections for beam impurities were made where necessary. Such corrections were made with a minor effect on the overall uncertainty. However, on the Cu anode fluorescent system the thick plastic data necessitated much larger corrections and was not used. The largest impurity correction was 16% at the F-K energy (with a CF_2 filter). All other corrections were less than 10%.

One uncertainty is not included in Fig. 4. For the K x-ray lines, data are plotted at the K-line energy. For the Ni-L line, the data are plotted at 810 eV instead of 852 eV. For the Ni-L line, we have evidence that the average energy is well below the line energy. This is probably due to the filtered bremsstrahlung continuum present in the final beam. Other L lines, and contaminant lines, may be present. With the present system we must admit to the possible existence of such contamination at energies somewhat below the actual energy of interest. Such problems would be more severe for L x-ray lines, but may also be present in other spectra. Energy-dispersive measurements will address the beam purity in subsequent work.

DISCUSSION

The straight line shown in Fig. 4 is an extension below 1 keV of an approximate power law dependence that was observed to fit the data of Ref.1 in the 1.5 to 10 keV energy range. This dependence is $C(E) = aE^x$, where x is about 0.46. Such a power law, with a somewhat different exponent, follows from the semi-empirical ionization quenching model discussed in Ref. 7. This model relates the light output from a particle to its energy loss rate. To apply this model, values for dE/dx must be known for all electron energies below the primary photoelectron energy. At some low energy, the Bethe-Bloch energy loss formula must become invalid, but several references suggest that it has some validity down to energies well below one keV. Using the parameters suggested in the literature for NE102[7], and assuming the validity of the Bethe-Bloch formula down to energies below 100 eV; a value for the exponential power x, of about 0.35 is calculated for the 1 to 10 keV range. Such a treatment is admittedly approximate and several other effects may complicate such a simple interpretation.

One effect that can be dismissed is loss of energy from the plastic from electron escape or gain of energy by the plastic from primary electrons leaving the substrate or window. Using an approximate value for dE/dx of 130 eV/μg/cm^2 below 1 keV (measured[8] for Al), negligible upper limits for such effects in this study are readily obtained. For different energies, or thinner foils, such effects should be considered (see Ref. 1).

In Fig. 4 the data indicate a rise in C(E) at low energies, but the character of that rise (whether a continuous increase, or with some discontinuity at the C-edge) is not known. The form of dE/dx is sufficiently uncertain that a test of the ionization quenching model much below 1 keV is not possible. However, a comparison of the C-K and O-K data values suggests that mechanisms other than simple ionization quenching are operable. In the C case, interactions are of photoelectric origin with C L- or H K-shell electrons — thus yielding an ~ 250 eV photoelectron. In the O case, interactions are virtually all with the C K-shell yielding an ~ 250 eV photoelectron and a K-shell vacancy that decays to yield an Auger electron of ~ 250 eV. Thus the C and O cases yield similar electron energies. This suggests that the conversion efficiencies should be equal.

Several effects could possibly explain the observed difference. One such explanation would involve the much greater attenuation coefficient of O-K x rays as compared to C-K x rays. But such an explanation leads to the suggestion of a dead layer that must be ~ 30 μg/cm^2 to explain the C/O data. This is unlikely since it is not supported by the data of Fig. 4 or Ref.1, or by reports[9] of heavy particle detectors using plastics of 10 μg/cm^2 thickness.

Still another effect involves the observation that O-K interactions are with inner shell electrons, while C-K interactions are with outer shell electrons. It can be speculated that a molecule that undergoes an inner shell interaction is sufficiently perturbed that it cannot participate in subsequent emission processes, while an outer shell interaction may be sufficiently gentle that the molecule may be useful in subsequent light production. It should be noted that only about 0.5 photons per O x ray are being emitted from the plastic, so any increased emission probability for an event becomes significant. This explanation, while certainly speculative, would be in greater favor if subsequent data showed a discontinuity at the C-K edge.

Perhaps the most likely hypothesis is that quenching interactions between the ionization clouds of the two electrons generated in the O case are important. Without further information, a choice between possible hypotheses will not be made.

Through these calibrations sub-keV x-ray conversion efficiencies for plastic scintillators have become available. The plastic scintillators offer several advantages for plasma diagnostic work. The plastic foils are inexpensive and are available in a wide range of thicknesses. Commercial foils as thin as 150 μg/cm^2 have been received and techniques exist[9] to fabricate much thinner foils. By using foils of various thicknesses and filters, the response of a detector can be tailored to peak at a desired energy. NE111 scintillators are quite fast (1.3 nsec FWHM) and new quenched plastics with a FWHM below 200 psec have been demonstrated [10]. No special vacuum requirements must be met. Light tight windows are needed, but these are common to virtually all detectors. Gain is readily possible with photomultipliers and output is directly compatible with fiber optics.

Photoelectric diodes can be built faster if enough effort is expended, 30 psec response has been demonstrated[11]. If time response in the nsec range is desired, the detector can be very simple. Photoelectric diodes are more sensitive than plastics below ~ 400 eV[12], while the plastic is much more sensitive at higher energies. However, they require excellent vacuum conditions.

PIN diodes have dead layers that restrict their use down to a few hundred eV. They are very slow (several nsec), fairly expensive and

sensitive to visible light. However, they do not require stringent vacuum conditions and are simple to use.

In conclusion, plastic scintillators offer several advantages in low energy x-ray diagnostics. A number of these detectors are in use in the Los Alamos laser-produced plasma diagnostics program.

ACKNOWLEDGMENTS

Many individuals contributed suggestions and materials used in this effort. Some coated anodes were made by R. Deck, J. Gursky, and E. Fullman of LASL; some were provided by K. Glibert and L. Morrison of Sandia Laboratories. Particularly helpful suggestions were received from B. Henke, University of Hawaii; R. Moler, Science Application, Inc.; R. Blake and D. Barrus of LASL.

REFERENCES

1. P.B. Lyons and D. W. Lier, IEEE Trans. Nuc. Sci.,NS-22(1975) p.88.

2. B. L. Henke, Advan. X-Ray Anal. 5 (1962) p. 285.

3. Available from Kimberly-Clark Corp., Peter J. Schweitzer Div., Lee, Mass.

4. Available from Nuclear Enterprises, Inc., San Carlos, CA.

5. B. L. Henke and E. S. Ebisu, Advan. X-Ray Anal., 17 (1973) p.150.

6. W.J. Veigele, E. Briggs, L. Bates, E. M. Henry, and B. Bracewell, Kaman Sciences Corporation (1971), DNA 2433F, KN-71-431 (R).

7. J. B. Birks, *The Theory and Practice of Scintillation Counting*, Pergamon Press (1964).

8. R. H. Ritchie, F. W. Garber, M. Y. Nakai, and R. D. Birkhoff, Adv. Rad. Biol.3 (1969) p. 1.

9. M. L. Muga, D. J. Burnsed, W. E. Steeger, and H.E. Taylor, Nucl.Instr. and Meth.83 (1970) pp. 135- 138.

10. P. B. Lyons, C. R. Hurlbut, L. P. Hocker, Nucl. Instr. and Meth. 133 (1976) p. 175.

11. X-Ray Diagnostics for Laser Syatems, L. F.Chase, R. K. Bardin, T. R. Fisher, H. A. Grench, W. C. Jordan, D. A. Kohler, R. K. Landshoff, T. D. Miller, and J. G. Pronko, Lockheed Research Lab. (1974), DNA 3404F.

12. R. H. Day and E. J. T. Burns, Adv. X-Ray Anal., 19 (1975) p. 597.

Proceedings, ERDA X-and Gamma-Ray Symp. Ann Arbor, MI, May 19-21, 1976 (Conf 760539)

SOFT X-RAY DETECTION WITH CHARGE COUPLED DEVICES

John L.Lowrance and George Renda
Department of Astrophysical Sciences
Princeton University
Telephone No.: 609-452-3803
Princeton, New Jersey 08540

Introduction

In nuclear fusion research it is important to measure the impurities in the plasma and the total energy being radiated. The sensitivity of silicon over a broad spectral range makes it very attractive and when configured as a CCD it is even more attractive because of its relative insensitivity to strong magnatic fields associated with plasma containment. The Fairchild 201-CCD has been illuminated with X-rays from a copper target to explore its applicability for X-ray imagery. The Reticon 512 B/24 self-scanned linear array has been evaluated using copper, aluminum and carbon targets.

Experiment Configuration

The measurements were made in a vacuum using a high intensity electron source to illuminate the targets as shown in Fig. 1. Both the CCD and the linear array were cooled to minimize the dark current. beryllium or aluminum filters blocked the visible light from the electron gun filament. The tests for the CCD were conducted at a pixel clock rate of 61 Khz, which resulted in frame rate of 3 3/4 frames per second. In order to obtain data over the X-ray energy range shown in Figs. 3 and 4, the period of integration was varied from 0.25 seconds to 5 minutes. Data was displayed as a single line (100 pixels) of video information on an oscilloscope and polaroid photographs made to record the information. The full scale signal for the CCD of approximately 5×10^5 electrons per pixel is used as a means of calibrating the detector since the CCD has a linear response. The Recticon was calibrated in a similar way, its full scale signal is approximately 2.5×10^7 electrons per pixel.

Fairchild 201-CCD

The photosensitive area of the 201-CCD is covered by about 1.5 microns of silicon and silicon dioxide that is "dead" in terms of visible radiation.That is, photons absorbed in this layer do not contribute to the signal. The shift registers are covered by an additional layer of aluminum 1.2 microns thick that is opaque to visible radiation. Figure 2 shows the transmission characteristics of the aluminum and silicon layers in the soft X-ray spectral region. As can be seen by the aluminum transmission characteristics, the shift register circuits behind the aluminum are also exposed to the X-ray photons. We have found that the problem of the X-ray sensitive shift register can be circumvented by rapid scanning the shift registers during the exposure time. Large doses of X-rays also cause permanent damage. A back illuminated CCD would protect the circuits from the X-ray damage and also allow a thinner dead layer with corresponding improvement in long wavelength response.

Reticon RL 512 B/24

The Reticon linear array of 512 one mil wide by 24 mil tall photosensitive elements has a dead layer of 50 Å of silicon making it potentially quite sensitive in the soft X-ray region. The signal is scanned out by 4 sets of interleaved shift registers that are an integral part of the silicon chip located on each side of the photosensitive area. This geometry allows the shift registers to be masked from the X-rays.

The disadvantage of the Reticon aside from its one-dimensional characteristics is that its readout noise is about 10,000 electrons rms compared to 250 for the Fairchild 201. However this readout noise could be reduced to about 1000 electrons by redesigning the Reticon preamplifier. The Reticon is, of course, well suited for spectral readout with its 1 x 24 mil elements.

X-ray Sensitivity

For light elements the equation for the continuous X-ray intensity can be written

$$N_E = K Z \frac{(E_o - E)}{E} \qquad (1)$$

Where: N_E is the number of photons per unit energy interval; E_o is the high energy limit of the spectrum (ev); E is any energy between E_o and O (ev). Z is the atomic number of the element and K is the continuous X-ray efficiency constant of the element (ev^{-1}). Taking into account the beryllium filter attenuation, and the polysilicon and silicon dioxide layers on the CCD, the equation for the number of X-rays per unit energy interval reaching the active silicon is

$$N_{EI} = K Z \frac{E_o - E}{E} e^{-u_1 x_1 E^{-Y_1}} e^{-u_2 x_2 E^{-Y_2}} \qquad (2)$$

where $e^{-u_1 x_1 E^{-Y_1}}$ is the transmission function for the Beryllium and the Silicon transmission is expressed by a similar term.

The silicon has a conversion efficiency of one electron-hole pair per 3.5 electron volts of energy. And for a given electron accelerating voltage E_o, the response of the CCD is

$$\sum_o^{E_o} N_{se} = \frac{K Z}{(3.5)(4\pi)} \int_o^{E_o} (E_o - E)\, e^{-u_1 x_1 E^{-Y_1}} e^{-u_2 x_2 E^{-Y_2}} dE$$

Signal electrons steradian^{-1} electron^{-1}. (3)

The characteristic X-ray spectra of interest for the copper target are the L shell lines $L\alpha_{1,2}$ and $L_{\beta 1}$ at at 0.928 and 0.948 Kev respectively.The other L series lines are either weak compared to these lines or are sufficiently attenuated by the beryllium filter so that they are negligible in these measurements

The empirically derived equation:(2)

$$N = n (E_o - E^*)^{1.63} \text{ photons electron}^{-1} \qquad (4)$$

gives the characteristic line strength where E* is the line of interest (Kev) and "n" is the efficiency coefficient. Efficiency coefficients for $L\alpha_{1,2}$ are published for heavier elements and have been extrapolated to yield a value of 3.4×10^{-5} for copper. The ratio

of $L\alpha_{1,2}$ to $L_{\beta 1}$ is 2. Therefore, the combined characteristic line strength is given by the equation:

$$N_e = n^* \left(C_\alpha (E_o - E_{L\alpha_{1,2}})^{1.63} E_{L\alpha_{1,2}} + \frac{C_\beta}{2} (E_o - E_{L_{\beta 1}})^{1.63} E_{L_{\beta 1}} \right)$$

Signal electrons steradian^{-1} electron^{-1} (5)

where C_α and C_β are the attenuation factors for the filter and dead layer at the characteristic line energy and

$$n^* = \frac{n \times 10^3}{(3.5)\ 4\pi} \qquad (6)$$

Similar equations for the characteristic lines of carbon and aluminum were solved. The characteristic lines of interest for aluminum are $K\alpha_1$, (1.487 Kev), $K\alpha_2$, (1.486 Kev), and $K\beta_1$, (1.553 Kev), and the carbon line of interest is $K\alpha_{1,2}$, (.282 Kev). The characteristic efficiency coefficient, n, used for the calculations was 6.3×10^{-5} for aluminum and 2×10^{-4} for the carbon target.

Test Results

Figure 3 shows the sum of equations (3) and (5) plotted as a solid line. For a copper target and the Fairchild 201-CCD the experimental results are plotted as points. There is a close agreement between the experimental data and the calculated response from 1.7 to 6 Kev. The roll off in response at lower energies is readily attributed to a somewhat thicker beryllium filter and/or thicker layers of polysilicon and silicon dioxide on the CCD.

The actual CCD signal current when converted to signal electrons in the silicon per steradian per incident electron on the copper X-ray target agrees with the calculated value when one uses a value for the continuous X-ray efficiency constant $(\frac{K}{2})$ of 1.3×10^{-9} ev^{-1} and an active CCD area of 7 mm^2 out of a total area of 12 mm^2. Figure 4 shows similar data for the Reticon RL 512 B/24 linear silicon array. Aluminum, carbon, and copper targets were tried and the predicted responses in each case is plotted on solid lines. For the carbon and aluminum targets, the continuous X-ray efficiency constant $(\frac{K}{2})$ used was $1.82 \times 10 \times 10^{-9}$ ev^{-1} and 1.55×10^{-9} ev^{-1} respectively. Here again there is fairly close agreement between the measured and predicted response and the differences are easily attributable to uncertainties in the filter thickness and/or target contamination.

Fe 55 Calibration and Resolution Test of CCD

The Fairchild 201-CCD was exposed to a radioactive Fe-55 source emitting 5.9 Kev X-rays. The measured CCD signal current when converted to units of input flux indicated a quantum efficiency of 100%, assuming a conversion factor of one electron hole pair per 3.5 volts of incident X-ray energy.

A metal aperture type test pattern was placed in contact with the silicon dioxide coated surface of the CCD and illuminated by the Fe-55 source. One aperture was 3 pixels (90 microns) in diameter, another aperture was 21 pixels in diameter. The results showed that the 3 pixel signal amplitude and the 21 pixel signal amplitude was approximately the same. This implied that there was little smearing of charge into adjacent pixels.

Phosphor Wavelength Converter

As a means of extending the sensitivity of the CCD to weaker energies we have measured the X-ray response of a red emitting phosphor that is a good match to the CCD response in the visible. The phosphor, RCA 33-Z-237A, was deposited on a glass slide and inserted in the X-ray beam near the CCD. Using the CCD as the detector, the effective phosphor efficiency in the region from 1.6 Kev to 5 Kev was measured to be between 8 and 15%. In the region from 0.6 to 1 Kev the effective efficiency was considerably higher. This increase at lower energies is not understood and may be due to some experimental error. As a next step we plan to coat the CCD photosensitive surface with the phosphor, as it would actually be used in an instrumental application.

Visible Light Excitation

In addition to the X-ray testing, the dynamic range of the CCD was evaluated with visible light excitation. The CCD was exposed to various levels of illumination and the data was stored on digital tape for analysis by digital computer. It was found that the predominant noise was coherent. This coherent noise was assumed to be caused by the gain variations in the silicon detectors and charge transfer inefficiency. A straight line equation, ax + b, seems to adequately fit the individual pixel data. The "a" term corresponds to the gain or sensitivity of each pixel and the "b" term corresponds to an initial "zero exposure" offset. A computer program was written to find the a's and b's of each pixel element. This full frame set of a's and b's were then used to process other data files. For a quantitative comparison of raw and processed data, the standard deviation was computed over a 50 x 50 pixel patch and for 100 pixels along a single line.

Tables 1 and 2 show the improvement in signal-to-noise ratio after point-by-point calibration of the data. This is compared with the predicted signal-to-noise that one would calculate, assuming that the signal-to-noise in the calibration files is Gaussian, i.e. $\sigma = (\text{number of electrons})^{1/2}$.

TABLE 1

S/N CHARACTERISTICS (50 x 50 PIXEL AREA)

Exposure Level % Full Scale	S/N Raw Data	S/N Processed Data	S/N Predicted	Ideal $(\text{Photoelectrons})^{1/2}$
24	62	195	236	380
84	71	313	446	710

TABLE 2

S/N CHARACTERISTICS (100 PIXEL LINE)

Exposure Level % Full Scale	S/N Raw Data	S/N Processed Data	S/N Predicted	Ideal $(\text{Photoelectrons})^{1/2}$
24	62	207	236	380
84	116	438	446	710

The discrepancy between Table 1 and Table 2 for the 84% file may be due to a small number of pixels in the 50 x 50 pixel patch that were several sigma away from the mean.

The processed data S/N is reasonably close to the

predicted S/N. Therefore the assumption of (photoelectron)$^{1/2}$ noise is valid. This implies that by averaging calibration data frames to achieve higher S/N in the calibration frames one can closely approach the ideal case. This makes the CCD uniquely attractive for low contrast applications. With the large gain associated with the X-ray photon conversion into signal electrons one can expect that the CCD will be quantum noise limited in the X-ray region. Our examination of raw X-ray data substantiates this conclusion. Computer reduction of X-ray data is planned for later this year.

Acknowledgements

The authors wish to thank Dr. Martin Green for his assistance in understanding the characteristic X-ray production efficiency. This work was supported by the Energy Research and Development Administration

References

(1) N.A. Dyson, "X-rays in Atomic and Nuclear Physics" (London: Longman Group Limited), pp. 7-61 (1973)

(2) M. Green, and V.E. Cosslett, Brit. J. Appl. Phys. (J. Phys. D.), 1, 425 (1968).

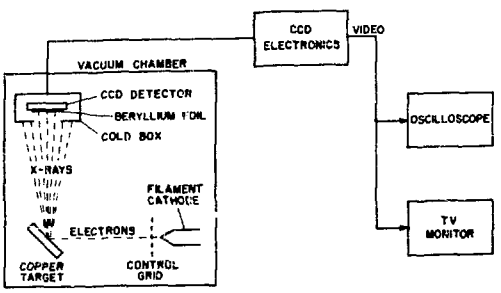

CCD X-RAY EXPERIMENT BLOCK DIAGRAM

Figure 1

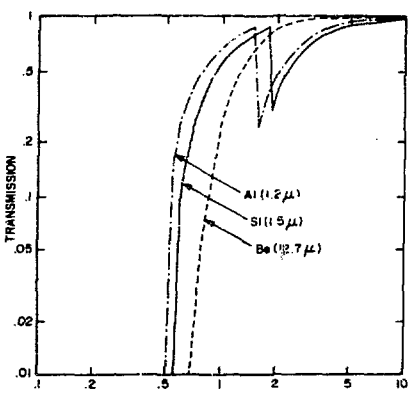

TRANSMISSION CHARACTERISTICS - Al, Si, Be

Figure 2

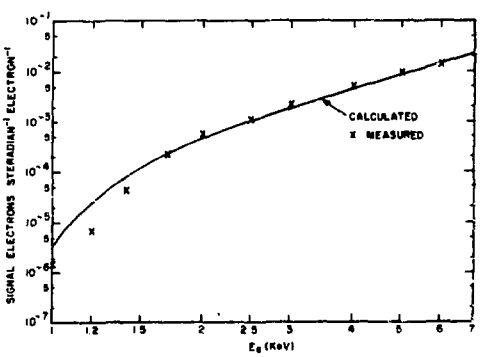

Fairchild CCD-201
Response to Soft X-rays

Figure 3

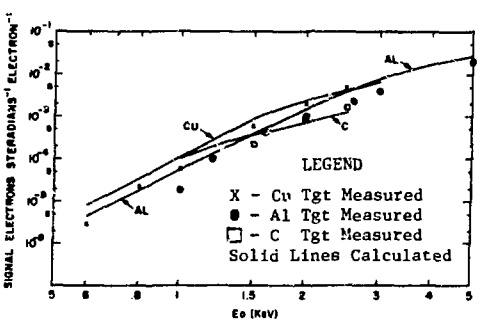

Reticon Linear Array
Response to Soft X-rays

Figure 4

Proceedings, ERDA X-and Gamma-Ray Symp. Ann Arbor, MI, May 19-21, 1976 (Conf 760539)

GAMMA, X-RAY DATA REDUCTION SYSTEM
VOLUME 1 - GAMMA

William H. Zimmer
Chemical Technology Laboratory
Atlantic Richfield Hanford Company
Richland, Washington 99352

SUMMARY

The starting premises for this data reduction system were (a) the individual researcher needs all the accuracy that can be achieved but he has neither the time nor the inclination to learn how to achieve it, and (b) if the data reduction system is to be centralized the people operating it will want to minimize conversation with the computer.

This is a working system. We put the detector/analyzer system where the work is: in the field, in the operating plant, in the research laboratory, or in the counting room. All spectral data are stored on Data General 4234 discs after background normalization and strip. Storage is initiated from magnetic tapes loaded by detached pulse height analyzers or directly from Scorpio pulse height analyzers. The only restrictions placed on the individual researchers are that the pulse height analyzer energy scale be set up consistently, that a recovery standard be run at least once every day of use, and the total acquisition system be calibrated to its range of use. In many instances, and if desirable, the latter is provided as a service.

At the time of writing this gamma data reduction system is actively being used to calculate net peak areas, activities with or without time correction, activations analysis results, counting precisions, and dynamic limits of detection for the spectral data output of 17 detached pulse height analyzers. To all modes of data reduction are applied background subtraction, random summing correction, detector recovery factor correction, peak interference correction (second-order product interference for activation analysis), geometry function correction, acquisition time decay corrections, external and internal sorber correction. All of this is accomplished and a customer report typed in a readable format after a half-line of noninteractive instruction.

Still being programmed are the data reduction of 8000 channel spectra, correction of irrradiation and decay time for cyclical activation analysis, and the calculation of accuracy, instead of counting precision.

CONCEPT

The basic concept of the GXDR system is to extend to all Atlantic Richfield Hanford Company (ARHCO) semiconductor detector users the accuracy, time, and labor-savings available through the use of modern automation techniques. Control of the detectors and their calibrations, control of the data acquisition equipment, and the timing of its use are left in the hands of the user. Data reduction is performed on the GXDR system. In this way each gamma unit can perform data reduction for up to 120 acquisition systems and neither type system need be purchased at the price of a stand-alone unit.

The detached or satellite analyzer consists of a minimum-priced pulse height analyzer interfaced to a Tracor Northern NS-111 magnetic tape cassette deck. The attached analyzers consist of ADC's and memory attached to a Scorpio Processor (see Figure 1). Spectra from magnetic tape and via the Scorpio Unibus interact in the Scorpio PDP-11/05 32K x 2^{16} Central Processing

FIGURE 1

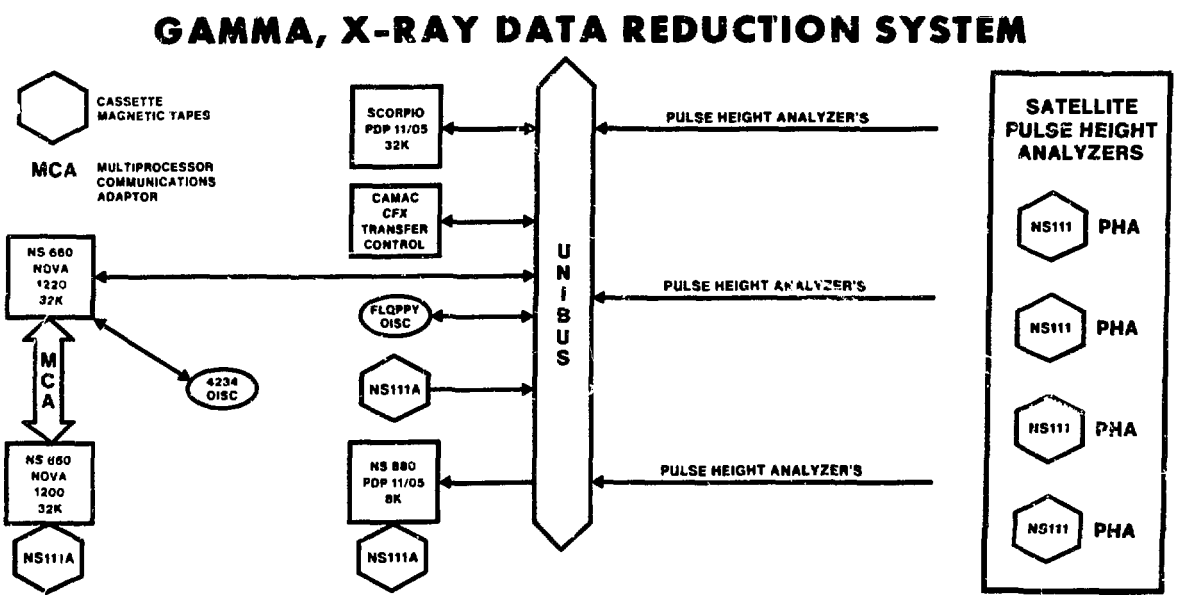

Unit (CPU) with background spectra stored on floppy disk. Here the backgrounds are normalized on the basis of acquisition time and stripped from the sample spectra. The data are then routed through a Data General 1220 for storage on a 4234 disc system.

CAPABILITIES

Figures 2 and 3 illustrate the capabilities and mechanics of GXDR-Gamma data reduction. The calculations used are as follows. Variables are called out by name in Figures 2 and 3 or specifically identified.

CALCULATIONS

$$\text{Activity} = \frac{\text{net area} \cdot BN \cdot GEO \cdot e^{\lambda T}}{UF}$$

where $\lambda = \ln 2 \div \text{half-life}$

T = time difference in days between Time of Count and Time Zero

$$ppm = \frac{\text{Activity}\ e^{\lambda \cdot TOR} \cdot e^{\lambda \cdot TC}}{\left(1-e^{-\lambda \cdot TR}\right) \cdot F \cdot CY}$$

where

$$TC = \frac{\ln 2}{966.425} \cdot \text{time difference in days between Time of Count and } ^{252}Cf \text{ Time Zero (for californium multiplier neutron source)}$$

F = neutron flux density

$$CY = \frac{M}{1-Q} - \frac{Q(1-Q^M)}{(1-Q)^2}$$

$$Q = e^{-\lambda \cdot TQ}$$

TQ = (TR + TOR + acquisition Clock Time)

The first item entered under "Sample Identification Input" is the customer's proper name followed by a carriage return and line feed. When the report is read to TI733 cassette magnetic tape, this portion of identification will act as the search code in assembling all item reports into a total report. The customer name is not typed when the report is read from the tape. The average reading time of the sample spectrum from the disc plus typing time for the full identification and the instruction line (Figures 2 and 3) is 10 seconds. The automatic data reduction plus typing and magnetic taping of up to 30 peak analyses takes less than 20 seconds. Output for each peak analyzed consists of a floating point activity or concentration, the units specified in the instruction line, the isotope or element name, and the 2σ percent counting precision, soon to be accuracy.

For additional details, references 1 and 2 are recommended.

REFERENCES

1. W. H. Zimmer, "Gamma, X-Ray Data Reduction System, Volume 1 - Gamma," ARH-ST-114-1, Atlantic Richfield Hanford Company, Richland, Washington, December 1974.
2. W. H. Zimmer, "Gamma, X-Ray Data Reduction System, Volume 2 - Gamma," ARH-ST-114-2, Atlantic Richfield Hanford Company, May 1976.

FIGURE 2

ACTIVITY ANALYSIS

(CNTRL) X

SAMPLE IDENTIFICATION INPUT (CNTRL) A

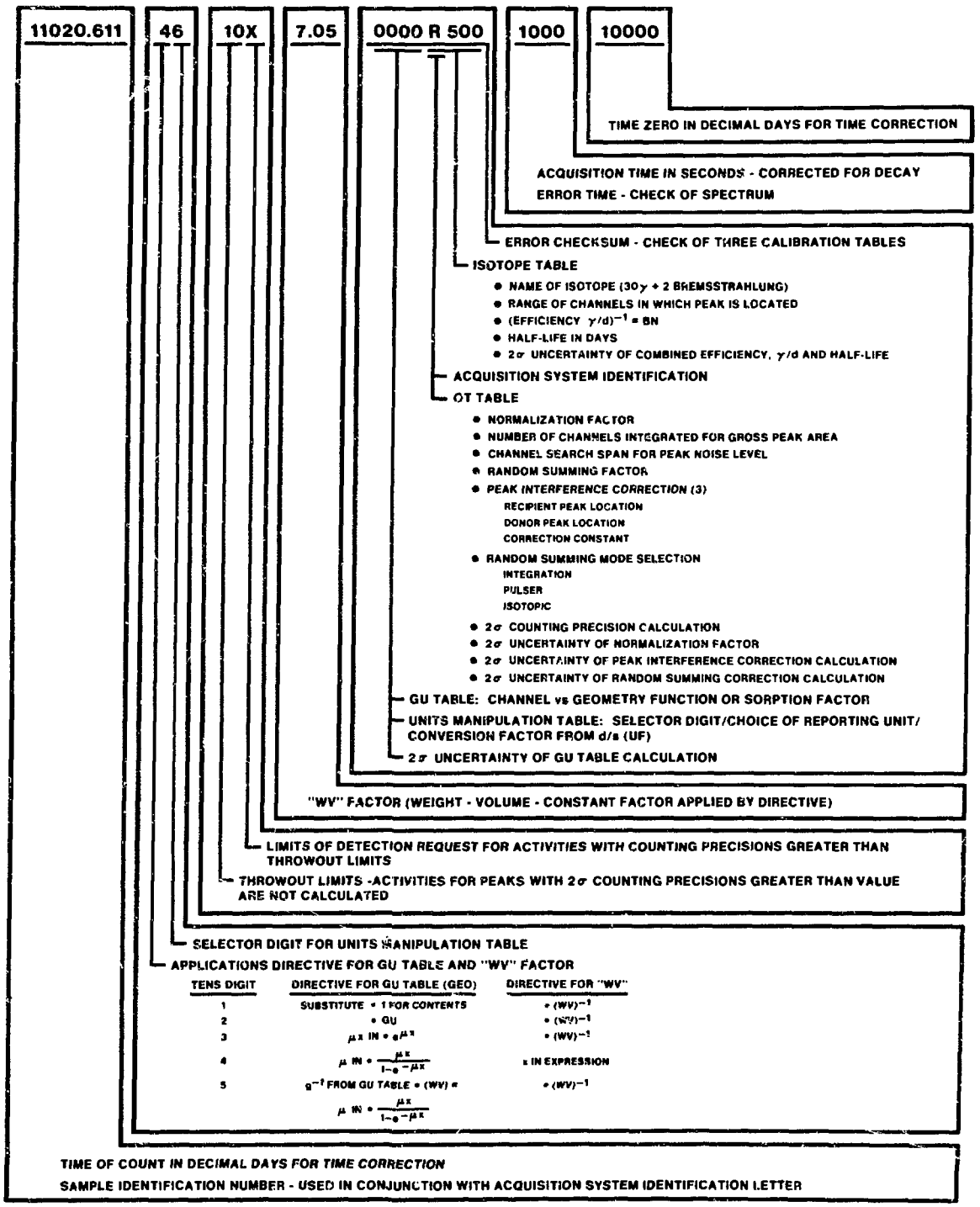

FIGURE 3

(CNTRL) Z

ACTIVATION ANALYSIS

SAMPLE IDENTIFICATION INPUT (CNTRL) A

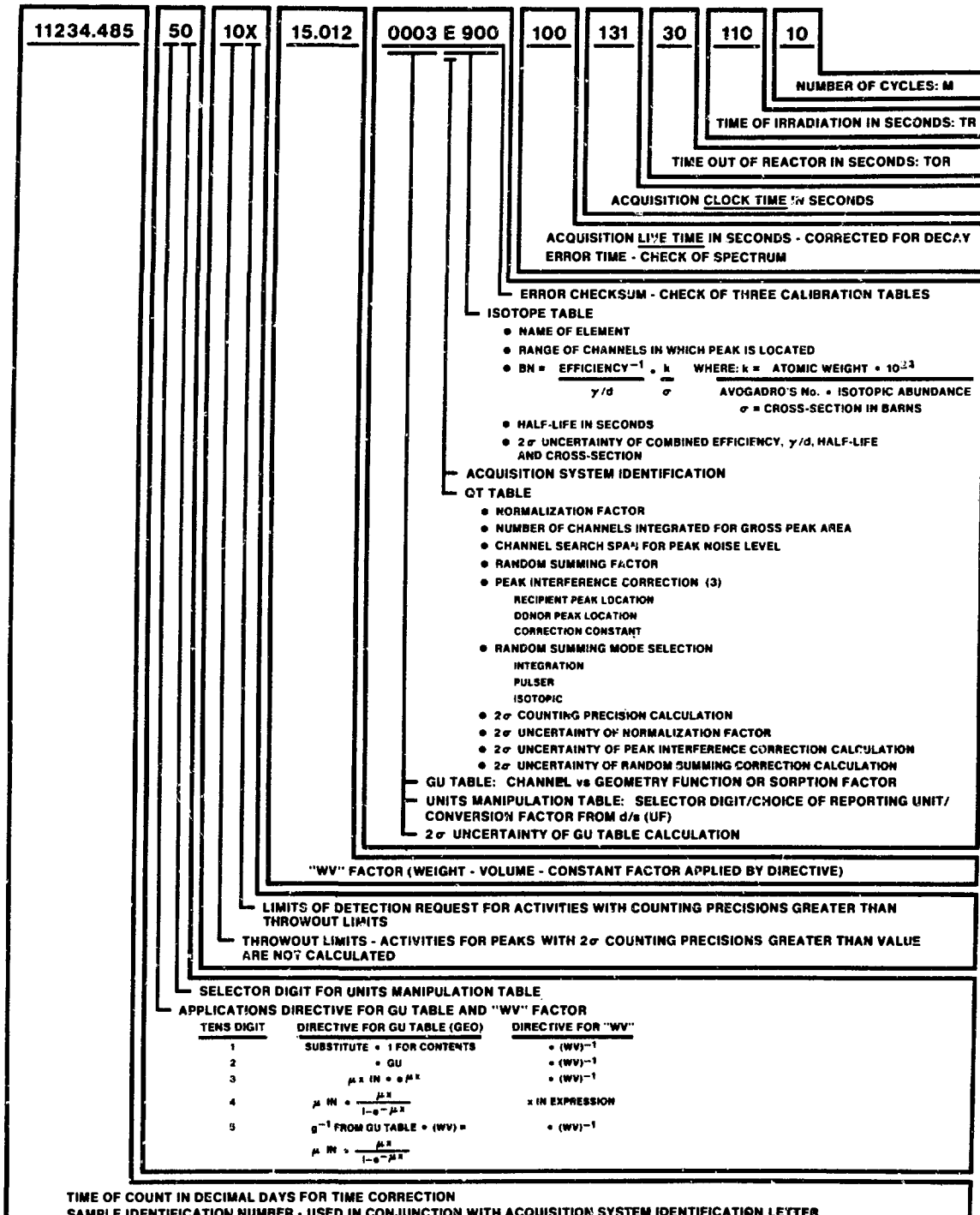

Proceedings, ERDA X-and Gamma-Ray Symp. Ann Arbor, MI, May 19-21, 1976 (Conf 760539)

GERMANIUM DETECTOR EFFICIENCY CALIBRATION WITH NBS STANDARDS

A. T. Hirshfeld, D. D. Hoppes and F. J. Schima
Radioactivity Section, National Bureau of Standards
Washington, D. C. 20234

Summary

The efficiency calibration of two complementary germanium detectors has provided a means of comparing the gamma-ray emission rates of all suitable radioactivity standards currently available at the National Bureau of Standards. This procedure has not only checked the activity calibrations and the accepted gamma-ray probability per decay for each gamma ray, but has served to illustrate precautions necessary for the use of the standards in accurate detector calibrations. Our approach has been initially to use rather idealized conditions (low rates, geometrical efficiencies of about 0.1% of 4π, well-separated peaks) to establish the characteristics of the detector systems, then to observe discrepancies as these conditions are relaxed. A constant-dead-time pulse-height-analysis system allows monitoring of the operating parameters during data collection and statistical evaluation from repeated measurements. An expansion of the logarithm of a detector efficiency in powers of the energy fits extensive energy regions with only small systematic deviations and provides an interpolation function. The calibration curve for a 30-cm^3 coaxial Ge(Li) detector contains 24 points between 88 and 2754 keV, with an average deviation from a fitted function of about 1/2%. The detector systems have been used to measure directly a probability per decay for many gamma rays from standards of ^{75}Se, ^{110m}Ag, and ^{152}Eu whose activities had been determined by methods essentially independent of decay-scheme parameters.

Spectrometer Systems and Data Analysis

Two germanium detector systems designed to check radionuclidic purity and the gamma-ray emission rates from current and proposed NBS radioactivity standards were calibrated for efficiency as a function of energy, with care taken to avoid some of the errors that may be responsible for discrepancies observed in the values for gamma-ray probabilities per decay, P_γ.

Detectors. For the energy region from 100 keV to 2 MeV, a coaxial Ge(Li) detector 34 mm in diameter and 33 mm long is used. With 2-μs amplifier time constants, the full width at half maximum (FWHM) is now 0.84 keV at 122 keV and 1.70 keV at 1332 keV. There has been a general improvement in resolution, with some fluctuations, over the past 2½ years, with an accompanying increase in efficiency of 1 to 1.5%. Peak-to-total ratios and peak shapes have remained essentially constant, as have pulse heights observed relative to that of a stable pulser.

In the region below 100 keV, the coaxial detector peaks have a low-energy tail that makes an area determination uncertain. A pure germanium planar detector with a 200 mm^2 nominal active area and a thickness of 5 mm is used for energies from a few keV to 400 keV. One such detector showed erratic and dramatic losses in efficiency and was replaced by another which lost less than 1% efficiency in almost a year. The detector is maintained at liquid nitrogen temperatures to avoid small efficiency changes that were observed when it was allowed to return temporarily to room temperature. The detector is equipped with a resistive-feedback preamplifier and has a resolution of 290 eV at 14 keV and 840 eV at 392 keV, when a 6-μs amplifier time constant is used. An original pulsed-optical-feedback preamplifier had a few percent better resolution, but was replaced because higher-energy gamma rays were selectively rejected. The pulse which triggers a reset of the FET, after the equivalent of 2 MeV of charge have been accumulated, is lost, and fewer higher-energy gamma rays are required for triggering.

Both the coaxial and planar detectors show efficiency variations of several percent for different possible bias voltage settings. Constant bias voltage and gain settings are used and both spectrometer systems are kept operational at all times.

Data Collection. Data are collected in 8192 channels with a fixed-dead-time, multiple input ADC under computer control. The use of the direct access mode for data storage in the computer permits concurrent peak-fitting and data analysis. The data required are collected and processed in cycles of preset duration for as long as necessary to allow statistical assessment of the accuracy of the determination of the collected peak areas. In this manner, the effect of possible gain shifts can be minimized, particularly when the counting extends beyond a day.

Stable 50 or 60 Hz pulsers are used for measuring counting losses, which are primarily due to pulse pile-up. Low pulse amplitudes permit the overshoot due to the finite pulser decay times to remain hidden in amplifier noise. The pulser peaks are analyzed in the same manner as spectral peaks, and provide a normalization good to 0.1% for total rates under 1000 s^{-1}.

Data Analysis. A computer program based on the method of first differences (four channels in a row have contents at least one standard deviation above the local background) locates peaks to the nearest half-channel and gives a rough measure of their area. We can then select those peaks whose areas are to be accurately determined. A linear background is fitted to a region starting above any channel containing significant counts due to the peak and extending upward for 40 channels or until a non-linear region is encountered, as observed with an oscilloscope display. This background is extrapolated under the peak and subtracted; a Gaussian function is then fitted to the peak region extending from the half-maximum height on the low energy side to the 0.1 maximum point on the high energy side. For isolated peaks on a background that changes slowly with energy, the fitted Gaussian locates the peak and determines the FWHM accurately for both detectors. The area of the Gaussian can be taken as the peak area, for both calibrants and unknowns, but a more reproducible area is obtained by summing the net channel contents between points 1.55 times the FWHM above and below the peak center. The ratio of the Gaussian area to the summed area averages about 0.975 for the coaxial detector for energies greater than 300 keV and is greater than 0.99 for the planar detector for energies greater than 40 keV. A statistically-significant ratio which differs by more than 1% from those values indicates a complex peak or incorrect background subtraction.

The above simple analysis suffices for the calibrants used, and for most of the gamma rays of radionuclides to be investigated. If a decomposition of a complex peak into components must be made, more complicated analytic peak shapes are used or known peak

shapes are used to synthesize the complex peak graphically or numerically. The uncertainty increases considerably. This has special significance for x-rays, where techniques suitable for measuring the usually complex peaks are still being investigated.

Source Mounting and Positioning. All of our sources use the usual low-absorption NBS configuration, namely, a 2-to-8 mm diameter dried deposit of the radionuclide between two layers of polyester tape 0.006 cm thick mounted on an aluminum annulus with a 3.8 cm inside diameter. Source holders use spring-loaded plastic discs to press the source tape against a raised plastic ring about 2 cm in diameter and are located at reproducible distances from the detectors by light, but rigid, plastic tubes. The positions of the detectors inside their cryostats were determined by x-ray photography, and source-detector distances are quoted with respect to the front face of the detector.

A large source-detector separation reduces errors due to source size and positioning. It also reduces the possibility of the loss of peak counts due to summing with coincident radiations, including beta particles and x rays. Our most-used calibration positions (25 cm for the coaxial detector and 10 cm for the planar) correspond to geometrical efficiencies of less than 0.2% and the largest correction for any of the calibrants is 0.17%. However, at 10 cm from the coaxial detector, the 1064-kev peak of a ^{207}Bi source must be corrected by 0.96%. For smaller separations, larger detectors, or several radiations in cascade, the corrections become larger.

Efficiency Calibrations

Calibrant Data. The pertinent data for all NBS standards used in the present efficiency determinations are shown in Table 1. The energies, P_γ values and uncertainties are those published by [1], or obtained directly from, the Nuclear Data Project at the Oak Ridge National Laboratory (except for the case of ^{207}Bi, where NBS values and uncertainties are given).

The uncertainties to be considered in each calibration point include, in general, that associated with P_γ, those involved in the calibration of the sources, and the standard error of the counting (maximum 0.3%). The errors quoted for P_γ represent one standard deviation plus, perhaps, the experimenter's estimate of systematic errors. The source uncertainty, in column 5, includes the statistical error, quoted at the 99% confidence level, plus a correspondingly conservative estimate of the conceivable systematic errors. In obtaining a least-squares fit of the efficiency data, we have arbitrarily taken the quoted P_γ uncertainty plus 1/3 the source activity calibration uncertainty plus the standard error of the counting, to arrive at a standard deviation to be used in weighting each point. However, for those cases where a γ appears in column 5, our sources were calibrated directly in terms of emission rate at the particular gamma-ray energy, so that the P_γ values and their uncertainties do not enter into the efficiency calculation.

Interpolation Functions. Although analytical expressions which have some physical basis are more satisfying for describing the energy dependence of a detector efficiency, we have found that, for the present calibrations, truncated power series in E_γ give satisfactory fits with non-iterative computer programs. An expansion of the logarithm of the efficiency in 5 powers of the energy yields curves with few systematic departures and no disturbing undulations within regions of interest. Where there is a paucity of points, such expressions may not give a reasonable approximation to the efficiency; the region between 166 keV and 279 keV may be ill-defined for this reason. But emission rates determined using the two detectors in that interval agree to better than 1.5%, despite the quite different energy dependences involved.

Table 1. Calibration Data

Energy	Nuclide	P_γ Value	P_γ Uncertainty %	Calibration Uncertainty %
88.037	^{109}Cd	3.72	3.0	γ 1.91
122.063	^{57}Co	85.59	.22	1.6
140.509	^{99m}Tc	88.96	.27	1.6
165.853	^{139}Ce	80.06	.16	1.0
279.189	^{203}Hg	81.5	.25	γ 1.37
320.078	^{51}Cr	9.8	1.0	1.5
364.480	^{131}I	91.2	1.47	1.80
391.688	^{113}Sn	64.9	.3[illegible]	γ 2.2
411.795	^{198}Au	95.47	.08	1.5
513.990	^{85}Sr	98.0	1.02	2.3
569.689	^{207}Bi	97.84	.10	1.4
604.699	^{134}Cs	97.6	.31	.93
702.627	^{94}Nb	100	.3	1.5
795.846	^{134}Cs	85.4	.47	.93
834.827	^{54}Mn	99.98	.00	γ 1.0
871.099	^{94}Nb	100	.3	1.5
1063.635	^{207}Bi	75.3	1.0	1.4
1173.208	^{60}Co	99.90	.02	1.22
1274.540	^{22}Na	99.9[illegible]	.02	γ 1.53
1332.460	^{60}Co	100	.00	1.22
1368.53	^{24}Na	100	.00	2.0
1836.040	^{88}Y	99.35	.03	γ 1.9
2754.09	^{24}Na	99.86	.01	2.0

Calibration Results. Tables 2 and 3 show the present results for the coaxial detector. Although a single fitting with the same five powers of E produced a maximum divergence from a point of 1.4%, there were regions with several consecutive points diverging in the same direction. Fitting in two separate regions, which is justified by the available degrees of freedom, produces a more acceptable distribution of the signs of the residuals. The figure displays the quality of the fit from 411 to 2754 keV. Plotting the product of the efficiency and the energy shows the deviations over an extended range, while permitting easy interpolation of the calculated efficiency.

A similar fitting for the efficiency of the planar detector, at 10 cm, is shown in Table 4. An extension of the curve to lower energies will require the development of consistent evaluation techniques for x-ray peaks, for the best calibration points will involve x rays.

Table 2. 30 cm^3 Detector Efficiency for $E_\gamma \leq 411$ keV, 25 cm

$\ln(eff) = 0.243866 \times 10^2 E^{-3} - 80121.8 E^{-2} + 830.623 E^{-1} - 9.9449 - 0.229637 \times 10^{-3} E$

Energy, keV	Efficiency x 10^5	Departure from Calculated Value, %
88.037	67.94	-0.04
122.063	74.72	+0.55
140.509	70.35	-1.65
165.853	64.15	+0.14
279.189	35.45	+0.51
320.078	29.15	-0.94
364.480	24.54	-1.02
391.688	22.48	-0.43
411.794	21.27	+0.45

Table 3. 30 cm^3 Detector Efficiency for $E_\gamma \geq 411$ keV, 25 cm

$\ln(eff) = -9.67280 \times 10^6 E^{-3} - 25936.3 E^{-2} + 762.103 E^{-1} - 9.85384 - 3.90268 \times 10^{-4} E$

Energy, keV	Efficiency x 10^5	Departure from Calculated Value, %
411.794	21.27	-0.02
513.990	16.03	+0.26
569.689	14.00	-0.29
604.699	13.09	+0.33
702.627	10.84	-0.54
795.845	9.524	+0.79
834.827	8.918	-0.42
871.099	8.549	+0.06
1063.635	6.880	-0.09
1173.208	6.204	-0.08
1274.540	5.722	+0.54
1332.46	5.431	-0.01
1368.53	5.297	+0.29
1836.04	3.841	-0.26
2754.09	2.358	+0.07

Table 4. Planar Detector Efficiency for 10 cm Separation

$\ln(eff) = 1.54998 \times 10^6 E^{-3} - 67721.6 E^{-2} + 1012.24 E^{-1} - 11.4735 - 1.54414 \times 10^{-3} E$

Energy, keV	Efficiency x 10^5	Departure from Calculated Value, %
59.537	179.3	+0.03
88.037	138.9	-0.16
122.063	86.23	+0.63
140.509	63.45	-0.49
165.853	43.19	+0.12
279.188	11.44	+0.07
391.688	4.982	+0.25
411.794	4.405	-0.18

Tests of the Efficiency Calibration. Not all radionuclides for which NBS activity or emission rate calibrations exist were used in constructing the efficiency functions. ^{95}Nb and ^{46}Sc were not available, but the P_γ values determined for the 1100 keV and 1292 keV gamma rays of ^{51}Fe differed from the evaluated ones (M. J. Martin, 1976) by only +.1% and -0.9%, respectively. We measure a 1.2% higher gamma-ray emission rate for the 662 keV transition in ^{137m}Ba than is determined from an interpolated ion chamber calibration. This possible discrepancy is under investigation. For ^{65}Zn, our emission rate value for the 1116 keV gamma ray is 1.1% greater than an indirect NBS calibration would indicate. The 898-keV gamma ray of ^{88}Y was found to have a P_γ 1.7% higher than the tabulated value, and our value of 0.950±0.005 has been adopted for use in NBS certificates.

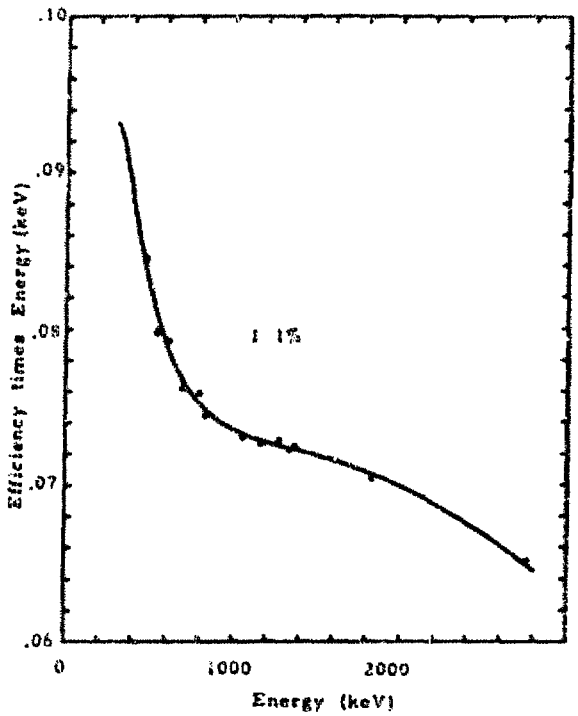

Figure 1. The calibration points for the 30-cm^3 detector are displayed. The data and fitted curve are from Table 3.

A further check for relative efficiencies was made with the 434-, 614- and 723-keV gamma rays of ^{110m}Ag, where well-established relative emission rates were checked to 0.3%.

The application of these efficiency-calibrated detectors to standards that emit many gamma rays requires that more elaborate evaluation techniques be used in many cases. However, the spectrum produced by the mixed-radionuclide NBS standards[2] is, by design, free of serious interferences for good-resolution detectors. The greater background around peaks contributes to the uncertainty in the gamma-ray emission rates, but the values agree to 1% with the source calibration values. Of the radionuclides used in the mixture only ^{60}Co and ^{88}Y are susceptible to large coincidence summing errors, with the fraction of counts lost from each peak corresponding to about

$\frac{1}{2}$ the fraction of 4π subtended by the detector. The summing corrections, and interferences observed for some peaks, are more significant for ^{75}Se, ^{110m}Ag and ^{152}Eu. Values of P_γ's measured for those nuclei, and a discussion of the evaluation techniques used, will be published elsewhere.

Acknowledgements

We are greatly indebted to L. M. Cavallo and B. M. Coursey for preparing a large number of special sources for the detector calibrations.

References

1. Martin, M. J., ORNL-5114, Oak Ridge National Laboratory, Oak Ridge, Tennessee 37830, March 1976

2. Coursey, B. M., in Proc. of a Symposium: Measurements for the Safe Use of Radiation, Gaithersburg, Maryland, March 1976

Proceedings, ERDA X-and Gamma-Ray Symp. Ann Arbor, MI, May 19-21, 1976 (Conf 760539)

PERFORMANCE OF A LARGE MULTI-DETECTOR ARRAY OF INTRINSIC GERMANIUM GAMMA-RAY DETECTORS

K.W. Marlow, G.W. Phillips and F.C. Young
Naval Research Laboratory, Washington, D.C. 20375

Summary

A twelve detector array of coaxial intrinsic germanium gamma-ray detectors is described. At one-meter source distance, the array has full energy peak efficiencies of 5.5×10^{-4} at 60 keV and 6.9×10^{-5} at 1332 keV. The energy resolution (FWHM) at 60 keV is 1.0 keV and at 1332 keV it is 2.07 keV. The efficiency and energy resolution of individual detectors are given for comparison. The array has been thermally cycled many times between room temperature and the operating temperature of liquid nitrogen with no apparent degradation of performance.

Introduction

Within the past few years the availability of high purity (intrinsic) germanium has led to the development of coaxial intrinsic germanium gamma-ray detectors. Since such detectors can, in principle, be warmed up without damage to the detector, it is possible to assemble a large volume array of high resolution germanium detectors without the risk of losing all as a result of a minor vacuum leak or failure to replenish liquid nitrogen.

In the sections below, results are reported on the performance of a twelve detector array of intrinsic germanium coaxial detectors.

System Description

Detectors

The detectors, preamplifiers, cryostats and dewar were obtained on contract from Princeton Gamma Tech, Inc. The detectors range in diameter from 44 to 46 mm and in length from 23 to 25 mm. Each is mounted in its own vacuum enclosure and all are connected to a common copper cold plate attached to a single dewar. Figure 1 shows the completed detector assembly mounted on a dolly. The cold plate can accommodate up to 18 detectors, however only twelve are currently installed.

Electronics

Preamplifiers. Each detector has its own preamplifier, the first stage of which is cooled and contained inside the respective detector cryostat. The remaining portions of the preamplifiers are mounted together above the detectors as shown in Fig. 1.

Amplifiers. Commercially-available amplifiers have been used, ORTEC Models 451 and 471. The latter are decidedly more stable than the former. The 2 microsecond time constants are adequate, but 4 microseconds would give slightly improved performance as indicated below.

Multiplexer. The commercially-available multiplexer, Model 459D of Northern Scientific, Inc., accepts as inputs the amplified detector signals. Each input channel possesses a discriminator and a linear gate. The linear gate is normally closed and the outputs of all of the linear gates are summed and amplified at the output of the multiplexer. If a signal appears at one of the inputs, the discriminator is triggered, which in turn opens the linear gate for that channel. The gated signal then appears at the output. This kind of operation avoids summing the noise from the detectors and therefore preserves the energy resolution. When two or more signals arrive at the multiplexer inputs within the pulse duration, a coincidence circuit detects such events and rejects their analysis. This is acceptable since the count rate is assumed to be low; otherwise one would probably not need an array of detectors. The single output of the multiplexer is applied to a conventional pulse-height analyzer. In order to provide a "super-fine" gain control, a variable resistance (0 - 3.3 Ω) was placed in series with each multiplexer input.

Performance

Individual Detectors

Energy Resolution and Efficiency. Calibrated sources of ^{241}Am and ^{60}Co were tested on each detector at 25 cm distance (source to detector housing). A Canberra Model 1412 amplifier with 4 microsecond time constants was used for these measurements. The results are shown in Table 1. The first six detectors in the Table have a dead layer of germanium of approximately 1 mm. The later detectors have a smaller dead layer (0.5 - 0.6 mm) as evidenced by the higher efficiency to 59.5 keV gamma rays.

Array

Alignment. Radioactive sources of ^{241}Am and ^{60}Co are used to adjust the baseline and gain, respectively, of each of the detectors. Measurements utilizing the array have been made with amplifier time constants set at 2 microseconds.

Energy Resolution. A portion of a ^{60}Co spectrum is given in Fig. 2, showing the region about the peak at 1332 keV, as well as a peak fit by the computer program HYPERMET.[1,2] The full-width at half maximum (FWHM) of 2.07 keV and full-width at one-tenth of maximum (FWTM) of 4.0 keV are also shown. The resolution (FWHM) is approximately 1.0 keV in the region 60 - 120 keV.

Efficiency. Since the detector array spans a distance of approximately 40 cm, an efficiency measurement made at 25 cm would not be useful for scaling purposes. Efficiency measurements, therefore, have been

made at one meter. At least on a semi-quantitative basis, the efficiency for larger distances can then be inferred using the inverse square law and air attenuation. The efficiency for ^{241}Am and ^{60}Co gamma rays are shown in Table 2.

Stability. There are several possible concerns on stability of the system. Some of these have been investigated and are reported here. The largest instability problem encountered has not been given a detailed quantitative treatment; namely the temperature induced change in gain and baseline of the amplifiers. Most importantly, the amplifiers do not have the same temperature coefficients, leading to distorted peaks when large ambient temperature changes occur ($\approx$ 10 - 20 deg C). Small temperature changes ($\approx$ 1 - 2 deg C) have a much smaller effect on the system as exemplified by the fact that spectra recorded for a duration of 2×10^4 seconds on each of five successive days showed that the ^{40}K gamma ray line at 1461 keV changed in position by less than 0.1 keV in the first three days and the resolution of 2.35 keV changed by less than 0.05 keV. A change of room temperature upwards by 2 deg C during the last two days resulted in the peak position decreasing by 0.15 keV and the resolution worsening to 2.5 keV. No realignment or changes in the electronics was made during this five day period. Measurements made on a single detector of the system indicate that the ^{60}Co gamma ray peak position changed by -0.08 keV/deg C. The same detector and associated electronics has been shown to drift 5.4×10^{-3} keV/hour for 30 hours at constant room temperature. Other amplifiers have temperature coefficients of the same order, but not necessarily of the same sign.

As a test of the capability of the detector to operate in the down-looking mode, the system as shown in Fig. 1 was tipped over and then elevated so that the faces of the detectors were 20 cm above the laboratory floor. A background spectrum was recorded in this position and is shown in Fig. 3. Prominent gamma ray peaks are identified by their energies in kiloelectron Volts. SE and DE refer to single escape and double escape peaks of the indicated gamma ray. ^{60}Co spectra recorded before and after tipping over gave resolutions of 2.0 keV and a peak shift of less than 0.1 keV.

The spectrum shown in Fig. 4 was recorded while the array was mounted in a stationary truck and operating on the power supplied by a motor-generator set. The spectrum of Fig. 4 is that of a typical background. The resolution for the system is the same whether operating in the truck or the laboratory; however with the truck in motion, the ^{60}Co resolution was degraded by approximately 0.2 keV.

Recyclability. The array has been recycled many times over a six month period. No change in efficiency or resolution has been observed.

References

1. G.W. Phillips and K.W. Marlow, "Automatic Analysis of Gamma-Ray Spectra from Germanium Detectors," submitted for publication.

2. G.W. Phillips and K.W. Marlow, "Program HYPERMET for Automatic Analysis of Gamma-Ray Spectra from Germanium Detectors," Naval Research Laboratory Memorandum Report 3198, January (1976).

Table 1

Energy Resolution and Efficiency of Individual Detectors

Detector Number	Resolution at 1332 keV	Absolute Efficiency 59.5 keV	Absolute Efficiency 1332 keV
217	1.77	7.1(-4)*	7.3(-5)
218	1.91	7.6(-4)	7.6(-5)
219	1.90	7.5(-4)	7.9(-5)
227	1.86	7.6(-4)	8.7(-5)
228	1.95	7.7(-4)	7.9(-5)
229	1.90	7.5(-4)	8.3(-5)
237	1.90	8.8(-4)	8.4(-5)
259	1.81	8.3(-4)	8.3(-5)
260	1.87	8.7(-4)	8.2(-5)
261	1.94	9.6(-4)	8.9(-5)
270	1.75	9.0(-4)	8.6(-5)
271	1.80	10.1(-4)	9.3(-5)

*This notation means that 7.1(-4) = 7.1×10^{-4}

Table 2

Energy Resolution and Efficiency of the Detector Array

Photon Energy (keV)	Resolution (keV)	Absolute Efficiency at one meter
59.5	1.0	5.5(-4)
1332	2.07	6.9(-5)

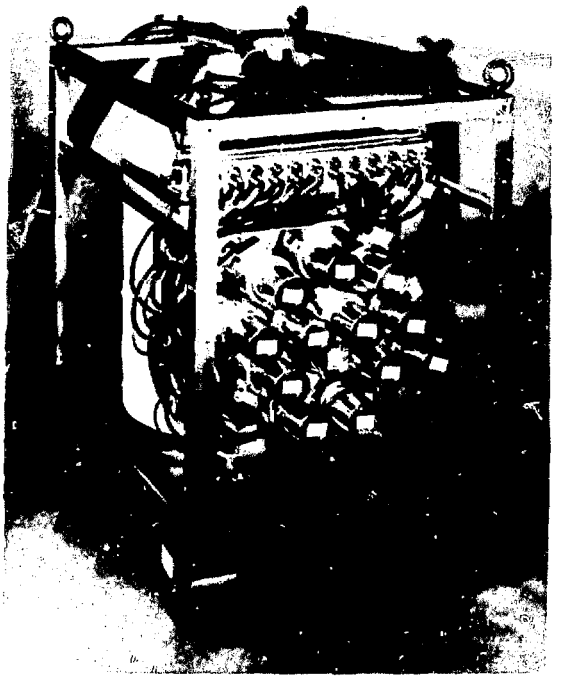

Figure 1. The twelve-detector array of intrinsic germanium detectors, including cryostat, preamplifiers and dewar.

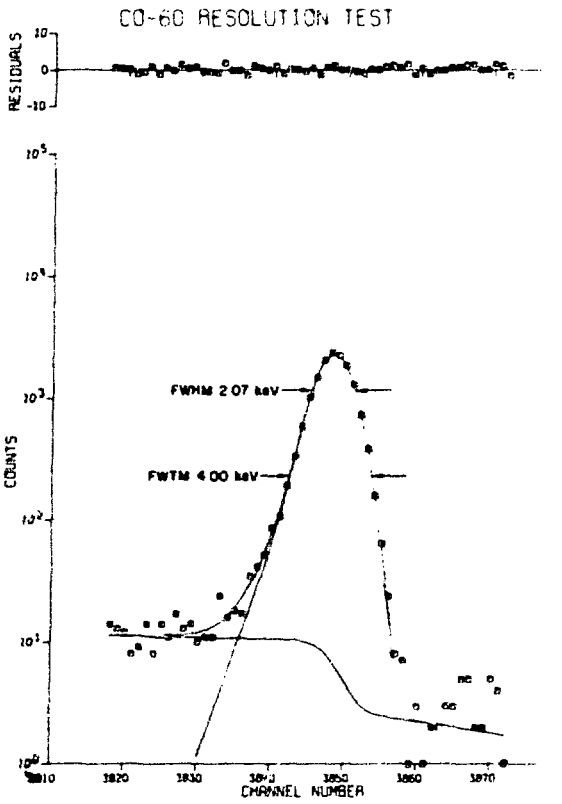

Figure 2. Resolution of the array for the 1332 keV gamma-ray from ^{60}Co. The solid lines show a computer fit to the data points which are represented by small squares.

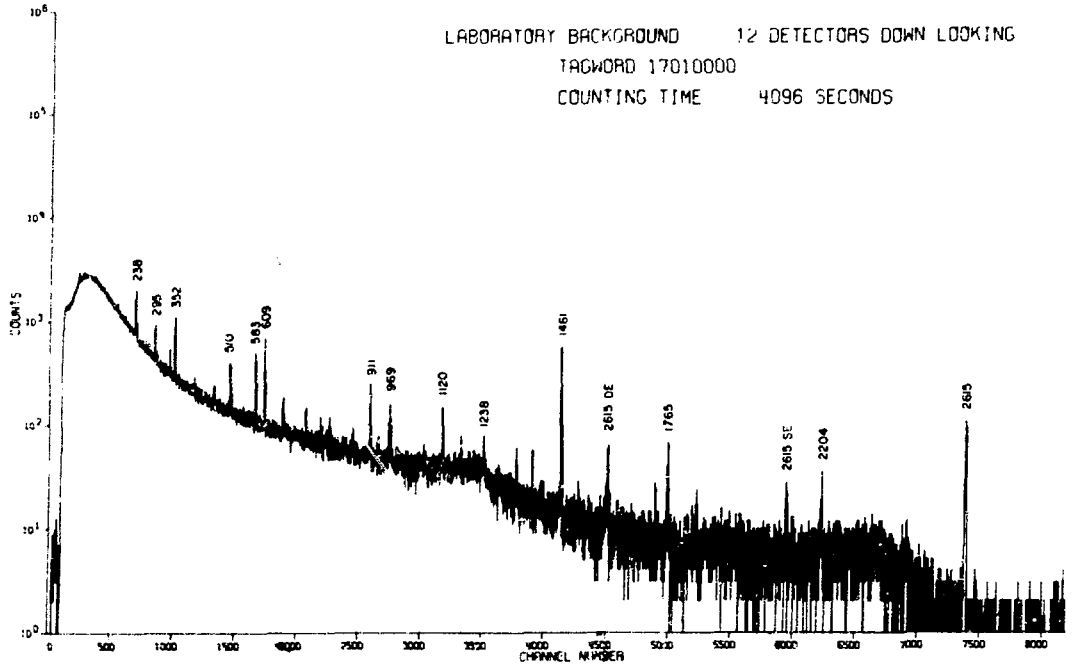

Figure 3. Background spectrum taken in the laboratory with the array suspended and pointing downward.

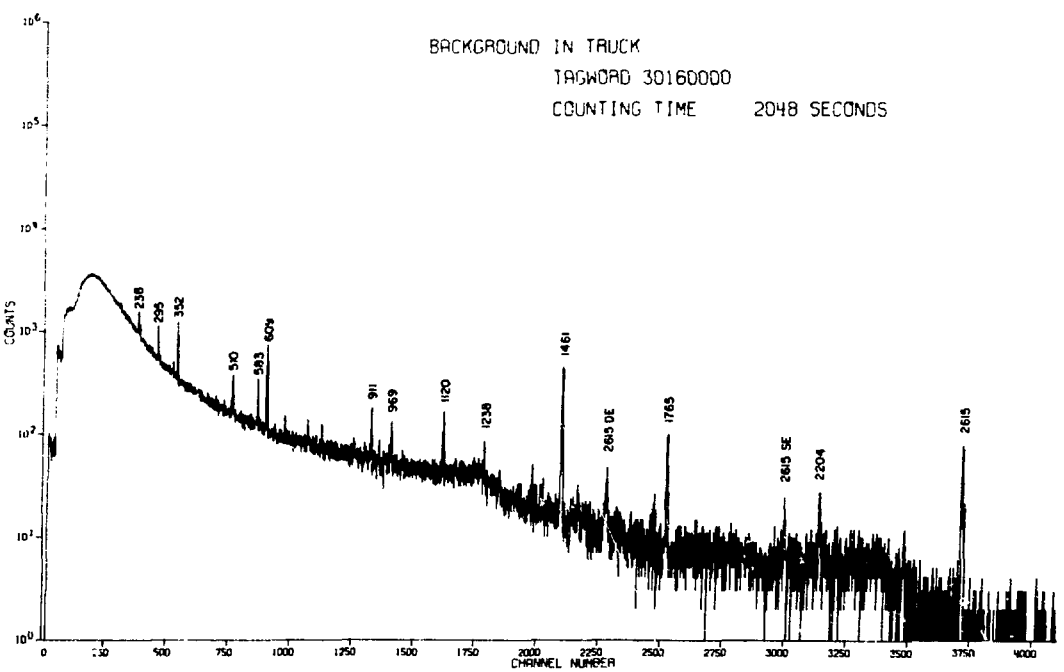

Figure 4. Background spectrum taken with the array in a stationary truck and the electronics powered by a motor generator.

Proceedings, ERDA X-and Gamma-Ray Symp. Ann Arbor, MI, May 19-21, 1976 (Conf 760539)

MEASUREMENT OF HIGH GAMMA DOSE RATES BY MEANS OF CONVERSION ELECTRON COUNTING

Joseph J. Law
Department of Natural Sciences
Longwood College
Farmville, Va. 23901

The induced activity of the internal conversion electrons emitted from the indium nuclei exposed to ^{60}Co gamma radiation can be used as a measure of the high dose rate delivered by the irradiation source. The sensitivity of measurement under the experimental conditions is calculated to be 5.6 krad hr^{-1}. It can be increased to about 8.0 X 10^2 rad hr^{-1} if the irradiation period is increased to 4.5 hr and the counting period to 1 hr. There is no upper limit of determination.

Introduction

Upon irradiation with gamma-rays the target nuclei of the elements having metastable isomers are excited and, consequently, release induced radiation which often includes internal conversion electrons. The induced gamma activity has been used as a measure of the dose rate, flux density, or activity of the irradiation source, when all other parameters are fixed.[1-5] The induced activity has been found linear with these quantities. There is no theoretical upper limit of the measurement. Dosimetry based on photonuclear excitation has advantages over chemical dosimetry as it is simple, rapid, and independent of temperature. Photonuclear dosimetry is specially useful in the comparison of strengths of different sources of the same radionuclide in a standard configuration.

The highest sensitivity of the dose rate measurement by photonuclear dosimetry was 2.75 X 10^5 rad hr^{-1}, reported by Ware et al.[5] However, the sensitivity can be increased if the efficiency of counting the induced activity is improved. This goal can be achieved by a better counting geometry such as the 4-pi counting. In this study the feasibility of using the liquid scintillation method (4-pi counting) for measuring the induced activity of conversion electrons and the high dose rate response of the photonuclear dosimeter were explored. The sensitivity of the method was calculated.

Materials and Methods

An indium dosimetric system was chosen for this study as indium has an isotopic abundance of 96% for ^{115}In and the cross-section for $^{115}In(\gamma,\gamma')^{115m}In$ is comparatively large. The metastable isomer has a half-life of 4.5 hr and emits 308 and 331 keV conversion electrons. The ratio of the conversion electron activity of ^{115m}In to that of ^{113m}In is calculated to be about 20:1 after 1-hr irradiation with ^{60}Co source. This ratio increases as the irradiation period increases. Therefore, the contribution of ^{113m}In to the total induced activity is minor.

The dosimetric systems investigated were aqueous $InCl_3$ solution with (1) 10 ml of Insta-Gel (Packard Instrument Co., Inc.) as the liquid scintillator; (2) 10 g of anthracene as the suspended scintillator. The concentration of the solution was 11.7 g of $InCl_3$ in 10 ml of solution. This concentration is slightly lower than the solubility of $InCl_3$ at 0 °C so that phase separation can be avoided when the dosimeters are prepared and placed in the liquid scintillation spectrometer for counting at a temperature of slightly above 0 °C.

Ten milliliters of $InCl_3$ solution was irradiated for 1 hr with the 4.7 X 10^4 Ci ^{60}Co source installed at the Atomic Reactor Facility of the University of Virginia. Calibration of the dose rate delivered by the source was by Fricke dosimetry. After irradiation the solution was transferred into a 22-ml borosilicate glass counting vial containing the scintillator. The vial had been chilled in ice-water before it was placed in a Packard Tricarb 3330 liquid scintillation spectrometer for 10-min counting at 5 °C. The activity from the dosimeter containing anthracene was counted in the same way without chilling. The gain control and discriminator settings of the spectrometer were optimized for recording no noise pulse and obtaining the maximum counting rate. Background rates were obtained by counting the blanks for 1 hr. The blanks were the same materials as those used in the dosimeters without irradiation. The time elapsed between the end of irradiation and the start of counting was 3 min. Three identically prepared dosimeters were made for each measurement.

Results and Discussion

The scintillation mixture containing Insta-Gel became a thin gel and appeared translucent. It was not milky and no suspension was seen. The average net count of the conversion electron activity was 4.86 X 10^4 counts. Since the dose rate determined by Fricke dosimetry was 1.03 Mrad hr^{-1}, each count was equivalent to 21 rad hr^{-1}. The background rate was 463 counts per 10 min. The lower limit of determination, which was arbitarily taken as 14.1 standard deviations of background rate,[6] was calculated to be 294 counts. This is equivalent to 6.0 krad hr^{-1}. For the dosimeters containing anthracene the average net count was 3.81 X 10^4 counts. Each count was equivalent to 27 rad hr^{-1}. The background rate was 220 counts per 10 min. The lower limit of determination was calculated to be 209 counts. It is equivalent to 5.6 krad hr^{-1}. The dosimeter is about 50 times as sensitive as the one developed by Ware et al. The limit can be increased to about 8.0 X 10^2 rad hr^{-1} if the irradiation period is increased to 4.5 hr and the counting period to 1 hr based on the calculation using the activation equation.

The sensitivity of measurement for sources other than ^{60}Co will change as the extent of photonuclear excitation changes with the spectral energy distribution of the radiation field.[7] It is necessary to calibrate the photonuclear dosimeter for each system studied.

Photonuclear dosimeters using cadmium solution as the target material are less sensitive than the corresponding indium system as the cross-section for the production of ^{111m}Cd is considerably smaller than

that of ^{115m}In and the isotopic abundance of ^{111}Cd is only 13%.

Acknowledgment

This work was supported jointly by a Virginia Academy of Science Research Grant and a Grant-in-Aid of Research from the Society of the Sigma Xi. The help of Mr. M. Pickle of the Department of Nuclear Engineering, University of Virginia, is gratefully acknowledged.

References

1. I.A. Abrams, L.L. Petekis, Latv. PSR Zinat. Akad. Vestis. Fiz. Teh., No. 2, 3 (1967).
2. J.J. Law, Health Phys., 17, 338 (1969).
3. K. Yoshihara, J. At. Energ. Soc. Japan, 12, 266 (1970).
4. I. Pavlicsek, V. Stenger, M. Csürös, L. Lakosi, A. Veres, Izotoptechnika, 14, 466 (1971).
5. A.R. Ware, S. Oldham, D.M. Pibby, Radiochem. Radioanal. Lett., 15, 107 (1973).
6. L.A. Currie, Anal. Chem., 40, 586 (1968).
7. G. Harbottle, Radiochem. Radioanal. Lett., 16, 263 (1974).

Proceedings, ERDA X-and Gamma-Ray Symp. Ann Arbor, MI, May 19-21, 1976 (Conf 760539)

GAMMA RAY DETECTOR OPTIMIZATION FOR MOBILE DETECTORS

Thomas E. Sampson
Los Alamos Scientific Laboratory
University of California
Los Alamos, New Mexico, 87545, USA

Introduction

The Energy Research and Development Administration supports a program[1,2] enabling a rapid response to situations requiring a mobile, detection-at-a-distance capability for locating lost or stolen nuclear materials. For this application, man-portable, vehicular-borne, and airborne detection systems are used. For gamma ray detection, NaI detectors are usually used. Because weight is a serious constraint, many systems employ unshielded detectors.

This paper presents results of optimization studies to determine a suitable thickness for 12.7cm diameter NaI detectors that are commonly used in these applications.

Measurements

Detectors. Table I displays the characteristics of the detectors used in this study. The optimization was directed toward the 1.27cm to 7.6cm thicknesses of NaI. The FIDLER and two Ge(Li) detectors were included because they are often mentioned as candidates for detectors for this scenario. All detectors were unshielded because shield weight is usually prohibitive for these applications.

Source. The source used for all measurements was 819g of PuO_2 doubly enclosed in "tomato can" geometry. The PuO_2 was contained in a right circular cylinder geometry of about 8.6cm diameter by 11.3cm high. For all measurements the source was placed 9.14m (30 ft) from the detectors. The Pu contained about 6.5% ^{240}Pu.

Source Shielding. Several thicknesses of different types of shielding were used around the source in 4π geometry. The shielding was chosen to be typical of low Z (140mm concrete), medium Z (25mm, 50mm iron), and high Z (3.2mm, 6.3mm, 12.7mm Pb). A "bare" spectrum was examined with 0.79mm of Cd shielding to remove the ^{241}Am 60 keV line that is usually not a factor when any shielding at all is present.

Data Accumulation and Analysis. Pulse height spectra were accumulated from four detectors simultaneously using a four-input mixer-router with a 4096 channel PHA. The 5x1 NaI was used with both sets of four inputs to provide normalization.

The spectrum of the net signal was isolated by a point-by-point background subtraction. The net and background spectra were computer searched to find the energy window that maximized the ratio (Net Signal)^2/Background (S^2/B). The S^2/B figure of merit is appropriate when detection is based on the ratio of the net signal to the background standard deviation. The minimum count time for detection is also related to S^2/B by

$$t_{min} = \frac{n^2}{S^2/B}$$

where n is the number of standard deviations or "σ level" used for detection. One must be careful in using the expression for t_{min} in situations involving a small number of counts since exact Poisson statistics must be used. In this case the usual false alarm probabilities derived from the normal distribution approximation are not valid. This S^2/B figure of merit was used to rank the detectors.

Results. Some typical spectra are illustrated in Figs. 1 and 2. Figure 1 shows the PuO_2 source spectra for a 5x1½ NaI with four source shielding configurations. In Fig. 2, the background spectra for all detectors -- except the LEPS -- are displayed. Table II summarizes the results for four shielding configurations. The results for the other iron and lead thicknesses studied are qualitatively similar to those listed. For the optimum energy windows listed, differences of a few keV are not significant. Window limits below ~ 20 keV should be interpreted as "above noise". The two listings in Table II for the 5x1 NaI illustrate the reproducibility between the two sets of four detector data for each shielding configuration. From Table II the following comments are made:

1) For high Z (Pb) shielded sources thicker NaI detectors improve detectability. The hardening effect of the Pb (Fig. 1) accents the high energy region of the Pu spectrum that makes thicker detectors more useful.

2) For "bare" (0.79mm Cd), low Z (concrete), and medium Z (Fe) shielding, detector thickness in the range from 1.3cm to 12.7cm has no significant effect on detectability.

3) The FIDLER is poorer than thicker NaI detectors in all cases but approaches thicker detectors for thick low Z shields. This is in general agreement with previous measurements at this laboratory. We find whenever the shield is thick enough to degrade the spectrum enough to make the FIDLER "competitive", it is thick enough to make detection impractical for realistic counting times.

4) For thicker detectors ($\geq$ 2.5cm) and high Z shielding, a window on the 400 keV complex maximizes S^2/B for this PuO_2 source.

5) For "bare", low Z, and medium Z shielded sources, a wide open window from above noise to $\sim$ 450 keV maximizes S^2/B in most cases. Our experience finds that this usually holds for other sources and spectral shapes where the upper edge of the window is set just above the principal energy emitted by the source.

6) Even for the high resolution Ge(Li) a wide open detector window offers superior detectability compared to narrow windows on a photopeak -- except for 6.35mm Pb shielding. The use of a larger Ge(Li) detector might change this result. However, the 127mm diameter NaI detectors will still give superior detectability because of the brute force effect of detector area.

Conclusions. These results indicate that the detectability of a PuO_2 source in various shielding configurations is insensitive to NaI detector thickness in the range from 1.27cm to 7.6cm. This means that outside factors such as cost, weight, geometry, and data analysis techniques can play the dominant role in selecting NaI detectors for mobile detection-at-a-distance applications.

Table I

Detector	Entrance Window	Quartz Light Pipe	Resolution
5x3 NaI 12.7cm diam 7.6cm thick	0.25 mm Be	2.5 cm	7.25% at 662 keV
5x1½ NaI 12.7cm diam 3.8cm thick	0.25 mm Al	2.5 cm	8.1% at 662 kev
5x1 NaI 12.7cm diam 2.5cm thick	0.51 mm Al	1.27 cm	8.1% at 662 keV
5x½ NaI 12.7cm diam 1.27cm thick	0.25 mm Al	5 cm	6.8% at 662 keV
FIDLER NaI 12.7cm diam 0.16cm thick	0.25 mm Be	5 cm	26% at 22 keV
Ge(Li) 42mm diam 31mm long 7.9%, $\sim$40cm^3	0.51 mm Al	-------	1.72 keV at 1332 keV
LEPS Ge(Li) 16mm diam 5mm thick	0.127 mm Be	-------	550 eV at 122 keV

References

1) W. H. Chambers, "Developments in Search and Survey Instrumentation," Trans. Am. Nucl. Soc., 21, 129 (1975).

2) John F. Doyle, "Search Methods for Radioactive Materials," Trans. Am. Nucl. Soc., 21, 129 (1975).

Table II

Maximum S^2/B [Window (keV)]

Detector	0.79mm Cd	6.35mm Pb	25mm Fe	140mm Concrete
5x3 NaI	1576 (8-456)	30.7 (353-448)	68.1 (16-457)	19.2 (0-447)
5x1.5 NaI	1688 (7-450)	26.6 (328-444)	71.7 (7-461)	21.3 (7-443)
5x1 NaI	1567 (8-453)	17.8 (330-447)	65.0 (10-460)	20.6 (0-446)
5x1 NaI	1582 (13-454)	20.0 (18-480)	65.8 (7-453)	23.4 (7-440)
5x0.5 NaI	1513 (6-446)	15.9 (8-484)	55.2 (6-452)	23.7 (6-440)
FIDLER	689 (5-414)	4.74 (5-481)	17.7 (3-422)	13.2 (6-227)
Ge(Li)	132 (9-416)	1.66 (414 peak)	6.19 (22-423)	1.76 (16-415)
LEPS	14 (10-270)	0.093 (14-424)	0.38 (10-381)	0.16 (9-180)

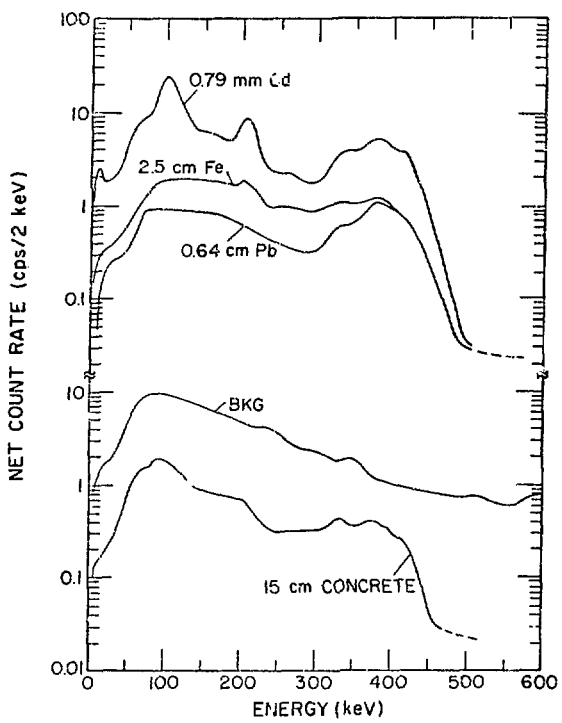

Fig. 1 PuO_2 source spectra with four source shielding configurations compared with background spectrum -- 5x1½ NaI detector.

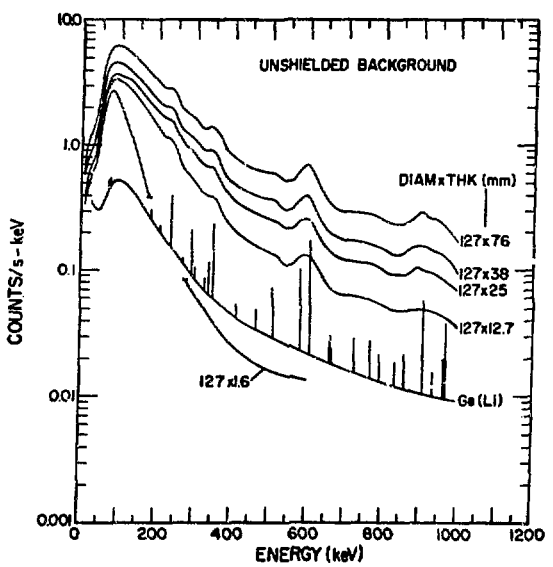

Fig. 2 Unshielded background spectra for six different detectors.

Proceedings, ERDA X-and Gamma-Ray Symp. Ann Arbor, MI, May 19-21, 1976 (Conf 760539)

FABRICATION OF GAMMA RAY DETECTORS FROM HIGH PURITY GERMANIUM*

A. S. Zolnay, P. A. Schlosser, B. K. Utts, M. C. Dudzik and I. G. Zubal
The Ohio State University
Department of Nuclear Engineering
206 W. 18th Avenue
Columbus, Ohio 43210

I. Summary

The distinguishing characteristic of high purity germanium (HPGe) detectors, as opposed to the lithium-drifted variety, is their ability to be cycled between ambient and liquid nitrogen temperatures without degradation of operating characteristics. Since the commercial introduction of HPGe crystals in 1972, several important applications of this unique material have been under development by the authors and by other investigators. The purpose of our research has been to develop detector fabrication techniques which are appropriate for the construction of gamma ray detector systems which have applications in nuclear medicine, portable gamma ray spectrometers, and orbiting satellite gamma ray telescopes. Over the past three-year period, approximately two dozen gamma ray detectors have been fabricated from high purity germanium in our laboratories. This paper gives a detailed discussion of the detector fabrication and testing process as it has evolved in our laboratory, presents some theoretical considerations which have a direct bearing upon proper fabrication and successful operation of HPGe spectrometers, and illustrates the above discussions with experimental results obtained in the operation of typical detectors.

II. Fabrication and Testing

The detector fabrication process involves the construction of an n^+pp^+ semiconductor structure which can be reverse biased with electric fields of sufficient strength to sweep out electron-hole pairs (generated by radiation interactions) without appreciable charge recombination. In addition, the reverse leakage current at full bias voltage must be maintained below some maximum value above which it degrades energy resolution. Fabrication of HPGe diode structures is similar to making lithium-drifted diodes but is considerably less difficult because the time consuming drift process is unnecessary. There are, however, several important differences between the two methods which are largely due to the very pure nature of the HPGe starting material. Consequently, in all process steps considerable care is taken to avoid contamination of the HPGe crystal.

All of the detectors which we have constructed have been planar devices from p-type crystals as large as 20 cm^3 in volume and 1.0 cm thick. We begin with a HPGe wafer which has a purity of about 2×10^{10} net acceptors/cm^3. The following process steps are employed:

1. The planar crystal is initially lapped lightly on both sides and cleaned by an acid etching solution (2 minutes in 3 parts HNO_3 plus 1 part HF) followed by a distilled water or methanol quench.

2. The crystal is mounted in a vacuum system and lithium metal is vacuum evaporated on one side through a mask which prevents lithium from reaching the sides.

3. The crystal is heated in an argon atmosphere at 275° for about 5 minutes. This forms the n^+ contact by thermal diffusion of lithium to a depth of about 0.015 inch.

4. The crystal is subsequently etched in acid ($3HNO_3$:1HF) for 30 seconds.

5. The lithium contact is covered with etch-resistant black wax and the wafer is etched for 2 minutes in acid and quenched in methanol.

6. The black wax is removed and the wafer is again mounted in the vacuum system.

7. Palladium metal is vacuum evaporated onto the reverse side of the wafer to a thickness of 500-1500 Angstroms. This forms the p^+ contact.

8. Both detector contacts are masked with black wax and the wafer is acid etched for 2 minutes with a methanol quench.

9. The wax is removed; the detector is boiled in methanol for 10 minutes, and quickly mounted in a vacuum cryostat.

After evacuating the cryostat and cooling the detector with liquid nitrogen, the initial electrical characteristics of the diode are evaluated. This includes measurement of the reverse current-voltage curve and the capacitance-voltage curve. Following this, energy resolution values are measured. Some representative current-voltage curves are shown in Figure 1 along with the structure of electric fields in the intrinsic region of the detector under various bias conditions. The theory which predicts electric field and bias current characteristics for both good and poor detectors is developed more fully in the next section. It is seen from Figure 1, however, that the upper limit for reverse leakage current at full overvoltage is about one nanoampere. Planar detectors fabricated using the above process have exhibited acceptably low leakage current and energy resolution of the order of 2 keV.

III. Theory

The objective of this section is to review the structure and depletion characteristics of HPGe radiation detectors giving a basis for some of the observed experimental results. The analysis should begin with the examination of the n^+pp^+ diode structure.

The n^+pp^+ diode structure commonly used in the construction of radiation detectors consists of a lithium diffused n^+p junction (+ indicating highly doped) on one surface and a metal to semiconductor surface barrier junction of palladium (or other

*This research has been supported by Contract No. NO1-NS-2-2323 with the National Institutes of Health, Department of Health, Education and Welfare.

suitable metal) on the other surface as shown in Figure 1. The high purity germanium used is generally p-type with an impurity concentration of approximately 2×10^{10} impurities/cm^3.

Detector operation involves the application of a reverse bias to the n^+p junction forming a depletion region which starts from the lithium side and extends all the way to the surface barrier contact. The depleted region should have sufficient electric field (about 100 V/mm) to impart saturation velocity to the charges produced by radiation interactions, thereby minimizing charge collection time and the possibility of recombination and trapping. The overvoltage criterion requires that the surface barrier contact remain noninjecting at least for electric fields which just produce saturation velocity of charge at this contact. For proper operation, these detector biasing conditions must be achieved with very low leakage currents, otherwise serious degradation of energy resolution will result due to leakage current noise.

The electric field structure of a depleted radiation detector is of interest. As expected, depletion of the electrically neutral p region results in a charged region, sometimes called the intrinsic region, where the potential and electric field distributions are obtained by the application of Poisson's equation. The charge density on both sides of the depleted junction is a constant consisting almost entirely of fully ionized, fixed donor and acceptor atoms. Thus, the electric field is linear as a function of distance from the n^+ junction and the potential is parabolic. Due to the very heavy doping of the lithium diffused region, the junction voltage drop occurs almost entirely in the depleted p-region. A representation of this situation is shown in Figure 2 for an overvoltaged detector.

Assuming that the potential changes only in the direction perpendicular to the surface, expressions for the electric field, potential, and depletion depth are obtained from Poisson's equation in one dimension for p-type germanium,

$$\frac{d^2V}{dx^2} = \frac{q}{\epsilon} , \qquad (1)$$

where V = electric potential in x direction (perpendicular to surface)
x = distance from the n^+p junction (+ toward p region)
q = net impurity concentration for p-type Ge
ϵ = dielectric constant of p-type Ge

Some simplifying assumptions used for the solution of Poisson's equation are:

1. The n^+p junction is abrupt.
2. The undepleted region is neutral (potential is constant).
3. The doping is much heavier in the n^+ region than the p region.
4. The applied bias voltage is much greater than the junction voltage.
5. There is no appreciable leakage current.

With these simplifying assumptions, Poisson's equation is readily solved by integration and is valid for the depleted portion of the p region.[1]

The electric field distribution is given by

$$E(x) = \frac{qd}{2\epsilon} + \frac{Va}{d} - \frac{qx}{\epsilon} , \qquad (2)$$

where d = depletion depth
Va = applied potential (reverse bias).

The potential distribution is given by

$$V(x) = \frac{qx^2}{2\epsilon} - \left\{ \frac{Va}{d} + \frac{qd}{2\epsilon} \right\} x + Va . \qquad (3)$$

By taking into account charge conservation, the depletion depth as a function of applied reverse bias is found from Equation 3,

$$d = \left\{ \frac{2\epsilon Va}{q} \right\}^{1/2} . \qquad (4)$$

Of course, the depletion depth cannot be greater than the detector thickness so that a reverse bias greater than that required for full depletion will produce a constant component of electric field across the entire depleted region provided the surface barrier contact remains noninjecting. This is shown in Figure 1b. The reverse bias voltage required for full depletion and two overvoltage conditions (100 V/mm at the surface barrier contact insures saturation velocity everywhere in the depleted region, whereas an electric field of 50 V/mm at the surface barrier contact probably results in negligible recombination) as a function of detector thickness and impurity concentration is shown in Figure 3.

The depleted region gives rise to a detector capacitance of

$$C = \frac{\epsilon A}{d} , \qquad (5)$$

where A = electrode surface area.

By substituting into Equation 5 the expression for the depletion depth we obtain the detector capacitance as a function of applied reverse bias for bias voltage less than full depletion (for bias voltages exceeding full depletion the capacitance remains constant).

$$C = A \left(\frac{\epsilon q}{2Va} \right)^{1/2} . \qquad (6)$$

With the aid of Equation 6, the depletion voltage is indicated when the capacitance becomes constant during a capacitance versus bias voltage measurement.

IV. Illustration of the Theory with Experimental Results

With an elementary understanding of the electric fields in a radiation detector provided in the previous section, some aspects of the current-voltage curve can be readily explained. Experimental current-voltage curves may exhibit one of the shapes illustrated in Figure 1c.

An acceptable diode will maintain low leakage current beyond the depletion voltage Vd. This is shown in Figure 1c along with the other cases that will be

discussed. Such a good diode current-voltage curve implies a rectifying n^+p junction, negligible surface leakage current, and a noninjecting surface barrier contact. At full depletion an injecting surface barrier contact will allow a sudden increase in leakage current. This is due to the electric field reaching the surface barrier contact. Such detectors cannot be overvoltaged and rework of the surface barrier contact is indicated. In some cases defects and contamination on the sides of the detector contribute an increasing surface leakage current (Figure 1c) as the depletion region becomes deeper with the application of reverse bias. This situation is usually corrected by re-etching the detector sides. A poor n^+ contact will result in current through the bulk of the detector immediately upon the application of bias. Correction of this defect is usually accomplished by lapping off the relatively thick n^+ contact and reprocessing the detector.

Verification of the depletion voltage calculated from the impurity concentration provided by the manufacturer of HPGe can be accomplished by taking a capacitance voltage curve. A typical experimental curve is shown in Figure 4. The leveling off of the capacitance indicates that full depletion voltage has been reached. Figure 4 also shows a current-voltage curve for a detector that can withstand a minimum overvoltage. The current shows a sharp increase just after depletion.

Although current-voltage curves of experimental devices may not exhibit the same shapes as presented in this section, a good indication of the basic problem can be surmised with the aid of Figure 1c.

V. Conclusion

Some basic considerations necessary for the understanding of high purity germanium detector operation have been reviewed. The detector fabrication procedure has been presented in detail as a means of approaching experimentally the ideal detector characteristics discussed. Experimental curves of radiation detector characteristics were interpreted in terms of theoretical considerations presented earlier with specific suggestions for repairing unacceptable detectors.

Reference

1. G. Bertolini and A. Coche, Semiconductor Detectors, John Wiley & Sons, 1968, p. 106.

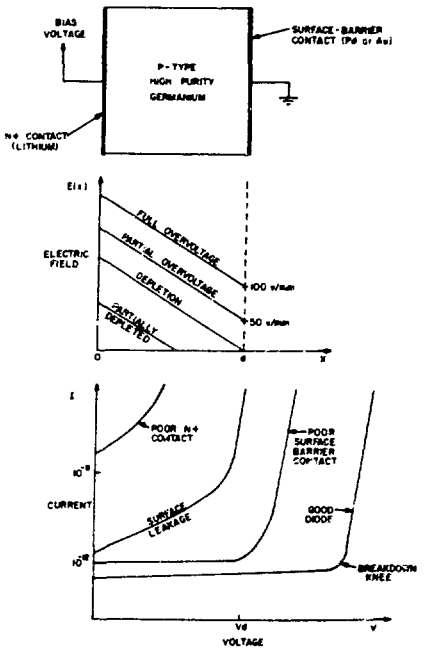

Figure 1. Typical electric fields and reverse current-voltage curves for various reverse bias conditions in high purity germanium detectors.

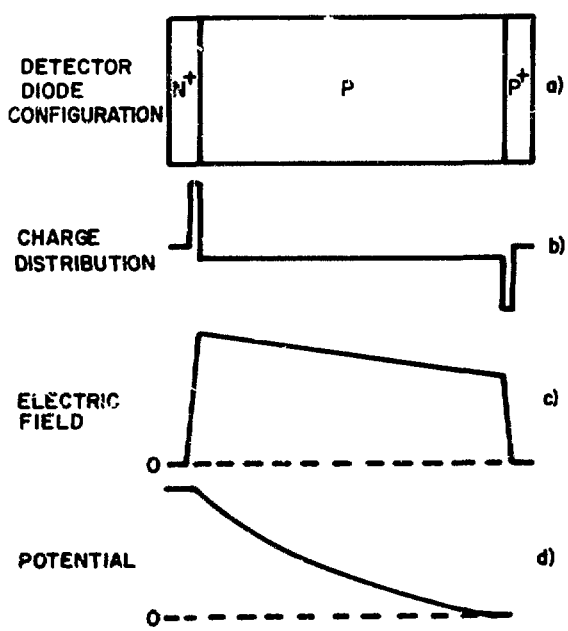

Figure 2. The reverse biased n^+pp^+ diode.

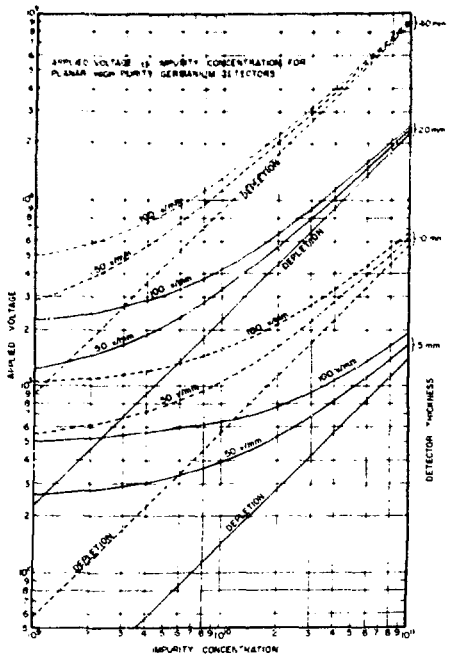

Figure 3. Depletion and overvoltage as a function of detector thickness and impurity concentration.

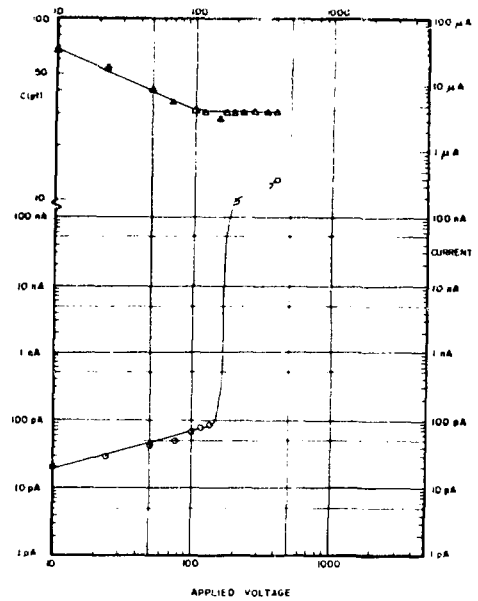

Figure 4. Experimental current-voltage and capacitance curves.

Proceedings, ERDA X-and Gamma-Ray Symp. Ann Arbor, MI, May 19-21, 1976 (Conf 760539)

PHOTON SOURCES FOR ABSORPTIOMETRIC MEASUREMENTS

Robert M. Witt, John M. Sandrik, and John R. Cameron
Medical Physics Section
University of Wisconsin
Madison, Wisconsin 53706

Summary

After defining photon absorptiometry, the paper describes the requirements of photon sources for these measurements. Both x-ray tubes and radionuclide sources are discussed including the advantages of each in absorptiometric systems.

Introduction

Photon absorptiometry is a non-invasive method of determining the masses of body components by direct, photon-transmission measurements in vivo. The method employs collimated, low energy (20 to 100 keV) photon beams from either radionuclide sources or x-ray tubes. The transmitted beams are monitored by collimated, electronic detectors including those used with nuclear counting instrumentation, such as NaI(Tl) crystals, Ge(Li) and Si(Li) diodes, and multiple wire proportional counters, and also image intensifiers coupled to TV chains. Photon absorptiometry has been used to determine the masses of the following body components: bone mineral content (BMC), iodine, lipid, and fluid. In theory as many components can be simultaneously analyzed as there are photon energies. One, two, and three energy systems have been devised. The single energy method can determine the mass of one component in a two component substance, but the requirement of constant total thickness of the components usually limits its application to measurements on the limbs. Dual energy absorptiometry allows measurements of the masses of two components (e.g. BMC and soft tissue), permitting measurements on any site of the body. Photon absorptiometry, especially the single energy method, has become widely accepted for the precise and accurate determination of BMC and for the evaluation of skeletal status in biomedical research and in clinical practice.[1-4] This report will review the radiation sources that have been used for photon absorptiometry.

Desired Characteristics of Radiation Sources

To be useful for photon absorptiometry the photon sources should have the following characteristics:

1. Suitable energies at fluence rates to allow measurements to be completed in short times (~ min),
2. Adequate monochromaticity of the radiation beams (energy spectrums),
3. Small dimensions to minimize the geometric effects of the collimation,
4. Stable and reproducible outputs.

The choice of photon energy and the source intensity are related to the statistical precision of the method and have been described by others.[5-8] The statistical precision depends upon (1) the energies of the photons, (2) the tissue mass and the proportions of the components, and (3) the total and relative intensities of each radiation beam.

For simulated measurements, analyses of the statistical errors allow prediction of the optimum energies for given tissue masses and component proportions. Optimum energies have been calculated for the single photon determination of BMC[5] (Fig. 1), and for dual-photon determinations of fat fractions[9] and BMC[10] (Figs. 2 and 3). For in vivo measurements, however, the proportions of the body components vary with position such that there is no one photon energy or energy pair optimal for the determinations of the masses of the tissue components. A compromise can be made by choosing the energies to be optimum for either the maximum or average amount of the tissue components encountered across the measurement site.

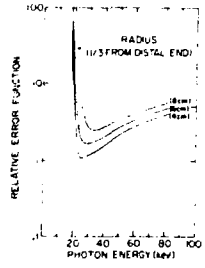

Fig. 1 The relative error function of BMC determined by the single energy method as a function of the photon energy.

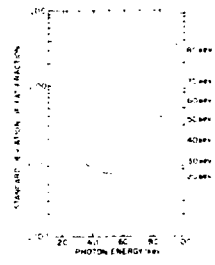

Fig. 2 The standard deviation of the fat fraction determined by the two-energy method as a function of the high energy for different low energies.

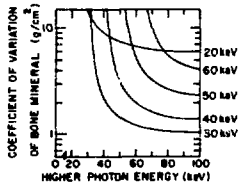

Fig. 3 The coefficient of variation of the BMC determined by the two-energy method as a function of the high energy for different low energies.

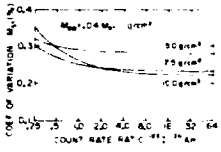

Fig. 4 The coefficient of variation of the soft-tissue mass determined by the two-energy method as a function of the relative intensities of 28 and 60 keV photons.

For specified beam energies, source intensities to achieve a given statistical precision can be estimated. With the single energy method a desired precision can be obtained with smaller source intensities or shorter measurement times than with the dual-energy method. In dual-photon absorptiometry, the precision of the measurement depends on the relative intensities of the radiation beams. For beams of 28 and 60 keV there is little improvement in the precision if the intensity of the low energy beam is four times greater than that of the high energy beam[10] (Fig. 4). Similar ratios would be expected for other energy pairs.

Mass determinations from photon absorptiometric measurements assume that Lambert's Law relates the incident to the transmitted intensities. Deviations from exponential attenuation may be due to detection of scattered radiation and the lack of monochromaticity of the radiation beams. For monochromatic sources if 10% of the detected beam is scattered radiation there is no effect on the measurement of BMC or soft-tissue mass[10,11] If multiple photon energies are present in the spectrum or the energy spectrum is continuous, as with x-ray tubes, the radiation beam will exhibit

hardening as it passes through the body tissues. Hardening has been investigated for single photon absorptiometry with ^{125}I[12] and dual photon absorptiometry with $^{125}I/^{241}Am$.[10] The results of these studies have indicated that hardening can be predicted by models and can be corrected by calibration.

An error is made in scanning transmission measurements when a photon beam of finite size crosses or overlaps the boundary between two substances with different attenuation properties. This geometric effect depends on the size of the radiation beam relative to the size of the object, geometry, photon energy, attenuation properties of the substances at the boundary, and the scan velocity of scanning systems. The effect has been theoretically analyzed for BMC measurements.[5,13-15] For BMC measurements the absolute error is negative and approximately constant provided that the bone diameter is about three times the beam diameter. The error is larger for slit sources. For large bones the errors can be as large as 20% as the beam diameter approaches the bone diameter. Geometric effects, however, do not affect the precision of photon absorptiometry.

The output of radiation sources should be stable. A radionuclide source has stable output that decreases according to its half life. An x-ray tube provides stable output if supplied by a constant potential generator; however, all types of x-ray generators have been employed. In some cases reference detectors[24,33,40,44,47] or band-pass filters[20,33] have been included in the detector system to correct for output fluctuations.

X-ray Sources

This discussion of x-ray sources concerns generators of electromagnetic radiation in which the primary photon source derives from the deceleration of electrons in a target material. Radiative interactions of the electrons with the nuclei of the target atoms yield a continuous spectrum of radiation, called bremsstrahlung, with x-ray energies ranging from zero to the maximum energy of the incident electrons. Characteristic radiation is emitted at discrete energies when incident electrons interact with the electrons of the target atoms. X-rays striking a second target material can produce monoenergetic, fluorescent radiation characteristic of the secondary target by means of photoelectric interactions. Finally, Bragg diffraction can be applied to an x-ray beam to produce monoenergetic radiation of an arbitrary wavelength.

Application of Monochromators

In 1925 Glocker and Frohmayer[16] described a dual energy absorptiometric system in which the x-rays emitted from a conventional, tungsten-anode Coolidge tube were passed through a crystal to produce monochromatic radiation by Bragg diffraction. Insensitivity of the output energy to fluctuations of the input spectrum is an advantage of crystal diffraction; lack of intensity is its main disadvantage. Analysis of a 1 cm thick, *in vitro* sample required 2 to 3 hr of exposure time to achieve an accuracy of ± 10%.

In vivo measurements with monochromator x-ray sources have been limited to the determination of BMC of finger bones. Fromhold and Schoknecht[17] applied stabilized current and high voltage supplies to a molybdenum anode tube and selected its $K_{\alpha 1}$ x-rays (17.5 keV) with a calcium carbonate monochromator. A BMC determination for the middle phalanx of the fifth finger required 3 min. Zwicker and Gebhart[18,19] described dual energy systems incorporating monochromators. Using various diffraction crystals they selected the $K_{\alpha 1}$ radiation produced in several x-ray tubes with different anode materials. A copper-anode tube provided the low energy radiation (8.1 keV) and either a silver- (22.1 keV) or tungsten-anode (59.3 keV) tube provided the high energy radiation.

Fluorescence Sources

Jacobson et al.[20-25] developed fluorescence x-ray sources intended for absorptiometry of thicker body sections. Three such sources were developed between 1953 and 1964. Only the most recent version will be discussed here.

The anode of the tube was a cylinder of gold-plated copper foil. The secondary radiators, shaped like the frustum of a cone, were placed within this cylinder to minimize the distance between anode and secondary targets and maximize the fluorescence output. The entire anode plus secondary target structure was rotated at 25 rps to provide heat distribution in the anode and switching of the output energy. The secondary radiator consisted of three sectors, allowing the simultaneous analysis of three body components. For the quantitation of iodine, bone mineral, and soft tissue the secondary sources were iodine ($K_{\alpha 1}$=28.6 keV), cerium ($K_{\alpha 1}$=34.7 keV) and tungsten. The secondary radiation from this source was of high spectral purity with the non-characteristic radiation accounting for less than 5% of the total output fluence; but the x-ray yield was in the range of 10^8 to 10^9 quanta/mA-s-sr.[23] A two component system (bone and soft tissue) could be analyzed in less than 2.5 s; but three component analysis required at least 20 s.[24]

Atkins et al.[26] described a fluorescence source for imaging and quantitation of iodine *in vivo*. The primary source was a water-cooled, end window, tungsten-anode tube connected to a constant potential generator. External to the tube were pellets containing the three elements used as secondary sources--barium ($K_{\alpha 1}$=32.2 keV), cerium, and neodymium ($K_{\alpha 1}$=37.4 keV). The three secondary radiators emitted simultaneously and the energies were separated using a Si(Li) detector and a three-channel analyzer. With this system thyroidal iodine measurements required at least 10 s per measuring point at a count rate of $\sim 10^4$/s.

Non-specialized Bremsstrahlung Sources

Measurements with absorptiometric systems incorporating conventional, continuous-spectrum x-ray tubes are typically extensions of clinical fluoroscopic examinations. An effort is deliberately made to obtain quantitative information with the least modification of the standard equipment. Determinations of lung ventilation[27-33] and perfusion[31-33] by fluoroscopic pulmonary densitometry and applications of videodensitometry[34-39] exemplify this type of measurement. Source modifications are generally limited to increased filtration,[31,33] small field sizes,[32] and stabilization and filtering of the high voltage supply.[38] Bürsch et al.[36] investigated the validity of the assumption of exponential attenuation of a continuous spectrum x-ray beam as applied to the videodensitometric determination of contrast medium concentration. The range of thickness over which the assumption was valid was a function of filtration of the x-ray beam. With 2mm of copper filtration the assumption was valid up to a thickness of 5 cm of 21 g% Urografin contrast medium.

Specialized Bremsstrahlung Sources

Other investigators have constructed more specialized systems for absorptiometric measurements. Smith[40] described a system for BMC determinations of the os calcis in which the photon source was a 50 kV x-ray microscope. Reiss[41] developed a dual energy system for determination of BMC and soft-tissue mass in which the x-ray tube potential was switched between two values (typically 70 and 150 kVp) by a thyristor circuit at a rate of ~5 Hz. Copper filtration of 1.5 to 4.5 mm was

added to balance the intensities of the two spectra. A narrow beam geometry was used for quantitative measurements that required ∿10 s.

Jacobson et al.[42-44] also developed a dual energy system in which varying potential was applied to the x-ray tube. Two spectra were obtained by using a high voltage waveform consisting of both AC and DC components. The magnitudes of both components were independently adjustable. A filter wheel placed in the output beam had sectors of samarium (K_{abs}=46.8 keV) and either lead (K_{abs}=88.0 keV) or thorium (K_{abs}=109.6 keV). Typical operating conditions for BMC measurements on adult humans were 110 peak kV, 65 kV DC level, 1.7 g/cm^2 of lead and 0.5 g/cm^2 of samarium. The filter wheel was rotated synchronously with the pulsation of the applied voltage such that the samarium filter was in the beam when the voltage was low and the lead filter was in the beam when it was high. Count rates at the detector of ∿5x10^5 for each energy permitted precise (±1%) BMC determinations of the femoral neck in 25 s and of the distal radius in 3 s.

Another class of specialized absorptiometric systems are the computerized transverse axial tomographic scanners.[45] Few details are known about the x-ray sources in these systems. The filtration has been estimated from half value layer measurements as being 4 to 5 mm Al.[46,47] The typical operating characteristics of 120 kVp, 32 mA or 140 kVp, 27 mA are necessitated by the requirement for low statistical noise. The use of a constant tissue thickness bolus system is one means of compensating for the polychromatic spectrum of the output beam.[47] Other compensatory mechanisms, particularly those used with non-bolus systems have not been disclosed, but seemingly might exist in the software rather than the hardware.

Radionuclide Sources

The increased use of radionuclides as sources for photon absorptiometry over the last 15 years has paralleled the increased acceptance of the absorptiometric method to determine BMC as developed by Cameron and Sorenson.[48,49] The number of radionuclides suitable as sources is limited (Table 1.).[48,50-58] Radionuclides emitting a single energy were used for single energy absorptiometry. For dual energy methods the sources were composed of either two radionuclides each emitting photons of a different energy or radionuclides that emit at two discrete energies. Some of the radionuclides useful for BMC determinations have been investigated.[51] The conclusions of these investigations agree with theoretical determinations of optimal energies. For single energy BMC determinations ^{125}I is almost the ideal source for measurements of small bones in the hands and forearms. Although the photon energy available from ^{145}Pm makes it a better choice for measurements of larger limb bones such as the humerus and femur, ^{241}Am has been used more commonly perhaps because of its availability and long half life.[13,59,60] For dichromatic absorptiometric BMC determinations the ^{125}I/^{241}Am combination is well suited for measurements on forearms and hands[10] while ^{153}Gd is preferable for measurements of large limbs, the spine and whole body BMC measurements.[61] For soft tissue analysis by dichromatic absorptiometry ^{109}Cd is better at a measurement site where the total soft-tissue mass is small, such as the hand, while ^{125}I/^{241}Am combination is the choice for measurements of the limbs.

To minimize measurement times the radionuclide sources should have high activities and small self-absorption. Sources of ^{125}I and ^{153}Gd are available with high activities (>10 GBq) in a size of a few (∿4) mm. High self-absorption limits the amount of ^{241}Am and ^{210}Pb that can be placed in a small volume.

The discrete levels of radioactive decays make the radiation beams from most radionuclides monoenergetic. Sources such as ^{241}Am with γ-rays widely separated in energy, at least in the region below 100 keV, are most desirable. Characteristic radiation emitters such as ^{125}I, ^{109}Cd, and ^{153}Gd emit K_α and K_β x-rays over a small energy range (∿5 keV). High resolution detectors can separate the characteristic x-rays but the more commonly used scintillation detectors can not resolve the separate energy peaks; they detect all the x-rays as a single energy beam. Lower energy characteristic x-ray sources such as ^{125}I and ^{109}Cd have a sufficiently large separation between the K_α and the K_β x-rays that the radiation beams exhibit hardening as they pass through large amounts of tissue.[12] The monochromaticity of these sources has been improved by using K-edge filters: 0.06 mm tin for ^{125}I[12] and 0.01 mm palladium for ^{109}Cd.[62]

The active volume of a radionuclide source is small, usually only a few mm in any dimension (Table 1). They can be enclosed in small source capsules making radionuclide sources compact and easy to collimate. The nature of radioactive decay makes radionuclide sources inherently stable with emitted intensities that only decrease as a function of their half lives. Sources with long half lives are desirable to minimize the frequency of source replacement. An exception may be ^{125}I. Its other desirable properties such as its nearly

Radionuclide	Half Life	Decay Mode	Type of Radiation	Principal Energy (keV)	Source Size (mm)	Typical Activity (mCi) Actual	"Eff"	Applications	Ref.
^{244}Cm	17.6y	α	Pu L x-ray	18	3	100	20	BMC, hand, small animals	50
^{125}I†	58.5d	EC	Te K x-ray	28	2	200-400	same	BMC, hand, forearm.	48
^{145}Pm	17.7	EC	Nd K x-ray	37	1x5x1	25	same	BMC, humerus.	50
^{210}Pb	22y	β-	γ	47		100		BMC, forearm.	51
^{241}Am	463y	α	γ	60	3	45	15	BMC, femur.	52
^{57}Co	270d	EC	Fe K x-ray	122	0.2x1				53

Table 1a. Radionuclide Sources for Single Photon Absorptiometry

^{109}Cd††	453d	EC	Ag K x-ray	22	<4	10-30		Soft tissue analysis, thin sections (hands).	54
			γ	88					
^{133}Xe	5.3d	β-	Cs K x-ray	31	3			Bone mineral and soft tissue analysis, limbs	55
			γ	81					
^{153}Gd	240d	EC	Eu K x-ray	44	3	500-2000	same	Bone mineral, larger limbs spine, and whole body	56
			γ	97,103					
^{125}I/^{241}Am†	60d	EC	Te K x-ray	28	2	50	50	Bone mineral and soft tissue analysis, forearm, upper arm, leg.	57
	463y	α	γ	60	3	45	15		
^{241}Am/^{137}Cs	463y	α	γ	60	7.2	100	30	Bone mineral, spine.	58
	26.6y	β-	γ	662	3	∞			

Table 1b. Radionuclide Sources for Dual Photon Absorptiometry

†Filtration: 0.06 mm tin ††Filtration: 0.10 mm palladium

optimal photon energy, high activity, and commercial availability as sealed sources apparently offset the necessity of frequent replacement. Typical ^{125}I sources have initial activities of 200 mCi, are used for two half lives (120 d), and require replacement three times per year.

Conclusion

Both radionuclide and x-ray sources have been utilized in photon absorptiometric measurements of body components. Radionuclide sources are compact, rugged, easy to collimate, and require no auxilliary power supply, making them particularly well suited for compact and portable instruments as needed for field studies and space flight applications. These sources emit discrete monoenergetic radiations which do not vary in energy. Their energy fluence rate is determined by the decay rate and is therefore predictable; monitor detectors are unnecessary.

The main advantage of the x-ray tube as a photon source is its high output, which allows rapid measurements in the thicker body sections. Beam energy is selectable; the optimum energy for a particular measurement can, in principle, be obtained. Although the output of most x-ray tubes is polychromatic, filtration can be added to achieve exponential attenuation over a useful range of subject thickness. An image intensifier can be used for visual verification of the measurement site to aid repositioning of serial measurements, with a concomitant increase of radiation dose to the subject. X-ray sources in absorptiometric systems are durable, do not require frequent replacement, and cost less per photon than radionuclide sources. The high intensity radiation beams necessary for computerized tomographic data acquisition in times of 5 to 20 s currently demand that the photon source be an x-ray tube.

References

1. Cameron, J.R. (ed.), Proc. of Bone Measurement Conf., USAEC, Div. of Tech. Inf., CONF-700515, Springfield, VA, 1970.
2. Mazess, R.B. (ed.), Internat'l Conf. on Bone Mineral Measurement, U.S. Dep't of Health, Ed. and Welfare, Pub. No. (NIH) 75-683, Wash., D.C., 1973.
3. Mazess, R.B. (ed.), Trans. Third Internat'l. Conf. on Bone Mineral Measurement, Am. J. Roent., in press.
4. Schmeling, P. (ed), Proc. of the Symp. on Bone Mineral Determinations, Aktiebolaget Atomenergi Pub. AE-489, Studsvik, Sweden, 1974.
5. Judy, P.F., in Ref. 1., pp. 1-21.
6. Judy, P.F., A Dichromatic Attenuation Technique for the In Vivo Determination of Bone Mineral Content, Ph.D. Thesis, U. of Wis., 1971.
7. Wooten, W.W., Bone Densitometry. The Two Photon Technique and Fat Content of the Bone, Thesis, U. of Cal., Los Angeles, 1971.
8. Watt, D.E., Br. J. Rad., 48, 265 (1975).
9. Hanson, J.A., USAEC Prog. Rep. COO-1422-151, 1973.
10. Witt, R.M., The Determination of Fluid Content by Dichromatic Absorptiometry, Ph.D. Thesis, U. of Wis., 1975.
11. Judy, P.F., in Ref. 2., pp. 1-10.
12. Sandrik, J.M. and P.F. Judy, Invest. Rad., 8, 143 (1973).
13. West, R.R. and G.W. Reed, Br. J. Rad., 43, 886 (1970).
14. Watt, D.E., Phys. Med. Biol., 18, 673 (1973).
15. Watt, D.E., and R. Logan, in Ref. 4., pp. 148-166.
16. Glocker, R. and W. Frohmayer, Ann. Phys., 76, 369 (1925).
17. Frommhold, W. and G. Schoknecht, Fort. Geb. Roent., 93, 358 (1960).
18. Zwicker, H. and M. Gebhart, Fort. Geb. Roert., 113, 576 (1970).
19. Gebhart, M. and H. Zwicker, in Ref. 2., pp. 108-112.
20. Jacobson, B., Acta Rad., 39, 437 (1953).
21. Jacobson, B., Science, 128, 1346 (1958).
22. Edholm, P. and B. Jacobson, Acta Rad., 52, 337 (1959).
23. Jacobson, B. and L. Nordberg, Rev. Sci. Inst., 34, 383 (1963).
24. Jacobson, B., Am. J. Roent., 92, 202 (1964).
25. Jacobson, B. and B. Lindberg, Rev. Sci. Inst., 35, 1316 (1964).
26. Atkins, H.L. et al., Am. J. Roent., 114, 176, (1972).
27. Andrews, A.H. et al., Dis. Chest, 35, 117 (1959).
28. *Marchal, M. and M.T. Marchal, in Proc. Second Internat'l. Conf. on Med. Electronics*, C.N. Smyth (ed.), Iliffe and Sons, London, 1960, pp. 533-536.
29. Kourilsky, R. et al., Dis. Chest, 42, 345 (1962).
30. Oderr, C., Am. J. Roent., 92, 501 (1964).
31. Standertskjöld-Norderstam, C., Acta Rad. Suppl., 239 (1965).
32. Laws, J.W. and R.E. Steiner, Br. J. Rad., 38, 512 (1965).
33. Robinson, A., Br. J. Rad., 40, 905 (1967).
34. Wood, E.H. et al., Mayo Clin. Proc., 39, 849 (1964).
35. Bürsch, J.H. et al., Eur. J. Card., 1, 437 (1974).
36. Bürsch, J.H. et al., in Roentgen-, Cine-, and Videodensitometry, P.H. Heintzen (ed.), Georg Thieme Verlag, Stuttgart, 1971, pp. 81-84.
37. Bürsch, J.H. et al., in Roentgen-, Cine-, and Videodensitometry, P.H. Heintzen (ed.), Georg Thieme Verlag, Stuttgart, 1971, pp. 119-132.
38. Silverman, N.R. and G. Hylander, Am. J. Roent., 110, 172 (1970).
39. Silverman, N.R., Radiology, 101, 597 (1971).
40. Smith, N.J.D., in Symposium Ossium, A.M. Jelliffe and B. Strickland (eds.), E. and S. Livingstone, Edinburgh, 1970, pp. 244-246.
41. Reiss, K.H. et al., in Ref. 2., pp. 80-87.
42. Jacobson, B., in Ref.1., pp. 237-242.
43. Dalén, N., in Ref. 2., pp. 60-65.
44. Gustafsson, L.B. et al., Med. Biol. Eng., 12, 113 (1974).
45. Hounsfield, G.N., Br. J. Rad., 46, 1016 (1973).
46. Perry, B.J. and C. Bridges, Br. J. Rad., 46, 1048 (1973).
47. McCullough, E.C. et al., Radiology, 111, 709 (1974).
48. Cameron, J.R. and J.A. Sorenson, Science, 142, 230 (1963).
49. Sorenson, J.A. and J.R. Cameron, J. Bone Jt. Surg., 49-A, 481 (1967).
50. Friedman, A.M. et al., J. Nuc. Med. 15, 335 (1974).
51. Sorenson, J.A., Invest. Rad., 5, 92 (1970).
52. Nilsson, B.E., Acta Orthop. Scand., 37, Supp. 91, 1966.
53. Reiss, K.H. et al., Quantitative Determination of the Mineral Salt in the Juvenile Skeleton. Physical Principles and Medical Results, paper pres. at Third Symp. in Erlangen on Roent. in Infancy and Childhood, 26 Nov 1968.
54. Preuss, L.E. and L.T. Kosnik, J. Nuc. Med., 10, 366 (1969) (abstract).
55. Schmeling, P. in Ref. 2., pp. 100-107.
56. Mazess, R.B. et al., in Ref. 1., pp. 308-312.
57. Mazess, R.B. et al., Nature, 228, 771 (1970).
58. Roos, B. et al., in Ref. 1., pp. 243-254.
59. Nilsson, B.E., in Symposium Ossium, A.M. Jelliffe and B. Strickland (eds.), E. and S. Livingstone, Edinburgh, 1970, pp. 148-150.
60. Overton, T.R. et al., in Ref. 2., pp. 11-29.
61. Madsen, M. et al., in Calcified Tissues 1975, S.P. Nielsen and E. Hjorting-Hansen (eds.), F.A.D.L. Pub., Copenhagen, 1976, in press.
62. Schmonsees, W.B. and L.E. Preuss, in Applications of Low Energy X- and Gamma Rays, C.A. Ziegler (ed.), Gordon & Breach Sci. Pub., New York, 1971, pp. 281-288.

Proceedings, ERDA X-and Gamma-Ray Symp. Ann Arbor, MI, May 19-21, 1976 (Conf 760539)

PROGRESS IN PHOTON ABSORPTIOMETRIC DETERMINATION OF BONE MINERAL AND BODY COMPOSITION

R.B. Mazess, R.M. Witt, W.W. Peppler and J.A. Hanson

Department of Radiology (Medical Physics)
University of Wisconsin Hospitals
Madison, Wisconsin 53706

Summary

Single-photon absorptiometry, with low energy radionuclides, has become widely accepted for measurement of bone mineral content in vivo. Dual-photon absorptiometry is a newer approach which overcomes previous limitations and allows measurement of total body and spinal bone mineral with high accuracy and precision (2% error). Dual-photon absorptiometry also permits measurement of the lean-fat composition of soft-tissue and the monitoring of shifts in body composition and/or fluid balance.

Introduction

Single-photon absorptiometry has become a widely accepted non-invasive method for the precise and accurate measurement of bone mineral content in vivo, and has proven useful in biomedical research and clinical practice[1,10,11,18] The basic technique was developed over a decade ago by Cameron and Sorenson[2,19] and involves use of a highly collimated beam of monoenergetic radiation from a low-energy (20 to 100 keV) radionuclide source. The beam intensity is monitored with a collimated scintillation detector and conventional nuclear counting instrumentation. The source (most often ^{125}I or ^{241}Am) and detector are mechanically linked and are passed across a body area, usually a limb such as the forearm. Changes of beam attenuation are proportional to the mass of bone mineral in the scan path. Several studies have shown that single-photon scans accurately indicate the local bone mineral content[3,9,12] Measurements on long bones also provide accurate estimates of the weights of long bones, total skeletal weight, and total body calcium[4-6,9] The high accuracy and precision of the method compared to other methods[13] together with ease of measurement, have fostered its use in evaluation of skeletal disorders[14] (osteoporosis, renal bone disease, anticonvulsant osteomalacia, corticosteroid demineralization, etc.) as well as in assessing normal changes of bone with growth and aging.

Dual-photon Absorptiometry of Bone

In recent years there has been an increasing interest in dual-photon absorptiometric methods for measuring both bone mineral content and soft-tissue composition[8,17] This approach uses a beam from two monoenergetic radionuclides ($^{125}I/^{241}Am$; $^{241}Am/^{137}Cs$) or radionuclides which emit at two discrete energies (^{153}Gd; ^{109}Cd). The dual-photon approach eliminates the need for surrounding the limb in a constant thickness of tissue equivalent material and permits measurement of bone mineral in otherwise inaccessible areas, such as the hips or spine. Dual-photon procedures and the sources of error have been detailed[7,15,16,20] In our laboratory we have concentrated on use of ^{153}Gd (44 and 100 keV; 242 day half-life) for determination of spinal and total body bone mineral, and on use of $^{125}I/^{241}Am$ (27.4 and 60 keV) for examination of soft-tissue composition (fat versus lean) and monitoring of fluid shifts.

A modified Ohio Nuclear rectilinear scanner was used with a 1-Ci (4 mm bead) source of ^{153}Gd to measure spinal and total body bone mineral[8] The source and detector move in a raster pattern and cover a 10-cm length of the spine in 1.25 cm steps for determinations on the lumbar spine or in 2.5 cm steps for total body mineral. The dose from a spinal measurement was 2 mrad and for total body mineral 0.1 mrad.

Precision of vertebral scans was evaluated on a phantom measured 35 times over 3-months (1.7%) and on 4 subjects measured 4 times over 6 weeks (2.3%)[8] The accuracy in estimating vertebral phantoms of known mass was very high (1.2%). Measurements on living subjects showed that aging bone loss occurred in the spine at half the rate of that in peripheral bones. This confirmed anatomical observations though it is contrary to prevailing clinical belief. The spine has been shown to demineralize and remineralize more rapidly than long bones in response to disease, immobilization, and therapy[17] and therefore is of clinical interest.

The precision of total body mineral was 2% over two weeks on an isolated skeleton and on a living subject. Long-term precision on the skeleton was 2% while on the living it was 3%. Measurements were made on normal subjects and patients and the bone was found to comprise about 4% of the lean body mass. There was also a very high correlation ($r = 0.96$) between bone mineral content of the radius and total body mineral ($n = 16$). The scan results have been outputted to a graphics display (Figure 1) to provide a quantitative "radiograph". Computer analysis allows assessment of any anatomical region (spine, hips, head, limbs) as well as information on the distribution and symmetry of bone.

Dual-photon absorptiometry can be utilized in many nuclear medicine departments with existing rectilinear scanners. The method permits for the first time detailed evaluations of the spine and total bone mineral and promises to be of great utility in skeletal disorders.

Dual-photon Absorptiometry of Soft Tissue

Dual-photon absorptiometry with a congruent source of $^{125}I/^{241}Am$ has been used for measuring soft-tissue composition on the limbs[21] The precision of these determinations was evaluated on 5 subjects over 5 weeks and on phantoms. The precision for soft-tissue mass was 2% on the subjects, while the precision for the fat-fraction was about 2% fat. On phantoms the precision for soft-tissue mass was 0.5%. The "fat" percentage of known mixtures was estimated with small error (1-2%). Measurements were made on 160 elderly women (mean age = 71 ± 15 years) and the bone mineral content of the limbs correlated more highly with lean mass of the limb ($r \sim 0.6$) than with height, weight or limb circumference ($r \sim 0.4$).

Soft-tissue measurements were also done to follow fluid shifts in surgery patients[21] Validation was provided by experiments on dogs that were exsanguinated, and infused while absorptiometric changes were recorded in the hind limb. There was high temporal correspondence ($r = 0.96$) between actual fluid shifts and absorptiometric changes. Fluid shifts were followed in 20 patients during and after surgery and a post-operative fluid loss was found in many patients.

Figure 1. Computer graphics display of total body bone mineral. Specific areas may be selected using a cursor for determination of regional bone mineral content.

Acknowledgements

F. Neil Case of Oak Ridge National Laboratories kindly supplied sources of ^{153}Gd for these studies. Supported by NASA-Y-NGR-50-002-051, NIH AM 17892, and NIH AM 16235.

References

1. Cameron, J.R. (ed) 1970. Proceedings of the Bone Measurement Conference. U.S. Atomic Energy Comm. Conf. (700515), U.S. Department of Commerce (CFSTI), Springfield, Va.

2. Cameron, J.R. and J.A. Sorenson 1963. Measurement of bone mineral in vivo: an improved method. Science 143: 230-232.

3. Cameron, J.R., R.B. Mazess and J.A. Sorenson 1968. Precision and accuracy of bone mineral determination by the direct photon absorptiometric method. Invest. Radiol. 3: 141-150.

4. Christiansen, C. and P. Rodbro 1975. Estimation of total body calcium from the bone mineral content of the forearm. Scand. J. Clin. Lab. Invest. 35: 425-431.

5. Cohn, S.H., K.J. Ellis, I. Zanzi, J.M. Letteri and J. Aloia 1974. Correlation of radial bone mineral content with total body calcium in various metabolic disorders. In: R.B. Mazess (ed), International Conference on Bone Mineral Measurement, U.S. Dept. of Health, Education and Welfare, DHEW Publ. 75-683, Washington, D.C.

6. Horsman, A., L. Bulusu, H.B. Bentley and B.E.C. Nordin 1970. Internal relationships between skeletal parameters in twenty-three male skeletons. In: J.R. Cameron (ed), Proceedings of the Bone Measurement Conference, U.S. Atomic Energy Comm. Conf. 700515, U.S. Dept. of Commerce (CFSTI), Springfield, Va., pp. 365-382.

7. Judy, P.F. 1971. A Dichromatic Attenuation Technique of Bone Mineral Content. Ph.D. Thesis in Radiological Sciences, University of Wisconsin, Madison, Wisconsin.

8. Madsen, M., W. Peppler and R.B. Mazess 1976. Vertebral and total body bone mineral by dual photon absorptiometry. In: S. Pors Nielsen and E. Hjorting-Hansen (eds), Calcified Tissues 1975, F.A.D.L. Publishing, Copenhagen.

9. Mazess, R.B. 1971. Estimation of bone and skeletal weight by direct photon absorptiometry. Invest. Radiol. 6: 52-60.

10. Mazess, R.B. (ed) 1974. International Conference on Bone Mineral Measurement. U.S. Department of Health, Education and Welfare, DHEW Publ. 75-683, Washington, D.C.

11. Mazess, R.B. (ed) 1976. Trans. III International Conference Bone Mineral Measurements. Am. J. Roentgen. (June, in press).

12. Mazess, R.B., J.R. Cameron, R. O'Connor, and D. Knutzen 1964. Accuracy of bone mineral measurement. Science 145: 388-389.

13. Mazess, R.B., J.R. Cameron and J.A. Sorenson 1970. A comparison of radiological methods for determining bone mineral content. In: G.D. Whedon and J.R. Cameron (eds), Progress in Methods of Bone Mineral Measurement, U.S. Department of Health, Education and Welfare, Supt. of Documents, Washington, D.C., pp. 455-479.

14. Mazess, R.B., P.F. Judy, C.R. Wilson and J.R. Cameron 1973. Progress in clinical use of photon absorptiometry. In: B. Frame et al. (eds), Clinical Aspects of Metabolic Bone Disease, Excerpta Medica Found. Int. Congr. No. 270, Amsterdam, pp. 37-43.

15. Mazess, R.B., C.R. Wilson, J. Hanson, W. Kan, M. Madsen, N. Pelc and R. Witt 1974. Progress in dual photon absorptiometry of bone. In: P. Schmeling (ed), Proc. Symp. Bone Mineral Determinations. Aktiebolaget Atomenergi Publ. AE-489, Studsvik, Nykoping, Sweden, Vol. 2, pp. 40-52.

16. Rassow, J. 1974. Systematische Fehler bei der radiolgischen Mineralgehaltbestimmung in Knochen. Fortschr. Rontgenstr. 121: 77-86.

17. Roos, B. 1974. Dual Photon Absorptiometry in Lumbar Vertebrae. Akademisk Avhaling, Goteborg.

18. Schmeling, P. (ed) 1974. Proceedings Symp. Bone Mineral Determinations. Aktiebolaget Atomenergi Publ. AE-489, Studsvik, Nykoping, Sweden.

19. Sorenson, J.A. and J.R. Cameron. 1967. A reliable in vivo measurement of bone mineral content. J. Bone Jt. Surg. 49(A): 481-497.

20. Watt, D.E. 1975. Optimum photon energies for the measurement of bone mineral and fat fractions. Br. J. Radiol. 48: 265-274.

21. Witt, R.M. 1975. The Determination of Fluid Content by Dichromatic Absorptiometry. Ph.D. thesis in Radiological Sciences, University of Wisconsin, Madison, Wisconsin.

Proceedings, ERDA X-and Gamma-Ray Symp. Ann Arbor, MI, May 19-21, 1976 (Conf 760539)

ABSOLUTE LUNG DENSITOMETER INCORPORATING A Gd-153 SOURCE AND CdTe DETECTORS

Leon Kaufman, Gordon Gamsu, Charles Savoca and Sybil Swann
University of California, San Francisco, CA 94143

ABSTRACT

A low-cost portable non-invasive densitometer is described. While the present system is optimized for lung densitometry, similar configurations can be used for bone densitometry and in industrial applications.

INTRODUCTION

The measurement of absolute lung density by a non-invasive technique is of importance in assessing the status of patients with pulmonary edema. Radiographic methods suffer because of the difficulties associated with calibration of the x-ray source-patient-film-developer system, and provide information only when large relative changes of density occur.

Figure 1. Conventional absorption densitometry cannot separate effects due to chest wall and varying path lengths through the lung.

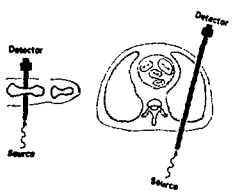

Transmission densitometry (Figure 1) provides an accurate relative value of density, but because chest wall thickness and path length in the lung are not known this method cannot be used to measure absolute density.

While the new body computerized x-ray scanners can provide a measure of lung density, the need exists for serial bedside sampling, and the cost, radiation dose and central location of these large scanners would make serial measurements impractical. There is also a need for measuring lung density in normal volunteers during pulmonary physiology experiments, and the same objections to the use of the x-ray scanners would preclude their use in this application.

We have developed an inexpensive system that measures lung density within a small volume, the results being independent of the thickness and respiratory movements of the chest wall and ribs.

FORMULATION

Density is obtained following two sequential measurements. A collimated source (S_A) is directed for a time t_1 at a co-linear collimated detector D_1 and the transmitted beam intensity through the subject, T_1, is measured (Figure 2). Another co-planar collimated detector (D_2) detects a scattered beam intensity S_1. For the second measurement a second source (S_B) co-linear with D_2 is directed for a time t_2 at the subject and the transmitted and scattered beam intensities, T_2 and S_2, respectively, are measured (Figure 3). If S_A and S_B represent the same radioisotope (i.e., same energy emissions), we can write [1,2]

$$\frac{S_1 S_2}{T_1 T_2} = g\sigma^2 \, V^2 \, \delta^2 \qquad \text{eq. (1)}$$

where g is a geometric factor dependent on the configuration of the collimators, σ is the differential Compton cross-section, V is the effective volume and δ is the mean electron density within that volume. Since the first three terms are constant, the electrons density can be written as

$$\delta = K\sqrt{\frac{S_1 S_2}{T_1 T_2}} \qquad \text{eq. (2)}$$

While K can be calculated from first principles, it is easily measured using a water phantom.

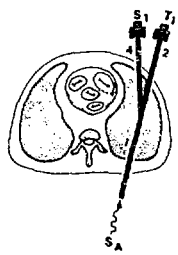

Figure 2. Arrangement for absolute densitometry, showing the first measurement of scattered and transmitted beams.

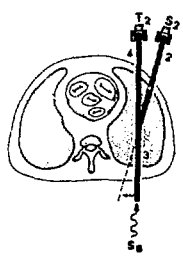

Figure 3. Second measurement of scattered and transmitted beams.

Electron density can be transformed to gravimetric density ρ through the relationship

$$\rho = 0.556\delta \, \frac{\Sigma A_j a_j}{\Sigma Z_j A_j} \qquad \text{eq. (3)}$$

where Z_j and A_j are the atomic number and atomic weights of constitutent elements of the sample, and a_j is the average number of such atoms per molecule of the material. The constant 0.556 represents $\Sigma Z_j a_j / \Sigma A_j a_j$ for water. For lung tissues and the accuracies desired, we assume $\rho \approx \delta$.

Equation 2 is only an approximation to δ. The validity of Equation 1 is dependent on the equality of the exit absorption paths (paths 2 and 4 in figures 2 and 3) seen by the transmitted and scattered beams. Since in Compton scattering the primary beam energy is decreased, the assumption of equal paths is not exact. Since at high (low) energies the change in energy is large (small), but the change in absorption cross-section is small (large), it can be estimated that for biologic tissues the error in equation 1 is minimized for primary beam energies in the range of 80 to 100 keV. This error can be eliminated if two different sources are used, choosing the energy of the second source to match the energy of the first source's scattered beam[3]. While exact, this approach is less convenient in that the system becomes more complex, source choice is more

restricted, and since geometric configuration depends on source availability, it becomes less versatile.

The scattering angle of 20-deg in this densitometer is chosen because the narrow angle is better adapted to measurements accross the eliptical chest cross-section. Also, narrow angles are advantageous because of the increased forward-scattering cross-section (which increases statistics), and because the change in energy due to the scattering process is smaller (minimizing the error of equation 1). Also, the sensitive volume is elongated, thus increasing the count rate.

HARDWARE

Configuration

The system is configured at a 20 deg angle with a 30cm working span between collimators. The assembly is part of a rigid plate which can be displaced vertically and rotated through a 180-deg angle. The densitometer is shown in Figure 4.

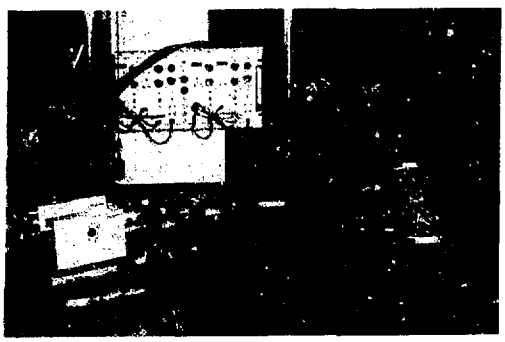

Figure 4. The densitometer shown in a horizontal position. On the left are the detector collimators and preamplifiers. On the right are the source collimators, in the movable source mount. Electronics are shown in the background.

To obtain a compact configuration while producing a relatively wide beam with narrow angular dispersion each collimator consists of 19 tantalum tubes, each of 0.224 m outside diameter, 0.010 cm wall thickness and 6.35 cm length, contained in a cylindrical lead holder of 3.3 cm diameter and 6.35 cm length. Figure 5 shows the end view of one of the four collimator assemblies used in the densitometer.

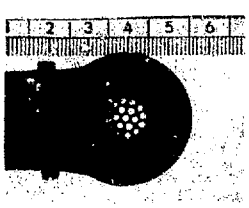

Figure 5. End view of a tantalum tube collimator.

Radiation Source

Gd-153 was chosen for the densitometer because of its spectrum, ready availability, adequately long half-life, and high specific activity[4]. Emitted photons at 100 keV as well as 41 keV are both adequate for lung densitometry. The source in use consists of 10Ci of Gd-153 in a steel capsule of 1.2 cm active diameter. It is moved between positions A and B (Figures 2 and 3) to obtain the two measurements necessary for each density determination. The resultant skin radiation exposure is less than 15mR per measurement.

Detectors and Electronics

Two Tycho CdTe detectors of 1 cm diameter (0.7 cm contacts), operated at room temperature are used in the densitometer. Their thicknesses are slightly different (2.35 and 2.15mm). The detectors are encapsulated in aluminum cans, as shown in Figure 6. Tennelec electronic components are used throughout the system: two TC 161A preamplifiers, two TC 203 BLR amplifiers, four TC 441 single-channel-analyzers, four TC 540A scalers, one TC 541 timer and one TC 911 NIM bin. Bias voltage is obtained from a battery pack.

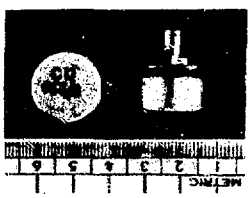

Figure 6. CdTe room temperature detectors used in the densitometer.

Operation of the CdTe detectors has to be set so as to optimize energy resolution, count-rate capability and charge collection. The first condition minimizes detection of multiple scatter photons which tend to produce a non-linear response vis-a-vis density, since they enhance the scattered beam intensities from dense samples. Count-rate capability has to be high because the transmitted beam has an extremely high intensity when compared to the scattered beam ($\sim 10^4$:1), and a rate-dependant response would introduce systematic errors. Finally, charge collection has to be maximized so as to collect as many events as possible within the photopeak region. The parameters of interest are dependent on bias voltage and amplifier shaping time, and they were optimized using the 122 keV peak of Co-57. The behaviour of peak-to-plateau ratios, i.e., charge collection, and energy resolution are shown as a function of bias voltage and amplifier time constant in Figure 7.

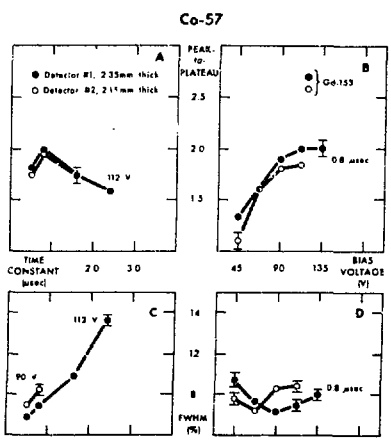

Figure 7. The dependance of peak-to-plateau ratio on amplifier time constant (7A) and on detector bias (7B) as well as energy resolution dependance on time constant (7C) and bias (7D) are shown for the two detectors used in the densitometer, measured for the 122 keV peak of Co-57. Peak-to-plateau ratios for the "100 keV" gamma-

rays of Gd-153 are also shown (7B).

As can be seen, operation at 100V with a time constant of 0.5 μsec offers an adequate compromise in performance at 122 keV, where conditions are more stringent than those necessary for the detection of 100 keV photons. Under these conditions count-rate response is linear with beam intensity when more than 5 cm of tissue absorber are present between source and detector collimators. The spectrum of Gd-153 measured with one of the CdTe detectors through 5 cm of absorber is shown in Figure 8.

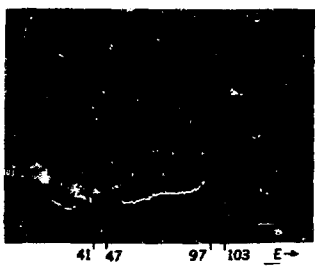

Figure 8. Gd-153 spectrum from a CdTe detector used in the densitometer.

The use of CdTe has allowed us to realize a compact system, with adequate energy resolution and drift-free operation.

PERFORMANCE

Characterization of the densitometer included measurement of the count-rate $\sqrt{S_1 S_2}$ as a function of scattering angle (Figure 9) and definition of the sensitive volume (Figure 10). Both were in close agreement with expected values.

Figure 9. The count rate $\sqrt{S_1 S_2}$ is shown as a function of scattering angle. The increase at narrow angles is due to the increases in sensitive volume and scattering cross-section.

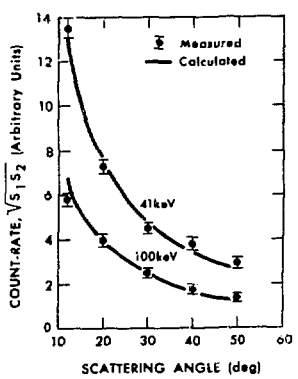

The effects of increasing tissue absorber were measured at 41 keV and 100 keV. For this purpose the beam traversed a 10 cm water path and tissue absorber was added first along one exit path up to 7.5 cm thickness, and then along the second exit path, for a total of 15 cm of absorber. The 100 keV measurements showed no significant shift, while at 41 keV a deviation of +8% was observed at the extreme range (Figure 11). Since the variation in chest thickness is not large (except for extreme cases), both beams are considered adequate for lung densitometry.

The response of the system to materials of different density was tested with blocks of wood surrounded by a 2.5cm-thick "chest wall". Response in the range

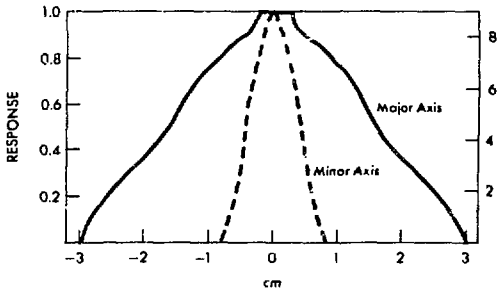

Figure 10. Measured response of the densitometer along an axis bisecting the two photon beams, centered at their intersection point (major axis); and an axis transverse to the previous one, also centered at the intersection point (minor axis).

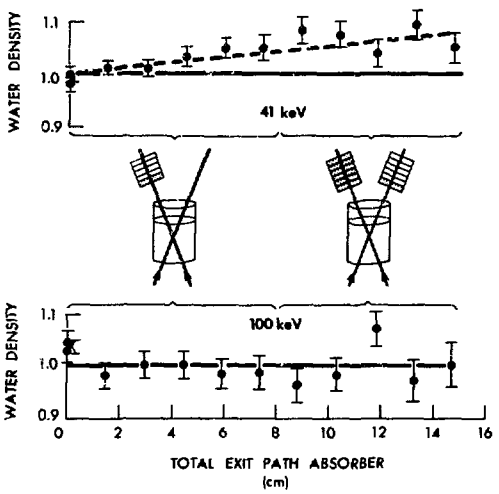

Figure 11. The effects of increasing tissue absorber in the exit paths from a 10cm water bath on measured density are shown for the 41 keV and 100 keV beams. Least square fits show a maximum +8% deviation at 41 keV, and no significant deviation at 100 keV.

of 0.14g/cm^3 to 1g/cm^3 is linear with standard deviations of 5.4% and 7.4% at 41 keV and 100 keV, respectively (Figure 12). These values are approximately twice as large as those expected from statistical considerations alone. Because the 41 keV and 100 keV measurements show an internal agreement of the order of 1.0% we believe that the measured standard deviations are due mainly to the fact that the average density of a 1500 cm^3 wood block will certainly differ from the local density in ~10cm^3 regions. Subsequent calibrations where the sensitive volume was positioned over different regions of the wood blocks, and the measurements averaged, yielded standard deviations of 2.0% at both energies.

The reproducibility of results depends on the number of counts S_1 and S_2, which in term depend on the absorption paths and on density in the sensitive volume. Figure 13 shows reproducibility for an "average chest" as a function of density and counting time. As can be seen a reproducibility of 5% or better is readily attained.

The effects of respiration, which brings different

amounts of absorber into the path of the beams, was determined by placing a birch block (ρ = 0.589g/cm^3) within the chest cavity of a dead dog. The chest was closed and density within the wood block was measured with the chest still (ρ(41) = 0.602 and ρ(100) = 0.596), and under forced respiration (ρ(41) = 0.598 and ρ(100) = 0.599). The differences of these three-minute measurements were not statistically significant.

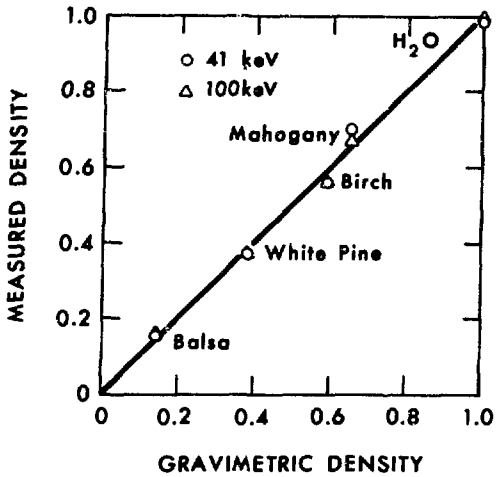

Figure 12. Response of the densitometer to blocks of wood of gravimetrically determined density, with water as the density standard.

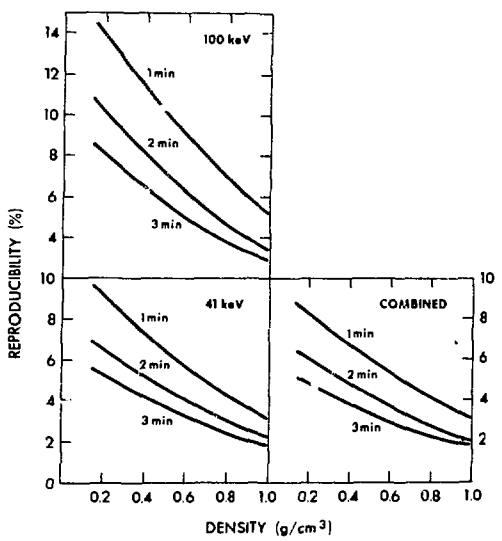

Figure 13. Reproducibility of measurements depends on count rate $\sqrt{S_1 S_2}$, which is in turn dependent on density within the sensitive volume and beam absorption. For an "average chest", the reproducibility is shown as a function of lung density for different single-measurement times.

We have also found that moving the sensitive region of the densitometer over the lower and central regions of the lung of a supine live dog yielded three-minute density measurements in the range of 0.276 - 0.321g/cm^3, with a mean of 0.302 ± 0.019g/cm^3. This indicates that the volume spanned by the system is sufficiently large to adequately average artifacts that could arise from local inhomogeneities produced by large blood vessels.

Initial density measurements in twelve sitting healthy young humans under normal tidal respiration have yielded a mean density of 0.296 ± 0.065 g/cm^3.

CONCLUSION

A low-cost portable non-invasive lung densitometer has been assembled and evaluated. The system is now being used to follow the progress of experimental pulmonary edema.

ACKNOWLEDGEMENTS

The CdTe detectors used in these investigations were fabricated by Dr. Gerald Entine, now at Radiation Monitoring Devices, Inc. The Gd-153 source was provided by Dr. F. Neil Case, of the Isotopes Development Center, ORNL.

The authors wish to acknowledge the assistance of Mr. B. Hruska and Mr. L. Murphey in assembling the densitometer, and the assistance of Dr. D. Palmer in measuring detector response.

This work is supported in part by USPHS Grant GM 21017 and Research Career Development Award GM-70598, both from the NIGMS.

REFERENCES

1. Clark RL, van Dyk G: The measurement of bone mineral content using transmitted and scattered beams of gamma rays. Carleton Univ internal report, Sept. 1972.

2. Kaufman L, Gamsu G, Savoca C, et al. Measurement of Absolute Lung Density by Compton-Scatter Densitometry. IEEE Trans Nuc Sci NS-23:599, 1976.

3. Garrett ES, Kenneth TJ, Keyyon DB, Webber CE: A Photon-Scattering Technique for the Measurement of Absolute Bone Density in Man. Radiol 106:209-219, 1973.

4. Case FN, Acree EH and Cutshall NH: Production study of Gd-153, ORNL-TM-2632, August, 1969.

Proceedings, ERDA X-and Gamma-Ray Symp. Ann Arbor, MI, May 19-21, 1976 (Conf 760539)

AUTOMATED FLUORESCENT EXCITATION ANALYSIS IN MEDICINE USING RADIOISOTOPIC EXCITATION SOURCES

Leon Kaufman and Frank Deconinck
University of California, San Francisco, CA

David C. Camp, Albert L. Voegele and Richard D. Friesen
Lawrence Livermore Laboratory, Livermore, CA

James A. Nelson
University of Utah Medical Center
Salt Lake City, Utah

ABSTRACT

An automated x-ray fluorescence system has been developed for application in clinical and investigative practice. The optimization of its major components permits the rapid and accurate quantitation of low levels of selected tracers in a cost-effective manner.

INTRODUCTION

The measurement of body compartments (such as extracellular fluid volume, red cell mass, plasma volume), and of organ function (for instance, glomerular filtration rate, hepatic metabolism) can be performed by studying the dilution volume and clearance of purposefully administered tracers[1]. The concentration volumes of these tracers in easily accessible fluids such as blood, urine and bile provide the information from which the physiologic parameters of interest can be calculated. Other physiologically significant information is found by analysis of the kinetics of the contrast agents used in conventional radiography as well as in computerized tomography.[1]

These tests provide data necessary in the diagnosis and therapy assessment of a diverse number of diseases, including cardiovascular and renal failure, malnutrition, anemia, hepatic dysfunction and metabolic disorders. They also provide data necessary for understanding the healthy state and for designing improved contrast agents and radiographic procedures.

The tests have certain common characteristics: The tracer is introduced by intravenous or oral routes and timed samples of the fluid of interest are assayed in-vitro for tracer concentration, the study rarely lasting more than 24 hours. In all cases serial determinations are needed, and studies encompass such critical population groups as children, pregnant women and normal volunteers.

Radiolabelled tracers offer a convenient and accurate method for performing the tests of interest, and have been successfully applied in such context[2,3]. On the other hand, they suffer of some basic disadvantages. There often exists interference between different tracers in closely spaced studies, as well as interference from radioisotopic imaging studies. More importantly, even a low radiation exposure per test becomes significant in serial studies, in children and in pregnancy, and their use in normal volunteers is being increasingly curtailed by stringent human experimentation guidelines. Finally, in animal experimentation radiolabelled tracers require expensive quarantine and disposal procedures.

Because of these factors, alternative chemical analysis methods for stable tracers have been used alongside radioisotopic techniques[4,5], although they are costly and lengthy: Often only a few samples per day can be accurately quantitated by a trained technician.

As an alternative to the above, the technique of x-ray fluorescence (where an atomic species is excited into emitting relatively penetrant x-rays through exposure to higher energy photons) can be combined with the use of stable tracers to provide medical tests synthesizing the simplicity, speed and accuracy of radioisotopic techniques with the safety and convenience associated with the use of stable indicators[6,7].

DESIGN CRITERIA

Foremost in the application of fluorescent excitation analysis (FEA) to medicine is the simultaneous need for large signal-to-background levels and for high count-rates of fluorescent x-rays, since these are the limiting factors in low level quantitation. The source of these limitations can be better understood after inspection of a typical spectrum obtained by fluorescence with Am-241 of an iodine-containing sample (Figure 1).

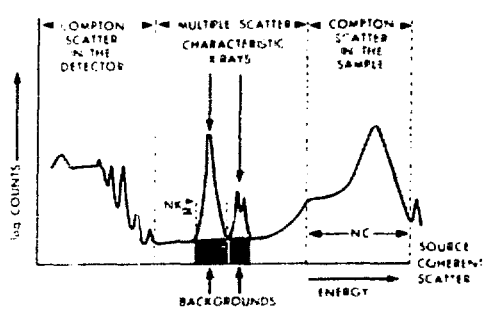

Figure 1. The spectrum resulting from Am-241 fluorescence of an iodine-containing sample.*

Compared to the Compton-scattered contribution, fluorescent photons can be equally abundant at very high concentrations, or account for less than 1 out of every 1000 detected photons at very low concentrations. Thus, count rate is limited mainly by the Compton contribution from the sample, and not by tracer levels.

The interaction of Compton-photons with the detector assembly also produces the background "valley" seen in Figure 1. This background decreases signal-to-noise levels, degrading quantitation accuracy. We have found that for a well designed FEA system most of the background counts arise in the detector assembly itself. This was varified by placing a hafnium filter in front of the detector entrance window, with thickness such that the absorption of background photons was increased 30 fold over that of Compton photons. If background arises outside the detector, the observed reduction in background to Compton counts should have been dramatic, while in actuality we observed a 10% reduction in this ratio. By counting without a sample in position, we also observed that cross-talk effects from the high

energy emissions of Am-241 account for less than 5% of the background count-rate in the Kα channel. A further confirmation of the internal origin of background is that this parameter will vary twenty five-fold when using the identical test set-up with different detectors. Thus, to minimize background and to increase effective count-rates, the detection system has to maximize the ratio of detected fluorescent to Compton photons. Within limits this can be accomplished by utilizing a 90-deg scatter geometry, by using collimator materials and designs that absorb rather than scatter x-rays, and by using "thin" detectors which are proportionally more transparent to Compton x-rays. Another promising approach, the use of polarized excitation sources[3], (which scatter at preferential angles) is now under investigation vis-a-vis its applicability to practical systems. A successful avenue to background reduction has been the development for this work of "low-background" detectors by the KeVex Corporation. A three-fold improvement has been achieved through this particular developmental effort.

Next to the parameters that affect accuracy of quantitation of low concentration tracers (background and count-rate), factors affecting dynamic range become important. Typically, quantitation limits at high concentration arise from count-rate limitations in the electronics and from self-absorption effects in the sample. Weaker excitation sources and smaller sensitive volumes will increase the high concentration range, but at the expense of also raising the minimum working levels. For the tracers of interest (bromine and higher atomic numbers), with 1cm-diameter vials the present FEA system spans a linear range of nearly 10^3 in concentration response. It must be pointed out that this is marginally adequate, since in a typical study bile may contain 20mg Iodine/g while blood levels may be as low as 0.001 mgI/g.

Another important need in a cost-effective medical system involves its ability to assay unprepared samples (i.e., samples requiring no ashing, pressing or weighing), since nearly 10,000 samples per year are assayed by FEA at our institution. Sample preparation would increase labor costs, delay turn-around time and decrease accuracy. Results independent of sample volume can be obtained if that volume is larger than the sensitive volume itself (the sensitive volume is defined by the source and detector collimators). Since the size of small animals and infants (and also serial sampling in large subjects) limit sample volume, the approach described above is severely limited. On the other hand, use of a region of the Compton peak to normalize the fluorescent counts yields concentrations that are independent of exact sample position, dead-time, source strength and counting time, while allowing for sensitive volumes of size comparable to that of the sample. Two ml disposable vials, filled with 0.5 to 1.5ml of sample, offer an adequate compromise.

Finally, because fluids such as whole blood tend to settle in the period prior to counting, a totally automated system has to be able to mix the sample prior to assay, and because the FEA system has to be used in a medical environment it should be drift-free, easily calibrated and easily operated. The resolution of these requirements is discussed below.

TRACER QUANTITATION

Referring to Figure 1, and from the considerations of the previous section, it can be seen that if the counts in the Kα and Compton windows are given by NK and NC, respectively, the concentration W can be expressed as

$$W = K\left(\frac{NK}{NC} - B\right), \qquad \text{equation (1)}$$

where B = NK/NC for a water sample and K is a constant that yields concentrations in the desired units, e.g., mg/g, ppm, mEq/l. K can be obtained by measuring NK and NC for a sample of known concentration W. We have found that the system is linear, that is, K and B are constant, for tracer concentration in the range of 1ppm to 2-4%. The error in W can be written as

$$\Delta W = K\frac{\sqrt{NK}}{NC}, \qquad \text{equation (2)}$$

This equation holds for NK > NC, which is typically the case for W > 1%. It can be seen that the fractional error Δ is no longer proportional to $1/\sqrt{NK}$, but that it is increased by the term $\sqrt{1 + KB/W}$. Note that the product KB is the background in absolute units of concentration.

SOFTWARE PARAMETERS

Once the hardware parameters are fixed, data processing criteria can be set to optimize system performance, for instance by setting NK window widths to match the concentration range of interest. For high tracer concentrations, KB << W, wide windows are preferred, since statistics are improved and signal-to-noise levels are not limiting factors. For low tracer concentrations, KB >> W, narrow windows increase accuracy by decreasing the term KB. Figure 2 shows the dependance of optimum window width on the ratio W/KB.

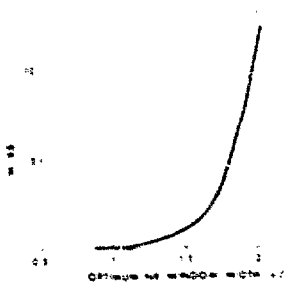

Figure 2. The optimum NK window width (1- = FWHM) is shown as a function of W/KB (for Iodine (KB=6 ppm).*

In a software-controlled system the calculation of W could be performed in a two-step process: First W would be calculated using a standard set of parameters and based on this value a new window would be used to recalculate W, extracting the appropriate K and B from a table. While such an approach would not be difficult to implement, the gain at the high concentration end would not be significant, and the system might as well be optimized for the lowest concentrations of interest. Unfortunately, the lower limit on window width is set by another consideration: Over the commonly found ambient temperature ranges, commercial analog-to-digital converters (ADCs) will drift one or two channels per 2,000 channels of digitization. The effect of this drift on quantitation accuracy is shown in Figure 3. It can be seen that to obtain quantitations free of systematic errors windows of 1.5 to 2σ (1σ = FWHM) need to be used. Note that for elements such as iodine this window has to be widened to account for the $K\alpha_1$ - $K\alpha_2$ separation.

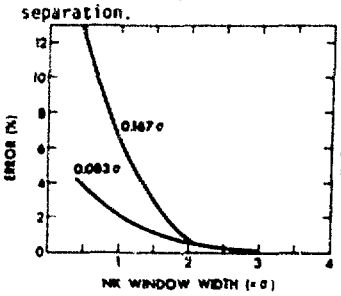

Figure 3. Measured systematic quantitation errors that are introduced by spectral shifts of one and two channels are shown as a function of Kα window width (1σ = FWHM)

HARDWARE

The automated FEA system consists of the following:

The central component is a 80mm^2, 5mm-thick KeVex "low background" Si(Li) detector with pulsed optical reset preamplifier, followed by a KeVex 4510P amplifier with a 2μsec pulse-shaping time constant.

Data storage and analysis is effected in a Ino-Tech Ultima programmable analyzer with 2,000 channels of display memory. The analyzer combines the simplicity and ease of operation of hardwired analyzers with the versatility allowed by programming all necessary functions through a paper tape.

The sample changer was designed expressly for this work[11]. It contains a removable tray with 48 disposable vials. Upon command each vial is raised to the sensitive volume through a mechanism that also has a mixing option. The basic functions of the changer are up (with or without mix), down, advance, return to home position and repeat, under analyzer or manual control.

In normal use the operator enters the six constants associated with a tracer: the NK and NC limits, K and B. The number of samples is entered, either for single or repeat analysis. Preset conditions include time, NK count, or combinations such as termination in no less than a time t_1, and then termination in either preset count or time t_2, whichever of the two comes first. Mix and repeat options are set at the sample changer. Printout for each sample includes sample number, counting time, NK and NC counts, and W and ΔW as given by equation 1 and 2. At the end of the cycle the counting period is printed and the sample changer returns to home position.

Radioisotopic excitation sources were selected for this system because compared to x-ray tubes they are compact, reliable and comparatively inexpensive, while they provide count rates that easily reach the maximum operating range of the electronics. The main tracers of interest are presently bromine, iodine and cesium. A 60 mCi Cd-109 is used for excitation of the first and a 600 mCi Am-241 source filtered with 0.025mm of hafnium is used for the latter two. Source energy is selected by reaching a compromise between two conflicting requirements: Since excitation cross-sections drop as $\sim E^{-3}$, the exciting photon should be close in energy to the absorption edge of the tracer. On the other hand, if its energy is too close Compton-scatterd photons overlap the region of interest and background increases. Other important considerations in selecting an excitation source involve the half-life, availability, spectral and radiopurity, self-absorption and cost of the radioisotope. Cd-109 has been found adequate for excitation of bromine, and Am-241 is quite ideal for iodine, and only slightly less so for cesium. A problem with Am-241 is posed by the presence of lower energy emissions, which are partially filtered by self-absorption and the hafnium. Even with this filtration, the 33 keV photons from Am-241 increase background for cesium by 65% over the value for iodine.

Detector and source collimators for Cd-109 are surfaced with cadmium, since fluorescence induced in this material by the source have an energy lower than the fluorescence of the tracers of interest. Cadmium is also attractive because of its high density, easy availability and machinability. For the same reasons Mallory 1000 (a tungsten alloy) is used for the Am-241 collimator. In both cases the Compton-scattering cross-section is low, since L-edge absorption dominates. To further reduce Compton-scattering in the collimators, they are configured as shown in Figure 4. Figure 5 shows the complete system.

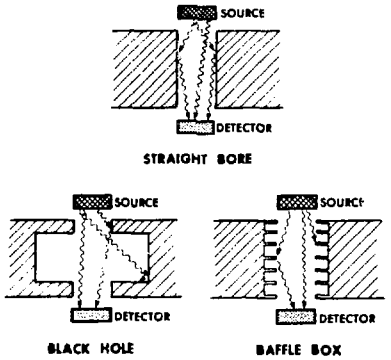

Figure 4. Collimator configurations that reduce scatter when compared to straight-bore designs.

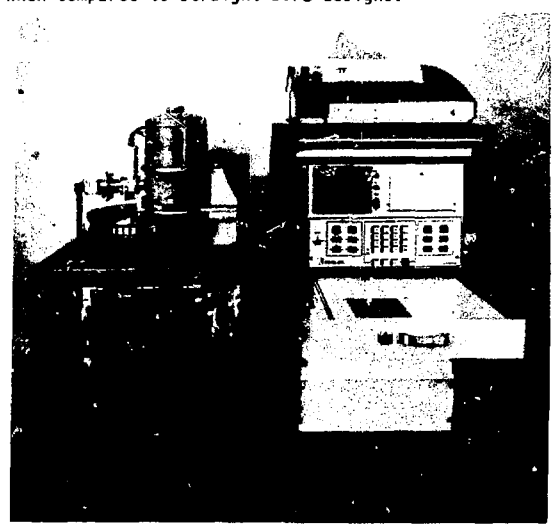

Figure 5. The automatef FEA system. On the left is the sample changer with KeVex "low-background" detector and Am-241 source in place. The Ultima programmable analyzer is on the right. Sample vials are shown on the analyzer shelf.

PERFORMANCE

The automated analyzer has been previously characterized[12]. The principal performance parameters are shown in Table I. "Sensitivity"[13] is shown because it is a parameter used widely in the industry, but its significance vis-a-vis quantitation is not great. A definitive indication of performance is given by the system's ability to quantitate tracer concentrations with a certain accuracy within a given time. Tables II, III and IV show experimentally determined quantitation accuracy for three tracers of interest.

CONCLUSION

The use of compact radioisotopic sources and specially designed "low-background" Si(Li) detectors, together with versatile electronic and mechanical peripheral components, has allowed the development of a FEA system suited for routine clinical and investigate work.

Further reductions in minimum working tracer levels together with the development of labelling techniques optimized for FEA will permit further diffusion of this powerful technology.

TABLE I

SYSTEM PERFORMANCE PARAMETERS

Tracer	Excitation Source	Net Count Rate (counts/sec/ppm)	Background (ppm)	"Sensitivity" (ppm)
Bromine	Cd 109	0.209	13.3	0.75
Iodine	Am 241	0.382	8.1	0.44
Cesium	Am 241	0.373	12.7	0.55

TABLE II

BROMINE

Counting Time	Concentration Range (ppm)	Reproducibility
10 sec	40,000 - 1,400	$\sigma < 2\%$
30 sec	40,000 - 2,200	$\sigma \leq 1\%$
1 min	1,000 190	$\sigma > 1\%$ $\sigma > 2\%$
2 min	100	$\sigma > 2\%$
15 min	6	$\sigma > 5\%$

TABLE III

IODINE

Counting Time	Concentration Range (ppm)	Reproducibility
10 sec	20,000 - 1,700	$\sigma > 1\%$
30 sec	20,000 - 550	$\sigma \leq 1\%$
1 min	300 75	$> 1\%$ $< 2\%$
5 min	30	$\sigma > 2\%$
30 min	~3	$\sigma > 2.3\%$
1 hr	~1	$\sigma > 3.4\%$

TABLE IV

CESIUM

Counting Time	Concentration Range (ppm)	Reproducibility
10 sec	20,000 - 1,600	$\sigma > 1\%$
30 sec	750	$\sigma \leq 1\%$
1 min	370 100	$\sigma > 1\%$ $\sigma > 2\%$
15 min	6	$\sigma > 3\%$
30 min	3	$\sigma > 6\%$
1 hr	1	$\sigma > 10\%$

ACKNOWLEDGEMENTS

The authors wish to thank Mr. Richard Frankel and Dr. Rolf Woldseth of the KeVex Corporation, and Mr. Garry Williams and Mr. Robert Anderson of Ino-Tech, Inc., for their cooperation. This research is supported in part by USPHS Research Grant GM-21017 and Career Development Award GM-70598, both from the National Institutes of General Medical Sciences.

REFERENCES

1. Price DC, Amberg JR, Benet LZ, et al. Biomedical Applications of Fluorescent Excitation Analysis. Semiconductor Detectors in Medicine, Kaufman L and Price DC, ed. USAEC CONF-730321, 1973, page 149.

2. Wilson CJ, Potter DE, Holliday MA. An Approach to the Comprehensive Treatment of Children with Chronic Renal Failure. Body Fluids in Pediatrics, Winters RW, ed., Boston, Little Brown, 1972.

3. Cohen ML, Smith FG, Mindell RS, et al. A Simple, Reliable Method of Measuring Glomerular Filtration Rate Using Single Low Dose Sodium Iothalamate I-131, Pediatrics 43: 407, 1969.

4. Cheek DB. Estimation of the Bromide Space With a Modification of Conway's Method. J. Appl. Physiol. 5: 639, 1953.

5. Dodge WF, Travis LB and Daeschner CN. Comparison of Endogenous Creatinine Clearance with Inulin Clearance. Amer. J. Dis. Child. 113: 683, 1967.

6. Kaufman L and Wilson CJ. Determination of Extracellular Fluid Volume by Fluorescent Excitation Analysis of Bromine. J. Nuc. Med. 14: 812, 1973.

7. Price DC, Swann SJ, Hung S, et al. The Measurement of Circulating Red Cell Volume Using Non-Radioactive Cesium and Fluorescent Excitation Analysis. J. Lab. Clin. Med. 87: 535, 1976.

8. Guesry P, Kaufman L, Orloff S, et al. Measurement of glomerular Filtration Rate by Fluorescent Excitation of Non-Radioactive Meglumine Iothalamate. Clinical Nephrology 3: 134, 1975.

9. Nelson JA, Pepper HN, Goldberg HI, et al. Effect of Phenobarbital on Iodipamide and Iopanoate Bile Excretion. Invest. Radiol. 8: 126, 1973.

10. Kaufman L and Camp DC. Polarized Radiation For X-Ray Fluorescence Analysis. Advances in X-Ray Analysis 18: 247, 1975.

11. Camp DC, Voegele AL, Friesen RD, et al. Automated Sample Changer for X-Ray Fluorescence Analysis of Bio-Medical Samples UCRL-76740, July 1975. Chem. Inst. (In Press)

12. Kaufman L, Guesry P, Hruska B, et al. An Automated Fluorescent Excitation Analysis System for Medical Applications. Invest. Radiol. May/June, 1976.

13. Sensitivity is defined as the tracer concentration for which NK is 3 standard deviations above background in 1000 seconds.

Proceedings, ERDA X-ray and Gamma Ray Symp. Ann Arbor, MI, May 19-21, 1976 (Conf 760539)

DYNAMIC TOMOGRAPHY IN DENTISTRY

Albert J. Richards, M.S.
School of Dentistry - University of Michigan
Ann Arbor, Michigan 48109

Dynamic tomography is a procedure in which a sandwich of eight underexposed radiographs is utilized to display sharp images of details lying in a thin layer at any chosen depth within a subject. When the sandwich of films is viewed by transmitted light, the location of this chosen layer can be moved up or down within the subject by simply mechanically moving the radiographs in a precise manner relative to each other. The amount of radiation used in exposing the eight radiographs is the same as would be used to fully expose two normal radiographs.

Radiographic films usually have an emulsion layer on each side of the film base. When a film is exposed, similar images record on each side of the film. When radiographs are viewed, the image seen by the observer is the sum of the perfectly superimposed images contained in the two emulsions. Hence, the image of a detail exhibiting correct density and contrast is actually the sum of two images, each displaying one-half the final density and contrast. This same property would apply if the two emulsions with their identical images were on separate film bases rather than one.

A radiograph differs from a photograph in that all details within a subject record on a radiograph but not on a photograph. Suppose metal markers are placed on a skull, one on the forehead and the other at the back of the head, and then two underexposed radiographs are made of the skull from slightly different directions. Both metal markers would be visible on each of the two radiographs, however, it would be possible to superimpose the images of only one marker at a time because the two radiographs were not identical. All details lying in the layer containing the superimposed marker would appear with normal contrast and density and would appear "in focus." All other details would be both underexposed and of low contrast to begin with, and in addition, would be superimposed on non-matching details displaying both low density and contrast. Proper movement of the two radiographs would cause the images of the second marker to superimpose and be "in focus." Thus, other orientations of the two radiographs could bring into focus details lying in any other parallel plane. Unwanted details can be blurred out more effectively, if instead of having the final image built up from two underexposed radiographs, eight underexposed radiographs are used.

A high degree of accuracy is necessary to make a successful dynamic tomography examination of a subject. Each detail must display the same amount of enlargement on each of the several radiographs used in the examination. The following expression describes the relationship between the factors that control enlargement:

$$\text{Percent enlargement} = 100 \times \frac{\text{Detail-to-film distance}}{\text{Source-to-detail distance}}$$

Excellent dynamic tomography surveys of a subject can be made by sequentially exposing eight films, with the source and film moving during the exposure, at each of the eight positions shown in Figure 1.

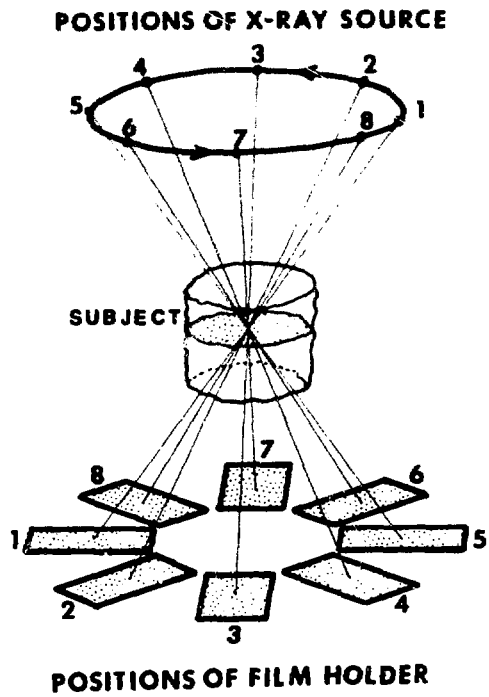

Figure 1. Both the source and film holder move along circular paths in parallel planes between exposures.

After exposure and processing, the eight radiographs are assembled as a sandwich on an illuminated viewing device. Turning the control knob on the viewer causes each radiograph to move radially toward or away from the center of the viewer to focus on details lying anywhere within the subject (Figure 2). Details in a layer only 0.5 mm thick are displayed routinely. The thinnest layer of details examined to date has been 0.3 mm.

Figure 2. Eight 6" x 12" radiographs located over the 6" diameter illuminated area of the Dynamic Tomography viewer. Control knob is in lower right-hand corner. Small circular area at top of viewer is a scale which indicates depth of the layer of detail within the subject that is currently in focus.

A few of the infinite number of possible sagittal sections of a skull are displayed in Figure 3.

(a) Calcified crown of the mandibular first molar.

(b) 1. Second mandibular primary molar

2. Tooth bud of mandibular second bicuspid

(c) 1. First mandibular primary molar

2. Calcified crown of mandibular first bicuspid

(d) 1. Primary mandibular cuspid

2. Calcified crown of permanent mandibular cuspid

(e) 1. Primary mandibular lateral incisor

2. Calcified crown of permanent mandibular lateral incisor

(f) 1. Primary mandibular central incisor

2. Calcified crown of permanent mandibular central incisor

Figure 1. Dynamic laminagraphy applied to dental examination. a. Cross-sectional view of human jaw showing the mandibular cuspid and lateral incisor. Age about 10 years.

[illegible] dynamic laminography examination [illegible] will provide the [illegible] information that will provide for the multiple [illegible] and jaw planes, a [illegible] film [illegible], the [illegible] a [illegible] the patient [illegible] the [illegible] a patient [illegible] [illegible] [illegible] problem, the [illegible] already been [illegible].

[illegible] applied to dynamic laminography are in medical practice, the teaching [illegible] and [illegible] to non-destructive testing in industry.

References

Fleischer and Flinders, B.G. Deri ek j.n, ... F rtscher. Bet. F ortgenstrahlen, 57:605-10, June 1938; Jerie:yy. A rail graphic method which makes it possible t view an infinite series f parallel planes in succession by means f a few exposures. Trans. j. 1 3-141. (In collected works of B.G. Fleischer and Flinders. Amsterdam, Experta Medica, 1973, vi + 227 p.

Richards, A.G. Variable depth laminography. Biomed. Sci. Instrument., 6:194-199, 1969.

Miller, E.R., McCurry, E.M. and Hruska, P.P. An infinite number of laminagrams from a finite number of radiographs. Radiology, 96:649-655, Sept., 1971.

Miller, E.R., McCurry, E.M. and Hruska, P.P. A simplified procedure for viewing multiple films to create an infinite number of laminagrams. Radiology, 110:365-367, February 1974.

Proceedings, IEEE/A.E.C. Gamma-Ray Symp. Ann Arbor, MI, May 19-21, 1976 (Conf-760539)

CODED APERTURE IMAGING IN NUCLEAR MEDICINE; REVIEW AND UPDATE

W. Leslie Rogers
University of Michigan Medical Center
Ann Arbor, Michigan 48109

Summary

Since mid-1972, a number of investigators have been studying the properties of coded apertures as applied to imaging distributions of gamma-emitting radiotracers in the human body. Aperture codes including the zone plate, annulus, stationary and time modulated random hole patterns and the rotating slit have been employed with a variety of detectors ranging from X-ray film to multi-wire proportional counters. These methods are described and discussed.

Introduction

In Nuclear Medicine, images of the in vivo distribution of radiolabeled compounds administered to patients are used for diagnostic purposes. Traditionally, a pinhole in lead or a collimating aperture is employed to form a gamma ray image of the radiotracer distribution on a position sensitive detector. The image is transferred to film or to a computer for viewing and analysis. Collimators and pinhole apertures subtend a small solid angle, and the resulting images are corrupted by statistical noise arising from the limited number of collected photons. The solid angle can be increased, but only at the expense of spatial resolution. For this reason, great interest was initially sparked when Barrett first demonstrated high quality gamma ray images obtained with a lead Fresnel zone plate aperture in mid 1972.[1] This aperture subtends a much greater solid angle than a pinhole for a given spatial resolution, and it was hoped that image signal-to-noise could thereby be improved. Coded apertures also give three-dimensional information about the source distribution and place a different set of restrictions on detector design than do conventional apertures. The potential advantages have been only partially realized as will be described later, but the ensuing research has developed a mature understanding of the gamma ray imaging problem and the many very interesting approaches to its solution.

Coded Aperture Imaging

Figure 1 illustrates a zone plate used as a coded aperture. The encoded image is shown for two representative points in the object. Of course the aperture transmission function need not be a zone plate and it may vary with time. To the extent that variations in aperture solid angle over the object can be ignored, the shadow image, or coded image, is a convolution of the object distribution O with the scaled coding function, T.

$$C(x,y,t) = O(x,y,z) * T(\alpha x,\alpha y,t)$$

The scale factor alpha, is a function of z and the aperture-detector spacing.

In order to recover an image which has some likeness to the object the coded image must be operated on with some decoding function. The results depend critically upon both the selection of the coding function and the means employed for decoding. The only restriction on the coding function is that it be real and positive since it represents the gamma ray transmission of the aperture which lies between zero and one.

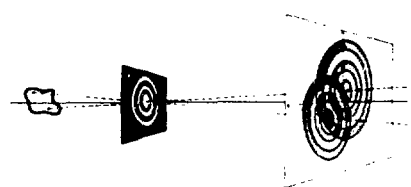

Figure 1. Example of coded aperture shadow casting for a zone plate aperture.

With two exceptions, namely the anulus [2,3] and Tanaka's rotating slit, [4,5] the coding functions which have been investigated are characterized by time averaged autocorrelation functions which have sharp central peaks and relatively flat sidelobes. Time averaging is included to encompass time varying code functions. When the autocorrelation function is peaked and the object is not a function of z, then the decoding is readily performed by correlating the coded image with the aperture function.

$$I(x,y,z_o) = \overline{C(x,y,t) * T(-\alpha x,-\alpha y,t)} \qquad (2)$$
$$= \overline{O(x,y,z_o) * T(\alpha x,\alpha y,t) * T(-\alpha x,-\alpha y,t)}$$
$$= O(x,y,z_o) * \Delta(x,y)$$

The bar denotes time averaging, and the delta represents the peaked autocorrelation function with wings. The resulting image is a smoothed version of the object distribution plus a constant bias. The decoding function is not constrained to be real and positive as is the encoding function, nor is it constrained to be identical to the encoding function.

In the event that the object is not planar, then the above reconstruction will yield the object at z_o with additional terms composed of

$$\overline{\sum_{i \neq o} O(x,y,z_i) * T(\alpha_o x,\alpha_o y,t) * T(-\alpha_i x,-\alpha_i y,t)}, \qquad (3)$$

Planes in the object distribution at different distances

from the aperture are enumerateed by i. The character of this out-of-focus information is determined by the cross correlation of the aperture functions at different scales.

When the autocorrelation function of the encoding function is not sharply peaked with flat sidelobes but has, for instance, 1/r tails as does a rotating slit and an annulus, then further processing is required to obtain a reconstructed image with usable contrast and resolution.[4,5] In this event equation 2 becomes:

$$I(x,y,z_o) = O(x,y,z_o) * P_s(x,y) * h(x,y). \quad (4)$$

P_s is the point spread function corresponding to the time averaged autocorrelation function of the aperture code, and h is a filter function such that

$$P_s(x,y) * h(x,y) = \Delta(x,y) \quad (5)$$

Tanaka [5] points out that this additional step can adversely affect the image signal-to-noise.

Image Reconstruction

Correlation of the coded image with the encoding function may be performed using either coherent or incoherent optical methods, digital computers, or analog electronic methods. Zone plate coded images are readily reconstructed by diffraction as originally pointed out by Mertz and Young.[6] A reduced scale transparency of the coded image is illuminated by coherent light and the required correlation with the zone plate function results from the diffraction integral and the nature of the free space propagation of light. Additional filtering may be performed in the Fourier transform plane of the optical system, and the resulting image viewed on a ground glass. Codes other than the zone plate may be optically reconstructed with coherent light using a matched filter in the Fourier plane of the optical system.[7,8,9] The matched filter is the complex conjugate of the Fourier transform of the encoding function.

Incoherent optical correlation is very simply performed by diffusely illuminating a transparency of the coded image and reimaging it back through the encoding aperture. Incoherent reconstruction is not very practical, however, since a bias term proportional to the mean transmission of the real, positive mask is superimposed on the image in the process of reconstruction.

The major attraction for optical processing is the speed at which the correlation is performed. The laboratory technique is fairly demanding, however, and even though computation is performed at the speed of light, film processing takes from twenty to forty minutes. Digital computers can readily compete with these times for the number of resolution elements involved, and they furthermore offer ready quantitation and subtractive processing steps. Although grid coded subtraction as described by Barrett, Stoner et al [3] may be used to accomplish subtraction on an optical processor, there remain the ever present problems of film dynamic range, grain noise, and fingerprints. Digital processing also offers a signal-to-noise advantage by avoiding conversion of amplitudes to intensities. For these reasons digital processing is often used even for zone plate images.

Survey of Methods and Results

Fresnel Zone Plate

The most well known and diligently studied of the apertures is the Fresnel zone plate. Its use as an imaging device was first proposed by Mertz and Young in 1961[6] for x-ray stars and later by Barrett[1] for Nuclear Medicine imaging. Both optical[1,6,8,10-25] and digital[26-31,55] reconstruction methods have been employed as well as electronic pulse compression.[10] Difficulty was encountered because reconstructions from a single on-axis zone plate aperture contain a strong DC component plus virtual and out-of-focus higher order images which greatly degrade the desired image. The DC component has been removed using a Schlieren stop in the Fourier plane[1] and by means of a Smith's polarimeter.[25] Also, Tipton[16,23] described a means of forming a dark image on a DC background by causing the two components to interfere destructively. These methods proved of limited value for DC removal, and the higher order out of focus images remained a problem until the off-axis zone plate with half-tone screen was used in conjunction with an x-ray film detector.[12]

With this combination, diagnostically useful images of both large and small organs have been obtained.[22,24] Quality was exceptionally good. Two optically reconstructed examples made using a zone plate half-tone screen are shown in Figure 2(b and d) compared to standard images (a and c) made using a collimator on an Anger camera.

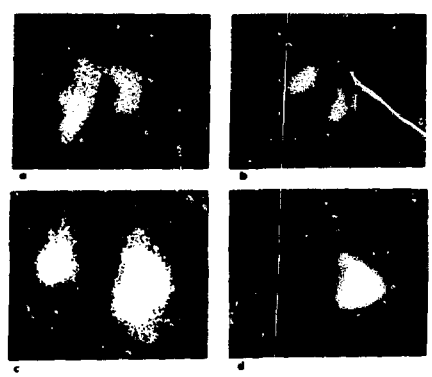

Figure 2. Anger camera (a) and zone plate/film cassette images (b) of normal liver. Zone plate exposure is 20 min-5mCi Tc s.colloid. Anger camera (c) and zone plate (d) images of lung perfusion. Zone plate exposure is 12 min.-10mCi Tc microspheres. Bar pattern at upper right from scratched lens. (Courtesy of H.H.Barrett, University of Arizona)

The off-axis zone plate camera, however, is limited by the following problems:

1. The detector resolution required for a given resolution is a factor of three higher for the off-axis zone plate compared to the on-axis zone plate or pinhole. This dictates the use of x-ray film as a detector with a resulting single photon detection efficiency about ten percent that of a standard gamma camera for the 140 KeV gamma rays of ^{99m}Tc.

2. The signal-to-noise performance of this combination is limited by poor detection efficiency, the 50% attenuation by the halftone screen, and reduced harmonic content of the first order diffraction pattern.

Extensive signal-to-noise analysis has been performed; by Barrett and DeMeester [20] for a single zone plate, aperture limited system; by Lundgren et al[32] for an off-axis zone plate with zone plate halftone screen and detector limited system; and by Joy and Houle [33] who compared the performance of an optimized off-axis zone plate camera with an optimized pinhole camera. Houle and Joy[34] have also examined the small signal performance of the off-axis zone plate camera.

The results vary widely depending upon the assumptions. The first two references examine the relative performance of the pinhole and zone plate for viewing uniform sources of varying size under the condition of identical geometry. For a source filling the field of view, Barrett shows that the signal-to-noise ratio of the pinhole is a factor of π times zone plate for optical decoding and $\pi/2\sqrt{2}$ for digital decoding. Lundgren, assuming optical reconstruction, calculates a signal-to-noise advantage of the pinhole for the filled field to be a factor of five greater than the off-axis zone plate with halftone screen. Signal-to-noise is taken as the ratio of mean to standard deviation, and it has been assumed that the photon detection efficiency of the two cameras is the same for both sets of results. When optimum cameras are compared,[33] the conclusion is reached that the detector space-bandwidth product must exceed that of the object by a factor of twenty, and the detector size must be 2 1/2 times the object size in order to obtain improvement with an off-axis zone plate camera and optical reconstruction.

These analytical results spurred interest in digital reconstruction and alternate aperture codes including time modulated apertures which will be described later. However, the on-axis zone plate discarded earlier was destined to be resurrected. The key to this resurrection was based on the knowledge that DC bias could be eliminated from the reconstructed image by taking a coded image with a positive zone plate and subtracting from it an image taken with a negative (180° out of phase) zone plate. Macdonald and Chang[26] demonstrated this technique using digital processing of coded images from a multiwire proportional chamber detector. Results were obtained equivalent to those from a hypothetical bi-polar aperture. Barrett, Stoner, Wilson and DeMeester [8] extended this method to remove conjugate image background by using a sequence of four zone plates 90° out of phase. Grid coding of the multiple zone plate images was used in order to perform the subtraction step optically. They also described grid coding phase information for spiral zone plates, inverse zone plates and the Girard grill, all of which posess peaked autocorrelation functions.

More recently Moore [31] has obtained some excellent images using four sequential on-axis zone plates, an x-ray film with intensifying screen detector, and digital reconstruction. Figure 3-a shows these results while 3-b shows the results obtained when only two zone plates were used. The background in 3-b is that of the out-of-focus conjugate and higher order images. Houle and Joy[55] have reported computer simulations of this method.

Digital processing and elimination of the halftone screen and off-axis zone plate are two very important improvements since a gain of at least $2\sqrt{2}$ is made in signal-to-noise [55] in addition to reducing detector resolution requirements by a factor of 3. This makes it feasible to use an Anger camera as a detector with approximately a gain of 10 in single photon detection efficiency over x-ray film cassettes.

Figure 3. Digitally reconstructed images of a thyroid phantom using 4 on-axis zone plates 90° out of phase (a) and 2 zone plates 180° out of phase. X-ray film was used as detector. (Courtesy of F.E. Moore, Searle Radiographic)

Figure 4. Reconstruction of image shown in Figure 3-a at varying focal depths. Note changes in polarity of defects. (Courtesy of F.E. Moore)

Zone Plate Out-of-Focus Response

One of the advantages cited for zone plates and other coded apertures is a tomographic response, that is, the ability to focus on a place at a given depth in the source. Unfortunately it has been recognized for some time [18] that, in the case of zone plates, out of focus information can interfere with in-focus data to produce spurious structure. The effect is worse with objects containing high spatial frequencies. Figure 4, which is also the work of Moore[31], illustrates the problem. The defects in the thyroid phantom actually reverse sign as the image is defocused. This problem is discussed by Gaskill et al [15] and by Whitehead[9] who

have attempted matched filtering in an attempt to eliminate both the spurious structure and out of focus information. They point out that the crosscorrelation of different scale zone plates results in annoying ring structure plus an out of focus image.

Webb and Parker[29] have obtained isolated tomograms of simple objects from simulated data for a 4 ring zone plate by matrix inversion. The equations are ill conditioned so the solution is very sensitive to noise. Figure 5 shows results for the letters H and T contained in separate planes. In this example 8 x 10^{10} counts were recorded. Images (a) and (b) are the unprocessed reconstruction while (c) and (d) are the result of matrix inversion.

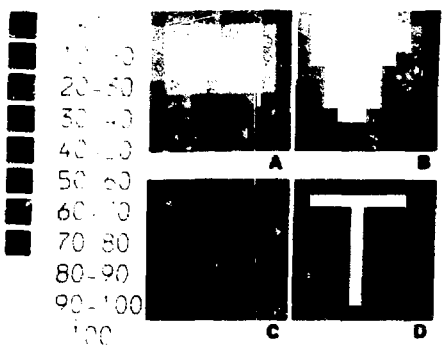

Figure 5. Computer simulation of 4-ring on-axis zone plate images of letter H at 10 and letter T at 8 cm. from aperture. T is double strength and 8 x 10^{10} counts collected. (a) and (b) are raw reconstructions. (c) and (d) after response matrix inversion. (Courtesy R.P. Parker and S. Webb, Royal Marsden Hospital, Sutton, Surrey, U.K.)

Solution for the isolated tomograms for any of the coded apertures is likely to be very difficult and sensitive to noise particularly when the objects have predominantly low spatial frequencies. This is because the limited cone of view angles employed severely restricts the volume in Fourier space for which information is directly available. Noise greatly hampers attempts to compute the missing coefficients.

Other Stationary Apertures

Annulus

An annulus has peaked autocorrelation function with approximately 1/r tails and a bump at the annulus radius. It was first suggested as an aperture code by Walton[2] who performed analog reconstruction by means of a spiral sweep read-out of the coded image from a scan converter. More recently[3], digital processing has been used with good sucess to remove the 1/r tails from the response function. The filter required for this purpose is the same 1/ρ filter employed for transaxial tomography. The bump remains, however, causing a ring in the reconstructed image which limits the field of view. The annulus is a dilute aperture being much leas than 50% open. This should give better signal-to-noise performance in cold regions of the object than is obtainable with the zone plate.

Random Arrays

A purely random array of pinholes will have the desired autocorrelation function if the array is large enough. Dicke[36] described the properties of such arrays and suggested both coherent and incoherent methods for decoding them. Both coherent[7,53] and incoherent[54] decoding for simple objects have been shown.

Non-redundundant Arrays

Golay[33] has described finite, non-redundant arrays of pinholes with compact autocorrelation functions. These are similar to Dicke's random arrays but have a much lower mean transmission. For this reason Chang et al[37] were able to obtain rather good images using incoherent optical reconstruction as described by Dicke[36] and demonstrated by Wouters.[52] See Figure 6 for an illustration of the method and result.

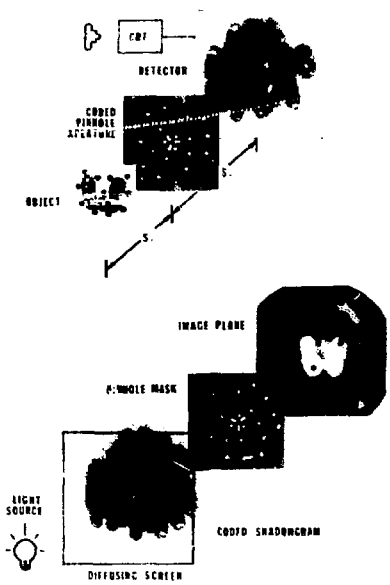

Figure 6. Non-redundant pinhole aperture used with multiwire proportional counter. Incoherent reconstruction scheme is illustrated. (Courtesy of B. Macdonald, Lawrence Berkely Laboratory)

Random Phase

A random phase code with remarkable out-of-focus performance has been described by Whitehead.[9] The aperture code is a focused image hologram of a ground glass made using an off-axis reference beam. Optical reconstruction with a holographic matched filter is employed. The unusual feature of this approach is that, as a point source image is defocussed, the core image vanishes before there is any appreciable blurring. Unfortunately when extended objects are imaged, a halftone screen is required which prevents the object spectrum from shifting out of the passband, and the core image does not disappear. Instead it expands with uniform blurring. This in itself is a desirable feature although not as desirable as having the image disappear altogether.

Time Modulated Apertures

The last group of apertures to be described are those whose transmission is a function of time. With these apertures it is necessary to record a sequence of coded images. In this sense the multiple phase zone plate is also a time modulated aperture, but in performance it has more in common with stationary apertures. By varying the aperture transmission so that the transmission at one point on the aperture is uncorrelated in time with the transmission at all other points, it is possible to calculate the object distribution seen by each detector element through each point on the aperture. Three methods of modulating the aperture to achieve this have been suggested: random modulation[38-41], pseudorandom modulation[40-45], and frequency modulation.[46] Random aperture performance has been computer modeled and pseudorandom apertures, which are simpler to realize, have been experimentally implemented. Decoding is accomplished by digital correlation. Figure 7 illustrates a pseudorandom aperture on an Anger camera and two tomographic images of a human thyroid compared to a standard pinhole image taken for the same time duration. Figure 8 shows the tomographic response of this aperture for three $99m_{Tc}$ filled letters. Images defocus smoothly with no high frequency structure.

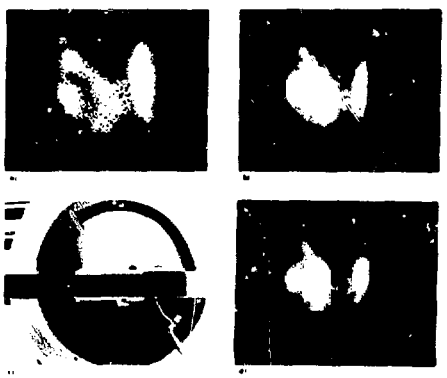

Figure 7. Human thyroid images obtained with a pinhole (a) and pseudorandom aperture (b and d). Image (b) is focused at 1.6cm and (d) at 2.3cm below skin surface. Motor driven aperture on Anger camera is depicted in (c).

Two key features distinguish these time modulated apertures from the stationary apertures. Since the correlation is performed in time, the shape of the point response function is independent of the amount of the aperture shadowed onto the detector, and objects may be positioned as close as a centimeter from the plate to maximize efficiency. For the same reason, the spatial distribution of the hole pattern over the aperture plate is completely arbitrary and may be specified to give optimum tomographic response or to tailor the signal-to-noise response in some manner. Work is now underway to calculate the isolated object plane using a matrix inversion technique described by Chang.[47]

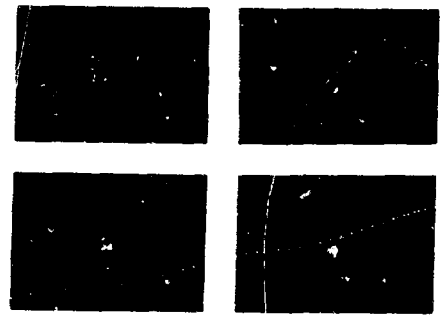

Figure 8. Illustration of tomographic response of pseudorandom aperture for $99m_{Tc}$ filled letters. Note smooth out-of-focus behavior.

A variation of the above aperture geometry is under investigation by Knoll and Williams.[48] The pseudorandom code is distributed on a cylinder which is free to rotate. A detector ring outside of the code cylinder views the object distribution inside the code cylinder. The prototype is illustrated in Figure 9 with the detectors removed.

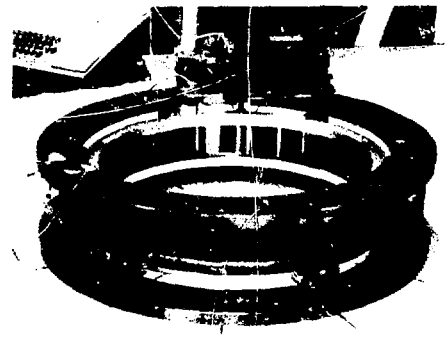

Figure 9. Prototype of pseudorandom coded ring aperture. The 2π geometry permits construction of transaxial section images. (Courtesy of G.F. Knoll and J. Williams, University of Michigan)

This geometry permits information to be gathered over a range of 360° so that transaxial tomographic slices may be reconstructed of the object distribution. Another version of this type of device is described by Price[49] who has simulated its response digitally using iterative reconstruction.

Rotating Slit

Figure 10 shows images of a thyroid phantom made with quite a different type of time varying aperture; a rotating slit.[4,5] This aperture is distinguished from all the others by not offering tomography since the slit rotates about its center. In view of the problems posed by tomographic response this need not be considered a deficiency. As mentioned earlier, the rotating

slit has a 1/r autocorrelation function similar to the annulus so that the appropriate filter is also 1/ρ. The images illustrated in Figure 10 compare two sets of pinhole images and two sets of rotating slit images. Each column of images is processed to have Gaussian point spread functions of equal FWHM. The noise texture of the slit images is seen to be quite different from the pinhole images, and the slit images have a very pleasing appearance.

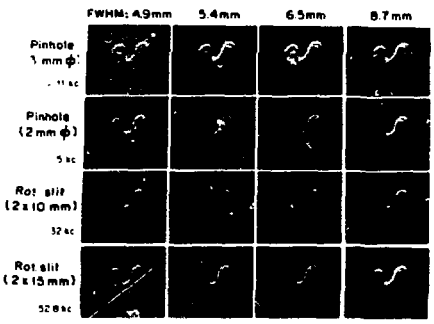

Figure 10. Rotating slit images of thyroid phantom compared to pinhole images at varying resolution. Imaging time is constant and total counts collected are indicated at left. (Courtesy E. Tanaka and T.A.Iinuma, National Institute of Radiological Sciences, Anagawa, Chiba-shi, Japan)

Discussion and Conclusions

Amidst the welter of various apertures, detectors, and processing schemes run two main themes: improve the signal-to-noise and obtain tomography without artifacts and preferably without out-of-focus background.

The nature of signal related noise is such that gains in signal-to-noise are achieved with coded apertures when the object distribution is not well matched to a compact, round detector. Thus when the object is either sparse or has a shape much different from the detector, gains in signal-to-noise can be realized by spatial multiplexing of the data. Digital processing appears to yield the best signal-to-noise.

Tomography with smooth defocussing has been accomplished, but actual decoupling of the depth information from different planes has been complicated by noise and the limited range of view angles. Any widespread medical application of coded apertures will likely depend on the solution of these problems coupled with fast, real-time decoding schemes.

Acknowledgements

I wish to extend my thanks to those who contributed the results of their own research to this paper.

References

1. Barrett HH: Fresnel zone plate imaging in Nuclear Medicine. J Nucl Med 13: 382-385. 1972

2. Walton PW: An aperture imaging system with instant decoding and tomographic capabilities. J Nucl Med 14: 861-863, 1973

3. Simpson RG, Barrett HH, Subach JA, Fisher HD: Digital Processing of annular coded-aperture imagery. Opt Eng 14: 490-494, 1975

4. Tanaka E, Iinuma TA: Image Formation in Coded Aperture Imaging and its applications to a rotating slit aperture. Proc. First World Congress of Nuclear Medicine, Tokyo, Japan, pp 9-13, 1974

5. Tanaka E, Iinuma TA: Image Processing for coded aperture imaging and an attempt at rotating slit imaging. Proc. of the 4th International Conference on Information Processing in Scintigraphy, Orsay, July 15-19, 1975

6. Mertz L, Young NO: Fresnel Transformations of Images. Proc. Conf. Opt. Instr. Tech., London 1961, KJ Habell, Ed., New York: John Wiley and Sons, Inc., pp. 305-312, 1962

7. Hayat GS: X-ray and γ-ray Imaging with Multiple Pinhole Cameras. Ph.D. Thesis, State Univ. of New York at Stony Brook, 1971

8. Barrett HH, Stoner WW, Wilson DT, and DeMeester GD: Coded apertures derived from the Fresnel zone plate. Opt Eng ., Nov-Dec. 1974

9. Whitehead FR: A comparison of coded aperture imaging systems containing zone plate and random-phase code functions. Ph.D. Dissertation, University of Arizona, 1976

10. Rogers WL, Han KS, Jones LW, Beierwaltes WH: Application of a Fresnel zone plate to gamma-ray imaging. J Nucl Med 15: 612-615, 1972

11. Rogers WL, Jones LW, Beierwaltes WH: Imaging in Nuclear Medicine with incoherent holography. Appl Opt Instr Med, I, Proc. SPIE 35: 165-179, 1972

12. Barrett HH, Wilson DT, DeMeester GD: The use of half-tone screens in Fresnel zone plate imaging of incoherent sources. Opt Comm 5: 398-401, 1972

13. Barrett HH, Wilson DT, DeMeester GD, Scharfman H: Fresnel zone plate imaging in radiology and nuclear medicine. Appl Opt Instr Med, I, Proc. SPIE 35: 199-205, 1972

14. Barrett HH, Horrigan FA: Fresnel zone plate imaging of gamma rays; theory. Appl Opt 12: 2686-2702, 1973

15. Gaskill JD, Whitehead FR, Gray JE, O'Mara RE: Matched filter restoration of coded gamma and x-ray imagery. Appl Opt Instr Med, I Proc. SPIE 35: 193-197, 1973

16. Tipton MD, Dowdey JE, Caulfield HJ: Coded aperture imaging with on-axis Fresnel zone plates. Opt Eng 12: 166-168, 1973

17. Wilson DT, DeMeester GD, Barrett HH, Barsack E: A new configuration for coded aperture imaging. Opt Comm 8: 384-386, 1973

18. Wilson DT, Barrett HH, DeMeester GD, Farmelant MH: Point Source artifacts in Fresnel zone plate imaging. Opt Eng 12: 133-134, 1973

19. Barrett HH, Garewal K, Wilson DT: A spatially-coded X-ray source. Radiology 104: 429-430, 1972

20. Barrett HH, DeMeester GD: Quantum noise in Fresnel zone plate imaging. Appl Opt 13: 1100-1109, 1974

21. Jaszczak RJ, Moore FE, Whitehead FR: Use of an array of three off-axis zone plates for large field of view gamma ray imaging. Appl Opt Instr Med, II, Proc, SPIE 43: 3-9, 1973

22. Farmelant MH: Improved anatomical definition by a Fresnel zone plate imager. J Nucl Med 14: 393 - 394, 1973

23. Tipton MD, Dowdey JE, Bonte FJ, Caulfield HJ: Coded aperture imaging using on-axis Fresnel zone plates & extended gamma-ray sources. Radiology 112: 155, 1974

24. Farmelant MH, DeMeester G, Wilson D, Barrett HH: Initial clinical experiences with a Fresnel zone plate imager. J Nucl Med 16: 183-187, 1975

25. Nicholas A, Parker RP: Optical reconstruction of radioisotope distributions obtained using a zone plate coded aperture. Proc. Conf Electro-optics/Laser '76 Ed. HG Jerrard (London: I.P.C.) In the press

26. Macdonald B, Chang LT, Perez-Mendez V, Shiraishi L: Gamma-ray imaging using a Fresnel zone plate aperture, multiwire proportional chamber detector, and computer reconstruction. IEEE Trans Nucl Sci NS-21: 678-684, 1974

27. Budinger TF, Macdonald B: Reconstruction of the Fresnel-coded gamma camera images by digital computer. J Nucl Med 16: 309-313, 1975

28. Parker RP, Dance DR, Nicholas A, Webb S, Wilson BC: The use of coded apertures with digital decoding. Presented at 7th L.H. Gray Conference on Medical Images, Leeds, April 13-15, 1976

29. Webb S, Parker RP, Dance DR, Nicholas A: Digital processing of longitudinal tomograms obtained with a zone plate camera. IEEE Trans Biomed Eng. 1976

30. Wilson BC, Parker RP, Dance DR: Digital processing of images from a zone plate camera. Phys Med Biol 20: 757-770, 1975

31. Moore FE: Digital computation of Fresnel zone plate images. To be submitted Phys Med Biol. 1976

32. Lindgren AG, Cuha OK, Spence JE: A noise analysis of Fresnel zone plate imaging systems. In Digest of Papers, 1974 International Optical Computing Conference, April 9-11, 1974 Zurich, Switzerland, IEEE Catalog #CH0862-3C.

33. Joy MLG, Houle S: The potential performance of off-axis Fresnel zone plate gamma imaging systems on arbitrary objects. IEEE Trans Nucl Sci NS-22: 364-368, 1975

34. Houle S, Joy MLG: Small signal suppression in coded aperture imaging in nuclear medicine. IEEE Trans Nucl Sci NS-22: 369-373, 1975

35. Golay MJE: Point arrays having compact, nonredundant autocorrelations. J Opt Soc Am 61: 272-273, 1971

36. Dicke RH: Scatter hole cameras for x-rays and gamma rays. Astro J 153: L101-L106, 1968

37. Chang LT, Kaplan SN, Macdonald B, Perez-Mendez V, Shiraishi L: A method of tomographic imaging using a multiple pinhole-coded aperture. J Nucl Med 15: 1063-1065, 1974

38. May RS: Gamma ray image formation by Stochastic Time Modulation. Ph.D. Thesis, The University of Michigan, 1974

39. May RS, Akcasu Z, Knoll GF: Gamma ray imaging with stochastic apertures. Appl Opt 13: 2589-2601, 1974

40. Akcasu AZ, May RS, Knoll GF, Rogers WL, Koral KF, Jones LW: Coded aperture gamma ray imaging with stochastic apertures. Appl Opt Instr Med, II, Proc. SPIE 43: 17-28, 1973 and Opt Eng 13: 117, 1974

41. Akcasu AZ, May RS, Knoll GF, Rogers WL, Koral KF, Jones LW: Time modulated coded apertures for γ-ray imaging in nuclear medicine. Int.Opt. Comp. Conf. IEEE Tech. Dig. 49-53, 1974. IEEE #CHO 862-3C

42. Knoll GF: Photon imaging using statistical filters. SRC Research Grant B/RG/3192 Final Report, Science Research Council, London, May 15, 1973

43. Knoll GF, May RS, Akcasu Z: Pseudorandom filters and correlation analysis applied to gamma ray imaging. J Nucl Med 15: 507, 1974

44. Koral KF, Rogers WL, Beierwaltes WH: Gamma ray imaging with a time-modulated pseudorandom aperture and an Anger camera. Abs J Nucl Med 15: 508, 1974

45. Koral KF, Rogers WL, Knoll GF: Digital Tomographic imaging with time-modulated pseudorandom coded aperture and Anger camera. J Nucl Med 16: 402-413, 1975

46. Macovski A: Gamma ray imaging system using modulated apertures. Phys Med Biol 19: 523, 1974

47. Chang LT, Macdonald B, Perez-Mendez V: Three dimensional image reconstruction from axial tomography. Proc. Meeting on Image Processing for 2-D and 3-D Reconstruction from Projections, Stanford, California August 4-7, 1975

48. Knoll GF, Williams J: A coded ring aperture for transaxial tomography. To be sub IEEE Trans.Nucl.Sci.

49. Price LR: CCA: A high resolution, high sensitivity, three dimensional imaging system for nuclear medicine. Nucl Inst Meth 131: 353-368, 1975

50. Barrett HH: Pulse compression techniques in nuclear medicine. Proc. IEEE 60: 723-724, 1972

51. Chang LT, Macdonald B, Perez-Mendez V, Shiraishi L: Coded aperture imaging of gamma rays using multiple pinhole arrays and multiwire proportional chamber detector. IEEE Trans Nucl Sci NS-22: 374-378, 1975

52. Wouters A, Simon KM, Hirschberg JG: Direct method of decoding multiple images. Appl Opt 12: 1871-1873, 1973

53. Groh G, Hayat GS, Stroke GW: X-ray and γ-ray imaging with multiple pinhole cameras using a posteriori image synthesis. Appl Opt 11: 931-933, 1972

54. Palmieri TM: The multiplexed pinhole camera. Livermore, Calif. University of California Preprint

55. Houle S, Joy MLG: On-axis multiple Fresnel zone-plate coded apertures. Report #16 Inst. of Biomedical Engineering, University of Toronto, Canada 1975

Proceedings, ERDA X-and Gamma Ray Symp. Ann Arbor, MI, May 19-21, 1976 (Conf 760539)

TRANSMISSION IMAGING WITH A CODED SOURCE

W. W. Stoner, J. P. Sage, M. Braun and D. T. Wilson
Raytheon Research Division
Waltham, Massachusetts 02154

H. H. Barrett
University of Arizona
Tucson, Arizona 85721

Introduction

What is a coded source? The conventional approach to transmission imaging is to use a rotating anode x-ray tube, which provides the small, brilliant x-ray source needed to cast sharp images of acceptable intensity. Stationary anode sources, although inherently less brilliant, are more compatible with the use of large area anodes, and so they can be made more powerful than rotating anode sources. Spatial modulation of the source distribution provides a way to introduce detailed structure in the transmission images cast by large area sources, and this permits the recovery of high resolution images, in spite of the source diameter. The spatial modulation is deliberately chosen to optimize recovery of image structure; the modulation pattern is therefore called a "code."

A variety of codes may be used; the essential mathematical property is that the code possess a sharply peaked autocorrelation function, because this property permits the decoding of the raw image cast by the coded source. Random point arrays, non-redundant point arrays, and the Fresnel zone pattern are examples of suitable codes. This paper is restricted to the case of the Fresnel zone pattern code, which has the unique additional property of generating raw images analogous to Fresnel holograms.[1] Because the spatial frequency of these raw images are extremely coarse compared with actual holograms, a photoreduction step onto a holographic plate is necessary before the decoded image may be displayed with the aid of coherent illumination.

Advantages of Coded Sources

There are two potential signal-to-noise ratio advantages of a coded source: a throughput or Jacquinot advantage, and a multiplex or Fellgett advantage. These terms are borrowed from the field of spectroscopy, where such gains were first recognized.[1,2] In diagnostic medicine, the need for improved image quality must always be weighed against the additional x-ray exposure needed to provide the improvement. For this reason, neither the throughput or the multiplex "advantages" are appropriate in diagnostic radiology. Indeed, the potential for a multiplex advantage occurs only if an image is to be obtained in the presence of a parasitic radiation background, or if the detector system introduces an objectionable noise background. These types of situations are simply not tolerated in diagnostic radiology. The potential for a throughput advantage only occurs with very special object structures which define the incident flux into largely non-overlapping beams; moreover, this "advantage" arises because a large area source can generate more radiation than a smaller area conventional source. Obviously, the throughput advantage is not applicable in situations where it is important to minimize the x-ray exposure of the object under study.

An analysis of the throughput and multiplex gains in coded source imaging is contained in a later section; this analysis points towards two areas where coded sources provide images with higher signal-to-noise ratios than conventional sources:

1. x-ray imaging in the presence of a substantial, undesired x-ray background
2. imaging of voids or cracks in radiation shields.

Additional virtues of coded sources are depth discrimination and the feasibility of using fluorescent radiation instead of bremsstrahlung. The depth discrimination of a coded source allows a series of images to be reconstructed from a single transmission image.

Holographic Reconstructions

Some of the characteristic properties of such holographically decoded images are demonstrated by the series of images shown in Fig. 1. The 1,2,3

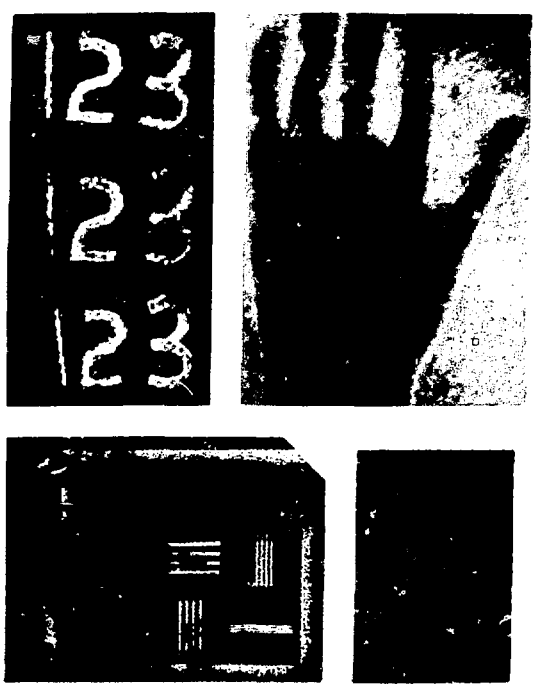

FIGURE 1

series demonstrates that a single raw image cast by the Fresnel zone pattern source can be holographically imaged at successive depths. Unfortunately, the out-of-focus point spread function (which will be treated analytically later on) does not adequately wash out the high spatial frequency image content, and so the utility of this focusing feature depends critically on the extent of the operator's a priori knowledge of the image content. The hand image was

made of a dummy hand, composed of genuine bones encased in plastic which simulated the x-ray transmission of flesh. This image illustrates that the range of x-ray transmission covered by the plastic and the bone is translated into an acceptable variation in grey level by the holographic decoding process. The resolution chart image illustrates two facts. One, the resolution limit (in this case 1 line pair per millimeter) is determined by the usual geometric factors, and by the width of the finest zones on the Fresnel zone pattern source. Two, the noise in the image varies spatially in proportion with the transmission of the object; since the source is extended, the noise pattern is smeared out over a width determined by the diameter by the source. Therefore, the noise is greatest in the transmitting proportions of the image, and lowest well inside the opaque areas, gradually increasing in the vicinity of the transmitting border. The worst case situation is that of a just resolved opaque element surrounded by a transmitting region; Fig. 1 shows an example of this

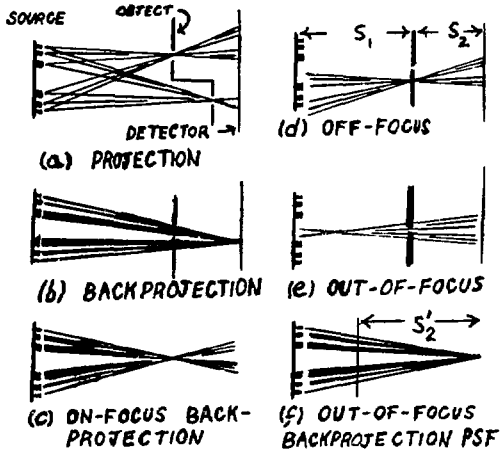

FIGURE 2

unfavorable situation - the noticeably noisy image of a 2 millimeter lead strip in air. In each instance, the raw transmission images were recorded on DuPont Cronex 4 film, exposed in a cassette with detail speed intensifying screens. These radiographs were then photoreduced onto Kodak high resolution plates, which were processed as phase holograms.

The Imaging Process

The imaging process can be fully understood in terms of the concepts of projection and backprojection, as depicted in Fig. 2. In the projection step, the volume around each point in the object attenuates the incident x-ray flux in accordance with the average absorption coefficient over the volume. This attenuation modulates a component of the flux over a Fresnel zone pattern region of the image. This process is most easily analyzed by thinking in terms of an object (such as that shown in Fig. 2a) consisting of a few pinholes in an opaque sheet. The lateral position of the Fresnel zone pattern images clearly corresponds to the lateral position of the pinholes, while depth is recorded by the scale of the Fresnel pattern image.

The raw image cast by a Fresnel zone pattern source obviously suffers from poor registration among the various spatial frequency components, because a pinhole is rendered as a scaled image of the source. This places the high spatial frequency components (the finer rings of the Fresnel zone pattern image) far away from the center of the image. To reconstruct a sharp image, it is necessary to shift each frequency component the appropriate distance back towards the center. One way to accomplish this is to backproject the raw image onto the source, as is shown in Fig. 2b. Since the detected image carries no trace of the direction from which each detected x-ray arose, each detected x-ray photon must be uniformly backprojected over the entire Fresnel pattern source. This creates an objectionable background in the reconstituted image. Nonetheless, backprojection definitely sharpens up the image, since the "density" of the backprojection increases twofold within the resolution volume about the pinhole images. This peaking occurs, because outside of the resolution volume corresponding to the pinhole, the backprojection is mismatched to admissible source regions (Figs. 2c, d and e). Viewed in two dimensions as in Fig. 3, the backprojection

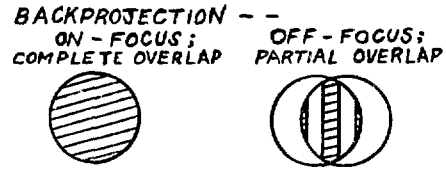

FIGURE 3

procedure is recognized as an autocorrelation of the raw image with the source function, and the sharpening of the raw image arises because the source pattern possesses a sharply peaked autocorrelation function.

The objectionable background which detracts from the backprojected image arises because the Fresnel zone pattern source behaves, in part, as a large, uniform disk source. The background can therefore be reproduced by recording an additional image cast by a uniform disk source. If the proper proportion of this additional image is subtracted from the raw Fresnel zone image, the background component is removed from the backprojected image. Later we shall see that this background subtraction may be implemented by replacing the on-axis Fresnel zone pattern source by an off-axis section of a Fresnel zone pattern, and by interposing a (properly scaled and oriented) lead grating between the off-axis source and the detector.

The Imaging Process MTF

It is worthwhile to analyze the operations of projection and backprojection through the frequency domain concept of MTF (the modulation transfer function). First, notice that the "output" of the projection is the "input" for backprojection, so the MTF for the overall imaging operation is the product of the projection MTF with the MTF for backprojection. This observation leads directly to a demonstration that the MTF for the overall "in focus" imaging process is positive. (A positive MTF indicates that all of the sinusoidal image components are properly registered with one another; a negative MTF corresponds to components which are misregistered by half a cycle, or "phase reversed".) The demonstration goes as follows: When an object slice is projected onto the detector and then backprojected onto the original slice plane, the MTFs for both operations turn out to be identical, so the overall MTF is just the square of the projection MTF. In the language of electrical engineering, backprojection is a "matched

filter" for the raw projected image.

The first job in calculating the overall MTF is to find the point spread functions (PSF) for projection and backprojection. As usual, the projection and backprojection MTFs are calculated by Fourier transforming the corresponding PSFs. It is tempting to accept the projection PSF in its form on the detection plane: (See Fig 2.)

$$\text{projection PSF(r) as found on the detector} = \cos\left[\pi\left(\frac{S_1}{S_2}\cdot\frac{r}{R}\right)^2\right]\cdot \text{circ}\left(\frac{S_1}{S_2}\,\frac{r}{R}\right) \quad (1)$$

(The notation is as follows: R, outside radius of the source, r_1, inside radius of the smallest source zone; s_1, object slice to source distance; s_2, object slice to detector distance; $D = s_1 + s_2$.) However, we are really interested in resolution within a given object slice, so a factor of (D/s_1) must be included as a scale parameter, to account for the magnification of an object slice on the detector plane:

$$\text{projection PSF(r) (interpreted on an object slice a distance } s_2 \text{ from the detector)} = \cos\left[\pi\left(\frac{D}{S_2}\cdot\frac{r}{r_1}\right)^2\right]\cdot \text{circ}\left(\frac{D}{S_2}\cdot\frac{r}{R}\right) \quad (2)$$

The backprojection PSF does not present this problem because it is directed within the object space:

$$\text{PSF(r) of backprojection a distance } s_2' \text{ inside object space from the detector plane} = \cos\left[\pi\left(\frac{D}{S_2'}\cdot\frac{r}{r_1}\right)^2\right]\cdot \text{circ}\left(\frac{D}{S_2'}\cdot\frac{r}{R}\right) \quad (3)$$

As anticipated, if $s_2 = s_2'$, the PSFs (and hence the MTFs) are identical; if $s_2 \neq s_2'$, the overall MTF is no longer a square, and hence the out-of-focus imaging is degraded by misregistrations among the frequency components.

The Fourier integral calculation of the exact MTFs is straightforward, but tedious, because of the large number of parameters, r_1, s_2, ... etc; in order to emphasize the concepts, these details are relegated to the Appendix. In the Appendix it is shown that the projection (and the backprojection) MTF has the following approximate functional dependency on spatial frequency f:

$$\text{projection MTF (or backprojection)} \leftrightarrow \sin(\beta f^2)\cdot \text{circ}(f/f_1) + \text{(a "DC" spike)} \quad (4)$$

The spike at f = 0 arises, because of the bias factor of 1/2 present in the projection (and the backprojection) PSF. The circ function cuts off the MTF at a limiting frequency f_1, which is determined by the width of the finest rings of the source. The parameter β varies with the distance s_2 of the object slice from the detector. If the previously discussed background subtraction step is applied - to both projection and backprojection - the "DC" spikes are removed from the MTFs. The overall MTF then takes the form:

$$\text{overall MTF after background subtraction} \leftrightarrow \sin(\beta f^2)\sin(\beta' f^2)\,\text{circ}(f/f_1)\cdot\text{circ}(f/f_1') \quad . \quad (5)$$

In the case of in-focus imaging, $\beta = \beta'$, and the overall MTF becomes a square.

In a noise-free imaging situation, the ideal MTF would be unity; noise is always present in radiologic imaging, so the MTF must be cut off above the highest frequency of interest. An in-focus MTF like $\sin^2(\beta f^2)\,\text{circ}(f/f_1)$ is deficient, because it completely fails to image the spatial frequencies at the zeros of the sine function. A much better MTF would be $(\sin^2(\beta f^2) + \cos^2(\beta f^2))\text{circ}(f/f_1))$, because $\sin^2\theta + \cos^2\theta = 1$. This MTF can be synthesized by including an additional Fresnel zone pattern source with a sine (in contrast to a cosine) dependency. With the addition of a term from a sine source, the out-of-focus MTF takes on the form

$$\text{out-of-focus MTF} \leftrightarrow \cos(\beta-\beta')f^2)\,\text{circ}(f/f_1)\text{circ}(f/f_1'). \quad (6)$$

It would be quite a nuisance record raw images cast by a sine source, a cosine source and a uniform disk source. The next section explains how this nuisance is avoided by using an off-axis section of a Fresnel zone pattern for a source, and by introducing a lead grating between source and detector.

Imaging with an Off-Axis Fresnel Source

Figure 4 shows the imaging configuration used with an off-axis Fresnel zone pattern source. A peephole is shown in the detection plane; from this vantage

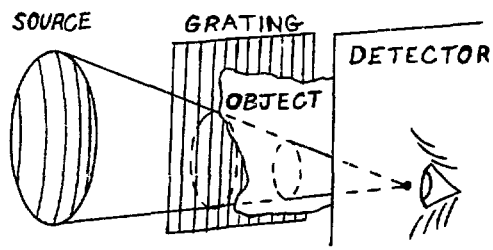

FIGURE 4

point, the source is seen masked by the lead grating, and the moiré between the grating and off-axis source is - an on-axis Fresnel zone pattern source! This occurs because an off-axis Fresnel pattern, $\cos(\alpha|\vec{r}-\vec{r_c}|^2)$ can be regarded as sinusoidal carriers, $\sin(2\alpha\vec{r}\cdot\vec{r_c} + |\vec{r_c}|^2)$ and $\cos(2\alpha\vec{r}\cdot\vec{r_c} + |\vec{r_c}|^2)$ modulated by on-axis Fresnel zone patterns, $\sin(\alpha|\vec{r}|^2$ and $\cos(\alpha|\vec{r}|^2)$:

$$\cos(\alpha|\vec{r}-\vec{r_c}|^2) = \sin(\alpha|\vec{r}|^2)\cdot\sin(2\alpha\vec{r}\cdot\vec{r_c} + |\vec{r_c}|^2) + \cos(\alpha|\vec{r}|^2)\cdot\cos(2\alpha\vec{r}\cdot\vec{r_c} + |\vec{r_c}|^2). \quad (7)$$

Masking an off-axis Fresnel pattern with a lead grating having the same spatial frequency as the carriers, $2\alpha\vec{r_c}$, therefore exposes the on-axis Fresnel zone pattern modulation. The phase of this on-axis Fresnel pattern source varies with the phase or registration of the lead grating.

Returning to Fig. 4, note that the frequency of the lead grating is chosen so that, as viewed from the detector plane peep-hole, it matches the carrier frequency of the off-axis source. Because the grating and source are in different planes, as the peep-hole is scanned across the detector, the phase of the on-axis Fresnel pattern moiré rapidly varies because of parallax between the grating and the source. By using a sufficiently far off-axis Fresnel zone pattern source and a sufficiently fine grating, this change of phase in the source pattern can be made to occur more rapidly across the detector than changes in the projection image due to the object structure. Because the phase of the source does not vary as the peep hole is scanned parallel to the bars of the grating, the raw images cast

along a discrete set of narrow strips on the detector sample the projection of the object from a fixed source pattern, for example, $(1/2 + 1/2 \cos(\alpha r^2)) \cdot \mathrm{circ}(r/R)$. Interleaved halfway between these strips is another set of strips which correspond to the projection of the object with the source pattern $(1/2 - 1/2 \cos(\alpha r^2)) \cdot \mathrm{circ}(r/R)$. The difference between these two sets of sampled projection images isolates the image corresponding to a cosine Fresnel source, without a background component. Similarly, the projection image corresponding to a sin Fresnel source, without a background, may also be isolated. Thus, the raw image cast with the off-axis system provides the same data base as the on-axis system collects with three separate raw images.

In terms of the holographic analogy, the on-axis system corresponds to Gabor holography, the off-axis system to Leith-Upatnieks holography.[3]

Fluorescent Sources

The intrinsic efficiency of fluorescent x-ray emission is quite high: for targets with atomic numbers greater than 40, more than 75 percent of the x-rays absorbed by a K shell photoelectric process result in the emission of K_α or K_β fluorescent x-rays. This is high compared to the efficiency (about one-half percent) of bremsstrahlung production in conventional rotating anode tubes. Consequently, there is no heat dissipation problem associated with fluorescent targets.

Although the intrinsic efficiency of fluorescent x-ray production is high, a conventional, small area fluorescent source collects only a fraction of the total emission from an excitation source. Since a coded fluorescent source can be made much larger in area, the overall conversion efficiency is more practical. A detailed calculation shows that a coded Barium source with 20 percent emission purity attains an average output of one K x-ray for every 10,000 electrons (125 KeV) incident at the primary target.

If alternate zones of the Fresnel source pattern are composed of two different fluorescent materials, for example, BaO and CeO_2, the radiation from both sets of rings is absorbed equally well by all chemical elements except iodine and xenon, because these elements have their K edge between the Barium K_α and the Cerium K_α emissions. Therefore, this source is specific to iodine and xenon. Other elements are not imaged in the reconstruction.

Noise Considerations

Consider once again the view of the object and source from a peep hole on the detector (Figs. 2b and 4). Imagine that the object is partitioned into many resolution volumes. A large area of the object, containing many of these resolution volumes, is within the line of sight with the source. Each detected x-ray photon is relatively valueless in measuring the x-ray absorption in any given resolution volume; in fact, it is most likely that the photon did not even pass through the resolution volume of interest, because there are so many other rays leading through the object to the detector!

In short, although a large source can generate a proportionately large flux, this is completely offset by the proportionately large increase in the section of the object a detected photon may have traversed - unless:

1. the object is like a slit or a pinhole, so that the paths taken by detected photons are well defined, in spite of the large source area. Or unless:
2. a background noise source dominates the imaging process.

In case (2), the quantum noise from the background dominates the image unless the transmission source is powerful enough to provide a larger flux over the entire projection area on the detector. If a conventional source cannot provide enough flux, a more powerful, larger area coded source is the answer.

Appendix

The PSF of the projection is given in Eq. (2) as the product of two factors. By the convolution theorem, its Fourier transform (the MTF of the raw projection image) is the convolution between the Fourier transforms of each factor:

$$\text{the projection} = \left(\frac{S_1 r_1}{D}\right)^2 \left(\frac{S_1 R}{D}\right)^2 \cdot \sin^2\left[\pi\left(\frac{S_1 r_1}{D} f\right)^2\right] \; * \; \text{MTF(f)} \; \frac{J_1\left(2\pi f \left(\frac{S_1 R}{D}\right)\right)}{2\pi f \left(\frac{S_1 R}{D}\right)} \qquad (8)$$

The spatial Fresnel factor transforms into a Fresnel factor in frequency; the circ factor transforms into a familiar Bessel factor. The Bessel function factor is sharply peaked, and so for small values of frequency, f, the convolution between the Fresnel factor and the Bessel factor merely reproduces the oscillations in the Fresnel factor. These oscillations, however, increase rapidly with f, and they are ultimately washed out at frequencies greater than those corresponding to the finest zones of the PSF. This frequency f_1, is given by:

$$\text{limiting frequency of the PSF, } f_1 = \frac{R}{r_1^2}\left(\frac{D}{S_1}\right)^2 . \qquad (9)$$

The MTF can be written in the approximate functional form:

$$\text{projection MTF(f)} \leftrightarrow \sin(\beta f^2) \cdot \mathrm{circ}(b/b_e) + \text{(a "DC" spike)} . \qquad (10)$$

The DC spike is added on here for correctness. It arises from a term of $1/2 \cdot \mathrm{circ}(D \cdot r/s_2 \cdot R)$ which belongs in Eq. (2) unless a background subtraction has been performed to the projection image.

References

1. L. Mertz, Transformations in Optics, (John Wiley and Sons, 1965).
2. G. A. Vanasse and H. Sakai, "Fourier Spectroscopy," Progress in Optics (North-Holland), Vol. VI, Chap. VII, p. 261 (1967).
3. H. H. Barrett and F. A. Horrigan, Applied Optics, Vol. 12, p. 2686 (November, 1973).

Proceedings, ERDA X-and Gamma-Ray Symp. Ann Arbor, MI, May 19-21, 1976 (Conf 760539)

A PROTOTYPE GAMMA RAY CAMERA FOR NUCLEAR MEDICINE BASED ON A HIGH PURITY GERMANIUM DETECTOR*

P. A. Schlosser, D. W. Miller, M. S. Gerber, J. W. Steidley, A. S. Zolnay and A. H. Deutchman
The Ohio State University
Department of Nuclear Engineering
206 W. 18th Avenue
Columbus, Ohio 43210

Summary

A prototype gamma ray camera system has been constructed based on high purity germanium detectors fabricated with orthogonal strip electrodes. Position sensitivity is obtained by connecting each contact strip on the detector to a charge dividing resistor network. The camera requires only three amplifier channels to measure the energy and location of gamma ray events. Excellent energy and spatial resolution have been achieved by cooling the resistor networks to 77°K and by proper selection of noise filtering parameters in the pulse shaping amplifier circuitry. This paper presents theoretical and experimental results obtained in the investigation of the charge splitting camera concept. These restuls indicate that it is possible to construct a high resolution germanium camera system which has sufficient field of view and sensitivity for routine use in nuclear medicine.

I. Introduction

In nuclear medicine the principal gamma ray imaging instrument is the NaI(Tl) scintillation camera, often referred to as the Anger camera. This instrument, which was first introduced by H. O. Anger[1] in 1956, has proved to be a powerful diagnostic tool and has led to the development of many innovative nuclear medical techniques for the diagnosis of disease. However, as has been shown by Anger[2], the in vivo resolution of the scintillation gamma camera is inherently limited by its energy resolution (about 20 keV for the 140 keV gamma rays of 99m-Technetium).

The scintillation camera is capable of resolving line sources and point sources in a nonscattering medium which are separated by less than 6 mm. For the same sources 7 to 10 cm deep in a scattering medium, however, the resolving distance widens to about 15 to 20 mm. Anger[2], Beck[3] and others have shown that the degradation of resolution is due to photons which Compton scatter with small energy loss in the patient to a trajectory allowing them to enter the collimator of the camera and be accepted in the pulse height analysis window. If the energy loss of the photon in the Compton interaction is less than the energy resolution of the imaging system, then the scattered photon will be recorded in the image as a false event originating at the point of the Compton interaction. With energy resolution of about 20 keV, photons which directionalize by Compton scattering at angles from 0° to 70° are recorded in the scintillation camera image and lead to significant loss of image contrast.

In order to improve the diagnostic capability of nuclear medicine, it has been suggested that germanium[4,5,6] be employed as the radiation detector in a gamma imaging instrument, since germanium detectors exhibit a factor of 5 to 10 improvement in energy resolution. With energy resolution of 3 keV or less for photon energies of interest, semiconductor detectors offer a fundamental solution to the problem of image quality and contrast. The importance of energy resolution for the improvement of nuclear medicine images has been documented in both theoretical[4] and experimental[7,8] studies.

II. The Charge Splitting Detector Concept

Our research has focused upon the development of position sensing germanium detectors which operate in the charge splitting mode. These detectors are based upon an orthogonal strip detector structure which has been studied previously by Parker[9,10] and Detko[11,12] and is shown in Figure 1. Both Parker and Detko have used a separate preamplifier-amplifier channel to read out each strip on the detector. Recently, Kauffman, et al.[13,14], have used a delay line readout method. Our work[15-18] has involved the investigation of orthogonal strip detectors which are read out using the resistor-divider network illustrated in Figure 1. The grooves between strips

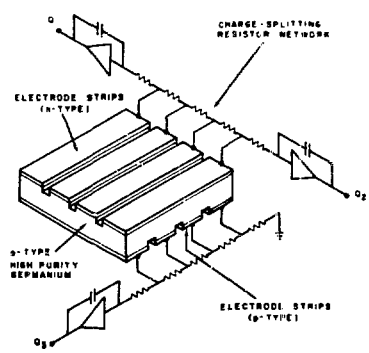

Figure 1. The charge splitting orthogonal strip detector.

create a matrix of relatively isolated diodes which are addressed in row and column fashion by the orthogonal set of electrodes. The function of the resistor network is to electronically locate the row and column positions of individual gamma ray interactions, using just three amplifier channels. In this sense, a pulse of charge which emerges from a given electrode will divide into the resistor network in relation to its location along the resistor string. The amount of charge, Q_1 or Q_2, which arrives at either end of the upper resistor network fixes the original location of the gamma ray event in one dimension and Q_3 provides the position in the second dimension. Energy information is obtained by summing Q_1 and Q_2.

Six orthogoanl strip detectors have been fabricated and evaluated in our laboratories. A photograph of one of these is shown in Figure 2, which is

*This work has been supported by the National Institutes of Health, National Institute of Neurological Diseases and Stroke, Contract No. NO1-NS-2-2323.

a 14 x 14 strip detector measuring 3 cm x 3 cm x 0.5 cm thick. The methods used in fabricating

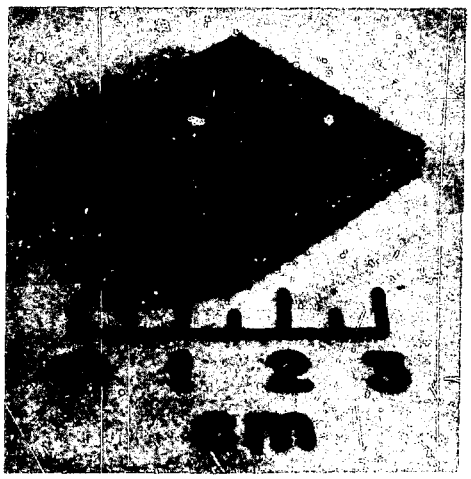

Figure 2. Photograph of the 3 cm x 3 cm x 0.5 cm thick detector which has 14 electrode strips on each side, spaced on 2 mm centers.

these detectors are outlined in a paper presented by Zolnay, et al. at this symposium.

III. The Electronic Readout System

The electronic readout and image display system for the charge splitting detector is shown in Figure 3. The detector and charge dividing resistor string

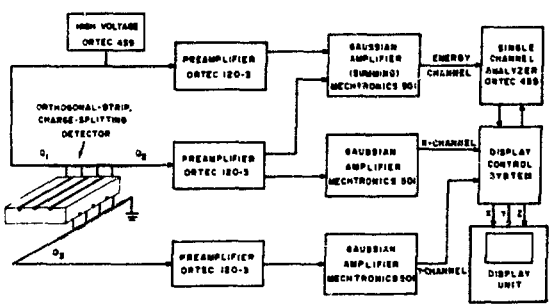

Figure 3. The electronic signal processing system which was used to evaluate charge splitting orthogonal strip detectors.

can be modeled[18] as a two-surface diffusive transmission line. Analysis of the noise properties of the model show that the minimum spatial resolution is obtained by using antisymmetric Gaussian Trapezoidal filtering. The FWHM spatial resolution is given by

$$\Delta X = \frac{3.11\ wL}{Eq}\left(\frac{4kT_D\tau_o}{R_D}\right)^{1/2}, \qquad (1)$$

where T_D is the detector temperature, L the length of the detector, E the energy of the incident gamma ray in keV, and τ_o is the peaking time of the Gaussian Trapezoidal filter. For minimum spatial resolution the peaking time is set equal to $.1\ R_DC_D$, where R_D is the resistance of one charge dividing string.

The best energy resolution is obtained by using a Gaussian filter operating at a long peaking time. The FWHM noise resolution in keV is

$$\Delta E(keV) = \frac{7.1 \times 10^{-3}}{q}\left(.88\ qi_D\tau_o + \frac{4kT_DC_D^2R_D}{6\tau_o}\right)^{1/2} \qquad (2)$$

where i_D is the detector leakage current. If the leakage current is less than 1 nA and τ_o is limited to a maximum of 6-8 μseconds, the leakage current term in Equation (2) can be neglected.

IV. Experimental Results

Several small prototype camera systems have been evaluated. The first one incorporated a position sensing detector which is 2 cm x 2 cm x 0.5 cm thick. This detector was grooved by cutting 10 parallel electrode strips on one side orthogonal to 10 parallel strips on the reverse side. The strips were placed on 0.080 in. centers and the grooves measured 0.015 in. wide and 0.050 in. deep. This 10-strip by 10-strip detector had 5.5 keV (FWHM) energy resolution and 1.66 mm (FWHM) noise limited spatial resolution at a gamma ray energy of 122 keV. A second prototype employed a 9 x 9 strip detector having strips on 0.10 in. centers. The detector had a noise limited energy reduction of 5.4 keV and a spatial resolution of 1.7 mm at a gamma ray energy of 122 keV. The measured results of these two and other detector systems correlates well with those calculated from the analytical model.

Imaging experiments were performed with each prototype camera. These experiments, illustrated in the images of Figure 4, demonstrated that two-point radioisotope sources with a center-to-center spacing of 2.15 mm could be clearly resolved. A number of other phantoms were also used to demonstrate the energy and spatial resolving capability of the germanium gamma ray camera concept.

V. Conclusions

The results of this research program have demonstrated the feasibility of constructing a germanium gamma ray camera for use in clinical nuclear medicine. This has led to a proposed design of a large scale clinical demonstration camera.[17] The proposed clinical camera will have an approximately 36-square-inch detector array (shown in Figure 5 inside of the usable field of view of an 11-1/2-inch scintillation camera) and is projected to exhibit an energy and spatial resolution of 3.5 keV and 3.8 mm, respectively. The camera detector element will be assembled from sixteen 3.8 cm x 3.8 cm x 2 cm strip electrode detectors electrically connected in quadrants measuring 7.6 cm x 7.6 cm.

The assembly of the proposed germanium camera head is illustrated in Figure 6, which shows a cutaway view of the shell of the head containing the detector array and environmental support system. The camera head encloses the vacuum chamber, preamplifier section, closed cycle detector cooling unit, and vacuum pump.

In summary, the feasibility of constructing a clinical semiconductor gamma camera employing an array of charge splitting orthogonal strip detectors has

been demonstrated. Energy and Spatial resolution values of less than 4 keV and 4 mm, respectively, are possible in such a system and would result in a significant improvement over scintillation cameras in image quality and clinical resolution.

References

(1) H. O. Anger,"Scintillation Camera," Rev. Sci. Instr. 29, 1958, p. 27.

(2) H. O. Anger and D. H. Davis, "Gamma Ray Detection Efficiency and Image Resolution in Sodium Iodide," Rev. Sci. Instr. 35, 1964, p. 693.

(3) R. N. Beck, M. W. Schuh, T. D. Cohen and N. Lembares, "Effects of Scattered Radiation and Scintillation Detector Response," Medical Radioisotope Scintigraphy, Vol. I, Vienna, IAEA, 1969, p. 595.

(4) R. N. Beck, M. W. Schuh, T. D. Cohen, and N. Lembares, "Medical Radioisotope Scintigraphy," Proccedings of a Symposium, IAEA, I, August 1968, p. 595.

(5) R. P. Parker, E. M. Gunnersen, J. L. Wankling and R. Ellis, "Medical Radicisotope Scintigraphy," Proceedings of a Symposium, IAEA, 1, August 1968, p. 71.

(6) J. F. Detko, Radiology 104, 1972, p. 431.

(7) A. B. Brill, J. A. Patten and R. J. Baglan, "An Experimental Comparison of Scintillation and Semiconductor Detectors for Isotope Imaging and Counting," IEEE Trans. Nuc. Sci. NS-19, No. 3, 1972, pp. 179-190.

(8) M. M. Dresser, G. F. Knoll, "Results of Scattering in Radioisotope Imaging," IEEE Trans. Nuc. Sci. NS-20, No. 1, 1973, pp. 266-270.

(9) R. P. Parker, E. M. Gunnersen, J. L. Wankling and R. Ellis, "A Semiconductor Gamma Camera with Quantitative Output," Medical Radioisotope Scintigraphy, Vol. I, IAEA, Vienna, 1969, p. 71.

(10) R. P Parker, E. M. Gunnersen, R. Ellis and J. Bell, "A Semiconductor Gamma Camera," Medical Radioisotope Scintigraphy, Vol. I, IAEA, Vienna, 1973, p. 193.

(11) J. F. Detko, "A Prototype, Ultra-Pure Germanium, Orthogonal-Strip Gamma Camera," Medical Radioisotope Scintigraphy, Vol. I, IAEA, Vienna, 1973, p. 241.

(12) J. F. Detko, "Progress Toward a Stable Orthogonal Strip Germanium Gamma Camera," IEEE Trans. Nuc. Sci. NS-23, No. 1, 1976, pp. 538-542.

(13) L. Kaufman, G. A. Armantrout, R. C. Camp, J. H. McQuaid and S. P. Swierkowski, "Delay Line Readouts for Intrinsic Germanium Medical Imaging Camera," IEEE Trans. Nuc. Sci. NS-21, No. 1, February 1974, p. 652.

(14) L. Kaufman, R. Hattner, D. Price, S. Swann, J. Huberty, G. Armantrout, D. Camp, J. McQuaid and J. H. Ewins, "Imaging with a Small Ultra-Pure Germanium Gamma Camera," IEEE Trans. Nuc. Sci. NS-21, No. 1, February 1974, p. 652.

(15) P. A. Schlosser, D. W. Miller, M. S. Gerber, R. F. Redmond, J. W. Harpster, W. J. Collis and W. W. Hunter, Jr., "A Practical Gamma Ray Camera System Using High Purity Germanium," presented at the 1973 IEEE Nuclear Science Symposium, San Francisco, November; also published in IEEE Trans. Nuc. Sci. NS-21, No. 1, February 1974, p. 658.

(16) D. W. Miller, P. A. Schlosser, M. S. Gerber, R. F. Redmond, and W. W. Hunter, Jr., "A Prototype Gamma Camera Systedm Based on a Strip-Electrode, High Purity, Germanium Detector, presented at the 1974 Society of Nuclear Medicine Meeting, San Diego, California, June 1974.

(17) P. A. Schlosser, M. S. Gerber, D. W. Miller and A. H. Deutchman, "A Large Scale Medical Gamma Camera System Based on Orthogonal Strip, High Purity Germanium Detectors," presented at the IEEE Nuclear Science Symposium, Washington, D.C., December 1974.

(18) M. S. Gerber, D. W. Miller, B. Gillespie, and R. S. Chemistruck, "Instrumentation for a High Purity Germanium Position Sensing Gamma Ray Detector," IEEE Trans. Nuc. Sci., NS-22, No. 1, February 1975, p. 416.

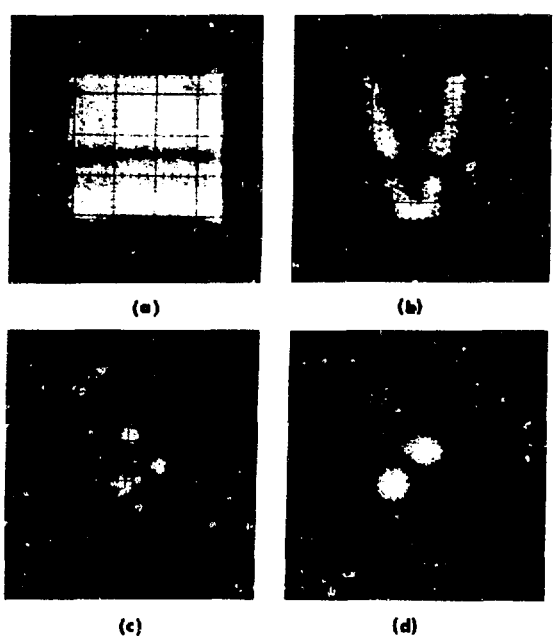

Figure 4. Photographs of images made using the 10 x 10 strip detector. Photograph (a) is a flood field image of the detector. Photograph (b) is an image of a V-shaped cut in a lead sheet. Photograph (c) is an image of three 1.25 mm diameter holes separated by 3.5 mm. Photograph (d) is an image of two 1.25 mm diameter holes separated by 2.15 mm.

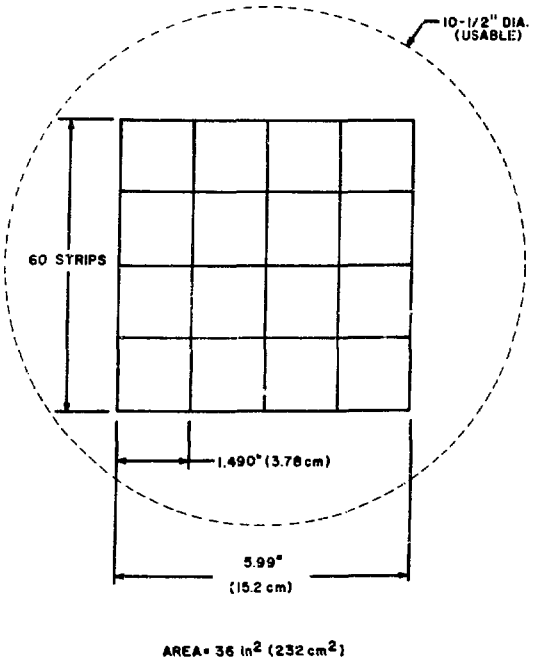

Figure 5. Illustration of the proposed germanium detector array and dimensions. The array is shown inside of the usable area (dashed circle) of a scintillation camera.

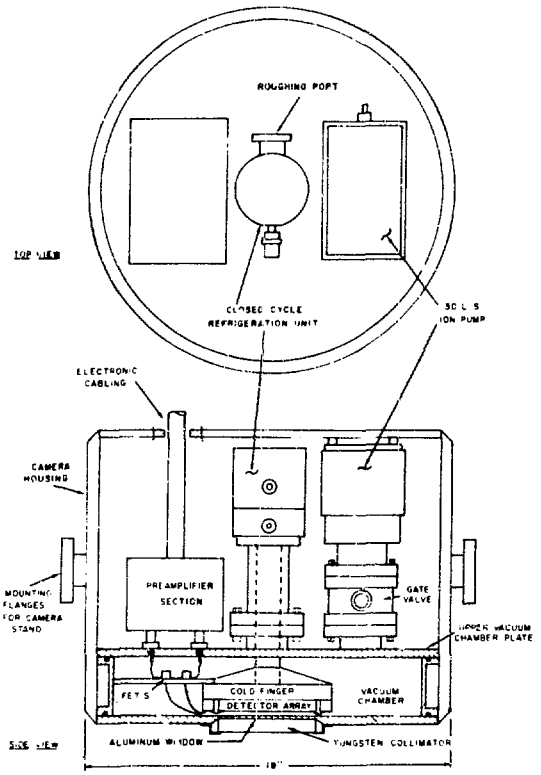

Figure 6. Cutaway view of the mechanical components of the proposed germanium camera head.

Proceedings, ERDA X-and Gamma-Ray Symp. Ann Arbor, MI, May 19-21, 1976 (Conf 760539)

A PORTABLE MULTIWIRE PROPORTIONAL CHAMBER IMAGING SYSTEM FOR HIGH RESOLUTION ^{125}I IMAGING

Joel L. Lazewatsky[†], Richard C. Lanza,[*°] Brian W. Murray[*+]

Craig Bolon[°], Ronald E. Burns,[+] Massimiliano Szulc[+]

Department of Nuclear Engineering[+] and the
Laboratory for Nuclear Science[°]
Massachusetts Institute of Technology
Cambridge, Mass. 02139

Physics Research Laboratory*
Massachusetta General Hospital
Boston, MA 02114

Summary

A dedicated multiwire proportional chamber aystem designed to image ^{125}I labeled venous thrombi is described. The chamber is filled with a Kr-CO_2 gas mixture at one atmosphere pressure and utilizes an externally mounted delay line readout. A pair of crosaed x-ray grids form a collimator which yields an optimum system efficiency of 3.1×10^{-4} for a fixed spatial resolution of 0.74 cm. The chamber is further designed to be light-weight and portable for in-hospital use.

Introduction

Despite the long history of the proportional chamber in the measurement of ionizing radiation, position-sensitive multiwire proportional chambers (MWPC) date only from approximately 1968.[1] It quickly became apparent that not only were such devices practical, but they offered as well a number of advantages over other position-sensitive radiation sensing devices in terms of cost, flexibility and spatial resolution.

Early in the era of renewed proportional chamber instrumentation development, it was suggested that the MWPC would have significant imaging applications in nuclear medicine and radiology.[2] The prospect of medical application remains undiminished and development has proceeded in many laboratories tc solve the attendant technical problems associated with in-hospital use.[3] Most devices reported to date, however, have been primarily laboratory instruments designed for general nuclear medicine applications.

The major advantages of a MWPC as compared with conventional scintillation cameras are low cost and flexibility in design, allowing a dedicated MWPC for a particular radioisotope and/or clinical application. The clinical advantages of a dedicated specialized MWPC include around-the-clock availability, bedside operation and inherently digital image information so that diagnostic information can be readily quantified.

Clinical Applications

The detection of deep venous thrombi by means of external detection of ^{125}I-labeled fibrin concentrations has provided useful clinical data.[4,5] The usual detection method[6] involves the repeated monitoring of a number of locations on the patient's leg performed using a hand-held 2" x 2" NaI(Tl) detector. This simple technique has significant drawbacks in detecting small thrombi (1-2 cm in length) or thrombi near healing surgical wounds[7] when compared to advanced X-ray venography.[8] Clearly the problem is a result of the poor spatial resolution of a single 2" x 2" NaI detector given the relatively low ratio of thrombus activity to blood pool or wound activity. Obtaining a one or two-dimensional image with a resolution better than 1 cm in both dimensions would enable the visualization of small thrombi by improving the spatial signal to noise ratio.

A tailored multiwire proportional chamber seems a reasonable approach to the achievement of such improvement. It has been shown[2] that spatial resolutions of the order of a few millimeters are readily achieved with distributions of low energy photon emitters such as ^{125}I (primarily 27 KeV $K_{\alpha 1}$ x-rays). Moreover a light, portable instrument possesses advantages in that it may be brought to the bedside of a post-surgical patient and positioned with a minimum of discomfort. Also, the relatively low cost of this sort of instrument (as compared with presently availsble scintillation cameras) makes the dedication of an imaging system to this one measurement quite attractive.

Chamber Construction

Figure 1 depicts the general arrangement of the electrodes and the overall dimensions of the assembled and electrically shielded detector in its ultimate form. Table 1 liats the characteristic dimensions, materials and electrical parameters of the chamber-delay line system. Not shown in Figure 1 are the delay lines which are mounted on a printed circuit board beneath the backplane and outside the chamber volume. Connections are made from the upper and lower cathodes to the delay line board via four fifty-conductor Scotchflex cables and card-edge connectors. The construction of each frame is by means of four layers of G10 glass-epoxy strips laminated with Shell Epon resin and overlapping at the corners in a technique described elsewhere.[9] The anode and spacer frames, are an exception to this in that substituted for

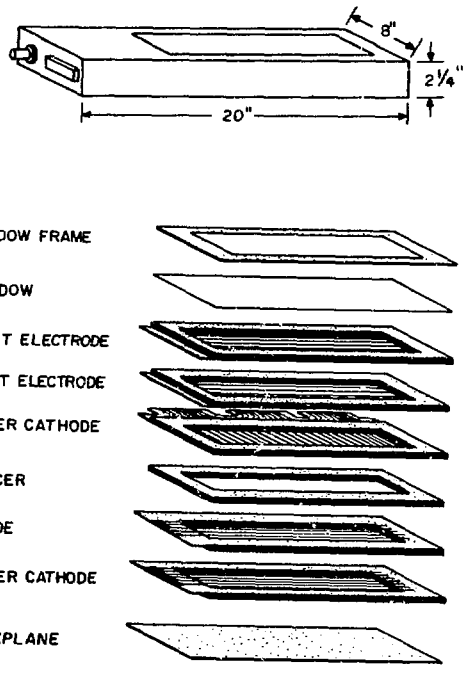

Figure 1 (above) External View of Chamber Including Shielding But Without Collimator and (below) Exploded View

the second layer beneath the wire-side of the frame is a layer of 0.8 mm brass protruding 3.2 mm into the gas forming a guard strip.

Table 1

Chamber Dimensions, Parameters and Materials

Exterior dimensions: 40.6 x 20.3 x 5.7 cm^3

Active volume: 31.1 x 10.8 x 4.0 cm^3

Anode-cathode spacing: 0.58 cm

Anode: 0.02 mm gold plated tungsten wire, 2.1 mm spacing, +3.0 KV.

Cathodes: 0.127 mm Cu-Be wire, 2.5 mm spacing, -300 V, -600 V.

Drift electrodes: 0.127 mm Cu-Be wire, 2.1 mm spacing, -300 V, -600 V.

Frame material: NEMA G10 fiberglass-epoxy, 1.78 mm

Backplane: NEMA G10, copper clad, 2 oz., -300 V.

Window: 0.051 mm aluminized mylar

Gas: Krypton, 90%; CO_2, 10%

Chamber capacitance: 167 pf

Delay lines: ESC Electronics, #200T401-10* 200 ohm impedence, 40 taps 10 ns. per tap

Delay line-chamber coupling: direct

Krypton (Z = 36) was chosen as the noble gas to be used due to its higher mass absorption coefficient for photons in the neighborhood of 30 KeV than that of Xenon (Z=54). This is a result of the energy of the Xenon K-absorption edge (34.6 KeV), which is above the energies of the X-rays of ^{125}I. The improvement in effective chamber efficiency is not, however, quite as dramatic as the increase in mass absorption would suggest. Inasmuch as Krypton has a 60% K-fluorescence yield, it may be expected that some fraction of the fluorescence photons produced will interact in the chamber. This will ultimately require circuitry to reject those events which produce two start pulses within the delay time of one delay line. Thus it has yet to be determined what increase in counting efficiency will result from using Krypton rather than Xenon.

Readout and Signal Processing

The analog readout arrangement presently being tested is depicted in figure 2. The

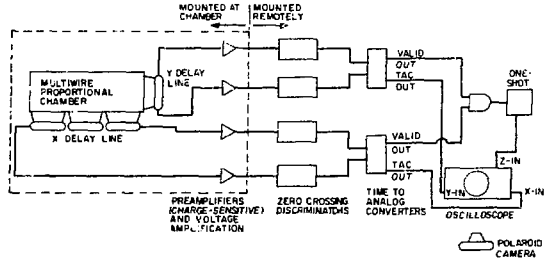

Figure 2 Analog MWPC Delay Line Readout System

delay lines are terminated using modified charge-sensitive amplifiers with electronically "cooled" terminations [10]. The signal then goes to standard tunnel diode zero-crossing discriminators (LRL 22X2151-P1). In the analog version, the time difference is converted to a pulse height via EG&G TH200A/n time-to-analog converters which is used to position an oscilloscope trace. The trace is then brightened only when a true event has occurred as determined by appropriate logic circuitry. The image is allowed to accumulate on Polaroid film using a Tektronix C-27 camera system.

In contrast to the relatively routine analog readout, the planned digital system (figure 3) directly digitizes the time difference using 250 MHz MECL counters yielding 4 ns. time resolution. The two numbers thus produced increment an appropriate location in the memory of a 16K minicomputer. The matrix of numbers which results may then be stored on tape and displayed on a 32 gray level CRT display which utilizes its own CCD memory to permit an adequate refresh rate.

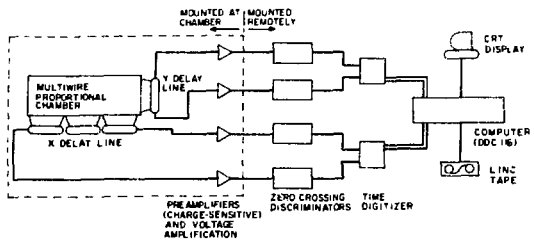

Figure 3 Digital MWPC Delay Line Readout System

It is hoped that all relevant programming may be accomplished via a high-level language such as FORTRAN which may readily be run on a machine of this sort. Subsequent versions may be further reduced in cost if an appropriate microprocessor-based computer system can be substituted for the minicomputer. All programming may then reside in read-only memory.

Collimator

Optimization

In order to optimize a system such as this one for greatest efficiency given the specified clinical situation, it is necessary to determine which parameters are dictated by physics and anatomy and/or feasibility and which may readily be varied. It is clear that the depth and size of the thrombus to be imaged are given in that they dictate, in large measure, the resolution (R) and the source-to-collimator distance (b). Additional quantities are primarily the materials properties (linear absorption coefficients) for the given X-ray energy.

Beyond these, all other parameters of the chamber-collimator system may be varied in such a manner as to maximize the ratio of detected counts to source photons. We have done this using a straightforward iterative optimization in BASIC. The program requires as input the linear absorption coefficients of all materials involved (septum, gas and any inter-septal material) the depth of the source and the desired resolution. It then calculates the optimal dimensions for a square-hole multichannel collimator given Anger's criteria[11] and iterates that optimization to determine the best chamber thickness consistent with the desired resolution and maximum efficiency.

The Optimal Collimator

When one considers a lead collimator with a spatial resolution of 0.5 cm for a thick detector (approx. 4 cm) and 30 KeV X-rays, severe mechanical limitations arise. Septa are less than 50 μm and channels less than 0.5 mm. It is clear that poured or corrugated lead collimators could not readily be built to these dimensions while maintaining necessary tolerances in terms of linearity.

Thus we have investigated a different construction method which does not have the disadvantages of the above techniques for this energy and solid angle. It is illustrated in figure 4 and consists essentially of two orthogonal laminated structures of alternating layers of high-Z (lead, e.g.) and low-Z

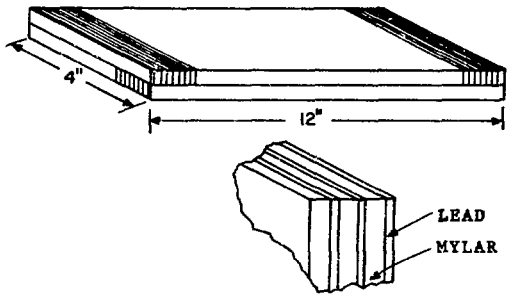

Figure 4 Laminated 2-Dimensional MWPC Collimator

(mylar, paper, e.g.) materials. Each laminated grid behaves as a one-dimensional collimator entirely independent of the other. The performance of a collimator in terms of transmission, septal penetration and resolution is entirely independent of its position between the source and detector. Thus it is clear that this collimator may be treated in essentially the same fashion as a square-hole multichannel collimator. Intuitively, what has been done is a separation of the two (orthogonal) dimensions of an "egg crate" collimator in a dimension over which their performance does not vary. In actual fact, there is a slight decrease in performance due to the additional source-to-collimator distance imposed by the additional thickness of collimator. For low energies, however, this is only a small fraction of the total source-to-detector distance and has little effect.

Quantitatively, Anger[11] has shown that the resolution of a square-hole multichannel collimator is given by

$$R = \frac{d(a_e + b + c)}{a_e} \qquad a_e = a - 2\mu^{-1} \qquad (1)$$

where "d" is the septal spacing, "a" the septum height, "b" the source-to-collimator distance, μ the septal linear X-ray absorption coefficient and "c" the detector half thickness. We define "c" not as the central plane of the detector medium but rather as the plane at which half of the total absorption has taken place. For highly absorptive materials this tends toward the collimator side of the detector medium, whereas for less absorptive materials it tends toward the center of the detector.

Equation 1 is not strictly accurate for this type of collimator. The geometric origin of (1) is evident in that $a_e + b + c$ is simply the source-to-detector-half plane distance. Thus the only a_e that is to be changed for our laminated collimator is the one in the numerator of the right side of equation 1.

Anger's expression for geometric

efficiency is

$$g = \frac{1}{4\pi}\left[\frac{d^2}{a_e(d + t)}\right]^2 \qquad (2)$$

where t is the septal thickness. It is clear that there is no parameter which will be altered by separation of the layers, since a_e is the septal height, not the collimator height.

Results of running the optimization with the above modification for lead septa, mylar spacer and 0.52 cm resolution are given in table 2 on the first line each of "resolution" and "system efficiency" for two different chamber sizes. Column one uses the optimal chamber as determined by our program.

Table 2

Chamber Thickness		9.4 cm	4.0 cm
System Efficiency	O:	1.73×10^{-4}	1.31×10^{-4}
	F:	4.03×10^{-4}	3.06×10^{-4}
	M:	1.27×10^{-4}	8.58×10^{-5}
Resolution	O:	0.517	0.456
	F:	0.835	0.739
	M:	0.472	0.418

O: Optimal F: "Fineline" (60/inch) M: "Microline" (80/inch)

Column 2 is the present chamber which is smaller in order to reduce its thickness and make positioning it under the leg of a recuperatint patient less difficult and less uncomfortable for the patient.

Practical Collimators

Building collimators of this type, although simpler than other methods, is still a considerable amount of work. However, if the resolution is not regarded as a precisely fixed quantity, then it is possible to use commercially available stationary X-ray grids with excellent results.

X-ray grids normally used for cleaning up scatter in medical radiographs are constructed in essentially the same fashion as the collimator described previously. We have made resolution and efficiency calculations for two stationary X-ray grids manufactured by Liebel-Flarsheim. The remaining entries of table 2 give the calculated resolution and efficiency of these two grids. If we then run the optimization and request the resolution given by the "Fineline" (F) collimator, the efficiency result is within 2% of that of the optimum collimator. That is, given the choice of spatial resolution, one cannot find a significantly better collimator of this sort.

We are presently testing a collimator made from a pair of "Finaline" 6:1 stationary grids kindly donated by Liebel-Flarsheim. These have yielded the expected FWHM of 0.75 cm (plus 0.2 cm for the diameter of the ^{125}I source used).

*Liebel Flarsheim, Sybron Corp., Cincinnati, OH

Count Rate Considerations

Calculations yield an overall system efficiency of 3.1×10^{-4}, or approximately 600 cpm/μCi. Thus a thrombus one inch long containing 0.3μCi of ^{125}I would yield 900 counts in five minutes in 4 resolution elements, or 225 counts/resolution element. The blood pool background might conservatively be estimated at 5μCi yielding 15000 counts in five minutes over all 412 resolution elements, or 36 counts per resolution element. This is a signal-to-noise ratio of nearly 6.3 to 1.

Conclusion

We have described the design and construction of a highly specialized multiwire proportional chamber system for imaging ^{125}I. Preliminary tests using Argon-CO_2 indicate that it should perform as expected once the initial problems are resolved. At present, we plan to evaluate the system with patients in collaboration with Dr. W. Harris at MGH using the analog readout system. However, it is anticipated that the digital system will offer a means to record and display a far wider dynamic range than is possible with Polaroid film and will permit more sophisticated treatment of the data, including background substraction and day-to-day comparisons.

Acknowledgements

We would like to express our thanks and appreciation to Dr. W.H. Harris of the MGH for providing the necessary clinical background. We would also wish to thank Mr. Robert Zimmerman for many helpful discussions. Two of us (J.L.L. and M.S.) wish to thank Prof. G.L. Brownell for his academic supervision and to acknowledge the support of the BME Fund through the Harvard-MIT Joint Program in Health Sciences and Technology. This work was supported by a grant from the Health Sciences Fund Inc., and in part by NIH grant #GM 22675.

References

1. G. Charpak, et al, Nucl. Inst. and Meth. 62 (1968) 262
2. S.N. Kaplan, Nucl. Inst. and Meth. 106 (1973) 397
3. C.J. Borkowski, and M.K. Kopp, IEEE Trans. Nucl. Sci. NS-19 (1972) 161
4. C. Flanc, et al, Brit.J. Surg. 55 (1968) 742
5. N.J. Browse, et al, Brit. Med. J.4 (1971)325
6. M.M. Kakkar, Arch. Surg. 104 (1972) 152
7. W.H. Harris, et al, N.E.J. Med 292(1975)665
8. K. Rabinov and F. Paulin, Arch. Surg. 106 (1972) 134
9. R.C. Lanza, and N. Hopkins, Nucl. Inst. and Meth. 102 (1972) 333
10. V. Radeka, IEEE Trans Nucl. Sci., NS-21 (1974) 51
11. Anger, H.O., ISA Trans. 5 (1966) 323

Proceedings, ERDA X-and Gamma-Ray Symp. Ann Arbor, MI, May 19-21, 1976 (Conf 760539)

APPLICATION OF A Ga-68/Ge-68 GENERATOR SYSTEM TO BRAIN IMAGING USING A MULTIWIRE PROPORTIONAL CHAMBER POSITRON CAMERA

R. S. Hattner, C. B. Lim, S. J. Swann, L. Kaufman, D. Chu, V. Perez-Mendez
University of California, School of Medicine
San Francisco, California
and
Lawrence Berkeley Laboratory
Berkeley, California

SUMMARY

A Ge-68/Ga-68 generator system has been applied to brain imaging in conjunction with a novel coincidence detection based positron camera. The camera consists of two opposed large area multiwire proportional chamber (MWPC) detectors interfaced to multichannel lead converter plates. Event localization is effected by delay lines.

Ten patients with brain lesions have been studied 1-2 hours after the administration of Ga-68 formulated as DTPA. The images were compared to conventional brain scans, and to x-ray section scans (CAT). The positron studies have shown significant mitigation of confusing superficial activity resulting from craniotomy compared to conventional brain scans. Central necrosis of lesions observed in positron images, but not in the conventional scans has been confirmed in CAT. The economy of MWPC positron cameras combined with the ideal characteristics of the Ge-68/Ga-68 generator promise a cost efficient imaging system for the future.

INTRODUCTION

Although a Ge-68/Ga-68 generator system with remarkable properties has been available for a decade, it has found little clinical utility because of the poor ability of conventional scintigraphic instrumentation to image annihilation photons (511 keV), and the unavailability of practical coincidence based positron cameras. Ge-68 has a 275 day $T_{\frac{1}{2}}$ and Ga-68, the daughter, has a 1.13 hour $T_{\frac{1}{2}}$. Thus, a single generator constitutes a 2 year supply of a high purity positron emitter (184% 511 keV photon/disintegration) with an ideal $T_{\frac{1}{2}}$ for physiologic imaging.

METHODS AND MATERIALS

An economical large area, large solid angle, positron camera using gas filled multiwire proportional chambers coupled to lead channel converters has been constructed and its imaging performance characterized.[1, 2] Use of the Ge-68/Ga-68 generator, its eluate formulated as Ga-68-DTPA, in conjunction with the MWPC positron camera follows.

Ten patients with brain lesions (primary neoplasms, 8; abscess, 1; metastases, 1) were studied 1.5-2 hours after administration of Ga-68 DTPA. 100-200K coincidence events were recorded over approximately 30 minutes. A single positioning with sagittal plane perpendicular to the detectors was used. Serial frontal images were reconstructed from the data set by determining the intersection of the annihilation vectors in planes separated by 1-2 cm after field uniformity correction, thresholding, and a single center-weighted smoothing, the images were displayed on the computers storage oscilloscope, and photographed with Polaroid film. Corroborative data included x-ray section scanning (CAT), conventional Tc-99m-DTPA scintigraphy, and surgical pathology in all patients.

RESULTS

The lesions were well visualized in eight patients. One glioma was poorly seen, and another glioma escaped detection because of technically suboptimal camera performance. The positron images demonstrated superb tomography. Positron images significantly mitigated the problem of interference of superficially increased activity from craniotomy in determining the presence of an intracranial lesion in conventional Tc-99m-DTPA scans, corroborated by CAT. Central necrosis of lesions shown in CAT, not evident in the Tc-99m-DTPA scans, was observed in the positron images (see Figure 1). Lesion extent appeared occasionally underestimated in conventional scans compared to the positron images and CAT. In this patient series the positron images, although crude, often provided more information than the conventional brain scans.

DISCUSSION

The MWPC positron camera potentially offers a number of advantages over the other systems. Some of these are: 1) low system cost; 2) low cost, large sensitive area detectors; 3) good efficiency for static imaging; 4) good spatial resolution; 5) good uniformity response; and 6) excellent tomography permitted by the large solid angle of large detectors.

Overall evaluation of diagnostic performance of the system, including patient factors suggest additional benefits. Ga-68 is conveniently obtained. The chemistry allows fabrication of a generator system, elutable every two hours, requiring replacement every 1.5-2 years. Delivery logistics and economic considerations of such a system permit very wide spread availability of the radiopharmaceutical. The low injected dose (1-2 mCi) required and the short $T_{\frac{1}{2}}$ result in a 50% reduction in radiation exposure compared to a conventional brain scan using 10-15 mCi Tc-99m.[3] A data set is accumulated from a single positioning of the patient, saving repositioning time. Planned system upgrading is anticipated to result in improved sensitivity and spatial resolution, the former to a degree permitting image deconvolution to subtract the influence of off axis planes.

ACKNOWLEDGEMENTS

Dr. Hattner is a Picker Scholar, James Picker Foundation, and Dr. Kaufman the recipient of a Career Development Award (N.I.H.-G.M.#70598). This work was supported by the RANN Division of the N.S.F. and the Cancer Research Coordinating Committee, University of California.

REFERENCES

1. Lim CB, Chu D, Kaufman L, et al: IEEE Trans Nucl Sci NS-22: 388, 1975.

2. Lim CB, Chu D, Kaufman L, et al: IEEE Trans Nucl Sci NS-21: 85, 1974.

3. M.I.R.D. Pamphlets, Society of Nuclear Medicine.

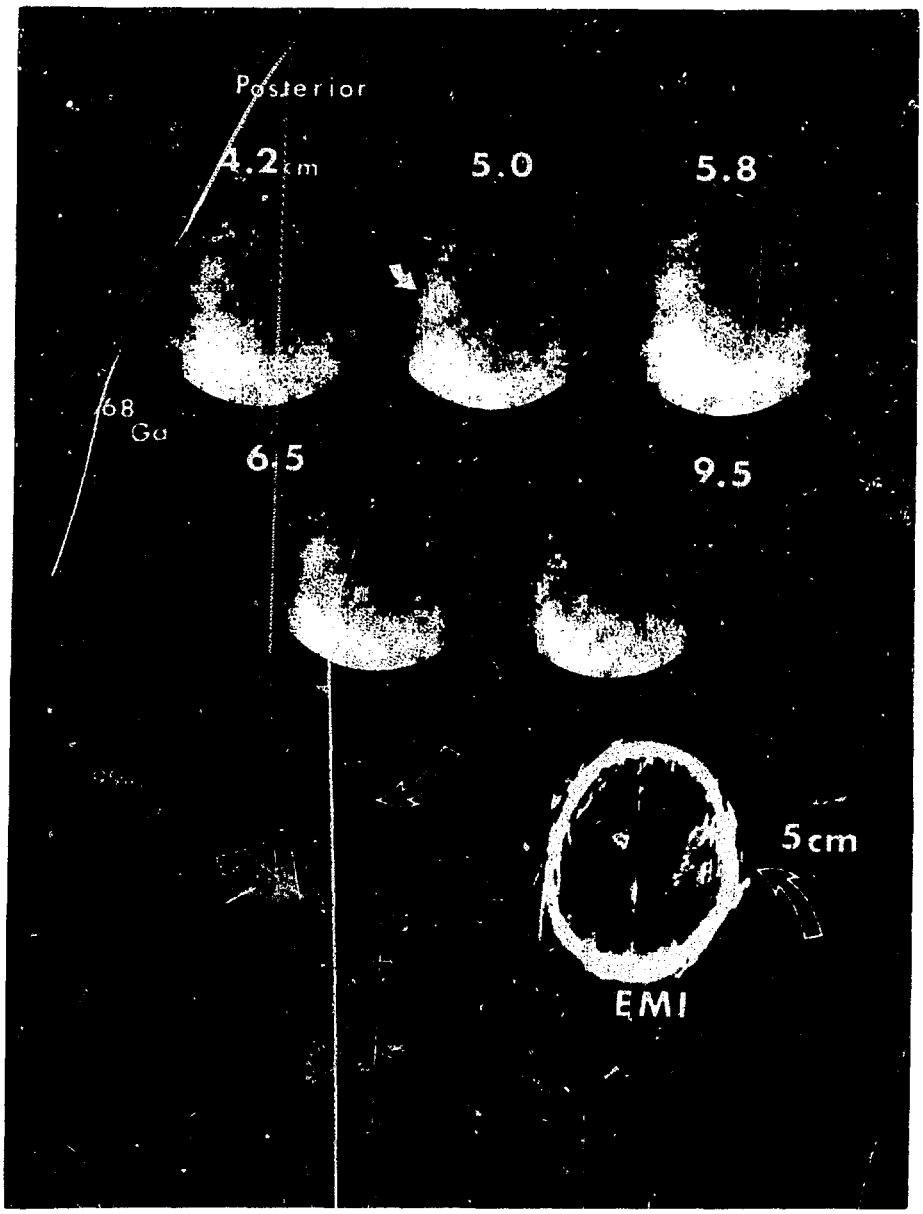

Figure 1. Positron images reconstructed in frontal planes at levels indicated from occiput (top five images). Note lesion (glioma) in sharp focus at 5 cm demonstrating central necrosis. Tc-99m-DTPA scintiphotograph (lower left image) in posterior projection. Note apparent homogeneous distribution of activity in lesion. CAT scan (lower right) corroborating central necrosis suggested in positron image.

Proceedings, ERDA X-and Gamma-Ray Symp. Ann Arbor, MI, May 19-21, 1976 (Conf 760539)

THE USE OF X- AND GAMMA RADIATION FOR SELECTIVE ANALYSIS OF BI-COMPONENT MATERIAL

F. P. Bolin, L. E. Preuss and C. K. Bugenis
Physics & Biophysics Department
Edsel B. Ford Institute for Medical Research
2799 W. Grand Blvd.
Detroit, Michigan 48202

ABSTRACT

The use of two monochromatic penetrating beams of appropriate energies makes it possible to selectively analyze for either fraction of a two component system. A key quantity is the R value, defined as: $R = Ln(I_{01}/I_1) / Ln(I_{02}/I_2)$ where 1 and 2 refer to the energies of the photon beams and "0" represents unattenuated intensity. For animal tissue, R is directly proportional to the fraction of either component of the absorber, but in general a linear transformation relates the two. The components to be analyzed determine the optimal photon energies needed for the system. Applications of dual photon absorptiometry have concentrated on biomedical measurements. The system can be extended to diverse applications. Our principal contribution to this work has been the development of soft tissue component assay. ^{109}Cd photons can analyze 10 cm thick tissue samples, with absolute lipid fraction assay accuracy of ± .015. Further developments have yielded a device for the assay of in vivo triceps tissue.

INTRODUCTION

To selectively analyze a bi-component material for the quantitative amount of either constituent, one may use two beams of monochromatic photons of the appropriate energies. To accomplish this the beams are passed through the material and the attenuation of each energy component is noted. The next step is to form the following function, known as the R value:

$$R = Ln(I_{01}/I_1) / Ln(I_{02}/I_2) \qquad (1)$$

where I_{01} and I_{02} are the unattenuated intensities of the two photon beams, and I_1 and I_2 are the attenuated intensities. The relationship between the R value and the fractional proportions, F_a and F_b, of the two substances present in the absorber is developed in the following equation. The exponential absorption law allows equation (1) to be written as:

$$R = \mu_1 \rho t / \mu_2 \rho t = \mu_1 / \mu_2 \qquad (2)$$

Where ρ and t are the absorber density and thickness, and μ_1 and μ_2 are the mass absorption coefficients of the absorber at the two energies of the dual photon beam. If the individual mass absorption coefficients of the two constituents of the absorber are referred to by subscripts a and b, then one can write:

$$\mu_1 = \mu_{a1} F_a + \mu_{b1} F_b \qquad (3)$$

$$\mu_2 = \mu_{a2} F_a + \mu_{b2} F_b \qquad (4)$$

where F_a and F_b are the fractional proportions of the individual absorber components.

Equation (5) follows from equations (2), (3), and (4) plus the fact that $F_a + F_b = 1$.

$$R = \frac{\mu_{b1} - (\mu_{b1} - \mu_{a1}) F_a}{\mu_{b2} - (\mu_{b2} - \mu_{a2}) F_a} \qquad (5)$$

Inversion gives F_a:

$$F_a = \frac{\mu_{b1} - \mu_{b2} R}{(\mu_{b1} - \mu_{a1}) - (\mu_{b2} - \mu_{a2}) R} \qquad (6)$$

Dividing by μ_{b2} and noting that $R_b = \mu_{b1}/\mu_{b2}$,

$$F_a = \frac{R_b - R}{\left(R_b - \frac{\mu_{a1}}{\mu_{b2}}\right) - \left(1 - \frac{\mu_{a2}}{\mu_{b2}}\right) R} \qquad (7)$$

If, as is sometimes the case, $\mu_{a2} \simeq \mu_{b2}$, then (7) can be simplified to:

$$F_a = \frac{R_b - R}{R_b - R_a} \qquad (8)$$

In the most general form, then, F_a is a function of R, which is experimentally measured using equation (1). For a given pair of substances to be analyzed, the mass absorption coefficients can be determined from tables or they may be experimentally determined from absorbers of known density and thickness. The experimental method is usually resorted to when the elemental breakdown of either substance is unknown.

In the case where the thickness of each component is required rather than the fractional proportion, the derivation proceeds differently. In this case the two exponential absorption equations are written as:

$$Ln(I_{01}/I_1) = \mu_{a1} \rho_a t_a + \mu_{b1} \rho_b t_b \qquad (9)$$

$$Ln(I_{02}/I_2) = \mu_{a2} \rho_a t_a + \mu_{b2} \rho_b t_b \qquad (10)$$

These are two simultaneous linear equations in two unknowns, t_a and t_b.

The solution will take the following form:

$$t_a = K_1 \text{ Ln } (I_{01}/I_1) + K_2 \text{ Ln } (I_{02}/I_2) \qquad (11)$$

$$t_b = K_3 \text{ Ln } (I_{01}/I_1) + K_4 \text{ Ln } (I_{02}/I_2) \qquad (12)$$

Where the K's are constants dependent on the densities ρ_a and ρ_b and on the energies of the two photon beams. The relationship between t and F is given by:

$$F_a = \frac{\rho_a t_a}{\rho_a t_a + \rho_b t_b} \qquad (13)$$

PHOTON ENERGIES

This section deals with the problem of selecting the appropriate energies for the two photon beams used for a bi-component analysis. It is instructive to begin a general inquiry into this area by examining the way in which the R value changes from one material to the next. For simplication, the materials considered will be limited to the elements. By use of equation (2) and a table of absorption values, an R value curve can be generated for each pair of energies under consideration.

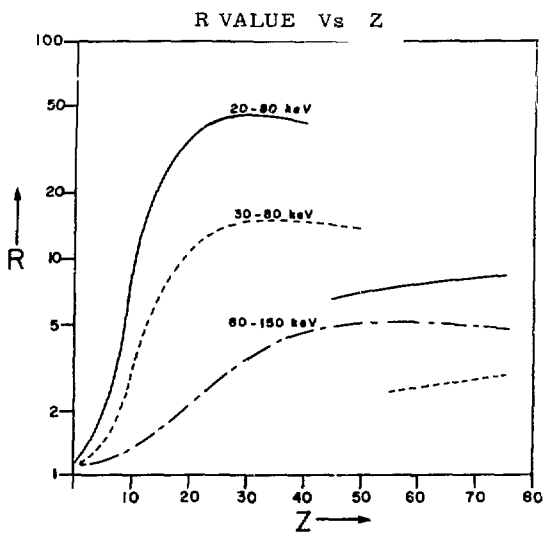

Fig. 1. The R value is plotted against elements of increasing Z number for 3 energy pairs.

Figure 1 illustrates the trend of the R value with increasing Z number for 3 pairs of photons. The discontinuities in the graphs are due to absorption edge effects. There are two items of information to be obtained from this graph. The first is the difference in R values between the two elements to be analyzed, and the second is the absolute size of the R values. Point one is very important. The greater the difference in R value between two substances, the greater will be the sensitivity of the system to small changes in composition. Point two is also informative. Large R values mean that the lower energy beam is much more highly absorbed than that of the upper energy. As a consequence, to avoid large poisson error, the intensity of the lower energy beam will need to be greatly augmented.

The greatest limiting factor to the precision obtainable at a given beam intensity is poisson statistical error. This error will change depending on the beam energy, substance analyzed, and sample density and thickness. Thus, it is advisable to determine the thickness range over which measurements of minimum statistical fluctuation can take place. Using the well-known formula for propagation of errors and equation (1) we find that

$$\sigma_R^2 = \frac{1}{\text{Ln } (I_{02}/I_2)} \left\{ \frac{1}{I_{01}} + \frac{1}{I_1} + R^2 \left[\frac{1}{I_{02}} + \frac{1}{I_2} \right] \right\} \qquad (14)$$

Where σ_R is the standard deviation of R. Given I_{01} and I_{02} as constants equation (14) can be expressed as a function of t if I_1 and I_2 are eliminated by using exponential absorption law.

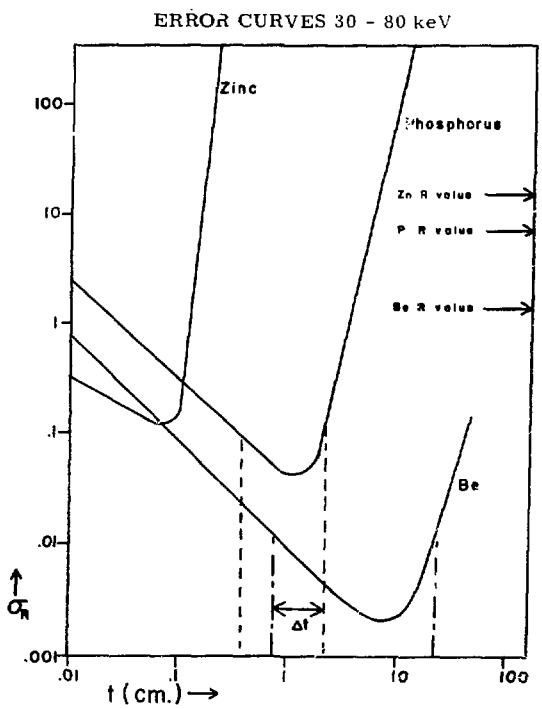

Fig. 2. The standard deviation of the R value is shown for three elements for an energy pair of 30 and 80 keV. $I_{01} = I_{02} = 10^6$.

The use of equation (14) in conjunction with the mass absorption coefficients of the substance to be analyzed can provide a practical means to determine the ideal thickness range for measurement. Fig. 2 shows plots of σ_R for three elements as a function of t. A plot can be made separately for each energy pair under consideration. (Graphs for more complex substances can likewise be drawn, but for simplicity's sake we limit this example to the elements). Since each element attains a minimum at a different point, it is necessary to impose two criteria to insure an efficient bi-component analysis. [1] $\sigma_R \leq .01\ R$ for either substance. [2] $\sigma_R \leq .01 |R_a - R_b|$. The first criterion keeps the statistical fluctuations at less than the 1% level for the R value measurement of either substance. The second criterion insures that the sensitivity of the system to a 1% change in composition will not be obscured by poisson fluctuation.*

The application of these criteria to a beryllium-phosphorus combination is shown in Fig. 2. Criterion [1] applied to phosphorus (R - 7.2) gives t intercepts at .4 and 3.2 cm. The same criterion applied to beryllium gives t intercepts at .75 and 30 cm. Criterion [2] gives intercepts nearly identical with those of phosphorus. Taking the innermost two intercepts, the allowable thickness range is .75 cm to 3.2 cm for a Be-P combination.

Graphs can be plotted for composite materials if the elemental composition is known. As an example, using the information provided by Omnell and Tipton, Fig. 3 depicts the error-curves of human fat and muscle tissue, using 22 and 88 keV radiations.

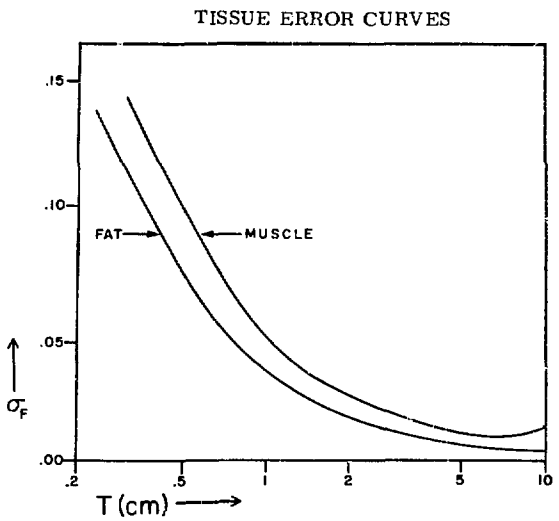

Fig. 3. Error curves for human fat and muscle tissue using 22 and 88 keV photons in the two photon method. Initial intensities are 10^6 for I_{022} and 1.7×10^5 for I_{088}.

*This assumes that $\mu_{a2} \simeq \mu_{b2}$. If not, then σ_f rather than σ_R should be plotted.

The ordinate is represented by the standard deviation in the fat fraction. It is evident that at thicknesses less than 1 cm there will be too much variation for the measurements to be considered accurate. More photons would be needed to reduce error or a different pair of energies used if measurements in that thickness range are to occupy a major portion of the work. At the other end of the scale a minimum error for muscle occurs at about 7 cm of tissue, and at 10 cm the error has begun to increase due to the heavy absorption. The error curve for fat will not turn upward until 15 cm is reached. Taking into account the range of fat to lean ratios in human tissue, the practical measurement range is about 2-12 cm for ^{109}Cd with the given intensity. Other isotopes, such as ^{133}Xe and 31 and 81 keV photons, will provide a different effective measurement range.

After demonstrating how to select photons by energy for various kinds of analysis, we would like to suggest some applications for which the two-photon system would be useful. The first possibility would be to monitor metallic alloy composition. Depending on whether thin foils or thick sheets were being measured, a different energy pair would be selected according to the methods outlined above. The system could also be used to monitor thickness if this were desirable.

Another possibility for application is in the chemical laboratory. A two-photon method could provide swift and accurate determinations of the level of concentration of a solution. The advantages of this method are manifold. For instance there would be no need of sampling the solution, since nothing is destroyed or neutralized. Another advantage is that the analysis, if so desired, could take place through a sealed container. On the other hand, one disadvantage is that the sensitivity of the system is generally restricted to the neighborhood of parts-per-hundred. Traditional methods would still be needed for higher sensitivity.

A final possibility touches on the area of biomedical studies. As Fig. 3 suggests, the two-photon method can be used to analyze tissue into its fat and fat-free components. There are several promising medical applications. One of the more interesting of these is a system designed to follow the course of a muscular wasting disease and thereby perhaps expediting diagnosis and treatment. In hopes of developing a system with such capabilities, our experimental work has been directed to the analysis of tissue into its fat and fat-free fractions.

Table I presents the results of a two-photon analysis on a series of beef tissue samples. For this set of samples the 31 and 81 keV radiations from ^{133}Xe have been utilized. The results of the photon analysis are compared with results of a chemical extraction of the fat. The samples were prepared by blending various amounts of lean and fat tissue together until the mixture was homogenous. The tissue was then packed into tubes for analysis and a small portion afterwards withdrawn for the ether extraction. Similar studies have also been done using ^{109}Cd. Results are comparable and slightly more accurate in this thickness range (4-7cm). These results show the feasibility of

using a two-photon system to obtain reliable fat-lean determinations.

ANALYSIS OF BEEF MUSCLE

Sample	Fat Fraction (by ^{133}Xe)	Fat Fraction (by extraction)	Difference
1	.08	.09	.01
2	.19	.16	.03
3	.30	.28	.02
4	.42	.40	.02
5	.44	.44	.00
6	.48	.46	.02
7	.51	.51	.00
8	.56	.59	.03

Table I. Experimentally determined fat fractions from beef tissue using ^{133}Xe.

From in vitro tissue the next step is to make in vivo measurements. For this task we assembled an apparatus to position and restrain the upper limb. The target was the triceps region which we chose as being readily accessible and hopefully representative of the remainder of the body tissue. An integrative scanning method was used to ascertain the average fat content of a cylindrical slice of triceps-biceps tissue. The data in Table II presents a selected sub-set of normal subjects from a larger initial volunteer study. All subjects were males and it is seen that although the weight of each varied considerably, the heights were all very close to 70 inches. The fourth column is the skinfold caliper thickness which is a measure of the thickness of the subcutaneous fat layer. It is therefore to be expected that the larger the skinfold reading the greater the fat fraction measured by photon analysis. This indeed was the case as the correlation coefficient between the data of the last two columns is .89, indicating a positive relationship. Not shown here, other body indices, such as arm girth, were also recorded in this study. A fuller evaluation and search for possible normative standards is presently being carried out.

PERCENT FAT BY TRANSVERSE SCAN

Subject	Height	Weight	Skinfold (mm)	% Fat
1	69.5	130	6	6.9
2	69.5	150	10.8	11.9
3	71	155	15	13
4	69	160	14	15.6
5	70	160	16	22.1
6	70	147	14.5	23.6
7	72	200	17.6	29.9
8	70.5	182	22	30
9	71	230	19	34
10	71	183	20	34

Table II. A comparison of the fat content values at the triceps muscle region for six subjects obtained by skinfold calipers and dual beam x-ray absorption using ^{109}Cd is shown here.

CONCLUSION

The two-photon system selectively analyzes the amount of each substance present in a two-component absorber. The choice of photon energies for the most accurate application is a function of absorber composition and thickness. The major limitation is the imprecision resulting from poisson fluctuation, this being a function of beam strength, composition, and thickness. The possibilities for application range from in vivo determination of tissue lipid level to industrial uses such as measurement of alloy composition.

Our own endeavors have been in the biomedical field. We have successfully measured lipid levels in beef tissue in vitro, as well as human triceps in vivo. In the latter case we have constructed an instrument for restraining limbs so as to attain a high degree of reproducibility by reducing positioning error.

UNCITED BIBLIOGRAPHY

1. Craig A. B. Jr., and Waterhouse C.: Body-Composition Changes in Patients With Advanced Cancer. Cancer 10:1106-09, Nov 1967

2. Mazess R. B., Cameron J. R., and Sorenson J. A.: Body Composition by Absorption of Monoenergetic radiation. AEC Report No. C00-1422-55, 1969

3. Omnell K. A.: Quantitative Roentgenologic Studies in Changes in Mineral Content of Bone In Vivo. Acta Radiological Suppl. 148 1957

4. Preuss L. E., Bolin F. P.: In Vivo Tissue Analysis with ^{109}Cd. Isotopes and Radiation Technology 9:501-509, 1972

5. Preuss L. E., and Bolin F. P.: In Vivo Analysis of Lipid-Protein Ratios in Human Muscle by Differential X-ray Absorption Using ^{109}Cd Photons. Advances in X-ray Analysis Vol. 16, New York Plenum, 1972

6. Preuss L. E. and Schmonsees W. G.: ^{109}Cd for Compositional Analysis of Soft Tissue. Int. J Appl Radiation and Isotopes 23:9-12, 1972

7. Preuss L. E., and Schmonsees W. G.: Two Photon Absorptiometric Analysis Using ^{109}Cd Proceedings of Bone Measurement Conference USAEC (TID-4500) Conf-700515

8. Seltzer C. C., Goldman T. T., Mayer, J. M.: The Triceps Skinfold As a Predictive Measure of Body Density and Body Fat in Obese Adolescent Girls. Pediatrics 36:212-18, Aug. 1965

9. Tipton I. H.: Stable Element Metabolism. Health Physics Division Annual Progress Report ORNL 4446:299-301, July 1969

Proceedings, ERDA X-and Gamma-Ray Symp. Ann Arbor, MI, May 19-21, 1976 (Conf 760539)

GAMMA RAY SCATTERING FOR DENSITY DETERMINATIONS

D. G. Piper and L. E. Preuss
Physics & Biophysics Department
Edsel B. Ford Institute for Medical Research
2799 W. Grand Blvd.
Detroit, Michigan 48202

ABSTRACT

A method is described which provides an absolute density determination by measuring the monoenergetic photons Compton scattered through a specific angle from a well defined volume of a material. Theoretically, the method measures density independent of geometry and surrounding material. A small geometrical dependence does exist, however, because of the finite cross-sectional area of the photon beam, and the degree of dependence changes with sample size, with density of shadowing material, and with type of collimation. Densities of organic liquids, water, lucite, crystalline materials, and zinc sulfate solution have been measured to verify the method. Differences between Compton densities and known densities are typically less than 3%. Samples of excised bovine bone have been measured, and density values correlate well (r = 0.97) with independent methods. In vivo human calcaneus determinations are proposed.

INTRODUCTION

Accurate density measurements are of importance in medicine, industry, and research. In some cases Archimedes' principle is impossible to apply and other methods are inadequate. Some methods, such as the dual beam absorptiometry technique for measuring bone density, measure only the related quantity g/cm^2. Compton scattering was used to determine density as early as the mid-1950's (1, 2), but only recently has the method been investigated in regard to absolute in vivo bone and lung measurements (3, 4, 5, 6, 7, 8).

In Compton scattering, the energy of the scattered photon is given by

$$E' = \frac{E}{1 + \frac{E}{511}(1-\cos\theta)} \qquad (1)$$

where E is the incident energy in keV and θ is the scattering angle. The number of photons scattered through a given angle is proportional to the density of electrons in the scatterer, and the electron density is related to physical density, ρ, by

$$\text{Electron density} = \rho \frac{Z}{A} N_a \qquad (2)$$

where N_a is Avogadro's number.

Measurement of Compton scattering is influenced by absorption within the material, which can be accounted for by using two monoenergetic beams of photons and by measuring both transmission and scattering in the following manner.

A narrow, monoenergetic beam of photons from a radioactive source is directed at the sample, and transmission through the sample (I_1) and Compton scattering at the desired angle (P_1) are measured, as illustrated in Figure 1. A photon beam from the second source, with energy equal to that of the scattered photons from the first source, is passed through the object along the path of the scattered beam. After

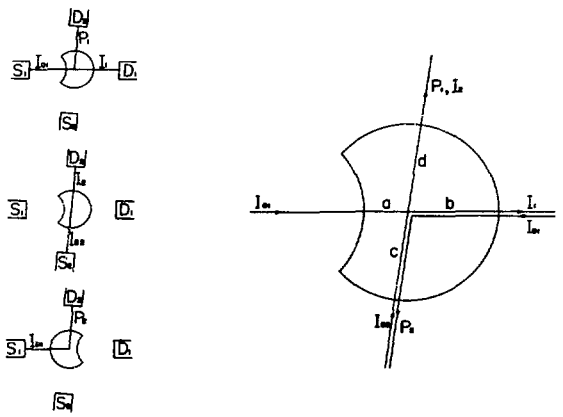

Fig. 1. Positions of sources (S), detectors (D), and sample during the required measurements (left). Detail at right indicates measured quantities as explained in the text. The density determination is at the beam intersection.

this transmission (I_2) is measured, the sample is rotated by 180°, and scattering from the first source is again assayed (P_2). Starting with the absorption law,

$$I_1 = I_{01} e^{-\mu_1 \rho (a+b)} \qquad (3)$$

$$I_2 = I_{02} e^{-\mu_2 \rho (c+d)} \qquad (4)$$

$$P_1 = I_{01} e^{-\mu_1 \rho a} B e^{-\mu_2 \rho d} \qquad (5)$$

$$P_2 = I_{01} e^{-\mu_1 \rho b} B e^{-\mu_2 \rho c} \qquad (6)$$

where μ is the mass attenuation coefficient, B is a function of electron density and Compton cross section. Since the Compton cross section is constant for the monoenergetic incident photons in a given medium

$$B \sim \rho \frac{Z}{A} N_a \qquad (7)$$

$$\text{or} \quad B = K\rho \qquad (8)$$

where K is a proportionality constant. Therefore,

$$P_1 = I_{01} e^{-\mu_1 \rho a} K\rho e^{-\mu_2 \rho d} \qquad (9)$$

$$P_2 = I_{01} e^{-\mu_1 \rho b} K\rho e^{-\mu_2 \rho c} \qquad (10)$$

Then

$$\frac{P_1}{I_1}\frac{P_2}{I_2} = \frac{I_{01}^2 e^{-\mu_1 \rho (a+b)} \left(K\rho\right)^2 e^{-\mu_2 \rho (c+d)}}{I_{01} e^{-\mu_1 \rho (a+b)} I_{02} e^{-\mu_2 \rho (c+d)}} \quad (11)$$

$$\frac{P_1}{I_1}\frac{P_2}{I_2} = \frac{I_{01}}{I_{02}} \left(K\rho\right)^2 \quad (12)$$

So that

$$\rho = \text{Constant} \left(\frac{P_1}{I_1}\frac{P_2}{I_2}\right)^{1/2} \quad (13)$$

The constant in equation (13) may be determined by measuring the scattered and transmitted values for a sample of known density, such as water. Unless the half-lives of the two radioactive sources are identical, this constant will change with time, so the system must be recalibrated periodically (8).

It should be noted that the derivation applies to any size or shape sample, independent of surrounding material, as long as the size and shape are constant during the measurement.

MATERIALS and METHODS

The optimum photon energy for in vivo bone density measurements, considering both radiation dose and scattering efficiency, is about 100 keV (3). Of the isotopic source combinations which could be of practical use (9), the ^{153}Gd-^{170}Tm pair, with gamma rays at 100 keV and 84 keV, respectively, was best suited for bone density determinations. An instrument was designed and constructed for use with these isotopes, with source collimators 0.5 cm in diameter and 2.0 cm long. The collimator for the transmission detector (D_1 in Figure 1) is 0.5 cm in diameter and 2.0 cm long, while that for the scattering detector (D_2) is 0.5 cm x 3.0 cm long. The scattering angle is 86° and separation between collimator faces is typically 10 cm, although both angle and separation are adjustable. An improved device with greater versatility is illustrated in Figure 2. The detectors are matched Na I (T1) 2" x 2" crystals with RCA 4523 photomultiplier tubes, and detection efficiency is approximately 100% at 100 keV. Analyzer windows are set at 94-106 keV for the 100 keV gamma of ^{153}Gd, and at 78-90 keV for the 84 keV photons of ^{170}Tm and the 84 keV scattered ^{153}Gd photons. The ^{153}Gd source is 100 mCi and was obtained from the Isotopes Development Center of Oak Ridge National Laboratory, and the 500 mCi ^{170}Tm source was supplied by International Chemical and Nuclear Corporation.

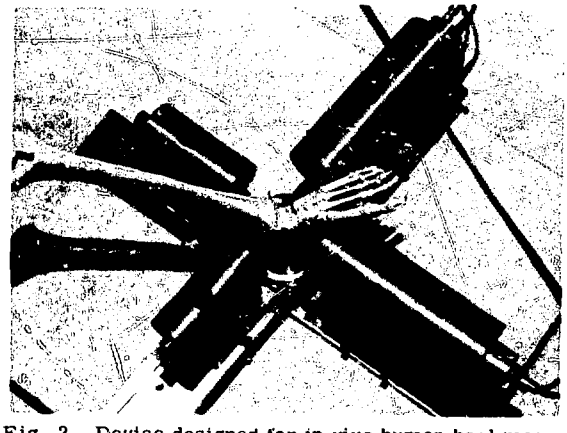

Fig. 2. Device designed for in vivo human heel measurements. The calcaneus is in the measurement position.

Water samples were used to calibrate the device, after which samples of petroleum ether, ethyl alcohol, lucite, carbon tetrachloride, quartz, and zinc sulfate solutions were measured repeatedly. Several excised ox bones were obtained, from which twenty samples of trabecular bone were prepared. These were immersed in alcohol which served as both preservative and crude soft tissue simulator, and were measured by the Compton scattering method and by Archimedes' principle.

RESULTS and DISCUSSION

Results of the measurement of samples of known density are listed in Table I. The errors are consistently small, the largest being 3.1% for CCl_4. Measurements of CCl_4 generally consisted of about 10^3 scattered counts (P_1+P_2), so statistical deviation is a significant fraction of the error. Standard deviations are usually about 2-3% of the density values, with only slight dependence on the number of measurements.

RESULTS OF KNOWN DENSITY SAMPLES

SAMPLE	ρ_C ± Std. Dev.	ρ_{True}	Error
Petroleum ether	.663 ± .026	.665	0.3 %
70% Ethyl alcohol	.888 ± .011	.890	0.2 %
Water	Standard	1.000	--
Lucite	1.195 ± .015	1.185	0.8 %
CCl_4	1.54 ± .05	1.59	3.1 %
Quartz	2.58 ± .02	2.65	2.6 %
$ZnSO_4$ solutions	1.043 ± .046	1.050	0.7 %
	1.089 ± .023	1.100	1.0 %
	1.141 ± .029	1.150	0.8 %
	1.193 ± .033	1.200	0.6 %
	1.227 ± .047	1.250	1.8 %

Table I. Results of the measurement of known density samples. Each sample was measured at least ten times. Total counts per measurement were: $P_1 \approx P_2 \approx 10^3$, $I_1 \approx 10^7$, $I_2 \approx 10^5$.

Table II gives the results of ox bone studies. Assuming that the Archimedean measurements are correct, the bone densities ranged from 1.13 g/cm^3 to 1.58 g/cm^3, which is also a typical variability for human trabecular bone in vivo. In only three cases did the measurement techniques disagree by more than 3%. These three samples were near the top of the density range, and each time the Compton density was higher than the Archimedes density. Overall, a

linear regression comparing the two techniques (Figure 3) indicates that

$$\rho_{Arch} = 0.799\ \rho_{Comp} + 0.256 \qquad (14)$$

with a correlation coefficient of 0.977 ($p < 0.001$).

COMPARISON OF OX BONE DENSITIES

Compton vs Archimedes Methods

Sample No.		Compton	Archimedes	% Difference
1		1.38 ± .01	1.42	- 2.8
2		1.68 ± .02	1.53	+ 9.8
3		1.23 ± .01	1.24	- 0.8
4		1.59 ± .02	1.58	+ 0.6
5		1.15 ± .01	1.17	- 1.7
6		1.36 ± .01	1.34	+ 1.5
7	end A	1.20 (4 trials)	1.22	- 1.6
	end B	1.39 (7 trials)	1.35	+ 3.0
8		1.36 ± .01	1.36	-
9		1.19 ± .01	1.19	-
10		1.48 ± .01	1.45	+ 2.1
11		1.20 ± .01	1.19	+ 0.8
12		1.50 ± .01	1.42	+ 5.6
13		1.59 ± .02	1.53	+ 3.9
14		1.24 ± .02	1.26	- 1.6
15		1.30 ± .01	1.31	- 0.8
16		1.12 ± .02	1.13	- 0.9
17		1.21 ± .01	1.23	- 1.6
18		1.24 ± .01	1.25	- 0.8
19		1.22 ± ~0	1.22	-
20		1.44 ± .01	1.43	+ 0.7

Table II. Results of measurements on twenty samples of trabecular ox bone. Unless otherwise noted, each bone was measured ten times. Total counts per measurement were: $P_1 \approx P_2 \approx 10^3$, $I_1 \approx 10^7$, $I_2 \approx 10^5$.

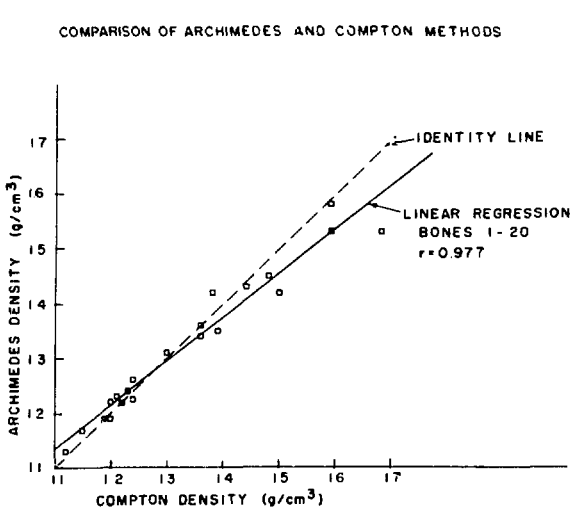

Fig. 3. Plot comparing Compton densities to Archimedes densities for the twenty bone samples. A linear regression of the data indicates a correlation coefficient of 0.977 between the points and the best fit.

Bone sample number 7 deserves some comment. In the course of the measurements, it was inverted so that the density of a new volume was measured. The two regions were found to have significantly different densities, and visual inspection revealed an epiphyseal seam through the center of the bone. The sample was divided along the seam, and each end then exhibited consistent results.

Experimental studies pointed out some factors that are not obvious from the theoretical coverage of the method. In practice, the photon beams have finite cross-sectional area, and are slightly divergent despite careful collimation. It is possible for some of the incident photons to be scattered through small angles, yet be accepted by the opposing detector collimator and analyzer window to be counted as transmission. The resulting inflated values for I_1 and I_2 cause an apparent decrease in density. With the broad beams used in the preliminary studies, effects of about 0.5% in density value were predicted. The problem can be reduced by narrowing the collimation of both sources and detectors, but larger sources and longer counting times are then required.

In addition to small angle scattering, it is possible that some ^{153}Gd photons may be scattered twice, ultimately reaching detector D_2 to be counted as primary scattering. At first glance, secondary scattering seems to be so unlikely as to be a negligible effect. However, we have observed experimentally that it may be of some importance, particularly when sample size is increased, as discussed below. If secondary scattering is significant, its effects can be reduced by restricting the beam solid angle. The resulting decrease in scattered count rate can be compensated for by introducing a slit collimator which follows an arc around the scattering volume at the desired angle. The primary scattered count rate is then enhanced in proportion to the area increase. The increased transmission from the second source (I_2) can be avoided by interchanging slit and hole collimators. A simple slit collimator was constructed for our device, and nine times as many scattered photons were detected. The slit area was nine times as large as the hole collimator.

A more efficient solution to the problem of multiple scattering is the inclusion on the scattering detector of a system of soller slits which focus on the scattering volume and follow an arc at the proper angle. A different focal length collimator would be necessary for each sample size if detector repositioning is required.

Measured density values were found to depend on sample size. With the hole collimator, increasing the diameter of a water sample by 50% produced a density reading 3.7% higher than the correct value. With the slit collimator, the same increase in sample size gave a density value 11.3% too high, indicating that the effect may be partially caused by multiple scattering. This problem can be avoided by calibrating the machine with a water standard of the same size as the sample being studied.

An investigation was made of the effect of placing various materials in the impinging photon beam to

"shadow" the sample. Samples ranging in density from 0.665 g/cm^3 to 1.59 g/cm^3 were shadowed by materials varying from 0.665 g/cm^3 to 2.72 g/cm^3. In nearly every case, the measured density was slightly higher (1% to 4%) than the true density, the larger errors generally coinciding with the more dense shadows. Since transmission was about 0.5% high due to small angle scattering, the density errors indicate that the P_1 and P_2 scatter values may have been 2% to 5% high because of the shadowing material.

Coherent scattering, which has been suggested as a complicating factor, has not been found to be a problem. The separation between incident and scattered energies (16 keV) is sufficient for electronic separation. In addition, coherent scattering at 86° is less than 1% of the total scattering, and the coherent peak is barely distinguishable in the scattering spectrum. It is conceivable that a smaller scattering angle, such as that used in the single source method (4, 5), could introduce a significant fraction of coherent scattering which could not easily be separated by the analyzer.

Applying the Compton scattering method to calcaneus density measurements in human subjects requires knowledge of the radiation dose administered to the subject. Assuming collimators 2 mm in diameter and 5 cm long for human studies, estimated source sizes are 1Ci of ^{153}Gd and 500 mCi of ^{170}Tm, with two one-minute exposures to Gd and one one-minute exposure to Tm being sufficient to assure 1% standard deviation. With these restrictions, dose to a patient would be about 330 mrad during one measurement of heel density.

While this is an acceptable dose, reduction would be desirable. Since 87% of the total dose arises from the 41.5 keV x-ray of ^{153}Gd (Eu k_α x-ray), filtering of this radiation will decrease exposure. Cerium, with K-absorption edge at 40.4 keV, is the most efficient filter at this energy. A foil of cerium metal 0.25 mm thick reduces the 42 keV x-ray to 1.4% of its initial intensity while allowing 66.1% of the 100 keV gamma to be transmitted. With this degree of filtering, the total radiation dose to the patient during one heel measurement drops to 33 mrad. Only 1.15 cm^3 of the bone is exposed to this relatively small dosage.

SUMMARY

While current applications of Compton scattering have concentrated on biomedical measurements, the method also has potential application in industry and research. It could be used to study liquid densities inside pipes for determination of composition or flow efficiency, to measure variations in soil composition, or to detect regions of gas or other impurities inside solid materials. Mixtures of solid-liquid, solid-gas, and liquid-gas are amenable to measurement by the technique. In theory, the Compton mechanism, coupled with the 180° reversal system, will provide true density at a point in an irregular object in g/cm^3. However, when applying this to measurements of human bone the several interacting factors of tissue dosage, beam dimension and flux, source size and distance are coupled to the geometric factors of the volume under assay. For example, bone density which is varying rapidly over small dimensions is inaccurately measured with a narrow beam and may be best assayed with a broad "averaging" beam; but the broad beam may be subject to error due to scattering events outside the assay volume. This is but a single example of many such interlocking problems of in vivo measurements. Since Compton densities from living human bone can be checked only by unacceptable biopsy, all of the factors of small angle and multiple scatter, collimator geometry, beam and source size, and photon energy require further investigation and understanding before the results can be accepted with full confidence. Nevertheless, the Compton principle in in vivo studies is most attractive and promising, and its further study is to be encouraged.

BIBLIOGRAPHY

1. E. Odeblad and A. Norhagen, "Measurements of Electron Densities with the Aid of the Compton Scattering Process;" Acta Radiologica 45:161, 1956.

2. P.G. Lale, "The Examination of Internal Tissues Using Gamma-ray Scatter with a Possible Extension to Megavoltage Radiography;" Physics in Medicine and Biology 4:159, 1959.

3. E.S. Garnett, T. J. Kennett, D.B. Kenyon, and C.E. Webber, "A Photon Scattering Technique for the Measurement of Absolute Bone Density in Man;" Radiology 106:209, 1973.

4. R.L. Clarke and G. VanDyk, "A New Method for Measurement of Bone Mineral Content using both Transmitted and Scattered Beams of Gamma-Rays;" Physics in Medicine and Biology 18:532, 1973.

5. H. Olkkonen and P. Karjalainen, "A ^{170}Tm Gamma Scattering Technique for the Determination of Absolute Bone Density;" British Journal of Radiology 48:594, 1975.

6. L. Kaufman, G. Gamsu, C. Savoca, S. Swann, L. Murphey, B. Hruska, D. Palmer, and J. Ullman, "Measurement of Absolute Lung Density by Compton-Scatter Densitometry;" IEEE Transactions on Nuclear Science. NS-23, No. 1, p 599, 1976.

7. K. H. Reiss and W. Schuster, "Quantitative Measurements of Lung Function in Children by Means of Compton Backscatter;" Radiology 102: 613, 1972.

8. L.E. Preuss, D.G. Piper, and C.K. Bugenis, "Bone Mineral (Apatite) Assay by Photon Scattering—A Survey of Sources and Experimental Evaluation;" Advances in X-ray Analysis, vol. 18, W. L. Pickles et al, editors, Plenum Press, New York, p 545, 1975

9. D.G. Piper, L.E. Preuss, and F.P. Bolin, "An Evaluation of Several Nuclides for Bone Density Determinations by Compton Scattering;" Proc. Int. Conf. on Bone Mineral Measurement, Chicago NIH 75-683 p 155, 1973.

10. I.H. Tipton, "Stable Element Metabolism;" Health Physics Division Annual Progress Report, USAEC Report ORNL - 4446, p 300, 1969.

Proceedings, ERDA X-and Gamma-Ray Symp. Ann Arbor, MI, May 19-21, 1976 (Conf 760539)

THE APPLICATION OF GD-153 TO STATIC AND DYNAMIC TRANSMISSION STUDIES*

R.R. Price, J. Wagner, K.H. Larsen, T. Stokes, J.A. Patton, and A.B. Brill
Vanderbilt University, Division of Nuclear Medicine
Nashville, Tennessee 37232

*Supported in part by E-(40-1)-2401 ERDA

Summary

A Gd-153 source has been utilized in a number of medical applications to measure body composition using photon attenuation techniques. Applications have included measurements of regional and whole-body bone mineral content and estimates of regional pulmonary perfusion pulse size.

Source-Detector Description

The Gd-153 source utilized for those studies was obtained from the Isotope Developments Division at Oak Ridge National Laboratory. The source is approximately 2 Ci and is encapsulated as a 1/8" diameter disk source on the tip of a 3/4" stainless steel cylinder. Spectra from the source taken with a high resolution intrinsic germanium detector is shown in Figures 1a and 1b. The Gd-153 spectrum is characterized by two primary photon groups. The lower energy group is usually assumed to have a mean of about 44 keV. The upper group consists of two lines one at 97 and the other at 103 keV with relative intensitiy of about 55 percent. Figure 1b is an expanded view of the 44 keV group and shows not only the expected Eu x-rays but also contains a number of additional lines. These have been identified as x-rays from Gd induced by interactions with its own 97-103 keV photons and an europium contaminant. The Gd x-rays have been measured to be approximately 30 percent as intense as the expected Eu x-rays.

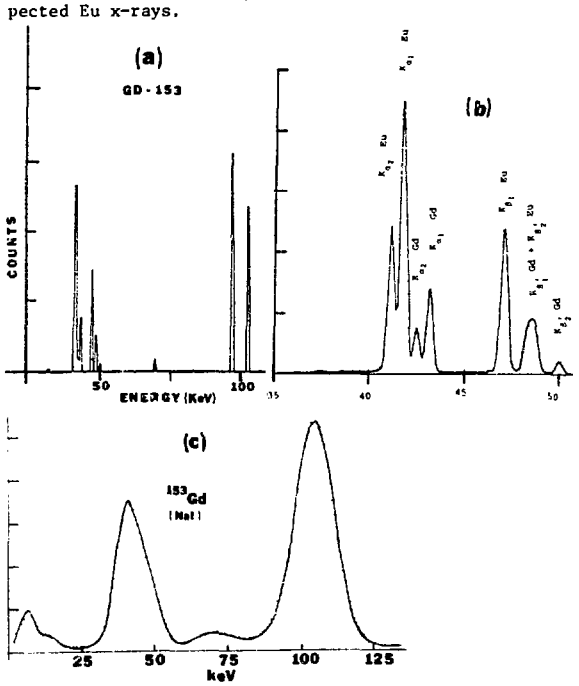

Fig. 1 (a) and (b) Gd-153 spectra from a high resolution Ge detector and (c) NaI detector.

For *in vivo* applications, we use a 2 x ½" thin window NaI crystal mounted as an integral unit with the photomultiplier tube. The detector system is capable of accommodating count rates of 100 KHz with no significant losses. The detector energy resolution has been measured to be approximately 10 percent at 100 keV (FWHM). The lower energy window for the NaI (Fig. 1c) detector has been chosen from 37-51 keV and 89-114 keV for the upper window.

All applications employ an opposed source/detector geometry. For all measurements except the measurements of the distal radius and ulna we have used a source/detector separation of approximately 15 inches with both source and detector collimated by cylindrical cadmium collimators. Cadmium was chosen instead of lead to minimize the production of lead x-rays (75 keV). Measurements of the radius and ulna are made with a source/detector separation of 8 inches. Different detector collimators were used, depending on the application. However, the source collimation is always 1/8".

Applications

Bone Mineral Content (BMC)

Methods for accurately determining bone mineral composition in weight-bearing bones are needed in order that bone demineralizing processes may be detected and monitored at locations most sensitive to fractures in patients with osteoporosis.

Photon attenuation measurements in bone density determinations have been carried out by many groups since the popularization of this technique by Cameron and Sorenson.[1,2] In the dual photon attenuation technique one uses the contrasting mass attenuation coefficients of the bone mineral and tissue at two photon energies to determine the amounts of both. The dual photon transmission equations are shown in equation 1 and 2. The

$$I^1_{xy} = I^1_0 \, e^{-\mu^1_t T - \mu^1_b B} \qquad (1)$$

$$I^2_{xy} = I^2_0 \, e^{-\mu^2_t T - \mu^2_b B} \qquad (2)$$

I^i_0 and $I^i_{x,y}$ refer to the initial and transmitted intensities at energy i; the μ^i_j refer to the mass attenuation coefficients of material j (bone mineral-b or tissue-t) at energy i; where B and T refer to the mass thickness (g/cm^2) of the bone mineral and tissue, respectively. The solution for the bone mineral at the particular position (x,y) of measurement is given as:

$$B_{xy} = \frac{\ln\left(\frac{I^1_0}{I^1_{xy}}\right) - \frac{\mu^1_t}{\mu^2_t}\ln\left(\frac{I^2_0}{I^2_{xy}}\right)}{\mu^1_b - \frac{\mu^1_t \mu^2_b}{\mu^2_t}} \ \frac{g}{cm^2} \qquad (3)$$

We have developed a system utilizing the two photon attenuation techniques and a modified dual-probe nuclear medicine whole-body scanner to make regional and whole-body estimates of BMC. With our system, signals from the scanner's x and y position encoders, the single channel analyzer pulses from the two photon groups and the pulses from a high frequency oscillator are monitored via CAMAC modules driven by a PDP/9 computer. The data are buffered into core and then dumped to disk at the end of each line. The recorded oscillator pulses make it possible to correct for scanner speed instabilities. The system was first used

to measure the BMC in the ulna and radius and more recently has been used for spine and total-body measurements. The Gd-153 source was chosen in particular for its suitability for measuring the deeper lying bones, including the vertebral column and represents an almost optimum choice of the two photon energies where the bone/soft tissue contrast is optimized with an acceptable total beam attenuation.

The routine arm scan uses a 256 point x 16 line scan field corresponding to a 0.5 mm x 1.5 mm spatial element. The simultaneous dual photon attenuation equations shown above are solved by the computer at each point of the scan matrix and intensity modulated images of the net bone mineral content are produced. An example is shown in Figure 2. The first image is from the 100 keV window, the second from the 40 keV and at the far right is shown the cell-by-cell derived bone mineral content distribution. It is our hypothesis that the mean bone mineral content determined from a number of parallel scan lines should be a more stable quantity by being less sensitive to repositioning errors, than measurements made at a single selected point or line. Our measurements have been found to have a precision of 1-2% as determined from repeated scans and phantom measurements.

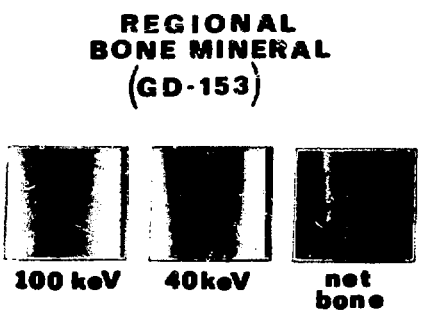

Figure 2. Rectilinear transmission scans of the ulna and radius using Cd-153 along with derived BMC distribution.

Rectilinear scanning techniques should prove most important when applied to the measurement of irregular objects such as the vertebral column. For such irregular objects accurate and reproducible repositioning techniques are essential since small variations in position would result in large changes in the measured bone mineral content and would compromise one's ability to measure small BMC changes in a given patient. Rectilinear scans allow one to visualize the vertebrae, thus making it possible to use internally recognizable and relocatable fiducal structures for locating regions of interest in the sampled data. With this technique the linear density (gm/cm)(which presents some difficulty in interpretation when applied to irregular objects) can be replaced by an estimate of the total grams or gm/cm^2 of bone mineral in the sampled region.

The vertebral scans are collected in a 64 x 64 image matrix corresponding to a 1.5 mm x 1.5 mm square spatial region. Scan time for a 20 cm segment of the spine is approximately 25 minutes and delivers an average radiation dose of $\leq$10 mrad. On repeated scans of human subjects and also on reference macerated vertebrae, we have estimated the precision of the vertebral measurements to be $\pm$5% independent of orientation to the scanning beam. Estimates of the bone mineral content using rectilinear scan techniques were made for six individual vertebrae from our reference spine placed in a 10 cm scattering medium. The bone mineral content was compared with the measured dry weight (as shown in Figure 3) and was found to be highly correlated (correlation coefficient of 0.98).

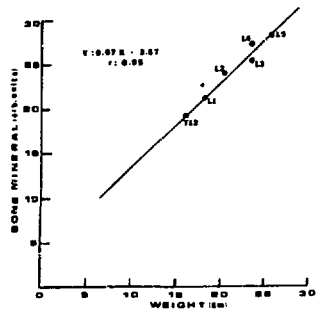

Figure 3. Comparison of BMC determined from photon attenuation to direct measurement of weight in macerated vertebrae.

Examples of intensity modulated images of the derived bone mineral content (gm/cm^2) of the T-12 to L-4 region of the spine along with the corresponding bone radiographs for a normal volunteer is shown in the Figure 4.

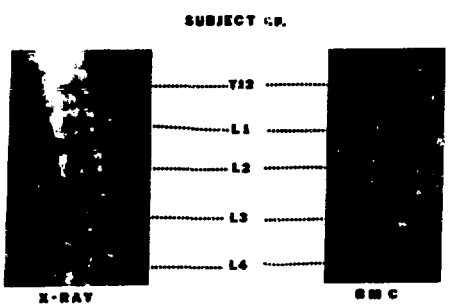

Figure 4. Comparison of vertebral x-ray to BMC rectilinear scan in a normal.

Although the spatial resolution of the transmission scan is quite poor relative to the x-ray, the images

are sufficiently clear to separate the individual vertebrae and recognize their characteristic structure.

BMC scans of the spine are shown in Figures 5 and 6 for three patients with varying degrees of osteoporosis. Figure 5 shows the BMC images while Figure 6 shows the total grams per cross sectional area (proportional to density) plotted for each vertebrae from the T-12 to L-4 level. Our hypothesis is that vertebral density is a normalizing quantity and should minimize the dependence of body size and sex, thus allowing direct comparison between patients and disease states.

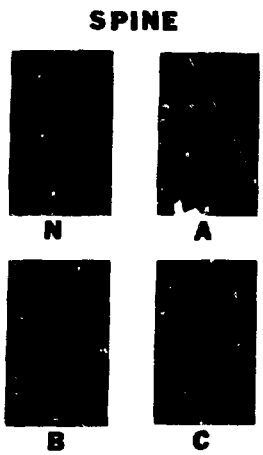

Figure 5. BMC scan images (N) normal, (A) premature osteoporosis after removal of ovaries, (B) and (C) senile osteoporosis.

In this small sample group, differentiation between known osteoporotics and normal volunteers is obvious with mass thickness (gm/cm^2) differing by as much as a factor of 2 in extreme cases. The BMC images are less quantitative but general demineralization associated with deformed and compressed vertebrae are easily appreciated. Since it is well known that demineralization takes place primarily within the traebecular bone it should be possible to detect losses from the vertebrae much sooner and more accurately than from measurements of the radius and ulna. An interesting artifact is apparent in the abnormal patient (A) at the bottom of the image in the L-5 region. The very dense region at L-5 was subsequently shown to be due to contrast medium given to the patient that had remained in this region. Observation of spine x-ray films taken during the same period confirms this.

We have also initiated measurements of total body BMC. In this application, the images generated are much coarser, as shown in Figure 7 although the various osseous structures are still discernible. Currently, data are collected in a 128 x 32 array. The individual cell sizes are approximately 1.3 x 1.3 cm. The time for a scan is approximately 30 minutes with an absorbed radiation dose of less than 10 mrads. From the scan we will obtain quantitative measurements of total body bone mineral as well as bone mineral in the various regions of the skeleton. A vertical profile scan is shown in Figure 8. Here we separate the body into right and left and then integrate the bone mineral along each line. All of the characteristic structure is observed and the symmetry of the body is apparent. The asymmetry in the head region is due to rotation, while the asymmetric chest region resulted from the exclusion of the left arm from the scan field.

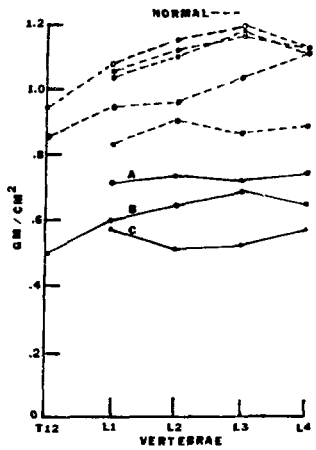

Figure 6. Total grams per unit cross sectional area of BMC for a group of normals and abnormals shown in Figure 5.

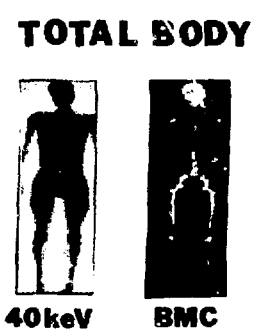

Figure 7. Whole body transmission scan using Gd-153 and derived BMC distribution.

Pulmonary Perfusion Pulse (PPP) Measurements

Variations in the attenuation of transmitted radiation through the lung provides an index of pulmonary perfusion and ventilation. A number of investigators have purported to measure pulmonary ventilation using densitometric techniques. These investigators have used both x-ray and radioactive sources. Close examination of the ventilation densitometric recordings reveal small fluctuations in the signal. These

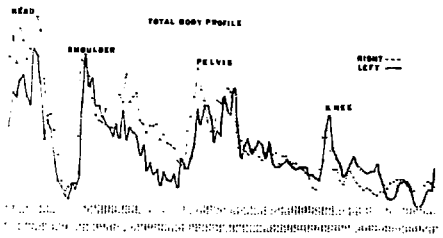

Figure 8. BMC profile derived from image shown in Figure 7.

fluctuations are known to be the result of density fluctuations in the lung resulting from the increasing and decreasing amount of blood in the pulmonary vasculature throughout the cardiac cycle. The amplitude of this perfusion pulse is related to the amount of blood ejected into the lungs. Studies are proposed in patients with pulmonary embolism to monitor the progress of the vascular block. In addition, the perfusion pulse amplitude in the normal upright individual increases from apex to base as does perfusion. However, this gradient in perfusion is often abolished or reversed in individuals with pulmonary hypertension. For this purpose, we are developing a computer based system employing a radioactive source and an opposed NaI detector to make regional PPP measurements in persons with suspected pulmonary hypertension.

Preliminary measurements on volunteers have shown that the change in lung density due to PPP results in a 1-3 percent change in beam transmission. We have found that changes of this magnitude can be measured reliably by signal averaging over multiple heart cycles using EKG gating information. Signals from the single channel analyzer and an EKG gating module are monitored by the PDP-9 computer at the rate of 60 samples per second and recorded on a digital disk for later analysis.

The optimum choice of the gamma ray energy and the intensity of the radioactive source to be employed requires a compromise between the amount of beam attenuation by the chest that can be accepted and the change of beam transmission (due to the changes in pulmonary perfusion) that is required to provide a statistically significant signal. As the gamma-ray energy increases, transmission increases, but at the expense of signal contrast. Preliminary calculations indicate that the optimum gamma energy is included within the range of 60-100keV. Thus, for these applications we have chosen to use the 100keV line (with preferential filtering of the 44keV) of our 2Ci Gd-153 source. Preliminary measurements in volunteers have been for 30-60 seconds (about 30-60 heart cycles) at 3 evenly spaced vertical positions along the lung. The exposure rate from the Gd-153 source in this configuration is approximately 75 mR/minute.

Figure 9 shows two typical traces, one taken from the apex and the other from the base of the lung in a normal volunteer. The sampling rate was 1/60 second with the occurance of the QRS gate pulse indicated as tick markers along the abscissa. The lower frequency ventilation variations are obvious; whereas, the cyclic variation due to pulmonary perfusion is obscured. Using signal averaging techniques, the pulmonary perfusion pulse can be extracted from these data as shown in Figure 10. These data are from measurements taken over the upper lobe of the right lung of a normal volunteer during breath holding and are the result of averaging all of the cardiac cycles sampled during 30 second measurements. In the presented data, 34 cardiac cycles were included in the average. Zero time in the figure corresponds to the occurance of the QRS pulse and is approximately equal to end-diastole and similarly the maximum density occurs at the approximate mid-point of the cycle, i.e. end-systole.

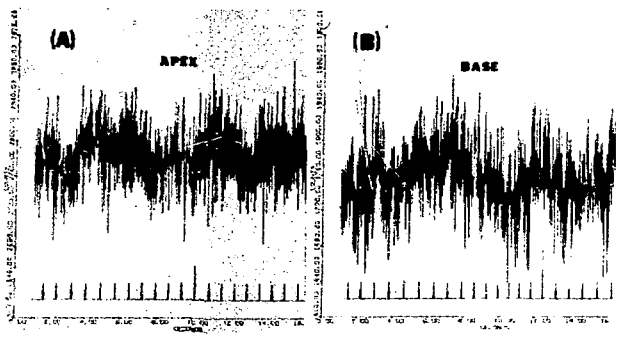

Figure 9 (a) Transmitted counts through the lung apex as a function of time. QRS gate signals shown as ticks along abscissa, (b) transmitted counts through lung base.

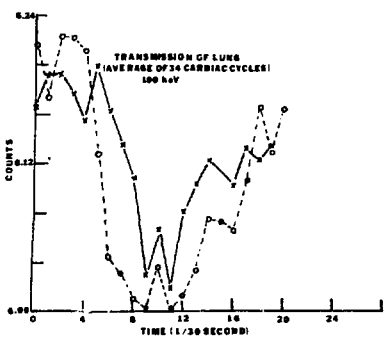

Figure 10. Signal averaged transmission data.

Conclusion

Gd-153 is proving to be an important new source for in vivo medical applications of quantitative photon attenuation techniques. The source is almost ideally suited for making dual photon measurements of bone mineral content in deep lying bones. The 100keV photon group (with filtering of the 44keV) is also well suited for measuring regional pulmonary perfusion. Preliminary measurements of regional and whole body bone mineral content and regional pulmonary perfusion have been very encouraging.

References

1. Cameron, J.R. and Sorenson, J.A. Measurement of bone mineral in vivo: an improved method. Science 142:230, (1963).

2. Cameron, J.R. R.B. Mazess and J.A. Sorenson. Precision and accuracy of bone mineral determination by direct photon absorptionmetry. Invest. Rad.3:141(1968).

Proceedings, ERDA X-and Gamma-Ray Symp. Ann Arbor, MI, May 19-21, 1976 (Conf 760539)

Regional Monitoring of Smog Aerosols*

T. A. Cahill
Department of Physics and the Crocker Nuclear Laboratory
University of California, Davis, California 95616

The atmospheric aerosol consists of a complex ensemble of particles in an infinite combination of physical and chemical states. Despite their importance in reducing visibility, affecting human health, and soiling materials, their complexity has hindered attempts to include detailed information on aerosols in air quality monitoring programs. Generally, only the total suspended particulate present at a site during a 24-hour period is measured. Some information on chemical composition is extracted from aerosol samples, but analytical costs limit such analyses to a few important species on representative samples.

A more complete effort at monitoring the atmospheric aerosol must include some information on the particle size profile, as health effects, transport behavior, and light scattering phenomena are all highly dependent upon the size of the particulate. Yet, instrumentation that can deliver a sample suitable for further chemical analysis generally yield very small amounts of mass for analysis. Thus, extreme sensitivity to the individual elemental components of the total mass loading becomes a requirement.

Another factor that must be considered in the study of the atmospheric aerosol is the wide range of elements that can be found in a typical sample. For example, 99% of the mass of an average set of gaseous pollutants in a city can usually be found in the five elements, H, C, N, O, and S. However, in order to inventory 99% of the mass of an average urban particulate sample, one would normally require the elements H, C, N, O, Na, Mg, Al, Si, S, Cl, K, Ca, Fe, Cu, Zn, Br, Ba, and Pb. More important yet, 88% of the mass is contained in elements lighter than potassium, so that any analytical method that selects elements or misses entirely the lighter elements will hinder any attempt to explain total mass loadings seen at a location. Table I illustrates a typical profile of elemental mass by elemental mass groups.

Table I

Prevalence of Elements in an Average Urban Aerosol (approximate)

Elemental Constituent	Prevalence	
	$\mu g/m^3$	%
Very Light Elements (H through F)	68	65%
Light Elements (Na through Cl)	22.6	22%
Medium Elements (K through Ba)	12.7	12%
Rare Earths	0.1	0.1%
Heavy Elements (Hf through Bi)	1.5	1.4%
Actinides (Th,U)	<< 0.1	<< 0.1%

For these reasons, most instrumental methods that are able to be used at the sampling site are inadequate for generation of detailed information on atmospheric particulates. The way is then open for the use of a central analytical laboratory that can be based upon the latest analytical methods and the best computational techniques. Such laboratories can be developed from existing accelerator laboratories, as the techniques of ion-excited x-ray analysis (I.X.A.) and ion-scattering analysis (I.S.A.) have proven themselves capable of performing precisely the type of broad range analyses covering the entire spectrum of elemental mass while using only milligrams of total sample. Ion-scattering analysis is normally used for the very light elements (H through F) which cannot be quantitatively measured by x-ray based methods due to x-ray attenuation effects in individual particles and sample layers. It is based upon the kinematic energy loss in the elastic scattering of protons or alpha particle beams from accelerators and thus performs a separation by elemental mass. It can be used in both a back-scattering mode or a forward scattering mode. Ion-excited x-ray analysis (also called PIXE, for particle induced x-ray emission) is used for elements sodium and heavier, and possesses excellent sensitivity, in the nanogram per centimeter squared range.

Development of the analysis techniques is of little use if the samples are collected in such a form as to destroy the advantages gained by use of advanced techniques. Thus, an integrated system of sample collection, sample handling, and sample analysis must be developed, as any error in any part of the entire scheme will be propagated into the error in the final result. Once this is done, however, one can visualize more complete aerosol monitoring efforts, including information on particle size and elemental content of aerosols at many locations for extended time periods.

Such a program has been established by the California Air Resources Board, working in conjunction with the University of California, Davis.[1] Up to 15 sites were selected at locations that were representative of large areas of the state. Aerosol samples were collected in three particle size ranges by means of Sierra Instrument's Multiday Impactors. These units are rotating drum impactors of the Lundgren type with after filters. Once a week, samples were sent to Davis and analyzed by ion-excited x-ray emission for elements sodium and heavier and ion scattering analysis for elements hydrogen through fluorine. Analytical error for elements aluminum and heavier has averaged less than 3% since January 1973.

The ability to generate large numbers of accurate elemental values brings with it both problems and possibilities. One aspect of energy dispersive x-ray analyses, excited either by ion beams or x-rays, is that they deliver large numbers of data on elements that are not generally toxic in ambient concentrations and normal chemical forms. These may be considered as a nuisance, and the elements of toxicological interest can be abstracted and utilized alone. However, these other elements can provide useful information as to sources of toxic elements, transport phenomena, chemical transformations, and particulate sinks. Correlation coefficients can be calculated between all pairs of elements seen during a period, normally one month in the California program. These statistical associations are often very strong, and they deliver elemental ratios that can be compared with suspected sources. Table 2 shows such a compilation of common associations.

Thus, non-toxic bromine is able to prove that lead at these sites is almost entirely of automotive origin. Many other such correlations exist for specific sources, including coal burning power plants and industrial operations. This type of information is

Table 2

Examples of Bivariate Elemental Correlations for Major Primary Aerosol Sources

Element	Correlation	Elemental Ratio	Elemental Ratio of Presumed Source (Typical)
Oceanic			
3.6 to 20μ			Sea Water
Na	0.97	1.13	0.56
Mg	0.81	0.26	0.07
S	0.88	0.094	0.047
Cl	=1.00	=1.00	=1.00
Soil			
0.65 to 20μ			Crustal Ave.
Al	0.96	0.28 ±0.04	0.282
Si	=1.00	=1.00	=1.00
K	0.93	0.095±0.005	0.094
Ca	0.87	0.20 ±0.07	0.131
Ti	0.89	0.027±0.005	0.016
Mn	0.81	0.008±0.001	0.003
Fe	0.97	0.285±0.03	0.181
Fuel Oil			
0.1 to 0.65μ			Fuel Oil
S	=1.00	=1.00	=1.00
V	0.95	0.016	0.018
Ni	0.97	0.021	0.025
Automotive			
0.1 to 3.6μ			PbClBr
Br	0.95	0.30	0.355
Pb	=1.00	=1.00	=1.00

only available from monitoring-type studies of extended duration using multi-element methods, and it is preferable to the use of "tracers" of dubious validity.

Once particulate sources have been established by these means, one can examine the sources of gaseous pollutants by fine particulate-gas pollutant correlations. The correlation between oxides of nitrogen and Pb at California sites possessing only automotive nitrogen sources averages at about 0.95. Using this fact, remarkably detailed breakdowns of automotive and non-automotive contributions to gaseous nitrogen compounds can be derived for comparison with source omission inventories.

Finally, studies of complicated effects such as visibility degradation can be undertaken when particulate data, by size and elemental composition, are combined with gaseous pollutant and weather data. Typically, 90 parameters will be generated per site per day, and thus at least 90 days of data on the dependent variable is required. Rather surprisingly, only a few parameters (~12) show any significant correlation with visibility in California. Intermediate-size suspended sulfate particulates, 0.6 to 2 μm diameter, derived from photochemical conversion of SO_2, appear to dominate haze formation at all California sites during the summer.

Thus, the development of energy dispersive x-ray detectors and improved methods of excitation have opened up new vistas in atmospheric science. The results of these studies will hopefully result in highly specific and cost-effective control strategies for air quality maintenance.

*Work supported in part by the California Air Resources Board. For a list of investigators, see reference 1. Analytical facility developed in part with support from the National Science Foundation, RANN.

References

1. "Monitoring California's Aerosols by Size and Elemental Composition", Robert G. Flocchini, Thomas A. Cahill, Danny J. Shadoan, Sandra J. Lange, Robert A. Eldred, Patrick J. Fieney, Gordon W. Wolfe, Dean C. Simmeroth, and Jack K. Suder, Environmental Science and Technology 10, 76 (1976).

Proceedings, ERDA X-and Gamma-Ray Symp. Ann Arbor, MI, May 19-21, 1976 (Conf 760539)

APPLICATION OF MULTI-STATION TIME SEQUENCE AEROSOL SAMPLING AND PROTON INDUCED X-RAY EMISSION ANALYSIS TECHNIQUES TO THE ST. LOUIS REGIONAL AIR POLLUTION STUDY FOR INVESTIGATING SULFUR-TRACE METAL RELATIONSHIPS

James O. Pilotte, J. William Nelson, and John W. Winchester
Depts. of Oceanography & Physics, Florida State University, Tallahassee, FL 32306

Time sequence streaker samplers[1], employing Nuclepore filters for aerosol collection, have been deployed over the 25-station St. Louis regional air monitoring network and operated for the months of July and August 1975 so as to determine aerosol composition variations with 2-hour time resolution. Elemental analysis of the 84 individual time steps per station for each week of sampling is carried out by 5 MeV proton irradiation and X-ray counting by Si(Li) detector, using a Van de Graaff accelerator with a special automated step drive sample handling device. Computer resolution of the X-ray spectra[2] for the elements S, Cl, K, Ca, Ti, V, Cr, Mn, Fe Ni, Cu, Zn, Br, and Pb is carried out at a rate equal to the proton irradiation rate, five minutes or less for each time step analysis.

The aerosol particle sampling equipment and conditions have been designed to take advantage of the high sensitivity of PIXE analysis[3], in the nanogram range for the elements determined. An air flow rate of two liters per minute or less is optimum and permits the use of light weight pumps and samplers which draw minimum electric current and are suitable for tower mounting. Nuclepore filters with 0.4 μm pore diameter are used to collect particles with high efficiency, by impaction for larger sizes and by diffusion for sizes smaller than the pore diameter. A test suite of samples from 11 stations and one week of sampling time has been analyzed for an evaluation of data handling and interpretation procedures. Stations selected in this study were #102, 104, 105, 106, 108, 111, and 113 in the Greater St. Louis area, #121 25 km north of the city center, and #122, 123, and 125 about 50 km to the north, east, and west of the city. From correlations of elemental concentrations in air with time and location and interelement time correlations at a single station we may infer the transport of elemental constituents from pollution and natural sources as well as gas-to-particle transformations of certain elements, such as sulfur. This study represents a field test of a combination of sampling, analysis, and interpretive techniques needed for large scale aerosol composition investigations. In it we have given special attention to the relations between particulate sulfur and trace metal constituents in the urban atmosphere.

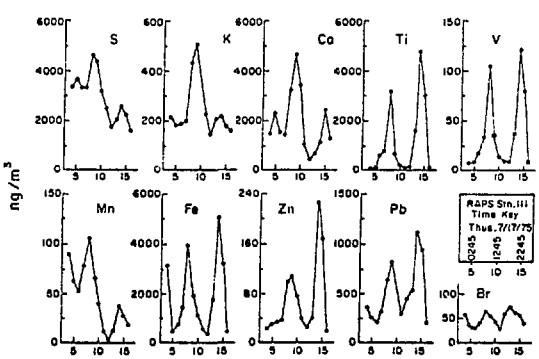

Figure 1

Figure 1 presents the time variations observed for ten elements measured for a 24-hour period at RAPS station 111, located in a residential neighborhood near an industrial area in the southern part of the city of St. Louis. Two prominent maxima are seen for all elements. However, when the exact times of the maxima are determined, they are not the same for all elements. The first maximum occurs at step 8 (about 0745-0945 in the morning) for S, Ti, V, Mn, Fe, and Br but at step 9 (two hours later) for K, Ca, Zn, and Pb. The second maximum occurs at step 14 (about 1945-2145 in the evening) for S, K, Ti, V, Mn, Fe, Zn, and Pb but at step 15 for Ca and step 13 for Br. As of this writing air trajectory analyses for this time period are not available. Nevertheless, it appears that the transport processes governing the sharp fluctuations in concentrations are complex and may include fumigation during the late morning bringing pollution-laden overlying air to ground level, horizontal transport from pollution sources, and local generation of pollution. It is noteworthy that both maxima for Pb occur two hours later than the corresponding Br maxima, and Pb at its maximum times is much greater in proportion to Br than can be ascribed to automotive sources of Pb alone.

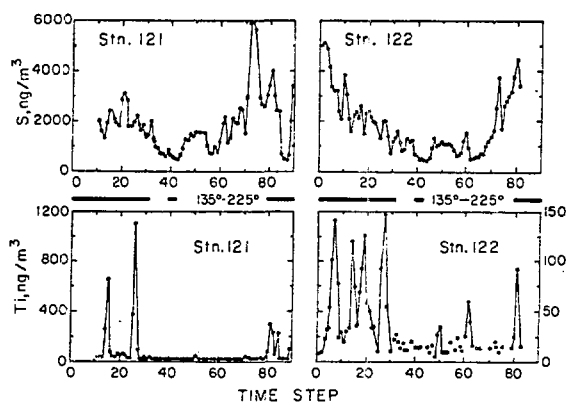

Figure 2

In Figure 2 the time variations of S and Ti concentrations are given for a full week of two hour time steps at two nonurban locations north of St. Louis, station 121 located 25 km NNW of the center of St. Louis and station 122 in Illinois 50 km due north of the city. Also given is an indication of times when air flow as measured at a representative city station was in the quadrant 135°-225°, SE to SW. These times are generally when strong Ti maxima are observed, confirming a source for Ti in the direction of the city. A strong pollution source for Ti is known to exist in the southern part of St. Louis, and this result is therefore expected. Apparently, horizontal transport, instead of vertical mixing, is dominant in governing the Ti fluctuations seen at stations 121 and 122. For S, however, the time variations do not appear to be tightly correlated. Although there is a generally higher concentration of S when air flow is southerly, suggesting a pollution source in the direction of the city, the positions of the times for maximum S concentrations are in no case the same as for Ti maxima.

Therefore, horizontal transport alone may not be sufficent to account for time fluctuations in aerosol S.

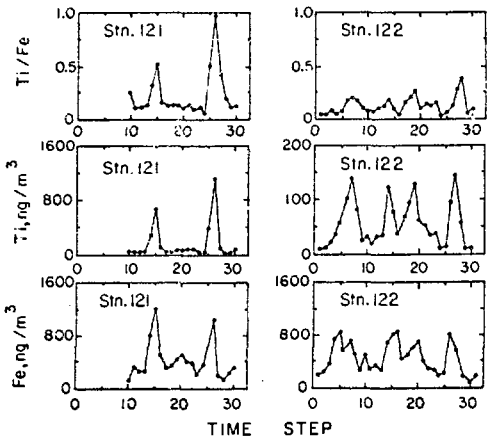

Figure 3

A further examination of aerosol concentrations at the same two nonurban stations is made by comparing Fe and Ti over the initial 2-1/2 day period, Figure 3, when air flow was southerly. At station 121 both Fe and Ti have two precisely synchronized maxima at steps 15 and 26 (about 2145-2345 on July 17 and 1945-2145 on July 18). The step 15 maximum occurs two hours later than the corresponding maximum at station 111 shown in Figure 1. At both maxima the ratio Ti/Fe is several times greater than the non-peak value around 0.1, typical of many earth's crust materials. It therefore appears that the source of Ti at peak times is an industrial emission, and peak Fe, by virtue of its time correlation with Ti, may also be of industrial origin. At station 122 the four Ti maxima correspond to anomalous Ti/Fe ratios. The four Fe maxima occur earlier in two instances and later in the other two instances, suggesting pollution Fe transport from a different source point but one in the general direction of the city.

The results exemplified by Figures 1, 2, and 3 suggest that several trace metals, when examined in the context of each other and if their principal source locations were identified, may be used as an indicator of aerosol transport over considerable distances. It may be assumed for the trace metals measured here that no significant interchange with the gas phase occurs, and therefore the aerosol transport inferred may be used as a reference for the more complicated case of sulfur where both transport of aerosol and gas-to-particle conversion reactions may occur during transport.

The time sequence trends of aerosol S over a 2-1/2 day period at six stations in or near St. Louis are shown in Figure 4. Qualitatively, the concentrations of S at the several stations vary in sympathy with each other, indicating that the processes governing the fluctuations are regional in extent. However, in detail the trends at stations 102 and 104 appear to lag the others by two to four hours. In no case is the relative degree of time variation of S as great as found for trace metals in the city, as shown for example in Figure 1 (station 111 a few days earlier). The shallow minimum at the city stations around time steps 65-70 corresponds to a similar minimum at station 122 north of St. Louis and less clearly to station 121, located nearer the city. Therefore, it should not be assumed that the causes of the time variations in aerosol S lie exclusively in transport or other processes associated with pollution sources. Instead, the processes may be larger scale than of urban dimensions and have underlying natural causes. Further examination of the matter is recommended.

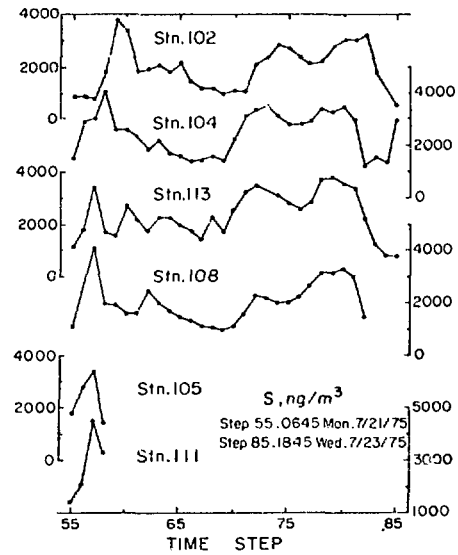

Figure 4

It was suggested in the discussion of Figure 1 that Pb may originate in both automotive and nonautomotive sources. The relative amounts of Br and Pb can serve as an indicator of nonautomotive Pb, since Br may be principally from the combustion of leaded gasoline but Pb may have industrial sources as well.

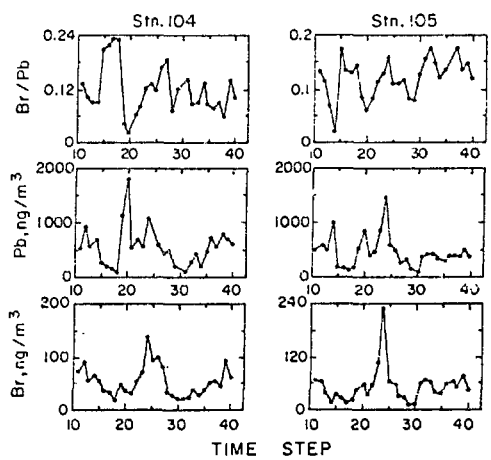

Figure 5

Figure 5 presents a time record over a 2-1/2 day period at city stations 104 and 105 for Pb and Br concentrations and the Br/Pb ratio. At both stations step 24 (1545-1745 on July 18) shows maxima for both Br and Pb and the ratio Br/Pb (0.13 and 0.16 at the two stations) is not anomalous. Increased automotive emissions apparently can account for the high Pb

concentrations. However, at step 20 (8 hours earlier) for both stations singularly high Pb concentrations are encountered which are not accompanied by Br maxima, and the Br/Pb ratios are accordingly very low. Step 14 at station 105 may be a similar case, although this is not also apparent at station 104.

The results of this investigation indicate that time variations in the concentrations of trace metals and sulfur in the St. Louis atmosphere are large, often well over a factor of 10, and occur over time periods of a few hours or less. Since the variations among several elements are often highly correlated, it appears that trace element associations have considerable promise an an indicator of aerosol transport from pollution sources. Moreover, the absence of a correlation between sulfur aerosol and trace metals may help in distinguishing between simple transport and other processes which may involve gas-particle interactions of sulfur and between local source effects and regional or larger scale effects. In the special case of Pb, its association with Br appears to have value in identifying nonautomotive Pb in the urban atmosphere. In general, the important associations needed for inferences of this kind require time resolution of the order of two hours and area-wide sampling at locations within the city and in surrounding areas. The combination of time sequence streaker sampling and PIXE analysis provides the necessary versatility in samplers and speed of analysis for this kind of investigation.

Acknowledgements

This work was supported in part by the Environmental Protection Agency for study of the sources and transport of trace metals in urban aerosols and by the National Science Foundation for accelerator operation.

References

1. J. W. Nelson, B. Jensen, G. G. Desmedeleer, K. R. Akselsson, and J. W. Winchester, Automatic time sequence filter sampling of aerosols for rapid multielement analysis by proton-induced X-ray emission, Advances in X-Ray Analysis, Vol. 19, R. W. Gould, C. S. Barrett, J. B. Newkirk, and C. O. Ruud, editors, pp. 415-425, 1976.

2. H. C. Kaufmann, K. R. Akselsson, and W. J. Courtney, REX: A computer program for PIXE spectrum resolution of aerosols, ibid., 355-366, 1976.

3. T. B. Johansson, R. E. Van Grieken, J. W. Nelson, and J. W. Winchester, Elemental trace analysis of small samples by proton induced X-ray emission, Anal. Chem., 47, 855-860, 1975.

Proceedings, ERDA X-and Gamma-Ray Symp. Ann Arbor, MI, May 19-21, 1976 (Conf 760539)

DENDRO-ANALYSIS: THE STUDY OF TRACE ELEMENTS IN TREE RINGS

W.B. Gilboy, R.E. Tout and N.M. Spyrou
Department of Physics, University of Surrey,
Guildford, Surrey, U.K. GU2 5XH

ABSTRACT

In attempts to study environmental contamination over long time scales into the past we have been measuring the levels of trace and minor elements in individual tree rings using instrumental neutron activation analysis. Most of our measurements so far have been done on elm tree samples which are widely available due to a current epidemic of Dutch Elm disease in southern England. Samples taken from every growth ring were individually activated for ten minutes in a therm. neutron flux of 1.5×10^{12}n cm^{-2}sec^{-1}in the 100 kW London University research reactor. The acivated samples were counted for ten minutes on a 42 cm^3 Ge(Li) gamma ray detector. These procedures enabled the following radioisotopes to be monitored for a large number of samples: ^{19}O, ^{24}Na, ^{27}Mg, ^{28}Al, ^{38}Cl, ^{42}K, ^{49}Ca, ^{56}Mn, ^{66}Cu, ^{80}Br, ^{87m}Sr, ^{41}Ar, ^{128}I, ^{139}Ba. Some of the above isotopes show striking systematic variations both from ring to ring in a radial direction, and also around individual rings. This paper describes these results in detail for samples taken from trees grown in various locations and assesses the potential of this technique for studying past environmental conditions.

INTRODUCTION

In an effort to measure environmental contamination over long periods we have been studying the possibility that the annual growth rings of trees might contain some record of past environmental conditions. This approach has already been used to study radiocarbon levels over very long periods and it was hoped that traces of other elements might also show interesting and useful variations. We have been systematically evaluating this idea since 1974 and this paper describes our experience to date.

EXPERIMENTAL

In recent years the elm tree population of southern England has been decimated by an epidemic of Dutch Elm disease. Consequently we have concentrated most of our measurements so far on this species, since samples are widely available from trees of useful age grown in interesting locations. Our most complete results are for a horizontal slice taken from an elm tree felled in 1974 which had been growing in a residential area of Guildford since early this century. Cylindrical samples 2.5 mm diameter (the width of one ring) and 15 mm long weighing about 70 mg were taken from every ring using a special steel boring tool. These were individually irradiated for ten minutes in a thermal neutron flux of 1.5×10^{12}n cm^{-2}sec^{-1} in the core of the 100 kW University of London reactor (ULRC). After a one minute cooling period the sample was counted for ten minutes on a 42 cm^3 Ge(Li) detector. The 4096 channel gamma ray spectra were recorded on magnetic tape for later analysis on the University of London CDC 6600 computer using the spectrum analysis program SAMPO plus additional routines for peak identification and estimation of elemental concentration; each peak requires an analysis time of about 0.8 seconds.

This irradiation and counting procedure enabled the following radioisotopes to be monitored from sample to sample: ^{19}O, ^{24}Na, ^{27}Mg, ^{28}Al, ^{38}Cl, ^{41}Ar, ^{42}K, ^{49}Ca, ^{56}Mn, ^{66}Cu, ^{80}Br, ^{87m}Sr, ^{128}I and ^{139}Ba were calibrated in a semi-absolute manner from a knowledge of the neutron flux and neutron cross-sections. We have assumed the (n,γ) reaction to be the dominant production process, but this may be an oversimplification for the cases of ^{28}Al and ^{19}O, where the ^{31}P(n,γ) ^{28}Al and ^{19}F(n,p) ^{19}O reactions may be contributing to the observed yields. The ULRC reactor has a relatively high fast neutron flux in the in-core irradiation tube, and as yet we have no way of checking the magnitude of these alternative production processes.

RESULTS

Some of the induced radioisotopes listed above show marked systematic variations, both from ring to ring in a radial direction, and also around individual rings. For example ^{42}K shows an increase of 80% in passing from the outer sapwood to the inner heartwood Fig. 1

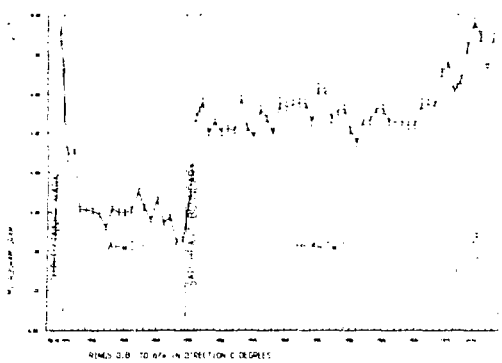

Figure 1 Radial variation of ^{42}K content in the Guildford elm.

which probably mirrors the natural biochemical change occurring at the sapwood/heartwood boundary (about the 1954 ring in this case). In contrast the ^{38}Cl signal shows a substantial drop on entering the heartwood zone, and both ^{27}Mg and ^{56}Mn show similar behaviour.

Some isotopes, principally ^{24}Na and ^{128}I, exhibit a strong oscillatory behaviour mostly in the sapwood zone. In one or two isolated rings the level of some elements (e.g. Ba, Ca, Sr in 1950) shows an extremely large increase which may be due to previous disease attacks. The persistence of these exceptionally high levels and their lack of radial diffusion, shows that these elements at least seem to be fixed fairly permanently which may allow their historic variations to be reliably measured.

Measurements within individual rings taken at varying angles around the tree show strong angular variations for some elements. For example the ^{24}Na, ^{38}Cl (Fig. 2) and ^{80}Br sapwood levels are much higher on that part of the tree which faces the prevailing wind, while the ^{128}I levels are higher at the leeward side. Most of the remaining isotopes show little systematic angular variation in sapwood,and in the heartwood region angular variations are virtually absent for all isotopes measured.

Since Guildford is not a centre of concentrated heavy industry, we have collected further elm samples from the city of Stoke-on-Trent which has been the centre of large scale ceramics manufacture since the Industrial Revolution and until recent years has possessed a highly polluted atmosphere. The first elm sample analysed from Stoke has an unusually narrow sapwood zone so it was only possible to analyse a range of rings

over the heartwood. An indication of the elemental concentrations in the Guildford and Stoke samples is given in Table 1. The comparative results show that the Stoke tree has generally lower levels for the range of elements analysed.

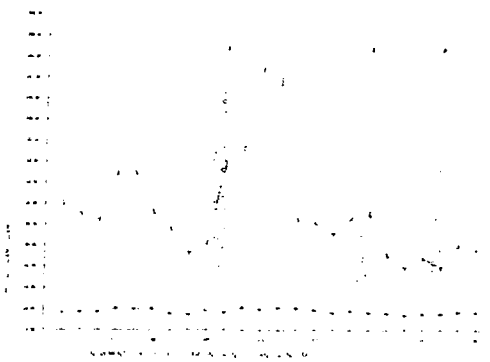

Figure 2 Angular variation of ^{38}Cl around sapwood (year 1960) and heartwood (year 1939) in the Guildford elm.

The radial variations in the Stoke heartwood (the sample goes back to 1930) show no simple correlation with the large reduction in atmosphere pollution levels in Stoke-on-Trent which has been achieved over the past two decades.

DISCUSSION

On the basis of our present results we have not as yet established any clearcut connection between the levels of trace and minor elements in tree rings and the environmental conditionsunder which they have grown.

We have until now only looked at a restricted range of isotopes in a limited number of samples, and we intend to extend these studies to both shorter and longer lived isotopes, and cover a more extensive set of samples, including soil samples. A few other workers have published more limited measurements of this type on other tree species [1,2], but the angular variations we have found do not appear to have been observed before.

The usefulness of this technique for environmental monitoring is not yet established but if successful for certain elements its special value would be for deducing the pre-industrial levels of environmental contamination against which the significance of modern levels can be sensibly judged. Since the method is related to the archaeological technique of dendrochronology, we suggest the term dendro-analysis to describe it.

ACKNOWLEDGEMENTS

We would like to thank Mr. D.S. Voss of our Physics Department, and Mr. Hoddle of the Parks Department, Stoke-on-Trent, for providing the Guildford and Stoke elm samples respectively, We are also indebted to Mr. M. Kerridge and his staff at the University of London Reactor Centre, for provision of irradiation and counting facilities.

REFERENCES

1. E. Ricci, Analytica Chimica Acta, 79 (1975) 109.
2. J.R. Vogt, Annals of the New York Academy of Sciences, 199 (1972) 137.

ISOTOPE	GUILDFORD ELM (µg/g)				STOKE-ON-TRENT ELM (µg/g)		
(ENERGY) keV	Av. Sapwood	Range	Av. Heartwood	Range	Sapwood Ring	Av. Heartwood	Range
^{19}O(197.4)	29, 300	ND-42,700	34,300	ND-47,300	38,500	40,100	26000-45,200
^{87m}Sr(388.5)	8.7	7.7-13.2	17.4	12.2-176.5	ND	6.3	3.8-12.6
^{128}I(442.7)	2.2	ND-6.4	0.4	ND-3.6	ND	0.07	ND-0.1
^{80}Br(617.0)	0.6	0.34-1.1	ND	ND-0.4	0.32	0.2	ND-0.3
^{27}Mg(844.0)	809	706-1,095	675	566-2,304	123	140	89-162
^{56}Mn(846.9)	1.9	1.5-2.5	1.1	0.64-3.2	1.0	1.0	0.7-1.5
^{66}Cu(1039.0)	0.91	ND-1.43	0.79	ND-1.49	0.54	0.44	ND-0.82
^{41}Ar(1293.6)	5.2	3.6-9.2	4.4	2.1-8.3	4.2	3.0	2.1-3.6
^{24}Na(1368.4)	115	81-162	110	84-162	36	22	17-51
^{42}K (1524.7)	3,022	2,257-3,541	5,477	4,749-6,789	2,106	1,888	1,114-3135
^{38}Cl(1642.0)	83	70-89	22	16-44	32	10.3	7.8-19.1
^{49}Ca(3083)	930	746-1,151	1,513	1,151-38,100	838	1,119	827-2,021
^{28}Al(1778.9)	0.4	0.2-0.6	0.6	0.2-1.5	0.5	0.3	0.2-1.0

Table 1. The average (Av.) concentrations and range of concentrations in the sapwood and heartwood in sections of elm trees from the Guildford area, and from the Stoke-on-Trent area. Values are in micrograms per gram.(ND = Below detection limit).

Proceedings, ERDA X-and Gamma-Ray Symp. Ann Arbor, MI, May 19-21, 1976 (Conf 760539)

DETERMINATION OF SULFUR IN WHOLE COAL BY X-RAY FLUORESCENCE SPECTROMETRY

William G. Lloyd and Henry E. Francis
Institute for Mining and Minerals Research
213 Bradley Hall, University of Kentucky
Lexington, KY 40506

Total sulfur in 26 Kentucky coals has been determined with a commercial energy-dispersive x-ray fluorescence spectrometer, correcting for the interactions of five other mineral elements by a simple multiple regression analysis. XRF results are not as good as properly conducted ASTM analyses, but are superior to several other fast methods.

ASTM Analyses

The determination of total sulfur in coal has traditionally been based upon the controlled combustion of pulverized coal samples, followed by the titrimetric, conductimetric or gravimetric measurement of the resulting sulfur oxides. Two of these classical procedures, both entailing the gravimetric determination of sulfur as barium sulfate, have been adopted as standard methods by the American Society for Testing Materials.[1] For both the Eschka and Bomb Wash procedures ASTM has specified the following:

sulfur content	repeatability	reproducibility
less than 2%	± 0.05%	± 0.10%
more than 2%	± 0.10%	± 0.20%

Thirteen bituminous coals were selected to provide total sulfur contents of 0.5-5.0%. Each was pulverized to -200 mesh, dried uniformly in a Brabender forced-air oven (110°C for 30 min.), mixed again, and split by riffle box into a number of analytical samples. Six sets of ASTM total sulfur analyses were obtained, from four different laboratories (Table 1). For each coal a "best ASTM" value was estimated by excluding the highest and lowest of the six analyses and then averaging the remaining four.

Table 1

ASTM Sulfur Analyses for Thirteen Kentucky Coals

	Eschka				Bomb Wash		Best
Coal	Lab A	Lab B	Lab C	Lab D	Lab C	Lab D	ASTM*
1	0.62%	0.63%	0.77%	0.61%	0.60%	0.59%	0.62%
2	0.84	0.83	1.07	0.84	0.83	0.83	0.84
3	1.09	1.13	1.26	1.09	1.01	0.98	1.08
4	0.95	0.96	1.02	0.92	0.93	0.95	0.95
5	1.45	1.44	1.61	1.41	1.38	1.33	1.42
6	2.26	2.23	2.45	2.22	2.17	2.17	2.22
7	0.54	0.60	0.72	0.53	0.54	0.63	0.57
8	1.94	1.88	2.14	1.90	1.88	1.67	1.90
9	3.08	3.00	3.12	2.99	2.99	2.65	3.01
10	3.91	3.87	4.00	3.81	3.66	3.44	3.81
11	3.63	3.70	3.73	3.53	3.49	3.49	3.59
12	4.98	4.88	5.05	4.81	4.78	4.53	4.86
13	2.03	2.02	2.23	2.00	1.96	1.77	2.00

* average of four after dropping highest and lowest

Three quality tests were built into this experimental block. These are described below.

Quality of ASTM Analyses

Each laboratory received 24 coal samples, among which were eleven pairs of blind-labelled duplicates. (A table of random numbers was used for serial labeling.) Analytical repeatability was estimated by averaging the spreads between the duplicate analyses. These data are shown in the first column of Table 2.

A second test makes use of the "best ASTM" values of Table 1. These are determined with fairly good specificity: standard deviations are often below 2% relative and in all cases below 5% relative. If it is assumed that these "best" values are close to true values, an empirical estimate of accuracy can be made by examining the spreads between individual analytical values and the "best ASTM" values for the same coals. Average spreads for these coals are shown in the second column of Table 2.

Table 2

Quality of the ASTM Sulfur Analyses in Table 1

Data Set	Repeatability*	Avg diff from "best ASTM"*	Avg rel error for NBS standards*
Eschka Lab A	0.020%	0.035%	1.0%
Eschka Lab B	0.028	0.030	4.4
Eschka Lab D	0.030	0.019	2.3
Bomb Wash Lab C	0.059	0.050	2.7
Bomb Wash Lab D	0.129	0.154	13.
Eschka Lab C	0.092	0.176	20.

* basis of estimate described in text

In addition, two of the coal samples in each set were blind-labelled NBS standard coals, for which the sulfur contents are known with confidence. Coals 7 and 13 are NBS materials 1631A and 1631B, containing (after drying) approximately 0.55% and 2.03% sulfur, respectively. The average relative error for these two NBS coals is shown in the right-hand column of Table 2.

[For this quality study analytical values were calculated to the nearest .001%. The data of Table 1, rounded to the nearest .01%, give slightly different figures.]

Table 2 shows that four of the six ASTM data sets clearly meet ASTM standards for repeatability and reproducibility. The presence of the two poorest data

sets is disturbing. Not every laboratory purporting to provide an "ASTM sulfur analysis" is capable of doing so.

Analysis by Energy-Dispersive X-Ray Fluorescence

A recent review[2] of the application of modern instrumental methods to elemental analysis of coal cites x-ray fluorescence as the only relevant instrumental method for sulfur in coal. In the past decade wavelength-dispersive XRF spectrometry has been shown to be directly applicable to the analysis of whole coal for sulfur and for many other elements.[3]

We have made use of a commercial energy-dispersive XRF spectrometer (Finnigan Corp. model 900), equipped with a 250-watt Rh-targeted x-ray tube. Work involving sulfur K fluorescence and other low-energy radiation is carried out under vacuum (0.1 torr), using a large (6 mm) collimator to minimize the effect of sample micro-inhomogeneity. In preliminary work we found better sample-to-sample reproducibility working with loose pulverized coal than with briquetted or planchetted coal samples. For the present work loosely powdered coal was loaded to a depth of 9-12 mm (substantially exceeding infinite thickness) in standard commercial 1-1/8 in. plastic sample cups with 0.10-mil mylar windows.

In our instrument the sulfur peak shows an optimum signal-to-background ratio at tube power of about 14 KeV. Data were acquired at this potential and with a tube current of 0.40 milliamperes, this setting providing a counting dead time of about 30%. The fluorescing x-rays were counted for 1000 sec in 1024 channels spanning the energy range 0.00-8.00 KeV, with a detector bias potential of 1000 v. Under these conditions the minimum detectable limits (3σ level) are, for Si, S, Ca and Fe, .006%, .002%, .001% and .0002%, respectively. The most prominent low-energy fluorescent peaks from western Kentucky coals are:[4]

Si Kαβ	at 1.74 KeV	typically 15-60 cps
S Kα	2.31	50-220
K Kα	3.31	5-60
Ca Kα	3.69	15-60
Ti Kα	4.51	10-75
Fe Kα	6.40	100-1200
Fe Kβ	7.06	(not used)

Other elements with fluorescent peaks in this energy range (Mg, Al, P, Cl, Sc, V, Cr, Mn, Ni) are present in sufficiently low concentrations that their intensities are insufficient to effect any substantial modification of the sulfur K peak intensity.

Interelement effects were calculated by an empirical approach similar to that of Lucas-Tooth and Pyne,[5] using a standard computer program for multiple regression analysis.[6] For our instrument under the conditions described above the coefficients obtained are:

$$\begin{aligned} S(\text{concn in ppm}) = {} & I(S)*[111.7 - .4817*I(S) \\ & +.1681*I(Fe) +4.527*I(Si) \\ & -1.092*I(K) -2.064*I(Ca) \\ & +3.039*I(Ti)] -12.88*I(Fe) \\ & -755.0*I(Si) +467.0*I(K) \\ & +110.1*I(Ca) +9.931*I(Ti) \end{aligned} \qquad (1)$$

where I(S), I(Si), etc., are the intensities in counts per second of the indicated fluorescent peaks.

The sulfur concentrations calculated from the raw XRF data by Eqn. (1) are shown, along with the "best ASTM" values for coals 1-13 in the first two columns of Table 3. A general agreement is evident between these two sets of data.

Table 3

Non-ASTM Sulfur Analyses for Thirteen Kentucky Coals

Coal	Best ASTM*	XRF this lab	Train 1 Lab E	Train 2 Lab F	Train 3 Lab G
1	0.62%	0.63%	0.68%	0.73%	0.67%
2	0.84	0.84	0.94	0.92	0.91
3	1.08	1.07	1.02	1.13	1.20
4	0.95	1.06	1.01	1.13	1.15
5	1.42	1.68	1.36	1.48	1.52
6	2.22	2.35	2.04	2.25	2.44
7	0.57	0.56	0.42	0.56	0.62
8	1.90	2.50	1.68	1.89	2.02
9	3.01	2.91	2.73	3.70	3.24
10	3.81	3.70	3.39	3.57	4.10
11	3.59	3.71	3.20	3.40	3.80
12	4.86	5.01	4.38	4.70	5.07
13	2.00	1.95	1.74	1.84	2.07

* from Table 1

Analysis by Fast Combustion Train Methods

The most widely used alternatives to the ASTM total sulfur analyses are variations of fast combustion train procedures, whereby weighed samples of coal are burned in oxygen at atmospheric or superatmospheric pressure and the sulfur oxide content of the combustion mixture is determined titrimetrically or conductimetrically.

Additional portions of coals 1-13 were analyzed by two well-established commercial analytical laboratories, both using fast combustion train methods incorporating some proprietary modifications. Results of these analyses are shown in Table 3 under the headings Lab E and Lab F.

In addition, two packaged laboratory sulfur-analyzing trains were evaluated by colleagues at the University of Kentucky. Analyses of coals 1-13 were conducted by chemists experienced with the use of these instrumental procedures. The data obtained from the better-known of these two trains is given in Table 3 under the heading Lab G. The other train failed to stand up to 24 successive sulfur analyses, notwithstanding many starts over a three-month period.

Quality of Non-ASTM Analyses

The same quality tests which were built into the ASTM test block are applied to the several non-ASTM data sets in Table 4. It is evident that none of these fast methods is as good as a properly-run ASTM analysis for total sulfur in coal. Among the fast procedures evaluated, however, the XRF procedure is the best of the group by each of the three criteria used in Table 4.

Discussion

The above findings have been based upon cross-analysis of a group of thirteen coal samples. A second group of thirteen coals has been similarly

split and analyzed by the Eschka procedure (two sets), by XRF using Eqn. (1), and by fast combustion train methods (two sets). Raw results are shown in Table 5. If the Eschka data from Lab A are taken as reference values, the XRF data conform most closely to these values (average difference 0.10%), followed by the combustion train data of Labs F (0.12%) and E (0.18%) and by the amazing data from Lab C (average difference 0.51%). These results with this second group of coals are generally consistent with expectations based upon the data of Tables 1-4.

Table 4

Quality of the Non-ASTM Sulfur Analyses in Table 3

Data Set	Repeatability*	Avg diff from "best ASTM"*	Avg rel error for NBS standards*
[best four ASTM sets]	.02-.06%	.02-.05%	1.0-4.4%
XRF this lab	.090	.128	2.7
Train 1 Lab E	.183	.212	19.
Train 2 Lab F	.195	.159	5.5
Train 3 Lab G	.093	.147	7.2

* calculated as in Table 2

Table 5

Sulfur Analyses of a Second Group of Kentucky Coals

Coal	Lab A Eschka	this lab XRF	Lab C Eschka	Lab E Train 1	Lab F Train 2
14	1.61%	1.66%	1.78%	1.42%	1.61%
15	0.67	0.67	0.89	0.63	0.60
16	0.67	0.47	1.18	0.78	0.90
17	1.95	1.89	1.71	1.85	1.96
18	0.59	0.58	0.30	0.59	0.69
19	2.12	1.93	1.64	2.04	2.26
20	2.97	3.30	2.74	2.87	3.00
21	0.80	1.15	0.68	0.81	1.37
22	4.78	4.80	3.47	4.52	4.81
23	3.91	3.98	4.40	3.50	4.10
24	0.52	0.51	...	0.57	0.53
25	5.02	5.02	3.50	4.39	5.12
26	4.77	4.73	...	4.44	4.92

The coals analyzed in Tables 1 and 3 have ash contents of 5 to 23% and total nitrogen contents of 1.0 to 2.0%. The pyritic sulfur fraction varies from 2% to 73% of the total sulfur, although this variation is not randomly distributed: the five coals of lowest total sulfur have pyritic fractions below 25%, while the eight higher sulfur coals have pyritic fractions above 40%. Analysis of error for each of the total sulfur data sets in Tables 1 and 3 failed to show significant correlations with any of these quasi-independent coal parameters. One combustion train data set shows probable systematic error associated with total sulfur content (i.e., a probable standardization error)

The properly conducted ASTM sulfur analysis (represented by the data of Labs A and B) is consistent and reliable, and in our judgment still provides the best measurement of total sulfur in coal. The drawback to both of the ASTM procedures is that they are slow and labor-intensive. Even with large groups of samples the investment in technician time cannot be reduced below about one man-hour per sample analyzed, and even with small groups of samples the analytical turnaround time is at least two days.

Among the fast methods for determination of total sulfur in coal, energy-dispersive x-ray fluorescence spectrometry appears to be the most consistent and the most accurate. In addition it has the obvious advantages of automated operation, concurrent simultaneous analysis of other fluorescing elements, and nondestructivity. We conclude that energy-dispersive XRF is now very close to meeting current ASTM standards of precision and accuracy for this analysis.

Acknowledgments

We are indebted to Prof. George F. Crewe (Chemical Engineering), Prof. Russell E. Puckett (Office of Research and Engineering Services), and Mr. Morgan R. Yewell (Mining Laboratory), all of the University of Kentucky, for technical advice and assistance. Dr. Gloria O. Kervyn of this laboratory provided valuable technical assistance. Mssrs. Russell Hubbard, Richard McAskill and Mark Davis assisted in the experimental work. We thank Dr. O. J. Hahn, Associate Director of the Institute, for support of this study.

References

1. American Society for Testing Materials, ASTM Standards, Part 26, Method D 3177-73 (1974).

2. B. Griefer and J. K. Taylor, "Pollutant Analysis Cost Survey", Rept. EPA-650/2-74-125, Dec. 1974.

3. L. T. Kiss, Anal. Chem., 38, 1731 (1966); M. Berman and S. Ergun, Fuel, 47, 285 (1968); C. H. Anderson and R. E. Jones, "Determination of Inorganic Constituents of Coal by X-Ray Fluorescence," Pittsburgh Conf. on Anal. Chem. and App. Spectroscopy, Mar. 1968; anon., "Rapid Determination of Sulphur in Coal by X-Ray Fluorescence Spectrometry", Coke Res. Rept. 71 (Brit. Coke Res. Assn.), 1972; S. D. Rasberry and K. F. J. Heinrich, in ref. 2, pp 49ff; R. R. Ruch, H. J. Gluskoter and N. F. Shimp, Environmental Geology Notes (Illinois) 72, 1974; J. K. Kuhn, W. F. Harfst and N. Shimp, in S. Babu, ed., "Trace Elements in Fuel", Advances in Chem. (Amer. Chem. Soc.), 144, 1975, pp 66ff.

4. W. G. Lloyd and H. E. Francis, Second Symposium on Coal Utilization (Natl. Coal Assn.) Proceedings, 324 (1975).

5. J. Lucas-Tooth and C. Pyne, Advan. X-Ray Anal., 7, 523 (1964).

6. J. Service, "A User's Guide to the Statistical Analysis System", North Carolina State Univ., 1972, pp 94ff.

Proceedings, ERDA X-and Gamma-Ray Symp. Ann Arbor, MI, May 19-21, 1976 (Conf 760539)

DETERMINATION OF SULFUR, ASH AND TRACE ELEMENT CONTENT OF COAL, COKE AND FLY ASH USING MULTIELEMENT TUBE-EXCITED X-RAY FLUORESCENCE ANALYSIS

J. A. Cooper, B. D. Wheeler, G. J. Wolfe, D. M. Bartell and D. B. Schlafke
ORTEC Incorporated
Oak Ridge, TN 37830

SUMMARY

A procedure using tube excited energy dispersive x-ray fluorescence analysis with interelement corrections has been developed for multielement analysis of major and trace elements and ash content of coal, coke and fly ash. The procedure uses pressed pellets and an exponential correction for interelement effects. The average deviations ranged from about 0.0003% for V at an average concentration of about .003% to 0.1% for S at an average concentration of about 4%. About 25 elements were measured and 100 second minimum detectable concentrations ranged from about one part per million for elements near arsenic to about one tenth of one percent for sodium.

INTRODUCTION

Coal is an important current energy source and will continue to play a major role in meeting our future energy needs. The quality and cost of coal currently depends on its sulfur and ash contents, and may depend on other specific elemental parameters in the future as environmental requirements become more restrictive. This paper describes a procedure using tube excited energy dispersive x-ray fluorescence which has been developed to measure about 25 elements in coal, coke and fly ash and to estimate the ash content of coal and coke.

EXPERIMENTAL CONDITIONS

An ORTEC 6110 TEFA (Tube-Excited Fluorescence Analyzer) System was used for this investigation. It included a PDP 11/05 Computer and dual drive floppy disk.

The samples analyzed in this study consisted of a variety of coals, cokes and coal ash samples.[1-4] They were ground for two minutes in a Spex Shatter Box[5] rotary swing mill using a variety of grinding aids and pelletized. The resulting pellets were loaded directly into the sample chamber which was then evacuated.

The samples were qualitatively analyzed using the optimum sensitivity excitation conditions listed in Table 1. Although the optimum excitation conditions are often required for the analysis of trace elements, the major and minor elements can usually be quantitatively analyzed simultaneously using only one excitation condition.

TABLE 1

Excitation Conditions For Optimum Sensitivities

Elemental Ranges	Line	Anode	Voltage	Filter
Na to Ca	K	Mo	10	None
Ca to Fe	K	W	25	Cu
Ce to Tb	L	W	25	Cu
Fe to Sr	K	Mo	35	Mo
Tb to Bi	L	Mo	35	Mo
Sr to Rh	K	W	40	Cd
Th and U	L	W	40	Cd
Rh to Ce	K	Mo	50	Mo

The resulting spectral data were quantitatively analyzed using ORTEC's FLINT[6] software which provides a linear least squares fit to the interelement corrected intensities. This program corrects the observed x-ray intensities for absorption and enhancement due to the presence of other elements. The concentration of the ith element is given by the equation

$$C_i = A' + B'I_i \left[\exp\left(-M_{ij} C_j\right)\right] \qquad (1)$$

where

M_{ij} is the interaction coefficient for element j on element i and

C_j is the concentration of the jth element.

The interaction coefficients are determined by a nonlinear multiple least squares fit of the standards concentration-intensity data. This requires a minimum of n + 2 standards where n is the number of interfering elements.

Elemental concentrations in unknown samples were calculated with an iterative process using Equation 1 and interaction coefficients calculated from standards.

RESULTS AND DISCUSSION

Representative x-ray spectra excited under different excitation conditions are illustrated in Figures 1 to 3. Figure 1 shows the semilogarithmic plot of the low energy portion of the x-ray spectrum of a fly ash specimen. This spectrum was excited with direct bremsstrahlung radiation from a rhodium anode which maximizes the sensitivity for the light elements including sulfur. This excitation condition provides for the simultaneous analysis of the major and minor elements from sodium to iron. Although there is considerable peak overlap in the sodium to silicon region of the spectrum, simple "region-of-interest" peak integrations can be used since the interelement correction program will minimize both the spectral interference and concentration variation effects.

Figure 2 shows the 0 to 10 keV portion of the x-ray spectrum of NBS standard coal (SRM 1632)[4] as excited with copper filtered tungsten radiation. This provides the best sensitivity for elements from Ca to Fe as can be seen from the clearly defined chromium and manganese peaks representing concentrations of about .002 and .004%, respectively.[7]

The optimum sensitivity for trace elements from iron to strontium, including elements near lead, is obtained by using molybdenum filtered radiation from a molybdenum anode as shown in the semilogarithmic plotted spectrum in Figure 3. Twenty elements are measurable in this single spectrum. Between twenty-five and thirty elements can be measured in these samples by using the different excitation conditions listed in Table 1. Upper limits can be set for many other elements based on the minimum detectable concentrations (MDC) shown in the 100 second MDC plots in Figure 4.

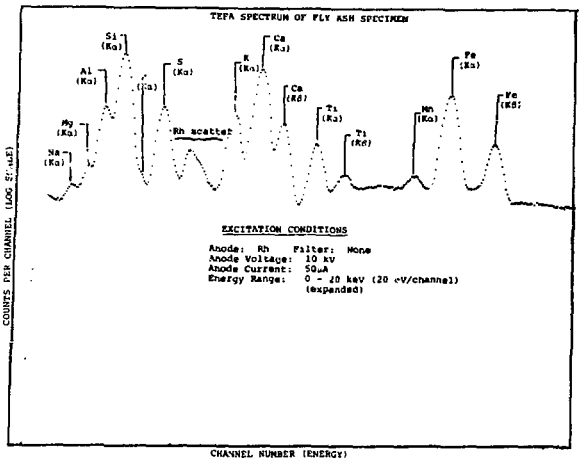

Figure 1. Logarithmic plot of the x-ray spectrum obtained from a specimen of fly ash obtained with a tube-excited fluorescence analyzer.

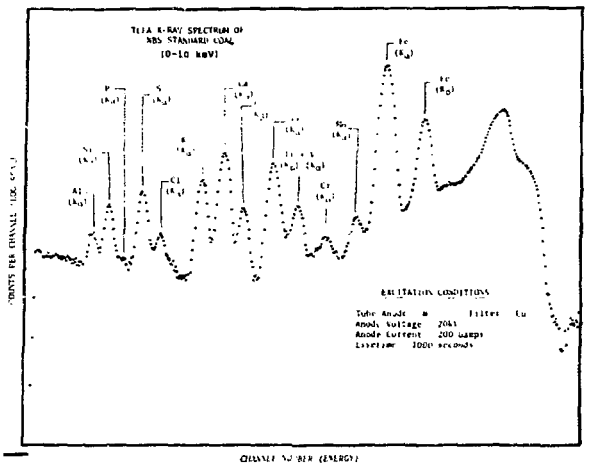

Figure 2. Logarithmic plot of the x-ray spectrum obtained from a specimen of NBS coal obtained with a tube-excited fluorescence analyzer.

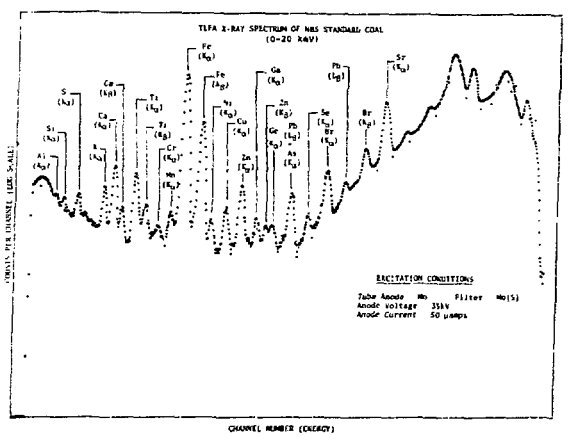

Figure 3. Logarithmic plot of the x-ray spectrum obtained from a specimen of coal obtained with a tube excited fluorescence analyzer.

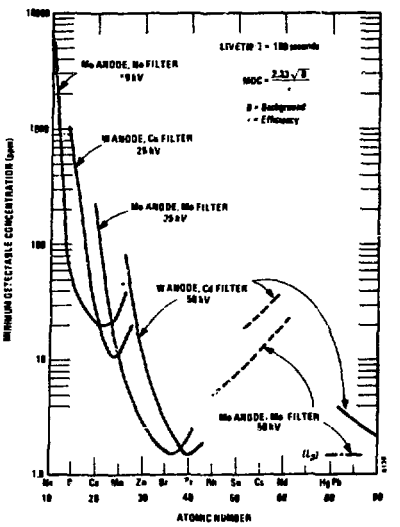

Figure 4. Minimum detectable concentration (MDC) in coal material.

The qualitative results for coal, coke and fly ash are summarized in Tables 2 to 4. Table 2 compares the results obtained by tube-excited fluorescence analysis (TEFA) with those listed by the Illinois State Geological Survey.[4] The TEFA results are not averages of replicate analyses but the results of a single analysis. Even so, the average deviations of about 0.02% represent relative accuracies of about 1%. These analyses, as well as the aluminum, sulfur and calcium, were corrected for interelement effects while the other elements did not require corrections.

The sums of the major element compositions are listed at the bottom of the table. The agreement with the listed ash values is relatively good despite the complex chemical changes taking place. The agreement is usually within 10% (relative) which is often adequate for estimation of the ash content. These coals, however, were quite similar in composition and a broader range of coal types should be studied before drawing general conclusions.

Table 3 compares the results of the coke analyses. Samples 4, 9 and 11 were blind unknowns, the results of which were not obtained until after the TEFA results were reported. The agreement of the TEFA values with the list values is excellent in most cases. The remaining small differences may be a result of significant

TABLE 2

Comparison Of Results Obtained For The Analysis Of Illinois State Geological Survey Coal Samples

	C15263		C15278		C16264		C16317		C16408		C16408* C16317		C16264* C16317		C15278* C16264		Unknown		Avg Deviation
	TEFA	LIST	TEFA	LIST	TEFA	LIST	TEFA	LIST	TEFA	LIST	TEFA	LIST	TEFA	LIST	TEFA	LIST	TEFA	LIST	
Percent																			
Na	.0300	.0140	.0300	.0460	.0300	.0510	.0300	.0170	.0300	.0070	.0300	.0120	.0300	.0370	.0300	.0050	.0300	.0310	.0200
Mg	.0400	.0400	.0400	.0500	.0400	.0400	.0400	.0500	.0400	.0300	.0400	.0400	.0400	.0450	.0400	.0450	.0400	.0450	.0050
Al	1.0100	1.0100	1.0500	1.1300	.9400	0.9200	1.1300	1.1200	1.0000	1.0200	1.0900	1.0700	1.0300	1.0200	1.0600	1.0200	1.0600	1.0700	.0205
Si	1.6400	1.6500	2.1700	2.1700	1.8900	1.9200	2.4000	2.4600	1.3800	1.4100	2.0700	1.9400	2.1900	2.2500	2.0800	2.0400	2.0200	1.9100	.0400
P	.0030	.0320	.0060	.0070	.0120	.0110	.0090	.0020	.0140	.0200	.0110	.0110	.0100	.0066	.0040	.0090	.0020	.0050	.0030
S	3.0500	3.1600	3.5800	3.3500	4.3200	4.5200	3.5100	3.2500	5.0300	4.9000	4.0200	4.0800	3.8000	3.8800	3.7700	3.9400	3.0000	3.2600	.1500
Cl	.0600	.0200	.0500	.1100	.0600	.0100	.0300	.0200	.0600	.1000	.0400	.0600	.0400	.0150	.0600	.0600	.0600	.0650	.0300
K	.1500	.1400	.1700	.1700	.1600	.1500	.1500	.1700	.1400	.1300	.1500	.1500	.1600	.1600	.1500	.1600	.1500	.1600	.0060
Ca	.1400	.1000	.6100	.8200	.6700	.5600	.7400	.7300	.2100	.2300	.4800	.4800	.7200	.6400	.6700	.6900	.4600	.4600	.0600
Ti	.0600	.0500	.0600	.0600	.0600	.0500	.0600	.0700	.0500	.0500	.0600	.0600	.0600	.0600	.0500	.0550	.0500	.0550	.0050
V	.0029	.0023	.0027	.0027	.0026	.0022	.0027	.0032	.0029	.0031	.0028	.0032	.0027	.0027	.0025	.0024	.0026	.0025	.0003
Fe	2.6400	2.6300	1.6000	1.6500	2.0500	2.0500	1.6100	1.570	3.5200	3.5100	2.5000	2.5400	1.8300	1.8100	1.6600	1.8500	2.1900	2.1400	.0200
Parts Per Million																			
Ni	42	40	18	8	16	22	23	30	24	26	26	28	25	26	21	15	30	24	.0004
Cu	40	46	7	8	5	10	22	29	15	16	21	18	19	15	13	9	24	26	.0003
Pb	106	96	30	9	43	53	53	72	41	40	52	56	52	62	37	30	46	52	.0015
Ash(%)	8.8	8.0	9.4	11.0	10.2	12.4	9.7	12.0	11.5	11.2	10.5	11.6	9.9	12.2		11.7	9.2	9.5	

*These samples were composed of 50% of each of the samples listed.

TABLE 3

ELEMENTAL CONCENTRATIONS (%) OF COKE SAMPLES

Sample Number	Al_2O_3* TEFA	Al_2O_3* WC**	SiO_2 TEFA	SiO_2 WC	S TEFA	K_2O TEFA	CaO TEFA	CaO WC	Ti TEFA	Cr TEFA	Mn TEFA	Fe_2O_3 TEFA	Fe_2O_3 WC
1	4.16	4.19	9.89	9.63	4.05	0.69	0.78	0.78	0.17	.0083	.0034	5.98	6.06
2	5.23	5.18	10.55	10.85	3.24	0.57	0.69	0.60	0.19	.0080	.0031	4.96	5.12
3	4.04	4.16	9.84	9.39	3.88	0.69	0.75	0.77	0.18	.0082	.0024	4.05	4.13
4	4.10	3.98	9.58	9.70	4.02	0.67	0.71	0.72	0.18	.0083	.0034	5.84	5.76
5	4.09	4.18	9.27	9.18	3.90	0.69	0.71	0.77	0.17	.0078	.0034	5.51	5.37
6	4.24	4.53	9.44	9.69	3.82	0.69	0.70	0.83	0.18	.0077	.0037	5.44	5.57
7	4.25	4.12	9.18	9.26	3.85	0.69	0.69	0.65	0.17	.0073	.0037	5.58	5.35
8	5.39	4.89	10.88	11.14	3.68	0.57	0.72	0.68	0.19	.0086	.0037	5.89	6.04
9	4.21	4.07	9.69	9.52	3.81	0.61	0.71	0.78	0.18	.0071	.0034	5.78	5.58
10	4.99	5.29	10.12	10.38	4.27	0.56	0.70	0.68	0.17	.0081	.0031	5.30	5.23
11	4.50	4.68	10.55	10.67	3.94	0.64	0.72	0.86	0.18	.0083	.0034	5.89	5.75

* TEFA - Tube-Excited Fluorescence Analyzer

** WC - Wet Chemical Methods

+ The Al_2O_3 concentrations have been corrected for the effect of SiO_2 and Fe_2O_3

uncertainties in the standards (wet chemical analysis methods were used to determine the listed values). Table 5 shows a comparison of the elemental iron concentration results obtained on three different days with three different excitation conditions. The deviations from the averages in most cases are less than 1% (relative) showing excellent analytical precision extending over a period of one month.

The concentration of the other elements listed in Table 4 were determined from the counting efficiencies established from the Si, Al, Fe and Ca counting efficiencies. That is, since the counting efficiencies are smoothly varying functions of atomic number, the counting efficiencies of S, K, Ti, Cr, and Mn were determined from the values established for Si, Al, Fe, and Ca. These values are in quite good agreement with what is expected and even better quantitative results could be obtained with appropriate standards.

The quantitative results of the fly ash analyses are listed in Table 4. All of the elements except Na, P, Ti and Sr were corrected for interelement effects. Although the agreement is not as good as might be expected, the average deviations are in all cases, less than the estimated wet chemical reproducibilities listed at the bottom of the table.

CONCLUSION

Tube-excited energy dispersive x-ray fluorescence can provide rapid and accurate multielement analyses of about 25 elements in coal, coke and fly ash ranging from sodium to lead. Accuracies approaching a tenth of a percent (absolute) can be achieved in the analysis of the major elements but require interelement corrections. One hundred second minimum detectable concentrations range from about one part per million for

TABLE 4

Comparison Of TEFA And Wet Chemical Analysis Results for Coal Ash

ELEMENTAL CONCENTRATIONS (%)

	SiO_2		Al_2O_3		Fe_2O_3		TiO_2 f		P_2O_5 f		CaO		MgO		So_3		Na_2O f		K_2O		Sr	TOTAL	
SAMPLE ID	TEFA	WC	TEFA	WC	TEFA	WC	TEFA	WC	TEFA	WC	TEFA	WC	TEFA	WC	TEFA	WC	TEFA	WC	TEFA	WC	TEFA	TEFA	WC
2819	47.76	48.15	14.72	15.70	3.08	2.86	.85	1.03	.25	.29	12.08	12.32	4.40	3.35	8.96	8.72	6.27	6.57	1.28	1.14	0.33	99.99	100.13
2822	53.00	53.50	16.73	17.95	4.42	3.52	.75	0.05	.25	.46	9.88	9.38	3.44	3.27	5.57	4.94	2.80	3.07	1.87	1.88	0.16	98.87	98.02
2840	39.60	39.79	25.68	25.80	6.89	7.01	.7	0.53	.36	.22	13.67	12.74	4.35	3.95	8.05	8.06	.19	0.22	.58	0.53	0.05	100.14	98.02
2843	40.67	39.59	28.35	27.75	5.25	5.38	.85	1.19	.37	.23	12.35	12.60	2.80	3.32	10.21	10.16	.19	0.15	.66	0.66	0.04	101.74	98.85
2844c	38.88	39.05	24.91	25.25	5.16	5.15	.69	0.89	.24	.19	17.18	17.70	4.39	4.32	6.35	6.24	.19	0.34	.80	0.87	0.04	98.83	101.03
2945	49.95	49.22	24.13	24.75	18.56	18.79	1.00	1.04	.46	.42	0.90	0.56	1.58	1.43	.75	0.67	.79	0.40	2.97	3.06	0.01	101.10	100.00
2946	47.00	46.54	21.89	22.12	17.11	17.02	.85	0.09	.45	.52	4.83	4.90	.79	1.06	4.82	5.12	.19	0.40	2.54	2.52	0.02	100.49	100.36
3003	42.33	43.67	27.43	26.90	20.12	20.02	1.09	1.10	.41	.83	2.72	3.25	.98	1.16	1.74	2.12	.38	0.91	1.79	1.66	0.05	99.04	101.64
3023-1	79.09	79.11	15.67	15.30	.78	.80	1.00	.88	.33	.15	.17	.14	.35	0.44	.40	.05	.46	.11	1.59	1.45	0.01	99.85	101.52
3048	48.69	49.22	27.70	28.00	3.91	3.43	.88	.85	.37	.17	8.17	8.40	3.31	2.74	6.31	6.24	.19	.28	1.30	1.46	0.07	100.90	98.43
3054	46.66	47.08	21.01	20.37	3.11	3.72	.87	.75	.21	.30	12.09	11.76	6.07	6.47	5.21	5.25	4.28	4.00	1.09	1.20	0.27	97.81	100.79
3055	47.90	46.54	18.54	18.25	3.76	4.00	.89	.78	.26	.33	11.02	11.20	5.67	6.22	6.70	7.19	4.76	4.62	1.10	1.15	0.30	100.92	100.90
3056	57.17	57.24	12.27	11.00	3.40	3.86	.70	.72	.19	.16	12.14	12.18	4.00	5.22	5.86	6.19	3.22	3.20	1.18	1.18	0.13	101.06	100.95
WC REPROD.	-	2.0	-	2.0	-	0.7	-	0.25	-	.15	-	0.40	-	0.5	-	-	-	0.3	-	0.3	-		6.60
TEFA AV DEV	0.55	-	0.59	-	0.30	-	0.13	-	.13	-	0.32	-	0.29	-	0.23	-	0.21	-	0.07	-	-	2.82	

f Ti, P, and Na were not corrected for interelement effects

TABLE 5

Comparison of Elemental Iron Concentrations Obtained on Three Different Days Under Three Different Excitation Conditions

Date	4/4/75	5/13/75	5/14/75	
Anode	W	W	Mo	
Filter	Cu	Cu	None	
Voltage	20	25	20	
Sample				Average
1	4.25	4.14	4.14	4.18
2	3.50	3.44	3.45	3.46
3	4.24	4.21	4.23	4.23
5	3.66	3.93	3.94	3.85
6	3.82	3.84	3.78	3.81
7	3.87	3.93	3.90	3.90
8	4.13	4.10	4.13	4.12
10	3.81	3.71	3.75	3.76

elements near arsenic to about one tenth of one percent for sodium.

ACKNOWLEDGMENTS

The authors thank John Kuhn of the Illinois State Geological Survey, Joe Corpening of Monsanto Industrial Chemicals Company and Bill Montgomery of Canadian Center for Mineral and Energy Technology for providing the coal, coke and fly ash samples used in this study. We also thank David Smiley for his assistance with the analysis.

REFERENCES

1. R. R. Ruch, H. J. Gluskotev and N. F. Shimp, "Occurrence and Distribution of Potentially Volatile Trace Elements in Coal", Environmental Geology Notes, Report Number EGN-72, Aug. 1974.

2. The coke samples were provided by the Monsanto Industrial Chemicals Company, Columbia, Tennessee.

3. The fly ash samples were provided by the Canadian Center for Mineral and Energy Technology, Ottawa, Canada.

4. National Bureau of Standards standard reference material 1632 and 1633.

5. Spex Industries Incorporated, P. O. Box 798, Metuchen, New Jersey, 08840.

6. J. A. Cooper, B. D. Wheeler, D. M. Bartell and D. A. Gedcke, "Analysis of Portland Cement, Clinker, Raw Mix and Associated Ceramic Materials Using An Energy Dispersive X-Ray Fluorescence Analyzer With Interelement Corrections", Advances in X-Ray Analysis, 19 213, 1976.

7. J. M. Ondov, W. H. Zoller, Ilhan Olmez, N. K. Aras, G. E. Fordon, L. A. Rancitelli, K. H. Abel, R. H. Filby, K. R. Shah and R. C. Ragaini, "Elemental Concentrations in the National Bureau of Standards Environmental Coal and Fly Ash Standard Reference Materials", Analytical Chemistry, 7 1102, 1975.

Proceedings, ERDA X-and Gamma-Ray Symp. Ann Arbor, MI. May 19-21, 1976 (Conf 760539)

RADIO-ISOTOPE INDUCED X-RAY FLUORESCENCE AS A TECHNIQUE FOR ANALYSIS OF HYDRODESULFURIZATION CATALYSTS, ELEMENTAL

J.J. LaBrecque, Centro de Petroleo Y Qumicia, Instituto Venezalano de Investigaciones Cientificos, Caracus, Venezuela

and

I.L. Preiss and S. Pandian, Rensselaer Polytechnic Institute, Troy, New York 12181

Introduction

The specific action of a catalyst is controlled to a large extent by the number of active centers it presents to the system under consideration. The number of active centers, in turn, are dependent on the composition of the catalyst. So, by all accounts, the composition of a catalyst is very critical to its efficient operation. Any change in the composition will inevitably change the number of active centers and may accelerate or retard the process. Desulfurization catalysts are not exceptions to the above rule and a quality control assay of these catalyst before, after and during utilization is an absolute necessity. A rapid, reliable method is desirable for determining the composition of these catalysts.

Atomic absorption and neutron activation methods have been employed in the past with some success[1]. In both these methods the procedures are very time consuming and require pretreatment or chemical processing leading to a very large uncertainty in the composition. In the case of atomic absorption, as the desulfurization catalysts consist of MoO_3 and CoO in a silica matrix dissolution of the catalysts in a suitable solvent mixture, within a short period is almost an impossible task. Hence, the quantitative analysis by these methods is dubious to a certain extent.

To avoid sample treatment one has to depend on X-ray spectrometry. For the catalysts under consideration, the two prime elements of interest are Co and Mo. In conventional X-ray fluorescence, using tube excitation with a Mo target, Mo in the sample can not be fluoresced. If one utilizes other targets, of higher Z, the underlying bremmstrahlung and scattered electrons associated with the tube excitation decrease the signal to noise ratio in the Co region making it difficult to determine the constituent with precision.

The use of low intensity (10mCi) radioisotope excitation source obviates the necessity for multitarget X-ray apparatus and extensive shielding and can cover the range of elements required. The capability of radioisotope induced fluorescence for multi element samples in the mass region of interest has been demonstrated[2,3,4]. The use of a single source, ^{109}Cd, with essentially monochromatic radiation meets all requirements predetermined for the analysis in question.

Experimental

The primary radiation source characteristics, sample configuration and the system configuration are discussed in ref (4).

Calibration: The system was calibrated using a precision digital pulser. A Cu foil was fluoresced and the peak channel due to CuKα was noted using a Northern NS-426 readout display. The pulse height of the pulser was adjusted such that the pulser amplitude corresponded to that determined for Cu. Exact doubling and tripling of the pulse amplitude of the digital amplifier made it possible to obtain a calibration plot with ease and precision.

Internal standard: $KBrO_3$ was used as an internal standard. A known amount of $KBrO_3$, $CoCl_2$ and MoO_3 mixture was ground together to achieve a homogeneous mixture. A portion of this mixture was fluoresced to obtain the relative correction factors for Kβ/Kα ratios, fluorescence yields, the K-shell ionization cross-sections and geometry and efficiency corrections. The sample configuration ensured thin samples, and one can assume that self-excitation and self-absorption corrections, are adequately determined by the empirical correction factor. Different compositions of $KBrO_3$, $CoCl_2$ and MoO_3 were fluoresced and the relative correction factors for these are shown in Table 1, and indicate that the mean relative correction factor 1:0.68:4:38::Br Mo:Co has a precision of better than ±1% (1σerror).

A known amount of each catalyst was ground together with a known amount of $KBrO_3$ and a portion of this homogeneous mixture was fluoresced in each case. Intensities of the Kα peaks along with the relative correction factors, determined previously, were used to make a quantitative analysis of the catalyst.

For each catalyst, portions of the mixture, with internal standard, was fluoresced three times and the mean value of the percentage of Mo was found with a precision of better than ±1.5% and that of Co, better than ±2.5%. From the same mixture, three different portions were fluoresced and the results showed a precision of better than ±0.7% for the percent of Mo, and of better than ±2.6% for the percentage of Co. The above results clearly indicate the homogeneity of the mixtures made with $KBrO_3$, as an internal standard.

Results and Discussion:

Figures 1, 2, and 3 show the X-ray spectra due to Co, Mo and Br respectively. Table II compares the analysis of X-ray fluorescence with that of atomic absorption, neutron activation and prompt gamma. The analysis with photon induced X-ray fluorescence was done with a precision of ±4% (1σ error). The other methods which are destructive involve inevitable systematic errors, and the precision in these methods is considerably lower. Optimization of the Si (Li) crystal size and the activity of the primary radiation is bound to increase the precision of the technique. This method would prove to be very useful on occasions where exact analysis of the catalysts, most of which are insoluble in most of solvents or even in most of solvent mixtures, is needed. Different radiation sources, depending on absorption edges of the elements of interest, can increase the precision, as well as sensitivity. However the precision, determined in this study would appear adequate over a wide range of elemental composition while the resolution of 151eV at MnK_α insures adequate elemental resolution. The sensitivity of 10^{14} to 10^{15} atoms requires that only thin, not absorbing samples can be utilized minimizing self excitation and absorption effects in multi element samples.

Table 1

Relative Correction factors

%$KBrO_3$	%MoO_3	%CoO	relative correction factors
			Br: Mo: Co
50	15	4	1: 0.68: 4:36
60	15	4	1: 0.69: 4.45
40	15	4	1: 0:68: 4:38
50	15	3	1: 0.67: 4:34
50	15	2	1: 0.68: 4:36
50	13	4	1: 0.67: 4:34
50	11	4	1: 0.68: 4.43

Table II Comparison of the analysis by X-ray fluorescence (x-ray) with that by neutron activation (NA), atomic absorption (AA) and prompt gamma (n,γ).

Sample	x-ray	AA	(n,γ)	NA
Venkat 75-1				
MoO_3	14.63±0.59	13.01	14.49	14.61
CoO	3.02±0.12	3.57	3.19	2.71
KetJenfire 124-1,5E(Ho)				
MoO_3	11.92±0.48	12.54	13.01	13.84
CoO	3.63±0.15	3.51	3.85	3.54
Filtrol SV-10-368B				
MoO_3	15.95±0.64	15.92	16.14	15.29
CoO	2.77±0.11	3.97	2.89	2.54
Cyanamid HOS-144-1A				
MoO_3	14.86±0.59	-	13.91	15.44
CoO	3.12±0.12	-	3.91	3.79

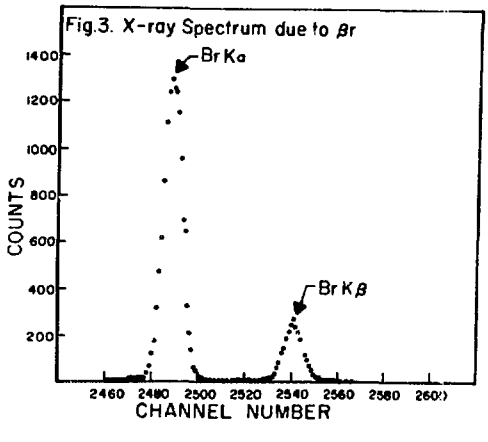

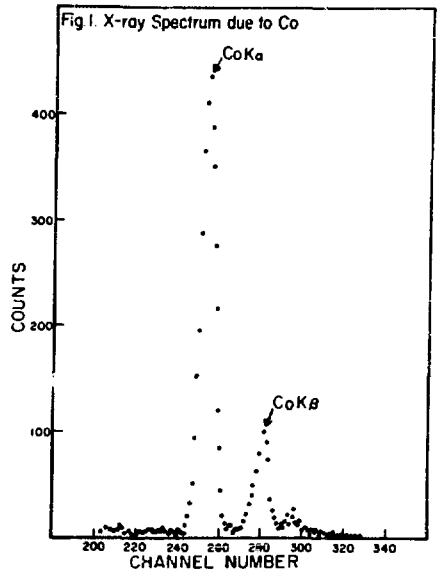

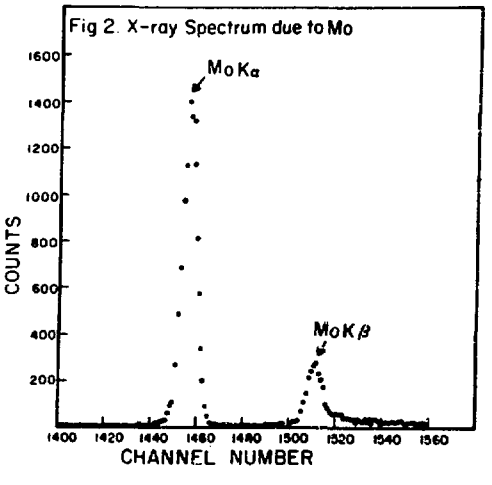

REFERENCES

1. J.J. LaBrecque, J. Radio Analy. Chem. (in press).
2. P.V. Kulkarni, I.L. Preiss, J. Radio Analytical Chem., 24, (1975) 425.
3. J.J. LaBrecque, P.V. Kulkarni, I.L. Preiss, J. Radio Analytical Chem., 14, (1973) 455.
4. S. Pandian, J.J. LaBrecque, I.L. Preiss, Applied Spectroscopy, 30, (1976) 31.

Proceedings, ERDA X-and Gamma-Ray Symp. Ann Arbor, MI, May 19-21, 1976 (Conf 760539)

DETERMINATION OF PPB CONCENTRATIONS OF URANIUM, THORIUM AND MOLYBDENUM IN WATER USING APDC PRECONCENTRATION AND RADIOISOTOPE EXCITED ENERGY DISPERSIVE X-RAY EMISSION SPECTROMETRY

A.H. Pradzynski, R.E. Henry, E.L. Draper, Jr.
Nuclear Reactor Laboratory
The University of Texas at Austin
Austin, Texas 78712

Summary

The determination of low ppb concentrations of uranium, thorium and associated elements in water has been extensively utilized as a prospecting method, and is, at present, being accomplished nationwide in a long range resource assessment program (National Uranium Resource Evaluation). In addition, such analyses are necessary for monitoring water for effluents from uranium mining and milling sites and for background level determinations in the vicinity of proposed sites. There is, thus, a need for a sensitive, rapid, multielement method of making such determinations. This paper describes a method of analysis which, in addition to meeting these criteria, eliminates one of the major problems associated with water sampling, viz., the adsorption of trace elements on the walls of the sample container. The technique combines sample preconcentration at the sampling site, with analysis by energy dispersive x-ray emission spectrometry. Calibration curves for uranium, thorium and molybdenum indicate the following respective lower determination limits: 0.7 μg (1.4 ppb); 0.9 μg (1.8 ppb); 0.5 μg (1.0 ppb).

Introduction

Trace element analysis of streams and ground waters has been successfully utilized in exploration for subterranean ore deposits. Hydrogeological prospecting methods are being applied to the search for deposits of uranium. Analyses of stream water and sediments for uranium, thorium, and elements showing a positive correlation with uranium have been the subjects of a number of papers presented at uranium panels, conferences and symposia over the past several years.[1,2]

Determination of ppb concentrations of uranium, thorium and their accompanying elements in water is gaining acceptance not only as a hydrogeological prospecting method for nuclear fuels but also as a method of monitoring effluents from uranium mining and milling sites, and for background level determinations in the vicinity of prospective sites.[3] For these reasons, research in this laboratory has been focused on developing a rapid, inexpensive and accurate method of determination of the fissionable elements: uranium and thorium and their pathfinder element: molybdenum.

The choice of analytical method for a particular application depends on the following factors: the elements to be determined, their concentrations, the required accuracy, the physical nature of the sample, the number of samples to be analyzed and the required speed of analysis. It also depends on whether single element or multielement analysis is required.

In this work multielement analysis was required for uranium, thorium, and molybdenum. The application of this method for other pathfinder elements, vanadium, copper, arsenic and selenium was published earlier. The required sensitivity was in the low ppb range. Speed and low cost were important factors since large numbers of samples should be analyzed.

Direct analysis of water for trace elements at ppb levels requires methods having extremely high sensitivity. Although such methods have been developed, they are expensive and the cost of analyzing large numbers of samples would be prohibitive. Therefore, most general methods of water analysis require the samples to be preconcentrated, either by evaporation or by chemical methods such as precipitation, ion exchange, solvent extraction, electrodeposition, etc., and subsequently analyzed by less expensive and less sensitive methods.

A problem often encountered in analyzing water for trace elements is the adsorption of these elements on the walls of the sample container. This process results in significant errors which can be avoided if, immediately after collection, the samples are processed into the final form for analysis. Such preconcentrated samples are stable and can then be measured on site in a mobile laboratory, or transported to a central laboratory for measurement.

Among analytical methods, the most practical for analysis of large numbers of samples for many elements is Energy Dispersive X-Ray Emission Spectrometry (EDXES). It is multielement, rapid, accurate, and sensitive when applied to properly preconcentrated samples.

In this work the method of coprecipitation of trace elements with a carrier was applied for preconcentration and sample preparation at the same time. Ammonium Pyrrolydine Dithiocarbamate (APDC), a powerful chelating agent, was used as precipitant. APDC coprecipitation has been described in our earlier papers[4,5] in its application to the analysis of trace quantities of vanadium, copper, arsenic, selenium, mercury and lead. In this work it was extended to uranium, thorium, and molybdenum.

Experimental

Sample Preparation

500 ml aliquots of deionized water were spiked with single elements: uranium, thorium and molybdenum in concentrations ranging from zero to 200 ppb. In a separate experiment water aliquots were spiked with all three elements together, covering the same range of concentrations. To each aliquot, 200 µg of Fe^{+++} was added as a carrier. The pH was adjusted to 4.0 and 10 ml of a freshly prepared 1% APDC solution was added with stirring. The precipitate was left standing for 30 minutes before being filtered through a Millipore membrane filter having a pore size of 0.45 micrometers.

Because the precipitate on the membrane filter is presented directly to the x-ray spectrometer, it must be uniformly deposited in order to assure accurate spectrometric measurement. For this purpose, the filtration device shown in Figure 1 was used.

Figure 1
Filtration Apparatus

A standard Millipore vacuum filtration apparatus, for filters 25 mm in diameter, was modified by extending the 15 ml glass funnel with a 500 ml conical flask. The filtration times ranged from 10 minutes to about 1 hour, depending on the total amount of trace elements in the sample and the flow rate of the filter. When processing a large number of samples, several filtration devices can be utilized, thus reducing the sample preparation time to about 10 minutes per sample.

X-Ray Spectrometry

Determinations of element concentrations in deposits on membrane filters were made using an energy dispersive x-ray emission spectrometer. An annular array of eight Cd-109 radioisotope sources, each having an activity of 8 mCi, was used for excitation of fluorescent x-rays in the samples. A lithium-drifted silicon detector, having a resolution of 180 eV, was used for spectrometric measurements. Counting time was 600 sec. per sample. Spectra were collected in 1024 channel memory groups and processed by an on-line Nova 800 minicomputer.

Results

Calibration curves were obtained by plotting the net count rate of the most prominent photopeak for each element (ULα, ThLα, MoKα) versus element concentration (Figure 2).

FIGURE 2
CALIBRATION CURVE

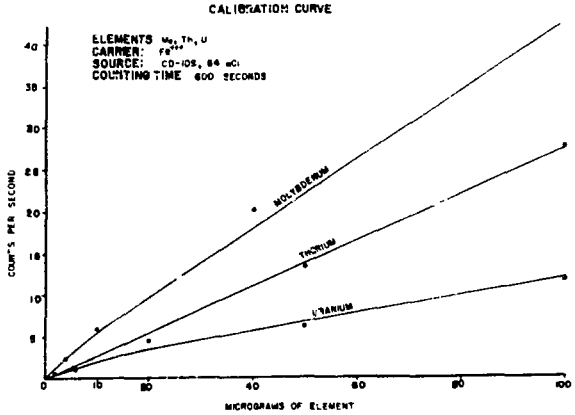

The efficiency of APDC precipitations was determined by measuring, along with the precipitates, standard samples prepared by deposition of calibrated solutions on membrane filters having the same diameter as the precipitate. For molybdenum and thorium the efficiency was 100% and for uranium 88%.

Lower determination limits (LDL) calculated as three times the standard deviation of the background in the photopeak area are given in Table 1. The background was determined by analyzing a blank containing the iron carrier only.

Table I

LOWER DETERMINATION LIMITS FOR MOLYBDENUM, THORIUM AND URANIUM

Element	X-Ray Line	Lower Determination Limit
Molybdenum	Kα	0.5 µg (1.0 ppb)
Thorium	Lα	0.9 µg (1.8 ppb)
Uranium	Lα	0.7 µg (1.4 ppb)

Conclusion

Using energy dispersive x-ray emission spectrometry combined with APDC coprecipitation, low ppb concentrations of uranium, thorium and associated elements in water can be determined rapidly, accurately and at low cost. Preconcentration on the spot of sampling, by APDC coprecipitation with a carrier, eliminates the problem of trace element losses due to adsorption on the walls of storage containers.

References

1. Otton, J.K., "Uranium and Trace Elements as an Exploration Tool:, Abstracts of the 1975 Uranium and Thorium Research and Resources Conference. N.S.G.S. Open file report 75-595, p. 34.

2. Fauth, H., "Hydrogeological Reconnaissance Prospecting", Uranium Exploration Methods, Proceedings of a Panel, IAEA, Vienna, STI/PUB/334, p. 209 (1973).

3. Clark, Don A., State-of-the-Art. Uranium Mining, Milling and Refining Industry. Environmental Protection Technology Series, EPA-660/2-74-038, p. 4 (June 1974).

4. Pradzynski, A.H., Henry, R.E., Stewart, J.L.S., "Determination of Selenium in Water on the ppb Level by Coprecipitation and Energy Dispersive X-Ray Spectrometry", Radiochem. Radioanal. Letters 21 (5) 277-285 (1975).

5. Pradzynski, A.H., Henry, R.E., Stewart, J.L.S., "Determination of ppb Concentrations of Transition Metals by Radioisotope Excited Energy Dispersive X-Ray Spectrometry", Trans. Am. Nucl. Soc., 21 (Suppl. 3) 34-35 (1975).

Proceedings, ERDA X-and Gamma-Ray Symp. Ann Arbor, MI, May 19-21, 1976 (Conf 760539)

APOLLO REMOTE ANALYSIS SYSTEM APPLIED TO SURFACE AND UNDERWATER IN-SITU ELEMENTAL ANALYSIS

Larry G. Evans, Michael J. Bielefeld
Computer Sciences Corporation, Silver Spring, Maryland 20910

Evan L. Eller, Richard L. Schmadebeck, Jacob I. Trombka, M. G. Mustafa*
Goddard Space Flight Center, Greenbelt, Maryland 20771

Frank E. Senftle
U. S. Geological Survey, Reston, Virginia 22092

Russell L. Heath
Aerojet-Nuclear Co., Idaho Falls, Idaho 83401

Kurt Stehling, Joseph Vadus
National Oceanic and Atmospheric Agency, Rockville, Maryland 20852

Summary

The surveying of the elemental composition of bulk samples over extended areas in near real-time would be an invaluable tool for surface and underwater environmental analysis. However, few techniques provide such a capability. Based on the experience from the orbital gamma-ray spectrometer experiments on Apollo 15 and 16 in which elemental composition of large portions of the moon were determined, an analysis system has been developed for terrestrial applications, which can fulfill these requirements. A portable, compact pulsed neutron generator and NaI(Tℓ) detector system coupled to associated electronics under mini-computer control can provide the timing and spectral characteristics necessary to determine elemental composition for many applications. Field trials of the system for underwater elemental analysis are planned during the next year.

Apollo System

As part of an orbital geochemical package carried in the service module of both the Apollo 15 and 16 missions, a gamma-ray spectrometer was used to collect information about the chemical composition of the surface of the moon. The gamma-ray spectrometer measured both the natural radioactivity and the radiation resulting from the interaction of cosmic ray protons with the lunar surface. The detector was a NaI(Tℓ) crystal mounted on a deployable boom. The output signal from the photomultiplier tube was pulse height analyzed into 512 channels and transmitted back to earth in interval samples of .33 seconds. Real time analysis of the digital signals was performed on earth and the results transmitted back to the astronauts, thus allowing information feed-back during the mission. The data were also recorded for subsequent and more detailed analysis. Results from the gamma-ray experiment have yielded regional concentrations for Th, U, K, Fe, Mg, Ti, Si, and O in the lunar surface.

With techniques described elsewhere [1,2], the discrete signal depicted in Figure 1, was separated from the interfering background signals which comprised more than 85% of the total measured spectrum. The unfolding of discrete line spectrum into chemical information was accomplished by synthesizing the spectrum under a least squares criterion with response functions characteristic of elements measured. Though showing only a few of the elements contributing to the signal, Figure 1 illustrates both complexity of the spectrum and the differentation of the spectrum by type of excitation process. For example, the inelastic neutron scatter line of iron Fe(n,n′γ) is prominent at .84 MeV whereas the capture line Fe(n,γ) is at 7.6 MeV. The signature of the natural radioactivity of thorium and uranium from the moon is easily identified at 2.6 MeV.

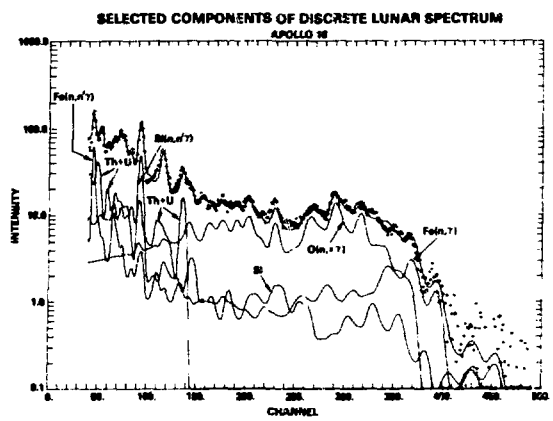

Figure 1. Pulse height spectrum of the lunar surface measured by the Apollo 16 gamma-ray experiment and the fit of selected components to the data. The energy scale is ~ 19.3 KeV/channel.

Apollo System Application

The systems approach and techniques that were successfully applied to the problem of lunar chemistry composition can also be adapted for gamma-ray analysis in terrestrial applications. Characteristics which were felt important, based on the experience of the Apollo program include: (a) ruggedness for the field environment; (b) the capability to pre-process the data for immediate digital transmission to a central accumulator; (c) real-time analysis of the data; and (d) a two-way transmission link to allow for feed-back and increased flexibility in the operation of the system. Figure 2 illustrates through a block diagram the essential characteristics of the Apollo gamma-ray experiment.

* NAS/NRC Research Associate

The one feature of a gamma-ray detection system which must be added for terrestrial applications is a source of neutrons. To this end, a portable compact neutron generator which can produce pulses of 14 MeV neutrons on a pulsed time scale of microseconds has been developed by Sandia Corporation for NASA and is currently being tested. The advantage of a pulsed neutron source over continuous isotopic sources is that the temporal features of the gamma radiation can be combined with the energy characteristics of the spectrum to facilitate determining elemental composition. A proposed gamma-ray analysis system for underwater studies is shown in block diagram form in Figure 2. The underwater probe consists of the neutron generator detector system, a pre-processor to digitize the data and a controller for experiment operational control. The data is transmitted to a real-time processor and the results used as inputs to control the experiment.

COMPARISON OF APOLLO AND UNDERWATER ANALYSIS SYSTEMS

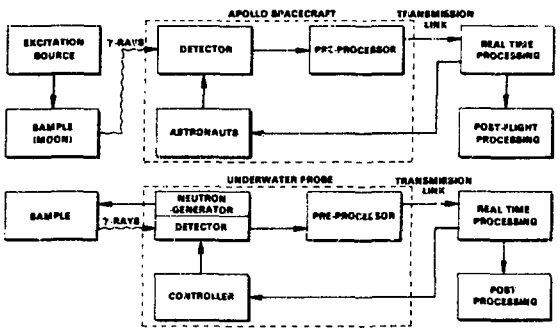

Figure 2. Block diagrams of the Apollo gamma-ray experiment and of a proposed underwater elemental analysis system.

Modes of Operation

The ability to pulse the neutron output and to collect spectra at specific times after a pulse, greatly simplifies the subsequent data analysis.[3] Prompt gamma-rays resulting from the inelastic scattering of fast neutrons occur only during the neutron burst. Gamma-rays from neutron capture have an intensity proportional to the number of thermal neutrons, which die away within a few hundred microseconds after each neutron pulse. Activation gamma-rays vary little in intensity over the time interval between bursts (e.g., 2 milliseconds). In addition to measuring the energy of prompt, capture and activation gamma-rays, the rate of die-away of thermal neutrons can also be measured and is related to the hydrogen content of the sample.

A block diagram of the complete experimental set-up is shown in Figure 3. The operation and timing of the neutron generator is done through a command controller. The controller also acts to discriminate in time for the collection of various spectra. A He^3 neutron detector has been incorporated into the system to measure epithermal neutron die-away. The system has been designed to run in two distinct modes. Mode 1 is a fast repetition mode, used to collect inelastic scattering spectra and epithermal die-away information. Mode 2 is a slower repetition mode, and is used to collect capture and activation spectra and to measure thermal die-away. The actual timing of each mode will be discussed below.

SYSTEM BLOCK DIAGRAM FOR GENERATOR-DETECTOR SYSTEM

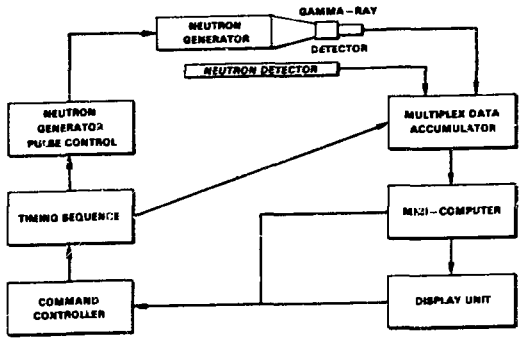

Figure 3. Block diagram of the neutron generator-detector system used for elemental analysis.

The neutron generator detector system has been in operation at the National Reactor Test Site since the beginning of April, 1976. Evaluation and optimization of the various modes of operation are being carried out. Sample spectra which were taken during the early phase of evaluation under non-optimized operation are presented here.

The neutron generator detector system was placed on a steel plate on the floor of the laboratory. The neutron generator was run with a pulse width of about 20 microseconds. Under mode 1 operation, the pulse rate was approximately 5000 pulses/second and the neutron output was about 500 neutrons/pulse. Figure 4 shows a sample inelastic scattering spectrum using a collection window that coincided with the burst duration. The obvious features which can be identified on this spectrum are the annihilation line at .511 MeV, the $Fe(n,n'\gamma)$ line at .84 MeV, the $Si(n,n'\gamma)$ line at 1.78 MeV and $Al(n,n'\gamma)$ lines at 1.0 and 2.2 MeV. Some indication of a 6.1 MeV triplet feature from $O(n,n'\gamma)$ can be seen in channels 230-290.

The capture and activation spectra shown in Figure 5 were collected under identical conditions to the spectrum in Figure 4. However, the pulse rate for mode 2 operation was approximately 500 pulses/second with 5000 neutrons/pulse. The capture spectrum was accumulated from 5 to 700 microseconds after each burst, while the activation spectrum was accumulated from about 1100 to 2000 microseconds after the pulse. Characteristic capture and activation lines are indicated on the figure. The capture spectrum includes any lines due to activation as well as any from the laboratory background. Two lines K^{40} at 1.37 MeV and Th at 2.6 MeV are from natural radioactivity probably present in the background. Subtraction of the activation spectra from the capture spectra, removes these two features as well as the $Si(n,p)$ activation line at 1.78 MeV confirming the origin of these lines. The remaining features in the capture spectrum can be identified as the 7.6 MeV triplet from $Fe(n,\gamma)$, the 2.2 MeV $H(n,\gamma)$ line, the 4.9 MeV triplet from $Si(n,\gamma)$ and possibly the 1.78 MeV $Al(n,\gamma)$ line. Many of these capture features show up in the activation spectrum indicating that the timing of the activation window may be moved to a greater time delay after the pulse.

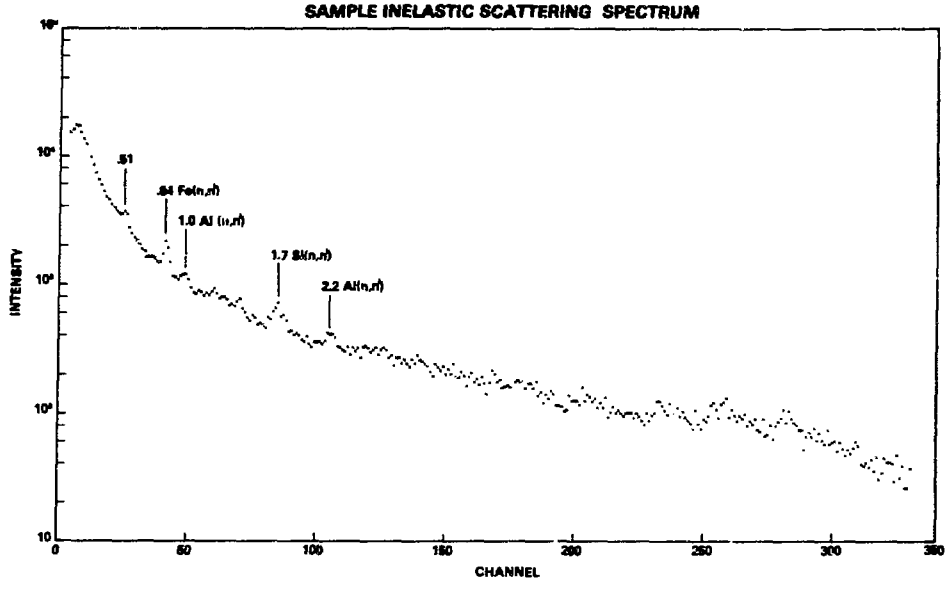

Figure 4. Sample inelastic scattering spectrum with major features identified in energy (MeV) and by element. The energy scale is $\sim$ 20.5 keV/channel.

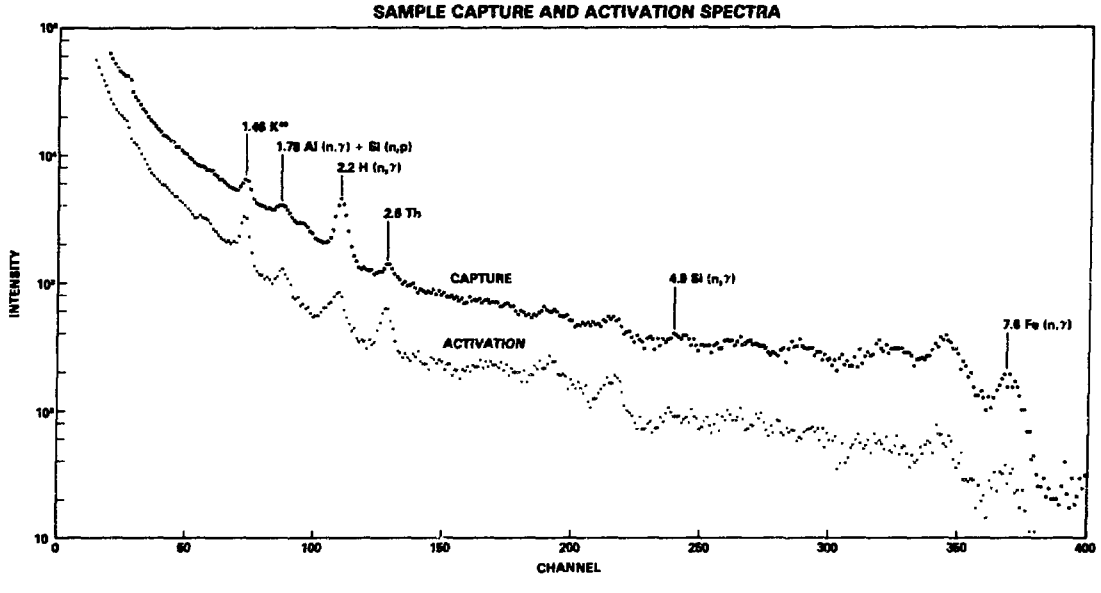

Figure 5. Sample capture and activation spectra with major features identified in energy (MeV), by element and by process. The spectrum labeled capture is actually capture plus activation and background. The energy scale is $\sim$ 20.5 keV/channel.

Future Plans

Laboratory and field trials of the system for underwater elemental analysis are planned during the next year. Problems which may be investigated include the distribution of particulate matter released during dredging operations and mapping of toxic metals in the bay floor. The sample site for these trials is Chesapeake Bay.

The problem of neutron and gamma-ray transport as a function of chemical composition is also being investigated. This is to establish correlations between the neutron flux distribution and the gamma-ray spectra for various chemical compositions. The calculated results and the experimental data will be used to determine the limits of quantitative analysis which can be obtained by this method.

Replacement, for certain applications, of the NaI crystal with an intrinsic Ge detector will greatly increase sensitivity and allow for the measurement of more elements than is presently possible. It will also greatly simplify the spectral analysis necessary to determine chemical composition from the data.

Acknowledgments

We wish to acknowledge the assistance of Drs. E. B. Nieschmidt and J. W. Mandler of Aerojet-Nuclear Corporation in obtaining the pulse height spectra used in this paper.

References

1. R. C. Reedy, J. R. Arnold and J. I. Trombka, Journal of Geophysical Research, 78, 5847, 1973.

2. M. J. Bielefeld, R. C. Reedy, A. E. Metzger, J. I. Trombka and J. R. Arnold, Proc. of Seventh Lunar Science Conference, 1976 (in press).

3. R. L. Caldwell, W. R. Mills, Jr., L. S. Allen, P. R. Bell and R. L. Heath, Science, 152, 457, 1966.

Proceedings, ERDA X-and Gamma-Ray Symp. Ann Arbor, MI, May 19-21, 1976 (Conf 760539)

PRECISION AND ACCURACY OF MULTI-ELEMENT ANALYSIS OF AEROSOLS USING ENERGY-DISPERSIVE X-RAY FLUORESCENCE.

F. Adams and P. Van Espen
Dept. of Chemistry
University of Antwerp (U.I.A.)
B-2610 Wilrijk, Belgium

Measurements have been carried out for the determination of the inherent errors of energy-dispersive X-ray fluorescence and for the evaluation of its precision and accuracy. The accuracy of the method is confirmed by independent determinations on the same samples using other analytical methods.

Introduction.

Energy dispersive X-ray fluorescence analysis has progressed from its rather modest status a number of years ago, into one of the most interesting methods for the routine multi-element analysis of environmental samples. The method compares favourably with alternative techniques as far as simplicity of the equipment and ease of analysis is concerned. Nevertheless its accuracy and precision are not always considered excellent. This study was undertaken to determine and evaluate sources of error associated with the method so that eventually they might be minimized. The precision obviously depends critically on the instrumentation used, the mathematical treatment of the results and finally on the homogeneity and complexity of the sample. The accuracy of the method, or the degree of agreement of the analytical results with the "true" accepted, or most reliably known concentration, is the result of the quantitation procedures used and can only be assessed with the aid of standard samples and other reliable analytical techniques. It has been tested mainly by intercomparison exercises [1] up to now. The results indicate quite large deviations between several authors for most elements.

The influence of erratic factors operating onto the system have to be evaluated. These are due mostly to the use of incorrect physical constants, undetected spectral interferences, blank and contamination problems, instabilities of the instrumentation and for the low atomic number elements radiation absorption and particle size effects.

Experimental

Instrumentation and data reduction

The instrumentation used consists of a secondary target-water cooled tube system, a 30 mm^2x3 mm Si(Li) detector and amplifier, a 16 position automatic sample changer, all from Kevex, Burlingame, California (Kevex Subsystem 0810) and a X-ray tube with tungsten-anode (Siemens AGW 61) with Kristalloflex 2 generator (4 KW). The Si(Li) detector is collimated with a 2 mm diameter aluminium aperture which limits the measurement from the fluorescence radiation to a poorly defined oval area with axes of 7 and 9 mm at 50 % intensity cut off [2]. The detector is mounted into a cryostath with a 0.012 mm beryllium window. A cooled FET-preamplifier with pulsed optical feedback (Kevex 2002) is used with an X-ray amplifier Kevex 4510P at a time constant of 6 µsec. The energy resolution amounts to 165 eV at 1000 cps and 5.9 KeV. The amplifier incorporates a base-line restorer and pulse pileup rejection circuitry. A Northern Econ II, 4096 channel analyser with 200 MHz ADC is used with a WANGCO 7 track magnetic tape unit for storage in BCD code and off-line transmission to and from the computing facility.

Calculations were performed on a 64 K PDP 11/45 system. The software available for the data reduction consists of the well known fitting technique based on the non-linear least squares algorithm of Marquandt [3]. The fitting function consists essentially of a number of Gauss functions and a third degree polynomial background. The method was thoroughly studied. A full description of the methods and the results for fluorescence spectra will be described separately [4]. The method provides optimum results however for small and medium intensity peaks below 5.10^5 counts integral intensity. For very high intensity peaks deviations from the Gaussian shape at the low energy side were taken into account.

The apparatus can be considered as a state of the art example of the energy dispersive instruments. The data reduction methods, however, are of a complexness typical for large off-line system.

The major factors which influence the precision can be divided as :
1. Electronical effects originating either in the high voltage power supply or the measuring electronics.
2. Imprecisions due to the sample or to the sample positioning.
3. Errors in the data reduction process.
4. Errors due to the standardisation.

The precision and accuracy that can be reached with the method depend to a non-negligible extent on the type and on the complexity of the samples. Therefore the present study was limited to typical aerosol samples collected on filter paper and to homogenised powder samples of comparable complexity which could be brought homogeneously on a filter paper type support.

The thin samples were positioned in a sample holder consisting of two concentric teflon rings between which they were flatly held. The sample holder could be accomodated reproducibly into the sample changer positions of the instrument.

Electronical sources of errors - High voltage generator instabilities.

The overall stability of the spectrometer was tested by measuring repeatedly the same sample which was reproducibly placed in a fixed counting position of the sample changer over periods ranging from 50 min to several days. The results of one series of measurements are shown in Fig. 1. It appears that the precision for 2000 sec measurements is of the order of 3% and that the spectrometer is subject to drift and oscillations [5]. Also the intensity variations appeared to be proportional to the anode current of the X-ray tube. A thin wire of a suitably chosen element can be placed reproducibly into the radiation path about 1 mm below the sample surface. Through its fluorescence radiation it provides a correction for the primary intensity fluctuations. Fig. 2 shows the normalised intensity fluctuations for a CsBr thin film standard counted over a 45 hrs period. Normalisation is achieved through a 50 µ thick zirconium wire. A spectrum which shows the Zr K radiation which is located conveniently just below the incoherent scatter peaks is shown in Fig. 3. The maximum instability left in the data of Fig. 2 is a small drift of 0.2 % per hour which could be traced back to a decrease of the tube voltage by circa 1 kV over the 45 hrs period.

The external wire reference also serves the purpose of behaving as an ideal purely random pulse generator. Consequently it accurately corrects for pulse pileup and dead time losses in the measurement equipment.

Errors due to the sample.

For an homogeneous thin sample the observed standard deviation for replicate measurements can be considered as a composite of individual variations and errors. These individual variations can be taken as independent.

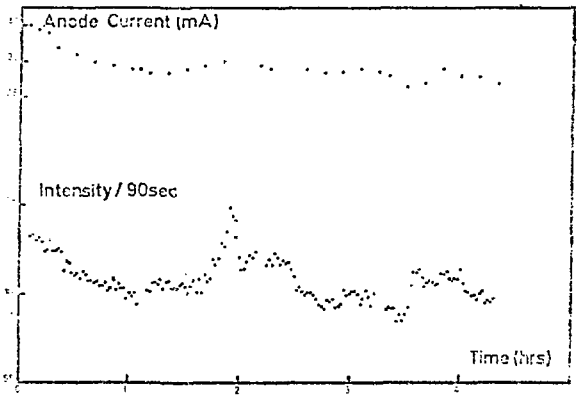

Fig. 1 : Fluorescence intensity and anode current stability

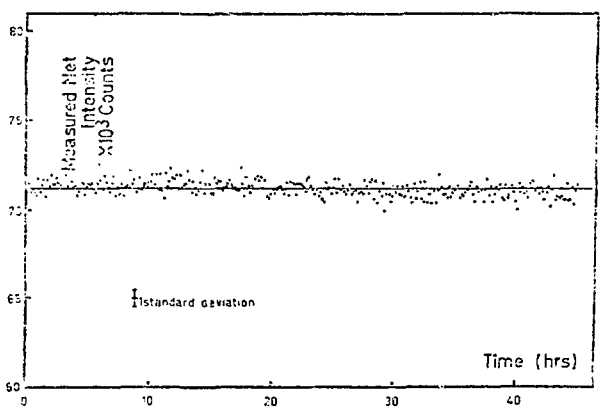

Fig. 2 : Normalised fluorescence intensity stability.

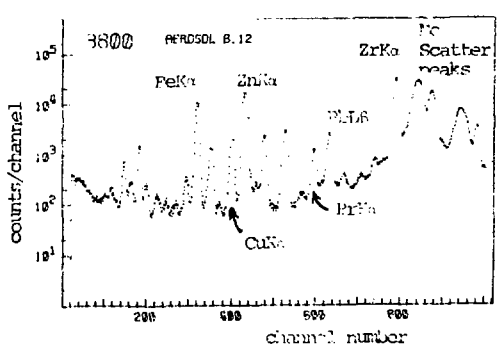

Fig. 3 : Spectrum of aerosol loaded cellulose filter with zirconium external reference.

The following sources of variations were considered : placement of the sample in a sample holder, placement of sample + holder in a sample changer position, variations between individual sample changer positions and between sample holders. The relative contributions of these errors could be obtained by repetitive measurements of iron in the aerosol loaded filter of Fig. 3. Other operational errors due to counting statistics, to drift of current or voltage and data reduction were minimised by selecting long measurements with the external wire reference and limiting the analysis to a high concentration element in a sample of excellent homogeneity.

The results of a number of replicate measurements are shown in Table I. The error due to differences in sample position amounts to $[(1.88)^2-(0.47)^2]^{1/2}$ = 1.82%, that due to placement of a sample in a single holder to $[(0.83)^2-(0.47)^2]^{1/2}$ = 0.68% and finally the error due to placement of the sample in its sampler holder in one position to $[(0.47)^2-(0.30)^2]^{1/2}$ = 0.36%. The use of different sample holders of a single construction batch proved to be no significant source of errors. Results obtained for other elements provided consistent results with those obtained for iron. These results can be compared with similar data obtained by Buchanan et al [6] who report a 0.12% deviation when the same sample was removed and reinserted in the sample holder of a Philips Universal Vacuum Spectrograph with crystal monochromator.

Table I : Iron K_α intensity normalised for tube fluctuations.

Measurement	Sample remaining in single holder; single sample changer position	Sample with single holder; different position.	Sample replaced in one sample holder; single sample changer position
1	181 187	184 417	181 734
2	181 826	184 911	181 041
3	181 755	176 191	180 439
4	180 544	184 355	182 738
5	182 845	179 851	178 959
6	-	181 387	179 848
s %☆	0.47	1.88	0.83
σ %☆☆	0.30	0.30	0.30

☆ : % standard deviation obtained
☆☆ : % standard deviation from counting statistics

Table II : Intensity dependence with vertical position.

Height above normal position (mm)	% deviation intensity
1.5	3.1
3	10.4
4.5	18.2
6.0	30.0
7.5	39.2

Table III : The precision of the normalised net peak intensity for the element and the radiation shown (11 measurements)

	Fe K_α	Cu K_α	Zn K_α	Br K_α	Pb L_β
s %	0.35	0.84	0.22	1.19	0.84
σ %	0.38	0.82	0.31	1.09	0.72
$\chi^2 = \frac{(n-1)s^2}{\sigma^2}$	8.7	10.4	4.8	12.0	13.7

The residual errors due to the placement of the sample in different sample changer positions can be traced back to height deviations in relation to a normal measuring position. Table II summarises the intensity variation as a function of the deviation from the standard position. The errors obtained corresponds to a 1 mm uncertainty only.

The results for the determination of the intensity when an aerosol sample is measured in the same sample changer position daily for 11 consecutive days are shown in Table III. Since χ^2 for 10 degrees of freedom is 18.3 at a 95 % probability level, there is no indication in this case for operational errors in the analysis of these high intensity peaks apart from counting statistics.

Data reduction.

For well-defined non-interfered peaks located onto a low continuous background, the calculation of the net intensity through peak integration is very easy by every means of calculation used. To obtain accurate results it is only necessary that the technique used is reproducible for all samples and standards. As the peaks become considerably less intense and the spectral complexity increases errors will become more important. Numerous computer programs exist for this aspect of the analysis but considerable caution should be excercised to evaluate the computer program initially and to routinely examine the results for validity. Powerful least-squares fitting can be considered as optimal but the user should be well aware that possible sources for operational and systematic errors are numerous and that automated routines are especially prone to produce more or less erroneous results.

The precision and the accuracy of the data reduction used was evaluated as a function of the complexity of the spectrum. The results will be described elsewhere[4]

Standardisation.

A widely used practice in fluorescence analysis especially ion induced analysis consists in using one or a few thin-film single element standards for the calibration and relying on many constants and corrections, amongst others : the photoelectric mass absorption coefficient, the jump ratio at the absorption edge, the Auger yield, the X-ray detection efficiency corrected for the absorption in the air path, the detector window and insensitive layers. We have been most reluctant to follow this practice because it relies very profoundly on the knowledge of accurate values for the physical constants which have errors ranging from a few percent to 20 percent or more.

Thin film standards obtained by vacuum evaporation[7] were employed for every element to be determined. The overall precision and accuracy of these was estimated at ± 5%. The precision of the measurement was of the order of 2%. One can assume that owing to the bichromatic excitation conditions of the secondary target, the specific K-intensity varies smoothly with atomic number. This is borne out by the experimental data shown in Fig. 4. The full line is a quadratic polynomial fit of the logarithm of the normalised intensity per µg of element versus the logarithm of the absorption jump energy. The mean deviation between the curve and 13 individual calibration points is 4%.

Accuracy.

Assessment of the accuracy of a technique is much more difficult than the assessment of its precision. The usual approach adopted is the analysis of an accepted standard. Several other analytical techniques have been used for gaining insight in the accuracy of the analytical results. Emphasis was laid onto the determination of the major elements of sufficiently high atomic number to prevent particle size effects and radiation absorption to influence the results.

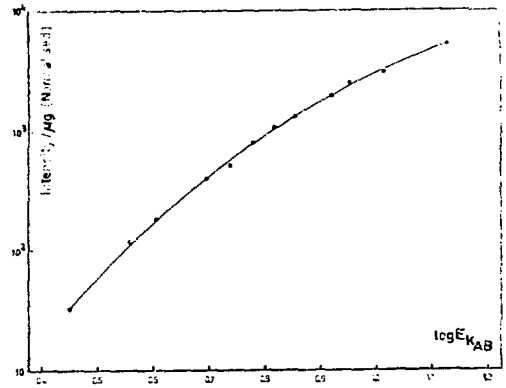

Fig. 4 : Normalised specific intensity for a number of elements versus absorption jump energy.

Atomic absorption spectrophotometry, and instrumental neutron activation analysis have been used. As an example Table IV shows a comparison of a few paired determinations by the fluorescence method and atomic absorption for the routine analysis of aerosols.

Table IV : Comparison between analysis performed routinely whit XRF and AAS for a number of elements. Concentration in µg cm^{-2}

	Fe		Cu	
Tagword of spectrum	XRF	AAS	XRF	AAS
3478	12.6	15.8	0.16	0.16
3479	10.9	13.0	0.15	0.22
3480	8.9	11.5	0.15	0.20
3695	5.4	4.8	0.24	0.29
3696	11.7	11.2	0.26	0.17
3697	8.4	7.6	0.21	0.12
	Zn		Pb	
Tagword	XRF	AAS	XRF	AAS
2478	2.5	2.6	4.0	4.9
2479	2.4	2.5	3.5	6.25
2480	1.5	1.6	6.7	8.15
3695	1.7	1.5	4.3	4.1
3696	2.0	2.2	4.5	—
3697	2.3	2.2	4.0	—

A few determinations of manganese, iron, copper and zinc in bovine liver are shown in Table V. The scatter on the results contrasts with the high precision of most of the data of Table III and was due to inferior counting statistics.

Table V : Analysis of Bovine liver.

	Concentration in µg/g material			
	Mn	Fe	Cu	Zn
Sample 1	10.8	337	139	101
Sample 2	8.7	267	149	109
Sample 3	8.9	287	144	116
mean and st. dev.	9.5±1	297±36	144±5	109±3
NBS values	10.3±1	270±20	193±10	130±10

Finally several intercomparison excersises show the accuracy of the particular analysis we use in comparison to the results obtained elsewhere by comparable methods. Fig. 5 shows the collection of results for a number of laboratories on the Denver II intercomparison study. Our results are marked in the figure. In each series of determinations the sequence of elements is Al, Si, S, K, Ca, Ti, Mn, Fe, Cu, Zn, Se, Br and Pb.

Radiation absorption effects may give rise to severe inaccuracies. A methodology for the correction for this effect has been thoroughly studied for homogeneous thin samples and also for samples which have an heterogeneous distribution in the z-direction [8,9]. A cellulose filter loaded with aerosols is typical for the latter situation. The methods used for the correction are based on the accurate measurement of the mass absorption coefficient by transmission measurements and of the front-to-back intensity ratio of the radiation. Experimental verification of the method has been obtained by :

1. Measuring filters analysed by other analytical techniques.
2. Using the "two-lines" method based on the intensity ratio of the PbM_α to PbL_β radiation. The latter high-energy line is virtually free of absorption and may serve as a reference whereas the former is subject to severe radiation absorption. It is thus a good indicator for the study of absorption in several samples.

Table VI [10] shows for 18 aerosol loaded cellulose filters with the loads indicated, the total absorption correction coefficient, the ratio of the corrected PbM_α intensity to the absorption free intensity. The latter intensity was obtained from the absorption free intensity ratio of PbM_α/PbL_β as obtained with ultra thin samples. The acceptable results were obtained by assuming an exponential concentration gradient of the aerosol through the filter.

Table VI : Radiation absorption of PbM_α radiation (2,34 keV) in aerosol loaded cellulose filters.

Sample	Aerosol load ($\mu g\ cm^{-2}$)	Calculated mean absorption correction	Ratio of corrected PbM_α intensity to absorption free intensity
1 - 3	250	1.70	1.08
4 - 15	400	1.75	1.03
16 - 18	650	1.74	1.14

Conclusion.

In conclusion one might state that the precision of the X-ray excited fluorescence analysis can compete in very favourable circumstances with that obtainable with wavelength dispersion.

Acknowledgments.

This work was financially supported by the "Nationaal Fonds voor Wetenschappelijk Onderzoek", Belgium.

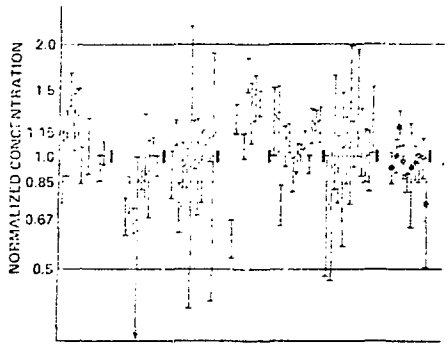

Fig. 5 : Normalised concentration for the determination of a number of elements by X-energy spectrometry as obtained by 7 laboratories. Our results are dotted (•).

References.

1. D.C. Camp, A.L. Van Lehn, J.R. Rhodes, A.H. Pradzynski, X-Ray Spectrometry, 1975, 4, 123.
2. J. Smits, Private communication
3. D.W. Marquandt, J. Soc. Ind. Appl. Math., 1963, 11, 431.
4. P. Van Espen, F. Adams, to be published
5. K.A.H. Hooton, M.L. Parsons, Anal. Chem., 1973, 45, 2218.
6. E.B. Buchanan Jr., Foo-Chong Tsai, Anal. Chem., 1974, 46, 1701.
7. P. Van Espen, F. Adams, Anal. Chim. Acta 1974, 75, 61.
8. F.C. Adams, R.E. Van Grieken, Anal. Chem., 1975, 47, 1767.
9. R.E. Van Grieken, F.C. Adams, Advances in X-ray Analysis, Eds. R.W. Gould, C.S. Barrett, J.B. Newkirk and C.O. Ruud, 1976 (vol. 19), Kendall-Hunt Publishing Co.
10. F.C. Adams, J. Billiet, X-ray spectrometry, in press.

Proceedings, ERDA X-and Gamma-Ray Symp. Ann Arbor, MI, May 19-21, 1976 (Conf 760539)

MODELING OF BACKSCATTER GAMMA RAY SEDIMENT GAGES.

L.D. Maus, J.R. Roney, V.C. Rose, and V.A. Nacci, Department of Ocean Engineering, University of Rhode Island, Kingston RI 02881.

SUMMARY

Semi-empirical mathematical models were developed to predict the response of gamma-scattering gages. A single scatter model was used to develop an equation describing the response of a close spaced gage. Laboratory experiments and Monte Carlo simulation were conducted to determine the effects of changes in the collimation angles and the source to detector spacing on the numerical coefficients. A more general model was developed to predict the response to both sediment density and equivalent atomic number. Water with a small amount of barium chloride was used to simulate a wide range of densities and chemical compositions to obtain numerical coefficients. The response was found to be a function of source to detector distance collimation angles, photon energies registered by the detector as well as sediment density and chemical composition.

INTRODUCTION

Sediment density and composition are important parameters in marine geology as well as in submarine soil mechanics and underwater acoustics. The process of obtaining core samples for laboratory analysis is costly and time consuming. In addition, results are subject to errors due to inadequate sampling and core disturbances. As a consequence, there has been interest in measuring sediment properties in-situ.

Gamma-ray backscattering has been used for a number of years for density measurement. It is particularly suited for in-situ measurements since it is capable of measuring bulk parameters while having access to only one surface. Commercial backscatter gages are available for measuring soil density while several developmental gages have been constructed to measure marine sediment density. In the design of the density gages, the emphasis is on reducing compositional effects which could bias the density measurements. Limited research has been conducted on backscatter compositional gages.

One purpose of this research was to develop semi-empirical mathematical models that could be used to reliably predict the response of gamma backscatter gages over the normal range of sediment density and composition. This required detailed information of the behavior of scattered gamma radiation as a function of sediment variables as well as gage parameters. In order to describe this behavior around the probe, an extensive research program was necessary. This involved mathematical analysis of the scattered radiation between the source and detector, Monte Carlo simulation of scattering in the near field, and laboratory experimentation.

BACKGROUND

In the gamma energy range considered practical for portable gages, there are two principal interactions between the gamma photons and the sediment: Compton scattering and photoelectric absorption. For these materials, Compton scattering is effectively independent of chemical composition and only a function of density. Photoelectric absorption, however, is a strong function of atomic number and is therefore very dependent on chemical composition. Compton scattering is the dominant process for photon energies above 200-300 kev while photoelectric absorption dominates for lower energies. The energy of the scattered photon depends on the angle of the scatter.

Two competing phenomena affect the detector response as the product of density and source to detector distance are increased: Compton scattering of photons back to the detector and photoelectric absorption of photons traveling toward the detector. At low values the first effect predominates. As the value of the product increases the second effect becomes dominant. The results, for a given geometry and source to detector distance, is for the count to increase with increasing density up to some maximum and then diminish with increasing density. The position of the maximum depends on the source to detector distance. The closer the source to detector distance the higher the value of density where the maximum occurs[1,2,3]. It is possible to design a backscatter sediment density gage to follow either the rising portion of the curve[4], or the falling portion of the curve[5].

A number of investigators including Tittman and Wahl[6], Czubek[7], and Christensen[8], have found that the effect of composition and density of the medium on the scattered gamma ray spectrum can be separated. Generally the magnitude of the upper region of the spectrum, above the energy where photoelectric absorption is significant, is a function of density but not chemical composition while the lower region is a function of both. At distances sufficiently far from the source (usually 3 or 4 mean free paths) the spectrum approaches a stable equilibrium spectra. At these distances the response of a detector is a separable function of density and composition.

Although there are serious limitations to the single scatter model, it is useful in analysing detector response for short source to detector distances and for detectors that only respond to the upper portion of the scattered gamma energy spectra. This model has been used in assuming that the highest energy photon reaching the detector corresponds to single scatters along the path defined by the minimum possible scatter angle[3,4,7].

Monte Carlo calculational techniques, which involve calculation of a large number of individual photon histories, are very useful for generating statistics on photon trajectories, energy and angle distributions number of scattering events, etc. Monte Carlo methods have been used to investigate the effects of source to detector distance,

source and detector collimation, source energy and compositional[10,11]. One result of these calculations is the conclusion that the single scatter model only holds for very low densities and short source to detector separations.

Because of the difficulty involved in obtaining exact agreement among the various analytical techniques, a semiempirical approach has been widely used. The most generally used model for density gaging is of the form

$$d^2I = A(\mu\rho d)^b \exp-(\mu\rho d)$$

where A and b are constants, ρ is the density of the medium, d is the source to detector distance and μ is an effective mass attenuation coefficient. The most common assumption has been that b = 1. This assumption is consistent with the results of the diffusion approximations[1,2] and has been used successfully to fit experimental data[12,13]. Czubek[6] has obtained values of b ranging from 0 to 1.25. Umiastowski[14] using Monte Carlo calculations and experimental data from 23 gages concludes that b falls in the range of 0.8 to 1.2 and that μ can be related empirically to μ_o, the mass attenuation coefficient at the source energy.

For density gaging, there have been a number of methods proposed to suppress compositional influences, all of which recognize the need to reduce the sensitivity of the gage to gamma photons in the photoelectric absorption range. These methods include collimation of the source and/or detector to enhance the high energy portion of the spectrum, suppression of the low energy portion of the spectrum by electronic discrimination of the detector output or by filtering the scattered photons through high Z materials and the dual gage techniques which permit cancellation of the effects of low energy photons.

Czubek (6, 16) presented the following model for gage response which includes the effect of composition:

$$d^2I = A\rho^b \exp(-c\rho + h Z_{eq}^{3.5}).$$

where d is the source to detector distances, ρ is the bulk density, A, b, c and h are gage constants, and Z_{eq} is the equivalent atomic number.

Gardner and Roberts[11] have proposed a model in the same general form. The Czubek model permits the exponent b to vary while the Gardner and Roberts model restricts it to a value of one. In the Czubek model, the composition effect is separable from the density effects. In addition, the Czubek model only applies for source to detector separations of 4 mean free paths or more while the Gardner and Roberts model appears to have been correlated with data obtained at distances of 4 mean free paths or less.

For compositional measurements Czubek[7] proposes the use of scintillation detectors and electronic discrimination of the output so that two signals are generated; one corresponding to the upper portion of the spectrum which would be a function of density only and one corresponding to lower portion of the spectrum which is a function of both density and composition. He then suggests that a ratio of these two intensities would be a function of Z_{eq} only.

MODEL DEVELOPMENT

Single Scatter Model

In the first phase of this research[17] (sponsored by the Atomic Energy Commission) the ultimate objective was to develop a sediment density gage for deployment on the Deep Ocean Sediment Probe (DOSP) along with other types of sensors. In order to provide accurate density profiles for use with the information from these other sensors, the gage had to be capable of accurately sensing small volumes of sediment. This can be accomplished with a collimated close spaced backscatter arrangement with associated energy discrimination. To provide data for the design of this probe a series of laboratory experiments and a Monte Carlo computer program were performed. Using a Monte Carlo computer program described by Roney[17], histories were accumulated for a backscatter arrangement. The geometry was a source emitted axially through a radical collimation into a medium of composition similar to marine sediments. Each photon was tracked from the source collimation port into the sediment through scattering until the history was terminated by escape, return to the wall of the probe, or absorption. The criteria for escape was passing a maximum radical or vertical distance of 30 centimeters. Spatial coordinates of the photon termination, its direction cosine, energy at termination and number of scatters were recorded.

Close to the source most photons experienced a single scatter while, with increasing distance from the source, the predominance shifted from single to double to multiple scatters. Beyond a distance of 7 centimeters, single scatters were no longer significant. The average energy of photons backscattered to a probe wall was found to diminish with distance from the source.

In the laboratory experiments, actual detector responses were recorded for a variety of source collimation angles, source to detector distances and sediment densities. Basically, the equipment consisted of a 20mCi Cs-137 source, a series of lead shields to provide various separation distances and collimation angles and a sodium iodide crystal. An aluminum tube closed on one end was used to align and contain these components. A 100 channel multichannel analyzer was used to obtain the energy spectrum of the radiation reaching the detector. Through the selection of collimating angles and separation distances photons undergoing single scatter or multiple small angle scatter were most likely to reach the detector. This resulted in a distinct peak in the higher energy region of the spectrum which could be recorded separately through the use of electronic discrimination.

In the experiments, the intensity of this peak was recorded as the gage and soil parameter were varied. Although the source collimation was fixed at 45°, the detector collimation was varied from 35 to 60° in four discrete steps. The source to detector

spacing was varied from 2 to 6 centimeters in 1 cm increments. Artificially layered sediment with densities ranging from 1.17 to 2.15 grams per cubic centimeter were used as the scattering medium.

As indicated by the Monte Carlo calculations, the single scatter model should apply over the range of conditions studied. The results were thus compared to a generalized form of the simplified detector response model developed by Pirie et al[3]. Good approximations were obtained in selected cases. Further analysis indicated that there was a relationship between the detector collimation angle and the distance of separation. This relationship is shown below where θ_d is the detector collimation angle and d_p the preferred source to detector distance.

θ_d	d_p(cm)
35^o	2.9
45^o	4.2
52.5	5.8
60	8.0

When the equation was modified by adding a term $c(\theta)$ to the exponent, further analysis indicated that $c(\theta) = 1.0 + 0.2\,(d_p - d)$. It was thus found that the response of a close spaced collimated backscatter gage could be expressed by the detector collimation angles of $35 - 52.5^o$).

$$I = A(\rho/d)\exp - (\mu\rho d\, c(\theta))$$

over the values of d up to 6 centimeters and for scattering angles of 80 to 97.5^o (in this case source collimation angles of $35 - 52.5^o$).

General Model

In the second phase of this research[18] the objective was to develop a semi-empirical model that could be used in the design of sediment composition gages. To provide the necessary data a series of experiments were performed. In these experiments, the actual detector responses were recorded for a variety of source and detector collimation angles, source to detector distances, and aqueous concentrations of $BaCl_2$. Basically the equipment consisted of a 25 mCi Cs-137 source, two lead shields mounted on a rack so that the collimation angles and source to detector distances could be varied, and a sodium iodide scintillation detector. A 400 channel multichannel analyzer was used to determine the energy spectrum of the radiation reaching the detector.

One prominent feature of these spectra was the few scatters peak in the higher energy half. This peak was the result of collimation selectively admitting only those photons approaching from a given angle. The peak is relatively narrow at low values of χ (scattering mean free path or $\mu\rho d$) but broadens as χ increases. This suggests that the photon histories are similar at low values but becomes more varied as χ increases.

Regression analysis was used to fit this data to a equation of the form: $d^2I = A\chi^b \exp(-c\chi)$. The constants A, b and c were assumed to be a funtion of collimation angles, Z_{eq}, and spectrum energy range over which the data was analyzed. Basically the spectrum was divided into low and high energy ranges with the cutoff energy varied. These analyses indicated that the response of a collimated backscatter gage to changes in sediment density and composition could be predicted by an equation of the form:

$$d^2I = A_o\chi^{(b_o - f Z_{eq}^{.35})}\exp - (C\chi + h Z_{eq}^{3.5})$$

where: $C = 0.560 + 0.005360\theta_s$, θ_s is the source collimation angle and A_o, b_o, c, f and h are a function of collimation angles, and photon energies registered by the detector. For values of χ greater than 4, this equation can be approximated by

$d^2I = A_o\chi^{b_o}\exp - (c\chi + h Z_{eq}^{3.5})$ which has the same form as the model of Czubek[16]. For values of χ between 1 and 2 the equation can be approximated by

$d^2I = A_o\chi^{b_o}\exp - (c\chi + 0.7 f\chi Z_{eq}^{3.5})$ which has the same dependence of Z_{eq} as the model of Gardiner and Roberts[12].

Since the actual values of the coefficients are specific to the gage parameters the general trends will be discussed.

All of the parameters except c were found to be definite functions of the photon energies registered by the detector. The magnitude parameter A_o increases as more of the available energy spectrum is included by the detector. The value of b_o is also a non linear function of energy. The composition parameters f and h both behave similarly with energy, being relatively high for low energies and rapidly decreasing with increasing energy. Above about 250 kev, these terms can be neglected for the range $10 \leq Z_{eq} \leq 20$.

In general, all of the parameters are functions of the source and/or detector angles. The value of A_o decreases with an increase in source or detector angle. This decrease is very pronounced for energies above about 250 kev. The parameter b_o also decreases with an increase in either source or detector angle, however, it is more influenced by the detector angle. The value of c was considered to be a function only of the source angle based on a double-scatter model and increases with θ_s. Similarly, the composition parameters f and h were found to be functions only of the source angle.

Considering the overall effect of the parameters b_o, c, and f on d^2I, it was concluded that for $\chi > 2.5$, the χ or density dependence could be considered independent of detector angle. The only one of these parameters exhibiting any dependence on detector angle was b_o; however, the influence of this parameter on overall response decreased with increasing χ.

A further conclusion from this research was that it would be impractical to design a sediment gage for which the effects of density and Z_{eq} are completely separable and that some correction for the density of the sediment will probably be required. Because sediments are relatively low in density,

excessively large source-detector separations would be required to ensure separability of density and composition effects for the minimum density in which the gage is to operate.

REFERENCES

1. Diad'kin, I.G., 1955. Izv. Akad. Nauk SSSR, Ser. Geof., 1, pp. 323-331. Transl. No. 710, U.S. Dep't Inter., Bur. Reclamation, Off. Er.. Ref., Denver, 19 pp.)
2. Voskoboinikov, G.M., 1957. Bull. Acad. Sci. U.S.S.R., Geophys. Ser., 5, pp. 94-107.
3. Pirie, E., Lin, K., and Taylor, D., 1968. Soil Sci., 106, pp. 411-414.
4. Preiss, K., 1968. Highway Research Record, No. 107, pp. 1-12.
5. Keller, G.H., 1965. Deep-Sea Res., 12, pp. 373-376.
6. Tittman, J. and Wahl, J.S., 1965. Geophys., XXX, pp. 284-294.
7. Czubek, J., 1966. Radioisotope Instruments in Industry and Geophysics, Vol. II, STI/PUB/112, IAEA, Vienna, pp. 249-275.
8. Christensen, E.R., 1971. Nucl. Instr. Meth., 91, pp. 461-468.
9. Taylor, D. and Kansara, M., 1968. Nucl. Instr. Meth., 59, pp. 305-308.
10. Umiastowski, K., 1970. Nukleonika, 15, pp. 259-266.
11. Preiss,K., and Livnat, R., 1972. Note on the Behaviour of Backscattered Gamma Ray Photons in the Scattering Medium. Rpt. 120, Negev Inst. for Arid Zone Res., Beer-Sheva, Israel, 24 pp.
12. Gardner, R.P., and Roberts, K.F., 1967. Density and Moisture Content Measurements by Nuclear Methods -- Final Report NCHRP Rpt. 43, Highway Res. Bd., 38 pp.
13. Devlin, G., Henderson, I.A., and Taylor, D., 1969. Nucl. Instr. Meth., 76, pp. 150-156.
14. Umiastowski, K., 1970. Nukleonika, pp. 259-266.
15. Rychlicki, S. and Umiastowski, K., 1970. Nukleonika, 15, pp. 42-49.
16. Czubek, J., 1970. Calibration of Radioisotope Probes for Soil Density Measurements. Rpt. No. 715/I, Inst. of Nucl. Physics, Cracow, 15 pp.
17. Roney, J.R., 1973. PhD dissertation, Univ. of R.I.
18. Maus, L.D., 1973. PhD dissertation, Univ. of R.I.

Proceedings, ERDA X-and Gamma-Ray Symp. Ann Arbor, MI, May 19-21, 1976 (Conf 760539)

ELEMENTAL ANALYSIS OF COAL BY PROTON-INDUCED X-RAY EMISSION ANALYSIS

S. M. Cronch and W. D. Ehmann, Department of Chemistry
University of Kentucky, Lexington, Ky. 40506

H. W. Laumer and F. Gabbard, Department of Physics and
Astronomy, University of Kentucky, Lexington, Ky. 40506

Summary

Proton-induced X-ray emission has been used to determine elemental concentrations in solid coal samples. The coal samples were irradiated with 2.5 to 5.5 MeV protons. Concentrations were determined from characteristic X-ray yields taking into account matrix absorption. The precision is shown by replicate analysis and the accuracy by comparison with results obtained by other laboratories using different techniques.

Introduction

Since the introduction of proton-induced X-ray emission analysis (PIXEA) by Johansson,[1] it has been used to analyze a great variety of materials. Its most successful application has been to thin targets, especially if the target material available is limited. The technique can, however, also be applied to thick targets. In this study the suitability of the technique for analyzing solid coal samples is investigated.

Experimental

The samples were bombarded with proton beams of 2.5 to 5.5 MeV generated with the University of Kentucky 5.5 MeV Van de Graaff accelerator. The beam diameter at the sample was 7 mm. The collimator and anti-scattering slits were made of graphite to keep the X-ray and γ-ray backgrounds to a minimum. A nickel foil was placed 130 cm from the target to homogenize the beam. A 75 micron nickel wire mounted horizontally on a 3 mm diameter plastic rod was moved vertically through the beam spot. By monitoring the Ni Kα peak, the beam density was determined. For proton energies of 2.5 MeV and 5.5 MeV using nickel foils 5 μ and 13 μ thick, respectively, produced beam densities homogeneous to 10%. Beam currents on target ranged from 5 nA to 70 nA. The target chamber was electrically insulated and acted as the Faraday cup for charge integration. Between the collimator and chamber, a 10 cm long and 4 cm diameter cylinder kept at -2000 V acted as an electron suppressor.

At the higher beam currents, the charge build-up on the target causes considerable background radiation by electron bremsstrahlung. A filament taken from a flashlight bulb was operated at 3V, the battery floating with the chamber. With the filament located 2 cm from the target, background radiation from this process was suppressed. No evidence of contamination by tungsten was observed.

The vacuum in the target chamber was usually 5 x 10^{-5} torr. Pump down time between target changes was about 10 minutes. Since irradiation time was approximately 15 minutes per sample and four targets could be mounted at one time, this is only a fraction of the accelerator time used.

The targets were mounted on a ladder such that the targets were at a 45° angle with respect to the proton beam. The X-rays were detected with a Nuclear Semiconductor Si(Li) detector which was situated at 90° to the proton beam and 45° to the target. The target was located 5 cm from the 25 μm beryllium window on the target chamber and 6 cm from the 25 μm beryllium window on the detector face. An aluminum absorber was usually placed between the two windows.

The 30 mm^2 x 3 mm Si(Li) detector has an energy resolution of 190 eV, FWHM, measured at 5.89 KeV. X-rays of the elements above atomic number 13, aluminum, can be detected.

Pulses from the Si(Li) detector and amplifier system were analyzed by a Canberra ADC on-line with a PDP-8/I computer. The resulting 1024 channel X-ray spectra were stored on magnetic tape. The PDP-8/I has an oscilloscope display and a light-pen unit for analyzing spectra. Previously accumulated data can be analyzed while recording the next X-ray spectrum.

To extract X-ray yields from the accumulated spectra the following procedure was employed. The areas of peaks which were relatively isolated and well resolved were determined on the PDP-8/I with a simple peak stripping routine which fits straight lines to the background. Peaks which are not well resolved, such as a small Cl peak in the presence of an intense S peak, were analyzed with the program SAMPO[2] on the University of Kentucky IBM-370 computer.

The coal samples obtained from the Illinois Geological Survey were ground in an agate mortar until the powdered coal would pass through a 200 mesh screen. The coal sample obtained from NBS required no further grinding. The samples were pelletized without a binder in a die at 35,000 lbs/in^2. The pellets, which were 1.3 cm in diameter, were attached to an aluminum square using three plastic screws to hold the pellet in the center of the square. The targets were then ready to be mounted on the target ladder for irradiation.

Standard stock solutions were prepared from reagent grade chemicals for the following elements: S, Cl, K, Ca, Mn, Fe, Co, Zn, Br, Sr, Ba, and Pb. Aliquot's of the stock solutions of 1000 μg/ml were diluted to 10 μg/ml. An Oxford micropipetter was used to deposit 10λ of the 10 μg/ml solution on to a thin formvar film (10-20 g/cm^2). The formvar film covered an aluminum frame with a 1.6 cm hole in the center. After the drop had air dried, the target was ready for irradiation. The yields obtained by irradiating these targets with a homogeneous beam formed the basis for determining detector efficiencies used in calculating concentrations of the coal targets. Detector efficiences for elements not in the set of standards were interpolated. This interpolation was based on a detector efficiency curve calculated for the detector and absorber combination.[3]

Spectra were accumulated at count rates below 1000 cps. Above this rate sum peaks for the intense X-ray lines start to become troublesome. Elements with Z<26 and bremsstrahlung X-rays in the low energy region of the spectrum represent the major contribution to the X-ray yield. For a constant count rate this indirectly limits the sensitivity which can be achieved for the higher Z elements. By introducing an absorber the low energy contribution to the count rate is reduced. The next limit encountered in trying to increase the count rate for elements with Z>26 is usually the stability of the target under high beam currents. A considerable increase in count rate, especially for solid targets, can be obtained by increasing beam energy; however, the general X-ray background also increases and sets a limit to the ultimate sensitivity

that can be achieved. Secondary effects may also become important and make data analysis more complex.

At a proton energy of 2.5 MeV, the highest sensitivities for the low atomic number elements, $14<Z<30$, were obtained without using an additional absorber. In this situation, the detector was count rate limited due to intense low energy X-rays for low Z elements. Because of this, beam currents were limited to very low values, approximately 5 nA. The sensitivities for the higher Z elements $Z>30$ were rather poor. To improve the sensitivities for these elements, a 0.24 mm aluminum absorber pierced by a 0.5 mm diameter hole was introduced. By using an absorber with a pinhole, the spectrum of X-rays from the low Z elements could still be detected, while the count rate of high Z was increased by increasing the beam current. The deadtime of the system didn't increase, since most of the intense low energy X-rays were absorbed and only a small fraction passed through the hole. For a 2.5 MeV proton beam, the highest count rates for the high Z elements were obtained by using a 0.32 mm aluminum absorber. With this absorber, low energy X-rays for the low Z elements didn't reach the detector, so the beam current could be increased again without increasing the detector deadtime. The limiting factor on increasing the beam current was the thermal stability of the coal sample in the proton beam. At 2.5 MeV the maximum permissible beam current was 70 nA. To increase the count rate at this maximum current, the proton beam energy was increased from 2.5 MeV to 5.5 MeV. The electron bremsstrahlung background increased at the higher proton energy, but the higher count rate yielded superior sensitivities for the same irradiation time.

All the samples were irradiation at least twice, once at 2.5 MeV with the aluminim absorber with the hole and once at 5.5 MeV with the solid aluminum absorber.

To correct for preamplifier and system deadtime a 60 cps pulser was fed into the preamplifier. The ratio of the number of pulses presented to the preamplifier and the number counted for the pulser peak in the spectrum was used as a yield correction factor.

Data Analysis

There are a number of strategies that can be adopted to determine concentrations from thick target data. A popular method, much used in X-ray fluorescence, is to use doped samples to establish an empirical concentration curve. They are often used in conjunction with statistical analysis programs to calculate regression coefficients and then take account of effects due to variations in the matrix. For a sample that contains n elements this may mean a minimum of (n-1) doped samples.[4] It appears that it is not a trivial undertaking to produce such a set of doped standards for coal samples in the face of the considerable variabilities of coal matrices encountered. An alternative is to calculate matrix effects by considering the physical processes important in producing and detecting characteristic X-ray.

A proton beam striking a carbon target surface with initial energy 2.5 MeV will penetrate a distance of about 60 μ at which point it will have lost most of its kinetic energy. The X-ray production cross-section will vary smoothly along this path. An X-ray produced at some point along the proton trajectory will therefore have to traverse some matrix material in addition to any absorbers in front of the detector before being counted. To calculate the concentration of an element, based on the number of X-rays counted per coulomb of integrated proton beam, the proton range was divided into segments. Each segment represented an energy loss of 0.1 MeV. The contribution below 0.5 MeV is negligible since the X-ray production cross-section falls off rapidly at low proton energy. This is fortunate, since stopping power values are least reliable in this region. The contribution to the yield from each range segment was determined as follows. It was assumed that the production cross-section for X-rays varied linearly in each segment. The absorption by the matrix of X-rays originating in the segment was calculated. The product of the average cross-section and X-ray attenuation was then weighted by the areal density of the range segment. The stopping powers used to calculate the range for protons were taken from J. F. Janni and are expected to be accurate to 3%.[5] For the purpose of calculating proton ranges in the coal matrix, the Bragg additivity rule was assumed to hold.[6]

$$(dE/dx)_{matrix} = \sum_i W_i \, (dE/dx)_i \qquad (1)$$

W_i is the mass fraction of element i in the matrix, and $(dE/dx)_i$ is the stopping power of element i at proton energy E. This is valid if the elements are fairly uniformly distributed in the coal matrix. If specific elements occur in grains, this technique will have the same difficulty as a method based on doped samples would have.

The X-ray production cross-section were based on the empirical curve of Akselsson and Johansson.[7] The cross-section averaged over energy is expected to deviate less from the experimental value than the variation of experimental values from the empirical curve at any specific energy, and thus should deviate by less than 10%.

The absorption cross-sections for X-rays are taken from Storm and Israel.[8] In calculating the absorption coefficients for the matrix, an equation similar to eq. 1 was used; where stopping powers were replaced by absorption coefficients.

Since the Kβ X-rays for some elements interfere with the Kα X-rays of others, the yields obtained from the spectra may have to be corrected for this overlap. The Kα/Kβ ratios were taken from Bambynek *et al.*[9] and the effects of matrix and window absorption applied to produce corrected Kα and Kβ yields.

It is evident that this technique is perfect only if the sample composition is known beforehand. This implies an iterative procedure must be employed. For a preliminary calculation, a likely composition was assumed and a first set of elemental concentrations was then determined. Subsequent calculations could then be based on the calculated concentrations. For the samples analyzed in this work there were only changes of the order of 5% between first calculations and subsequent iterations. Elements which are abundant in the coal, but for which PIXEA yields no information, are a potential source for error. Varying the carbon-oxygen abundances from 65% and 20% to 75% and 10% caused changes of the order of 10% for elements such as sulfur, which have K X-rays which are strongly absorbed by the matrix.

Results

Table I gives the PIXEA results for the coal samples provided by the Illinois Geological Survey and compares them to published values.[10] Table II compares PIXEA concentrations determined for NBS SRM 1632 with published analyses by other laboratories.[10,11,12] Errors cited for PIXEA in Table II are standard deviations based on four measurements and do not include systematic errors discussed below. S showed very good agreement while Si concentrations were found to be consistently low. The values for Zn were erratic, sometimes agreeing and at other times differing by a factor of 5. Se, Zr, Br, and Cl also compared poorly.

Table III presents the results of the replicate analyses of a coal sample issued by the EPA for a round-robin study.

Nine targets were made and analyzed with a proton beam at 2.5 MeV. The yields for Z≤26 were obtained from spectra collected with the 0.24 mm aluminum absorber having a 0.5$ mm hole. For Z>26 data was obtained with a 0.32 mm aluminum absorber. Standard deviations are generally within the variation due to peak fitting and target geometry, except for the elements Zn and Br.

For a proton energy of 3.5 MeV preliminary results yield concentrations which are higher than those obtained with 2.5 MeV protons. We suspect this is caused by secondary fluorescence which is negligible for these targets at a proton energy of 2.5 MeV. We intend to investigate the phenomenon further.

Error Analysis

To arrive at the error estimates quoted in Table I, the following error contributions were considered. Geometry variation for the detector-sample distance contributes 7%. Beam integration and deadtime correction are assigned 3%. The error introduced in calculating matrix effects varies with the element identified. Range of the proton beam is based on values which are accurate to 5%, but the uncertainty in composition will introduce an error of at least 6%. The absorber coefficients are expected to be accurate to 10%. Thus for silicon and other strongly absorbed x-rays the error contributed by this factor is close to 10% while for iron at 2.5 MeV proton energy this becomes 1%. These errors and the statistical error due to variation in peak fitting are summed by squares and entered in Table I. It is apparent in Table III that these errors do not always justify the observed variation in replicate analysis which must be ascribed to sample variation.

Table I. Comparison of PIXEA with Values Obtained by the Illinois Geological Survey*[10] (Concentrations, μg/g unless % indicated)

		C13464		C14684		C15231		C16139		C16317	
Element	% Error	PIXEA†	I.G.S.	PIXEA	I.G.S.	PIXEA	I.G.S.	PIXEA	I.G.S.	PIXEA	I.G.S.
Si %	13	1.1	2.65	0.76	2.10	.92	2.87	.80	2.95	0.81	2.48
S %	12	4.3	4.08	2.6	2.46	4.1	4.12	4.0	4.01	3.1	3.22
Cl %	20	0.52	0.33	0.53	0.42	0.38	0.14	0.34	0.22	0.58	0.02
K %	11	0.11	0.17	0.09	0.15	0.12	0.17	0.11	0.16	0.11	0.17
Ca %	11	0.58	0.50	0.34	0.54	0.46	0.90	0.38	0.71	0.83	0.73
Ti %	10	0.08	0.05	0.04	0.06	0.07	0.06	0.06	0.06	0.07	0.07
Fe %	10	1.9	2.34	1.4	1.72	1.5	1.83	1.3	1.78	1.4	1.57
Zn	16	27	26	21	30	51	289	40	89	2300	2668
Se	16	5	2.3	2	1.2	4	1.6	6	7.7	2	2.4
Br	14	19	15	21	19	13	13	7	12	15	14
Zr	15	19	103	17	40	21	28	20	-	19	20
Cd	24	-	0.5	-	<0.3	-	1.4	-	0.09	23	28

*Samples provided by the Illinois Geological Survey.

†PIXEA values are the average of two determinations at 2.5 MeV.

Table II. Concentrations Determined by PIXEA Are Compared to Values Obtained by Other Laboratories for NBS SRM 1632. (concentration, μg/g unless % indicated)

Element	PIXEA *	Inter-Laboratory Comparison ave. values[a]	I.G.S.[b]	NBS[c]
Si %	1.7 ± 0.07	-	3.92	3.2[d]
S %	1.4 ± 0.04	-	1.25	-
Cl	1060 ± 150	890 ± 125	1000	-
K %	0.28 ± 0.01	0.28 ± 0.03	0.33	
Ca %	0.46 ± 0.01	0.43 ± 0.05		
Ti	1010 ± 16	1049 ± 110	1100	800[d]
Fe %	0.81 ± 0.03	0.84 ± 0.04	1.11	0.87 ± .03
Zn	59 ± 38	30 ± 10		37.0 ± 4
Se	12 ± 2	3.4 ± .2	2.8	2.9 ± 0.30
Br	14 ± 1	19.3 ± 1.9	20	-
Rb	24 ± 4	21 ± 2	-	-
Sr	163 ± 4	161 ± 16		
Y	23 ± 2	-	-	-
Zr	44 ± 7			
Ba	770 ± 170	352 ± 30		

*PIXEA values obtained at 2.5 MeV; errors are standard deviations based on 4 measurements.

[a] Ref. 11, [b] Ref. 10, [c] Ref. 12, [d] Information only.

Table III. Replicate Analysis of a Coal Sample* (concentrations, μg/g unless % indicated)

Element	# of Determinations (9)	Mean+	σ
Si %		1.3	0.08
S %		1.2	0.1
Cl %		0.12	0.03
K %		0.25	0.01
Ca %		0.42	0.02
Ti		850	36
Fe %		0.73	0.4
Zn		32	8
Br		12	4
Rb		22	3
Sr		171	30
Zr		85	8

*Coal sample issued by EPA for round-robin study.[13]

+Values were obtained by irradiation at 2.5 MeV.

Acknowledgments

This work was supported in part by the Institute of Mines and Minerals Research at the University of Kentucky, Lexington, Ky. The authors thank the Coal Section of the Illinois Geological Survey for providing analyzed coal samples.

References

1. T. B. Johansson, R. Akselsson, and S. A. E. Johansson, Nucl. Instrum. Meth. 84, 141 (1970).
2. J. T. Routti, and S. G. Prussin, Nucl. Instrum. Meth. 72, 125 (1969).
3. W. J. Gallagher and S. J. Cipolla, Nucl. Instrum. Meth. 122, 405 (1974).
4. S. D. Ramberry and K. F. J. Heinrich, Anal. Chem. 46, 81 (1974).
5. J. F. Janni, Technical Report No. AFWL-TR-65-150. Air Force Weapons Laboratory, 1966.
6. L. C. Northcliffe and R. F. Schilling, Nuclear Data Tables A 7, 233 (1970).
7. R. Akselsson and T. B. Johansson, Z. Physik 266, 245 (1974).
8. E. Storm and H. I. Israel, Nuclear Data Tables A 7, 565 (1970).
9. W. Bambynek, B. Crasemann, R. W. Fink, H. U. Freund, H. Mark, C. D. Swift, R. E. Price, and P. Venugopala Rao, Rev. Mod. Phys. 44, 716 (1972).
10. H. H. Ruch, H. J. Gluskoter, and N. F. Shimp, Ill. Geol. Survey, Environmental Geology Note No. 72, 96 p. (1974).
11. J. M. Ondov, W. H. Zoller, Ilhan Olmez, N. K. Aras, G. E. Gordon, L. A. Rancitelli, K. N. Abel, R. H. Filby, K. R. Shah, and R. C. Ragaini, Anal. Chem. 47, 1102 (1975).
12. Certificates of Analysis, Standard Reference Material SRM 1632, Office of Standard Reference Materials, National Bureau of Standards, U.S. Dept. of Commerce, Washington, D.C. 20234.
13. D. J. VonLehmden, R. H. Jungers and R. E. Lee, Jr., Anal. Chem. 46, 239 (1974).

Proceedings, ERDA X-and Gamma-Ray Symp. Ann Arbor, MI, May 19-21, 1976 (Conf 760539)

A RADIOISOTOPE IMMERSION PROBE FOR CONTINUOUS OR DISCRETE MEASUREMENTS OF SULPHUR IN CRUDE OILS AND LEAD IN REFINERY PRODUCTS

Steen Teller
Isotopcentralen, 2, Skelbaekgade, DK-1717 Copenhagen V, Denmark

SUMMARY

The sulphur content of fuel oils and the lead content of gasolines can be determined in a single measurement by a simultaneous detection of scattered and transmitted low-energy X-rays. A prototype immersion probe has been developed and a precision of 0.02 % sulphur and 20 ppm lead obtained for a counting period of 1 minute.

INTRODUCTION

During the last 20 years radioisotope instruments for the determination of sulphur and lead in petroleum products have been an attractive alternative to the more time consuming chemical methods. The need for rapid methods of analysis for these elements increases with the realization, that the levels of sulphur and lead in fuels are hamful to the environment and in some countries legislation has already been introduced to limit the concentrations. In a recently published "Proposal for a Council Directive" for the member states of EEC[1] the sulphur content of most fuel oils should not exceed 2 % by weight from 1 June 1978 and 1 % by weight from 1 June 1983, and "measures of control in particular by means of random sampling, should be provided to check to sulphur content of fuel oils placed on the market".

Direct analysis of sulphur or lead in hydrocarbons by non-dispersive X-ray fluorescence has been reported[2], but the majority of sulphur monitors are based on the absorption of soft gamma- or X-rays emitted from radioisotope sources[3-5]. Instrumentation for the laboratory as well as plant process control are commercially available. None of the methods however, are well suited for the design of a portable instrument intended for rapid analysis in various places. The X-ray absorption technique is strongly dependent on the sample density, whereby compensation for density variations must be achieved either by presenting a sample of constant mass per unit area[4] or by a simultaneous measurement of the sample density[3,5] (weighing by nucleonic or other means). The low energy radiation from sulphur (2.4 keV) causes difficulties for the X-ray fluorescence technique, e.g. thin fragile windows, window contamination and influence from variations in density and humidity in the ambient air.

It is the purpose of this paper to present a measuring principle, which can be applied for the construction of a portable immersion probe giving the sulphur or lead content of different petroleum products in a single reading.

ANALYSIS BY ABSORPTION OF LOW-ENERGY X-RAYS

Transmission

The intensity I_t of monochromatic gamma- or X-rays transmitted through a measuring cell of thickness x containing a hydrocarbon with the density ρ, is given by

$$\frac{I_t}{Ito} = \exp\left(-\Sigma \mu_i C_i \cdot \rho x\right) \qquad (1)$$

where I_{to} is the intensity for the empty cell and μ_i and C_i are the mass attenuation coefficients and the weight fractions of the respective elements, hydrogen (H), carbon (C) and sulphur (S). Using gamma- or X-rays of energy about 20 keV, where $\mu_H = \mu_C << \mu_S$, it is possible to determine small variations in C_S, if a constant value of ρ (and x) is maintained.

Back-scattering

The intensity I_s of gamma- or X-rays back-scattered from a layer of hydrocarbon of thickness x and density ρ is given by

$$\frac{I_s}{I_{so}} = K \frac{\Sigma \sigma_i C_i}{\Sigma(\mu_i+\mu_i) C_i} \left(1-\exp(-\Sigma(\mu_i+\mu_i)\rho x)\right) \qquad (2)$$

where I_{so} is related to the source emmission, σ_i is the scattering coefficient (a sum of Compton and coherent scattering coefficient) and $(\mu_i+\mu_i)$ is the sum of the mass attuation coefficient for the incident and the scattered radiation. K is the overall efficiency of detection.

The equation (2) indicates, that it is possible to determine the weight fraction of sulphur independent of the density, if the thickness of the hydrocarbon layer is large (the exponential term drops to zero). Experimentally however, one finds that the overall detection efficiency K depends on the density, because the average path length travelled by the incident and scattered radiation changes with the density. The backscattered intensity also depends on the C/H-ratio, because there is no radiation energy for which both $\mu_H = \mu_C$ and $\sigma_H = \sigma_C$ are fulfilled.

It is well-known from the design of in-situ density meters for coal and soil[6], that the relation between the intensity of the scattered radiation and the sample density can be expressed as

$$I_s \approx (\mu\rho)^m e^{-\mu\rho r} \qquad (3)$$

where r is the distance between source and detector and where m is an empirical constant for the instrument, typical of the magnitude 1.5-2. The equation (3) is illustrated in fig. 1 for two samples of different average atomic number(Z). The intensity of the scattered radiation decreases with increasing atomic number (increasing sulphur content), but the density range around the maximum for the response curve (3), where an accurate determination

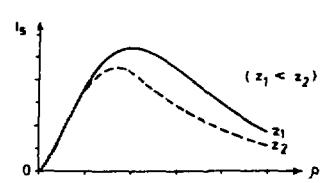

Fig 1 Back-scatter intensity versus density and average atomic number

With the low source activity of 2 mCi, the radiation dose rate is negligible on the probe surface except for the circumference of the reflector, where it amounts to 35 mrem/hour. The dose rate is less than 0.3 mrem/hour in a distance of 30 cm from the reflector.

RESULTS AND DISCUSSIONS

Probe parameters

Pure hydrocarbons with butyl sulfide added covering the following ranges of density (0.75-0.98 g/cm^3), C/H-ratio (6.7-10.0) and sulphur content (0-3 %) was used to examine the probe parameters.

The smallest influence on the detected X-rays (≈ 20 keV) due to variations in the C/H-ratio was obtained using a silver or a tin reflector, while a molybdenum reflector proved to be the best choice regarding the sensitivity of the sulphur content and the independence of the density, at the expense of a slight but tolerable increase in the dependence on the C/H-ratio (± 0.05 % sulphur for C/H-ratio between 8.0 - 9.0). With a source-reflector distance about 17 mm the influence from densities in the range 0.80 - 0.97 g/cm^3 were less than ± 0.02 % sulphur.

Sulphur in fuel oils

Samples of fuel oils (approx. 500 cm^3 each) were supplied by two petroleum companies in Denmark (B.P. and Esso) and the Danish Boiler Owners Ass. (analysis of fuel oils etc.). Results from analysis for the sulphur content (X-rays transmission and chemical methods) were also provided by the suppliers and both light and heavy gasoils and light and heavy fuel oils were represented among the samples.

The probe was immersed in the different samples and the countrate measured. Fig. 6 shows the dependence of the countrate on the sulphur content and a hyperbolical calibration curve is expected. The results however indicates, that a good approximation is obtained with two linear calibration curves in the range 0 - 3.5 % sulphur.

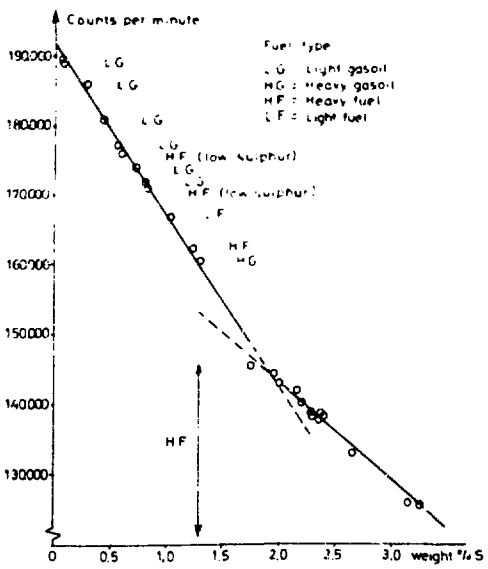

Fig 6 Determination of Sulphur content.

The precision for a counting period of 1 minute (repeated measurements on the same sample involving only counting statistics and electronical drift) is 0.02 % sulphur by weight (1 standard deviation) at a level of 1 % sulphur.

The accuracy expressed as the standard deviation for the linear calibration curves is ± 0.03 % in the range 0 - 1.5 % sulphur and ± 0.07 % in the range 1.5 - 3.5 % sulphur.

Trace impurities in fuel oils

The measured radiation intensity depends on the average atomic number of the hydrocarbons and is therefore influenced by trace impurities in the fuel oils. In a sulphur monitor uging X-rays of 20 keV in a transmission geometry[2] the following concentrations of contaminants have been calculated causing a change of 0.01 % in the sulphur reading: 40 ppm Va, 20 ppm Ni, 320 ppm Na, 85 ppm Cl, and 650 ppm H_2O.

The same concentrations are expected for the immersion probe. This is verified by adding small amounts of Ferrocene ($C_{10}H_{10}Fe$) to pure hydrocarbons. The calculated concentration of Fe, which causes a change of 0.01 % in sulphur reading is 25 ppm Fe, where values from 20 to 30 ppm Fe are found experimentally.

Influence of temperature

An increase in the temperature of the samples to 40 - 50 °C does not influence the responce of the probe, if the period of immersion is only a few minutes. A cooling mantle however will be necessary, if the probe is immersed in large preheated tanks (e.g. to determine the sulphur contents in different depths - "sedimentation") or in preheated process-streams (on-line installation).

Lead in gasolines

Samples of different gasolines covering the relevant range in lead content were prepared and the relationship between the probe countrate and the lead content established. The results are shown at fig. 7, and again a good approximation is obtained using two linear calibration curves. In fact with an expected limitation of the lead content to about 0.5 g/l only one linear calibration curve is necessary.

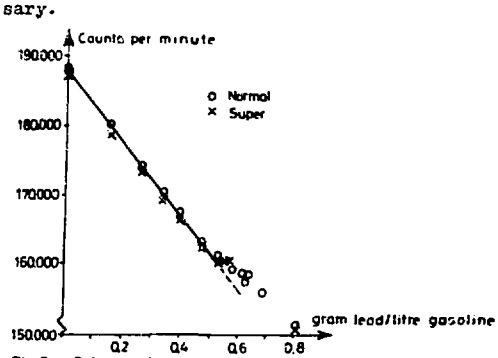

Fig 7 Determination of lead content

of the sulphur content independent of the density is theoretical possible, is much smaller than the variations encountered for petroleum products (o.7 - 1.o g/cm^3).

Transmission + Back-scatter

From equation (1) one finds, that $dI_t/d\rho$ is negative, from equation (2) that $dI_s/d\rho$ is positive and from equation (3) that $dI_s/d\rho$ is both positive and negative. It is therefor suggested[7], that a combination of transmitted and scattered gamma- or X-rays will lead to a method of analysis for high Z elements in a matrix of low Z elements which method is independent of the density over a wide range.

A series expansion in the density for the sum of e.g. the equations (1) and (2) will show that the detected intensity $I = I_t + I_s$ to the first order is independent of the density, if a proper choice of measurement geometry, source strength and radiation energy is made. The mathematical details will not be dealt with, but the principle is illustrated in fig. 2, where the intensity is given as a function of the density with the mass absorption coefficient as parameter. The sum of the curves with the same μ is independent of the density over a wide range about ρ_o.

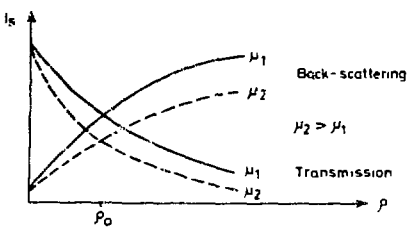

Fig 2 Transmission and backscatter intensity versus density.

The measuring principle is also illustrated in table 1 for 2 X-ray energies. X-rays of 6o keV give a poor sensitivity for sulphur but reduce the influence from the C/H-ratio. A further reduction is obtained utilizing an empirical relationship (fig. 3)[8] between the density and the hydrogen content valid for most petroleum products. In stead of being independent of the density the detected intensity can be adjusted to increase slightly with the density to compensate for the decrease in the intensity due to decreased hydrogen content.

Tabel 1 *)

X-rays	Energy	ρ(+)	C/H(+)	S or Pb(+)
Transmitted	6o keV	-	+	-
Transmitted	2o keV	-	o	-
Back-scattered	6o keV	+	-	-
Back-scattered	2o keV	+	-	-

*) Increase (+) or decrease (-) in intensity or parameter.

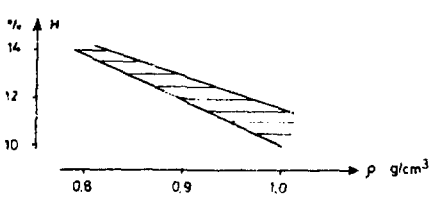

Fig 3 Hydrogen - density relationship

THE PROTOTYPE IMMERSION PROBE

A source-detector arrangement with a reflector a short distance apart (fig. 4) is chosen in order to obtain a compact measurement geometry, in which the sample in the same time acts as a scatterer for incident radiation from one source and as an absorber for transmitted radiation from another source (the reflector). The diameter of the probe is less than 2" which ensures easy access to drums, tanks or other containers for petroleum products.

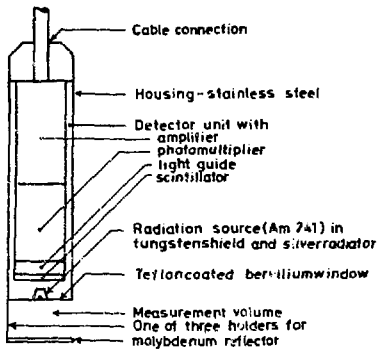

Fig.4 Sulphur - lead probe

X-rays of energy 21 keV and gamma-rays of 6o keV are obtained from an americium-241 source (2mCi) covered by a silver foil. The scintillator receives transmitted X-rays from the reflector and scattered X-rays from the sample with energies about 2o keV and scattered gamma-rays from the sample with energies of 5o-6o keV. A combination of a physical and electronical discrimination against the unwanted gamma-rays is obtained with a crystal (1 mm x 1 1/2 "Ø) of CaF_2 (Eu). The energy resolution of this crystal is inferior to that of a thin crystal of NaI (Tl), but better than the energy resolution of plastscintillators. The use of a thin crystal of NaI (Tl) is precluded because the scattered gamma-rays of 6o keV interfere with the X-rays of 2o keV through the iodine escape peak in this crystal.

A typical spectrum for the probe immersed in a fuel oil is shown in fig. 5. The first measurements were made with a single-channel analyser (BASC-battery scaler, NEA, Copenhagen), but later an instrumentation specially designed for the probe was developed. This instrumentation includes zero suppression, inversion and slope selection for a direct reading of sulphur or lead content together with spectrum stabilization, where the difference between the countrates in two channels (fig. 5) controls the high voltage for the photomultiplier.

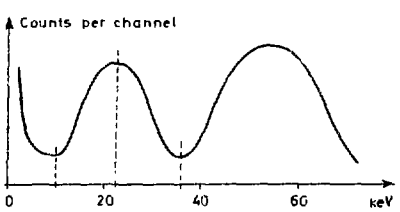

Fig.5 Probe spectrum with discriminator levels

The precision for a counting period of 1 minute is o.ol g/l (1 standard deviation).

The accuracy expressed as the standard deviation for the linear calibration curve is o.ol5 g/l (≈ 2o ppm) in the range o - o.5 g/l.

The probe parameters were unchanged from the sulphur measurements, and it is therefore expected, that the small though significant difference observed in fig. 7 between the "normal" and "super" types of gasolines can be removed by slight adjustments of the parameters improoving the accuracy further.

CONCLUSION

The analysis of sulphur or lead content in petroleum products with a radioisotope immersion probe has been demonstrated. The measuring principle is based on the simultaneous detection of transmitted and scattered low-energy X-rays. The portable probe which may be used in conjunction with standard electronic instrumentation, is very suitable for measurements in the field and in the laboratory. With minor modifications on-line installation is also possible.

REFERENCES

1. Commission of the European Communities, COM (75) 681 final, Brussels, december 1975.

2. Price, B. J. and Field, K. M., Int. Laboratory 39 (sept./okt. 1974).

3. Cameron, J. F. and Piper, D. G., IEE Conf.Publ. 84, 1o9, (1972).

4. Gilpin, R. L. and Franks, M. C., Proc. Amer. Petr. Inst. 43, 258, (1963).

5. Tröst, A., Erdöl und Kohle. Erdgas, Petrochemie 22, 548, (1969).

6. Semmler, R. A., "Gamma-scattering Density Meters"Univ. of Chicago (1961) TID-14178.

7. Teller, S., U.S. Patent 3.928.765 (1975).

8. Guthrie, V. B., "Petroleum Products Handbook", Table 14-2", McGraw-Hill (196o).

Proceedings, ERDA X-and Gamma-Ray Symp. Ann Arbor, MI, May 19-21, 1976 (Conf 760539)

ON THE ANALYSIS OF LOW RADIOACTIVITY LEVEL ENVIRONMENTAL SAMPLES

H. P. Yule
NUS Corporation
4 Research Place
Rockville, Maryland 20850

Summary

A comparison of counting times and accuracies and precisions of results for low radioactivity level environmental samples shows that a NaI(Tl) counting system coupled with a proper least-squares spectrum analysis permits the counting of many more samples than does a Ge(Li) detector counting system. Utilization of this system will also liberate the Ge(Li) detector for non-routine work.

Introduction

Analysis of environmental samples for low activity levels of gamma-ray emitters is often accomplished by counting for an extended period (e.g. 1,000 minutes) with a large volume Ge(Li) detector spectrometer. Because of the long counting time, the number of samples which may be processed is limited to perhaps one or two per day. An alternative method would be to count the samples using an NaI(Tl) spectrometer to take advantage of the substantially higher counting efficiency, and, hence, much reduced counting time. However, the analysis of the data produced this way is likely to be very difficult.

As an example, consider a milk sample (Figure 1).

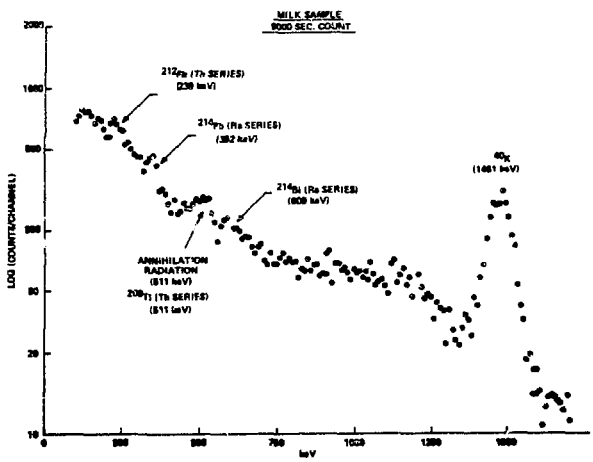

Figure 1

Milk having no demonstrable radioactive contamination has about 35 percent gross gamma-ray activity above background, which is caused by ^{40}K (half-life 1.2×10^9 years) naturally present in milk. The NaI(Tl) spectrum of milk contains a pronounced peak at 1461-keV and smaller background peaks. Approximately 18 percent of the ^{40}K peak is from counter background, and the remainder is from the ^{40}K in the milk. The 239-keV peak and some of the 511-keV peak are attributed to naturally occurring radioisotopes of the ^{232}Th series. The remainder of the 511-keV is annihilation radiation from various sources. The 352- and 609-keV peaks are counter background associated with ^{226}Ra daughters.

Small amounts of the fission product radioactivities, ^{131}I (364-keV) and ^{137}Cs (662-keV) would be difficult to observe because of the interferences from the naturally occurring peaks at 352- and 609-keV. Therefore, it could be concluded that NaI(Tl) detectors are useless for this kind of sample since there are no observable peaks from ^{131}I and ^{137}Cs at low levels of radioactivity.

In this paper, we shall demonstrate that the desired information on fission product radioactivities is available from sodium iodide spectra with the aid of a moderately sophisticated mathematical analysis of the spectra.[1-5] This method obviates the need for photopeak analysis and furthermore permits the counting of many more samples on a sodium iodide detector than may be counted in the same amount of time with a Ge(Li) detector. It has been found in our laboratory that samples which require 1,000 minute long counts with our large volume Ge(Li) detector may be counted for only 50-150 minutes with our NaI(Tl) spectrometer. Accuracy and precision of the answers provided by the two systems are indistinguishable. Thus, instead of counting one sample per day on the Ge(Li) detector, we can count up to ten times as many samples on the NaI(Tl) system.

Laboratory Procedures

Samples are counted in our laboratory on a three inch by three inch NaI(Tl) detector coupled to a Tracor-Northern hardwired multi-channel analyzer. Data are output on punched paper tape. The Ge(Li) detector has an effective volume of 60 cm^3 and a relative efficiency of 11.6 percent. Data from the Ge(Li) detector are processed by a Tracor-Northern model TN-11 dedicated mini-computer.

Examples of samples counted with these systems are water, milk, soil, sediment, vegetation, air filters, charcoal samples, and aquatic life. Water and milk samples were typically counted in a three liter Marinelli beaker, while the other classes of samples were counted in a small glass dish which contained typically 200 grams of soil or 100 grams of vegetation. Aquatic life samples were usually counted in the dish since there was not enough samples to anywhere near fill the three liter beaker.

Computational Procedures

For the Ge(Li) detector, the intensity of the photopeak in counts-per-second was calculated using the total peak area method.[4,5] After applying suitable correction factors, the amount of radioactivities (picoCuries) was computed by comparison with a calibrated source.

The NaI(Tl) data were input to a computer via a Teletype (Model ASR-33), and subsequently checked for errors using a computer program. The data were then reduced by the least-squares technique.[1-3] References 4 and 5 review and critique this method, and also present numerous references to publications concerning the method. The least-squares analysis involves solving eqt. (1):

$$\sum_{j=k}^{n} w_j \left(U_j - \sum_{i=1}^{M} \alpha_i S_{ij} \right)^2 = \text{MINIMUM} \qquad (1)$$

(For a full explanation, see reference 4.) The solution to eqt. (1) is the vector alpha, and if, for example, the unknown spectrum contained 10 picoCuries of ^{137}Cs and the standard spectrum of ^{137}Cs contained 100 picoCuries of ^{137}Cs then the least-squares technique should generate alpha equal to 0.1 for ^{137}Cs, ignoring any requisite decay corrections and assuming all spectra have been normalized to the same counting times.

A number of problems are associated with application of the least-squares technique. These include gain- and baseline shifts and the proper selection of the components in the solution. There is one further source of error in the final answer, and that is whether the number of picoCuries in the standard is accurately known, since the final picoCurie level in the unknown will be calculated from the product of alpha and the source strength of the standard.

In the present work we have utilized the ALPHA-M computer program[1-3] which makes all necessary decay corrections, and is able to compensate for gain- and baseline shifts provided such shifts are not extremely large. Therefore, the utilization of this program for our purposes reduces to (1) the accumulation of a good set of standard spectra having accurately known picoCurie levels for each standard, and (2) a method of selection of those component isotopes which were actually present in the unknown spectrum.

The problem of selecting the isotopes to be included in the solution is generally not trivial. The final solution should contain all those isotopes which are actually present and no others, and contributors having large relative uncertainties should also be excluded.

A common practice is to perform the fit with all possible contributors in the set of standard spectra. This approach often gives rise to inaccuracies in those components which turn out to be positive and/or absurd results such as answers with errors in excess of 100 percent are also obtained. A particularly disturbing feature is that some components are indicated to be negative, i.e., have calculated negative picoCurie levels, very often with relatively small errors, such as 20 percent.

What has been done in the present work therefore is to devise a method of approaching the final solution utilizing insofar as possible a knowledge of sample composition. Thus, for a milk sample we would expect the sample to contain ^{40}K, and we would first solve the least-squares equation utilizing ^{40}K and background as the only components of the spectrum. Other components which could be present, such as ^{137}Cs and ^{131}I, are tried one by one with the potasium and background components. The procedure is to add in first components which are most likely to be present and then components which are less likely to be present. Thus, what happens for the milk is that the solution with only background and ^{40}K is likely to give a satisfactory fit (or nearly so) as measured by the normalized chi-square statistic. The next step is to try ^{137}Cs, since that is often found in milk. Thus, ^{137}Cs would then be added to the list of components, and the solution repeated with background, ^{40}K and ^{137}Cs. If ^{137}Cs is present then the least-squares technique will produce a positive value of alpha for the cesium, a small relative error in cesium result, and a significant improvement in the fit, as indicated by the chi-squared statistic. If it is not present, the chi-squared statistic will change little, the alpha for ^{137}Cs will have a large relation error or may be negative. If the newly added component, in this instance ^{137}Cs, is deemed to be present, based on the criteria set forth immediately above, it is retained in the list of component isotopes; otherwise, it is discarded from the list.

The next iteration is then to add, for example, ^{131}I to the list of isotopes. If ^{137}Cs is present, the list will now contain background, ^{40}K, ^{137}Cs and ^{131}I; otherwise it is omitted from the list. The fit is then repeated using the updated component list. This process is repeated until all candidates have been processed.

The final solution, then, contains (1) those isotopes expected to be present, ^{40}K, and background, in the present example, and (2) zero, one, or more isotopes which might be either present or absent. If these tentative isotopes improved the fit significantly when incorporated in the list of isotopes, they are retained for the solution. Intermediate solutions would have tried and resulted in discarding as not detectable ^{137}Cs, radium and its daughters, ^{131}I, ^{59}Fe, ^{51}Cr, ^{60}Co, ^{65}Zn, ^{106}Ru, ^{134}Cs, and ^{140}Ba-^{140}La. In the present example, the final solution has only background and ^{40}K in the fit. This fit is best because it contains only components which are actually present in the sample. In practice, not even this solution is accepted unless the "goodness of fit" as determined by the chi-squared statistic lies in an acceptable range (0.85-1.50).

An advantage of the present approach is that not only does the final solution tell us that background and ^{40}K are present in the unknown spectrum and how much ^{40}K is present, but also that all the other isotopes tried during various iterations were not detected.

In the event of improper selection of the order in which isotopes are added to the list of candidates to be fitted, the solution finally reached may not correct. The code is programmed to flag this condition so that the run may be repeated with the order of fitting truly reflecting the decreasing probability of presence of each candidate with increased position in the list.

Results

Comparisons of results obtained for various samples as obtained through Ge(Li) spectrometry and NaI(Tl) spectrometry coupled with least-squares spectral analysis is shown in Tables 1-3. Examination of the numbers in Tables 1-3 shows that the accuracies and precisions of the results are comparable. It may be noted that for milk the counting time for the NaI(Tl) system is 150 minutes, approximately 1/7 of the 1,000 minute counting time utilized on the germanium detection system. It is clear that in an 8 hour shift it would not be possible to count seven times as many milk samples, but it would be possible to count four milk samples rather than one milk sample per day if the NaI(Tl) system is left counting at the end of the working day. (It is also clear that for milk counting time of 1,000 minutes for the Ge(Li) detector is substantially more than is necessary but the same is doubtedly true for the NaI(Tl) system.)

The ^{144}Ce number for sample C is marked as doubtful (by the code) since its two sigma error is rather large. In sample E, ^{137}Cs was detected by the Ge (Li) system but not by the NaI(Tl) system. In this instance, the error on the cesium result is quite substantial.

Figure 2 shows an NaI(Tl) spectrum of a soil sample counted for 50 minutes. Prominent peaks from the thorium- and radium series are visible, as is ^{40}K. A hint of ^{137}Cs (662-keV) is seen on the right of the prominent 609-keV peak from ^{214}Bi.

Table 3 shows results for soil samples and also results obtained by an independent laboratory which utilizes 100 minute counts for the Ge(Li) detectors. For sample A, it may be seen that the antimony may have been detected by the 1,000 minute Ge(Li) but has a 100 percent error. Antimony 125 was detected by the 200 minute Ge(Li) count and was not detected by NaI(Tl) count. In sample B, the ^{95}Zr-^{95}Nb numbers for both counters are in agreement with one another whereas the shorter Ge(Li) count did not detect them. On the other hand, ^{144}Ce was detected by both Ge(Li) methods, although results do not agree.

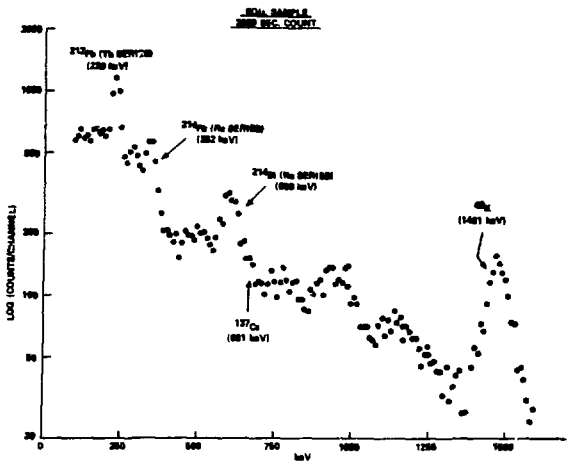

Figure 2

Reviewing the results in Tables 1, 2, and 3, leads to the conclusion that a long count on a Ge(Li) detector is not necessarily superior to a short count on a NaI(Tl) detector when the NaI(Tl) spectrum is properly analyzed with the least-squares technique. Occasionally, the least-squares technique will miss a component which makes a very small contribution to the spectrum such that the error in the results is very nearly as large as the answer. The same is true when comparing a long Ge(Li) and a short Ge(Li) count. Minor components will be missed in the short count. Furthermore, the precision and accuracy of the long Ge(Li) count and the short NaI(Tl) count will be in most cases very much better than the accuracy and precision obtained from the short Ge(Li) count.

In view of the much shorter counting time needed for the NaI(Tl) system, it seems clear that there is a definite place in the environmental laboratory for the NaI(Tl) detector for processing low activity gamma-ray spectra.

Table 1

Gamma-Ray Spectrometry of Milk

1000-min Ge(Li) vs 150-min NaI(Tl) Results

NUS Sample	Nuclide	pCi/l ± 2σ 1000-min Ge(Li)	150-min NaI(Tl)
"H"	^{40}K	1041 ± 90	923 ± 54
	^{137}Cs	17 ± 3	16 ± 3
"I"	^{40}K	987 ± 63	939 ± 79
	^{137}Cs	10 ± 4	9 ± 4
"J"	^{40}K	1056 ± 83	1000 ± 80
	^{137}Cs	12 ± 3	11 ± 4
"K"	^{40}K	988 ± 79	1023 ± 66
	^{137}Cs	12 ± 3	12 ± 5

Table 2

VEGETATION
Comparison of Results
of
150-min NaI(Tl) and 1000-min Ge(Li) Measurements

	Radioactivity Concentration, pCi/g-dry ± 2σ	
	1000 - Min Ge(Li)	150 - Min NaI(Tl)
	Sample "C" Corn Silage	
^{40}K	19 ± 2	20 ± 2
^{137}Cs	ND	ND
^{144}Ce	0.58 ± 0.33	(0.53 ± 0.38 "Doubtful")
	Sample "D" Grass Silage	
^{40}K	16 ± 4	17 ± 4
^{137}Cs	*0.40 ± 0.11*	*0.62 ± 0.24*
^{144}Ce	3.0 ± 0.6	2.7 ± 0.7
	Sample "E" Hay	
^{40}K	21 ± 4	22 ± 5
^{137}Cs	0.19 ± 0.14	ND
^{144}Ce	2.1 ± 0.8	1.5 ± 0.9
	Sample "F" Hay	
^{40}K	22 ± 3	25 ± 2
^{137}Cs	0.13 ± 0.08	(0.12 ± 0.10 "Doubtful")
^{144}Ce	1.0 ± 0.5	0.9 ± 0.3
	Sample "G" Grain	
^{40}K	8.6 ± 1.0	6.6 ± 1.2
^{137}Cs	ND	ND
^{144}Ce	ND	ND
^{226}Ra	0.43 ± 0.09	0.39 ± 0.11

ND - Not Detected

Table 3

Comparison of Gamma-Ray Spectrometry Results for Soils
Measured by a NaI(Tl) Detector (NUS) and Ge(Li) Detectors
(NUS and Independent Laboratory)
pCi/g - dry ± 2σ

	Sample "A"		
	NUS		IND
	50-min NaI(Tl)	1000-min Ge(Li)	100-min Ge(Li)
^{40}K	8.4 ± 1.1	9.0 ± 0.7	5.0 ± 3.3
^{95}Zr	-	-	-
^{95}Nb	-	-	-
$^{95}Zr + ^{95}Nb$	ND	ND	ND
^{125}Sb	ND	(0.03 ± 0.03)	ND
^{137}Cs	3.1 ± 0.1	3.1 ± 0.1	3.4 ± 0.5
^{144}Ce	ND	ND	ND
	Sample "B"		
	NUS		IND
	50-min NaI(Tl)	1000-min Ge(Li)	100-min Ge(Li)
^{40}K	9.6 ± 1.3	8.8 ± 0.8	4.0 ± 3.5
^{95}Zr	-	2.6 ± 2.2	-
^{95}Nb	-	2.0 ± 1.4	-
$^{95}Zr + ^{95}Nb$	2.7 ± 2.4*	4.6 ± 2.6	ND
^{125}Sb	ND	0.16 ± 0.04	ND
^{137}Cs	7.3 ± 0.2	7.5 ± 0.1	6.8 ± 0.7
^{144}Ce	ND	0.7 ± 0.4	2.7 ± 1.9

* Doubtful

Acknowledgement

The author is indebted to John D. Buchanan for providing the Ge(Li) results given here.

References

1. Schonfeld, E., Proceedings, 1965 Intl. Conf., "Modern Trends in Activation Analysis," College Station, Texas, April, 1965, p. 279.

2. Schonfeld, E.; Kibbey, A.H.; and Davis, W., Jr.: Nucl. Instrum. Methods 45, 1 (1966).

3. Schonfeld, E., Nucl. Instrum Methods 52, 177 (1967).

4. Yule, H.P., in "1968 Intl. Conf. on Modern Trends in Activation Analysis," J. R. DeVoe, Ed, N.B.S. Special Publication 312, June, 1969, pp. 1155-1204.

5. Yule, H.P., in "Activation Analysis in Geochemistry and Cosmochemistry," A. O. Brunfelt and E. Steines, Ed., Universitetsforlaget, Oslo, 1971, pp. 145-166.

Proceedings, ERDA X-and Gamma-Ray Symp. Ann Arbor, MI, May 19-21, 1976 (Conf 760539)

APPLICATION OF GAMMA-RAY SPECTROSCOPY IN ENVIRONMENTAL MONITORING

B. B. Hobbs, L. G. Kanipe, W. R. Clayton, E. A. Belvin
Radiological Hygiene Branch
Tennessee Valley Authority
Muscle Shoals, Alabama 35660

Gamma-ray spectroscopy is used as the primary analytical method in the Tennessee Valley Authority's environmental monitoring program. Routine sample screening is done by means of least-squares analysis of spectra from NaI(Tℓ) detectors. Nonroutine or suspicious samples are analyzed by means of Ge(Li) spectral analysis. A laboratory quality control program provides internal and external checks on the reliability of analyses.

Introduction

The extent to which the Tennessee Valley Authority is committed to nuclear power generation is evidenced by the fact that TVA now has seventeen nuclear reactors in seven separate nuclear plants that are either operating, under construction, or in various stages of planning and licensing. In addition to these light-water-reactor nuclear power plants, TVA will also operate the Clinch River Breeder Reactor Project and uranium milling and mining operations in several western states. The result of these commitments has been the development of an extensive radiological environmental monitoring program. The projected time schedules for analyses of samples from the nuclear power plants are listed in table 1.

Table 1. Projected Schedule of Environmental Monitoring and Sample and Analysis Rate for TVA's Radiochemical Laboratory

Year	Plant	Samples	Analyses
1968	BFNP	2,000	8,800
1969		6,300	13,500
1970		8,100	18,700
1971		8,000	24,000
1972	SNP	7,500	30,000
1973		8,000	36,000
1974		6,316	32,613
1975		7,058	30,819
1976*	SNP	8,868	39,392
1977	WBNP	13,400	60,000
1978	BNP	18,000	80,000
1979	HNP	20,000	90,000
1980	PBNP	22,200	100,000
1981	YCNP CRBRP	30,000	140,000

*Estimates beginning in mid-1976 are projections.

From a relatively modest two thousand samples and eighty-eight hundred analyses per year in 1968, the number of samples has risen to over eight thousand per year and the number of analyses has risen to over thirty-nine thousand per year. There will be a four-fold increase over the next five years as new areas are added to the monitoring program.

Radiological Environmental Monitoring Program

TVA's environmental monitoring program has been in operation since 1968. It began with a preoperational program in a wide area around Browns Ferry Nuclear Plant to determine the levels of natural and manmade radiation present before plant operation. For reliable evaluation, TVA, in undertaking the survey, had to consider all routes by which radionuclides might be released from the power plant. In addition, the survey had to establish environmental levels of radioactive fallout, naturally occurring radiation, and contributions from other nuclear facilities. Consideration of the many routes by which radionuclides could be released from the plant led to the decision that the survey should include both terrestrial and aquatic monitoring. In the terrestrial environment, air, soil, rain, heavy particle fallout, milk, vegetation, well and surface waters, and food crops are being sampled. River water, fish, clams, sediment, and plankton are monitored to give a broad picture of the overall effect of the nuclear facility upon the ecology of the area.

A critical decision had to be made about the extent to which the samples should be analyzed. Would it be sufficient to measure gross radiation only and rely upon the difference before and after plant operation as a measure of the plant's contribution to the environment? Or, in addition to this gross measurement, select a few biologically significant isotopes for specific analysis? Should more extensive analyses, not only of biologically significant isotopes, but also of those that might aid in identifying the source of radioactivity be made? After considering the many factors involved, TVA decided that the last approach would be best if methods could be found to accomplish it without excessive manpower and equipment.

Analytical Method

In view of the large number of samples to be analyzed and our desire to identify and analyze for specific isotopic content, the only method by which this task could be accomplished without an extremely large laboratory activity appeared to be to do the larger part of the analyses by gamma spectrometry. This method of analysis seemed to offer at least three advantages:

1. It would allow the simultaneous identification and measurement of a mixture of radionuclides.

2. It would allow the screening of samples for the presence of radionuclides before deciding on more complicated chemical separation and measurement.

3. It would allow large bulk samples to be measured, partially offsetting the low specific activities expected in our samples.

The decision was made to use NaI(Tℓ) detectors as the primary analytical tool for gamma spectroscopy. Semiconductor detectors had not been developed to a point of economical use in a program of this type.

Spectral Analysis

Because of the large number of environmental samples planned for analysis and the variety of radionuclides under investigation, it was recognized that some effective means for resolving complex spectra would be needed. With slight modification, the Alpha M Computer Program developed at Oak Ridge National Laboratory by Schonfeld[1] would meet these needs. Also, TVA's IBM 360 Computer at Chattanooga was available for running such a program. Thus, it was decided to resolve any complex gamma spectra by use of least-squares analysis,

depending upon this as the principal method by which specific radioisotopes would be identified and measured.

Isotope Selection

The criteria for selecting isotopes to be identified and measured were as follows:

1. Does it have high biological significance?

2. Will there be large enough quantities to measure?

3. Will the isotope reflect the condition of the reactor and its steam system?

4. Can the isotope be easily identified?

Using these criteria, sixteen isotopes were selected for analysis. It is obvious that some isotopes cannot be analyzed by gamma spectrometry. It might be worthwhile to add that all of the samples are subjected to a gross beta analysis, and a few selected samples are counted for gross alpha content. Strontium isotopes are chemically separated and counted, and tritium is analyzed by liquid scintillation techniques.

Some of the reasons for the isotopic selections may be obvious, while others may be obscure. The strontium isotopes were selected because they are prominent as fission products and have biological significance. Isotopes ^{95}Zr, ^{137}Cs, and ^{131}I were selected because, as principal fission products with a range of half-lives, they provide the information necessary for determining the condition of the operating reactor and time of release of radioactivity. This information can be obtained by establishing the relative abundance of these isotopes at the time of sample analysis. Isotope ^{40}K was selected as a common source of interference and the greatest contributor among sources of what may be termed as naturally occurring radiation.

The selection of ^{106}Ru represents a compromise. Because of sampling frequency, it was felt that ^{106}Ru with its 1-year half-life would be the most appropriate selection, but ^{103}Ru is produced in greater abundance as a fission product and has a higher gamma counting efficiency; therefore, it greatly increases the total count. If unusually large results are reported from the ^{106}Ru analysis, then ruthenium can be chemically separated and identified. The same reasoning is applicable to the selection of ^{144}Ce. That is, the multiple isotopes $^{141-144}Ce$-Pr are expected to be analyzed under this label; when unusually large results are reported, isotopic identification will be made. Actually, we prefer to label these analyses as $^{103-106}Ru$ and $^{141-144}Ce$-Pr. The ^{140}Ba analysis represents another of the compromises made. The most significant photopeak for ^{140}Ba (0.53 MeV) is within the span of detection for the ruthenium isotopes (0.51 MeV). However, if it is assumed that ^{140}Ba will always be in equilibrium with its daughter ^{140}La, then the 1.6 MeV photopeak of ^{140}La can be used as a method of analysis for the barium and the barium interference can be minimized with the ruthenium analysis.

As for the neutron-activated corrosion products, our selection was primarily based on the longer half-life material which not only is of radiobiological significance but also is expected to give some indication of the corrosion rates of certain reactor systems. For example, zinc could be contributed to the reactor coolant system by corrosion of the admiralty tubing in the steam condenser. In the same manner, ^{54}Mn analysis coupled with ^{60}Co analysis may specifically indicate corrosion in certain stainless steel components. Contributions that may be made by the iron isotopes, such as ^{54}Fe are not ignored. If an unusually high result is reported for the zinc and cobalt analysis, then the isotopes can be chemically separated and specifically identified.

Three isotopes, ^{51}Cr, ^{58}Co, and ^{134}Cs, were first included in the isotope spectra library in 1970. The latter two had been found in significant amounts in effluent water from a nuclear power reactor similar in design to those being built by TVA[2]. The other, ^{51}Cr, was not found in effluents, but was found in primary coolant water as a corrosion product from cladding or construction materials. It was included as a potential contributor to environmental releases.

Sample Preparation

The preparation of environmental samples is an essential part of radiochemical analysis. The normal routine in the TVA laboratory is to first blend, dry, and grind or shred the sample to a predetermined fineness suitable for gamma-scanning in a standard geometry. Different types of samples require slightly different preparation; however, the general procedures are similar. Food products are prepared as for home use; rinds, seeds, cores, shells, or other material not normally eaten are removed before drying. Foreign objects are removed from soil and silt samples by screening through a collander. Samples are pulverized or ground to 32 mesh as necessary. Waters may be filtered depending on the type of analysis desired.

Sample Analysis

Samples are normally screened by NaI(Tl) gamma-spectroscopy for an initial estimate of radionuclide activity. Samples with an unusually high activity are further examined by Ge(Li) gamma-spectroscopy to confirm specific radioisotope activity. TVA's Muscle Shoals Radioanalytical Laboratory has been using this method of analysis for nine years. Samples of known or suspected high activity are not screened, but analyzed directly by Ge(Li) gamma-ray spectroscopy. Although considerable capability has been developed in analyzing gamma spectra obtained with Ge(Li) detectors, the NaI-Alpha M method is the first line of analysis for environmental monitoring.

The laboratory recently completed a detailed study of the capabilities and limitations of NaI least-squares gamma-spectroscopy. As a result of this study, changes have been made in the use of some of the options in the program. The study also showed that the program was correctly applied to this type of work. In brief, we now have documentation of what is considered to be the limitations and sensitivities of the program, and that the program can reliably determine environmental levels of radioactivity. This NaI-Alpha M combination, coupled with the Ge(Li) capabilities, has enhanced the entire monitoring program. By recognizing the disadvantages of each type of detector and by utilizing these advantages, a two-pronged approach to gamma-ray analyses has been developed.

From laboratory experience, the following standard conditions are now used routinely for determining gamma radioactivity in environmental samples. These conditions are applicable to over 90 percent of the samples analyzed.

NaI(Tℓ)

Counting time	-	4,000 seconds
Calibration	-	10 KeV/PHu
Soil Analysis	-	1-pint container (average weight 500 g) inverted on the 4- by 4-inch NaI(Tℓ) crystal
Vegetation	-	1-pint container (average weight 160 g) inverted on the 4- by 4-inch NaI(Tℓ) crystal
Water and Milk	-	3.5-ℓ volume in a Marinelli beaker, surrounding the 4- by 4-inch crystal
Air Filters	-	Inserted in a plastic vial and counted in a 4- by 5-inch NaI(Tℓ) well crystal
Charcoal Filters	-	Inserted in a plastic vial and counted in a 4- by 5-inch NaI(Tℓ) well crystal

Ge(Li)

Counting time	-	14400 seconds
Calibration	-	1 KeV/PHu
Standard Geometry	-	0.5-ℓ volume in a Marinelli beaker surrounding the detector crystal
Air Filters	-	Placed in a petri dish and placed on the detector crystal

Gamma-ray spectra are acquired in 256 channels of a multichannel analyzer from 4 x 4 solid or 5 x 4 well NaI(Tℓ) crystals. The data are punched onto paper tape, spooled, and transferred to magnetic tape. They are then transferred via the remote terminal at Muscle Shoals to a disk pack at TVA's central computing center in Chattanooga. The data are then input to the least-square program for data reduction.

A new system recently installed should considerably simplify data-handling procedures. A minicomputer stores sample information for up to eight experiments and handles data transfer between several input-output devices. A magnetic tape transport is intended to be the primary input/output device for transfer of gamma spectra to the central computer for analysis. This system can also transfer data to or from the computerized system used for Ge(Li) spectroscopy.

The exact technique to be followed in analyzing gamma-spectra by least-squares methods involve choices among several data-handling and mathematical procedures. Some of the parameters involve weighting schemes, gain and shift compensation, sample stripping and library content. There is no single best technique that can be applied in every case. The best compromise among the several choices has been made to optimize the results for environmental samples.

One of the first parameters to be studied involved background subtraction. Samples have, in the past, been counted with a daily background stripped from the sample spectrum. A qualitative interpretation of many results led to the belief that as the sample spectra approached background levels, less reliance could be placed on results. Statistical indicators included with computer analysis tended to show poor fit at low levels of activity. On occassion, a spurious high activity would result when improbable gain or shift values were calculated and false fits were obtained. An averaged background spectrum was added to the spectrum library to allow study of the effects of stripped versus unstripped spectra. Synthetic spectra were generated that contained a standard background plus a 50 pCi/ℓ activity component for single nuclides from the spectra library. Each spectrum was randomized before analysis. The results are shown in table 2 for purposes of comparison of stripped versus unstripped spectra. Both accuracy and precision are considerably improved when the background is included in the analysis.

Table 2. Comparison of Analyses of Single Isotope Spectra[3] With Background Stripped and Background Included.

	Error, %	
Isotope*	Background Included	Background Subtracted
^{65}Zn	5.5	45.1
^{95}Zr	37.5	54.3
^{137}Cs	12.9	72.5
^{134}Cs	16.4	15.3
^{58}Co	17.8	33.0
^{106}Ru	15.7	65.2
^{131}I	25.2	44.6
^{51}Cr	60.8	182.0
^{144}Ce	52.0	70.7
^{60}Co	9.4	8.5

*Activities are all at 50 pCi/ℓ.

Quality Control

The laboratory staff routinely assesses the precision and accuracy of its analyses to document the quality of work performed. Collaborative testing programs with other laboratories are carried out to evaluate the performance with respect to others. Cross-check programs, such as those provided by EPA and the International Atomic Energy Agency, provide a wide variety of simulated samples with well-known values. The results of one such series are given in table 3. The three samples represented water samples and were analyzed as such by the standard procedures for both NaI(Tℓ) and Ge(Li) spectroscopy. The results agree well with values provided by EPA. The two methods of analysis also agree well with each other.

The isotope that was most difficult to analyze precisely in this series was ^{106}Ru. The small peak-to-Compton ratio of the principle photopeak and its location in a high-background region causes problems in properly locating and quantitatively identifying this peak by automatic peak search methods in Ge(Li) spectroscopy. The problem in using NaI(Tℓ) spectroscopy is the high correlation between the ^{106}Ru spectra and atmospheric radon daughter radiation. Fluctuations in radon activity adversely affect the analytical results for ^{106}Ru.

Table 3. EPA Crosscheck, Gamma in Water.

		TVA	
Isotope	EPA(±3σ)	NaI(Tℓ)	Ge(Li)
#1			
^{51}Cr	0	0	0
^{60}Co	203±31	206	193
^{65}Zn	201±30	184	198
^{106}Ru	181±27	196	249
^{134}Cs	202±30	181	179
^{137}Cs	151±23	151	159
#2			
^{51}Cr	0	0	0
^{60}Co	271±41	279	272
^{65}Zn	250±38	268	274
^{106}Ru	247±37	246	224
^{134}Cs	349±52	345	349
^{137}Cs	274±41	281	264

Table 3. EPA Crosscheck, Gamma in Water (Continued)

Isotopes	EPA(±3σ)	TVA NaI(Tl)	TVA Ge(Li)
#3			
^{51}Cr	255±38	272	279
^{60}Co	307±46	308	307
^{65}Zn	281±42	291	320
^{106}Ru	379±57	590	360
^{134}Cs	256±38	248	231
^{137}Cs	307±46	295	301
#4			
^{51}Cr	0	0	0
^{60}Co	350±53	352	365
^{65}Zn	327±49	299	325
^{106}Ru	325±49	322	349
^{134}Cs	304±46	273	260
^{137}Cs	378±57	382	392

Approximately seven percent of the analyses performed in the laboratory are run in duplicate as an internal check on laboratory performance. Table 4 summarizes data on replicate measurement for water samples analyzed by NaI-gamma spectroscopy. The results are generally within statistically predicted ranges. About one percent of the values lie outside statistically expected values. After inspection of these particular results, these variations are attributed to fluctuations in the background due to variations in radon daughter radiation.

Table 4. Quality Control Data. Replicate Measurements of Some 3.5-ℓ Water Samples.

Number per Reporting Period	Range Analysis* <1σ	<2σ	<3σ	>3σ
203	185	13	1	4
245	239	4	0	2
444	409	26	5	4
TOTAL	93.4%	4.8%	0.7%	1.1%

* 1σ = 5 pCi/ℓ below 100 pCi/ℓ
= 5% above 100 pCi/ℓ

One of the most difficult parameters to evaluate is the minimum detectible amount for individual isotopes. The degree of interaction between radioisotopes and the effect of systematic variations complicates the assessment of detection limits. The statistical component of minimum detectable amounts (MDA) for selected individual radioisotopes has been estimated by two different methods (table 5) and found to be in reasonable agreement. There is a systematic difference, with MDA's calculated from photopeak areas slightly less than those calculated from the entire spectrum. This advantage is rapidly lost when multiple isotopes appear. Table 6 compares analyses from multiple radioisotopes contained in a composite standard. Least-squares results agree quite well with the activities known to be present. Individual photopeaks are not resolved well enough to duplicate this analysis by photopeak fitting.

Table 5. Minimum Detectable Amounts of Selected Radionuclides at the 95% Confidence Level (pCi/ℓ)

Isotope	Least-Squares	Photopeak Only
^{40}K	72	57
^{65}Zn	18	5
^{140}Ba	5	6
^{60}Co	6	-
^{54}Mn	5	4
^{95}Zr	15	-
^{137}Cs	6	4
^{134}Cs	7	-
^{106}Ru	15	-
^{58}Co	11	-
^{131}I	7	4
^{51}Cr	45	33
^{144}Ce	26	22

Table 6. 3.5ℓ Std Laboratory Composites (pCi/ℓ)

Isotope	Added	Found	Added	Found
^{144}Ce	181	142±43	174	182±20
^{51}Cr	0	0±128	0	0±76
^{131}I	0	0±64	0	0±35
^{134}Cs	630	628±18	100	91±8
^{137}Cs	260	248±18	126	126±8
^{58}Co	408	419±30	0	0±22
^{54}Mn	542	472±29	167	171±9
^{95}Zr	0	0±70	0	0±12
^{65}Zn	0	0±154	1289	1154±25
^{60}Co	1323	1356±22	103	113±12
^{40}K	3209	3001±198	0	0±20
^{140}Ba	0	0±36	0	0±16
^{106}Ru	349	197±28	92	66±28

Future Plans

The current investigations concerning practical aspects of gamma-ray spectroscopy will be a continuing part of laboratory operations. Experimental studies on parameters that influence analytical accuracy and minimum detection levels are being carried out and will be extended. A number of theoretical or calculated parameters need experimental confirmation. A study is also planned that will have the primary objective of optimizing experimental techniques for the use of Ge(Li) spectroscopy in environmental monitoring.

References

1. E. Schonfeld. "Alpha M - An Improved Computer Program for Determining Radioisotopes by Least-Squares Resolution of the Gamma-Ray Spectra." ORNL-3975, Oak Ridge National Laboratory, Oak Ridge, Tennessee, September 1966.

2. B. Kahn, R. L. Blanchard, H. L. Krieger, H. E. Kolde, D. B. Smith, A. Martin, S. Gold, W. J. Averett, W. L. Brinck, G. J. Karches. "Radiological Surveillance Studies at a Boiling Water Nuclear Power Reactor." BRH/DER 70-1, U.S. Department of Health, Education, and Welfare, Public Health Service, Environmental Health Service, March 1970.

3. S. Seale, unpublished report, Fundamental Research Branch, Tennessee Valley Authority, Muscle Shoals, Alabama, November 1975.

Proceedings, ERDA X-and Gamma-Ray Symp. Ann Arbor, MI. May 19-21, 1976 (Conf 760539)

GAMMA RAY MONITORING OF SEDIMENT SAMPLES

L. D. Maus, A. B. Chace, V. C. Rose, and V. A. Nacci
Department of Ocean Engineering
University of Rhode Island
Kingston, Rhode Island 02881

A gamma ray transmission method has been developed to monitor changes in pressurized samples. The method permits obtaining information for sediment cores while still in the core lining, thereby eliminating several sources of error. The cylindrical sample contained in a plastic core line rests on a porous disc within a pressure vessel. A narrow beam of gamma rays is passed through the sample and pressure vessel. The attenuation of this beam is a function of sample density. By changing the fluid surrounding the sample, either consolidation or degassing tests can be performed.

Numerous instances arise where cored sediment samples are inadequate for laboratory testing due to sample disturbances originating from the coring operations, sample transportation or laboratory handling. Poor samples may also result from the expansion of dissolved gasses when deep sea sediments are brought to the ocean surface. In such cases special soil treatment methods or testing procedures may be required in order that the sample may more accurately reflect undisturbed sediment properties.

In response to these needs, a method of eliminating most of the sources of core disturbances prior to laboratory consolidation testing has been developed. When applied, those errors due to the sample disturbances caused by sample extrusion, trimming, and handling are eliminated. The resulting consolidation parameters should reflect disturbances primarily from the sampling operation itself.

The sample disturbance resulting from the reduction of confining pressure and the subsequent expansion of gasses as the sample is recovered from the sea floor, while less obvious than other causes, can be just as devastating.

The purpose of this paper is to show how gamma-ray monitoring methods have been developed to handle these two problems. In one dimensional consolidation tests, the sample is surrounded by air and the gamma ray attenuation can be shown to be a function of the void ratio or water content of the sample. In the degassing studies, the sample is surrounded by water and the attenuation is used as a measure of the gas volume.

Gamma-Ray Monitoring of Sediment Consolidation Tests

The purpose of a consolidation test is to consider the diffusion of water through a porous medium under varying consolidation stresses. The resistance to water diffusion is supplied by the sediment permeability and stiffness. The effect of sample disturbance unduly influences laboratory results by reducing sample stiffness[1,2].

The standard consolidation test makes use of a sample extruded from a core liner and trimmed to testing size. The sample is then loaded and the overall change in sample thickness is noted. The data obtained is influenced by any disturbances resulting from the procurement and transportation of the sample as well as the laboratory extrusion and trimming operations.

In order to reduce the effects of distrubance due to extrusion and trimming, it would be desirable to measure void ratio only at the mid-thickness of the sample while still in its core liner. Gamma-ray transmission[3] was chosen because it is capable of measuring void ratio along a narrow beam which can be positioned at any desired elevation.

The cylindrical sample is contained within a section of plastic core liner and rests on a porous disc within a pressure vessel. Air pressure in the vessel is transmitted through a floating piston to the sample. The sample can drain through the porous disc. A beam of monoenergetic gamma-rays of energy E is emitted from a radioisotope source through a narrow collimating hole in the source shield. This beam passes through the pressure vessel, liner, and sample and arrives at a scintillating detector through another collimating hole in the detector shield.

For this arrangement, the change in gamma attenuation is due only to variation in sample parameters along the beam and the following narrow-beam attenuation relationship applies:

$$N = N_o \exp(-\mu_m \gamma D) \quad (1)$$

where N_o = gamma photons counted with no sample present
N = gamma photons counted with sample present
μ_m = sample mass attenuation coefficient, $cm^2 g$
γ = sample bulk density g/cm^3
D = sample diameter, cm

In equation (1), it is assumed that the counts N and N_o are made over the same time interval and that only unattenuated photons of energy E are counted.

The value of μ_m for water and for several of the elements common to sediments is a function of photon energy. In the range of energies between about 0.3 and 3 meV, μ_m is approximately the same for all elements of interest, except hydrogen. To understand this phenomena, one should consider the following expression for μ_m:

$$\mu_m = 6.02 \times 10^{23} \tau_e \frac{Z}{A} \quad (2)$$

where

τ_e = scattering cross-sections per electron, cm^2
Z = atomic number
A = atomic weight

In the range 0.3-3 MeV and for elements with atomic numbers of about 26 or lower, τ_e is almost entirely due to Compton scattering, an elastic collision between a photon and an orbital electron. Since all electrons are equally effective scatterers, the only compositional variable in equation (2) is the ratio Z/A. Values of Z/A for all elements of interest, except hydrogen, are relatively constant. The effective value of Z/A or μ_m for combinations of elements may be calculated by weighting the appropriate value for each element by its weight fraction in the compound.

Table 1 Z/A for Typical Sediment Compound

Compound	Formula	Z/A
Water	H_2O	.5551
Kaolinite	$Al_4Si_4O_{10}(OH)_8$	.5036
Montmorillonite	$(Al_{1.67}Mg_{0.33})Si_4O_{10}(OH)_2$	.1994
Quartz	SiO_2	.4993
Orthoclase	$KAlSi_3O_8$	.4958
Calcite	$CaCo_3$	.4996
Magnetite	Fe_3O_4	.4751

Based on the above table, it is reasonable to assume that the solid phase of sediment composition can be characterized by a Z/A of 0.500 and the water phase by a ratio of 0.555.

Assuming a saturated sediment and calculating an overall Z/A for the bulk sediment according to the weight fractions of water and solid particles:

$$Z/A = \frac{0.500(1+1.11w)}{1+w} \tag{3}$$

where w is the water content of the sediment expressed as the ratio of water weight to dry sediment weight. Substituting equation (3) into equation (2):

$$\mu_m = \mu_{ms}\frac{(1+1.11w)}{1+w} \tag{4}$$

where μ_{ms} is the Compton mass attenuation coefficient for sediment particles (assuming Z/A = 0.500).

The bulk density, γ, of saturated sediment can be written:

$$\gamma = \frac{G(1+w)}{1+Gw}\gamma_w \tag{5}$$

where G = specific gravity of solid particles;
γ_w = density of pure water at 4° C.

Combining equation (1), (4), and (5):

$$N = N_o \exp\left[-\mu_{ms} G \gamma_w D \frac{(1+1.11w)}{(1+Gw)}\right]$$

or

$$\ln \frac{N_o}{N} = \mu_{ms} G \gamma_w D \frac{1+1.11w}{1+Gw} \tag{6}$$

The term μ_{ms}, G, γ_w, D, is designated as C and is a constant for a given sample, source energy and collimation design. C is usually determined following the final count of a test, N_f, and after removing the sample, a final water content, w_f, is determined.

$$C = \frac{1+Gw_f}{1+1.11w_f}\ln\frac{N_o}{N_f} \tag{7}$$

Incorporating the value of C into the solution of equation (6) for w

$$w = \frac{C - \ln\frac{N_o}{N}}{C\ln\frac{N_o}{N} - 1.11C} \tag{8}$$

Experimental Verification

Laboratory consolidation of undisturbed samples results in a recognizable water content (or void ratio) vs. log pressure relationship. To test this method of obtaining this relationship the following test apparatus and sediment sample was used[4]. The collimating holes in the source and detector shields were 0.64 cm in diameter and the distance from the source to the face of the detector was 36 cm. The lead shielding around the source and detector was a minimum of 5 cm thick. The sediment, prepared from a kaolinite slurry and preconsolidated at 0.25 psi, was 5.8 cm in diameter.

The source was 21 mCi of cesium-137. The counting equipment consisted of a scintillation detector, amplifier, single channel analyzer, and counter. The discrimination level of the analyzer was set to pass only those counts representing unattenuated photons. The results of the test are usually given in this form:

$$C_c = \frac{\delta e}{\delta \log p} \tag{9}$$

where C_c is compression index and

e is void ratio

Values, typical of undisturbed Kaolinite were obtained.

Gamma-Ray Monitoring of Sediment Bulk Density

The thrust of this study was to monitor changes in sediment bulk density as a measure of the degree of saturation of the sediment. Marine sediments are not completely saturated as is often assumed. Thus a change in fluid pressure can result in a change in bulk density by changing:

1. the degree of saturation (S),
2. the density of pore water (γ_w) or
3. the density of the soil solids (γ_s).

The change in bulk density during an increase in pressure can be represented[5]:

$$\delta v = \frac{1}{v}\{V_{vi}(1-Si)(\gamma_{wa} - \gamma_{aa}) + \delta p\,\gamma_w[v - v_{Si}(1-B_s\,\delta p)] + \delta p W_s B_s\} \tag{10}$$

where p is gage pressure
V_{vi} is initial volume of void ratio
Si is initial degree of saturation
γ_{wa} is density of water at atmospheric pressure
γ_{aa} is density of air at atmospheric pressure
v is initial volume of solids
v_{Si} is initial volume of solids
B_s is compressibility of solids

In these experiments, sands and clays were cyclically pressurized to 1500 psi resulting in density changes. As in the consolidation studies, narrow beam geometry was maintained resulting in the relationship given in equation (1).

$$N = N_o \exp(-\mu_m \gamma D)$$

Rearrangement of this equation yields:

$$\mu_m \gamma = -\frac{1}{D}\ln\frac{N_o}{N}$$

Over a range of density, γ, from 1.57 to 1.98 g/cm^3 and degrees of saturation from 0 to 1.0, μ_m was calculated

to change from 0.074 to 0.076; $\mu_m\gamma$, therefore can be assumed to be proportioned to γ or:

$$\gamma = \frac{1}{D\mu_{air}} \ln \frac{N_o}{N} \qquad (11)$$

As a result it is possible to follow changes in bulk density by measuring the attenuation of the gamma radiation.

The change in bulk density of a typical test run involved a sand with an initial degree of saturation of 0.969. When subjected to a pressure increase of 1500 psi, the density change, equation (10), was computed to be 1.799×10^{-2} g/cc while, γ, from equation (11) gave a value of 1.93×10^{-2} g/cc. It should be noted that the density change is due primarily to the diffusion of air into water, 82 percent; 15 percent due to water compressibility and the remaining three percent to solid grain compressibility.

The main conclusions from the study were that ocean sediments lifted from 3000 ft. depths undergo bulk density changes up to five percent, primarily due to air coming out of solution, and that the gamma-ray density technique proved sensitive enough to detect density variations of water due to changes in confining pressure.

Conclusion

Gamma-ray transmission is a feasible method of measuring water content and void ratio during one-dimensional consolidation of saturated soil samples, particularly where it is desirable to eliminate the effects of disturbance due to laboratory handling.

The technique can also be considered quite capable of providing density information changes in bulk density of unsaturated sediments in response to changes in confining pressure.

References

1. Calhoon, M. L., Effect of sample disturbance on the strength of a clay. Trans. ASCE, 121, 1956, 925-939.

2. Preiss, K. Non-destructive laboratory measurement of marine sediment density in a core barrel using gamma radiation, Deep-Sea Res. 15, 1968, 401-407.

3. Evans, H.B. GRAPE--A device for continuous determineation of material density and porosity. Trans Sixth Ann. Logging Symp. Society of Professional Well Log Analysts, 2, 1965, B1-B25.

4. Maus, L. D. Gamma-ray measurement of changes in sediment sample water content. Thesis presented to the University of Rhode Island at Kingston, R. I., in partial fulfillment of the requirements for the degree of Master of Science, 1971.

5. Chase, A. B., Pressure and density in marine sediment. Thesis presented to the University of Rhode Island at Kingston, R. I., in partial fulfillment of the requirement for the degree of Doctor of Philosophy, 1975.

Proceedings, ERDA X-and Gamma-Ray Symp. Ann Arbor, MI, May 19-21, 1976 (Conf 760539)

ENERGY DISPERSIVE X-RAY FLUORESCENCE ANALYSIS OF COAL

E. L. DeKalb and V. A. Fassel

Ames Laboratory-ERDA
and
Department of Chemistry
Iowa State University
Ames, Iowa 50011

Summary

The X-ray fluorescence determination of sulfur and other constituents in coal ordinarily requires correction for a variety of interelement effects, which can be troublesome and time consuming. For mineral specimens with 6 to 10 major constituent elements, a large number of well characterized samples or synthetic standards are required to establish appropriate correction factors when bulk samples are analyzed. However, when the sample is prepared as a thin film specimen by the Chung procedure, interelement corrections can be neglected, and only a few samples which have been analyzed previously for the elements of interest are needed for calibration. The adaptation of the Chung method of sample preparation to coal samples will be described and illustrated in detail. Precision and accuracy data for the determination of sulfur in thin-film coal samples are presented.

Introduction

The determination of sulfur in coal is of considerable interest because of the environmental impact of sulfur oxides released into the atmosphere with flue gases. Among the various analytical techniques available for the determination of sulfur, X-ray fluorescence spectroscopy has been successfully applied by Kuhn (1), Frigge (2), Hurley and White (3), Berman and Ergun (4), and others.

Matrix Corrections for Thick Coal Samples

The data reported in this paper were obtained with an energy dispersive X-ray fluorescence spectrometer (Nuclear Semiconductor Model 440 with Tracor Northern Model 880 data analyzer). Initial measurements on briquetted two-gram coal samples of known sulfur concentrations and with widely varying ash content indicated that matrix effects were considerably more serious than had been anticipated. Consequently, an attempt was made to use the Rasberry-Heinrich method of matrix correction (5) as supplied in a software package from Tracor Northern.

Efforts to determine the appropriate correction factors for the Rasberry-Heinrich method on a series of synthetic reference samples that simulated the Al, Si, S, K, Ca and Mg contents of coal were unsuccessful when the software package supplied by Tracor-Northern was used.†

†A new software program, also based on the Rasberry-Heinrich procedure, has recently been received from Tracor-Northern. This revised program has not been evaluated in our laboratories.

Thin Film Method

Chung has described a sample preparation procedure (6) which converts a powdered sample into a thin film, and provided data which indicated that matrix effects were thus rendered negligibly small. In view of the earlier failure of the program for matrix correction, we decided to try the Chung approach.

Sample Preparation

Coal samples were first dry-milled to pass a 60 mesh screen, and blended by tumbling to minimize inhomogeneity. Samples were combined with Y_2O_3 as an added reference element, and with steel balls and a film-forming polymer fluid as listed in Table I. The container and its contents were placed in a metal capsule and vigorously shaken for 15 minutes in a Spex Industries Mixer-Mill (Model 8000). This ball-milling operation reduces most particles to only a few microns diameter, and thoroughly blends all ingrediants. An eye dropper was used to transfer a few drops of the black suspension onto a 2 by 6 inch strip of Type A Mylar ®. These strips were cut from 20 x 50 inch sheets, of 0.003 inch thickness, obtained from Franklin Fibre-Lamitex Corp., Wilmington, DE. The suspension was quickly drawn down to a thin coating with a Teflon ® wiper blade set for a 0.003 inch gap. The polymer dried in about 2 minutes to a film approximately 0.002 inch thick. A disc cut from the Mylar strip served as the X-ray fluorescence sample.

X-Ray Analyses

The thin film coal samples were analyzed with the operating conditions listed in Table II. The background corrected integrated counts from the sulfur region were ratioed to those from the yttrium region. Coal samples with known sulfur content were used to construct an analytical calibration curve.

Analytical Data

Precision. Because of the inhomogeneous nature of coal, duplicate samples were always prepared and analyzed. Sulfur values from the duplicates agreed to within ± 4% relative for about 80% of the samples. If the disagreement was greater than ± 5% (about 10% of the samples), the sample was rerun in duplicate.

Accuracy. Sixty samples were analyzed for sulfur by thin film X-ray fluorescence and by the Eschka fusion method (ASTM D-271). Data from the two methods were in agreement to within ± 5% relative for 30 samples and to within ± 10% for 47 samples. For two samples the disagreement was greater than 20%. The reasons for occasional large variances have not yet been determined. It is equally possible that the variances have occured in the Eschka fusion determinations.

Bibliography

1. J. H. Kuhn, Norelco Reporter, 20, 7 (Dec. 1973).
2. J. Frigge, Erdolund Kohle, Erdgas Petrochemie, 25, 447 (1972).
3. R. G. Hurley and E. W. White, Anal. Chem., 46, 2234 (1974).
4. M. Berman and S. Ergun, Bureau of Mines, RI 7124.
5. S. D. Rasberry and K.F.J. Heinrich, Anal. Chem., 46, 81 (1974).
6. F. H. Chung, Advan. X-Ray Anal., 19, 181 (1976).

Table I

Sample Preparation

Sample Weight	0.500 g coal.
Reference Element	0.200 g Y_2O_3.
Milling Balls	10 ml of 0.125 inch diam. steel balls (McMaster-Carr Cat. No. 9528 K11).
Film-forming Fluid	15 ml of polymer solution prepared by dissolving 250 g of poly(methyl)methacrylate (Aldrich Cat. No. 18,244-9) into 1000 ml of toluene.
Container	30 ml linear polyethylene wide mouth bottle (Nalgene Cat. No. 2104-0001).

Table II

X-Ray Operating Conditions

Tube	Mo target
Voltage	12 kV
Amperage	0.80 mA
Incident Beam Filter	Paper to remove Mo L lines
Amplifier Time Constant	Set for 20,000 maximum counts per sec
Dead Time	Approximately 50%
Live Time Integration	500 sec
Sulfur K Lines Region	2.22 through 2.40 eV
Yttrium L Lines Region	1.88 through 2.04 eV

Proceedings, ERDA X-and γ-amma-Ray Symp. Ann Arbor, MI, May 19-21, 1976 (Conf 760539)

MULTIELEMENTS PARTICLE SIZE ANALYSIS BY MEANS OF ENERGY DISPERSIVE X-RAY FLUORESCENCE WITH THE AID OF SEDIMENTATION

Hiroshi Tominaga, Shigemasa Enomoto, Muneaki Senoo, Noboru Tachikawa

Radioisotope Center, Japan Atomic Energy Research Institute
Oarai-machi, Higashi-ibaraki-gun, Ibaraki-ken, Japan

Summary

Application of the energy dispersive X-ray fluorescence technique to a sedimentation method for particle size analysis has been studied. Two types of apparatuses are proposed which enable to determine the size distribution for each component of a powder mixture, in wide ranges of particle size and atomic number, using a small quantity of sample. Examples are given of the analysis of airborne particulates and rock powder.

Introduction

The method of particle size analysis employing sedimentation in a liquid, based on Stokes' relationship between the diameter of particle and its rate of fall, is widely used as the most practical to determine the effective size distribution of powder samples. Various types of devices are used to measure the rate of suspension or deposition; for instance, gravitymeter, sedimentation balance, and photo- or X-ray- sedimentometer. However, none of them can determine the particle size of each component in the powder mixture; only the size distribution in weight is determined independently of the particle composition. Though the classical method with Andreasen pipette gives fractionized samples, the wet chemical analysis of them is troublesome.

The technique of energy dispersive X-ray fluorescence using a high resolution semiconductor detector with a radioisotope source or small X-ray tube can potentially solve the problem. Three methods were considered of using the X-ray fluorescence in the sedimentation method. First was the most simple idea, i.e. analysis of the samples extracted by Andreasen pipette. However, it was not easy to prepare the sample so as to be adaptable to the X-ray analysis. Second, measurement of the concentration of each component suspended in a liquid by X-ray analyzer through a side window of sedimentation cell. Third, analysis of the deposited powder from the bottom window of the cell. The latter two (cf. Fig. 1) are discussed comparatively in the following section, and the last of the three is described further as an advanced form.

Theoretical and Preliminary Investigation

Formulas of X-Ray Intensities

The intensities of X-rays of component i in the two methods shown in Fig. 1 are expressed as

$$\text{Side window:} \quad I_i \simeq \frac{K_i M_i}{\Sigma \mu_j M_j + \mu_\ell \rho_\ell} \tag{1}$$

$$\text{Bottom window:} \quad I_i \simeq K_i' m_i \frac{1 - e^{-\Sigma \mu_j m_j}}{\Sigma \mu_j m_j} \tag{2}$$

where K_i and K_i' are the constants including excitation and detection efficiencies, M_i is the concentration of component i in the suspension (g/ml), and m_i the weight thickness of component i in the deposition; μ_j is the mass absorption coefficient of component j for primary and fluorescent X-rays, ρ is the density, and suffix ℓ indicates the liquid.

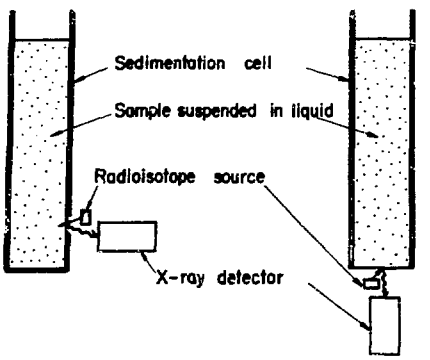

Side window method Bottom window method

Fig. 1. Two methods of the energy dispersive X-ray fluorescence applied to sedimentation.

Side Window vs. Bottom Window

For convenient data processing, the X-ray intensity is desired to be proportional to the quantity of powder. In concentration measurement by the side window method, the proportionality usually holds because the absorption of X-rays by the medium is larger than that by the suspended material (except the case of heavy elements) as far as the concentration is less than about 0.01 g/ml, which is the practical limit to prevent particle coagulation. The matrix effect is also hardly problem due to the dilution by the medium.

In deposition measurement by the bottom window method, the thickness of deposit must be less than the quantity limited by

$$\Sigma \mu_j m_j \leq 0.1 \tag{3}$$

in order to keep the deviation from the proportionality within 5 %. Figure 2 shows a result of experiment on the proportionality. Though the X-ray intensity in water is less than that of 'dried' due to the absorption by water contained in the deposit, the difference is small in the range limited by Eq.(3). Because of the limitation in final thickness of the deposit, the initial concentration of suspension must be very low; e.g. less than 0.1 mg/ml for Fe_2O_3 in water of depth 10 cm (cf. Fig. 2). The limitation must be satisfied for all the matrix components in the case of a powder mixture. The matrix effect is possibly severe in analysis for a minor component of low atomic-number element.

Comparison of X-Ray Intensities

The ratio of X-ray intensities of the two methods is obtained by using Eqs.(1), (2), and (3), and $M_i = 0.01$, $\Sigma \mu_j M_j \ll \mu_\ell \rho_\ell$, and $\rho_\ell = 1$.

$$R = \frac{I_i(\text{bottom})}{I_i(\text{side})} = 10 \frac{K_i' \mu_\ell}{K_i \mu_i} \tag{4}$$

With $K_i = K_i'$, the ratio is calculated;

Source	Pu-238				Am-241
Element	Ca	Ti	Fe	Zn	Ba
R	6	4	1.7	0.8	0.16

In practice, the width of side window must be sufficiently small to reduce the uncertainty in diameter calculation, whereas there is no limitation in the area of bottom window, though collimation is necessary in the case of high atomic-number elements to avoid measuring the X-rays coming from particles not yet deposited. After all, the bottom window method is advantageous for low atomic-number elements despite of the limit of quantity for measurement. On the other hand, the side window method is suitable for high atomic-number elements.

Experiments with the Bottom Window Method

Preliminary experiments were carried out by using an ORTEC vertical type Si(Li) detector of 30 mm^2 sensitive area and 180 eV resolution (FWHM) coupled with an acrylic tube cell having a bottom window of 50 μm polyester film, Lumirror. First experiment was made for $BaTiO_3$ powder the size distribution of which was known by other sedimentation methods (Andreasen pipette and X-ray transmission), using a 100 mCi Am-241 γ-ray source with a collimator mentioned above. The material was suspended in water containing 0.025 % sodium hexametaphosphate as dispersing agent (also in other experiments).

The size distribution was calculated by a desk calculator according to Eq.(5),[1] from the recorded count-rate of Ba K_α X-rays.

$$W = P - t\frac{dP}{dt} \qquad (5)$$

where P is the count-rate of the X-rays from material deposited in time t, and W is the fraction of material larger in size than the Stokes' diameter D corresponding to t;

$$D = \left[\frac{18\eta h}{g(\rho_s - \rho_\ell)t}\right]^{\frac{1}{2}} \qquad (6)$$

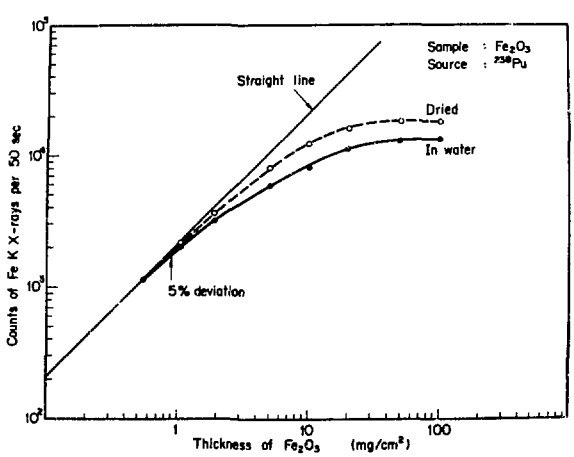

Fig. 2. Experimental test on the relation between the X-ray count and the deposition.

where η is the coefficient of viscosity of suspending medium, h the settling depth, g the gravitational acceleration constant, and ρ_s the density of settling particle; all in CGS units. The result agreed well with the known value.

Experiment was also made for powders of Ni_2O_3 and CuO and their mixture, using a 30 mCi Pu-238 X-ray source, to see if the size distribution of the two components can be correctly determined in the mixture without any interference such as coprecipitation. The results in the mixture agreed excellently with those in the respective components, with the correction made only for the superposition of Ni K_β counting on the channel of Cu K_α counting.

Proposal for New Apparatuses

In cumulative measurement by the bottom window method, the limitation in final thickness of the deposition due to the self-absorption or matrix absorption necessitates small thickness in the measurement with weak intensity of X-rays, especially at the early time of sedimentation. In order to solve the problem so that the quantity of deposition will be increased at any time near to the upper limit, new apparatus was designed.

Deposit Transfer Type[2]

In the apparatus shown in Fig. 3, thin film as a belt extending at the bottom of the cell is moved continuously or intermittently. An amount of measuring deposit is then kept less than the limit, since the measured deposits remove along. As the measurement is performed in real time for particles just settled on the belt, the apparatus is suitable for rapid and automatic measurement. In the apparatus, the gap between the bottom of tube and the belt has to be less than a certain value (e.g. 0.5 mm) to prevent the exchange of the sample suspension and the liquid outside tube. The belt must be in close contact with the Be window not to cause the attenuation of X-rays in the liquid.

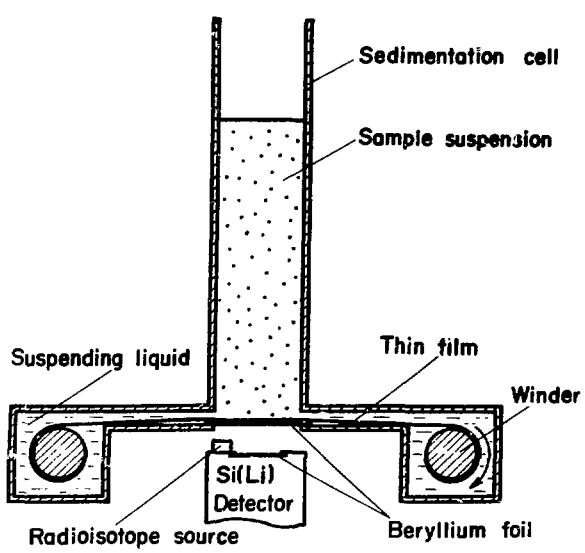

Fig. 3. Schematic drawing of the deposit transfer type apparatus.

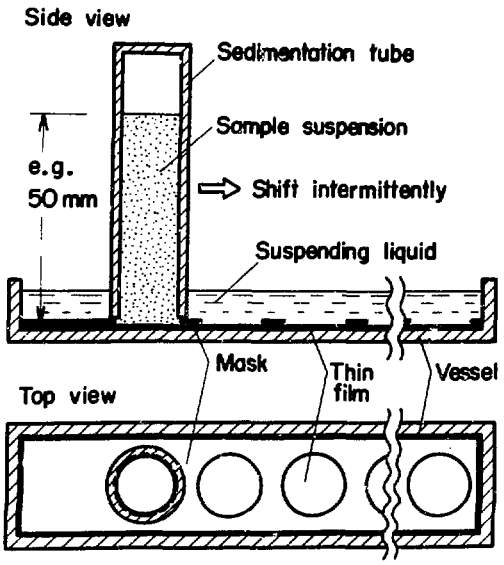

Fig. 4. Schematic drawing of the fraction preparation type apparatus.

Fraction Preparation Type[3]

Apparatus was so designed as to produce fractional deposits for analysis outside the liquid. A sedimentation cell filled with the suspension of appropriate depth is placed upside down as shown in Fig. 4, initially with a lid. Then, the top-sealed, bottom-opened cell is manually moved successively onto sampling positions in a shallow vessel filled with the liquid. The sampling positions are fixed with holes bored in a mask plate of thickness 0.4 mm, and the particles are deposited on a thin film spread on the base. After deposition is all complete, the liquid is sucked off with a pipette. And the deposited samples, after drying, are analyzed by an energy dispersive X-ray spectrometer. In this apparatus, time and trouble are involved, but the samples can be directly analyzed by the X-ray technique, elaborately as occasion demands, and also by other means. Therefore, even minor components can be measured.

Applications

Analysis of Airborne Particulates

By using the apparatus of Fig. 4, An airborne dust sample, AS-1,[4] was analyzed, which was collected by a filter for air-conditioning of a building in Tokyo; it was prepared as a sample for intercomparison by neutron activation analysis. A sample of about 10 mg was dispersed in distilled water containing 0.025 % sodium hexametaphosphate with the aid of supersonic waves for about 1 hour to obtain sufficient dispersion. A sedimentation tube of 14 mm inner diameter filled with the suspension of depth 5 or 10 cm was moved manually on a Millipore membrane filter intermittently for 2 or 3 days to get about 12 fractionized samples. Finally, the residual particles in the water were deposited by means of centrifuge. Dried samples were thinly coated with acrylic resin to protect the surface. Each sample was measured by the Si(Li) spectrometer with 130 mCi Pu-238 X-ray source for 2000 sec to determine K, Ca, Ti, V, Cr, Mn, Fe, Cu, Zn, and Pb, and later by neutron activation for other trace elements.

The calculation of size distribution from the fluorescent X-ray count was carried out in a similar manner as the preliminary experiment with bottom window method, by using the summed-up count of fractional deposits for P in Eq.(5). In the calculation, ρ_s was taken as 2 equally for every component; $\rho_\ell = 1$. Then, the particle size is expressed as Stokes' diameter multiplied by the square root of $\rho_s - \rho_\ell$ (cf. Fig. 5, ρ_w is the density of water). This expression may be meaningful because the elements whose particle size distribution curves coincide with each other can be considered to be in the same particle. For example, Ti, Fe, and Sc probably are the case, in the results shown in Table 1 and Fig. 5, and similarly Br and Pb.

In the experiment, however, the water soluble components can not be measured. About 40 % of Ca and 30 % of Zn were found in the residual liquid. For such components, an organic solvent is recommended as the suspending liquid.

Table 1. Particle size distribution parameters measured in the airborne dust sample, AS-1.

Element	MMD *	Cumulative % ≤ 2 μm	Cumulative % ≤ 1 μm
Br	3.6	30	15
Pb	3.8	30	16
Zn	3.9	30	17
Sb	4.2	28	16
V	4.3	25	13
Hf	4.6	27	18
K	5.2	21	10
Mn	5.6	18	8.0
Cu	5.3	13	7.1
Cr	6.0	13	7.6
Ti	6.0	13	5.5
Fe	6.0	12	5.5
Sc	6.0	10	5.0
Co	6.5	16	6.8
Sm	6.6	5.5	2.0
Ca	7.5	16	8.8

* Mass median diameter, in μm.
All the particle size is expressed in $D(\rho_s - 1)^{\frac{1}{2}}$.

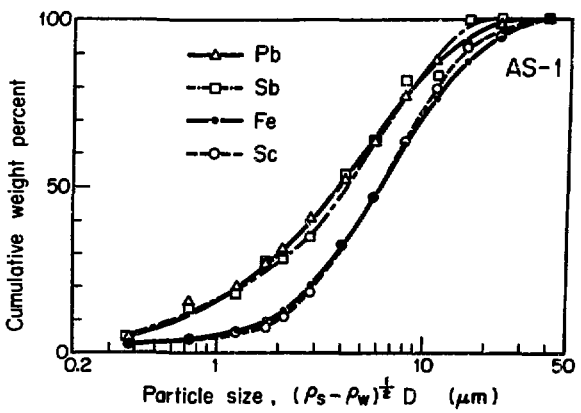

Fig. 5. Cumulative size distributions of typical elements in the sample AS-1.

The analysis of airborne particulates may not be a good example, since the apparatus does not directly measure sizes of the particles flying in the atmosphere. However, the method may be useful to samples collected but not fractionized.

Analysis of Rock Powder Mixture

Analysis was made by the same procedure to determine the size distribution of Si and K components in the mixture of quartz, feldspar, and potash feldspar supplied from a ceramics industry. Care was taken in both preparation and measurement of the deposits, to minimize the attenuation of soft X-rays of Si and K. To prevent entry of small particles into the film (filter papers are the case), a polypropylene film, 20 μm thick, less impurity, was used. A wetting agent for photographic film, Driwel, was added in 0.5 % to the liquid in the vessel, to prevent localized separation of the liquid from the film surface at the time of drying. The amount of powder used was about 3 mg, and the fractionized deposits without coating were measured in vacuum by the Si(Li) spectrometer with a 30 mCi Fe-55 X-ray source.

Figure 6 shows the measured spectrum for a deposit, and Fig. 7 the result of analysis. All the deposits possibly consist of a monolayer of particles. The correction factor[5] in X-ray intensity was calculated from the absorption effect in single fluorescent particles, integrating over the size distribution. For simplicity, the material was taken as $K_2O\,Al_2O_3\,6SiO_2$ alone, and the size distribution of each deposit was derived from that calculated without the correction. It is seen in Fig. 7 that the correction is of course larger for Si than K; but it is not so large owing to the continuous size distribution in a fractionized deposit, though the attenuation in a single large particle is considerable (for instance, the correction factor becomes 10 at 40 μm for Si K_α). The results show that the method is well applicable also to low atomic-number elements whose accurate analysis is not easily possible by the X-ray technique.

Conclusion

A combination of the energy dispersive X-ray fluorescence and the sedimentation is capable of particle size analysis for each element in a powder mixture, in wide ranges of particle size and atomic number, using a small quantity of sample. The side window method is suitable for higher atomic-number elements, while the bottom window method is useful in lower atomic-number elements, except the case of very low atomic-number elements and minor components. The deposit transfer type apparatus is further useful. The fraction preparation type apparatus is especially advantageous for elaborate measurement, not only in the X-ray analysis but also in other analyses. In the X-ray analysis, particle sizes of multielements higher than Al in atomic number, even for minor components, can be measured in the range of 0.2 to 50 μm, usually using water as a suspending liquid. Several to ten mg of sample material is sufficient, but in the case of high atomic-number elements or in other analyses larger quantities may have to be used. The methods are applicable to the analysis of powder samples including dust collected but not fractionized, and also to examination in pulverizing process of ore etc.

Acknowledgments

The authors wish to thank T. Imahashi for neutron activation analysis of airborne particulates and also K. Yamaguchi for his helpful discussion about the preparation of rock powder deposits.

References

1. S. Odén, Bull. Geol. Inst. Univ. Upsala 16, 15 (1918); cited in A. M. Gaudin et al., J. Phys. Chem. 46, 902 (1942).
2. M. Senoo, H. Tominaga, N. Tachikawa, and S. Enomoto, Patent Pending (1975).
3. M. Senoo and H. Tominaga, Patent Pending (1975).
4. Y. Hashimoto, Bunseki, 1975-(4), 250 (1975).
5. J. R. Rhodes and C. B. Hunter, X-Ray Spectrom. 1, 113 (1972).

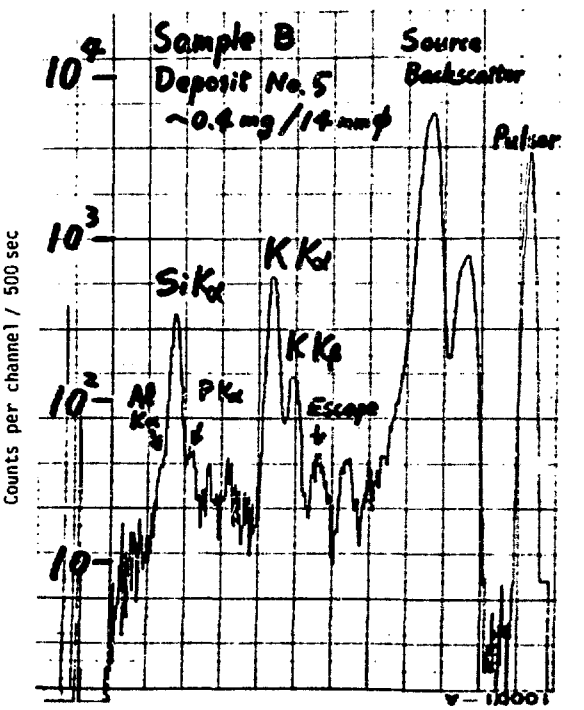

Fig. 6. X-ray spectrum of a deposit prepared from the rock powder mixture, measured by the Si(Li) analyzer with a 30 mCi Fe-55 source.

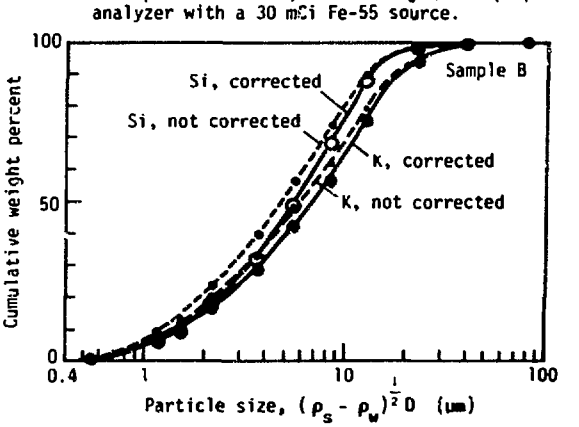

Fig. 7. Cumulative size distributions in the mixture of quartz, feldspar, and potash feldspar.

Proceedings, ERDA X and Gamma Ray Symp. Ann Arbor, MI, May 19-21, 1976 (Conf-760539)

APPLICATION OF ENERGY DISPERSIVE X-RAY FLUORESCENCE ANALYSIS IN PROCESS CONTROL

A. M. Delmastro
Allied Chemical Corporation
550 Second Street
Idaho Falls, Idaho 83401

INTRODUCTION

The Idaho Chemical Reprocessing Plant, located at the Idaho National Engineering Laboratory, is engaged in a program of reprocessing a wide variety of irradiated nuclear fuels. Several types of fuels to be processed cannot be dissolved in accordance with existing plant procedures, and therefore require the development of new dissolution, or "headend", processing techniques. Individual classes of fuels to be processed by the new techniques have diverse compositions. Three typical fuels are:

1. PNR fuel: a zircaloy clad fuel consisting of ZrO_2-UO_2-CaO wafers.
2. TRIGA fuel: a zirconium-uranium hydride element with either aluminum or stainless steel cladding.
3. THTR fuel: BeO-UO_2 ceramics with no cladding.

   This fuel is received in aluminum cans.

In order to accomplish the dissolution of these and other fuels with differing composition, several stepwise processing systems using a variety of dissolvent matrices will be used. In general, the fuel element will be placed in a dissolver tank and the appropriate acid dissolvent system will be employed to sustain dissolution. Many of the fuels will be treated with hydrofluoric acid which contains cadmium as a soluble nuclear poison. Subsequent steps require the use of solutions such as sulfuric acid, nitric acid, or aluminum nitrate.

Analytical requirements for this process necessitated the development of a rapid, accurate method for analyzing these complex samples. Several of the unique analytical problems involved are:

1. During dissolution of nonirradiated fuels in pilot plant studies, rapid analysis of process samples for certain key constituents is required in order to maintain suitable dissolution rates. Analytical results with an accuracy of ± 5-10% are needed within approximately 20 minutes to determine when the next processing step can be initiated. Current methods for analyzing fuel reprocessing samples at the ICPP are too time-consuming.
2. Because pilot plant personnel, rather than the analytical support group will be required to perform these analyses during process development studies, new procedures must be simple and involve a minimum of operator time.
3. The analytical procedures must be applicable ultimately to the determination of varying concentrations of the elements of interest in solutions of significantly differing matrices with a minimum of interferences and matrix effects.
4. During the dissolution of irradiated fuels, radioactive contamination and personnel exposure must be maintained as low as reasonably achievable.

EXPERIMENTAL

Instrumentation

Of various multielement analytical techniques available, X-ray fluorescence analysis was considered to be the most feasible. For pilot plant studies, a computer-controlled, energy dispersive X-ray spectrometer was selected. The system consists of a Nuclear Semiconductor Spectrace 420 spectrometer with associated electronics and a Tracor Northern NS-880 data analysis system. A low power molybdenum X-ray transmission tube with a yttrium-bromide filter is used as the excitation source.

Sample Composition

Initial development work has involved the use of simulated fuel dissolver solutions containing zirconium, uranium, and niobium in an 8M hydrofluoric acid matrix. Cadmium, used as a nuclear poison to prevent criticality in the dissolver is also of interest. As studies progress, other acid matrices will be considered and additional elements will need to be determined in the samples.

Sample Preparation

Although the samples received for analysis are in solution form, conventional solution techniques used in X-ray fluorescence analysis[1] presented several major drawbacks in this application. The principal analytical problems in the development of an X-ray fluorescence method were the possibilities of interelement effects among the elements present in the fuel material as their concentration levels changed during dissolution, and of significant matrix effects from the various acid dissolvent systems. Of concern also were the problems of personnel exposure to high levels of radiation and of potential contamination during the analysis of irradiated fuel samples.

Consequently, a filter-paper technique was used to produce a thin film type specimen. In principle for a thin film, the absorption-enhancement effects of the matrix are significantly reduced[1,2,3]. The reduction of sample size from several milliliters for solution methods to a 100 µl aliquot on a filter paper helped in minimizing radiation exposure levels. The possibility of spilling the sample is also reduced.

In order to obtain the necessary detectability within the necessary time limit for the analysis of several of the elements present in the sample initially at low concentrations, the minimum sample size was 100 µl. Because this volume was too great to be absorbed by a single 24-mm Whatman filter paper, a double layer of the filter papers was used. These filter papers were sandwiched between two sheets of ¼ mil Mylar and mounted on a Somar Spectro-Cup (Fig. 1a). The inner sheet of Mylar contained a small hole through which the solution aliquot could be pipetted (Fig. 1b). The samples and standards were analyzed while still wet, in contrast to the usual procedure of first drying the sample on the substrate[1,4]. The principal advantages of this procedure are:

1. Considerable time is saved by not having to dry the sample.
2. The need for remote drying facilities is eliminated.
3. There is less possibility for the sample to contaminate the area than as a dry powder.

No significant loss of precision was observed by analyzing the wet filter paper aliquots as long as the samples were counted immediately after pipetting.

FIGURE 1. SAMPLE CUP CONFIGURATION

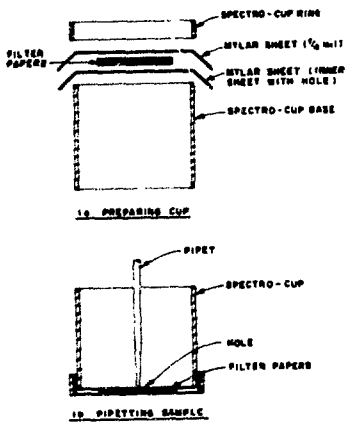

Calibration

In order to evaluate the effectiveness of the filter paper technique in minimizing interelement effects and to establish the appropriate calibration function for each of the elements to be determined, a series of 15 standards were prepared such that the concentration level of each element relative to the others was not constant. The composition of these standards is listed in Table I.

TABLE I. STANDARDS CONCENTRATION

STD. #	Zr, g/l	U, g/l	Nb, g/l	Cd, g/l
1	98.1	15.0	4.0	12.0
2	12.5	0.5	2.0	6.0
3	101.0	10.0	1.0	12.0
4	25.0	1.1	0.25	4.0
5	113.0	0.5	0.5	12.0
6	126.0	0	0	0
7	75.5	5.0	5.0	12.0
8	93.8	4.4	15.0	10.0
9	107.0	1.0	3.0	12.0
10	106.0	6.7	7.5	7.5
11	101.0	8.0	2.0	12.0
12	119.0	2.0	1.0	2.0
13	50.0	5.6	0.75	1.0
14	81.2	13.4	6.2	5.0
15	106.0	3.0	10.0	3.0

An internal standard was added to each standard solution to correct for the following:

1. Variations in the filter paper surface.
2. Any nonuniform dispersion or nonreproducibility of the sample on the filter paper.
3. Instrument drift and/or fluctuations so that standards would not have to be analyzed with each sample.

The choice of a suitable element for internal standardization was restricted by the necessity to select an element with the following characteristics:

1. The element could not be present in any of the fuel materials or the dissolvent acid matrices.
2. It must be soluble in all dissolvent matrices.
3. It could not interfere with the analysis of any elements of interest.
4. It could not be subject to absorption-enhancement effects from the matrix or the fuel materials.
5. Its energy spectrum should be in the same range as the elements to be determined.

Antimony was selected as the most feasible element, despite the fact that the cadmium Kβ peak at 26.15 Kev overlaps the antimony Kα peak at 26.27 Kev. The amount of the cadmium Kβ contribution to the antimony peak can be determined from the intensity of the cadmium Kα peak. Using background corrected peak areas for several pure cadmium solutions, the ratio of that part of the cadmium Kβ peak which overlaps the antimony Kα area to the cadmium Kα peak area was determined (Fig. 2). In the standards and samples, that fraction of the cadmium Kα peak is subtracted from the antimony Kα area to obtain the net antimony intensity. A certain error is introduced by this correction procedure; however, the accuracy of the results is still within the required ± 5-10% RSD.

FIGURE 2. CALCULATION OF CADMIUM CONTRIBUTION TO ANTIMONY

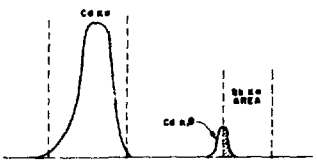

USING PURE SOLUTIONS:

$$\text{CORRECTION FACTOR} = CF = \frac{\text{PEAK AREA AT Sb Kα (CROSSMATCHED)}}{\text{PEAK AREA AT Cd Kα}}$$

$$\text{Sb}_{\text{NET INTENSITY}} = (\text{Sb Kα AREA}) - (CF)(\text{Cd Kα AREA})$$

The precision of analysis for this "wet filter paper procedure" was calculated to be ± 2% RSD, based upon 18 replicate determinations of the concentration of one of the elements. At or near the detection limit of each element, however, precision as well as accuracy was significantly poorer.

Three aliquots of each standard were analyzed. The integrated area above background for each element peak was ratioed to the net area of the antimony peak. Multiple regression techniques were used to evaluate whether there were any significant matrix effects. For zirconium, uranium, and cadmium, no mathematical matrix corrections were required to obtain a good fit to basic calibration curves.

For zirconium, a second degree calibration curve, covering the range of 10 to 130 g/l was obtained for the Kα peak (Fig. 3). Several typical dissolver solutions prepared in pilot plant studies and a control sample of known composition were analyzed for zirconium. In order to estimate the accuracy of the X-ray fluorescence method, the zirconium in these samples was also determined by an atomic absorption procedure, which has an accuracy of ± 4-6% RSD. The results are listed in Table II. Agreement between the two methods is excellent throughout the range of analysis.

In the case of uranium, a second degree equation using the Lα peak is obtained for the range of 0-15 g/l (Fig. 4). The uranium concentrations in most of the pilot plant samples were at or near the lower limits of detection for the X-ray fluorescence method. The reported accuracy of the uranium values obtained for comparison by a colorimetric method used in routine process control was about ± 6-10% RSD on the average. Nevertheless, agreement between the two sets

of results, listed in Table III, is good. The uranium values determined for the control sample are in excellent agreement with the known concentration.

FIGURE 3: ZIRCONIUM CALIBRATION CURVE

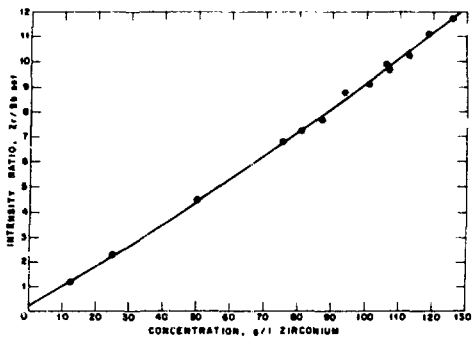

TABLE II. DETERMINATION OF Zr IN DISSOLVER SOLUTIONS

Sample #	Zr, g/l X-Ray	Zr, g/l AA	Known Control Value, g/l
1	105	97	
2	103	98	
3	71	64	
4	117	118	
5	60	55	
6	88	79	
7	52	52	
8	92	94	
9	63	57	
10	57	53	
11	54	49	
12	23	24	
13	114	121	
14	22	21	
15	48	42	
16	25	24	
17	62	57	
18	111	111	
19	109	110	
Control	101	100	100

FIGURE 4: URANIUM CALIBRATION CURVE

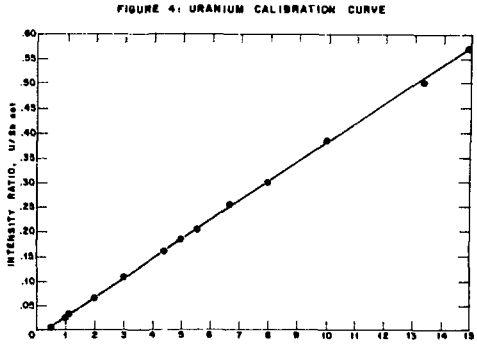

TABLE III. DETERMINATION OF U IN DISSOLVER SOLUTIONS

Sample #	U, g/l X-Ray	U, g/l Colorimetric	Known Control Value, g/l
1	0.88	0.82	
2	0.78	0.78	
3	0.90	0.77	
4	0.56	0.58	
5	0.90	0.70	
6	4.00	4.10	
7	0.32	0.29	
8	0.31	0.29	
9	0.65	0.58	
10	0.50	0.63	
11	1.84	2.20	
Control	2.25	2.18	2.22

A linear calibration curve was used for cadmium in the range of 0-12 g/l (Fig. 5). No cadmium was present in the pilot plant samples. However, the control sample was analyzed and a value of 9.92 g/l determined, compared with a known value of 10.0 g/l.

The principal problem in the determination of niobium in these samples is the spectral interference from the Lβ2 peak of uranium (16.43 Kev) on the Kα peak of niobium (16.58 Kev), which is the primary analytical peak. When the niobium standards data are plotted without any correction (Fig. 6), correlation is poor. The fit of the data points to the calibration curve appears to be dependent primarily upon the concentration of uranium in the solutions. Those standards with high levels of uranium (15,13.4,10, and

FIGURE 5: CADMIUM CALIBRATION CURVE

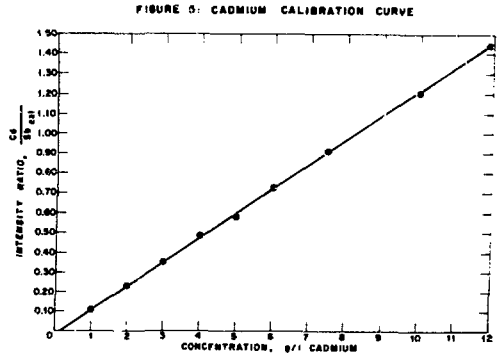

FIGURE 6: UNCORRECTED NIOBIUM CALIBRATION CURVE

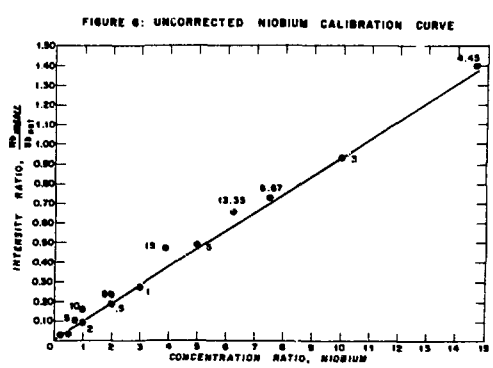

8 g/l) deviated most from the curve. Standards with lower concentrations of uranium (0.5, 1, and 2 g/l) and the standards with higher niobium relative to the uranium (4.4 g/l U with 15 g/l Nb; 3 g/l U with 10 g/l Nb) are in much better agreement with the calibration fit.

When a mathematical correction was applied to remove the contribution of the uranium to the niobium peak area, a significantly better fit of the data was obtained. A matrix correction factor for the effect of zirconium on the niobium intensity was also applied. The corrected data fit the calibration curve over the range of 0-15 g/l with excellent correlation (Fig.7).

FIGURE 7 CORRECTED NIOBIUM CALIBRATION CURVE

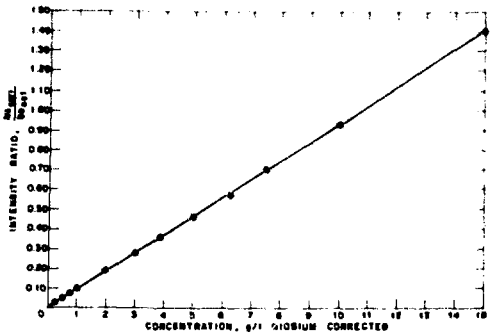

Niobium in several of the pilot plant samples was determined by the X-ray fluorescence procedure and compared with results from a colorimetric procedure with an estimated accuracy of ± 4-8% RSD. As with the uranium, the concentrations of niobium in most of the samples analyzed were at or near the lower limits of detection for the X-ray fluorescence method. The results, listed in Table IV, are in fair agreement. The niobium values determined for the control sample, with a concentration in the middle of the analysis range, are highly accurate.

TABLE IV. DETERMINATION OF Nb IN DISSOLVER SOLUTIONS

Sample #	Nb, g/l X-Ray	Nb, g/l Colorimetric	Known Control Value, g/l
1	0.69	0.73	
2	0.31	0.42	
3	0.34	0.47	
4	0.14	0.18	
5	0.46	0.64	
6	0.56	0.67	
7	0.26	0.35	
8	0.38	0.42	
9	5.7	6.2	
10	4.2	4.2	
Control	2.0	2.0	2.0

For these samples at low concentrations of niobium, there appears to be a bias between the two methods. The X-ray fluorescence results are consistently lower than the results from the colorimetric method. Future studies are planned to further evaluate the causes of this bias. In any event, the concentrations of both niobium and uranium in samples to be analyzed from actual process runs will be considerably higher.

Computer Programming

To permit operators who have a minimum of knowledge and experience with regard to X-ray analysis techniques and computer operation to obtain a sample analysis, a master control program has been written in the Tracor Northern Flextran interpreter language. The program initially outputs information regarding instrument set-up and necessary parameter checks. Once a sample code has been input by the operator, all else is automatic. The following operations are carried out without operator supervision or input:

1. Control of spectral data acquisition.
2. Storage of the sample spectrum on the tape cassette for future reference.
3. Calculation of the net peak area above background for all elements of interest.
4. Calculation of the corrected antimony intensity.
5. Calculation of the intensity ratio of each element to the net antimony intensity.
6. Calculation of the concentration of each element in both g/l and molar units.
7. Determination of the percentage change in concentration from the previous sample in the process run. This value indicates when dissolution is complete and the next step in the process can be initiated.
8. Output of the necessary data for each sample.

The entire procedure, which includes internal standardization, pipetting onto the filter paper, analysis of the sample, and printout of results, can be performed within twenty minutes.

DISCUSSION AND FUTURE WORK

The results of this initial development study have demonstrated that the X-ray fluorescence technique can achieve the necessary requirements for simplicity of sample handling, ease of operation, speed of analysis, and accuracy. The concentration levels of uranium and niobium will be higher in actual samples and improved accuracy can be expected.

Future development work will include the study of additional elements to be determined and of different acid dissolvent matrices. The use of various types of filter substrates to improve surface uniformity, sample dispersion, and absorbancy will be evaluated. The applicability of X-ray analysis in monitoring for corrosion products from the dissolver tanks will also be studied.

The possible effects of high levels of radioactivity on sample analysis must be evaluated. If the energy dispersive spectrometer cannot function efficiently in high radiation fields, a sequential wavelength spectrometer will be considered.

ACKNOWLEDGMENTS

The author wishes to thank W. A. Ryder for his technical guidance and assistance.

REFERENCES

1. E. P. Bertin, Principles and Practices of X-Ray Spectrometric Analysis, p 499, Plenum Press, N.Y., (1970).
2. F. H. Chung, "A New Approach to Quantitative Multielement X-Ray Fluorescence Analysis", in R. W. Gould et al., Editors, Advances in X-Ray Analysis, Vol. 19, in Press (1976).
3. E. L. Gunn, "X-Ray Fluorescent Intensity of Elements Evaporated from Solution onto Thin Film", Anal. Chem. 33, 921 (1961).
4. A.H.E. von Baeckmann, D. Ertel, and J. Neuber, "Determination of Actinide Elements in Nuclear Fuels by X-Ray Analysis", in W.L. Pickles et al., Editors, Advances in X-Ray Analysis, Vol. 18, p. 62-75, Plenum Press (1975).

Proceedings, ERDA X-ray and Gamma-ray Symp. Ann Arbor, MI, May 19-21, 1976 (Conf 760539)

BULK SAMPLE SELF-ATTENUATION CORRECTION BY TRANSMISSION MEASUREMENT

J. L. Parker and T. D. Reilly
Nuclear Safeguards Research Group, R-1
Los Alamos Scientific Laboratory
Los Alamos, New Mexico 87545

Frequently in the passive gamma-ray assay of bulk samples, the most difficult part of the assay problem is the correction for the gamma-ray attenuation within the sample itself, the difficulty arising from often unknown chemical compositions (and therefore unknown attenuation coefficients) and sample volumes which may range up to many liters. The problem is clearly most severe in the assay of samples containing high-Z elements because of the relatively higher mass attenuation coefficients for those elements. The studies described herein were stimulated, in fact, by the difficulty encountered in assaying bulk samples of uranium and plutonium, which are often such as to make a passive gamma-ray assay impossible. Nevertheless, there are many cases and classes of materials for which a careful passive gamma-ray assay is the most precise and accurate as well as the cheapest method for uranium and plutonium determinations, and the same is true for many other gamma-ray emitting materials. Because of the difficulties just mentioned, however, the usual calibration and attenuation correction methods involving direct comparison to standards or exploitation of prior knowledge of chemical composition are often not applicable. Determination of the sample attenuation coefficient (μ) by a separate transmission measurement with an external source has proven to be the most generally useful procedure.[1,2,3] This paper briefly reviews the various procedures in use and presents some results of a detailed study of the transmission method of attenuation correction applied to the most important geometrical classes of assay samples, namely box-shaped and cylindrically-shaped samples. These classes include most of the containers met in practice.

General Comments and Definitions

We assume that the mixture of material to be assayed and matrix (everything other than the assay material) is reasonably uniform and that the particles of assay material are small enough to ignore self-attenuation within the individual emitting particles. In effect, this assumption states that the sample attenuation is characterized by a single linear attenuation coefficient, μ. Then knowing μ of the sample, the sample dimensions and the distance of the sample from the detector, it is possible to calculate the correction factor for the sample self-attenuation. Few closed forms exist for the correction factors and exact calculations must most often be done by numeric methods, but frequently it is possible to use an approximate analytic form of sufficient accuracy as discussed below.

The correction factor may be defined in several ways. Because assays are usually done by comparison to known standards of the same or nearly the same shape as the unknowns, the most generally useful form is the so-called correction factor (CF) with respect to the nonattenuating sample. Symbolically, the definition may be expressed as

$$CF = \frac{C(\mu=0)}{C(\mu\neq0)} \qquad (1)$$

where $C(\mu=0)$ equals the count that would have been obtained from the sample with no attenuation, and $C(\mu\neq0)$ equals the actual count from the sample. $C(\mu=0)$, the quantity to be obtained in an analysis, is generally called the corrected count (CC) and is computed from the above definition, that is, $CC = CF \times C(\mu\neq0)$, where CF is computed from the sample μ and the assay geometry, and $C(\mu\neq0)$ is measured. Thus defined, the corrected count per gram of material assayed is constant, that is, the calibration curve is linear in terms of mass and corrected count.

Another useful correction factor form may be termed the correction factor with respect to a nonattenuating point (CF_p). Symbolically, this form is expressed as

$$CF_p = \frac{C_p(\mu=0)}{C(\mu\neq0)} \qquad (2)$$

where $C_p(\mu=0)$ equals the count that would have been obtained if the sample had been condensed to a nonattenuating point at the center of the sample, and $C(\mu\neq0)$ equals the actual count from the sample, precisely as in the previous definition. This form of the correction factor is particularly useful when it is necessary to assay a large sample (such as a 55-gal drum) with respect to a small standard. If the sample μ and the appropriate dimensions are known, the two forms of the correction factor are equally difficult to compute; however, because it is of more general use, the rest of the discussion herein deals only with the correction factor with respect to the nonattenuating sample.

Outline of Methods Used to Determine Correction Factors

The various methods used in either finding or avoiding the attenuation correction will be recapitulated briefly.

Representative Standards. The oldest and perhaps still most used (and abused) method is that of avoiding the issue by using representative standards. In this procedure a set of standards is prepared as nearly identical as possible in size, shape, and composition to the unknowns, with varying concentrations of the material to be assayed. The standards are counted to prepare a calibration curve and the assay is accomplished by counting the unknowns and comparing the count directly to the calibration curve. This procedure will produce good results if (and only if) the unknowns and standards are sufficiently similar that the same concentration of assay material in each gives rise to the same sample μ and, therefore, to the same correction factor. In other words, at the same concentration of assay material the exact same fraction of gamma rays must escape from both sample and standard. This method is only applicable in cases where the nature and composition of the assay samples are well known and unvarying as in the case, for example, with carefully prepared solutions.

Computation from Knowledge of Composition. A second method exploits previous knowledge of the chemical composition, mass, and shape to compute μ of the sample from which in turn the correction factor can then be computed. Sufficient prior knowledge to compute the sample μ does not necessarily imply that the assay result is known in advance. In many cases the assay material is a small and unknown fraction of the total sample mass and it is certain that μ is almost purely dependent on the matrix composition and mass.[1,2] When highest accuracy is not necessary and the required knowledge is available, this approach is useful.

Gamma Ray Intensity Ratios. Another method of determining attenuation corrections, more discussed than actually used, involves measuring the relative intensity of two gamma rays of different energy emitted by the material under assay.[4] However, in general, μ of the sample for a given energy is not uniquely related to the intensity ratio, and again some prior knowledge of the nature of the sample is required. Furthermore, nature has not endowed all materials of assay interest with a pair of gamma rays of the appropriate energies. Nevertheless, the method has proved useful in particular cases, and it does have the potential for raising a warning flag when the assumption of reasonable uniformity is not met.[5,6]

Transmission Method. A fourth and the most general method of obtaining the attenuation correction involves experimental determination of the sample μ directly by measuring the transmission through the sample of a beam of gamma rays from an external source.[1,2,7] This method requires no knowledge of the chemical composition of the sample, just the basic assumptions on uniformity and particle size. As such, it is the only practical way to proceed in the "black box" cases and is often the preferred method even when some knowledge of the sample composition is available, especially if the best obtainable accuracy is desired. The balance of this paper will be devoted to this method.

Detailed Consideration of Transmission Method

The sample transmission is defined as the fraction of gamma rays from the external source that pass through the sample unabsorbed and unscattered. From the fundamental law of gamma-ray attenuation, the sample transmission T is related to the sample μ by the relation $T = \exp(-\mu x)$, where x is the thickness of sample penetrated. Obviously, correction factors can be expressed either as functions of μ or of T; however, because T is the measured quantity and the relationships are most conveniently graphed as functions of T, this parameter is used in the following discussions. It is assumed that T is measured normal to the center of a face of box-type samples and along a diameter passing through the midpoint of the axis of cylindrical samples. It is also assumed that the transmission is determined at the energy of the gamma ray used in the assay. The far-field correction factor for box-type samples has a simple closed form

$$CF = -\frac{\ln T}{1-T} \quad . \qquad (3)$$

The dependence of the CF(T) is shown in Fig. 1. Although not exact for near field situations, this form is useful for assays where the distance to the detector from the face of the box is only ~5 times the maximum dimension of the box. This is especially true in cases of large, somewhat heterogeneous containers where a 10% error resulting from an approximate correction factor is much preferable to a ≥100% error resulting from neglect of the correction altogether. The discussion below with respect to cylindrical samples will help put the limitations in perspective.

No exact expressions for the CF of cylindrical samples can be written in terms of elementary functions. For the far-field case (cylinder radius and height negligible with respect to the distance to the detector), however, an expression exists in terms of Bessel functions and Struve functions,[8] but for near-field cases no exact expression of any form is known. The far-field case is conveniently taken as a reference case with which to demonstrate the general behavior of the CF for cylinders. Figure 1 shows the cylindrical far-field CF as a function of T as well as the far-field CF for a slab-type sample.

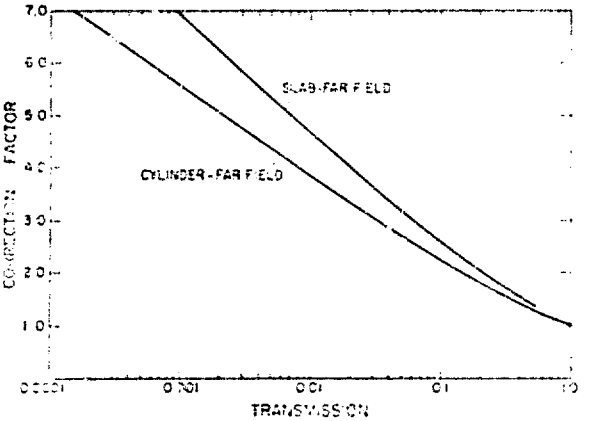

Fig. 1
Far-field correction factor for cylindrical and slab-type samples as functions of transmission.

Note that for T<0.1, that CF≈log(T) applies for both cases. It is also noteworthy that because transmissions of less than 0.001 are very difficult to measure accurately, the range of readily accessible CF is about $1 \leq CF \leq 6$.

Because of the lack of exact analytical forms for near-field cases, much use has been made of approximate forms for cylindrical samples, the most useful of which has been

$$CF = k \ln(T)/(T^k-1) \qquad (4)$$

where k is a constant of value ~0.8. This form is a slight modification of the exact far-field correction factor for a slab-type sample for which k=1. A first-order approximation of the exact far-field form for the cylinder gives $k = \pi/4 = 0.785$, whereas empirical and numerical studies indicate k = 0.82 is better. Figure 2 shows the deviation from the correct far-field values of this approximate form for various values of k. For k = 0.82, CF is within 1-1/2% of the correct value for $0.01 \leq T \leq 1$ and within ±3% for $0.001 \leq T \leq 1$.

It appears that the value k = 0.82 is better than k = π/4 or k = 0.85 for far-field assays of cylindrical samples. However, the consequences of using an incorrect CF function over a restricted range of T and the

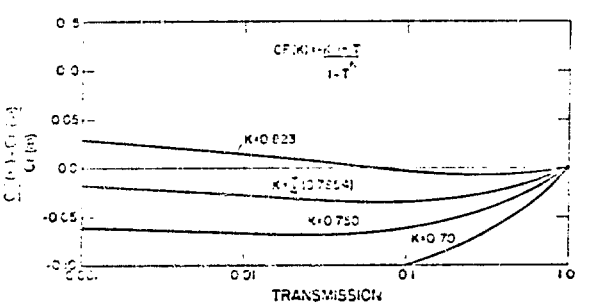

Fig. 2
Deviations from the correct far-field cylindrical correction factors of the approximate form CF(T) = k ln(T)/(T^k-1) for several values of k.

relationship of the error in the computed CF to the error in the measured value of T should be explored. Assume that an approximate form with functional dependence on T, CF (T), has been used and that the correct function is $CF_o(T)$. The calibration constant is determined from a standard of transmission T_s and the unknown sample has transmission T_u. Next, let G be the unknown mass determined by using CF(T) and G_o be the "correct mass," that is, the mass that would have been determined from $CF_o(T)$. Algebraic manipulation then yields the relationship

$$\frac{G}{G_o} = \frac{CF(T_u)}{CF_o(T_u)} \Big/ \frac{CF(T_s)}{CF_o(T_s)} \quad . \tag{5}$$

Thus the ratio of measured to true mass depends not on the actual magnitude of the errors in CF(T), but only on the ratio of "used to true" CF ratios for the transmissions of the unknown and the standard. Figure 2 shows that for transmissions in the range $0.001 \leq T \leq 0.1$ the value k = 0.75 would give better results than k = 0.82 even though the absolute error in CF(k = 0.75) is greater over the range. However, if the range of transmission were $0.1 \leq T \leq 1.0$, the value k = 0.82 would be better. The best value of k to use for this approximate analytic form will depend on the range of T encountered, and a judicious choice may well reduce systematic errors by a few percent.

Now consider the fractional error in CF caused by a given fractional error in T. For the functional form, use $CF(T) = k \ln(T)/(T^k-1)$. Then differentiating, we obtain

$$(dCF/CF)/(dT/T) = \left(\frac{1}{\ln T} + \frac{kT^k}{1-T^k}\right) \quad . \tag{6}$$

Figure 3 shows this expression as a function of T for several values of k. Note that as T becomes smaller, and therefore more difficult to measure accurately, the fractional error in CF becomes smaller relative to the fractional error in T, thus compensating somewhat for the larger expected fractional errors in T. It should be emphasized that when only a small fraction of the gamma rays escape (small T and large CF) the sample, large fractional errors in the assay can result. A transmission measurement to determine the CF is the best way to proceed in such cases.

In the near field, cylindrical correction factors become functions not only of sample transmission, but also of the sample radius, height, and distance from the detector. A simple two-dimensional model is adequate to demonstrate the dependencies and is sufficiently accurate for much practical work. The model assmes a sample of radius R and zero height whose center is at a distance D from a point detector. The detector is in the plane of the now plane circular sample. In this model the CF is a function of T and the ratio D/R only, which means, for example, that given the same value of T, a sample of R = 1 cm with D = 10 cm has the same CF as a sample of R = 1 m with D = 10 m. Figure 4 gives the CF as a function of D/R for various values of T. These and all other near-field results were obtained by computer-executed numerical integrations. The essential point obtained from Fig. 4 is that the CF decreases as D/R decreases with the more drastic changes occurring for the smaller values of T. Remembering that the CFs are with respect to the nonattenuating cylinder, the behavior just described can be seen qualitatively to be a consequence of the inverse square law. To show quantitatively the deviations from the far-field case as D/R decreases, the deviations are plotted in Fig. 5 as a function of T for various values of D/R. For $D/R \geq 50$, the deviation from the far-field condition is less than 1% for T>0.001. Therefore, $D/R \geq 50$ can be regarded as the far-field condition for most purposes.

Obviously, no real samples are of zero height as assumed in the two-dimensional model, and the height of the cylindrical sample will influence the values of the CF. Numerical computations can again be performed for the three-dimensional case. Qualitative arguments show that the assumption of a point detector is good for nearly every case where the sample is at least several times the volume of the detector, and this assumption has been used in calculations of CF for a cylindrical sample of finite height. It is of interest to get a qualitative understanding of how the CF for a cylinder of finite height varies from those of the corresponding two-dimensional case. Figure 6 gives the deviation for a cylinder whose height H is twice its diameter from the pure two-dimensional case for three values of D/R. The data quantitatively confirm what is qualitatively expected. The D/R>10 deviations from the two-dimensional

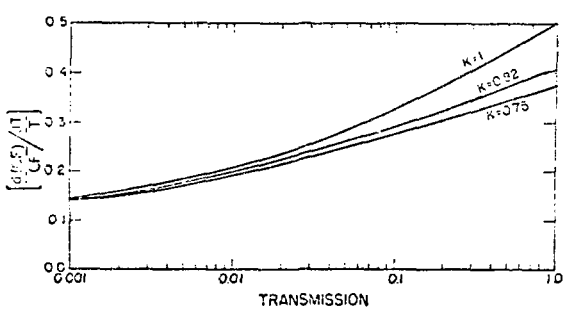

Fig. 3
The differential change in the correction factor relative to the differential change in transmission for several values of k in the approximate form $CF(T) = k \ln(T)/(T^k-1)$.

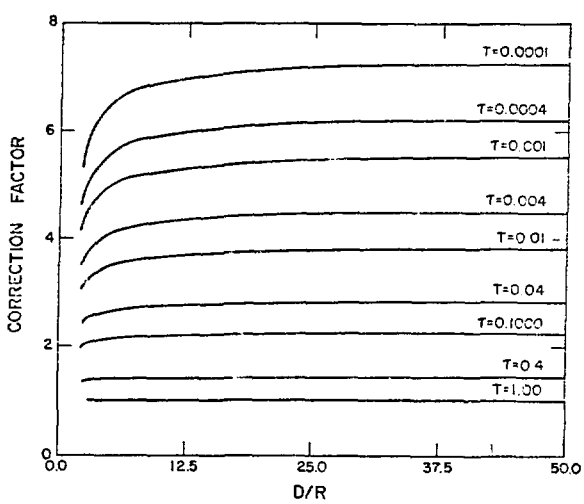

Fig. 4
Near-field correction factors for the two-dimensional cylinder as a function of the ratio of the sample center-detector distance to the sample radius for various values of transmission.

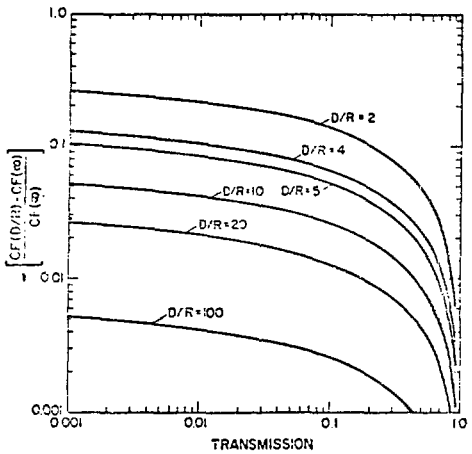

Fig. 5
Deviations as a function of transmission of the near-field correction factors for the two-dimensional cylinder from the far-field cylindrical correction factors. D/R is the ratio of the sample-center to detector distance to the sample radius.

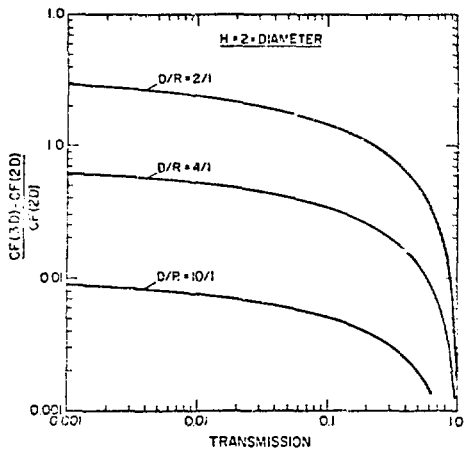

Fig. 6
Deviations of the three-dimensional cylindrical correction factors from the corresponding two-dimensional case for cylindrical sample whose height is twice its diameter. D/R is the ratio of the sample center to detector distance to the sample radius.

limit are <1%. The deviations are greater for smaller values of T and for smaller values of D/R. Clearly, the deviations for given D/R also become smaller as H decreases relative to D.

Conclusions

When possible, a "far-field" assay geometry is preferred because of less stringent requirements of sample positioning and less dependency of the CF on the exact dimensions of the sample. Unfortunately, count rate considerations usually force the use of a near-field geometry to some degree. In any case, but especially in near-field situations, (D/R<10 for cylinders), it is best to use the CF values computed for that geometry. However, obtaining those values is often awkward because of the lack of analytic forms for CF(T).

Two reasonable alternatives are suggested. The first is to prepare a graph similar to Fig. 2 for the particular geometry in order to choose an approximate form (such as the one discussed herein) that will give adequate accuracy over the anticipated range of T. In doing so, it is important to remember that the CF(T) function may be in error in an absolute sense, but still provide adequately accurate assays over large ranges of T. The second alternative, useful when a computer does the analysis, is to store enough previously calculated CF values for the geometry in the computer to allow accurate interpolation. Although this paper deals with cylindrical and box-type samples viewed from the side, other configurations can obviously be dealt with in similar fashion.

Just a word about experimental standards is in order. In principle, a single standard will suffice if the proper selection of CF(T) has been made, but clearly, it is prudent to have two or more standards spanning the expected range of values of T. It should be emphasized that the standards need not have the same or even similar chemical composition as the unknowns inasmuch as the CF is dependent only upon the transmission value, sample shape, and assay geometry.

In all that has been done, high resolution detectors have been assumed so that only a negligible number of Compton scattered gamma rays are included in the full energy peak areas. Coherent scattering does introduce a rather fundamental limitation in that the measured transmission may not yield quite the correct effective μ for the sample. For large samples the effect may be $\sim$1%. Most often the sample heterogeneity will determine the accuracy attainable.

This paper has not discussed the hardware problems involved in the determination of the transmission and the intensity of the emitted gamma rays. Quality assays must include skillful data acquisition as well as proper treatment of the sample self-attenuation. Nevertheless, in frequently met cases neglect or improper handling of the self-attenuation correction can give rise to very large errors ($\geq$100%), which sloppy acquisition techniques can rarely equal, hence the emphasis of this paper on the sample self-attenuation problem.

References

1. T. D. Reilly and J. L. Parker, "A Guide to Gamma-Ray Assay for Nuclear Material Accountability," Los Alamos Scientific Laboratory report LA-5794-M (March 1975), Chap. 5.

2. R. H. Augustson and T. D. Reilly, in: "Fundamentals of Passive Nondestructive Assay of Fissionable Material: Laboratory Workbook," Los Alamos Scientific Laboratory report LA-5651-M (September 1975), Chap. 5.

3. R. B. Walton, E. I. Whitted, and R. A. Forster, "Gamma-Ray Assay of Low-Enriched Uranium Waste," Nucl. Technol. 24, 81-92 (October 1972).

4. T. D. Reilly and J. L. Parker, Los Alamos Scientific Laboratory report LA-5889-PR (April 1975), pp. 16-18.

5. J. E. Cline, "A Relatively Simple and Precise Technique for the Assay of Plutonium Waste," Aerojet Nuclear Company report ANCR-1055 (February 1972).

6. J. E. Cline, E. B. Nieschmidt, A. L. Connelly, and E. L. Murri, "A Technique for Assay of L-10 Bottles of Plutonium Nitrate," Idaho Nuclear Corporation report IN-1433 (October 1970).

7. J. L. Parker, T. D. Reilly, R. B. Walton, D. B. Smith, and L. V. East, Los Alamos Scientific Laboratory report LA-4705-MS (May 1971), pp. 12-15.

8. E. I. Whitted, "Derivation of a Far-Field Gamma-Ray Correction Factor," Nuclear Analysis and Research Group internal memo (June 1972).

Proceedings, ERDA X-and Gamma-Ray Symp. Ann Arbor, MI, May 19-21, 1976 (Conf 760539)

AUTORADIOGRAPHIC TECHNIQUES TO DETERMINE NOBLE METAL DISTRIBUTION IN AUTOMOTIVE CATALYST SUBSTRATES

Walter H. Lange
Analytical Chemistry Dept.,
GM Research Laboratories
Warren, Mich. 48090

Summary

The distribution of noble metals in the ceramic substrates of automotive catalytic converter systems is important to the functional characteristics of the systems. A radiotracer technique involving microtomy of bead substrate samples and autoradiography using the resultant thin sections has been developed to produce detailed images of the metal distributions. The method is particularly valuable to determine the distribution of one metal in the presence of another to aid in the development of more efficient systems.

Introduction

Automotive catalytic exhaust converters reduce carbon monoxide and hydrocarbon emissions by oxidation reactions with a catalyst consisting of noble metals in a ceramic substrate. One of the substrate forms is alumina beads and the noble metals are added to them as a solution which diffuses into the beads. The final distribution of the noble metals, depending upon several factors including substrate structure and impregnation technique, can significantly affect the performance of the catalyst[1-4].

Methods used to define noble metal distribution in alumina beads have included electron microprobe analysis and various optical procedures combined with chemical reaction coloring (staining) of cleaved samples[1]. The microprobe analysis provides photomicrographs specific for each element of interest, but information may be limited by the minimum detectable concentrations. Although some optical methods are useful and usually rapid for many evaluations, they may not be applicable when certain combinations of elements are present. The autoradiographic technique described here was developed to provide distribution data 1) with maximum sensitivity to distribution variations, 2) with virtually any impregnation element, and most importantly 3) with the capability to study the effect of one metal upon the distribution of another in the beads.

Technical Considerations

In brief, autoradiography involves the placement of a sample containing radioactive elements in contact with a photosensitive emulsion for a time sufficient to produce a latent image through the interaction of ionizing radiation with the silver halide grains in the emulsion. Development of the image produces an autoradiogram showing the distribution of the radioactivity. In the experiments with catalyst beads, radioisotopes of platinum, palladium and rhodium have been utilized; their pertinent nuclear characteristics are listed in Table 1. These radionuclides may be incorporated into catalyst substrates following either of two general procedures, namely, by *in vitro* procedures with radioactive solutions or by *in situ* activation of the elements.

In Vitro Autoradiography. In this approach, the catalyst beads are impregnated with a radioactive solution of the appropriate metal(s). This method offers two important advantages; first, it allows the study of one element exclusive of other elements present, which is especially valuable in the study of synergistic effects. Secondly, this method assures that the images produced result only from the chosen element. With regard to the latter, care must be taken when choosing a particular radioisotope to represent the distribution of that element to make certain that radiation from daughter products does not give misleading information. As an example, when natural platinum is irradiated the predominant radionuclide produced is ^{199}Pt. However, by the time the H_2PtCl_6 solution can be prepared for impregnation into the beads, the 30-minute ^{199}Pt will have decayed to the 3.1 day ^{199}Au. Subsequent autoradiographic images will reveal gold distribution, which is not necessarily the same as that of the platinum. The use of ^{195m}Pt or the *in situ* activation of platinum avoids this problem.

Table 1

RADIONUCLIDES USED IN CATALYST DISTRIBUTION STUDIES

Element	Radioisotope	Half-life	Decay Mode
Platinum	^{199}Pt, ^{199}Au	30 min., 3.1 d	Beta
	^{195m}Pt	4.1 d	Isomeric Transition
Palladium	^{103}Pd	17 d	Electron Capture
Rhodium	^{99}Rh	4.7 hr, 15 d	Electron Capture

The *in vitro* method offers the additional benefit that radiometric as well as autoradiographic data may be obtained. For example, by comparing the radioactivity of a bead, or that of other samples obtained during catalyst preparation or testing, to the specific activity of the impregnation solution, one can quantify the amount of noble metal in a bead as well as the amount lost in processing. Similar procedures have been used to determine the attrition rate of platinum and palladium from automotive catalysts under engine operating conditions[5].

In Situ Autoradiography. In this approach, previously impregnated catalyst substrates are irradiated with neutrons to produce radioactive species of the noble metals.

The in situ neutron irradiation of materials is often advantageous when one wishes to demonstrate the effects of field testing upon elemental distributions when previously irradiated materials would have disappeared through decay or their use would otherwise not be practical. This method is generally limited to small samples; additionally, one must be certain that the distribution patterns obtained are produced by only the element of interest and not by other elements present.

Experimental

Radionuclides

Two means of producing radionuclides are the (n,γ) reaction in a nuclear reactor and the (p,n) reaction in a cyclotron. In the present work, ^{199}Pt and ^{195m}Pt were produced by neutron irradiation of natural platinum and ^{194}Pt, respectively, in the University of Michigan reactor. The radioactive metals were then dissolved to provide chloride solutions for subsequent bead impregnation. The radionuclides ^{103}Pd and ^{99}Rh were produced by the (p,n) reaction with ^{103}Rh and ^{99}Ru, respectively, and were purchased as chloride solutions from Amersham-Searle Corporation and New England Nuclear Corporation, respectively.

Substrate Impregnation

Alumina bead substrates were impregnated with radioactive species of noble metals following published procedures[6,7]; element concentrations of about 0.1% platinum, 0.025% palladium, and 0.0026% rhodium were used. The radioactive metal, as a chloride solution, was added directly to the appropriate quantity of beads. They were then dried for about five hours with occasional stirring, followed by calcining in a tube furnace at 550°C for 5 h. Samples of beads were taken randomly from the batches following the impregnation procedure, after calcining, and in some cases after engine tests.

Sample Preparation

The method used to obtain detailed images of the spatial distribution of the noble metals is an extension of a technique developed earlier which utilized ^{35}S to define the distribution of sulfate in battery reactions[8]. The technique includes the use of a microtome to obtain thin sections of the samples which are then placed in contact with a film for autoradiographic exposure.

To facilitate microtomy of the small, round beads and the collection of the thin sections, the impregnated beads were cast in 2.54-cm x 2.54-cm blocks of hard dental wax using aluminum forms (several beads can be included in each block). The sections which would normally curl and crumble as microtome cuts were made were preserved by pressing a piece of cellophane tape in contact with the wax block surface prior to making each cut. As the block passes under the knife blade, the tape and the section adhering to it are lifted away as illustrated in Fig. 1. The several beads in the block are sectioned simultaneously, and any number of successive sections can be taken with ease and retained for autoradiography. Usually, autoradiographic exposures are delayed until all samples from a given experiment have been sectioned. This is to guarantee equal exposure among all samples, thereby allowing direct comparison of image densities representing noble metal distributions.

Thin sections provide several advantages. For example, since the tape strips (and thin specimens) are flexible, they can be backed with plastic sponge and weighted, forcing the specimens to make the best possible contact with the emulsion; good autoradiographic image resolution depends upon such contact. Also, the sections do not include the relatively large mass of bead material beyond the surface of interest (the hemisphere of a cleaved bead) which otherwise would also expose the film and reduce total image sharpness through unwanted background exposure. Finally, thin sections provide the opportunity to examine many specimens of each sample for reliability of results and to allow for the detailed study of patterns through the bulk of the object, layer by layer.

Microtome sections of the beads are normally 0.05-mm thick, but handling is an easy task when they are affixed to the tape. Even so, the ceramic bead material of some samples tends to powder and fall away from the tape after the cut is made. The integrity of such samples is ensured by vacuum impregnation of the beads with wax prior to casting in the wax block. This is accomplished by placing the beads in the wax at about 70°C for 5 min at reduced pressure. This treatment does not affect the distribution of the radioactivity.

Fig. 1. Microtome Sectioning of Alumina Catalyst Substrate Beads for Autoradiographic Examination.

Autoradiography

The gamma photon energies of the radionuclides listed in Table 1 are not given because they have little influence upon exposure in autoradiography, especially when determining distributions in low density ceramic bead substrates. Exposure times are determined, rather, by the energy and abundance of beta particles, electrons and low

energy x-rays, and the half-life of the nuclide. Thus, radioactivity requirements and exposure times are usually determined empirically. As an example, for alumina beads impregnated with a solution tagged with ^{195m}Pt, excellent exposures were achieved in 4 days on Kodak Type T Industrial X-ray film with the exposure beginning when the radioactivity level was 1 uCi per gram of substrate.

Fortunately, the fine-grain commercial x-ray film generally used for this work exhibits a broad exposure latitude when the latent image is produced by electron interaction, and the emulsion integrates the exposure provided by the decaying radionuclides. Thus, even with relatively low radioactivity concentrations and short half-lives, usable images usually can be obtained. Exposures seldom have to be longer than two weeks with microcurie levels of radioactivity and the judicious choice of a commercial film.

Usually one or two strips containing four sections each are retained for autoradiography and as many as six strips are placed on each 12.7-cm x 17.8-cm piece of film for exposure. Sufficient numbers of the sections are taken to allow exposure of several film types as well as additional single sections for test exposures on small pieces of the selected films. Termination of exposure for a particular full-size film is then determined by development of the small test pieces after reasonable exposure times in a light-tight box.

In some cases, the major exposing radiation is sufficiently energetic to produce exposure of both emulsions of a double emulsion film such as Kodak Type T. This additional exposure of the emulsion on the back side of the film (that not in contact with the sample) may be undesirable because it adversely affects resolution. To avoid this problem, the film is developed while taped to a slightly larger plastic sheet to prevent development of the back emulsion. After development is complete, the plastic sheet is removed to allow the "hypo" solution to dissolve the undeveloped silver halide from the back emulsion. When radiation intensity levels are sufficient, a slower finer-grain film consisting of a single emulsion, such as Kodak Type R, may be substituted to avoid this extra handling. Once the films are developed they are examined by magnification or photographic enlargement.

Results and Discussion

The autoradiographic technique is effective in showing noble metal distribution pattern differences caused by the physical characteristics of particular substrates as well as variations in impregnation techniques. Possibly of greatest importance is the ability to demonstrate the distribution of one metal in the presence of another and to determine the distribution of relatively low concentrations of metals. The examples that follow were chosen from several different experiments, not as a total evaluation of any catalyst system, but principally to demonstrate the versatility of the radiotracer method.

Figure 2 shows autoradiograms obtained with two commercial substrates (designated A and B) impregnated with chloride solutions of platinum and palladium, but only the palladium was radioactive (^{103}Pd). The autoradiogram on the left (substrate A) shows a palladium pattern which is typical for this material and impregnation technique, either with or without platinum included in the impregnation solution. The sharply defined impregnation band measures about 0.24 mm in width, and there is no evidence of metal penetration beyond the band. The type B substrate, however, demonstrates a definite distribution pattern change when chloroplatinic acid is included in the impregnation solution. Without platinum the B material has a palladium distribution identical to A material; when platinum is present, the palladium impregnation band width doubles to about 0.50mm, as shown in the example, with the greatest palladium concentration occurring at the inner periphery of the band.

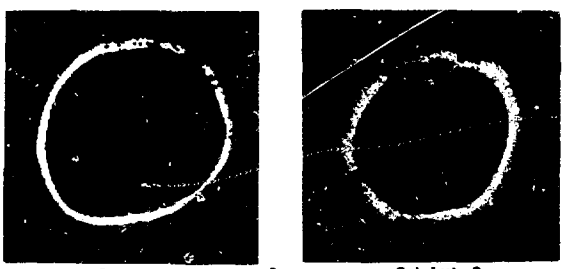

Fig. 2. Autoradiograms Showing Palladium Distribution in Two Commercial Alumina Substrates.

An alteration of impregnation pattern was observed also when studying platinum distributions, but this occurred in the A substrate material rather than the B. Figure 3 autoradiograms show the distribution of platinum (^{195m}Pt) in B substrate material with and without palladium. The platinum obviously extends throughout the bead in both cases. Figure 4, in comparison, shows a dramatic change in platinum distribution in substrate A when palladium chloride is included in the impregnation solution. With palladium absent, platinum penetrated about half way into the bead. When palladium was included, the platinum penetrated throughout the whole bead.

It has been shown that the physical characteristics of substrates, such as pore structure can also influence the distribution of impregnated metals[9]. Other physical differences such as overall bead size could also influence impregnation patterns. This may be the explanation for the patterns observed in a study of rhodium distributions using ^{99}Rh. In this study, autoradiography showed that small beads (2 to 3-mm diameter) typically retained rhodium in a concentrated band at the surface with a lesser but relatively uniform distribution through the remainder of the bead, as illustrated in Fig. 5, right. Larger beads

(3.5 to 5.0-mm diameter), Fig. 5, left, showed a similar surface concentration but also a second heavy concentration of the metal in the central area of the bead.

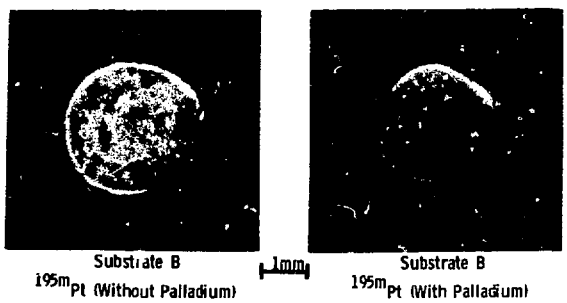

Fig. 3. Autoradiograms Showing Platinum Distribution Unaffected by the Presence of Palladium in One Substrate Type.

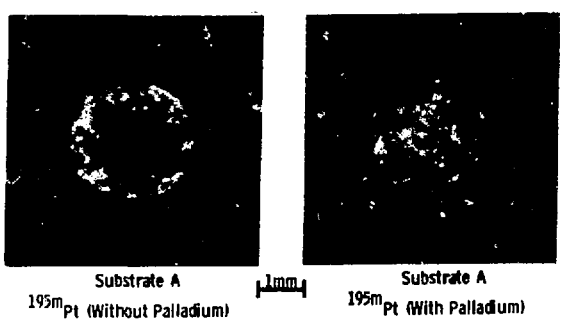

Fig. 4. Autoradiograms Showing the Effect of Palladium on Platinum Distribution in One Substrate Type.

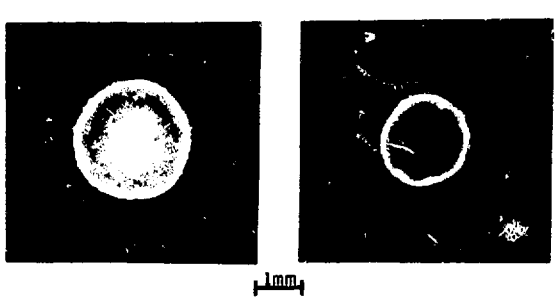

Fig. 5. Autoradiograms Showing Typical Rhodium Distribution Patterns in Large and Small Bead Substrates.

Conclusion

The adaptation of autoradiographic techniques to the study of noble metal distributions in catalyst substrates illustrates but another of the valuable applications of applied nucleonics in industrial research and development. It is not unusual to work long and hard collecting numerical data to provide some sort of visualization or imaging of phenomena under study. Autoradiography provides such information directly.

References

1. Hegedus, L. L. and Summers, J. C., "Improving Automobile Catalysts' Tolerance to Poisoning", presented to the Catalysis Society, Toronto, Ontario, Canada, February, 1975.

2. Shadman-Yazdi, F. and Petersen, E. E., Chem. Eng. Sci., 27, 227, (1972).

3. Corbett, W. E. and Luss, D., Chem. Eng. Sci., 29, 1473, (1974).

4. Wei, J. and Becker, E. R., "The Optimum Thickness of Catalytic Layers in Automotive Catalysis", presented to ACS, Los Angeles, California, April 1974.

5. Hill, R. F. and Mayer, W. J., "Radiometric Method for Determining the Attrition of Platinum and Palladium from Automotive Catalysts", International J. Applied Rad. and Isotopes, (in press).

6. Klimisch, R. L. and Taylor, K. C., Environmental Science and Technology, 7, 127, (1973).

7. Gallopoulos, N. E., Summers, J. C., and Klimisch, R. L., "Effects of Engine Oil Composition on the Activity of Exhaust Emissions Oxidation Catalysts", SAE Paper No. 730598, May, 1973.

8. Lange, W. H. and Smith, V. V., Electrochemical Technology, 6, (11-12), 405, (1968).

9. Hegedus, L. L., GM Research Laboratories, Private Communication, April, 1976.

Proceedings, ERDA X-and Gamma-Ray Symp. Ann Arbor, MI, May 19-21, 1976 (Conf 760539)

ANALYSIS OF NOBLE METAL ON AUTOMOTIVE EXHAUST CATALYSTS BY RADIOISOTOPE-INDUCED X-RAY FLUORESCENCE

M. F. Elgart
Engineering and Research Staff - Research
Ford Motor Company
Dearborn, Michigan 48121

Summary

A technique has been developed for the in-situ analysis of noble metals deposited on monolithic automotive exhaust catalysts. This technique is based on radioisotope-induced X-ray fluorescence, and provides a detailed picture of the distribution of palladium and platinum on catalyst samples. The experimental results for the cross section of a monolithic exhaust catalyst, analyzed in increments of 0.2 cm^3, are compared with analyses for palladium and platinum obtained by instrumental neutron activation analysis.

Introduction

The extensive use of automotive exhaust catalysts to comply with State and Federal regulations for automobile exhaust emissions has necessitated the development of various analytical techniques for measuring catalyst composition. Properties such as activity and durability have been related to catalyst compositions determined by wavelength-dispersive X-ray fluorescence, neutron activation, atomic absorption, and electron microprobe analyses. Tracer studies have been used to evaluate the durability of experimental catalysts.

Each of these techniques used for the analysis of platinum and palladium, and other elements, on monolithic exhaust catalysts requires the physical and/or chemical destruction of the catalyst sample. The various techniques are required so that the analysis of samples over a wide range of sizes can be optimized. These factors prompted the development of radioisotope-induced X-ray fluorescence as an analytical technique. A low energy photon spectrometer [planar Ge(Li) detector] was used to enable information for several elements to be obtained simultaneously, thus decreasing the time for analysis of each sample considerably. Suitable source-detector geometry and collimation were used to provide "active" volumes in space of various dimensions. A catalyst sample placed in such an "active" volume fluoresced only in that part of itself which intersected the collimated beam from the radioactive source. The collimated detector measured the X-ray fluorescence spectrum from only that part of the catalyst sample coincident with both the beam from the source and the "view" of the detector. The distribution of palladium and platinum throughout the catalyst was obtained using this technique. For comparison purposes, the cross section of a monolithic catalyst analyzed by X-ray fluorescence for palladium and platinum in increments of 0.2 cm^3 was also analyzed by instrumental neutron activation analysis.

Experimental

Sources

The radioactive isotope used in these experiments was thulium-170, which has a half-life of 128 d and decays with the emission of a gamma-ray of 84 kev in energy. Thulium oxide was compressed into pellets and sealed in high-purity quartz tubing. The ampoules were then irradiated in a thermal neutron flux of approximately 3×10^{13} $n/cm^2/sec$ for different periods of time to provide sources of various intensities. Thulium-170 is produced by the n, gamma reaction of thulium-169, which has an isotopic abundance of 100% and a thermal neutron capture cross section of 125 barns. Each ampoule was removed from its aluminum irradiation container approximately two weeks after the end of irradiation and placed in a combination source holder and shield. These holders were fabricated from lead and aluminum at the Phoenix Memorial Project, University of Michigan. Each sample holder was designed to have interchangeable inserts, which could provide a simple way of changing the collimation for a particular source.

Equipment

The detector used for these experiments was a low-energy photon spectrometer (Ortec, Inc.) which was connected to an Ortec model 472 spectroscopy amplifier. Spectra were acquired on a Nuclear Data model 4410 computer-based multichannel analyzer, which was also used to deconvolute the spectra. Samples analyzed by instrumental neutron activation analysis utilized the same analyzer and a 15.7% Ge(Li) detector (Ortec, Inc.) used simultaneously with the low-energy photon spectrometer.

Analysis by X-Ray Fluorescence

A one centimeter thick monolithic catalyst cross section was analyzed in increments of approximately 1 x 6 channels (0.2 cm^3) for palladium and platinum by radioisotope-induced X-ray fluorescence. Suitable collimation inserts were determined by the specific source-sample-detector geometry used. Catalyst cross sections were analyzed for 1200 seconds at each incremental position. The sample was then reversed (so that the side closer to the detector was now closer to the source) and the procedure repeated. Background from the catalyst substrate was obtained by analyzing a sample blank (a catalyst with no palladium or platinum present) and this background was subtracted from each spectrum. The $K\alpha_1$ line of platinum (66.820 kev) and the $K\alpha_1$ plus $K\alpha_2$ lines of palladium (21.175 kev and 21.018 kev respectively) were integrated for each incremental position of the catalyst cross section, corrected for the decay of the radioactive source. Comparison of the X-ray fluorescence spectra for palladium and platinum intensities for the two sample orientations at the same

channel position agreed to be better than ± 5% in all cases. Therefore, the X-ray intensities at each position were taken to be the sum of the two measurements. These intensities were used as a comparative measure of palladium and platinum present.

Analysis of Instrumental Neutron Activation Analysis

After analysis by radioisotope-induced X-ray fluorescence, the catalyst sample was cut up into appropriate 1 x 6 channel segments to provide samples for instrumental neutron activation analysis. These samples were irradiated together for 15 minutes in a thermal neutron flux of approximately 1 x 10^{13} n/cm^2/sec. During irradiation, the samples were rotated at 15 rpm to minimize any flux variations. Samples were then analyzed (30 hours after irradiation) simultaneously by the low-energy photon spectrometer and the 15.7% Ge(Li) detector. The 88 kev gamma-ray of silver-190 m (low-energy photon spectrometer) was used for the analysis of palladium, and the 158 kev gamma-ray of gold-199 [15.7% Ge(Li) detector] was used for the analysis of platinum. Integrated counts from a Gaussian peak-fit program for each incremental position were corrected for decay and used for the comparative measure of palladium and platinum present.

Results

Data for palladium and platinum loadings on small increments (1 x 6 channels) on a one centimeter thick cross section of a monolithic catalyst were normalized to the position closest to the edge of the catalyst (channel 1). Figure 1 (palladium) and 2 (platinum).

To compare the results of the two techniques, a constant k (for each specific position) was defined to be

$$k = \frac{\text{Ratio by XRF}}{\text{Ratio by INAA}},$$

where: XRF = radioisotope-induced X-ray fluorescence
INAA = instrumental neutron activation analysis

Ideally k should be constant for the platinum XRF/INAA ratio and constant for the palladium XRF/INAA ratio.

The values obtained were:

$$k_{Pd} = 1.00 \pm 0.04$$

$$k_{Pt} = 1.03 \pm 0.02.$$

These k values indicate that results obtained by radioisotope-induced X-ray fluorescence and by instrumental neutron activation analysis are in good agreement. Inspection of the data indicates that the distribution of palladium and of platinum differ somewhat on the same catalyst cross section sample.

The technique of radioisotope-induced X-ray fluorescence has also been applied to the analysis of palladium and platinum in whole catalysts and in increments of a single channel on a catalyst cross section. Other results indicate that this technique can be used for the analysis of platinum on exhaust catalysts sealed in steel containers.

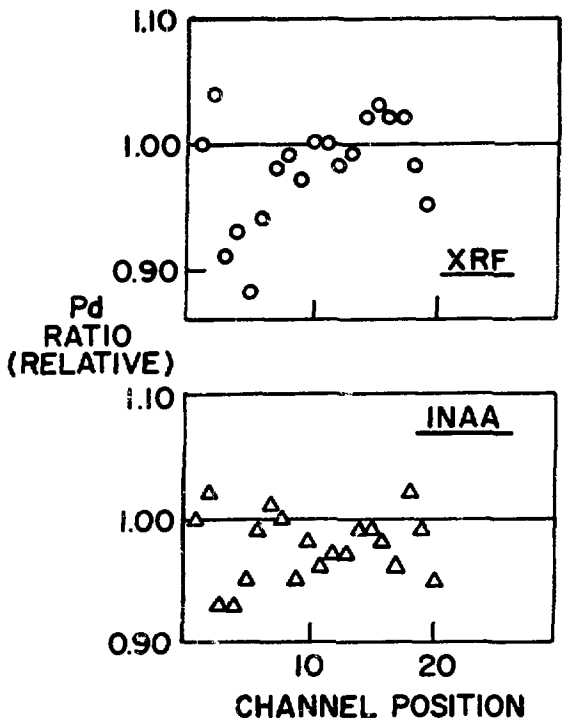

Figure 1. Distribution of Palladium on a Monolithic Catalyst Cross Section

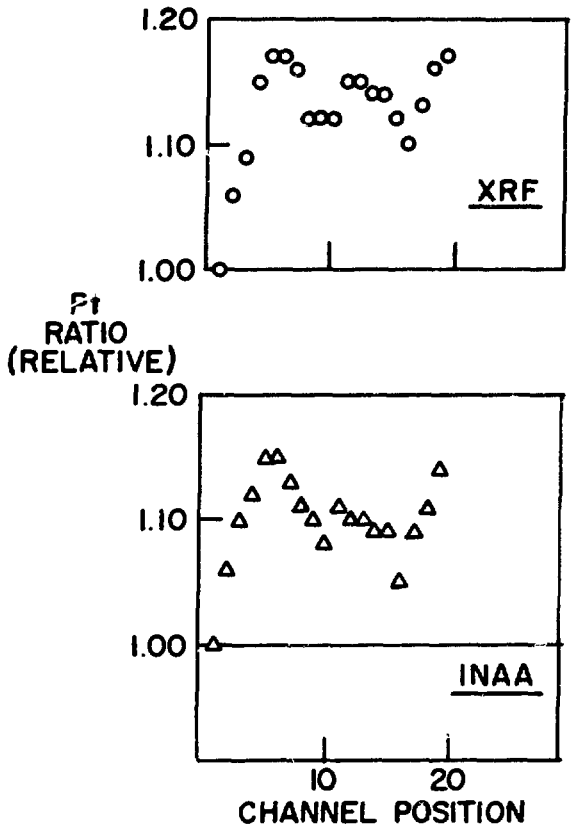

Figure 2. Distribution of Platinum on a Monolithic Catalyst Cross Section

Acknowledgement

The author wishes to acknowledge the collaboration of J. Jones, Laboratory Manager of the Phoenix Memorial Project (University of Michigan) in the preparation of the various sources used in this work.

Proceedings, ERDA X-and Gamma-Ray Symp. Ann Arbor, MI, May 19-21, 1976 (Conf 760539)

A STUDY ON THE APPLICATIONS OF BACKSCATTERED GAMMA-RAYS TO GAUGING

Masao KATO, Otomaru SATO and Hideo SAITO

Institute of Industrial Science, Univ. of Tokyo
22-1, Roppongi 7 chome, Minato-ku, Tokyo 106 Tel. 03-402-6231

Summary

Backscattering of gamma-rays has for the past long time been used for measuring density, concentration and thickness. And the input of these gauges is usually composed of mixture of single and multiple backscattered gamma-rays. In the present experiment, these two components were measured separately by changing collimators of different size which were placed in front of detector. The experimental configuration is shown in Fig. 1.

^{60}Co, ^{137}Cs and ^{192}Ir of several tens mCi respectively were used as gamma sources, their beams were projected in direction of 45° to the surface of scatterer and the detector, scintillation counter with 2"ϕ x 2" NaI(Tl) scintillator, was directed normally to the surface of scatterer and was installed on a small push-car movable parallel to the surface.

In case of low atomic number scatterer the multiple backscatter component increases to considerable extent. Comparison of thickness measurements by detecting multiple backscatter component only and single backscatter one only showed that the former was, for instance, 1.4 times as long as the latter in the maximum measurable range with carbon brick wall. Conventional thickness measurement using total backscatter is almost as same as single backscatter type in the maximum measurable range.

A new application of single backscattered gamma-rays was tried in density gauging. With conventional total backscatter type density gauge, there is a peak of backscatter at about 1 g/cm^3 and hence such a density gauge is available in the small range as only a little more than or less than 1 g/cm^3. In comparison with this conventional gauge a newly developed one is able to measure density over the range from 0.5 to 3 g/cm^3 by setting the distance between source and detector, for instance, tens cm in the configuration of Fig. 1.

Introduction

Taking advantage of the phenomena that the intensity of scattered gamma-rays varies depending on thickness and density of scatterers backscatter type thickness and density gauges have been well developed and in routine use. Backscattered gamma-rays involve single and multiple scatter components. In order to measure these components selectively the following means can be used: One is to fit up detector head with collimater and another to analyze pulse height of signals from detector.

By detecting multiple scatter component with the aid of the above techniques it can be done to extend measurable range of thickness of low atomic number materials. On the other hand, by detecting single scatter component only and by fixing the distance between source and detector to be a few tens cm in the configuration as shown Fig. 1 it is achieved to measure the density linearly over such a wide range as from 0.5 to 3 g/cm^3.

Thickness Gauge[1]

The experiment was carried out using gamma-rays of ^{137}Cs and in the configuration as shown in Fig. 1.

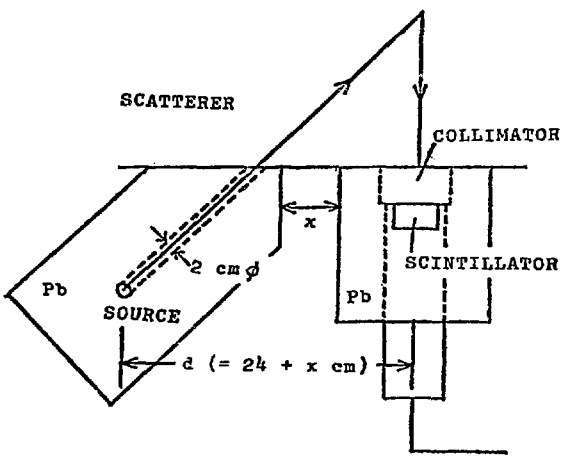

Fig. 1 Configuration of backscatter type gamma-ray thickness and density gauges developed in the present study

Incident angle of gamma-rays collimated to 20 mm in diameter upon a scatterer was 45° and 135° backscattered gamma-rays was detected with 2"ϕ x 2" NaI(Tl) scintillator. When fitting detector head with collimaters of different size backscattered gamma-ray energy spectra were observed as shown in Fig. 2. It is found from the result that multiple backscatter component disappears by degrees as inner diameter of collimater is lessened, mostly disappearing in case of 10 mm inner diameter.

For detecting multiple backscattered gamma-rays a combination method using collimater of 50 mm inner diameter and pulse height analyzer was adopted. Fig. 3 shows gamma-ray spectra of saturated scattering corresponding to the respective

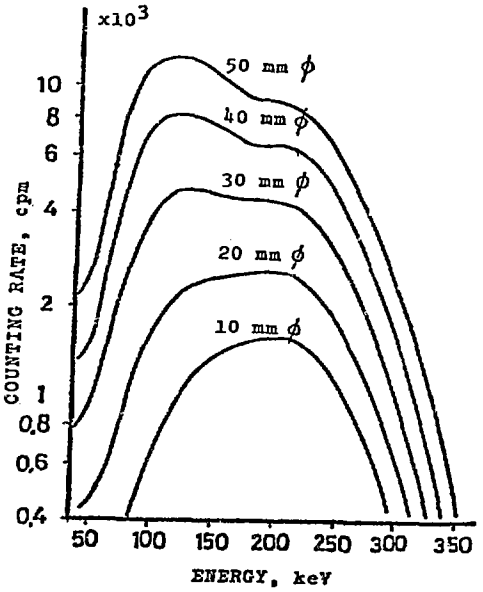

Fig. 2 Energy spectra of 135° back-scattered photons (^{137}Cs) corresponding to inner diameter of collimater

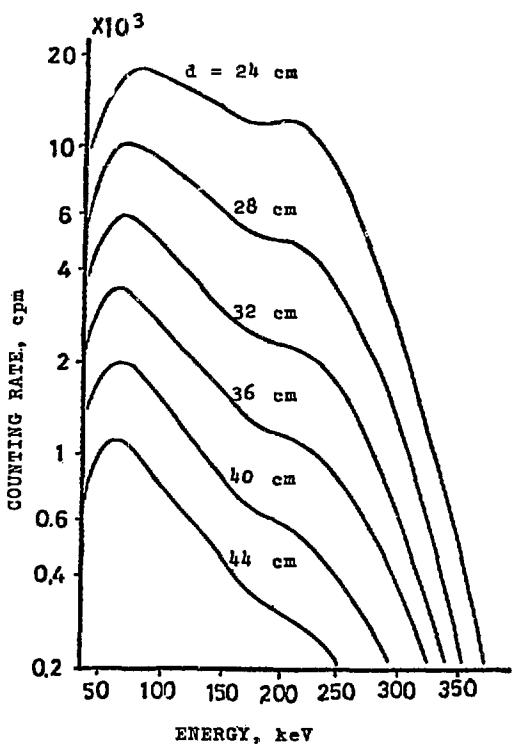

Fig. 3 Energy spectra of backscattered photons corresponding to source—detector distance, where inner diameter of collimeter is 50 mm

lengths of distance (d) between source and detector of 24, 28, 32, 36, 40 and 44 cm. As the length increases the single scatter component decreases and thus the multiple scatter component comes to have the majority. When the thickness of scatterer is changed under the same condition the integration value of multiple scattered gamma-ray energy spectrum, that is the number of multiple scattered photons, must be changed. This kind of experiment was carried out with carbon brick work as a scatterer and resulted in Fig. 4, where the energy range was 29~158 keV and the inner diameter of collimater 50 mm. In comparison with this the number of single scattered photons only was measured, where the energy range 116~262 keV and the inner diameter of collimater 10 mm. The number of photons in the latter experiment was lowered one order, which is mainly due to the reduction of diameter of collimater.

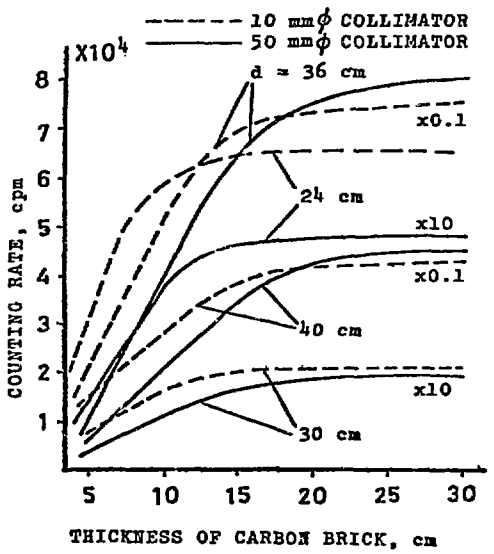

Fig. 4 Counting rate of backscattered photons depending on thickness of carbon brick (gamma source: ^{137}Cs)

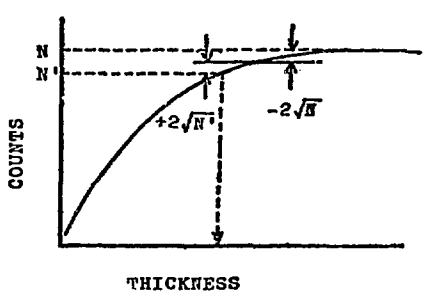

Fig. 5 Determination of measurable range of thickness

Now, as shown in Fig. 5, the counting rate corresponding to saturation thickness is N, the one a little lower than N is N', and the thickness corresponding to N' is the upper limit of measurement provided that the following equation holds:

$$N - 2\sqrt{N} = N' + 2\sqrt{N'} \qquad (1)$$

The equation (2) can be derived from (1),

$$N' = (\sqrt{N} - 2)^2 \fallingdotseq N - 4\sqrt{N} \qquad (2)$$

Thus, the measurable range of thickness can easily be calculated.

In this way, these values on aluminium, concrete, carbon and wood using ^{137}Cs gamma-rays were obtained as shown in Table 1. The values in parentheses are the ones obtained by measurement of single scattered photons only.

Table 1 Measurable ranges of thickness of low atomic number materials

Materials \ d (cm)	24	30	36	40
Aluminium	13(9)	14(11)	16(12)	16(13)
Concrete	13(9)	15(12)	18(14)	19(15)
Carbon brick	20(13)	22(15)	25(16)	26(16)
Wood	33(13)	35(22)	39(25)	43(32)

It is concluded that in the backscatter type thickness gauging of low atomic number materials the measurable range can be extended by measur ing mainly multiple scattered photons and some fractions of single scattered ones.

Density Gauge

Conventional backscatter type density gauge is usually used in the configuration of surface contact. And the output is generally maximized at a certain density of scatterer, $\rho_m(g/cm^3)$, when the distance, d(cm), between source and detector is fixed.[2]

On the other hand, in general, the following equation holds between d, ρ_m and mass attenuation coefficient, $k(cm^2/g)$:

$$d \cdot \rho_m = 1/k$$

In the case when primary gamma-rays (0.662 MeV) from ^{137}Cs attenuate their energy in consequence of Compton scattering k shows approximately constant value, 0.07 cm^2/g, for various kinds of scatterer. In accordance with this, it can be said that when d increases ρ_m must decrease. Fig. 6 seems to show the above tendency though it is not so clear, which may be due to the experimental condition that both primary and scattered gamma-rays are strongly collimated in the

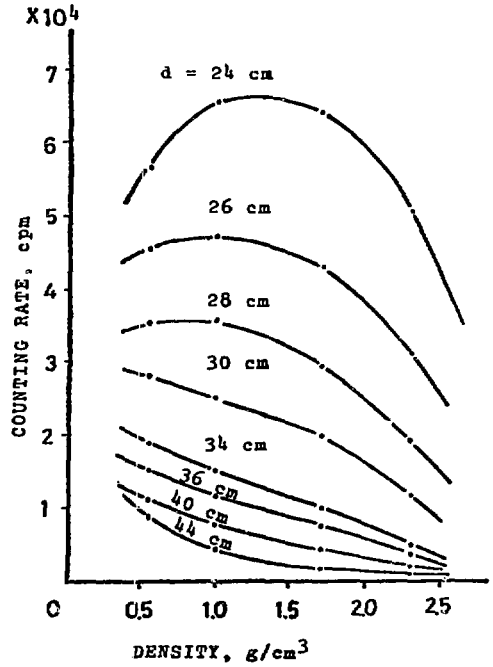

Fig. 6 Characteristic curves of single backscatter type density gauge

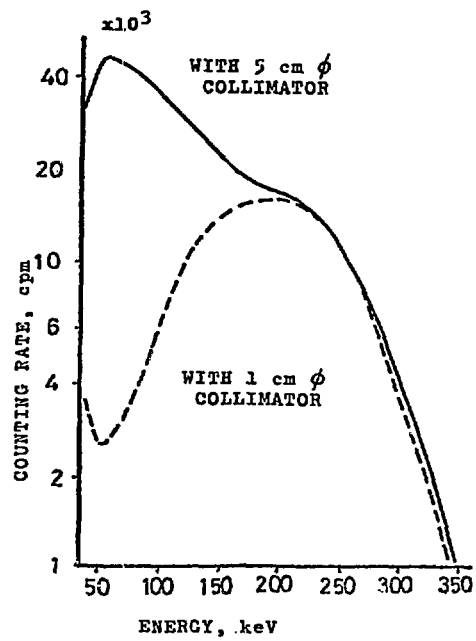

Fig. 7 Energy spectra of 135° backscattered photons (gamma source: ^{137}Cs)

present case. The authors intend to clear this point of question in another experiment.

When source-detector distance increases the convex curve of output vs density is flattened to sloped linear line and simultaneously the peak of curve moves toward lower density, (Fig. 6) and the above tendency comes to more remarkable as multiple scatter component is eliminated from the output of single scatter component by strong collimation, the obvious effect of which can be seen in Fig. 7. For carrying out these experiments, wood block, water, carbon brick and concrete block were used as materials of different density. And the characteristic curve was changed from convex into pseudo-linear at d = 34~36 cm and furthermore into concave curve at a little longer than the above length.

Making use of this pseudo-linear line it can be done to measure the density over wide range from 0.5 g/cm^3 to 3.0 g/cm^3. The characteristic holds as same even with the other gamma-ray sources such as ^{60}Co and ^{192}Ir as ^{137}Cs does, which is shown in Fig. 8. The result that the slope of characteristic line is steepest for ^{137}Cs shows the highest sensitivity in density gauging with the gamma-ray source of ^{137}Cs.

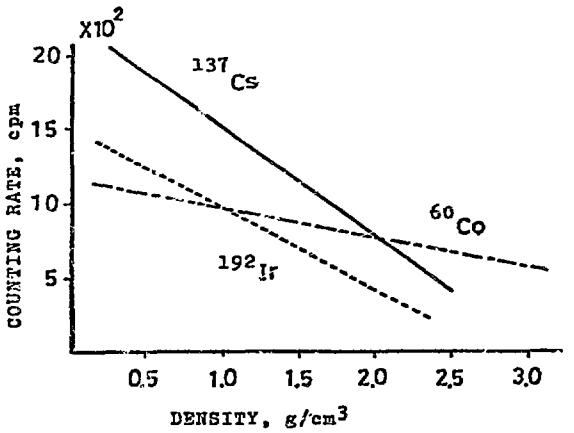

Fig. 8 Characteristics of density gauging

References

1. M. KATO, O. SATO and H. SAITO: "Thickness measurement of carbon brick by multiple backscattered γ rays" Seisankenkyu 25 (12), 541, 1973 (in Japanese)

2. D. Taylor and E. Pirie: "The design of gamma backscatter density gauges" IEEE Trans. on Nucl. Sci. NS-19 (1) 233, 1972

Proceedings, ERDA X-and Gamma-Ray Symp. Ann Arbor, MI, May 19-21, 1976 (Conf 760539)

COMPOSITION COMPENSATED PAPER ASH GAUGE

Orval L. Utt and Boong Y. Cho
Industrial Nucleonics Corporation
Columbus, Ohio

Introduction

In 1960, Murray and Johns measured clay coating on paper using a low-energy x-ray spectrometer.[1] They found variations in raw stock, adhesive and types of clay did not influence the measurement significantly. They also stated that titanium dioxide and calcium carbonate can be measured as easily as clay by using different mass attenuation coefficients. In the paper industry, however, clay and TiO_2 are frequently mixed with each other, often with unknown and variable proportions.

We have recently developed a low-energy x-ray gauge which measures the total ash content regardless of the relative proportion of the above binary mixture. The technique also applies for the mixtures of calcium carbonate and clay, and of calcium carbonate and titanium dioxide.

The transmittance of low-energy x-rays is dependent on the basis weight (weight per unit area) and moisture content of the sample in addition to its dependence on ash. Therefore, it is necessary to measure and correct for the changes of basis weight and moisture before the ash content can be determined.

Measurement Principle

The transmittance of low-energy x-rays through paper can be expressed as:[2]

$$T = \exp\left(-(\mu_A W_A + \mu_f W_f + \mu_w W_w)\right) \quad (1)$$

where μ_A, μ_f and μ_w are the total attenuation coefficients, and W_A, W_f and W_w are the weights per unit area of ash, fibre and water, respectively. Re-arranging the equation, one obtains:

$$W_A = \frac{1}{(\mu_A-\mu_f)}\left\{\ln(1/T) - \mu_f BW - (\mu_w-\mu_f)W_w\right\} \quad (2)$$

where $BW = W_f + W_A + W_w$. For most applications, the weight of water is generally less than 10% of the basis weight, and $(\mu_w-\mu_f)$ is approximately 30% of μ_f. Thus, the last term in the curly bracket of equation (2) is a relatively minor correction term. From equation (1),

$$\ln(1/T) = (\mu_A-\mu_f)W_A + \mu_f BW + (\mu_w-\mu_f)W_w \quad (3)$$

If true basis weight and the water weight per unit area are accurately known, then the weight of ash can be determined within the accuracy limit of the x-ray transmittance measurements. The sensitivity, or the percent change in transmittance per percent change in clay content is obtained from:

$$\frac{\partial T/T}{\partial W_A/BW} = \frac{BW}{T}\frac{\partial T}{\partial W_A} = -(\mu_A-\mu_f)BW \quad (4)$$

which is directly proportional to the basis weight. This value becomes approximately unity at 60#/3000 feet squared with the particular x-ray spectrum designed for the gauge. Thus, 0.1% transmittance measurement accuracy corresponds to 0.1% ash measurement accuracy.

The effect of moisture measurement error is negligible since the whole moisture term is only a minor correction term. The effect of basis weight measurement error can be estimated from:

$$\frac{dT}{T} = -(\mu_A-\mu_f)dW_A - \mu_f d(BW) - (\mu_w-\mu_f)dW_w = 0 \quad (5)$$

or

$$\frac{\partial W_A}{\partial (BW)} = \frac{-\mu_f}{(\mu_A-\mu_f)} \quad (6)$$

Since $(\mu_A-\mu_f)$ is approximately three times μ_f, 1% error in the basis weight measurement will cause 0.33% error in the computed percent ash.

Attenuation Coefficients of Clay

Since the x-ray method of ash measurement is based on the preferential absorption by higher atomic number elements, the atomic composition of ash is an important parameter. Even though Murray and Johns observed no significant effects from various types of clay, chemical composition of clay was obtained from the Handbook of Chemistry and Physics, and also from a TAPPI monograph. Table I shows the contributions from various molecular compounds in and the total attenuation coefficients of various types of clays, crude and washed, at 6 keV. Georgia, South Carolina and English clays represent most of the clay additives used in the paper industry. The variations in the total attenuation coefficients are ±1.4% from the mean. Since the total percent ash content seldom exceeds 30%, the actual measurement error due to these variations is typically ±0.1% to ±0.25% and will not generally exceed ±0.4%. In extreme cases, the measurement accuracy can be improved by calibrating the gauge for the specific source of clay.

Description of the Gauge

The complete measurement system consists of:

(a) X-ray transmission modules;
(b) Beta gauge for basis weight measurement;
(c) Moisture gauge for water weight measurement and;
(d) ash computer which performs the mathematical operations indicated by equation (2).

The x-ray transmission heads further consist of:

(a) Low-energy, low power x-ray tube,
(b) Reference x-ray detector,
(c) Measurement x-ray detector,
(d) Regulated anode and filament power supplies,
(e) Anode current control circuitry and,
(f) Temperature controllers and window air-wipe.

The x-ray measurement device intended for on-line industrial process measurement has to meet rather stringent qualifications, such as:

(a) Simplicity,
(b) Stability both in intensity and spectral quality,
(c) Reliability,
(d) Immunity to changing environmental conditions,
(e) Immunity to geometrical misalignments, and
(f) Small size and light weight.

Simplicity is one of the most important qualifications of any on-line measurement device. It is the fundamental basis of achieving other qualifications listed above. For example, if a guage is designed to produce a minimum amount of heat, it will considerably simplify the gauge, since no forced cooling is required. This, in turn, greatly improves the reliability of the system. Furthermore, the possibility of the loss of stability due to improper functioning of the cooling system will not exist. The tube used for the measurement system consumes less than 5 watts total electrical power including the filament.

The stability of the system has been achieved through several steps of stabilization techniques. The anode voltage and current are monitored and controlled at the x-ray tube. The actual x-ray output is monitored using a transmission-type ionization chamber. Thus, the transmittance of x-rays through the sample is computed by taking the ratio of the measurement detector signal to the reference detector signal, eliminating the effect of

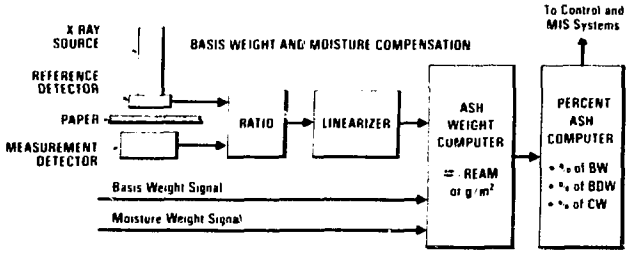

FIGURE 1: SIGNAL PROCESSOR

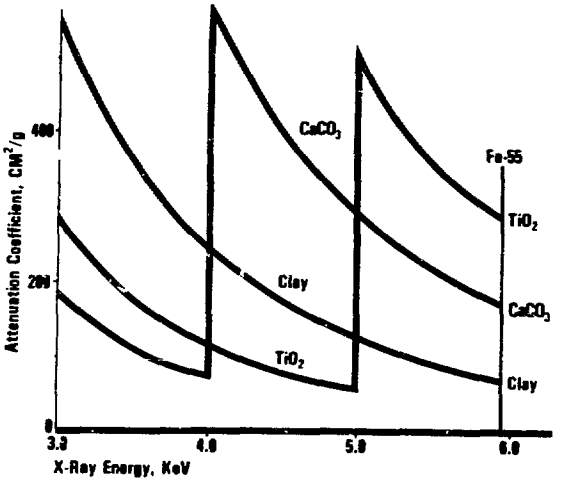

FIGURE 2: ATTENUATION COEFFICIENTS

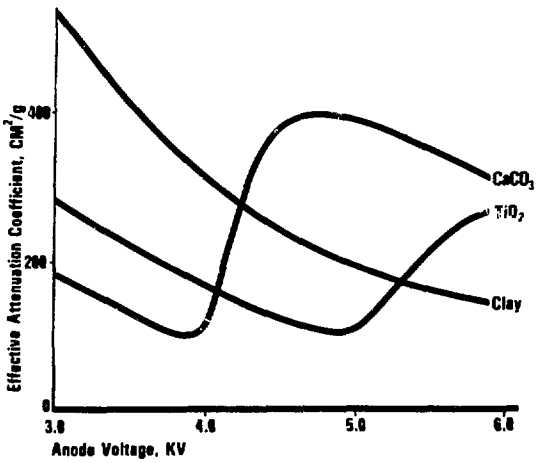

FIGURE 3: ANODE VOLTAGE DEPENDENCE OF EFFECTIVE ATTENUATION COEFFICIENTS

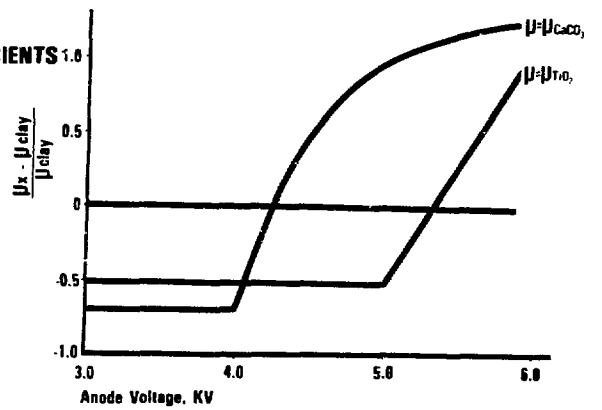

FIGURE 4: NORMALIZED ATTENUATION COEFFICIENTS

any short term fluctuation of the anode current. Periodically, the measurement modules are scanned off the paper web and the transmittance signal is compared against a reference voltage to eliminate the long-term drift which may still exist.

The reliability of the system is achieved by general selection of high reliability components and by derating and shock mounting critical components. For example, the actual anode current is essentially one-tenth of rated currents of the high voltage supply and of the x-ray tube. Up-times exceeding 99% are essential in industrial process measurement and control; conservative design insures that these objectives will be met.

The gauge generally needs to be scanned across the paper web to determine the distribution and the average value of ash content. Since the x-ray source module and the detector module are scanned separately using a pair of chains or metal tapes, misalignment of modules may occur during the scanning. Thus it is important to design the modules such that they are immune to misalignment.[3]

Composition Compensation

In laboratory type measurements, the instrument designers are often concerned with the ultimate detection limits. This is obvious if one inspects the review articles of various measurement techniques including those of low-energy x-rays. For on-line measurements, however, the ultimate success of most measurement devices heavily depends on the immunity to extraneous variables such as temperature changes, geometrical misalignments, accumulation of dirt, etc. Even the laboratory measurements, the matrix effects and the elemental interference problems have been the major concern in the analytical measurement field. Thus, the elimination of the effects of changing paper ash composition was a major objective in designing the gauge.

The ash in paper is mainly made of clay, titanium dioxide and calcium carbonate. As described in the previous section, the composition of clay is reasonably consistent regardless of its origin with respect to the x-ray technique of ash measurement. Many different types of paper contain clay and clay ash only. For these, the x-ray spectrum may be selected to achieve proper sensitivity and measurement range of basis weight and percent ash only. However, quite frequently some quantity of titanium dioxide is added in the United States to increase brightness and opacity of the paper. In Europe, pure clay, pure calcium carbonate and sometimes their mixture are used.

Referring to Figure 2, it is clear that if a monoenergetic source of low-energy x-ray above K-edge of titanium (4.966 keV) is used, then 1% of titanium dioxide is equivalent to approximately 4% of clay, in attenuating the x-rays. This will create 3% ash measurement error per percent TiO_2. It is one of the dominating reasons why an Fe-55 ash gauge is not as successful as it could be. Often an approach of manually inputting the percent TiO_2 value is used to minimize this error. However, even within a given grade of paper, this percentage will vary since it is controlled to obtain proper brightness and opacity rather than to a fixed percentage. The problem becomes more severe as more recycles are used.

With a broad-band x-ray source, the effective clay attenuation coefficient can be computed from:

$$\mu_{eff} = \int_0^{E_{max}} I(E)\,\mu(E)\,dE \Big/ \int_0^{E_{max}} I(E)\,dE$$

Where I(E) is the x-ray intensity spectrum, $\mu(E)$ is the attenuation coefficient of clay and E_{max} is equal to the anode voltage of the source.

The intensity spectrum, I(E), is a function of the anode voltage and the degree of hardening of the x-rays, and $\mu(E)$ is inversely proportional to approximately third power of energy, E. Above K-edge of titanium

$$\mu_{TiO_2}(E) \simeq 4\,\mu(E),$$

and below K-edge,

$$\mu_{TiO_2}(E) \simeq 0.5\,\mu(E),$$

since there is a factor of 8 jump in the attenuation coefficient of TiO_2 at the K-edge. Thus, the effective attenuation coefficient of TiO_2 is:

$$\mu(TiO_2) = \left[0.5\int_0^{E_K} I(E)\,\mu(E)\,dE + 4\int_{E_K}^{E_{max}} I(E)\,\mu(E)\,dE\right] \Big/ \int_0^{E_{max}} I(E)\,dE$$

This value is a function of the anode voltage and the degree of hardening of x-rays after emission at the target. With an effective hardening that corresponds to 70 mg/cm² of paper fibres, the values of $\mu_{eff}(TiO_2)$ has been computed as a function of anode voltage and plotted in Figure 3. The attenuation coefficient for clay is obtained from

$$\mu_{eff}(Clay) = \int_0^{E_{max}} I(E)\,\mu(E)\,dE \Big/ \int_0^{E_{max}} I(E)\,dE$$

It is seen from the figure that at the anode voltages of 4.2 and 5.3 KV, the attenuation coefficients of $CaCO_3$ and of TiO_2, respectively becomes identical with that of clay. The curves representing the attenuation coefficients of $CaCO_3$ and TiO_2 cross at an anode voltage of slightly above 6 kV. At these cross-over points, the x-ray ash gauge will correctly measure the total ash content of these binary mixtures regardless of their percentages.

By taking the ratio of $\mu_{eff}(TiO_2)/\mu_{eff}(Clay)$ and setting:

$$X = \frac{\int_{E_K}^{E_{max}} I(E)\,\mu(E)\,de}{\int_0^{E_{max}} I(E)\,\mu(E)\,dE}$$

one obtains

$$\frac{\mu_{eff}(TiO_2)}{\mu_{eff}(Clay)} = 0.5\,(1-X) + 4X = 3.5\,X + 0.5$$

At 5.3 KV anode voltage, this ratio becomes unity and therefore,

$$X = \frac{0.5}{3.5} = 0.143$$

If the spectrum is narrow enough to consider $\mu(E)$ to be approximately constant, then the spectrum of source should be shaped such that approximately 14% intensity is above 5 keV to measure clay/TiO_2 mixtures. If the anode voltage deviates from that value both effective attenuation coefficients will change, and the fractional error due to this voltage deviation can be computed from:

$$E = \frac{\mu_{eff}(TiO_2) - \mu_{eff}(Clay)}{\mu_{eff}(Clay)}$$

These values are plotted in Figure 4. It should be noted that even at 5.9 KV anode voltage, the error due to 1% change in TiO_2 will result in approximately 0.9% ash error compared to 3% error for Fe-55 isotope ash gauge. This is, of course, due to the fact that a significant quantity of x-ray photons has energies below titanium K-edge. It should also be noted that below 5.3 KV, the error is always less than 0.5% per percent change in TiO_2.

The first ash system was shipped to Mohawk Paper Company in the state of New York. The test results over a period of approximately two months for various paper types are shown in Figure 5. The basis weight ranged from 31# to 115# per 3,000 square feet, the moisture 4% to 6% and the ash 7% to 20%. The ash consisted of various mixtures of clay, hi-sil and titanium dioxide. A laboratory sample was taken at the end of each reel of paper produced and compared against the last scan average of gauge percent ash to produce the correlation data. The standard deviation was 0.35% ash. A significant portion of this error can be attributed to the fact that the laboratory samples did not represent the total on-line measurement portion of the paper web. Two to three-tenths of one percent ash difference

between two laboratory samples taken from the same paper web is not uncommon.

Conclusion

Both from the laboratory test and on-line experience, it was definitely proven that the Industrial Nucleonics design of-machine x-ray paper ash gauge was insensitive to the relative mixtures of clay and titanium dioxide. The gauge was also tested for the mixtures of clay and calcium carbonate in a limited range of basis weight with a good success. The first gauge shipped has been operating for approximately ten months without a problem of either failure or drift.

References

1. Murray, H.H. and Johns, W.D.: An x-ray absorption technique for measurement of coat weight on paper, Advanced in X-Ray Analysis, Volume 4, Page 309 thru 318 (1960).

2. Hess, C.T.P A laboratory ash gauge for low basis weight paper, TAPPI, Volume 57, Number 12, Page 150 thru 151 (1974).

3. Cho, B.Y. and Utt, O.L.: A new TiO_2 compensated x-ray ash sensor for paper, ISA Industry Oriented Conference and Exhibit, Paper Number 75-611 (1975).

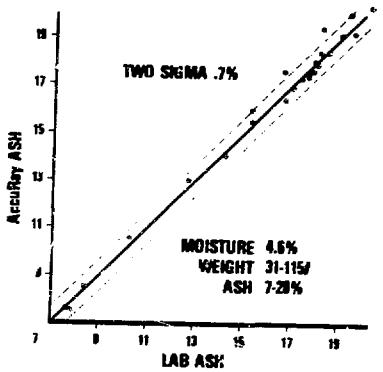

FIGURE 5: ASH CORRELATION

TABLE I

Attenuation Coefficient of Clay at 6 keV.

Chemical Species	Attenuation Coefficient	Chemistry Handbook	Macon, Ga. Crude	Langley, S.C. Crude	English Washed	Dry Bank, Ga. Washed
SiO_2	79.0	35.79	35.71	34.73	36.95	35.63
Al_2O_3	70.2	26.94	26.11	26.75	26.53	27.54
Fe_2O_3	61.3	0.18	0.20	0.83	0.34	0.19
TiO_2	280.2	4.03	3.53	3.92	0.06	3.13
MgO	63.7	0.16	0.30	-----	0.15	-----
CaO	280.9	0.14	1.46	-----	0.37	-----
Na_2O	56.2	0.15	0.20	-----	0.03	-----
K_2O	274.1	0.11	1.34	-----	4.08	-----
H_2O	22.7	3.17	3.36	3.25	2.90	3.16
P_2O_5	82.9	-----	-----	-----	0.08	-----
Fe	76.5	-----	-----	-----	0.18	-----
Total Attenuation Coefficient		70.67	72.21	69.68	71.67	69.65

Proceedings, ERDA X-and Gamma-Ray Symp. Ann Arbor, MI, May 19-21, 1976 (Conf 760539)

THE USE OF ALPHA-PARTICLE EXCITED X-RAYS TO MEASURE THE THICKNESS OF THIN FILMS CONTAINING LOW-Z ELEMENTS

Frederick A. Hanser, Bach Sellers, and Charles A. Ziegler
Panametrics, Inc.
Waltham, MA 02154

Summary

The thickness of thin surface films containing low Z elements can be determined by measuring the K x-ray yields from alpha particle excitation. The samples are irradiated in a helium atmosphere by a 5 mCi polonium-210 source, and the low energy x-rays detected by a flow counter with a thin stretched polypropylene window. The flow counter output is pulse height sorted by a single channel analyzer (SCA) and counted to give the x-ray yield. Best results have been obtained with Z = 6 to 9 (C, N, O and F), but usable yields are obtained even for Z = 13 or 14 (Al and Si). The low energy of the x-rays (0.28 to 1.74 keV) limits the method to films of several hundred nm thickness or less and to situations where the substrate does not produce interfering x-rays. It is possible to determine the film thickness with 50% accuracy by direct calculation using the measured alpha-particle spectrum and known or calculated K x-ray excitation cross sections. By calibration with known standards the accuracy can be increased substantially. The system has thus far been applied to SiO_2 on Si, Al_2O_3 on Al, and CH_2 on Al.

Equipment and Operation

The geometry of the x-ray excitation and detection is shown in Fig. 1. A 5 mCi 210-Po source irradiates a 2.5 cm x 2 cm sample area in a He flow atmosphere. The low energy x-rays are detected by a flow counter about 3 cm below the sample. The flow counter window is 80 $\mu g/cm^2$ stretched polypropylene supported by a 70% open conducting grid. With a 100 cc/min flow of 96% He + 4% isobutane the counter operated stably with 1700V on the central 1 mil wire, and gave about 75% resolution (FWHM) for the 0.28 keV C K x-ray. The flow counter output was amplified, energy selected by a SCA, and counted, generally for one minute periods. The flow for the He atmosphere was about 800 cc/min, with the input near the sample. At this flow rate less than a minute is required to reestablish equilibrium after a sample change, provided the sample opening is not uncovered for more than a few seconds. The He atmosphere is necessary to reduce alpha-particle energy loss and x-ray attenuation. For surface films containing C, N, O, or F, it is also necessary to reduce the background x-rays generated in the air that would otherwise be present.

The x-ray count yields from thick samples were about 3000/min for O x-rays in SiO_2 and Al_2O_3, both for a 5 mCi source and with a background (measured from Si and Al samples) of 2000/min subtracted. For CH_2 on Al the C x-ray count yield was about 13000/min with a background of 3000/min subtracted. For unknown samples the measured count yield (= actual count-background) is generally divided by the count yield from a thick sample to give a relative yield between 0 and 1. This eliminates variations from source decay (210-Po has a 138 day half life), from gas density variations due to pressure and temperature changes, and from small electronic drifts.

The alpha particle irradiated area around the sample was Al for the C and O x-ray measurements, which reduced background for these low energy x-rays. For Al or Si x-ray detection this area around the sample should be covered with a low-Z material like plastic (CH_2) to reduce the background in the Al or Si x-ray region.

Care must be taken to avoid any alpha-particle irradiation of the flow counter window, which would produce a large count rate from detected C K x-rays. The count rate of the detector must be minimized both to avoid excessive dead times with the associated drift problems, and to reduce statistical error from background subtraction.

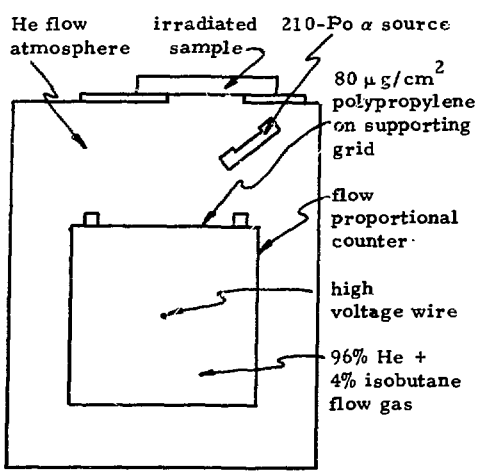

Fig. 1. Outline of x-ray excitation and detection geometry.

Theoretical Analysis

The x-ray count yield from a sample with a surface film thickness t is

$$C_x = T_{He}\, T_W \left(1 - T_{FG}\right) \int_o^t \frac{dt'}{\cos\theta_\alpha} \; x$$

$$\int_o^{E_{max}(t')} dE\; e^{-\mu t'/\cos\theta_x}\, \omega_K\, \sigma_K(E) \; x$$

$$\frac{dN_\alpha}{dE}\left(E_o(E)\right) \frac{S\left(E_o(E)\right)}{S(E)}\; f_W\, \frac{\rho N_A}{M}\; \Omega_d \qquad (1)$$

where the T's are the x-ray transmissions through the He gas, the flow counter window (including the 70% grid transmission), and the 5 cm depth of the flow counter gas, θ_α and θ_x the angles to the sample normal for alpha particle irradiation and x-ray detection, μ the x-ray absorption coefficient in the surface film for the x-ray of interest, ω_K the K-shell fluorescent yield and $\sigma_K(E)$ the K-shell ionization cross section for the element of interest, dN_α/dE the alpha particle spectrum at the sample surface, S the stopping power of the surface film for alpha particles, $E_o(E)$ the energy an alpha particle of energy E at depth t' had at the sample surface, f_W the mass fraction and M the atomic mass of the element of interest in the surface film, ρ the density of the surface film, N_A the Avogadro constant, and Ω_d the detector solid angle as seen from the sample. The energy $E_{max}(t')$ is the maximum alpha particle energy at depth t'.

The x-ray absorption coefficients needed to calculate the T's, and the values for μ, were interpolated from a tabulation by Henke et al.,[1] with compounds not listed being calculated from the component mass fractions and the elemental absorption coefficients. The stopping powers S were calculated from mass fractions and analytic fits to the tabulation of Hill et al.[2]. The K-shell ionization cross sections, σ_K, have not been measured for all elements of interest. The tabulation of Rutledge and Watson[3] gives data for C and Al, but not for O. The theoretical formulation for σ_K by Merzbacher and Lewis[4] shows that $Z_K^4\, \sigma_K/z^2$ should be an approximate universal function of $\eta_K = mE/(MZ_K^2\, Ry)$, where m = electron mass, $Z_K = Z - 0.3$ with Z the atomic number of the target atoms, z = 2, M is the alpha particle mass, and $Ry = 2\pi^2 m e^4/(h^3 c)$ is the Rydberg constant. Using this formulation the universal curve is constructed from the C and Al data, and then used to obtain the O cross sections. Values for ω_K are obtained from the listings of Bambynek et al.[5].

A solid state detector, reduced in effective area to avoid excessive count rates, was used to measure the alpha particle spectrum at several points of the irradiated sample surface. These measurements were averaged to give dN_α/dE. Although θ_α and θ_x vary somewhat over the sample area, as seen in Fig. 1, no attempt was made to correct for these variations, because of the complexity of introducing two additional integrations - as well as a variation in dN_α/dE and Ω_d - in (1). Additional uncertainty is introduced by variations in the T's from gas density changes (temperature and pressure variations), and there are also uncertainties in σ_K, ω_K, the x-ray absorption coefficients, and imprecise measurement of the geometry of Fig. 1. To reduce or eliminate most of the uncertainties the relative x-ray count yield is calculated as

$$Y_x(t) = \left(C_x(t) - B_x\right) / \left(C_x(\infty) - B_x\right) \qquad (2)$$

where B_x is the measured count yield from a blank substrate (e. g., Si), $C_x(t)$ is for the sample (e. g., SiO_2 on Si), and $C_x(\infty)$ is for an infinitely thick (relative to x-ray attenuation and alpha particle ranges) coating (e. g., SiO_2 - thick fused quartz).

The calculated values for (2) ($B_x = 0$ for the calculations) are estimated to be accurate to only about 50% in surface film thickness, primarily because of the neglect of variations in θ_α and θ_x. It is expected that the shape of $Y_x(t)$ vs. t will be more accurate, and that calibration with at least one known sample t should give a correction factor for the thickness scale and thus reduce the error to 10% or less.

Calibration

The measured alpha-particle spectrum for the 210-Po foil source[6], of 5 mCi initial intensity, is roughly flat from 0 to 2 MeV and falls off between 2 and 4 MeV. Using the measured, average spectrum and $\theta_\alpha = \theta_x = 30^\circ$ the relative yield curves were calculated for SiO_2 on Si, Al_2O_3 on Al, and CH_2 on Al. The yield curves were then normalized using measurements on several standards with the surface film thickness measured by other methods.

The SiO_2 on Si results are shown in Fig. 2. Two samples were obtained with 500 Å and 2000 Å of SiO_2 vacuum deposited on Si substrates. The film thicknesses were measured by monitoring the change in the wavelength dependence of the reflection coefficient of a SiO_2 on Si standard which had the same increase in SiO_2 film thickness deposited on it. Using a density of 2.2 g/cm^3, the relative O x-ray yield measurements gave a correction factor of 0.84, i. e., the true SiO_2 thickness is 0.84 times that obtained from the calculated relative yield. Considering the neglect in θ_α, θ_x, and dN_α/dE variations over the sample area, this is good agreement between

calculation and measurement.

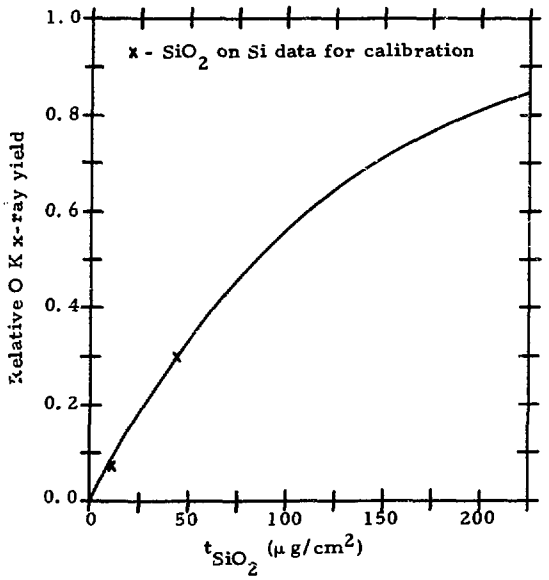

Fig. 2. Experimental O x-ray yields from SiO_2 on Si, and normalized theoretical curve.

The Al_2O_3 on Al results are shown in Fig. 3. Several samples with varying film thicknesses were analyzed by backscattering of 2 MeV [illegible] to give the absolute film thickness in $\mu g/cm^2$. The average correction factor obtained is 0.57, and this has been used to obtain the corrected curve in Fig. 3. The overall agreement is quite good, although the larger deviation of the correction factor from 1 indicates a possible systematic error in the x-ray absorption coefficient or the alpha-particle stopping powers used for Al_2O_3.

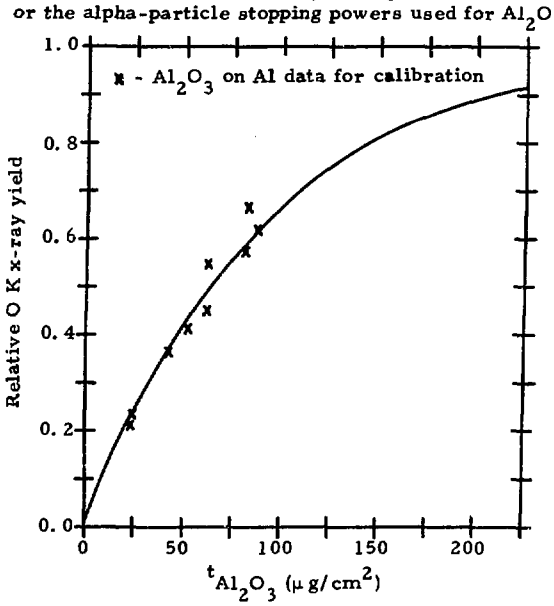

Fig. 3. Experimental O x-ray yields from Al_2O_3 on Al, and normalized theoretical curve.

The results for CH_2 on Al are shown in Fig. 4, where the theoretical curve has been corrected by a factor of 0.91. The various CH_2 films were made by stretching polypropylene with the thicknesses being calculated from the measured transmission energy loss of 5.48 MeV alpha particles from a thin 241-Am source, and the stopping powers from Hill et al.[2]. The agreement between the calculated and experimental relative yields is excellent.

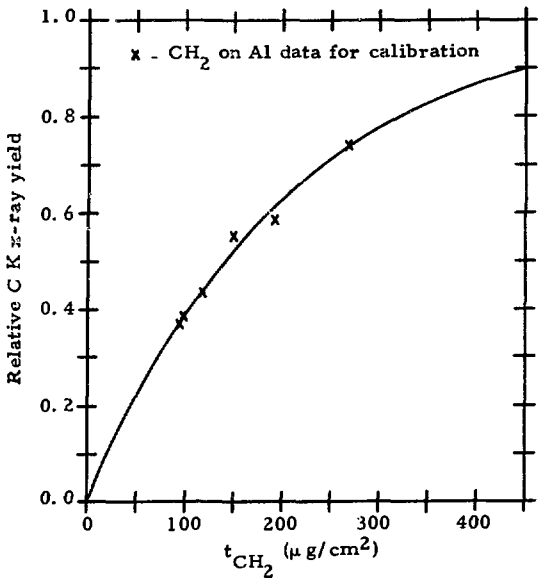

Fig. 4. Experimental relative C x-ray yields from CH_2 on Al, and normalized theoretical curve.

The data in Figs. 2, 3 and 4 show that even without calibration the approximate relative x-ray yield calculations can give 50% accuracy in film thickness measurements. Calibration can increase the accuracy to 10% for relative yields less than 0.75 or so. Because of saturation for thick films, the accuracy becomes increasingly worse for relative yields above about 0.75.

Discussion

The alpha-particle excited K x-ray system, calibrated as described above, has been used for over a year, primarily in making Al_2O_3 on Al film measurements. The system has proved stable for extended periods of time. The 210-Po alpha source was originally 5 mCi, but still proved useful at 0.5 mCi. Since the source spectrum should not change, the same relative yield curve can be used with only the statistical error worsening because of source decay. At 5 mCi the statistical error for a four minute count time per sample is about $\pm$ 2.5 $\mu g/cm^2$ Al_2O_3 at 50 $\mu g/cm^2$ Al_2O_3, and increases to about $\pm$ 10 $\mu g/cm^2$ for 0.5 mCi. The calibration curve (Fig. 3) has at least a $\pm$ 5% error from uncertainties in the standards, so the overall error per measurement is generally about $\pm$ 7% (for a 5 mCi source).

Replacement of the alpha source may require recalibration, if the alpha-particle spectrum is significantly different from that of the old source. Rechecking with the standards should minimize this as a problem. Because of high x-ray backgrounds associated with other available alpha emitters (such as 241-Am), 210-Po with its 138 day half-life may be the optimum source for this system.

By calibration with suitable standards the system can be used readily for C, N, O or F containing films. Best results are obtained if other elements in the substrate do not produce an x-ray (K, L, etc.) near enough in energy to the x-ray being detected to provide interference. Contaminating elements in the film could actually be helpful, since they increase the x-ray count and vary proportionately with the element being measured. What is necessary is that film composition be uniform and that suitable standards be available for calibration.

Sealed proportional counters may be usable with Al, Si, and higher Z elements. A two mil Be window transmits about 20% of the 1.49 keV Al K x-ray, so a sealed counter with reasonable detection efficiency is possible. While this eliminates the flow counter gas and associated equipment, the He flow atmosphere for the alpha-particle irradiation is still required. The K x-ray yield diminishes rapidly as Z increases, so measurements for elements beyond Si become more difficult. For Ca (Z = 20) and above the detection of L x-rays should become possible, though this has not yet been investigated with the system described here.

The system can also be used to measure film thicknesses where the film itself does not produce a detectable x-ray, but the substrate does. For such a case the attenuation of the substrate x-ray can be used to determine the overlying film thickness. Calibration with suitable standards would be necessary to obtain quantitative results, although for very thin, highly x-ray attenuating films, the thickness may be calculable solely from the x-ray attenuation coefficient.

The system outlined in Fig. 1 has proven quite useful in one program where it was desired to make many measurements of Al_2O_3 film thicknesses. The alpha-particle excited x-ray system was quicker and less expensive than the He^+ backscattering method, which required an accelerator and was used primarily to calibrate samples for the x-ray method. The calibrations shown in Figs. 2, 3 and 4 demonstrate the capability of the x-ray method for three different film-substrate combinations. Calibration standards should make it usable for many other combinations.

References

1. B. L. Henke, R. L. Elgin, R. E. Lent, and R. B. Ledingham, "X-Ray Absorption in the 2-to-200 Å Region," Report AFOSR 67-1254 (AD654315) (1967).
2. C. W. Hill, W. B. Ritchie, and K. M. Simpson, "Data Compilation and Evaluation of Space Shielding Problems, Vol. I, Range and Stopping Power Data," Report ER 7777 (N66-15586), Lockheed-Georgia Co. (1966).
3. C. H. Rutledge and R. L. Watson, Atomic Data and Nucl. Data Tables 12, 195-216 (1973).
4. E. Merzbacher and H. W. Lewis, "X-Ray Production by Heavy Charged Particles," in Handbuch der Physik, Vol. 34, 166-192, Springer-Werlag, Berlin (1958).
5. W. Bambynek, B. Crasemann, R. W. Fink, H. U. Freund, H. Mark, C. D. Swift, R. E. Price, and P. V. Rao, Rev. Mod. Phys. 44, 716 (1972).
6. Obtained from Amersham/Searle, Inc., Arlington Heights, Illinois.

Proceedings, ERDA X-and Gamma-Ray Symp. Ann Arbor, MI, May 19-21, 1976 (Conf 760539)

THE APPLICATION OF X-RAY FLUORESCENCE TO THE MEASUREMENT OF ADDITIVES IN PAPER

A. Buchnea and L.A. McNelles
Sentrol Systems Ltd.
Downsview, Ontario, Canada

AND

A. H. Sinclair and J.S. Hewitt
Department of Chemical Engineering & Applied Chemistry
University of Toronto
Toronto, Ontario, Canada

Summary

Titanium dioxide content in paper has been measured by X-ray fluorescence analysis using an ^{55}Fe source and an X-ray proportional counter to determine the feasibility of an on-line instrument. X-ray calibration curves for 60 and 100 g/m^2 paper samples were obtained using neutron activation to measure the titanium dioxide concentration. The predictions of a simple model were in good agreement with the experimental calibration curves. The measurements and calculations were extended to investigate the effects of clay and moisture. The presence of clay has a significant affect on the X-ray fluorescence determination of the titanium dioxide concentration, however, this can be well accounted for by the model. The calculations indicated that the affect of typical moisture levels on the titanium dioxide determination was small and can be ignored.

It is not possible to measure the clay content by X-ray fluorescence, however, preliminary results for the determination of calcium carbonate concentration are promising.

1. Introduction

The papermaking industry has shown increased interest in on-line methods for monitoring the quantities of chemical additives applied in the papermaking process. The primary additives namely, titanium dioxide (TiO_2), calcium carbonate ($CaCO_3$), and "clay" ($Al_2O_3 \cdot 2SiO_2 \cdot 2H_2O$), may serve as filler to improve paper qualities such as brightness and opacity. In order to ensure desired paper properties at acceptable cost, it is necessary to continuously monitor the concentrations of the various types of filler appearing in the end product.

Although concentrations of the various additives can be analyzed chemically in the quality control laboratories associated with each paper plant, the analytical "turn around" time can lead to the production of a significant quantity of sub-standard product. On the other hand, the continuous monitoring of the product during production enables immediate adjustment to the rate of filler addition.

Various types of on-line monitors for filler (or ash) content have been investigated previously. These have been based on techniques of preferential absorption and/or backscattering of ionizing radiation [1,2]. In most of the applications of these techniques, the emphasis has been placed on the measurement of total filler (or ash) content, without regard to the relative quantities of the individual filler constituents. In fact, significant advances have been made [3] in making the measurement of total filler content independent of filler composition. The present paper, in contrast, is concerned with developments toward the monitoring of filler constituents individually. For example, one objective is to monitor the TiO_2 content independently of the clay content. It is anticipated that such advances in additive monitoring, when applied in conjunction with the more conventional basis weight and moisture gauges, will permit the implementation of more efficient plant control strategies to be executed under computer control [4].

Until recently [5], the analytic capability of X-ray fluorescence has not been widely exploited in paper chemistry analysis, particularly for on-line application. This is presumably because of the anticipated difficulty associated with the operation of X-ray sources and detectors under conditions attending the paper making process. It would appear, however, that an instrument based on a radioisotope X-ray source and an X-ray proportional detector would provide continuous information on additive concentrations present in the finished product emerging from the paper machine. The purpose of the present paper is to elaborate on this concept and to report on laboratory studies to assess the feasibility of an on-line instrument composed of relatively simple and reliable components.

The studies have concentrated on the calibration of a prototype X-ray fluorescence analyzer suitable for monitoring either titanium dioxide or calcium carbonate additives. Special attention is given to the affect of basis weight, moisture content, clay content and geometry on the calibration of the instrument for TiO_2. Neutron activation analysis was used to determine the actual concentrations of additives in the paper samples used in the study.

2. Basic Principles

Through an X-ray fluorescence technique, the concentrations of TiO_2, $CaCO_3$ and clay can in principle be determined in the following manner: Photons of suitable energy emitted by a radioactive source are allowed to eject electrons from the K-shells of Ti, Ca, Si and Al, thus producing vacancies in the electronic structure. The subsequent de-excitation of these vacancies produces X-ray fluorescence spectra with photon energies characteristic of the elements. The intensities at the characteristic energies provide information on the quantities of elements present.

The principal components of the K-shell fluorescent spectra for Ti, Ca, Si and Al are shown in Table 1. Although the intensities of Ti and Ca are readily determined, as will be demonstrated, the determination of the aluminum or silicon and hence clay concentration, does not appear feasible using a practical X-ray fluorescence gauge. This is due mainly to the technical difficulties associated with the strong attenuation of the low energy (< 2 KeV) X-rays emitted by the fluorescing silicon and aluminum. Thus an auxiliary technique will be required to monitor the clay content.

There are further possible complicating factors in relating the measured X-ray intensities to the filler concentrations. For example, the Ti X-rays are attenuated by cellulose, water, and any additives present in a particular grade of paper.

Table 1

List of Principal X-ray Lines Excited in Various Filler Constituents by an ^{55}Fe Source (5.9 KeV)

Additive	Chemical Formula	X-Ray Fluorescence Line (KeV)
Clay (Kaolin)	$Al_2O_3.2SiO_2.2H_2O$	1.49 (Al) 1.74 (Si)
Titanium Dioxide	TiO_2	4.51 (Ti)
Calcium Carbonate	$CaCO_3$	3.69 (Ca)

Thus, the Ti X-rays detected for a particular TiO_2 content is somewhat dependent on the total basis weight of the paper and the concentrations of other constituents. Similar effects are also important in determining the concentrations of $CaCO_3$, and clay. Although these effects can be considered negligible in certain ideal operating situations, ways must be found to apply self-consistent corrections to validate information obtained in less ideal situations. A partial assessment of the affect of these inter-component dependencies on the measurement of TiO_2 is obtained experimentally in the present work, and the results are used in conjunction with theoretical calculations to extend the assessment over a wide range of additive concentrations.

3. Experimental

3.1 Prototype Instrumentation

A 5 mCi source of ^{55}Fe (half-life 2.6 years) provided the exciting radiation in these experiments. The absence of higher energy transitions in this pure electron capture decay minimizes background due to backscattered photons. The energies of the Mn KX-ray series are very appropriate for K-shell excitation of Ti and Ca, since they lie just above the K-absorption edge of both elements. The exciting photons penetrate the paper at an angle of ∿60° from the normal. The angle of acceptance of the detector for fluorescence originating in the paper sample was ∿130°. The detector is shielded from the source by a lead absorber. Further details on the geometry can be found in Reference 5.

The fluorescent X-rays were detected with a Reuter-Stokes Model RSG-61 xenon filled proportional counter. This detector has a flat response curve over the energy region of interest; thus, the detection process does not complicate the observed spectrum. The electronic instrumentation, including amplifiers and pulse height analyzers, are conventional.

A specially designed apparatus was constructed from aluminum to hold the paper samples. No part of the holder was in close direct view of the exciting source, thus minimizing background. With this holder, the paper samples could be moved laterally and vertically in a controlled manner to permit the scanning of a desired area of the paper surface.

An X-ray spectrum acquired on an expanded vertical scale with no sample present is shown in Figure 1. The backscattered primary radiation is evident at 5.90 KeV (channel 220). Another peak is present at 2.96 KeV (channel 115). Auxiliary investigations indicated this peak to be due to fluorescent X-rays from the argon in air.

Figure 2 shows an X-ray spectrum acquired for a paper sample containing TiO_2 . The Ti X-ray peak is evident at 4.51 KeV (channel 173). The argon X-ray intensity is diminished in this spectrum relative to that of Figure 1, since a smaller volume of air is being excited.

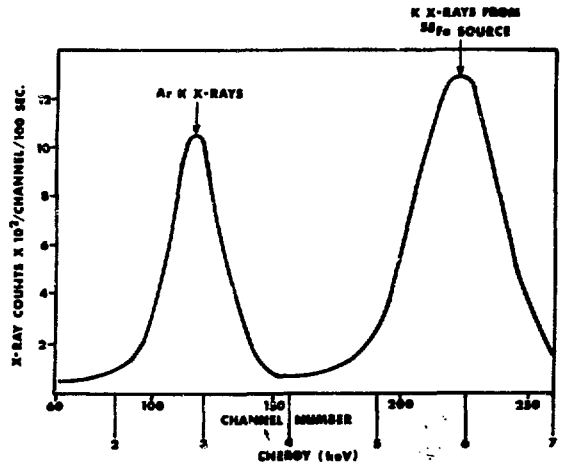

Figure 1. Background X-ray spectrum recorded in prototype ash analyser showing (on an expanded vertical scale) residual intensities at the source energy and at argon X-ray fluorescence energy.

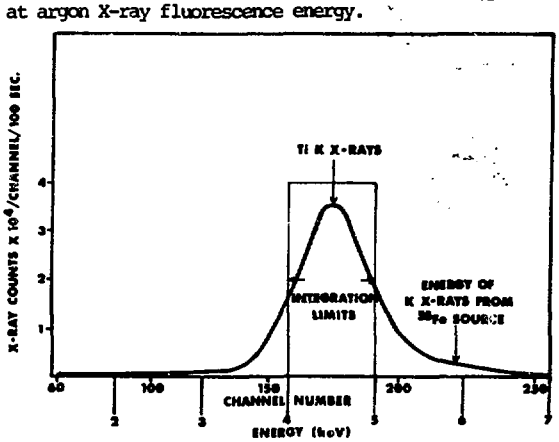

Figure 2. X-ray spectrum recorded for paper sample with typical levels of TiO_2 present.

3.2 TiO_2 Analysis by X-ray Fluorescence Analysis

Experiments The affect of basis weight on the determination of TiO_2 concentration by X-ray fluorescence analysis was investigated. Two groups of paper samples were prepared at total basis weights of approximately 60 and 100 g/m^2 for various concentrations of TiO_2. They were prepared at Abitibi Provincial Papers Limited and were analyzed by colorimetric methods to determine the approximate concentration of TiO_2. In this series of samples, the TiO_2 concentration varied from 0 to 16 g/m^2 and the clay concentration was less than 0.2 g/m^2 for each sample.

In a further study, samples which contained significant concentrations of both TiO_2 and clay were prepared. These were also analyzed by X-ray fluorescence analysis to investigate the attenuation of Ti X-rays due to the presence of clay.

All samples were calibrated for additive content by neutron activation analysis using the SLOWPOKE reactor facility at the University of Toronto. Reference standards were prepared by dissolving accurately weighed amounts of TiO_2 and Al_2O_3 in sulphuric acid. The intensities of the predominent gamma rays in the decay of ^{51}Ti (319.8 KeV, 5.8 min),

and ^{28}Al (1780 KeV 2.31 min) were determined using a large-volume Ge(Li) detector. A typical irradiation time was 3 min. with adequate counting statistics being acquired in a 200 second counting interval.

Titanium X-ray intensities were determined for each of the samples using the set-up previously described. Earlier work [5] had indicated insensitivity to paper-detector distance over a range of 6 mm. The optimum sample position was chosen to obtain maximum reproducibility. The spectra were acquired for 20 seconds and the intensity of Ti X-rays was obtained by summing over the channels 160 to 185 as shown in Figure 2. Fluorescent X-rays from both faces of the samples were counted to determine the effect of possible inhomogeneity of TiO_2 in the paper.

Results The basic experimental results are presented in the form of calibration curves (Figures 3 and 4) showing the counting intensity of the titanium X-rays versus the TiO_2 content, as determined by neutron activation analysis. For this determination, uncertainties due to counting statistics amounted to approximately 0.5% at the one standard deviation level.

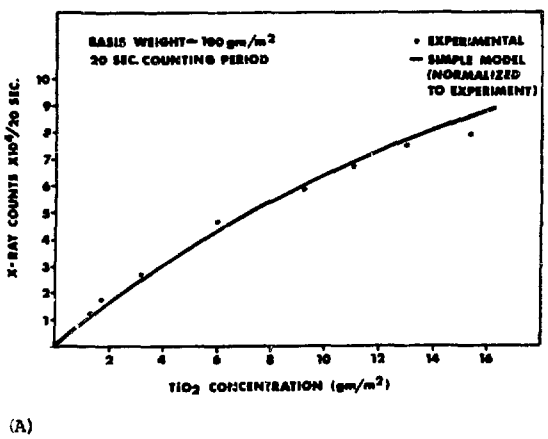

(A)

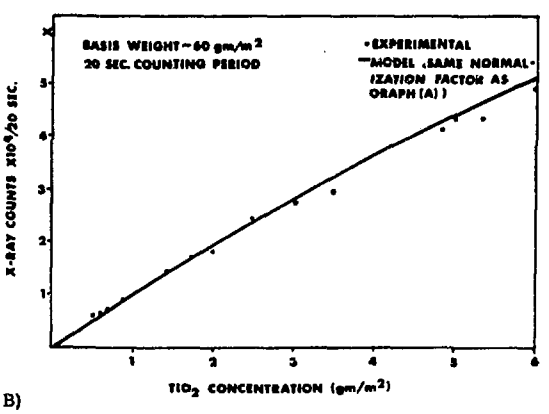

B)

Figure 3. Experimental TiO_2 calibration curves (dots) at basis weights of (A); 100 g/m^2; and (B) 60 g/m^2. Solid lines are predicted curves based on a simple theory in which only one free parameter was obtained by normalizing to the experimental data of (A)

The plotted points in Figures 3A and 3B represent the experimental calibration data which relate the X-ray intensity (measured from one side of the paper) to TiO_2 concentration for total basis weights of 60 and 100 g/m^2, respectively. No other additives were present in significant concentrations. The solid lines in Figure 3 represent the results of a simple theoretical calculation [6,7,1] which accounts for the absorption of the exciting and the fluorescent radiation in the sample. The geometric and efficiency constant K, defined in the calculation, was determined at 100 g/m^2 basis weight by normalizing the theoretical curve to a visual best fit to the data of Figure 3A. The solid line in Figure 3B showing the results of the calculation for the lower basis weight (~60 g/m^2) was determined using the same normalization constant.

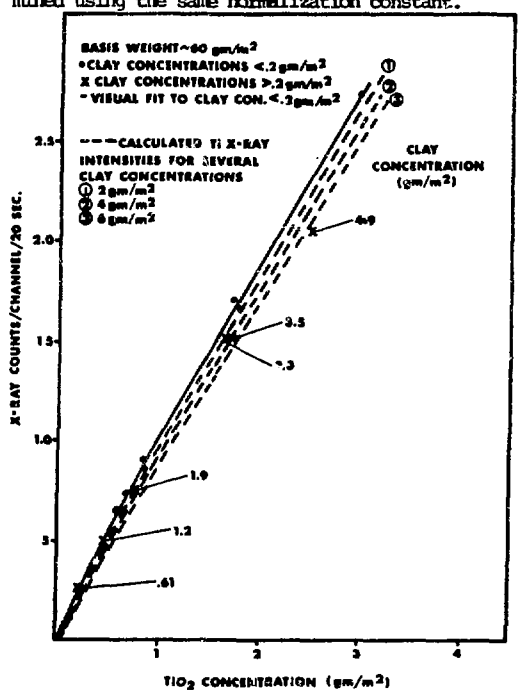

Figure 4. Calibration curves for TiO_2 showing the effect of clay content. Points are from experiments while broken lines are from calculations.

The dotted points of Figure 4 show the experimental calibration curve for the 60 g/m^2 paper samples each of which contain less than 0.2 g/m^2 of clay, as for Figure 3B. The solid line is the best visual fit to the data. The few results for samples of basis weight 60 g/m^2 which contained significant concentrations (>.2 g/m^2) of clay are shown as the crosses (X). The broken curves, also in Figure 4, predict the effect of clay concentration on the titanium X-ray intensities. These curves were obtained using the theoretical model with again the same normalization constant defined for the 100 g/m^2 calibration curve (Figure 3A).

Implications for an On-line Instrument The experimental calibration curves given in Figure 3 provide a realistic indication of the circumstances which would prevail in an operating instrument. For constant basis weight, the X-ray counting intensity is observed to remain sensitive to TiO_2 concentration over a large range extending up to 16 g/m^2. It is also verified that the calibration curve is only

moderately dependent on the basis weight. The theoretical model 6, which takes into account the internal absorption of both the primary and secondary radiation, predicts calibration curves which are consistent with the experimental curves. This confirms that the departure of the experimental curves from a straight line form is due to internal absorption. It is anticipated that such data along with theoretical curves extending to other basis weight regions will provide the basis for performing on-line corrections for basis weight affects on titanium dioxide monitoring in an operating plant. A similar comment may be made with regard to the utilization of the data in Figure 4 to correct for the influence of clay content on the titanium measurements.

All calibration curves shown here are based on the counting rate from one side of the paper sample. The studies of production paper samples have indicated that there is a constant ratio between the X-ray counting rates from the two sides of the paper. Since the ratio is constant at typically, 1.1, the monitoring of only one side of the paper, as would be the case in application, does not introduce systematic error in the determined concentrations.

3.3 Calcium Carbonate

Calcium carbonate is primarily used as a coating in paper production. The relation between detected Ca X-rays and $CaCO_3$ concentration is somewhat more direct in this sample geometry, since basis weight dependence is small. However, the ratio of the concentration of $CaCO_3$ coatings on the sides of the paper may differ widely, depending on the type of paper being produced. For this reason it is expected that a more complex calibration procedure may be necessary for the monitoring of calcium carbonate concentration.

The Ca X-ray counting rate from a coated sample was determined to ascertain the feasibility of determining $CaCO_3$ concentration in this manner. The basis weight of the paper was 80 g/m^2 with a calcium concentration of 4%. An X-ray pulse height spectrum from the coated side is shown in Figure 5. The counting rate of the calcium X-ray peak is sufficient to allow the detection of typical concentrations of calcium carbonate found in paper.

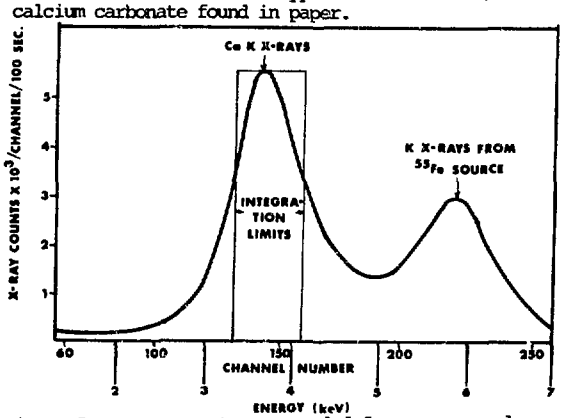

Figure 5. X-ray spectrum recorded for paper sample with typical level of $CaCO_3$ coating present.

In general, calcium carbonate and TiO_2 are not present simultaneously. However, if a particular type of paper were to contain both of these additives the Ti, and Ca X-rays would not be resolved sufficiently by the proportional counter to allow the accurate determination of the additive concentrations. In this situation the replacement of the proportional counter by a solid state X-ray detector would be advantageous.

3.4 Effects of Moisture

The experiments of Section 3.2 indicate the extent to which the TiO_2 measurements using the X-ray fluorescence technique may be affected by variation in basis weight and clay content. A method, based on a calculational procedure, in conjunction with continuous monitoring of these parameters, was indicated for adjusting the calibration data to compensate for these variations. A third parameter which is also subject to variation, but which is generally also monitored continuously, is the moisture content.

To estimate the interference of moisture content on the TiO_2 analysis, the mathametical model mentioned earlier was used to compute the fractional decrease in counting intensity as a function of moisture content for several different TiO_2 concentrations. The results for the case of 100 g/m^2 basis weight are shown in Figure 6.

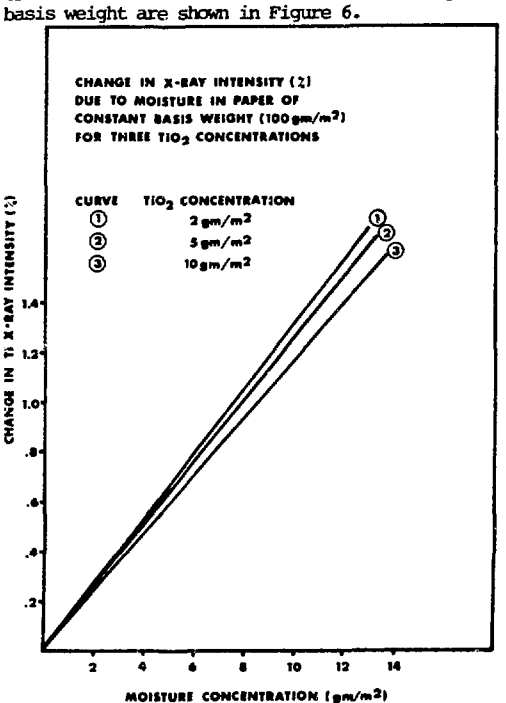

Figure 6. Results of a calculation to show the influence of moisture content on the measurement of TiO_2 by X-ray fluorescence.

It appears from these results that moisture has very little affect on the TiO_2 measurement; in fact, moisture at the level of 10% of the total basis weight would decrease the TiO_2 measurement by only about 1.6%. It is anticipated that in most cases such a small effect can be ignored. In any event, the correction could be applied on a more-or-less continual basis, if necessary.

(cont. on p. 283)

Proceedings, ERDA X-and Gamma-Ray Symp. Ann Arbor, MI, May 19-21, 1976 (Conf 760539)

PLUTONIUM ISOTOPIC MEASUREMENTS BY GAMMA-RAY SPECTROSCOPY

F. X. Haas and J. F. Lemming
Monsanto Research Corporation, Mound Laboratory*
Miamisburg, OH 45342

The nondestructive assay of plutonium is important as a safeguard tool in accounting for strategic nuclear material. Several nondestructive assay techniques, e.g., calorimetry and spontaneous fission assay detectors, require a knowledge of plutonium and americium isotopic ratios to convert their raw data to total grams of plutonium. This paper describes a nondestructive technique for calculating plutonium-238, plutonium-240, plutonium-241 and americium-241 relative to plutonium-239 from measured peak areas in the high resolution gamma-ray spectra of solid plutonium samples. Gamma-ray attenuation effects have been minimized by selecting sets of neighboring peaks in the spectrum whose components are due to the different isotopes. Since the detector efficiencies are approximately the same for adjacent peaks, the accuracy of the isotopic ratios are dependent on the half-lives, branching intensities and measured peak areas. The data presented describes the results obtained by analyzing gamma-ray spectra in the energy region from 120 to 700 keV. The majority of the data analyzed was obtained from plutonium material containing 6% plutonium-240. Sample weights varied from 0.25 g to approximately 1.2 kg. The methods have also been applied to plutonium samples containing up to 23% plutonium-240 with weights of 0.25 to 200 g. Results obtained by gamma-ray spectroscopy are compared to chemical analyses of aliquots taken from the bulk samples.

Nondestructive assay (NDA) is important in safeguarding plutonium since it provides the means to measure all of the feed, product and scrap material generated in the fuel fabrication process. Calorimetry and spontaneous fission detection are two important NDA techniques which can be used to account for plutonium. In order to convert the raw data from these measurements to grams of plutonium, the relative isotopic composition of the samples must be known. This isotopic ratio data can be provided by traditional chemical methods, gamma-ray analysis of solutions or gamma-ray analysis of the bulk sample itself.

Gamma-ray analysis of the bulk sample is attractive because it allows a totally nondestructive measurement. We have taken data principally on three size containers: 1) gallon cans containing 20 to 400 g of plutonium; 2) quart cans containing between 10 and 2500 g of plutonium; and 3) analytical vials containing 1 to 10 g of plutonium. The sample categories include plutonium oxide, plutonium metal, scrap, incinerator ash, ash heels, fluorides, crucibles, slag, scarfings, green cake and mixed plutonium-uranium oxides.

The desired accuracy for all the isotopic ratios is less than 3%. With these uncertainties and a calorimetric uncertainty of 0.25%, the total uncertainty in the plutonium analysis is less than 1%.

*Mound Laboratory is operated by Monsanto Research Corporation for the U. S. Energy Research and Development Administration under contract No. E-33-1-GEN-53.

The basis for the nondestructive measurement of plutonium isotopic ratios using gamma-ray spectroscopy involves the analysis of a spectral group whose members belong to different isotopes. Ratios of the areas of neighboring gamma-ray peaks are related to the isotopic abundance ratios by the expression

$$\frac{I_i}{I_j} = \frac{N_i \lambda_i B_i \varepsilon_i S_i}{N_j \lambda_j B_j \varepsilon_j S_j}$$

where I, N, λ, B, ε, and S are the measured peak area, the number of nuclei, the nuclear decay constant, the absolute branching intensity, the detector efficiency and the self-absorption for the gamma rays with energies E_i and E_j from isotopes i and j, respectively.

The ratios of the relative efficiencies, $(\varepsilon_i S_i)/(\varepsilon_j S_j)$, is assumed to be 1 for gamma rays whose energies differ by less than 10 keV. For the bulk samples, the further assumption is made that the plutonium isotopic composition is constant throughout the volume of the sample.

A high resolution Ge(Li) detector is used to acquire the gamma-ray spectra. The sample is rotated while acquiring data to reduce the effects of inhomogeneities due to the distribution of plutonium in the sample. A four-inch thick lead collimator with a 0.25" wide vertical slit is used to reduce the response to material located near the edge of the container. This allows the detector essentially to view the sample only along a diameter and improves the signal-to-background ratio by absorbing photons which are Compton scattered in the sample. A 0.030" (0.8 mm) cadmium absorber is used to further reduce the effects of low energy gamma rays. The data for all the isotopic ratios is measured with one detector.

Figure 1 shows the spectrum of a plutonium sample containing 94% plutonium-239 and 6% plutonium-240. The prominent gamma rays from each isotope of interest are indicated.

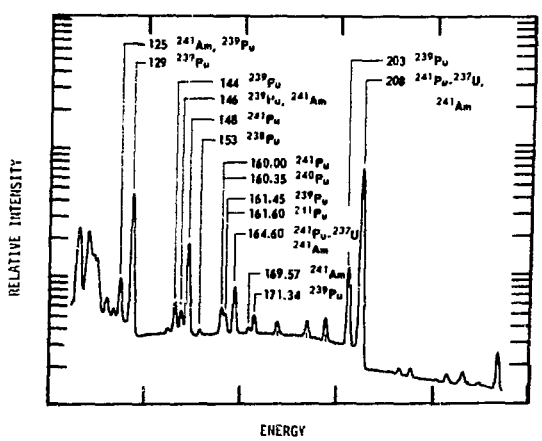

Fig. 1A - Gamma-ray Spectrum of Plutonium Sample Containing 94% Pu-239 Showing Energy Region from 120 to 220 keV.

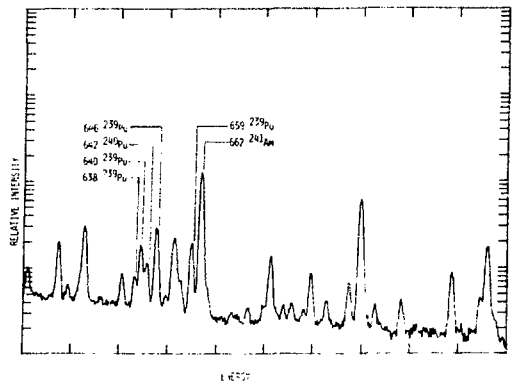

Fig 18 - Gamma-ray Spectrum of Plutonium Sample Containing 94% Pu-239 Showing 600 keV Energy Region.

The gamma rays used for each isotopic ratio are shown in Table 1. Also listed in the table are the conversion factors calculated using the branching intensities and half-life values of Gunnink and Morrow[1]. Peak areas are extracted using the programs GAUSS V[2] or GRPANL[3]. Both are nonlinear least squares fitting routines. The former runs on an IBM-360 computer; the latter on PDP-8 computers. The program used is dependent upon the spectroscopy system employed in the acquisition of the spectrum. Both programs give equally valid results when applied to the same spectrum.

TABLE 1

GAMMA-RAYS AND CONVERSION FACTORS USED FOR ISOTOPIC DETERMINATIONS

Isotopic Ratio	Gamma-rays	Conversion Factors to Express Ratio in ppm
$\frac{^{238}Pu}{^{239}Pu}$	$\frac{153\ keV}{144\ keV}$	$1010\ \frac{I_{153}}{I_{144}}$
$\frac{^{238}Pu}{^{241}Pu}$	$\frac{153\ keV}{148\ keV}$	$1.185\ \frac{I_{153}}{I_{148}}$
$\frac{^{240}Pu}{^{239}Pu}$	$\frac{642\ keV}{640\ keV}$	$148300\ \frac{I_{642}}{I_{640}}$
$\frac{^{240}Pu}{^{241}Pu}$	$\frac{160.35\ keV}{164.6\ keV}$	$50.7\ \frac{I_{160}}{I_{165}}$
$\frac{^{241}Pu}{^{239}Pu}$	$\frac{208\ keV}{203\ keV}$	$623.7\ \frac{I_{208}}{I_{203}}$
$\frac{^{241}Pu}{^{239}Pu}$	$\frac{148\ keV}{144\ keV}$	$852.7\ \frac{I_{148}}{I_{144}}$
$\frac{^{241}Am}{^{239}Pu}$	$\frac{662\ keV}{659\ keV}$	$487.5\ \frac{I_{662}}{I_{659}}$

The accuracy of nondestructive techniques can be established by comparing the results on aliquots with their subsequent chemical analysis.

Over the past three years, we have compared the nondestructive (NDA) and chemical analysis (DA) results for forty-five 9 g plutonium metal samples (93% plutonium-239). The average percent differences $\left(\frac{NDA-DA}{DA}\right)$ are: plutonium-238 (1.0 ± 11.7)%; plutonium-240 (-5.2 ± 6.4)%; plutonium-241 (4.2 ± 5.7)% and americium-241 (-2.9 ± 4.9)%.

The majority of the bulk samples investigated have been 93% plutonium-239. They are sent to Mound Laboratory for calorimetric assay as a part of a plutonium verification program[4]. Analytical aliquots are chosen from selected samples prior to shipment to Mound Laboratory. A combination of chemical and nondestructive measurements of the isotopic ratio is used with the calorimetry data to give an uncertainty in the plutonium content of less than 1%. Because of the overall time commitments of the program, samples can be counted for only four hours. In the most recent sample exchange, 20 aliquots and 79 samples were processed. The percent differences for the aliquots $\left(\frac{NDA-DA}{DA}\right)$ are: plutonium-238 (-1 ± 7)%; plutonium-240 (-7 ± 11)%; plutonium-241 (-2 ± 3)% and americium-241 (1 ± 7)%. When the isotopic ratios of the aliquots (A) are compared to the cans (C) from which they were drawn, the average percent differences $\frac{(C-A)}{A}$ are: plutonium-238 (1 ± 14)%; plutonium-240 (1 ± 18)%; plutonium-241 (1±2)%; americium-241 (1± 7)%. If we use uncertainties of 15% for $^{238}Pu/^{239}Pu$, 15% for $^{240}Pu/^{239}Pu$, 3% $^{241}Pu/^{239}Pu$ and 7% $^{241}Am/^{239}Pu$, the resulting uncertainty in the calorimetric assay would be 3%.

We are presently extending these techniques to lower fissile material. As a final example of our results, we analyzed five reactor fuel pins containing 86% plutonium-239. Comparison of the gamma-ray analysis of the pins with chemical analysis of the fuel at the time of fabrication yields the following differences: plutonium-238 (5.2 ± 6.5)%; plutonium-240 (-0.8 ± 5.8)%; plutonium-241 (0.2 ± 1.4)%; americium-241 (-5.1 ± 2.4)%. The use of gamma-ray isotopics in a calorimetric assay would yield total plutonium values which are 0.43% higher than corresponding values using chemical isotopics.

The technique we have developed in general meets the goals we have established for the program[5]. We have applied it to small samples with promising results as indicated by the results of the plutonium metal and fuel pin data. We feel it also shows promise for application to bulk samples as indicated by the verification program results. We use it routinely for plutonium-241 and americium-241 isotopic data and to verify that the aliquot is representative of the bulk sample. The results do not meet the 3% accuracy we set for the plutonium-238 and plutonium-240 isotopics. Plutonium-238 fails as a result of the weak intensity of the 153 keV peak at the 100 ppm level of plutonium-238. The plutonium-240 fails because of the low intensity of the 640 keV peaks and the requirement that all isotopic data be obtained in four-hour data acquisition time. We are guardedly optimistic that using a two detector system, one to examine the region up to 210 keV and the second the region at 600 keV, this goal can be achieved. These efforts are presently underway.

REFERENCES

1. R. Gunnink and R. J. Morrow, "Gamma-ray Energies and Absolute Branching Intensities for $^{238,239,240,241}Pu$ and ^{241}Am", UCRL-51087, University of California Radiation Laboratory, Livermore, California, July 22, 1971.

2. R. G. Helmer and M. H. Putnam, "GAUSS V: A Computer Program for the Analysis of Gamma-ray Spectra from Ge(Li) Spectrometers", ANCR-1043, Aerojet Nuclear Corporation, Idaho Falls, Idaho (January, 1972).

3. R. Gunnink, "A System for Plutonium Analysis by Gamma-ray Spectrometry - Part 2: Computer Programs for Data Reduction and Interpretation", UCRL-51577 Part 2 University of California Radiation Laboratory, Livermore, California (April 18, 1974).

4. Raymond S. George and Roy B. Crouch, "Inspector Measurement Verification Activities", Proceedings of the Sixteenth Annual Meeting of the INMM, June, 1975, p. 327-336.

5. Nuclear Safeguards Progress Reports, Mound Laboratory, MLM-2302 (April, 1976), MLM-2286 (December. 1975), MLM-2186 (December, 1974).

Proceedings, ERDA X-and Gamma-Ray Symp. Ann Arbor, MI, May 19-21, 1976 (Conf 760539)

MEASUREMENT OF K FLUORESCENCE YIELDS IN ACTINIDE ELEMENTS*

I. Ahmad and R. K. Sjoblom
Chemistry Division, Argonne National Laboratory,
Argonne, Illinois 60439

The K fluorescence yields (ω_K) for several actinide elements have been determined from the K Auger electron and K x-ray intensities. The electron spectra were measured with a cooled Si(Li) spectrometer and the K x-ray intensities were measured with a Ge(Li) diode. From our present measurements the following values of K fluorescence yield have been obtained: Np, 97.1 ± 0.5%; Pu, 97.3 ± 0.5%; Cm, 97.2 ± 0.7%; Cf, 97.2 ± 0.5%; and Es, 97.1 ± 0.5%. These numbers indicate that the K fluorescence yield in the Z = 93 to Z = 99 region remains constant within the experimental error.

Introduction

Absolute intensities of γ-rays associated with electron capture (EC) decays of nuclides are usually obtained by balancing transition intensities and normalizing the total γ, e^-, and direct EC intensities to the ground state to 100%. In such cases a knowledge of K fluorescence yields (ω_K) is essential in order to relate the K x-ray intensity to K-shell vacancies. Also, since K Auger electron lines often interfer with conversion-electron lines in an electron spectrum their intensities can be used to extract conversion-electron intensities. Although K fluorescence yields have been measured[1] for most elements up to lead, very little data is available for higher Z elements. Beyond lead, K fluorescence yield has only been measured for uranium[2] and americium.[3] For this reason we have measured the K fluorescence yields in several transuranic elements.

In the present paper we describe our measurement of K fluorescence yields in neptunium, plutonium, curium, californium, and einsteinium. Most of these results have been obtained as a by-product of our decay scheme study program. The K fluorescence yields have been determined by measuring electron spectra with a cooled Si(Li) detector and K x-ray intensities with a Ge(Li) spectrometer. The use of isotope separator prepared samples has enabled us to obtain accurate values of ω_K.

Source Preparation

Samples of ^{237}Pu(45.6 d), ^{238}Am(98 min), ^{239}Am(11.9 h), ^{245}Bk(4.90 d), ^{246}Bk(1.80 d), ^{249}Es(1.70 h), ^{251}Es(33 h) and ^{251}Fm(5.30 h) were prepared by the irradiation of appropriate target materials with α-particles or deuterons in the Argonne 60-in cyclotron. The irradiated target was dissolved in HCl or HNO_3 and the element of interest was separated from other actinide elements either by a cation-exchange resin column[4] or by a solvent extraction procedure.[5] The fission products were removed by a liquid-liquid extraction chromatographic column.[6] The chemically purified element was then run through the Argonne electromagnetic isotope separator[7] to prepare thin isotopically enriched sources. These sources were used for the measurement of photon and electron spectra.

Measurements

The K x-ray intensities of the mass-separated sources were measured either with a 25 cm^3 coaxial Ge(Li) detector or a 2 cm^2 x 5 mm planar Ge(Li) detector. The spectra were taken at large source-to-detector distances in order to minimize error due to any difference in the geometries of the source and the standard. The absolute efficiencies of these spectrometers were measured with IAEA standards and a calibrated ^{243}Am source.[8] The decays of these spectra were followed in order to determine the contributions to the K x-ray intensity from the decays of the adjacent masses.

The electron spectra of isotope separator prepared sources were measured with an 80 mm^2 x 3 mm lithium-drifted silicon detector. The detector was coupled to a low-noise preamplifier and the detector and the input stage field-effect transistor (FET) were cooled to liquid nitrogen temperature. The spectrometer[9] had a resolution (FWHM) of 900 eV at 100 keV and 1.5 keV at 600 keV electron energy. We found that the electron lines appeared lower with respect to the photon energies measured with the same Si(Li) detector by 0.5 keV at 100 keV electron energy. The different response of the detector to electrons and γ-rays could be accounted for by an electron energy loss in the detector "window".

The K Auger electron spectra of ^{237}Pu, ^{239}Am, ^{249}Es and ^{251}Fm measured in the present study are shown in Figs. 1-4. These spectra were taken at an efficiency-geometry product of 1.1%. The efficiency-geometry product of the Si(Li) detector was determined with a calibrated ^{203}Hg standard. As can be seen the Auger lines are intermixed with conversion electron lines and K x-ray peaks. Hence in some cases spectra of more than one isotope of the same element were measured in order to obtain the intensities of all K Auger lines.

The K Auger electron energies for the actinide elements lie in the range of 70- to 140-keV. With the resolution of our electron spectrometer the K Auger lines appear as six peaks:

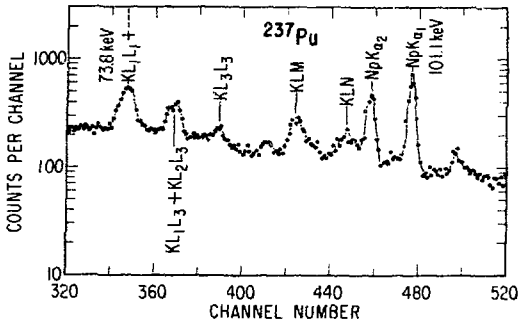

Fig. 1. ^{237}Pu electron spectrum showing the K Auger electron lines in Np (Z = 93). The spectrum was measured with a cooled Si(Li) detector at an efficiency-geometry product of 1.1%. The energy scale is 0.21 keV per channel.

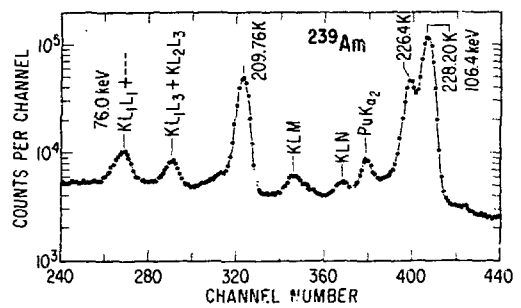

Fig. 2. ^{239}Am electron spectrum showing the K Auger lines in Pu. The efficiency-geometry product of the detector was 1.1% and the energy scale is 0.22 keV per channel.

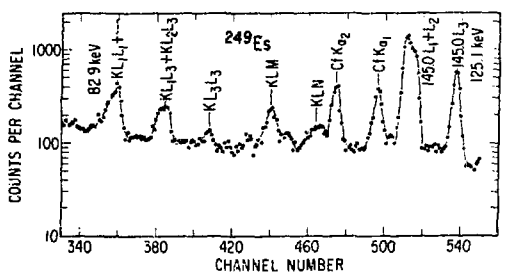

Fig. 3. ^{249}Es electron spectrum showing the K Auger peaks in Cf. The spectrum was measured at an efficiency-geometry product of 1.1% and the energy scale is 0.23 keV per channel.

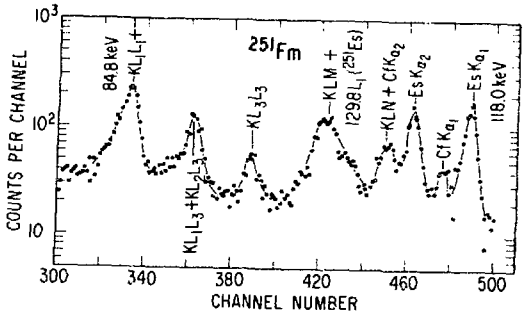

Fig. 4. ^{251}Fm electron spectrum showing the K Auger transitions in Es. The efficiency-geometry product of the detector was 1.1% and the energy scale is 0.22 keV per channel.

$(KL_1L_1 + KL_1L_2 + KL_2L_2)$, $(KL_1L_3 + KL_2L_3)$, KL_3L_3, KLM, (KLN + KLO ...), and KXY, where X and Y denote M and higher shells. In a spectrum free from conversion-electron lines all Auger lines except KLO + KLP and KXY were observed. We could not measure the intensity of the KXY peak because part of this peak is indistinguishable from the background and part of this peak falls under the $K_{\beta_1'}$ x-ray peak. The intensity of this peak, which corresponds to only 6% of the total K Auger intensity, was obtained using the theoretical[1] KXY/KLL ratio. The KLO + KLP line falls at the same energy as the K_{α_2} x-ray peak. We obtained the intensity of this peak from the increase in the K_{α_2} intensity relative to that of the K_{α_1} peak. The $K_{\alpha_2}/K_{\alpha_1}$ ratio has been very accurately determined in our decay scheme studies.

Discussion

The K x-ray spectrum, after correction for the detector efficiency, gave the K x-ray dis/min in the source. The number of K Auger electrons emitted per minute was obtained by dividing the peak area by the efficiency-geometry product of the electron detector. The Auger electron counts were also corrected for relative decay because the x-ray and electron spectra were measured at different times. The K fluorescence yield was then obtained by the equation

$$\omega_K = \frac{I_{K\ x\text{-ray}}}{I_{K\ x\text{-ray}} + \sum I_{KXY}}. \qquad (1)$$

In the above equation X and Y denote L,M,... shells and KXY denotes the six Auger electron peaks mentioned earlier.

From the present work the following values of K fluorescence yield have been obtained: NP, 97.1 ± 0.5%; Pu, 97.3 ± 0.5%; Cm, 97.2 ± 0.7%; Cf, 97.2 ± 0.5%; and Es, 97.1 ± 0.5%. The error denotes one standard deviation, σ, and it includes contributions from the counting statistics and the efficiencies of γ-ray and electron detectors. The measured K fluorescence yields are plotted against the atomic number Z in Fig. 5.

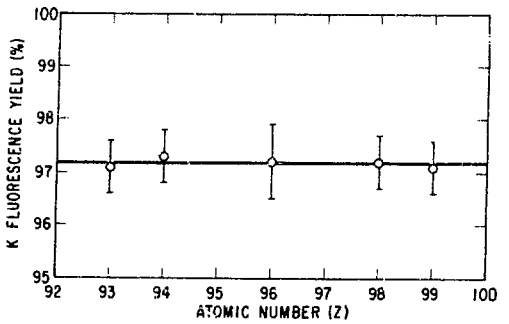

Fig. 5. A plot of K fluorescence yield against the atomic number Z.

It is evident from this figure that the K fluorescence yield remains constant in the Z = 93 to Z = 99 region within the experimental error. It should be pointed out that the same experimental arrangement was used for all measurements. Hence any change in the detector efficiency will not change the relative values of ω_K.

The relative intensities of K Auger lines obtained in the present study are in good agreement with the theoretical[10] values, as shown in Table I. No calculations for K fluorescence yields in actinide elements are available in literature. However, our values are in excellent agreement with previous measurements of K fluorescence yield in uranium[2] (97.0 ± 0.5%) and americium[3] (96.5 ± 0.4%).

Table I. Comparison of relative KLL and KLY intensities in Z = 93.

Auger Line	Experimental Intensity	Theoretical[10] Intensity
$KL_1L_1+KL_1L_2+KL_2L_2$	100 (norm)	100 (norm)
$KL_1L_3+KL_2L_3$	50 ± 5	61
KL_3L_3	13 ± 2	15
KLM	50 ± 5[a]	70
KLN+KLO+...	40 ± 4	

[a] A part of the KLM intensity is lost to the KLN+... peak. Hence the measured KLM intensity should be somewhat higher than 50.

*Work performed under the auspices of the U. S. Energy Research and Development Administration.

References

1. W. Bambynek, B. Crasemann, R. W. Fink, H. -U. Freund, H. Mark, C. D. Swift, R. E. Price and P. Venugopala Rao, Rev. Mod. Phys. 44, 716 (1972).

2. J. S. Hansen, J. C. McGeorge, R. W. Fink, R. E. Wood, P. Venugopala Rao and J. M. Palms, Z. Physik 249, 373 (1972).

3. F. T. Porter, I. Ahmad, M. S. Freedman, J. Milsted and A. M. Friedman, Phys. Rev. C10, 803 (1974).

4. G. R. Choppin, B. G. Harvey and S. G. Thompson, J. Inorg. Nucl. Chem. 2, 66 (1956).

5. I. Ahmad, D. D. Sharma and R. K. Sjoblom, Nucl. Phys. A258, 221 (1976).

6. I. Ahmad, R. F. Barnes, R. K. Sjoblom and P. R. Fields, J. Inorg. Nucl. Chem. 34, 3335 (1972).

7. J. Lerner, Nucl. Instrum. Methods 102, 373 (1972).

8. I. Ahmad and M. Wahlgren, Nucl. Instrum. Methods 99, 333 (1972).

9. I. Ahmad and F. Wagner, Nucl. Instrum. Methods 116, 465 (1974).

10. C. P. Bhalla and D. J. Ramsdale, Z. Physik 239, 95 (1970).

Proceedings, ERDA X-and Gamma-Ray Symp. Ann Arbor, MI, May 19-21, 1976 (Conf 760539)

COLLIMATOR-MAGNET ASSEMBLY TO ENABLE MICROPROBE EXAMINATION OF HIGHLY RADIOACTIVE MATERIALS BY ENERGY DISPERSIVE METHODS*

by

W. F. Zelezny, J. D. Farr, D. J. Hoard and E. A. Hakkila
Los Alamos Scientific Laboratory
University of California
Los Alamos, New Mexico 87545

Summary

Use of energy dispersive x-ray spectroscopy in the microprobe examination of highly radioactive materials, such as irradiated fuels of interest in the fast breeder reactor program, could increase the speed and scope of the examinations. Typical fuel materials that have undergone burnups up to 10 at. %, and have combined beta-gamma radioactivity levels up to 500 R/hr at contact for a sample of reasonable size, have previously been examined in a shielded electron microprobe, using wavelength dispersive (crystal) spectrometers. Attempts to replace a crystal spectrometer with an EDS system having a Si(Li) detector resulted in the EDS system being swamped and rendered inoperative by the background from samples of even relatively low levels of radioactivity. A collimator-magnet assembly has been produced which largely eliminates beta-gamma radiation at the detector and enables energy dispersive analysis of highly radioactive materials with the shielded microprobe.

Introduction.

Microprobe examination of irradiated nuclear fuels (and other highly radioactive materials) customarily uses a shielded electron microprobe equipped with wavelength dispersive (crystal) spectrometers. An energy dispersive spectrometer (EDS) coupled with the shielded electron microprobe would offer the advantage of acquiring a complete x-ray spectrum much more rapidly than is possible with a crystal spectrometer. Since the solid state detector of the EDS system must be in a direct line of sight with the specimen, it unavoidably receives β and γ radiation from the radioactive specimen as well as the x-rays produced by the finely focused electron beam. If the β and γ radiation is sufficiently intense, as is usually the case with any sample of practical interest, the detector is swamped and rendered inoperative. The samples examined at LASL, which are almost invariably complete cross-sections of highly irradiated fuel pins, require that activities of 100 R/hr β-γ at 100 mm, or greater, must be tolerated without swamping the detector.

One approach which has been tried[1] with a reasonable degree of success interposed a cylindrical lead collimator, having a conically tapered aperture hole concentric with the axis of the cylinder, with the small end of the cone closest to the specimen. Thus the detector could "see" only a limited area of the specimen surface containing the region of impact of the electron beam. This appreciably reduced the β-γ radiation reaching the detector and made possible the examination by microprobe of samples of intermediate levels of radioactivity. A similar approach applied to a scanning electron microscope (SEM) employed a tapered aluminum collimator lined with graphite[2], enabling samples reading 10 R/hr combined β-γ at two inches to be examined satisfactorily. A tapered tantalum-tungsten alloy collimator[3], also applied to a SEM, permitted the examination of samples with activities up to 11 R/hr at 2 inches. An extension of this idea applied to an x-ray fluorescence spectrometer with a solid state detector added a magnet to the collimator for the purpose of trapping the beta radiation. LASL has applied the magnet-collimator system to a shielded electron microprobe.

Apparatus.

The collimator-magnet assembly, shown diagrammatically in Fig. 1, was constructed** for LASL from a

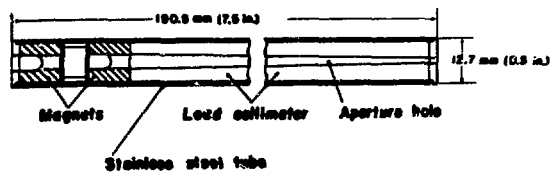

Fig. 1. Diagram of collimator-magnet assembly.

cylindrical length of lead containing a tapered axial aperture hole and a two-magnet system. All components were contained in a cylindrical stainless steel tube. In use the small opening of the collimator was closest to the sample, and the magnet assembly was next to the Si(Li) detector, as shown by the sketch in Fig. 2.

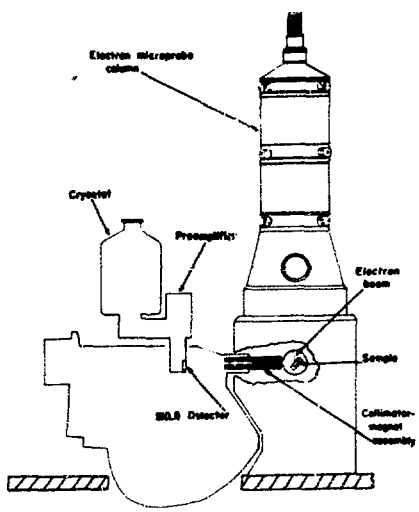

Fig. 2. Schematic of shielded electron microprobe showing collimator-magnet assembly in place, and Si(Li) detector inserted through crystal port of spectrometer.

*Work performed under the auspices of the U. S. Energy Research and Development Administration.

**Manufactured by Microspec Corporation of Sunnyvale, California.

The shielded microprobe was a MAC Model 450, which provided 109 mm of tungsten alloy shielding surrounding the specimen. The lithium-drifted silicon solid-state detector, pulsed optical feedback preamplifier, and linear amplifier were supplied by Nuclear Semiconductor. The amplifier output was processed by a Canberra Model 8050 analog-to-digital converter and a Canberra Model 8700 multi-channel analyzer.

Experimental Results.

The effectiveness of this magnet-collimator system is demonstrated by Figs. 3A and 3B. Fig. 3A represents a spectrum collected in 100 seconds by rapidly sweeping the electron beam in a 160 μm square raster over the fuel-cladding interface of a high-burnup, highly radioactive, nuclear fuel sample. The presence of the fuel components (unresolved), the stainless steel cladding components (resolved), and the fission product, cesium, is readily apparent. The magnitude of the background contribution from the radioactive sample is indicated by Fig. 3B which was obtained with the sample remaining in the same position, but with the electron beam turned off. It will be observed that the radioactive background reaching the detector has been reduced almost to zero.

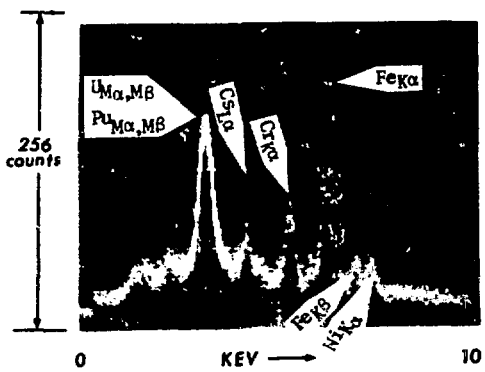

Fig. 3A. Spectrum showing x-ray lines of fuel and cladding constituents in a nuclear fuel sample of 7 at. % burnup. Combined β-γ field: 80 R/hr at 100 mm. Collection time: 100 sec. Deadtime: 10%. Microprobe electron beam: 25 keV, 0.015 microamperes. Spectrum display was enhanced over the U M - Pu M region.

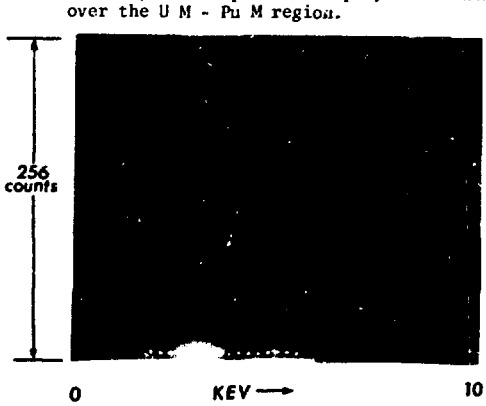

Fig. 3B. Same as Fig. 3A, except that electron beam was turned off.

In another test involving two-dimensional scans on an extremely highly radioactive sample (450 R/hr at 100 mm) the multi-channel analyzer was operated as a single channel analyzer to yield x-ray pulses in real time. These pulses were fed into a video system to obtain two-dimensional elemental distribution (x-ray images) for comparison with the x-ray images made with a crystal spectrometer over the same area. The photomicrograph in Fig. 4A shows the area of cladding failure and fuel-cladding interaction which was scanned in this test. Figs. 4B and 4D compare the Fe Kα x-ray images from a LiF crystal spectrometer, and the EDS system, respectively. Similarly, Fig. 4C compares the U Mα x-ray image taken by a PET crystal spectrometer with the combined uranium and plutonium Mα and Mβ x-ray image from the EDS system.

Conclusions.

The system effectively reduces the beta and gamma radiation from sample radioactivity and provides reliable data using a solid state detector with samples as radioactive (β+γ) as 500 R/hr at contact.

References.

1. Private communication from T. E. Lannin and R. C. Wolf.

2. C. Baker and G. K. Rickards, "Modification of an Energy Dispersive X-ray Spectrometer to Allow Analysis of Radioactive Specimens," Central Electricity Generating Board report RD/B/N-3221, Berkeley, England.

3. U. E. Wolff and R. C. Wolf, "Collimator for Energy Dispersive X-ray Analysis of Radioactive Materials in a Scanning Electron Microscope," Ninth Annual Conference of the Microbeam Analysis Society, Carleton University, Ottawa, Canada, July 22-26, 1974, Paper 25.

4. W. L. Pickles and J. L. Cate, Jr., "Quantitative Nondispersive X-ray Fluorescence Analysis of Highly Radioactive Samples for Uranium and Plutonium Concentration," Lawrence Livermore Laboratory report UCRL-74717 (August 14, 1974).

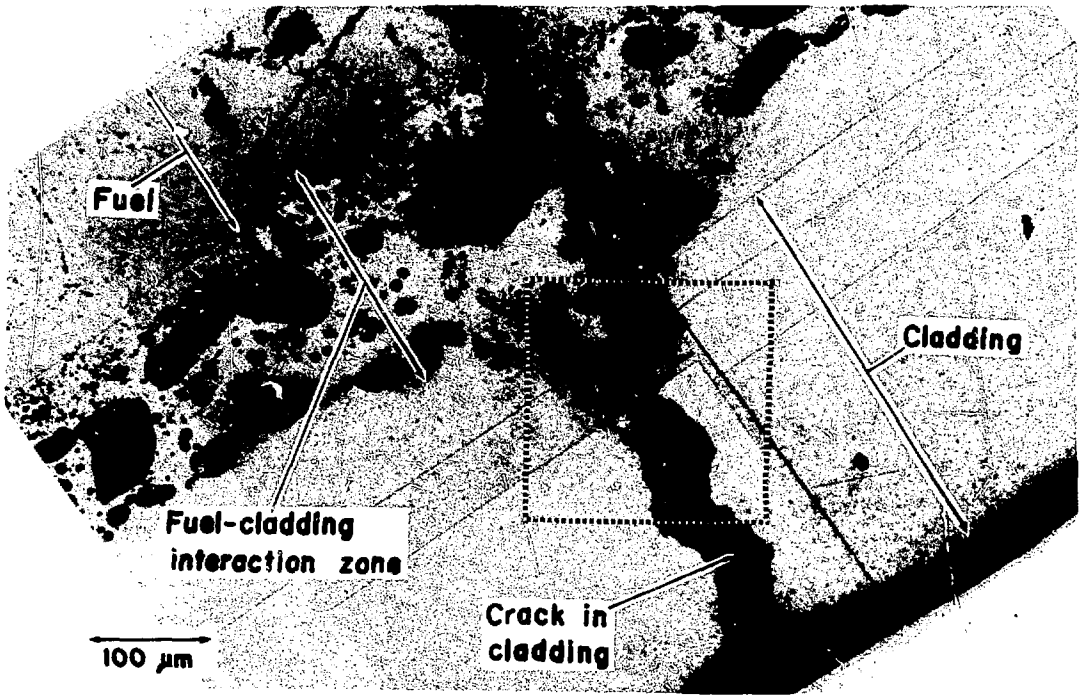

Fig. 4A. Photomicrograph of fuel-cladding interface region of irradiated (U,Pu)C fuel showing fuel-cladding interaction and cladding failure by cracking. X-ray images shown below correspond to dashed square on photomicrograph.

Crystal spectrometers

Fig. 4B. FeKα X-ray image taken with LiF crystal spectrometer.

Fig. 4C. U Mα X-ray image taken with PET crystal spectrometer.

EDS

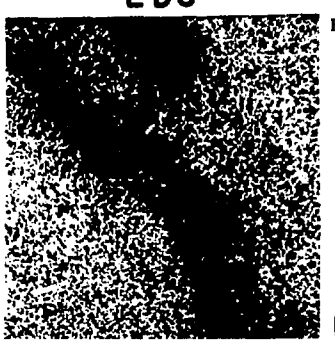

Fig. 4D. FeKα X-ray image taken with EDS.

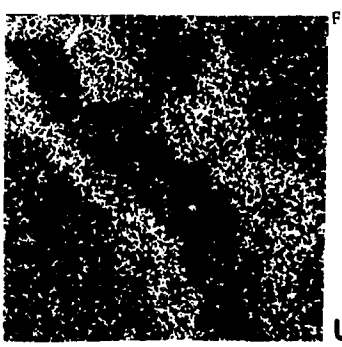

Fig. 4E. (U-Pu) Mα & β X-ray image taken with EDS.

Proceedings, ERDA X-and Gamma-Ray Symp. Ann Arbor, MI, May 19-21, 1976 (Conf 760539)

APPLICATION OF HIGH-INTENSITY, ROTATING-ANODE X-RAY TUBES FOR DIFFUSE X-RAY SCATTERING STUDIES OF CRYSTAL DEFECT STRUCTURES

H.-G. Haubold
Institut für Festkörperforschung der Kernforschungsanlage Jülich
D 517 Jülich, Germany

Summary

High power rotating anode X-ray tubes yield high X-ray luminosities up to 10^{17} monoenergetic quanta steradian^{-1} s^{-1} cm^{-2} from focal spot areas of about 1.5 x 1.5 mm^2. Their use in scattering experiments allows the statistical errors to be made small enough for very precise determinations of scattering cross sections. Thus it is possible to separate the diffuse scattering from lattice defects, such as isolated interstitials or vacancies or clusters of them, from the Compton and thermal diffuse scattering from the perfect crystal.

Using a 100 kW rotating anode tube and a multidetector system with 100 detectors, the scattering of 100 ppm self-interstitials in aluminum or copper could be measured even at scattering angles for which the Compton background scattering was up to 100 times greater. In both materials the interstitial structure was found to be the ⟨100⟩-split dumbbell.

Introduction

For many reasons, especially for a better understanding of radiation damage processes, there is a strong interest in methods that yield detailed information on the atomistic structure of lattice defects in crystalline solids.

For an illustration of some typical questions of interest Fig. 1 shows in a fcc lattice the basic lattice

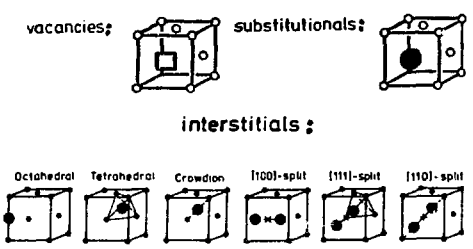

Fig. 1 Basic lattice defects in fcc lattices.

defects: a vacancy, a substitutional atom and interstitials in the six possible self interstitial configurations. In all cases the interest is in the resultant displacements of the surrounding lattice atoms; especially for interstitials the unresolved question is very often its specific configuration.

Electron microscope studies generally allow structure determinations only for those defects which are appreciable larger than single atoms. The method of the diffuse X-ray scattering, however, yields detailed structural information on atomistic point defects such as interstitials, vacancies and substitutionals as well as on larger clusters of them.

The principle of the method is simple. The intensity of X-rays which are scattered elastically from the sample, is measured as a function of the scattering vector $\vec{K}$, as shown schematically in Fig. 2. As illustrated in Fig. 3, in crystals without lattice defects (due to the perfect atomic order) elastically scattered intensity is observed only in sharp Bragg reflections for scattering vectors $\vec{K}$ equal to the vectors $\vec{K}_{Bragg}$ of the reciprocal lattice with a lattice parameter $2\pi/a$ (a = crystal lattice parameter). In crystals with lattice defects the Bragg intensities decrease due to the atomic disorder, and the elastically scattered X-ray waves cannot interfere to zero intensity out between the Bragg reflections. This results in a diffuse scattering with maxima around the Bragg reflections. In Fig. 3 this intensity between the Bragg peaks is shown schematically (exaggerated).

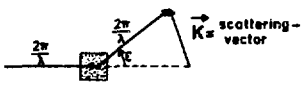

Fig. 2 Scattering vector for elastic scattering.

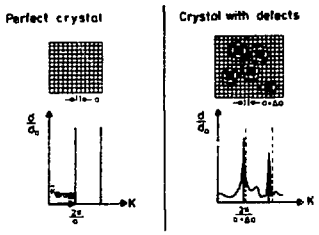

Fig. 3 Elastic scattering cross sections.

The scattered intensity is the square of the scattering amplitudes from all atoms within the distorted crystal. These are displaced by $\vec{S}_n$ from their regular lattice sites $\vec{r}_n$ as it is illustrated in Fig. 4, which shows a small part of the lattice distorted by an interstitial defect on a site $\vec{R}_D$.

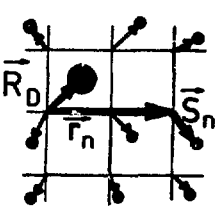

Fig. 4 Atomic displacements around defects.

In a single defect approximation, valid for small defect concentrations c, for instance below 1 %, the diffuse intensity I_{diff} is then given by:

$$I_{diff}(\vec{K}) = c\cdot\Big|f_D + \sum_n f\exp i\vec{K}(\vec{r}_n+\vec{S}_n+\vec{R}_D) - \sum_n f\exp i\vec{K}(\vec{r}_n+\vec{R}_D)\Big|^2, \quad (1)$$

where f_D is the scattering amplitude of the defect itself, and f that of the lattice atoms. The first summation gives the scattering amplitude from all lattice atoms on the distorted sites $\vec{r}_n + \vec{S}_n$; in order to relate all the phases to $\vec{R}_D$, $\vec{K}\cdot\vec{R}_D$ is included in both summations. The second summation, which gives the Bragg amplitudes from atoms on lattice sites, is subtracted so as to obtain only the diffuse scattering.[1]

Often the product $\vec{K}\cdot\vec{S}_n$ is small and an expansion yields as a first order term in the displacements:

$$I_{diff}(\vec{K}) = c\cdot\Big|f_D + f i\vec{K}\cdot\sum_n \vec{S}_n \exp i\vec{K}(\vec{r}_n+\vec{R}_D) + \dots\Big|^2 \approx c\cdot\Big|f_D + f i\vec{K}\cdot\vec{S}(\vec{K}) + \dots\Big|^2 \quad (2)$$

One sees that what is actually measured with elastic diffuse X-ray scattering, in addition to the defect scattering itself, is the projection of the scattering vector $\vec{K}$ on the vector $\vec{S}(\vec{K})$, which is the Fourier trans-

form of the lattice displacements $\vec{S}_n$. Therefore an evaluation of the diffuse intensity as measured in an extended area of the reciprocal lattice gives full information on both the defect type and its displacement field.[2,3]

Unfortunately in the region between the Bragg reflections measurements are difficult, since there the elastic diffuse scattering cross section from small fractions of point defects is appreciably weaker than the inelastic Compton- and thermal diffuse scattering cross sections from the lattice atoms. By energy discrimination this inelastic scattering is in practice not or only partially separable and masks, as a very intense background scattering, the elastic defect scattering. For the scattering of typically 500 ppm self interstitials in aluminum Fig. 5 shows that the Compton and thermal diffuse background scattering is up to two orders of magnitude more intense.

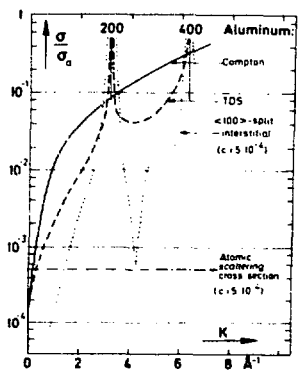

Fig. 5 Scattering cross sections in aluminum for scattering vectors $\vec{K}$ along a 100 direction of reciprocal space: <100> -split interstitials ($c = 5 \cdot 10^{-4}$), Compton- and thermal diffuse scattering (4K).

To separate the weak defect scattering from the background one must compare the cross sections from the crystal with defects with that from the identical crystal, either after all defects are annealed out or before they are introduced. This requires a precision measurement of scattering cross sections with an accuracy of the order of 0,01 %. Within reasonable measuring times the necessary small statistical error in the counting rates can be achieved only by using X-ray sources that are more intense than commonly used X-ray tubes.

High power rotating anode X-ray tubes: Optimum sources for diffuse scattering experiments

As the upper part of Fig. 6 illustrates, the admissable angle of aperture β and the resolution in the scattering angle ε together with the area A of the sample determines the optimum size of the X-ray source. If these parameters are given, optimum sources are then those with the highest luminosity, i.e. those which emit the maximum monoenergetic quanta $cm^{-2}s^{-1}$ steradian^{-1}. With very high luminosities of about 10^{17} quanta $cm^{-2}s^{-1}$ steradian^{-1} (copper K_α-radiation) rotating anode X-ray tubes prove to be preferable sources.

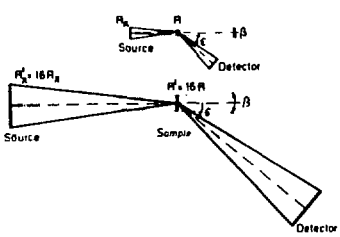

Fig. 6 Gain of measuring time by illuminating greater samples with unaltered resolution.

A further increase of the scattered intensity can be achieved by bringing more lattice defects into the primary beam. For a given defect concentration that means larger samples. The lower part of Fig. 6 demonstrates that an increase of the illuminated sample area can only be reached by enlarging all dimensions of the whole scattering arrangement. As is shown, an increase of the whole geometry by a factor of four in all linear dimensions yields an increase of the sample area A and thus of the scattered intensity by a factor of 16.

It is in general easy to use large samples and larger detectors. The size of the X-ray source, however, is strongly limited by the admissable electrical loads of the rotating anode X-ray tubes. As is discussed in more detail elsewhere[4], samples not larger than 1 cm^2 can be illuminated under optimum geometrical conditions with 100 kW rotating anode tubes, the strongest that are commercially available today.

Fig. 7 gives a schematic view of the equipment that was successfully used for measurements of the elastic diffuse scattering from lattice defects.[4,5] As an X-ray

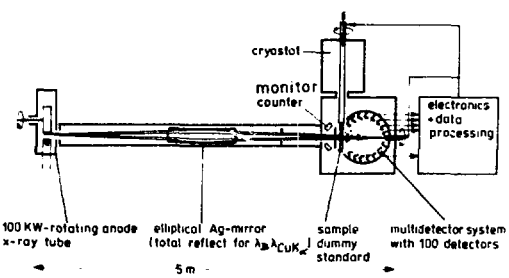

Fig. 7 Schematic view of the set up used for precision measurement of diffuse scattering between Bragg reflections.[5]

source, a powerful 100 kW rotating anode tube with a copper anode is used. The characteristic copper K_α radiation is focused by total reflection from an elliptical mirror. By use of 100 detectors arranged at different scattering angles on a focusing circle, a predetermined set of scattering intensities are measured simultaneously, and the incoming data are processed online by a data processing system.

The samples are single crystals typically of 1 cm^2 area, and for transmission measurements with thicknesses between 10 and 100 microns. To make highly accurate measurements possible, a differential technique is applied: Each 3 minutes the sample containing the defects is interchanged with a dummy sample, which serves as a standard to which all measurements are compared. In this manner within typical measuring times of several hours fluctuations in counting efficiencies have no influence on the accuracy of the measurement.

The necessary measuring time for a given accuracy of diffuse scattering cross sections is about a factor of 10^4 shorter than conventional set-ups would require. This factor results first from using the 100 kW rotating anode X-ray tube instead of a 1 kW tube, and second from using the multicounter system with 100 detectors instead of only 1 detector.

This gain in measuring time allows the minimization of statistical errors so that diffuse scattering cross sections can be measured with errors of the order of 0,01 %. Thus the weak defect scattering from some 100 ppm interstitials can be separated after several hours measuring time from the Compton and thermal diffuse background scattering of the lattice atoms. This is illustrated in Fig. 8 for a scattering pattern which was measured in aluminum along the indicated Ewald circle in the (110)-plane of the reciprocal lattice. The measurement was made at 8 K and the scattering due to the defects was derived from the upper curve by a subtraction

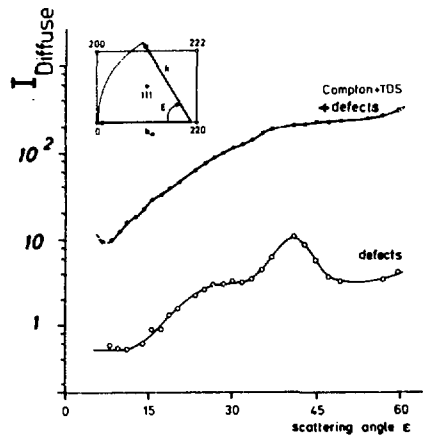

Fig. 8 Background and defect scattering at 5 K from aluminum with 340 ppm interstitials and vacancies.

of the background intensity, which was measured on the same sample, after all defects were annealed out.

Determination of defect structures from diffuse scattering cross sections

From the absolute value of the scattering cross section and the dependence of its magnitude on the scattering vector both the concentration and the configuration of the lattice defects can be determined rather unambiguously, if it had been measured in such areas of reciprocal space where different configurations yield different characteristic intensity distributions.

These regions can be found best if one looks at the amplitude of the scattering from the displacement field. According to eq. 2 in a first approximation this is proportional to $\vec{K}\cdot\vec{S}(\vec{K})$. For the example of substitutional atoms and interstitials on octahedral sites $\vec{R}_D$ Fig. 9 shows the vectors $\vec{S}(\vec{K})$ around some reciprocal lattice points. As can be seen, $\vec{S}(\vec{K})$ is periodic in reciprocal space. According to eq. 2 the different directions of the vectors $\vec{S}(\vec{K})$ around the reciprocal lattice points is due to the sign of the phasefactor $\exp(i\vec{K}\cdot\vec{R}_D)$, which only depends on the site $\vec{R}_D$ of the defects within the lattice.

Within the dotted regions the scattering vector $\vec{K}$ is parallel to the vectors $\vec{S}(\vec{K})$. This results in a positive amplitude of the scattering from the displacement field in these regions. Mostly around the (111)-point these regions are different for substitutionals and octahedrals; for substitutionals the direction of the vectors $\vec{S}(\vec{K})$ is inward at this point and is outward for octahedrals, giving opposite signs for the amplitudes. Since the scattering from the displacement field must be zero on the lines, on which the sign of $\vec{K}\cdot\vec{S}(\vec{K})$ changes, these differences in the amplitudes result in different characteristic lines on which no first order scattering from the displacement field is observed. Since these zero lines are specific for different defects, they result in characteristic differences in the isointensity lines for diffuse scattering from lattice defects in different configurations.

As an illustration, Fig. 10 shows the strongly different isointensity lines for self interstitials in the <100>-split and the octahedral configuration in aluminum and copper. They were calculated numerically from eq. 2 with an additional inclusion of higher order terms in the displacements. For the calculation of the lattice displacements the simplest defect models were used with defect forces acting only on the nearest

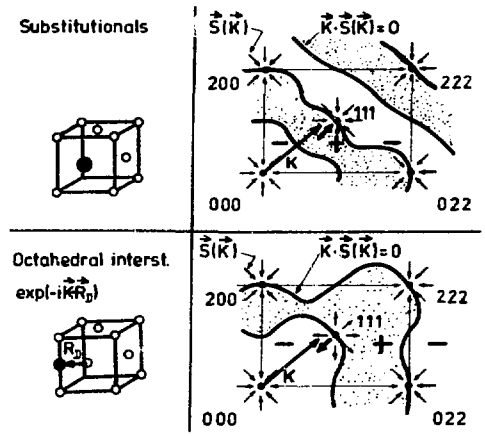

Fig. 9 Schematic view of the regions with positive and negative sign of $\vec{K}\cdot\vec{S}(\vec{K})$ for substitutional atoms and octahedral interstitials in fcc-metals.

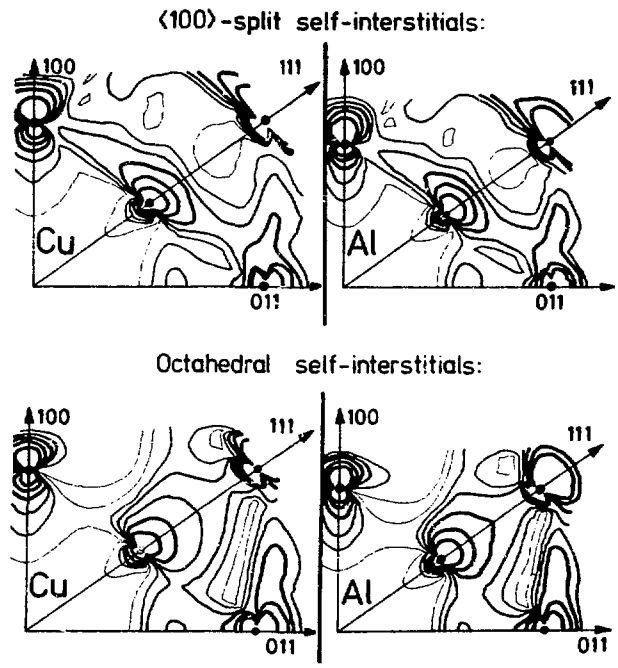

Fig. 10 Isointensity contours for interstitials in <100>-split and octahedral configurations in copper and aluminum.

neighbours.[2] The magnitude of these forces was evaluated from the known volume relaxation around the interstitial.[5,6]

The isointensity lines correspond to 1, 5, 10, 20, 40 and 80 times the atomic scattering cross section. Whereas a strong but very similar scattering is observed near the reciprocal lattice points (in that region the nearly identical long ranging part of the displacement field is Fourier transformed; the inverse relation of the displacement with distance from the defect results in an increase of their Fourier transforms), the scattering cross sections between the Bragg reflections are quite different.

For both metals the intensity minima for the <100>-split

configuration coincide approximately with the zero lines for the first order displacement field scattering for a substitutional atom as shown in Fig. 9, since the center for the displacements around split interstitials is on a lattice site. The strongly different minima for the octahedral configuration are also a direct consequence of the different zero lines for octahedrals. Although there are small differences in the responses of the lattice atoms for aluminum and copper (different anisotropy of the elastic constants), they are small compared to the differences between the interstitial configurations, and do not hinder configuration determinations from the diffuse scattering measurements.

Typical results

For the example of self-interstitials and vacancies in copper and aluminum Figs. 11, 12 and 13 show some typical results, that were obtained with the apparatus as described above from samples after an irradiation at 4 K with 3 MeV electrons.

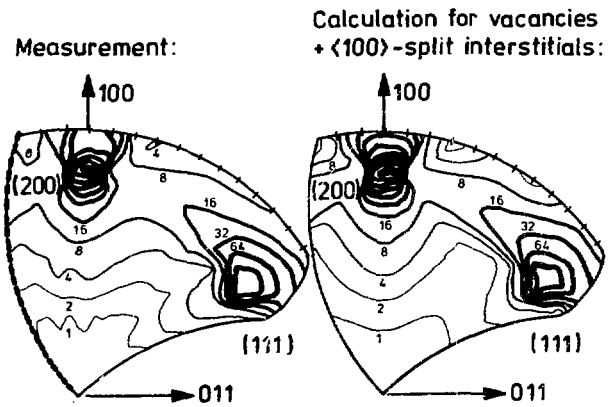

Fig. 11 Comparison of diffuse scattering contours measured on electron irradiated copper (4 K) with the results of model calculations.[6]

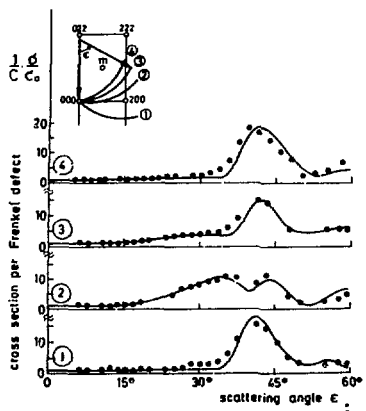

Fig. 12 Comparison of an optimum fit for <100>-split interstitials and vacancies to experimental points measured at 8 K on electron irradiated aluminum.[5]

120 ppm interstitials and vacancies, both produced in equal number during the irradiation, gave lines of constant scattering cross section that are plotted in the left part of Fig. 11.[6] These unsmoothened isointensity lines were constructed directly from about 700 cross section values, that were measured by rotating the sample with respect to the multidetector system, whose resolutions elements are given at the edge of the plot of the measured values.

For a comparison the calculated isointensity lines are plotted for vacancies and interstitials in a <100>-split configuration. Both the magnitude of the scattering

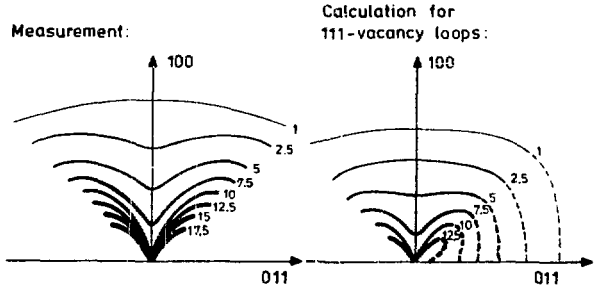

Fig. 13 Comparison of diffuse scattering contours for copper, electron irradiated at 4 K and annealed to 300 K, with the results of a model calculation for vacancy loops on (111)-planes with 7 Å radii.[5]

cross section along the calculated profiles and their shape correspond very well to the measured ones. Since the shape of these profiles are determined mainly not by vacancies but by the scattering from the displacement fields of the interstitials because of the much stronger displacements around them, by a comparison with the strongly different profiles calculated for other configurations, for instance that for octahedrals in Fig. 10, all other possible configurations for the self-interstitial in copper could be ruled out clearly.

In a similar way, the stable configuration of self interstitials in aluminum was determined. Again, the <100>-split interstitial was found to be the stable configuration.[5] In Fig. 12 is shown a quantitative fit of the calculated curves to the experimental data, which were measured as a function of the scattering angle at a defect concentration of about 400 ppm along the four Ewald circles in the (110)-plane of reciprocal space, as indicated in the insert. The curves were calculated with assumed interstitial parameters which gave an optimal fit: The distance between the two dumbbell atoms was found to be 0.6 lattice constants. As an illustrative number the displacements of the nearest neighbours were determined to be 0.1 lattice constants. From the scattering cross sections at low scattering angles, which is most sensitive on local density changes due to vacancies, the volume relaxation around a vacancy could be determined to be nearly zero.

Scattering in the region of small scattering angles is also very useful for studies of small vacancy agglomerates, which produce an increase of the small angle scattering intensity. For scattering angles up to 9 degrees Fig. 13 shows results on agglomerates that were formed an irradiated copper after annealing at a temperature of 300 K.[6] The lines for equal scattering cross sections, as obtained from the measurement, are compared to lines which were calculated for vacancy loops on <111>-lattice planes. Since measurement and calculation yield nearly identical lines, it was concluded that these agglomerates were <111>-loops with radii of about 7 Å. Since these agglomerates are so small, it has not been possible to detect them in transmission electron microscope studies.

Conclusions

The application of X-ray diffuse scattering for detailed studies of point defects and their clusters has recently become possible as a result of recent advances in X-ray sources and detector systems. Diffuse X-ray scattering yield direct information on structures of lattice defects which was not available before from other methods.

References

1 Dederichs, P.H., J. Phys. F: Metal Phys. 3 (1973) 471-496

2 Haubold, H.-G. Rev. Phys. Appl. 11 (1976) 73-81

(cont. on p. 283)

Proceedings, ERDA X-and Gamma-Ray Symp. Ann Arbor, MI, May 19-21, 1976 (Conf 760539)

THE DETERMINATION OF IMPURITIES IN BORON BY X-RAY SPECTROSCOPY

A. J. Busch

U. S. Energy Research and Development Administration
New Brunswick Laboratory
P. O. Box 150
New Brunswick, New Jersey 08903

X-ray spectroscopy has been used at the New Brunswick Laboratory for many years for the determination of a variety of impurities in elemental boron. As requirements for improvements in precision, accuracy,and sensitivity have become more stringent the basic technique has been modified both with improved instrumentation and methodology to meet these new requirements. This paper deals with the current procedures for the measurement of the concentrations of bromine, chlorine, fluorine and sulfur in high purity boron powder.

Experimental

Apparatus

Spectrometer - Phillips PW 1410

Source - Phillips X RG-3000

X-Ray Tube - Chromium,

Analyzing Crystals - Lithium fluoride (LiF, 220), thallaium acid phthallate (TAP) and germanium (Ge 111).

Detectors - Proportional counter, scintillation (Tl activated NaI).

Mixer Mill - Spex 8000.

Press - Buehler Metallurgical with a 1¼-inch mold and electric heater.

Materials

High Purity Boron.

Bakelite Resin Powder, Union Carbide Corp. BRP-5095.

Sodium Chloride, reagent grade.

Sodium Bromide, reagent grade.

Sodium Fluoride, reagent grade.

Sodium Sulfate, reagent grade.

Procedure

Preparation of Standards

Add appropriate amounts of standard solutions containing NaCl, NaBr, NaF, or Na_2SO_4 to weighed quantities of boron (70-80 µ) in Teflon dishes. Adjust the amount of liquid added to form a thick slurry. Dry in oven set at 110°C for 12 hours. Homogenize the mixture, sieve through a 40 mesh nylon screen into a V-blender. Blend for 30 minutes. Place blended material in bottles for later use.

Preparation of Pellets for Measurements

Mix on a mixer mill for a minimum of five minutes 1.5 g of the powdered sample or standard material with 0.45 g of Bakelite resin powder contained in a ten ml polystyrene vial, containing one 3/8 inch plastic ball. Pour the mixture into a 1¼-inch (3.18 cm) mold with 1/16-inch Teflon disk on the base of the die and place in the press. Turn on the heater and increase pressure to 4000 psi. When temperature reaches 140°C, turn off heat. When temperature falls to about 70°C, release pressure and eject pellet. Remove the Teflon disk when pressing pellets for fluoride analysis.

Measurements

Count the side of each pellet (both sides of fluoride pellets may be counted) exposed to Teflon. Measure impurity peaks and backgrounds for 100 seconds in accordance with the operating parameters summarized in Table I. Make background corrections and plot net intensities (counts per second) vs. element concentration for graphic display or calculate the regression equations.

TABLE I

OPERATING PARAMETERS FOR CHROMIUM X-RAY TUBE

Element	Voltage (KV)	Current (ma)	Analyzing Crystal	Detector	2Θ Peak Setting	Background Setting
Br	40	40	LiF(220)	Scint.	42.88	39.88 45.88
Cl	40	40	Ge 111	Proportional	92.76	96.00
F	40	60	TAP	Proportional	90.60	96.00
S	40	40	Ge 111	Proportional	110.68	114.00

RESULTS AND DISCUSSION

Table II summarizes the data obtained for each set of standards. The data are plotted in Figures 1, 2, 3 and 4. These plots indicate that the analytical curves cannot be represented as straight line functions over the concentration ranges investigated, however, linear regression equations have been

TABLE II

CALIBRATION DATA

Element	Conc. (µg/g)	Cross Counting: Element Peak	Cross Counting: Background	Net Intensity (c/s)
Bromine	Blank	27005	26806	2
	100	51545	32136	194
	110	51613	31318	203
	125	56047	32308	237
	150	61835	32396	294
	200	75122	32249	429
	300	102389	32188	702
Chlorine	25	16077	9026	70
	50	19462	8743	107
	100	24261	8614	156
	200	36389	8823	276
Fluorine	Blank	5875	2964	29
	10,000	6711	2974	37
	20,000	8212	2783	54
	40,000	13965	2681	113
Sulfur	Blank	11422	8669	28
	10	12040	8349	37
	25	14143	8489	56
	50	16490	8373	81
	100	21579	8168	134
	200	29836	8575	213

estimated for each element (except fluorine) in the range of 0-100 µg/g. Thus:

$$I_{Br} = 1.92\ C_B$$

$$I_{Cl} = 1.16\ C_{Cl} + 44$$

$$I_S = 1.06\ C_S + 28$$

Standard errors of estimate* $S_{I \cdot C} = \left(\frac{\Sigma (C-\bar{C})^2}{N-2} \right)^{\frac{1}{2}}$ have been calculated for each of the regression equations above holding intensity constant; values are ± 3 µg/g for Br, ± 3 µg/g for Cl, and ± 1 µg/g for S. Thus detection limits (µg/g) based on the Pantony and Hurley equation[1],

$$C_{D \cdot L} = \frac{(0.8\ I_B)^{\frac{1}{2}}}{m} ,$$

(where I_B is the intensity of the average background and m is the slope of the linear regression curve), may be expressed as 7 ± 3 µg Br/g B, 6 ± 3 µg Cl/g B, and 7 ± 1 µg S/g B.

* where C = standard value, $\bar{C}$ = regressed value

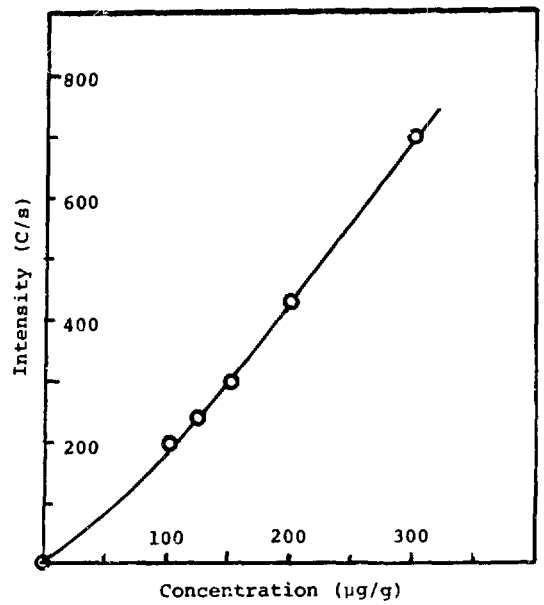

FIGURE 1. BROMINE

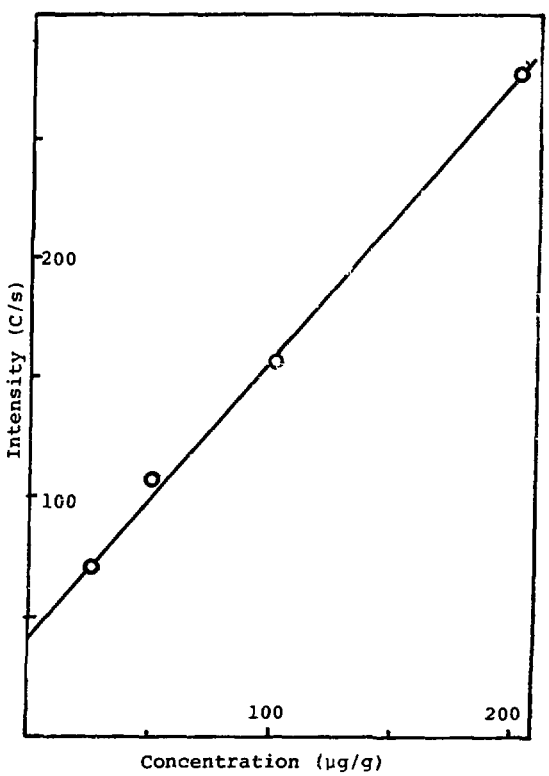

FIGURE 2. CHLORINE

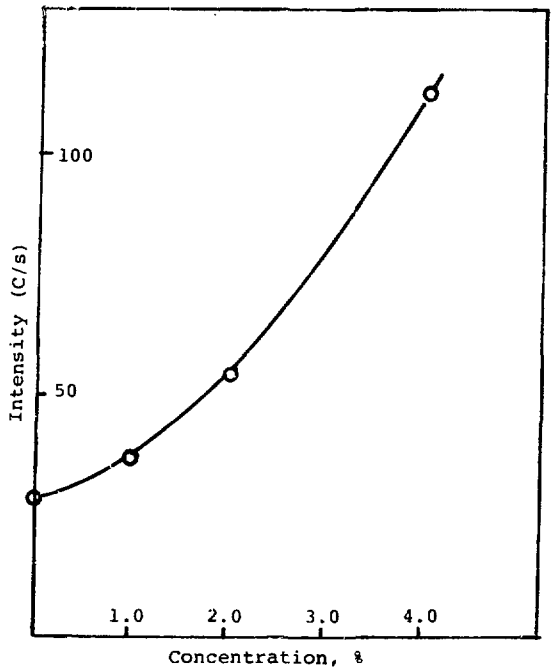

FIGURE 3. FLUORINE

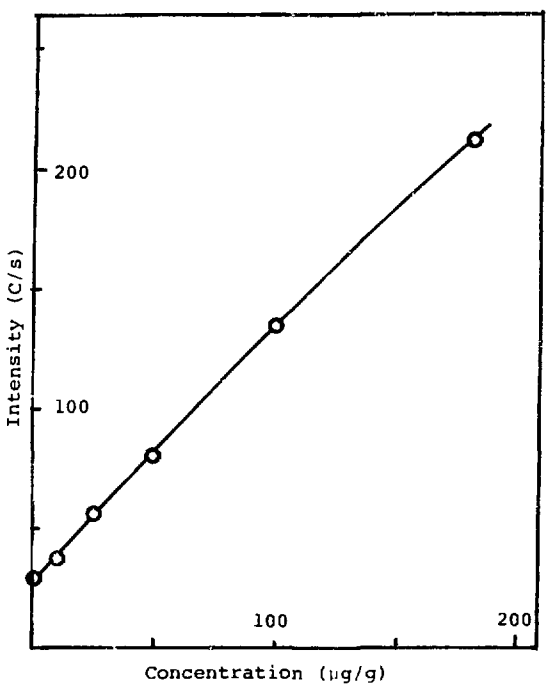

FIGURE 4. SULFUR

Prior to the studies reported here, other matrices and operating conditions were investigated. For instance, the use of filter pulp in place of Bakelite powder in forming the pellets did not significantly improve the measurements. In addition, the pellets made with filter pulp were not as durable as the Bakelite pellets.

Bromine was measured using a molybdenum target tube in place of chromium along with a LiF(200) analyzing crystal. Sensitivity was excellent and a satisfactory working curve was obtained (see Figure 5). The only advantage in recommending the conditions specified in Table I for bromine analysis is the fact that X-ray tubes do not need to be changed during sample measurement.

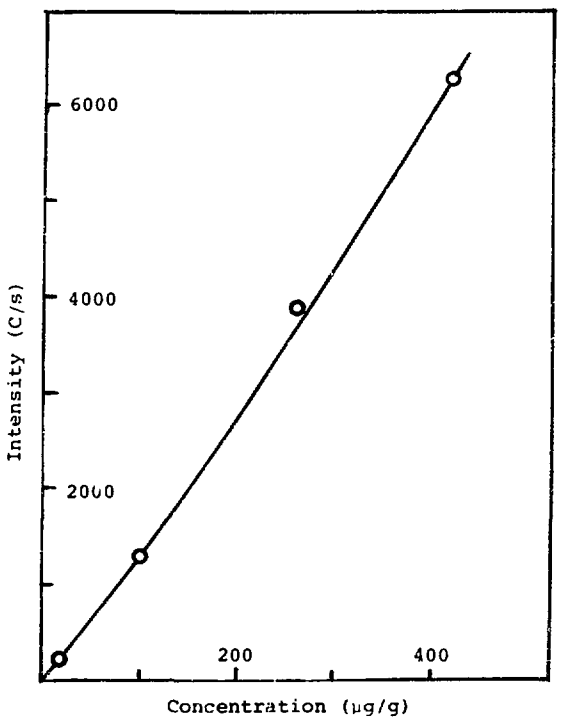

FIGURE 5. BROMINE (Mo TUBE)

Some interesting effects were noted when the chromium target tube was used in combination with a pentaerythritol analyzing crystal to measure sulfur concentration. Although this combination has been used successfully in determining sulfur in high Z matrices, results with low Z materials (boron in Bakelite) are less than satisfactory. High erratic blank values not identified as contributions from sulfur were observed. Investigation revealed interferring second order effects and an escape peak of chromium in the area of the sulfur peak. Replacing the PET crystal with a germanium (Ge 111) crystal re-

sulted in the elimination of both interferences.

Preliminary data for fluoride measurements listed in Table II and plotted in Figure 3 show that X-ray spectroscopy may be useful in estimating fractional percentages of fluorine in boron materials. Further refinement of this technique is planned.

Future efforts to improve the sensitivity and accuracy of Br, Cl and S measurements include the substitution of high purity graphite for Bakelite with pellets pressed at significantly higher pressures.

Reference

1. Eugene P. Bertin, "Principles and Practice of X-Ray Spectrometric Analysis", Plenum Press, N.Y. (1975).

Proceedings, ERDA X-and Gamma-Ray Symp. Ann Arbor, MI, May 19-21, 1976 (Conf 760539)

A MILLIANALYSER BY X-RAY FLUORESCENCE

A. Kawamoto, O. Hirao, J. Kashiwakura and Y. Gohshi
Toshiba R&D Center,
Komukai-Toshiba, Saiwai,
Kawasaki, 210 Japan.

Abstract

Research on the possibility of mm-size non-destructive analysis was carried out by the fluorescent X-ray method. With 0.2 mm pin-hole slit, source X-rays from a Cu target diffraction tube were collimated to a spot smaller than 1 mmϕ at a slide stage placed about 5 cm distant from the pin-hole slit. Resultant X-rays from a sample placed on the slide stage, which is excited by the collimated X-ray, were detected with a head-on-type 6 mm SSD, placed so that its 12.5 micron Be window was about 5 cm beneath the stage. X-ray intensities sufficient for analysis (500-5000 CPS) could be obtained for various metallic samples with up to 40 kV-10 mA excitation. This instrument proved to be useful for mm-size qualitative analysis in measurements of tiny samples. Furthermore the possibility of distribution analysis is expected based on the result of an investigation on c.a. 0.1% Cr in $LiNbO_3$, where the ratios of Cr-Kα intensity to scattered Cu-Kα intensity varied between 0.094 and 0.19, with deviations of less than 7.5% at five successive points located at 2 mm intervals along the direction of growth.

Introduction

Energy dispersive X-ray spectrometry (EDS) using an Si(Li) detector has become popular in the field of X-ray fluorescence analysis[1][2], as well as in that of EPMA (Electron Probe Micro Analysis)[3]. However, it seems still limited in measurements at a low count rate below 10K CPS, due to decrease in resolving power, unless intentionally ignoring a succeeding pulse with well devised techniques, such as anticoincidence[4]. On the other hand, it has large detection efficiency, which can be estimated as $10^3 \sim 10^4$ times that of an ordinary wavelength dispersive spectrometer (WDS) where crystals are used. In actual X-ray fluorescence analysis with EDS, it is necessary to take into account the limitation of the count rate for utilizing this merit of high detection efficiency. Photon flux density consumed to excite the sample can be reduced, or have to be reduced to $10^{-3} \sim 10^{-4}$ times of that is required in WDS, as long as the detection efficiency is not reduced. Or rather, an area excited by primary X-ray can be narrowed to $10^{-3} \sim 10^{-4}$ times of that in WDS, as long as the exciting photon flux density (photons/cm^2 sec) is unchanged. Since the excited area of a typical WDS X-ray fluorescence apparatus is about 10 cm^2 (= 10^3 mm^2), micro analysis in mm order seems to be feasible when the EDS spectrometer is employed.

In general, the EPMA method is adoped in micron order analysis, whereas WDS X-ray fluorescence method is employed in centimeter order analysis. A millianalyser by X-ray fluorescence with energy dispersive spectrometer using Si(Li) detector, which is the subject of this paper, can cover the intermediate region lying between the two methods.

Design and Construction

a) Mechanism

Figure 1 shows mechanical details of the apparatus. It includes the following three components and other mechanical parts holding them.

(1) Si(Li) Solid State Detector
(2) Sample Stage
(3) X-ray Tube

These three components are held so that the excited area is unchanged, no matter what arrangement variation occurs.

A top-hat and head-on type Si(Li) SSD (ORTEC-7016), whose effective area is 6 mmϕ with 12.5 micron Be window, was used. It was placed vertically under the sample stage. By shifting the SSD up and down, distance between the excited region and its Be window can be varied from 30 to 100 mm, so that the detection efficiency could be changed. Over the SSD, a sample stage (50 x 50 mm) made of Aluminum was held. The angle, formed between its face and a hypothetical horizontal surface, can be varied from -30° to 90°. It can be slid for x and y direction on its surface to change the excited region on a sample that is analysed in the millimeter order.

An ordinary Cu-target X-ray tube for diffractometry was used to provide primary X-ray for excitation. To collimate the X-ray beam, a Cu-made 0.2 mmϕ slit is attached to the tube. It has an empty cylindrical structure, having 0.2 mmϕ pin-holes on both bottom surfaces. By moving the tube, the angle formed between the primary X-ray beam and resultant secondary X-ray flux to be detected with SSD can be varied from zero to 180°, so that the appearance of diffraction peaks can be avoided when a crystalline sample is investigated. Distance between the slit exit and the excited point on a sample can be varied from 50 to 200 mm, to change the size of the excited area.

All of the results described in this paper were given under the following conditions. The distance between the slit and the excited point on the sample was fixed at about 5 cm. Also, the distance between the SSD's window and the excited point was fixed at about 5 cm. The angle formed between the surface of the sample stage and the primary X-ray beam was fixed at about 90°. The angle formed between the surface and the resultant secondary X-ray to be detected with the SSD was fixed at about 45°.

b) Electronics

Figure 2 shows a blockdiagram of a pulse height analysis system used in this millianalyser. It was proved to have a resolving power of 200 eV FWHM (Mn-Kα line) at 1000 CPS. Linearity between incident X-ray energy values and peak-channel numbers was found to be kept

correct with error of less than 1% in the region between 3 keV and 40 keV.

Experimental Observations and Results

a) Excited area size

On the arrangement described above, the diameter of the collimated primary X-ray was measured by the photographic method. An image on an X-ray film put on the sample stage revealed that the diameter is about 1 mm, as is shown in Fig. 3.

b) Secondary X-ray yield

Secondary X-ray intensities for various pure metallic samples were measured at 40 kV-2 mA operation of the X-ray tube. Both characteristic and continuous spectrum region of Cu-target emission were used for excitation. Obtained X-ray fluorescence spectrum consists of the characteristic X-rays of the sample elements and of scattered Cu characteristic X-rays. Results are listed in Table 1. Characteristic X-ray peaks could be seen obviously in each obtained spectrum, so that these secondary X-ray intensities could be considered sufficient for principal component analysis.

c) Qualitative analysis by millianalyser

Figure 4 shows an X-ray fluorescence spectrum obtained from a sintered lead oxide. It was measured at 25 kV-4 mA operation of the primary X-ray tube, and accumulated for 8^3 sec at a count rate of c.a. 200 CPS. Then, peak identification was carried out with TOSBAC-5400 TSS search system. In Table 2, the result of chemical analysis is listed for comparison. Obviously, it was found that qualitative analysis about elements, whose contents are more than 1% and whose atomic numbers are more than 22 (Ti), is feasible with this method.

To demonstrate usefulness of the millianalyser for qualitative analyses, a part article of an electron capture type detector (c.a. 10 x 15 x 20 mm as shown in Fig. 5) for a Gas-Chromatograph was investigated. It is made of ceramic. An unknown metallic material (about 1 mmφ) is molded into it. In addition, a wire (about 1 mmφ) is contacted to the metallic material with a solder like substance. Fluorescence spectra were measured for three points with 40 kV-0.5 mA operation. They were:

(A) Wire, (B) Molded material,
(C) Solder like substances.

Each spectrum was accumulated for 8^3 sec at about 1000 CPS. Those spectra are shown in Fig. 6a, in Fig. 6b and in Fig. 6c, respectively. From the spectra, it was found that both (A) and (B) are made of Nickel, and that (C) is a kind of silver solder which contains Ag, Cd, Zn and Fe. Furthermore, by investigating the spectra carefully, it was also found that manganese was used to contact (B) with the ceramic, or that manganese is contained in (B), as is shown in Fig. 6a' and in Fig. 6b'.

d) Distribution analysis

Generally, quantitative analysis by X-ray fluorescence method, with WDS spectrometer, adopts a photon counting method with stopping scanning of a goniometer at the angles corresponding to the characteristic X-ray of the measured element in question. Whereas, when EDS spectrometer is employed, intensity of characteristic X-ray has to be measured, after analysing data obtained from the fluorescence spectrum. When peak width is not influenced by count rate, and when overlapping of neighboring peaks does not occur in a spectrum, intensity of characteristic X-ray can be measured as a peak height.

For a preliminary experiment, Mo contents in Fe-Mo binary alloys were measured, because this sample is famous for resulting in a good linear calibration curve. Data were collected about FX-series standard samples, made by the Iron and Steel Institute of Japan, with 30 kV-8 mA operation. Spectra data were accumulated for 8^3 sec at about 3000 CPS, with a channel width of 19.6 eV/cm. Countrate decreased slightly as Mo concentration increases, because the fluorescence yield is higher at Fe than at Mo (shown in Table 1). However, Mo-Kα line peak width was mostly unchanged. Figure 7 shows a calibration curve obtained with plotting the peak heights of Mo-Kα lines versus concentrations of Mo after smoothing the spectra. It shows a good linear curve. Thus, it can be concluded that, as long as the condition described above is maintained and the matrix is not changed, quantitative analysis is possible with measuring peak height.

Based on the result of these preliminary experiments, the possibility of distribution analysis was examined. As a sample, $LiNbO_3$ crystal that contains c.a. 0.1% Cr was prepared. As to $LiNbO_3$ crystals made in the same way, it had been known previously from results of other destructive analyses that concentration of doped Cr is varied on a spot to spot. Using the millianalyser, which can non-destructively analyze, the distribution of doped Cr content was investigated. At as high an X-ray tube operation voltage as 30 ∿ 40 kV, K emission from contained Nb is too strong. In addition, concentration of doped Cr is very low. Time consumed for analysis seemed too long when reasonable resolution was maintained under such a high operation voltage. Then, the X-ray tube was operated at 15 kV to subdue the K emission (Nb-Kα = 16.6 keV, Nb - Kβ = 18.6 keV). To raise the Cr-Kα fluorescence yield, the X-ray tube was operated at 13 mA. Under such conditions, spectrum was accumulated for 2 x 8^3 sec at 40 CPS with a channel width of 20.0 eV/ch. Obtained typical X-ray fluorescence spectrum is shown in Fig. 8. Measurements were carried out on five successive points with 2 mm intervals along the direction of growth, i.e. A,B,C,D and E, in order. Using scattered Cu-Kα line intensities to compensate for primary X-ray beam intensity drifting, Cr-Kα line peak height ratios to that of the Cu-Kα line were compared. Since suitable standard samples could not be prepared, the absolute amount of doped Cr could not be determined. However, from the fact that the ratio varied from 0.094 to 0.19 as shown in Table 3, Cr distribution can be seen as relatively such that the doped Cr concentration increased from point C to point E.

Acknowledgements

The authors thank Mr. K. Hori and Mr. A. Kudo for their contributions in designing and manufacturing the apparatus. The authors also thank Mr. Matsumura for supplying the $LiNbO_3$.

References

[1] R. L. Heath
Advances in X-ray Analys. vol.15
pp. 1 - 35 (1972)

[2] D. E. Porter and R. Woldseth
Anal. Chem. 45(7), 704A (1973)

[3] E. Waldl, H. Wolfermann, N. Rusovic, and H. Warlimont
Anal. Chem. 47(7), 1017 (1975)

[4] F. S. Goulding, J. M. Jaklevic, B. V. Jarrett and D. A. Landis
Advances in X-ray Analys. vol.15
pp. 470 - 482 (1972)

A	SSD
B	X ray tube
C	Slit
D	Sample Stage
F	Post
J	Main Shaft

K	Worm Wheel
L	Worm
M	Handle
N	Worm Case
O	Worm Wheel
P	Worm
Q	Handle
R	Worm Case
S	Stage
T	Steering Arm
U	Tube-holding Shaft
V	Linear Motion Ball Bearings
W	Handle

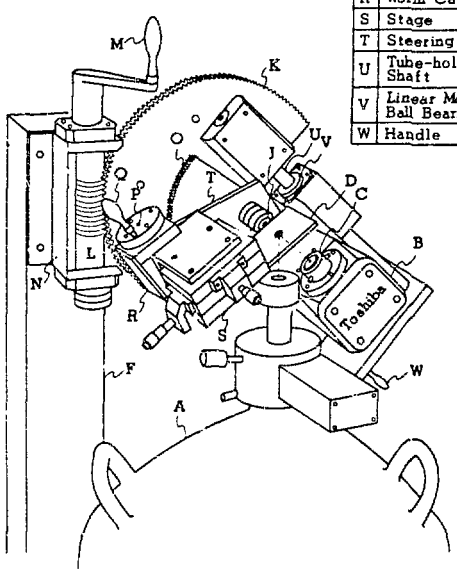

Fig.1 Detail of the Mechanical Part

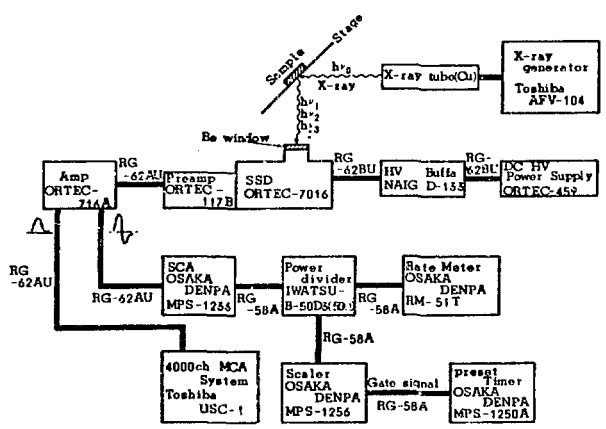

Fig.2 Block diagram of SSD X-ray Fluorescence Spectrometer

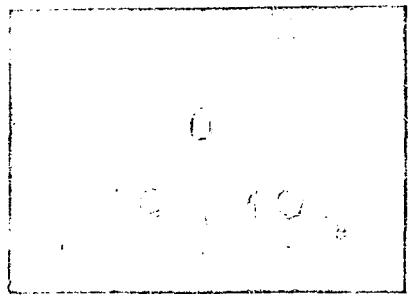

Fig.3 Photograph of Primary X-Ray Image

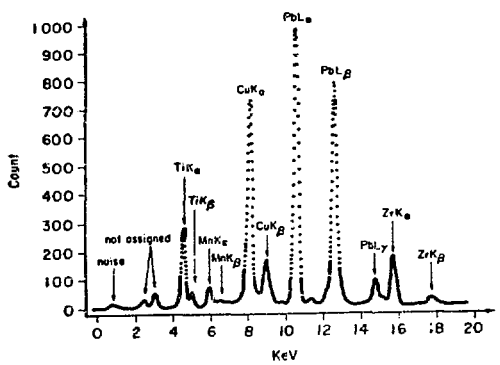

Fig 4 X-ray Fluorescence Srectrum of Sintered Lead Oxide

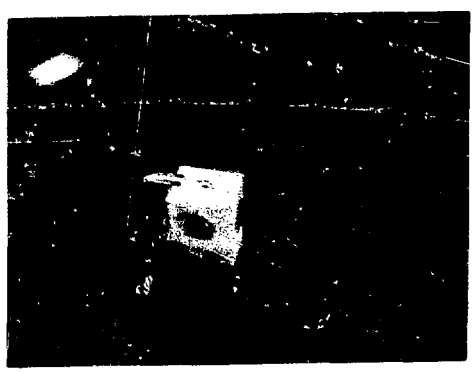

Fig. 5 Photograph of a part article used in ECD for Gas Chromatograph

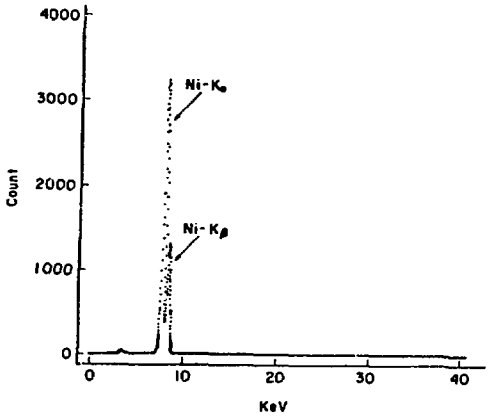

Fig 6a X-ray Fluorescence Spectrum of Wire Part

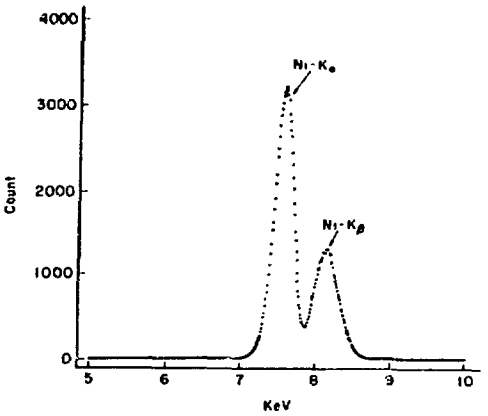

Fig. 6a' Expansion of Fig 6a

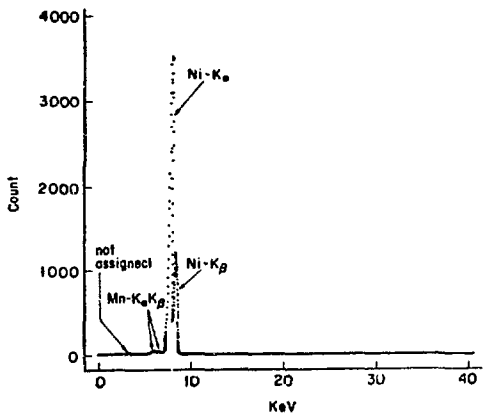

Fig. 6b X-ray Fluorescence Spectrum of Molded Part

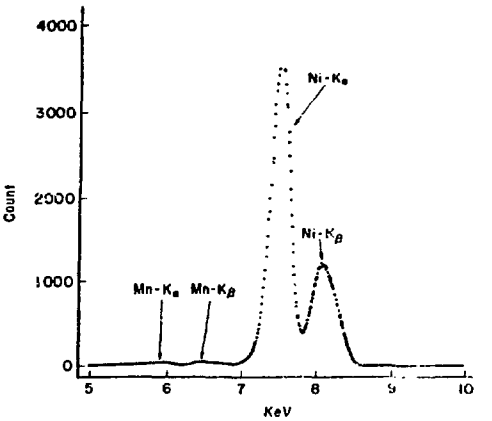

Fig 6b' Expansion of Fig 6b

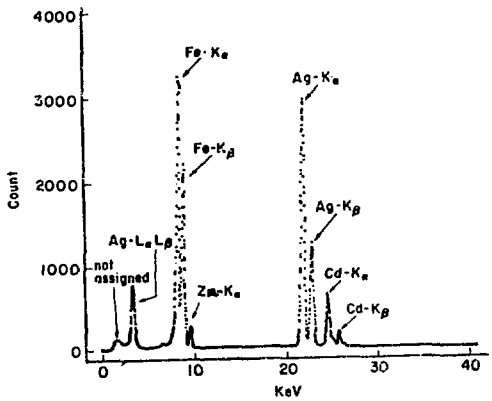

Fig. 6c X-ray Fluorescence Spectrum of Solder Like Part

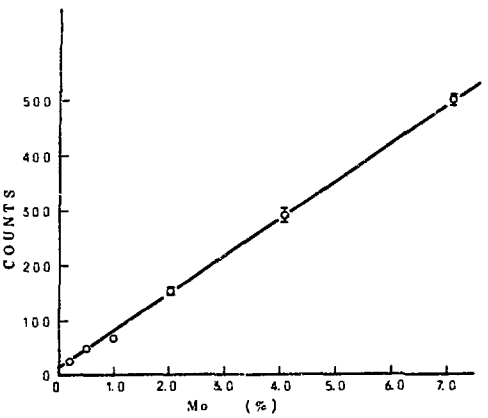

Fig. 7 Calibration Curve of Mo in Fe-Mo Binary Alloy

(cont. on p. 284)

Proceedings, ERDA X-and Gamma-Ray Symp. Ann Arbor, MI, May 19-21, 1976 (Conf 760539)

X-RAY THICKNESS MEASUREMENT OF ALUMINUM ALLOYS

J.J.Albert, Consultant, New York (212) 325-9422

The theory of X-Ray thickness gauging is extended to reveal the conditions under which a fixed anode voltage is ideal. A mathematical model of an alloy and computations reveal that two voltages can be used to measure the aluminum alloys with an error of roughly one percent, determined by the tolerance on manganese content, rather than the large errors ordinarilly a consequence of the tolerances on copper and zinc content. Implementation is discussed.

Extended Theory

Much of the theory of transmission thickness gauging begins with the equation

$$I = I_o \varepsilon^{-\mu x}$$

where:

I is intensity incident on the detector when thickness, x, is interposed between source and detector

I_o is the intensity incident on the detector when thickness is zero

μ is the linear absorption coefficient

When an X-Ray tube is used as the source, the substantial spectrum renders this model a rough approximation (and thickness gauge designers characteristically rely heavily on empiricism, rather than make calculations over the spectrum).

However, even the approximate theory, when extended, reveals useful additional information about thickness gauging.

Consider the derivable signal-to-noise equation (Appendix 1):

$$\frac{\Delta I_d}{I_{d_n}} \cong -\mu h x \sqrt{\frac{I_o T}{h\nu} \varepsilon^{-\mu x}}$$

where:

ΔI_d is the change of detector current consistent with a fixed change in thickness,

$\Delta x = hx$ (for purposes of analysis)

I_{d_n} is the RMS fluctuation of detector current (observed after integration)

μ is linear absorption coefficient (CM^{-1})

x is thickness (CM)

I_o is intensity incident on the detector when thickness is zero (ERGS/SEC)

T is integration time (seconds) of circuit prior to observation of detected signals

$h\nu$ is photon energy (ERGS)

This equation has the well known maximum at $\mu x = 2$ which can easily be demonstrated by adjusting thickness. However, when coefficient is adjusted, via anode voltage, intensity and photon energy also change so that it is necessary to examine performance in terms of anode voltage.

Intensity vs. Anode Voltage

Intensity can be related to anode voltage, E, by

$I_o \propto E^{n+1}$ $\left(\frac{I_o}{I_{o'}} \propto E^n\right)$

where n+1 may be between 2 and 5, depending on the X-Ray tube and the voltage range involved.[1]

Coefficient vs. Anode Voltage

Coefficient can be related to anode voltage by $\mu \propto \frac{1}{E^m}$

where m may be between 2 and 4. (Such an approximation is appropriate if one is well removed from a critical absorption edge).[1]

Signal-to-Noise vs. Anode Voltage

Substituting for intensity, coefficient and photon energy in the signal-to-noise equation and differentiating with respect to voltage, one finds that the coefficient-thickness product at "best voltage" is (Appendix II):

$$\mu x = 2 - \frac{m}{n+m}$$

Alternatively, the thickness for which a given voltage is the best voltage is

$$x_a = \frac{1}{\mu}\left(2 - \frac{m}{n+m}\right)$$

which is, in general, much smaller than best thickness

$$x_b = \frac{2}{\mu}$$

The Consequences

If a maximum voltage is assumed and S/N plotted vs. thickness, one finds that "fixed" anode voltage is ideal in that no improvement in S/N is attainable, via voltage reduction, in the region below best thickness, $x_b = \frac{2}{\mu}$

down to $x_a = \frac{1}{\mu}\left(2 - \frac{m}{n+m}\right)$

(the thickness for which maximum voltage is the best voltage).

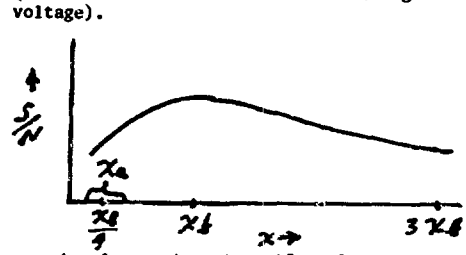

An alternative view, if anode voltage is to be chosen, one finds that S/N is maximized at a small coefficient-thickness product (generally less than one), whereas the requirement for detector and circuit stability is relaxed at high coefficient-thickness products. Thus, if one has stable components, "fixed" voltage, (yielding small coefficient-thickness products) is a desirable choice for gauge design.

Alloy Measurement

In the neighborhood of one angstrom, where many aluminum measurements are made, the photoelectric effect predominates in determining absorption coefficients. The aluminum alloys can thus be regarded as being composed of layers of the constituent components since the atoms retain their X-Ray absorption characteristics, independent of their location along the X-Ray beam.

Thus, at one "fixed" voltage, the intensity yielded by a two component alloy can be represented as

$$I = I_0 \, \varepsilon^{-(\mu_1 x_1 + \mu_2 x_2)}$$

where

μ_i is linear absorption coefficient
and xi is equivalent geometric thickness

At another voltage, chosen to yield differential changes in coefficients,

$$I_2 = I_{02} \, \varepsilon^{-(\mu_{12} x_1 + \mu_{22} x_2)}$$

Simultaneous solution of these equations will yield the unknowns, x_1 and x_2. The calculation x_1 plus x_2 is the geometric thickness of the two component alloy.
(The subscript 2 is used to designate parameters at the lower voltage)

Implementation

Observe that these equations can be written as

$$\frac{1}{\mu_1} \log \frac{I_0}{I} = x_1 + \frac{\mu_2}{\mu_1} x_2$$

$$\frac{1}{\mu_{12}} \log \frac{I_{02}}{I_2} = x_1 + \frac{\mu_{22}}{\mu_{12}} x_2$$

Note that these are

apparent thicknesses, as though measuring only one component. In fact, if only one component is introduced, x_1 ,(aluminum), it is possible to calibrate the thickness measurements to establish the numbers

$\frac{1}{\mu_1} \log \frac{I_0}{I}$ and $\frac{1}{\mu_{12}} \log \frac{I_{02}}{I_2}$

over the range of thickness to be measured.

Since $\frac{\mu_2}{\mu_1}$ and $\frac{\mu_{22}}{\mu_{12}}$ easily measured, by substituting material, the only unknowns in the two equations are the component thicknesses, x_1 and x_2

Let x_a and x_{a2} be the apparent thicknesses. The two equations are then

$$x_a = x_1 + \frac{\mu_2}{\mu_1} x_2$$

$$x_{a2} = x_1 + \frac{\mu_{22}}{\mu_{12}} x_2$$

Simultaneous solution yields the computed thicknesses

$$x_{2c} = \frac{x_a - x_{a2}}{\frac{\mu_2}{\mu_1} - \frac{\mu_{22}}{\mu_{12}}} = x_2$$

$$x_{1c} = x_a - \frac{\mu_2}{\mu_1} x_2 = x_1$$

Computed total thickness is

$$x_c = x_{1c} + x_{2c} = x_1 + x_2$$

(true thickness) independent of how x_1 and x_2 vary, in total, or with respect to each other.

Additional Components

To evaluate the effect of a third component, note that the apparent thicknesses are then

$$x_a = x_1 + \frac{\mu_2}{\mu_1} x_2 + \frac{\mu_3}{\mu_1} x_3$$

$$x_{a2} = x_1 + \frac{\mu_{22}}{\mu_{12}} x_2 + \frac{\mu_{32}}{\mu_{12}} x_3$$

The computed value of thickness is then

$$x_c = x_{1c} + x_{2c} = x_1 + x_2 +$$

$$+ x_3 \left[\frac{\mu_3}{\mu_1} + \frac{\frac{\mu_3}{\mu_1} - \frac{\mu_{32}}{\mu_{12}}}{\frac{\mu_2}{\mu_1} - \frac{\mu_{22}}{\mu_{12}}} \left(1 - \frac{\mu_2}{\mu_1} \right) \right]$$

Note that a third component does not influence the measurement of x_1 and x_2 so that they can vary in content, as before, without introducing error in thickness measurement.

The third term is an apparent thickness since the equivalent geometric thickness, x_3 , is multiplied by a factor which could be as much as $\frac{\mu_3}{\mu_1}$

The average value of the third (and other) terms are easily "calibrated out" of the final readout (one time for each alloy), but tolerance on content permits errors, the magnitude of which are determined by the departure of these terms from geometric thickness, x_3 , x_4 , etc. (the closer these terms are to geometric thickness, the smaller the errors).

The Aluminum Alloys

To illustrate the value of the two voltage measurement, consider alloy 2024.[2] Using a single voltage measurement and assuming a sinusoidal fluctuation of content, the RMS equivalent aluminum of the copper fluctuation is about 4%. Using the two voltage measurement there is theoretically zero error due to changes in copper content.

(The component limiting performance is manganese, since the absorption edge at 1.89Å. permits little differential change of coefficient, voltage-to-voltage, relative to aluminum. That is,

$$\frac{\mu_3}{\mu_1} - \frac{\mu_{3c}}{\mu_{1c}}$$

is closer to zero, for manganese, than is the case for any other component, resulting in an error of roughly 1% for those alloys containing the most manganese)

Measuring Thick Specimens

To measure thick material high voltage (short wavelength) is required for good S/N ratio and, on the other hand, it's necessary to exploit the critical absorption edges of copper and zinc (at 1.38 Å and 1.28 Å), to develop significant differential changes in coefficients, by choosing the low voltage to get some of the spectrum above these edges. In consequence, the measurement at the low voltage and hence computed thicknesses may be noisy.

Rather than use them directly for thickness measurements (by adding components) consider developing a calibration signal.

At the high voltage where S/N is good one measures

$$x_a = x_1 + \frac{\mu_2}{\mu_1} x_2$$

What function would correct this to yield true thickness

$$x_1 + x_2$$

Let this calibration signal be "C"

$$\left(x_1 + \frac{\mu_2}{\mu_1} x_2\right) C = x_1 + x_2$$

$$C = \frac{1 + \left(\frac{x_2}{x_1}\right)}{1 + \frac{\mu_2}{\mu_1}\left(\frac{x_2}{x_1}\right)}$$

Note that x_2/x_1 is not a function of thickness. (For example, at a given alloy composition, a 3% change in thickness would produce a 3% change in both components). It is, however, a function of alloy composition, which changes more slowly with time. As a consequence x_2/x_1 can be computed and averaged a relatively long time to yield the calibration signal, which, when multiplied by the high voltage measurement, will yield thickness measurement with good S/N ratio.

Hardware

The X-Ray Source

To compensate for the large difference in intensity (with X-Ray tube energy either side of the copper and zinc absorption edges)[1] it is desirable to have 8 pulses at the low voltage for every pulse at the high voltage. A high pulse repetition frequency (PRF = 600 Hz) was therefore used in experimental equipment in order to realize a reasonable PRF for the high voltage measurement.

The Detector

The Silicon detector (Nuclear-Semiconductor model L200-(2) CS, 200 mm^2 x 2 mm) is an excellent choice for the low energy photons involved, and, by using it as a pulse detector (10^4-10^6 photons per pulse), there was no problem with leakage current.

Digital Computation

The approach to digital computation can be appreciated by noting the correspondence between the functions:

$$I = I_0 \varepsilon^{-\mu x} \qquad e = E \varepsilon^{-\frac{t}{RC}}$$

("e" is the voltage across a parallel RC circuit as the capacitor discharges with time, t)

The steps in the process are:

1. Charge a capacitor to a "detected" voltage corresponding to zero thickness.
2. When this voltage is removed from the capacitor, (commencing discharge), start the count of a clock.
3. When this voltage drops to equal the currently detected voltage, stop the count.

In consequence of the correspondence between the two functions there is a one-to-one correspondence between thickness and time (the count of the clock).

Due to the spectrum yielded by as X-Ray tube, the actual functions must be approximated with two or three RC circuits, which are calibrated to establish the numbers

$$\frac{1}{\mu_1} \log \frac{I_0}{I} \quad \text{and} \quad \frac{1}{\mu_{1c}} \log \frac{I_{0c}}{I_c}$$

Conclusions and Comments

The extended theory of thickness gauging reveals that, under very reasonable conditions, "fixed" anode voltage is a desirable choice for gauge design. In particular, two "fixed" voltages can be used to measure the aluminum alloys, eliminating the large errors ordinarily a consequence of the tolerances on copper and zinc content.

Appendix I

Average detector current is proportional to intensity

$$I_d = k_3 I_0 \varepsilon^{-\mu x}$$

(definition of terms is given in the text)

since $\Delta I_d \cong \frac{d I_d}{dx} \Delta x$

and $\Delta x = k x$ (fixed, for analysis)

$$\Delta I_d \cong -k k_3 \mu x I_0 \varepsilon^{-\mu x}$$

To find the RMS noise, I_{dn}, note that[3]

$$\frac{I_d}{I_{dn}} = \sqrt{n_i}$$

(n_i is the average number of photons in an integration interval, T)

$$n_i = \frac{I T}{h\nu}$$

so that there is an equivalent noise

$$I_{dn} = k_3 \sqrt{I_0 \varepsilon^{-\mu x}} \sqrt{\frac{h\nu}{T}}$$

Thus:

$$\frac{\Delta I_d}{I_{dn}} = -k \mu x \sqrt{\frac{I_0 T}{h\nu} \varepsilon^{-\mu x}}$$

Appendix II

Let: $I_0 \propto E^{n+1}$

$h\nu \propto E$

$$\frac{I_0 T}{h\nu} = k_1 E^n$$

$$\mu = \frac{k_2}{E^m}$$

$$\frac{\Delta I_d}{I_{dn}} = -\frac{k_2}{E^m} k x \sqrt{k_1 E^n \varepsilon^{-\frac{k_2}{E^m} x}}$$

Since differentiation is with respect to voltage, with x constant, let

$$k_2 k x \sqrt{k_1} = K$$

$$\frac{\Delta I_d}{I_{dn}} = -K \left[E^{\frac{n}{2}-m} \varepsilon^{-\frac{k_2 x}{2E^m}} \right]$$

$$\frac{d\left(\frac{\Delta I_d}{I_{dn}}\right)}{dE} = -K \varepsilon^{-\frac{k_2 x}{2E^m}} \left[E^{\frac{n}{2}-m} \left(\frac{k_2 x}{2} m E^{-m-1} \right) + \left(\frac{n}{2} - m \right) E^{\frac{n}{2}-m-1} \right]$$

Setting this equal to zero:

$$\frac{k_2 x}{2} m \varepsilon^{-m} + \left(\frac{n}{2} - m \right) = 0$$

$$\frac{k_2}{E^m} x = 2 - \frac{n}{m}$$

But: $\frac{k_2}{E^m} = \mu$

Thus: $\mu x = 2 - \frac{n}{m}$

Test for maximum is omitted for simplicity. Solution for anode voltage and maximum S/N is not presented since the coefficient- thickness product at "best" voltage is more easily compared with that at best thickness, "2".

Acknowledgement

The work on alloy measurement was inspired by Vossberg, (see, for example, the general suggestions in patent 3,121,166 - 2/1964).

References

1. Emmett F. Kaeble, "Handbook of X-Rays," McGraw Hill, 1967.

2. Registration Record of Aluminum Association Alloy Designation and Chemical Composition Limits for Wrought Aluminum Alloys, The Aluminum Association, New York, June 1, 1974

3. B. M. Oliver, "Thermal and Quantum Noise", Proceedings of The IEEE, May, 1965

Proceedings, ERDA X-and Gamma-Ray Symp. Ann Arbor, MI, May 19-21, 1976 (Conf 760539)

LATTICE DYNAMICS OF INTERCALATION AND LAYER COMPOUNDS BY ^{119}Sn MOSSBAUER EFFECT SPECTROSCOPY

R. H. Herber and R. F. Davis
School of Chemistry, Rutgers University
New Brunswick, N. J. 08903

A class of inorganic compounds which has received a great deal attention in the past few years is that comprised by the "layer" compounds represented by the transition metal and main group dichalcogenides of general stoichiometry ML_2, where M = Ta,Nb,Ti,Zr,Hf,Sn... and L is S or Se. These materials, which generally have the CdI_2 crystal structure, are referred to as "layer" compounds because the adjacent planes of chalcogen atoms are held together by relatively weak (van der Waals) forces, and the solid is readily cleaved in a direction parallel to these layers in contrast to cleavage orthogonal to this plane. Moreover, one consequence of this anisotropy in the bonding properties is the interesting observation[1] that atoms and molecular species can be inserted (intercalated) into the van der Waals layer, forcing these layers apart, with a concomitant change in both the crystallographic and electrical properties of the intercalate.

Numerous physico-chemical techniques have been employed to characterize these compounds and to elucidate their solid state properties. In the present study, we have focussed on the application of nuclear gamma ray resonance spectroscopy[2] - specifically that using the 23.8 keV radiation in ^{119}Sn - to examine in detail the lattice dynamics of layer compounds and some of their metal atom intercalates.

I. Background

Among the parameters which can be extracted from Mossbauer effect spectra, the isomer shift (IS) and quadrupole splitting (QS) hyperfine interactions have received the greatest attention from chemistry because they are most directly connectible with the chemical nature of the subject material. The former arises from the small change in the nuclear energy levels, caused by the interaction between the nucleus and the orbital electrons, while the latter reflects the departure from cubic symmetry of the electric charge distribution about the nucleus. In terms of experimentally accessible quantities the isomer shift is given by

$$IS = E_o - E_{o_R} = \frac{2}{5}\pi Ze^2\left\{\psi(0)^2_a - \psi(0)^2_s\right\}\frac{\Delta r}{r} \qquad (1)$$

where E_o is the energy of the resonance maximum for the material (absorber) under study, E_{o_R} is the resonance maximum for a reference absorber, the two electron densities $\psi(0)^2$, are evaluated at the nucleus for the absorber and source, respectively, and $\frac{\Delta r}{r}$ is the fractional change in the nuclear radius in going from the nuclear ground state to the nuclear excited state in the Mossbauer transition. The IS is usually expressed in velocity units (mm/sec) as a shift from the resonance maximum for a standard reference absorber material which, in the present study, is $BaSnO_3$ at 294 ± 2°K. The quadrupole splitting parameter reflects the details of the shape of the electric change distribution around the nucleus and is given by

$$QS = \frac{1}{2}e^2qQ\left(1 + \frac{\eta^2}{3}\right)^{1/2} \qquad (2)$$

in which q is the electric field gradient tensor, $\partial^2V/\partial z^2$, along the principal field direction, Q is the nuclear quadrupole moment, and η is an asymmetry parameter given by

$$\eta = \frac{\partial^2V/\partial x^2 - \partial^2V/\partial y^2}{\partial^2V/\partial z^2} = \frac{V_{xx} - V_{yy}}{V_{zz}} \qquad (3)$$

with the axes chosen so that $|V_{xx}| \leq |V_{yy}| \leq |V_{zz}|$.

In addition to these two hyperfine interactions, another parameter which can be used to elucidate the physico-chemical properties of the solid under study is the recoil-free fraction of the absorber, f_a, which can be related to the mean square amplitude of vibration $\langle x^2\rangle$ of the Mossbauer active atom by the relationship

$$f = e^{-\langle x^2\rangle \bar{\lambda}^{-2}} \qquad (4)$$

where $\bar{\lambda} = \lambda/2\pi = hc/2\pi E_\gamma$, with E_γ equal to the Mossbauer transition energy. In the case of ^{119}Sn, E_γ = 23.87 x 10^4 eV, so that $\bar{\lambda}$ = 8.266 x 10^{-10} cm. The recoil-free fraction can be extracted from a Mossbauer spectrum which has essentially a Lorentzian line shape from the total area, A, under the resonance curve, that is

$$A = \frac{\pi\Gamma}{2} f_a L(t) a \qquad (5)$$

in which Γ is twice the natural line width of the Mossbauer transition ($= \frac{\hbar}{2\pi c}$ = 0.6 mm sec^{-1} for ^{119}Sn), L(t) is a thickness dependent line broadening function related to $t = n\sigma_o f$, and a is a proportionality constant. Values of L(t) have been tabulated in the literature.[3] For resonance spectra with more than one resonance line these equations are appropriately summed over all components of the spectrum.

For the purposes of the present discussion it is important to realize that the temperature dependence of the area under the resonance curve reflects the temperature dependence of f_a; that is, d ln A/dT = d ln f/dT, and thus it is possible to extract the temperature dependence of the recoil-free fraction from the temperature dependence of the area under the resonance curve without the need for determining absolute values of the recoil-free fraction. The temperature dependence, d ln f/dT, in turn, can be interpreted in terms of a characteristic lattice temperature, θ_M, which would be a Debye temperature if the solid under examination met the criteria for a Debye solid. In general, however, the compounds of interest are not monoatomic, cubic (isotropic), arrays and thus the temperature characterized by recoil-free fraction experiments is judiciously referred to as a Mossbauer or Debye-Waller temperature.

In the Debye approximation

$$\ln f = -\frac{3}{2}\left\{\frac{E_R}{k\theta}\left[1 + 4\left(\frac{T}{\theta}\right)^2\int_0^{\theta/T}\frac{x}{e^x - 1}dx\right]\right\} = -2W \qquad (6)$$

where W is sometimes referred to as the Mossbauer-Lamb factor. In the high temperature limit, that is for $T > \frac{\theta}{2}$, the integral in (6) goes to (θ/T) so that

$$\frac{d \ln f}{dT} = -\frac{6E_R}{k\Theta_M^2} \qquad (7)$$

where E_R is the recoil energy calculated from conservation of momentum considerations, and is given by

$$E_R = \frac{E_\gamma^2}{2mc^2} \qquad (8)$$

so that (7) becomes

$$\frac{d \ln f}{dT} = -\frac{3E_\gamma^2}{mc^2 k\Theta_M^2} \qquad (9)$$

and for a free atom recoil-process (ie: m is the mass of the ^{119}Sn atom), a Mossbauer temperature can be calculated from the relationship

$$\Theta_M = \frac{E_\gamma}{c}\left[\frac{3}{mk \; d \ln f/dT}\right]^{1/2} \qquad (10)$$

$$= \frac{9.460}{(d\ln f/dT)^{1/2}} \quad \text{degrees}$$

A somewhat different procedure to obtain a characteristic lattice temperature from temperature dependent Mossbauer effect measurements has been proposed by Taylor and Craig[4] who define a dimensionless parameter, S_T, by the relationship

$$S_T = \ln f_T/(\delta v/c) \qquad (11)$$

where $(\frac{\delta v}{c})$ is the isomer shift expressed in dimensionless units. This parameter can be separated into a temperature dependent and independent (zero point) term, that is

$$\frac{\delta v}{c} = \left(\frac{\delta v}{c}\right)_T + \left(\frac{\delta v}{c}\right)_0 \qquad (12)$$

and is equal to $\frac{-3kT}{2mc^2}$ for $T \geq 2\Theta_D$

Craig and Taylor[4] show that in the high temperature limit (that is $T \geq (\Theta/2)$) it is possible to calculate a characteristic lattice temperature from the equation

$$\Theta_{CT} = \left(\frac{E}{k}\right)\left[\left(\frac{2}{S_T}\right)\right]^{1/2} \qquad (13)$$

where S_T is calculated from the relationship

$$S_T = \frac{d \ln f}{d(\frac{\Delta E}{E})} = \frac{d \ln A}{d(\frac{\Delta E}{E})} \qquad (14)$$

which differs from the relationship implied by (11) in that a knowledge of the absolute value of the recoil-free fraction is not needed, but only its change with $(\Delta E/E)$. The term $\frac{\Delta E}{E}$ is a dimensionless fractional energy change given by the isomer shift; that is

$$\frac{\Delta E}{E} = IS(mm/sec)\ \frac{0.1}{2.9979 \times 10^{10}} \cdot \qquad (15)$$

Combining (13) and (15), and making the substitution $E/k = 2.7702 \times 10^8$ deg for the Mossbauer transition in ^{119}Sn, leads to the relationship

$$\Theta_{CT} = 2.7702 \times 10^8 \left(\frac{2}{d \ln A/d \frac{\Delta E}{E}}\right)^{1/2} \qquad (16)$$

in which the denominator of the second term is derived directly from the slope of a plot of ln A versus isomer shift.

In the present study we have attempted to characterize a number of van der Waals layer compounds and their intercalates by determining IS, QS, Θ_M, Θ_{CT}, and related parameters, from temperature dependent Mossbauer effect measurements. The relationship of these parameters to the structure and bonding in these compounds will be considered.

II. Experimental

The samples used in the present study were prepared by literature methods.[5] TaS_2·Sn was obtained[6] by an evacuated hot tube technique using HCl as a vapor transport agent, and an independently prepared sample was generously made available to us by F. J. DiSalvo of Bell Telephone Laboratories, who also supplied us with a sample of TaS_2·$Sn_{1/3}$ which had been carefully characterized. SnS_2 was grown both with and without I_2 (~5 mgm/cm^3) as a vapor transport agent,[7] and these samples were compared with analogous samples obtained through the courtesy of P. A. Lee of Brighton College and R. Schöllhorn of the Westfalische Wilhelms Universitat. A single crystal sample of SnTe was generously furnished by M. Schaub at CENG, Grenoble. To all of these workers we are greatly indebted.

The Mossbauer experiments were carried out as described previously,[8] and the remaining aspects of the nuclear gamma resonance methodology have been detailed in earlier communications,[9] and need not be repeated here.

III. Results and Discussion

The ^{119}Sn Mossbauer parameters of the subject compounds are summarized in Table 1. The IS and QS parameters are in satisfactory agreement with previously published values and will be referred to below. In the present study, the primary focus has been on the lattice dynamics of the Mossbauer active atom in these compounds, and thus the parameter of greatest interest is the temperature dependence of the recoil-free fraction and the characteristic temperatures derived from such data, as well as from the temperature dependence of the isomer shift. In the following discussion the individual compounds will be briefly considered in terms of these parameters and their implications in the context of the lattice forces in these solids.

SnS_2. In common with numerous other dichalocogenides, stannic sulfide has the CdI_2 structure (C6)[10] with primarily covalent sp^3d^2 hybridization of the tin bonding orbitals. The lattice is simple hexagonal with one molecule per primitive cell.[11] The two unit cell dimensions are[12] $a = 3.639 \pm 0.005$ and $c = 5.884 \pm 0.005$ Å. Stannic sulfide can be grown either[12,13,14] directly from the elements, or in the presence of a vapor transport agent such as I_2, normally added at a concentration of ~5 mgm cm^{-3} of reaction tube volume. The optical[11] and electrical properties[15,16] of SnS_2 have been reported in detail. Of particular interest is the observation[17] that crystals grown in the presence of I_2 and examined by X-ray topographic methods, show an unusually low concentration of lattice defects, and it is clear that this synthetic method yields large single nearly perfect crystals. Although there have been some reports of anomalous color changes on heating SnS_2 obtained by I_2 transport, compared to samples obtained from the neat stoichiometric mixture, the presence of iodine in the lattice cannot be determined analytical-

ly,[14] at least down to the 10^{17} atoms per cm^3 (200 ppm) level.

The temperature dependence of the recoil-free fraction, d ln f/dT, obtained from a linear regression (least squares) fit of the temperature dependence of the area under the ^{119}Sn resonance curve, is $-(4.59 \pm 0.07) \times 10^{-3}$ deg^{-1} for the samples prepared in the presence of I_2, and $-(4.96 \pm 0.07) \times 10^{-3}$ deg^{-1} for samples prepared from the neat reactants. The larger temperature dependence for the latter is reflected in the θ_M value calculated from equation (10), which is 190 ± 3 for SnS_2 and 198 ± 3 for $SnS_2(I_2)$. There is no difference in the isomer shift observed for the SnS_2 and $SnS_2(I_2)$ samples, the 78°K value of 1.062 ± 0.003 mm sec^{-1} observed in the present study being in reasonably good agreement with the value of 1.11 ± 0.02 mm sec^{-1} reported[16] by Baggio and Sonino and in slightly less satisfactory agreement with the value of 1.16 ± 0.09 mm sec^{-1} reported[19] by Stockler and Sano. The characteristic temperature, θ_{CT}, calculated from the Craig-Taylor relationship, equation (16), is 160 ± 3°K for SnS_2 and 160 ± 3°K for $SnS_2(I_2)$. The difference between the θ_M and θ_{CT} values reflect the assumptions concerning the magnitude of the effective recoiling mass made in the derivation of equation (10). Clearly the significance of these lattice temperatures lies not in their absolute values, but rather in their relative magnitudes, as well as the changes which can be observed in this parameter with systematic changes in the solid absorbers.

$TaS_2 \cdot Sn_{1/3}$. The preparation, crystallographic properties, and intercalate behavior of this van der Waals layer compound have been discussed in detail[20] and the ^{119}Sn temperature dependent Mossbauer parameters have been reported.[21] The θ_M value calculated from the ln f versus T behavior in the temperature range $78 \leq T \leq 294$°K is 226°K. The isomer shift of the singlet resonance is 3.933 ± 0.009 mm sec^{-1} at 78°K and the temperature dependence of this hyperfine interaction parameter, d(IS)/dT, is $(4.66 \pm 0.20) \times 10^{-4}$ mm sec^{-1} deg^{-1}. The characteristic lattice temperature, θ_{CT}, calculated by means of equation (16) is 270 ± 5°K, but this value must be considered as only tentative since it is based on a rather limited IS(T) data set. At the present time a more detailed comparison between θ_M and θ_{SOD} for $TaS_2 \cdot Sn_{1/3}$ would be premature.

$TaS_2 \cdot Sn$. The preparation and solid state properties of the 1:1 intercalate have been reported in considerable detail[20,22] as have the ^{119}Sn Mossbauer effect parameters.[21] The controversy raised by the Sn ESCA data of Haas[23] concerning the question of whether or not the ^{119}Sn Mossbauer doublet spectrum is appropriately interpreted on the basis of a single tin site in the lattice, or, on the other hand by the existence of two distinct cubic symmetry sites, appears to have been definitively settled by the single crystal Mossbauer study of Herber and Davis,[5] and the data analysis reported in the present study has been carried out under the assumption that there is a single unique Sn site in the $TaS_2 \cdot Sn$ intercalate. The isomer shift at 78°K is 3.165 ± 0.004 mm/sec and the quadrupole splitting is 1.120 ± 0.007 mm/sec. The θ_M value calculated for a polycrystalline sample of $TaS_2 \cdot Sn$ is 179 ± 5°K and and that for a single crystal sample examined at an orientation angle of 0° between the optical axis and the crystallographic c-axis is 176 ± 5°K. The characteristic lattice temperature, θ_{CT}, calculated from the Craig-Taylor procedure is 183 ± 5°K. The satisfactory agreement in the case of $TaS_2 \cdot Sn$ between θ_M and θ_{CT} is presumably due to the fact that the intercalated tin atom exists as a quasi free entity within the van der Waals layer and its lattice dynamics are governed by forces acting on a nearly isolated tin atom rather than on an extensively covalently bonded moiety. This interpretation is consistent with the agreement between the calculated value of the temperature dependence of the isomer shift obtained from the high temperature limit Thirring expansion,

$$d(IS)/dT = -\frac{3}{2}\frac{E_\gamma k}{mc^2} = -3.497 \times 10^{-4}$$

mm sec^{-1} deg^{-1}, and the experimentally observed value of this dependence of -3.38×10^{-4} mm sec^{-1} deg^{-1}, as shown graphically in Fig. 4 of ref. 11.

SnTe. The preparation and crystallographic properties of tin telluride have been extensively reported in the literature, and it is clear[24] that SnTe exists only on the Te-rich side of the stoichiometric composition and has a melting point of 804-806°C. The temperature dependence of the recoil-free fraction of both the ^{119}Sn resonance and the 35.46 keV ^{125}Te resonance have been reported by Bukshpan[25] who finds $\theta_M(^{119}Sn) = 132 \pm 3$°K and $\theta_M(^{125}Te) = 141 \pm 5$°K in the range $85 \leq T \leq 250$°K. Lin and Rothberg[26] have carried out ^{119}Sn Mossbauer experiments on SnTe in the temperature range $300 \leq T \leq 500$°K and report data for samples having a range of hole concentrations ranging from 4.5×10^{19} cm^{-3} to 1.6×10^{21} cm^{-3}. Further temperature dependent Mossbauer measurements have also been discussed by Keune,[27] and Bryukhanov et al.,[28] who finds $\theta_M(^{119}Sn) = 139 \pm 3$°K and by Taylor and Craig[4] who found $\theta_{CT} = 154$°K using the ^{119}Sn resonance.

In order to compare directly the θ_M and θ_{CT} values from a given data set, we have repeated the ^{119}Sn resonance measurements on tin telluride over the temperature range $4.2 \leq T \leq 320$°K. The 78°K isomer shift of 3.433 ± 0.002 mm sec^{-1} is in excellent agreement with the value of 3.43 ± 0.02 mm sec^{-1} at 300°K reported earlier.[18] We have been unable to confirm the existence[29] of a quadrupole hyperfine interaction of ~0.31 mm sec^{-1} in the temperature range $78 \leq T \leq 160$°K. The temperature dependence of the recoil-free fraction in the range $174 \leq T \leq 320$°K is found to be -8.70×10^{-3} deg^{-1} from which $\theta_M(^{119}Sn) = 143 \pm 2$°K. The temperature dependence of the isomer shift extracted from these data is d IS/dT = -2.77×10^{-4} mm sec^{-1} deg^{-1} which yields, by the Craig Taylor procedure, the value $\theta_{CT} = 140 \pm 2$°K, in good agreement with θ_M calculated from the same data set.

These results may be interpreted as follows: In solids in which the (^{119}Sn) Mossbauer atom is held either as an ion or as an isolated atom in the structure, both the θ_M value calculated from the temperature dependence of the recoil-free fraction (evaluated in the high temperature limit where $T > \theta/2$ and in the absence of significant anharmonic effects) and the θ_{CT} value calculated by the Craig-Taylor procedure, give internally consistent values for the lattice temperature of the solid as probed by the Mossbauer atom.

In cases where this probe atom is part of a covalently bonded structure, as for example in the extended polymeric SnS_2, $SnSe_2$ and related solids, the difference between θ_M and θ_{CT} will be significant, and this difference should be useful in the elucidation of the intermolecular and bonding forces in such solids and their relationship to the solid state properties of these materials.

Finally, it is worth noting that the experimental determination of a unique lattice temperature by Mossbauer spectroscopic methods provides the solid state physicist with an additional parameter which should be useful in the characterization of solids, and, more importantly, may serve as a diagnostic tool in the assessment of the effects of systematic changes (such as, for example, compositional variations, radiation damage effects, implantation and intercalation consequences, etc.) brought about in such materials. The further application of these ideas to the study of van der Waals layer

compounds is currently underway in these laboratories.

IV. Acknowledgements

The authors are indebted to Drs. F. J. DiSalvo, R. Schollhorn, P. A. Lee, M. Schaub and L. J. Vieland for several of the samples used in the present study. This research has been supported in part by the Research Council, Rutgers University and the National Science Foundation under grants NP 28053 and DMR 76-00139. The award of summer research fellowships to RFD by the School of Chemistry and of support for the computational aspects of this work by the Center for Computer and Information Services, Rutgers University is also gratefully acknowledged.

References

[1]See for example: S. F. Meyer, R. E. Howard, G. R. Stewart, J. V. Acrivos and T. H. Geballe, J. Chem. Phys. 62, 4411 (1975); M. B. Dines, Science, 188, 1210 (1975); see also refs. 20 and 22.

[2]For an introduction to this technique, see G. K. Wertheim, "The Mossbauer Effect-Principles and Applications," Academic Press, New York 1964; Chemical Applications of Mossbauer Spectroscopy," V. I. Goldanskii and R. H. Herber, Eds., Academic Press, New York, 1968.

[3]D. W. Hafemeister and E. B. Shera, Nucl. Instr. and Methods, 41, 133 (1966); G. Land, ibid. 24, 425 (1963).

[4]R. D. Taylor and P. P. Craig, Phys. Rev. 175, 762 (1968).

[5]For details, see the AB Thesis of R. F. Davis, Rutgers University, 1976, and R. H. Herber and R. F. Davis, J. Chem. Phys. (in press 1976).

[6]F. R. Gamble, F. J. DiSalvo, R. A. Klemm and T. H. Geballe, Science, 168, 568 (1970).

[7]R. Nitsche, H. U. Bolsterli and M. Lichtensteiger, J. Phys. Chem. Solids, 21, 199 (1961).

[8]A. J. Rein and R. H. Herber, J. Chem. Phys. 63, 1021 (1975).

[9]R. H. Herber, M. F. Leahy and Y. Hazony, J. Chem. Phys. 60, 5070 (1974); Y. Hazony and R. H. Herber, J. de Physique, C6, 131 (1974); Y. Hazony and R. H. Herber, "Mossbauer Effect Methodology," Vol. 8, I. Gruverman, Editor, Plenum Press, New York 1973.

[10]A. F. Wells, "Structural Inorganic Chemistry," Oxford University Press, Oxford 1962, p. 512.

[11]M. Y. Au-Yang and M. L. Cohen, Phys. Rev. 178, 1279 (1969).

[12]D. L. Greenaway and R. Nitsche, J. Phys. Chem. Solids, 26, 1445 (1965).

[13]M. Baudler in "Handbook of Preparative Inorganic Chemistry," G. Brauer, Ed., Volume 1, p.741, Academic Press, New York 1963.

[14]G. Domingo, R. S. Itoga and C. R. Kannewurf, Phys. Rev. 143, 536 (1966); L. E. Conroy and K. C. Park, Inorganic Chemistry 7, 459 (1968).

[15]P. A. Lee, G. Said and R. Davis, Solid State Comm. 7, 1359 (1969); S. G. Patil, J. Phys. Chem. Solid State, 5, 2881 (1972); G. Said and P. A. Lee, Phys. Stat. Sol. 15, 99 (1973).

[16]J. P. Jowers and P. A. Lee, Solid State Comm. 8, 1447 (1970).

[17]H.P.B. Rimmington, A. A. Balchin and B. K. Tanner, J. Cryst. Growth, 15, 81 (1972).

[18]E. M. Baggio and T. Sonnino, J. Chem. Phys. 52, 5786 (1970).

[19]H. A. Stockler and H. Sano, J. Chem. Phys. 50, 3813 (1969).

[20]F. J. DiSalvo, G. W. Hull, Jr., L. H. Schwartz, J. M. Voorhoeve and J. V. Waszczak, J. Chem. Phys. 59, 1922 (1973).

[21]R. H. Herber and R. F. Davis, J. Chem. Phys. 63, 3668 (1975).

[22]F. R. Gamble, J. H. Osiecki, M. Cais, R. Pisharody, F. J. DiSalvo and T. H. Geballe, Science, 174, 493 (1971); F. R. Gamble, J. H. Osiecki and F. J. DiSalvo, J. Chem. Phys. 55, 3525 (1971).

[23]C. Haas, private communication; G. K. Wertheim, private communication.

[24]F. A. Shunk, "Constitution of Binary Alloys" Second Supplement, McGraw Hill Book Co., New York, p.689.

[25]S. Bukshpan, Solid State Comm. 6, 477 (1968).

[26]S. T. Lin and G. M. Rothberg, J. Nonmetals 1, 335 (1973).

[27]W. Keune, Phys. Rev. B10, 5057 (1975).

[28]V. A. Bryukhanov, N. N. Delyagin, R. N. Kuz'min and V. S. Shpinel, Zh. Eksper. Teor. Fiz. 46, 1996 (1964) [Engl. Transl. Sov. Phys. JETP 19, 1344 (1964)].

[29]V. Fano and I. Ortalli, J. Chem. Phys., 61, 5017 (1974).

Table I - Summary of Mossbauer Results

Compound	d lnA/dT (deg^{-1})	d (IS)/dT (mm/sec deg)	d lnA / d (ΔE_Q)	θ_M (deg K)	θ_{CT} (deg K)
SnS_2	$(-4.18\pm0.03)\times10^{-3}$[a]	-2.40×10^{-4}	6.06×10^{-12}	201±3*	160±3
$SnS_2(\perp_2)$	$(-4.10\pm0.02)\times10^{-3}$	-2.27×10^{-4}	6.05×10^{-12}	210±3*	160±3
$TaS_2\cdot Sn_{0.33}$	-3.50×10^{-3}	-4.66×10^{-4}	2.10×10^{-12}	226±5	270±5
$TaS_2\cdot Sn$[b]	-5.78×10^{-3}	-3.38×10^{-4}	4.54×10^{-12}	179±5	183±5
SnTe	-8.70×10^{-3}	-2.77×10^{-4}	7.88×10^{-13}	143±5	140±5

[a] In the temperature range: $77 \leq T \leq 180$°K.

[b] $TaS_2\cdot Sn$ single crystal absorber.

Proceedings, ERDA X-and Gamma-Ray Symp. Ann Arbor, MI, May 19-21, 1976 (Conf 760539)

MÖSSBAUER EFFECT EMISSION SPECTROSCOPY - A USEFUL SURFACE TECHNIQUE?[+]

C. R. Anderson and R. W. Hoffman
Department of Physics
Case Western Reserve University
Cleveland, Ohio 44106

The Mössbauer effect has been of considerable use in studying materials because of the detailed information obtained at the nuclear site. Mössbauer Effect Emission Spectroscopy (MEES), in which the specimen of interest is also the Mössbauer source, has < 0.01 monolayer sensitivity and thus is of interest in surface and thin film investigations. An in-situ UHV spectrometer has been constructed which permits the measurement of Mössbauer spectra at low temperatures as well as LEED and AES. It is suggested that the MEES technique, although specialized, may be useful in surface studies. The main differences from the usual absorption geometry are the production of the radioactive sample and possible relaxation effects resulting from the decay. The Mössbauer parameters are determined from the spectra in the usual manner. The MEES technique has been applied to the study of the magnetization and superparamagnetic relaxation in thin Fe - 0.01 at.% ^{57}Co films and to the changes in hyperfine field and line breadth in the amorphous crystalline transition in Co. Measurements of the true surface magnetization (111) Ni are in progress. The alloy films show effectively bulk behavior for average thicknesses > 15 Å and no superposition of ferromagnetic and paramagnetic spectra. Only 0.5 T increases in the internal field were found with crystallization of the pure Co films although a 30% decrease in line breath was observed.

Introduction

Mössbauer spectroscopy has most commonly been practiced in the absorption mode, in which gamma-ray sources having a precisely defined energy determined by the emitter nucleus and its environment are transmitted through an absorber containing identical nuclei but in a different environment. For the zero phonon population of gamma-rays, resonance absorption may now be observed by the appropriate Doppler shifting of their energy. Since the recoil energy must be small the γ ray energy is limited; in practice Mössbauer spectroscopy is confined to about 26 elements, the most common in usage being iron and tin.

The importance of the Mössbauer effect lies in its ability to fingerprint the local environment. The isomer shift provides a useful way to determine s electron densities and hence valencies in solids even when several valencies are present. The nuclear quadrupole splitting allows the determination of electric field gradients at sites with lower than cubic symmetry. The nuclear hyperfine structure is the result of the magnetic field acting at the nucleus. In ^{57}Fe this gives rise to a six-line spectrum from which the internal field and its direction may be determined . If the fields at the nucleus fluctuate at a rate of perhaps 10^9 per sec relaxation effects enter and the spectrum reflects the time averaged value of the field. As we shall see later the superparamagnetic relaxation in thin films is of special interest. Lattice dynamics may be studied through the temperature dependence of the Mössbauer fraction and the second order Doppler shift.

In the past 15 years applications of Mössbauer effect absorption spectroscopy have been numerous and been described in a series of books[1] and reviews.[2] The purpose of this paper, however, is to describe the Mössbauer effect emission spectroscopy (MEES) technique and to point out some of the advantages and disadvantages. With certain possible exceptions MEES yields the same information in absorption spectroscopy.

Emission and Scattering Modes

In MEES, the specimen is doped with a radioactive Mössbauer isotope and serves as the source. Hence the γ-emitting specimen contains the information concerning the desired nuclear environment. The absorber nuclei are placed in a host such that there is only a single sharp transition between the ground and the first excited states. This is the inverse of the usual absorption geometry in which the single energy gammas serve as the source and the environmental information is contained in the non-radioactive (absorber) sample. The equipment for providing the relative motion between the source and absorber as well as the detector circuitry and signal processing is the same in both techniques.

Since it is obvious that in MEES a new radioactive sample must be prepared for each experiment, we must justify the use of a technique that requires a more difficult sample preparation. The value of MEES lies in its greatly increased sensitivity. In order to deal with samples of smaller size, or concentration, and especially to carry out investigations of surface and near surface phenomonon one desires useful data from a sample containing perhaps 10^{13} Mössbauer nuclei in times of a few hours. Thus the signal-to-background ratio must be improved by at least 4 orders of magnitude over the usual absorption geometry, even if extremely strong sources were used to reduce the counting time. Although ^{57}Fe enrichment[3] and multilayer samples have been used to increase the sensitivity, but in the limit of small samples (< 10^{16} Mössbauer nuclei) the absorption geometry is not at all practical because the total number of resonant events is too small.

Mössbauer scattering geometries in either the forward[4] or backward[5,6] directions have also been used to reduce the background. In come cases the 6.3 keV internal conversion X-rays are detected,[7] and this provides energy discrimination. The internal conversion elections have also been used in the scattering geometry as a Mössbauer indicator.[8] In this case the experiment must be carried out in vacuum and rough depth profiling may be done by energy analyzing the emitted electrons. A spatial resolution of about 20A and a total depth that may be explored of some 600 Å has been found[9] for the K electrons ^{57}Fe.

In spite of the poorer than 10 monolayer sensitivity or resolution, backscatter geometries have seen increased use partially because the sample need not be either thin or "two-sided."[10-12]

One of the earlier applications of the MEES technique is that of the alkalide halides by Mullen[13] and others.[14] Tracer (0.1 mc) amounts of $^{57}CoCl_2$ were vacuum evaporated onto a NaCl crystal face and

thermally diffused into the lattice with some precipitation taking place. The same deposition technique is presently being used in studies of color centers in KCl and NaCl.[15]

Characteristics Unique to MEES

An early study by Wertheim[16] suggested that multiple charge states might exist in insulators because the Co Auger cascade relaxation process is incomplete before the excited ^{57}Fe nucleus decays with the emission of the 14.4 keV x-ray carrying the environmental information. Thus, unlike the absorption mode, the local nuclear signature may not be known in advance. The physics is essentially that of which charge state(s) exist in the just-decayed daughter on the time scale of the nuclear lifetime, which for iron is 10^{-7} sec. If the relaxation is sufficiently rapid then only a single charge state is involved and the observed Mössbauer spectrum is not mixed. This case seems to commonly happen for ^{57}Co in metals. A rapid relaxation was also observed for ^{57}Co/$CoCl_2$ and ^{57}Co/NaCl.[13] The case of ^{57}Co/CoO is complex and controversial. Measurements of delay-coincidence Mössbauer spectra in ^{57}Co/CoO and ^{57}Co/NiO show no evidence of metastable charge states,[17] although other interpretations of the Mössbauer data is given.[18,19] The temperature dependence of ^{57}Co/CoO spectra for material prepared at high temperatures has been interpreted as evidence for electron hopping charge fluctuations.[20] MEES is suggested as a sensitive technique to investigate charge averaging and fluctuations in solids.[20] With the present state of understanding direct comparison of emission and absorption spectra may be needed to establish the charge state for insulating samples as has been done for $LiNbO_3$ [21]

A second feature concerns the line shapes. Because of saturation effects in thicher absorbers, the peak heights or areas in a spectrum are seldom those calculated from the transition probabilities. In particular the nuclear Zeeman line intensities tend to become the same instead of the 3:2:1 ratio expected for a random magnetic field direction. Some applications envisage using the intensities to determine the average field directions and infer magnetic anisotropies. In this case MEES has an advantage as the absorber is fixed from sample to sample and may be made sufficiently thin to avoid saturation at the expense of counting time. Self-absorption in the sample is eliminated as the radioactive emitters are confined near the surface.

We establish the sensitivity of MEES with the following example. Consider a specimen of 1 cm^2 area doped with 10^{13} ^{57}Co atoms. This represents a concentration of about 10^{-2} monolayers with the atoms spaced some 30 Å apart on the surface. The working equation for the counting rate is:

$$N_c = \frac{\ln 2}{\tau} N_d \alpha_\gamma f_s F_a P$$

where N_d is the number of radioactive source atoms, τ their half-life, α_γ the Mössbauer decay branching ratio, f_s the source recoilless fraction. F_a is an absorber constant combining the f fraction, ^{57}Fe concentration and cross-sections and represents the absorber design comprimises between line breadth and counting rate. We have used 1 mg/cm^2 ^{57}Fe in stainless steel with F_a = 0.4 and 0.25 mg/cm^2 ^{57}Fe in sodium ferrocyanide. The constant P is the source-absorber-detector geometry factor and includes the transmission through the 0.010 in Be windows and Al radiation shield as well as the counter efficiency. For our spectrometer using 0.01 monolayer ^{57}Co the sample activity is 10 μCi and the counting rate is about 10 c/sec or roughly 100 counts per channel-hour.

UHV In-situ Emission Spectrometer

The UHV/MES apparatus has evolved over a period of several years. The first system had a reentrant cavity with a thin beryllium window for the Mössbauer radiation to reach the external coaxial absorber and proportional counter. An asymmetric constant acceleration drive was used to facilitate the data analysis.[22] The Mössbauer electronics are straightforward with the exception of the asymmetric drive. The cantilevered absorber and end window proportional counter complete the counting system and necessitated custom drive speakers to minimize unwanted vibrations. The system design and operation prior to the present modifications is described in references 22, 23 and 24. Presently the experimental linewidth for the spectrometer is <0.5 mm/sec FWHM.

Substrates were mounted on a variable temperature helium dewar and deposition carried out in the ultrahigh vacuum. A ^{57}Co Fe alloy was evaporated from a pyrolytic BN crucible in order to condense oligatomic films on glass substrates.[23] In spite of the low diffusion rate perpendicular to the BN basal plane, it was nevertheless difficult to deposit 10^{16} atoms by this technique. A pendant-drop electron beam heated source was designed to minimize the thermal flux and facilitate the condensation on helium temperature substrates.[24]

The system has now been redesigned to include LEED and AES (CMA) for surface studies. Figure 1 shows the geometry for the various techniques. The UHV pumping station is based on a 12" Varian ion/sublimation system with RGA. A 15" high collar

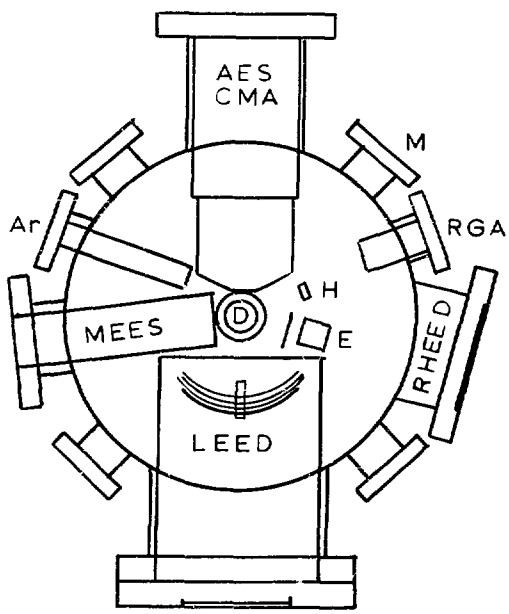

Figure 1 UHV in-situ MEES System. The sample is attached to the He dewar D, surrounded by a radiation shield. The pendant drop evaporator E and heater H are shown. Not drawn are RHEED electron gun and sample manipulator operating through port M

section, fabricated by Ultek, houses the MEES,LEED, single-pass CMA and Ar sputtering gun. Additional ports will allow the later addition of RHEED. The variable temperature dewar, custom fabricated by Janis Research on a 10" UHV flange is fastened to the top of the collar with its vacuum insulation common to the UHV. Pressures of 2 x 10^{-9} Pa are easily obtained after overnight bakeout and before the dewar is filled.

Because the specimen must be heated after argon bombardment for cleaning and annealing and then low temperatures maintained to avoid surface and bulk diffusion of the ^{57}Co, the sample holder design is rather complicated and will not be detailed here. In addition provision must be made to rotate the sample for the various surface analyses. The LEED pattern must be viewed from the back side of the screen since the specimen is mounted on a rather large cold finger, which in turn, is surrounded by a N_2 thermal radiation shield. The present system thus incorporates multiple surface techniques in addition to the in-situ MEES spectrometer even though some design compromises were necessary.

Examples

In-situ MEES has been applied to monolayer films by Varma and Hoffman.[23,25] Briefly these Fe 0.1 at.% ^{57}Co films were deposited on nitrogen cooled substrates at 10^{-8} Pa and spectra obtained from near helium to above room temperature. Films thicker than 10 Å (4 atomic layers) showed a hyperfine splitting over the entire temperature range, although the internal field decreased somewhat more rapidly with increasing temperature for the thinner samples. For the 0.2 monolayer specimen only a poorly resolved doublet related to rapid superparamagnetic fluctuations was noted. Several samples were produced in which the transition between these two behaviors could be followed and the usual six-line spectra would undergo a broadening and collapse. Submonolayer films showed a well resolved doublet interpreted as a quadrupole splitting at a particular nucleation site on the substrate. From the point of view of the ferromagnetic dead layers the films whose thickness exceeded the superparamagnetic transition never showed coexistence of a hyperfine spectrum with a central line. Thus, one must conclude that either no dead layer exists at the surface of these films or that the relaxation times are so changed near the surface that a paramagnetic contribution would not be observed.

For comparison Walker and his co-workers[12] have used the Mössbauer scattering geometry to reduce the background and obtain measurements on enriched samples. Epitaxial samples were prepared in UHV and then overcoated to protect them for the Mössbauer measurements made under ambient conditions. Their results agreed with those of Varma and Hoffman with the exception of two features. First, single and six-line spectra coexisted in some samples of average thickness up to about 30 Å and secondly, hyperfine fields in excess of the iron 33.0T were observed. The importance of trace impurities trapped in the sample during preparation and the difficulty of adequately protecting the sample were later recognized as a result of AES analysis indicating the presence of iron oxides. It should be emphasized that only the in-situ experiments do not show the superposition of ferro- and para-magnetic spectra.

100 Å ^{57}Co/Co films were deposited on helium temperature substrates by Kwan and Hoffman.[24] An amorphous crystalline phase transition was found at ~ 53 K by observing a rapid fourfold decrease in electrical resistivity upon warming. In contrast to data in less pure metallic amorphous ferromagnetics these Co films showed only a 0.5T increase in the internal field in going to the crystalline phase. The linewidth decreases from 0.8 to 0.6 mm/sec and can be interpreted in terms of a smearing of the atomic positrons in the randomized material. The other Mössbauer parameters were essentially unchanged.

Data for a 0.01 monolayer Co-Fe alloy deposited on a glass substrate but measured under ambient is shown in Fig. 2. The spectrum shows a splitting of 2.2 mm/sec, interpreted as a quadrupole splitting, and an isomer shift possibly corresponding to Fe^{2+}. The width of the lines was about 1.5 times the experimental resolution. The continuous function superimposed on the data is a Lorentzian function.

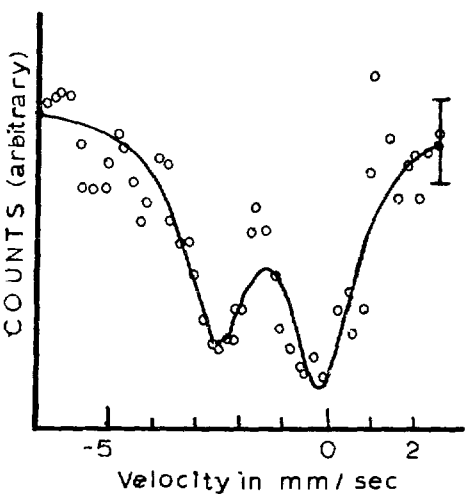

Figure 2 First MEES spectrum of 0.01 monolayer ^{57}Co/Fe sample. Isomer shift with respect to sodium nitroprusside.

The distinct features of the spectrum for this sample are consistent with the assumption of isolated atoms on the surface. At this low surface density the distance between atoms is about 10 atomic diameters, implying that about 99% of the substrate area is empty. This would indicate that the resonant fraction is for the most part due to substrate-iron bonding, and may thus be characteristic of isolated atoms on the surface.

It is also possible that monomers are not stable on the surface and the smallest stable nucleus consists of 3 or more atoms. The spectrum of Fig. 2 implies if this were the case, then the majority of emitting atoms have roughly the same quadrupole splitting, and isomer shift, and consequently implies that the majority of film atoms are either clusters of one atom, two atoms, three atoms, etc., but not a mixture of one, two, etc., atoms. This is in contrast to the normal interpretation of the nucleation and growth models which would predict a distribution of sizes of atomic cluster. Similar in-situ spectra with the same splitting but different isomer shift have been observed.[25] Upon annealing the usual six-line spectrum is observed corresponding to the growth of the n-mer cluster to a size greater than about 100 Å such that the superparamagnetic fluctuations are slow.

The examples given show that MEES has applications to thin film and amorphous magnetics, nucleation site identification and growth of small clusters and hence to catalysis. Additional data may be found in the references cited. Experiments are in progress to measure the surface magnetization and anisotropy direction by deposition of ^{57}Co on well-characterized single crystal magnetic surfaces. This field of surface Mössbauer effects has been reviewed by a number of authors, but experimental data are scarce.[27,28] MEES should fill that gap.

References

1. Mössbauer Effect Methodology, I.J. Gruverman, ed. (Plenum Press, New York).
2. For instance: B.W. Dale, Contemp. Phys. 16, 127 (1975).
3. E.H. Lee, P.L. Bolduc and C.E. Violet, Phys. Rev. Letters 13, 800 (1964).
4. N. Hershkowitz and J.C. Walker, Nucl. Instr. Methods 53, 273 (1967).
5. P. Debrunner, Mössbauer Effect Methodology 1 97 (1965).
6. R.N. Ord and C.L. Christensen, Nucl. Instr. Methods 91, 293 (1971).
7. J.C. Walker and B.T. Cleveland, Bull. Am. Phys. Soc. 15, 108 (1970).
8. R. Oswald and M. Ohring, J. Vac. Sci. Tech 13, 40 (1976).
9. T. Toriyama, M. Kigawa, M. Fujioku and K. Hisatke, Japan J. Appl. Phys. Suppl. 2 PT1, 733 (1974).
10. K.R. Swanson and J.J. Spijkerman, Journ. Appl. Phys. 41, 3155 (1970).
11. R.L. Collins, Mössbauer Effect Methodology 4, 129 (1968).
12. J.C. Walker, C.R. Guarnieri, and R. Semper, 18th Magnetism and Magnetic Materials Conference, AIP Conf. Series 1539, 1973.
13. J.G. Mullen, Phys. Rev. 131, 1410 (1963).
14. M. de Coster and S. Amelinckx, Phys. Letters 1, 245 (1962).
15. R. Kamal and R.G. Mendinetta, Phys. Rev. B7, 80 (1973).
16. C.K. Wertheim, Phys. Rev. 124, 764 (1961).
17. W. Triftshauser and P.P. Craig, Phys. Rev. Letters 16, 1161 (1966).
18. P. Molland, F. de Bergeuin, P. Gerni, M. Figlarz and F. Fievet-Vincent, Phys. Rev. B8, 1265 (1973).
19. J.G. Mullen, Phys. Rev. B8, 1267 (1973).
20. C. Song and J.G. Mullen, Solid State Communications 17, 549 (1975).
21. W. Keune, S.K. Dote, I. Dezsi and U. Goneri, Journ. Appl. Phys. 46, 3914 (1975).
22. A.C. Zuppero and R.W. Hoffman, J. Vac. Sci. Tech. 7, 118 (1970).
23. M.N. Varma and R.W. Hoffman, J. Appl. Phys. 42, 1727 (1971).
24. R.W. Hoffman and M.M.L. Kwan, Japan J. Appl. Phys. Suppl. 2 PT1, 729 (1974).
25. M.N. Varma and R.W. Hoffman, J. Vac. Sci. Tech. 9, 177 (1972).
26. R.S. Semper, C.R. Guarnieri, and J.C. Walker, Bull. Am. Phys. Soc. 20, 609 (1975).
27. V.I. Goldanskii and I.P. Suzdakev, Russian Chemical Reviews 39, 609 (1970).
29. W. Zinn, Czech. J. Phys. B21, 391 (1971).

† MEES system initiated under ERDA support.

Proceedings, ERDA X-and Gamma-Ray Symp. Ann Arbor, MI, May 19-21, 1976 (Conf 760539)

MOSSBAUER DOWN - HOLE GRAVITY METER

Jon J. Spijkerman*, Jag J. Singh**, David H. Bohlen***, Kenneth H. Brown***, Richard A. Mazak*

Summary

The application of the Mossbauer Effect for a proposed down - hole gravitometer is described. The inherent precision of the Mossbauer Effect presents a comparitively simpler and lower cost alternative technique for the measurement of gravitational anomalies, which have yielded the most definite information on oil reservoir location.

Introduction

The first demonstration of the Mossbauer Effect (ME) in gravitational measurements was the Pound and Reoka[1] experiment in 1960. The relationship between ME and gravity can be derived from the apparent weight of the photon.

In survey uses for the location of hydrocarbon and mineral reserves, the precision of the Mossbauer measurement must be increased by many orders of magnitude. Existing Mossbauer isotopes do not have sufficient sensitivity; however, there are several long lived isotopes available, and Rh-103 is the most suitable for this application. Long lived metastable isotopes have higher order transitions, resulting in very complex spectra. Analysis has shown that magnetic polarization greatly reduces the number of allowed transitions. Magnetic modulation can be used to measure the gravitational shift.

Theory

A. Gravity Measurements. The main purpose of the gravitometer is to provide on substrate formations, either with an airborne pad or downhole tool[2]. McCulloh[3] has shown that the gravity difference between two vertically separated points underground is:

$$\frac{\Delta G}{\Delta Z} = (F_\ell - 4\pi\kappa\rho) + \Delta C_t + \Delta C_g + \Delta C_b \qquad [1]$$

where: F_ℓ = local free air gradient, mgal/ft

κ = the gravitational constant

ρ = the average rock density within the ΔZ

ΔC_t = the surface terrain effect correction

ΔC_g = the correction due to dipping beds

ΔC_b = the correction due to borehole effects in mgal/ft

The ΔC corrections are small below 3000 ft for a homogeneous lithology and a short ΔZ spacing[3]. Solving for the density, and using the gravitational constant and an average value for the free air gradient,

$$\rho = 3.687 - 39.185\ (\Delta G/\Delta Z) \qquad [2]$$

For resevoir evaluation a precision of 10 microgals at 30 feet intervals would be desired to give a density[4] accuracy of 0.02 gm/cm^3. The success of borehole gravimetry[5] is attributed to its large volume capability and the absence of wellbore a d near wellbore effects. Present gravitometers use a vibrating mass or astatized spring, and require a large borehole diameter. The Mossbauer devise can be constructed with a much smaller diameter, and without moving parts.

B. Mossbauer Effect. The Mossbauer gravitometer is based upon the general theory of relativity equivalence principle, or[6]

$$\Delta E = \frac{E_\gamma}{c^2} g \Delta Z \qquad [3]$$

where E_γ is the Mossbauer gamma ray energy.

The fluctuation in ΔE from changes in the value of g, is:

$$\Delta E = (E_\gamma/c^2) gh(\Delta g/g) = E_\gamma(\Delta g/g)\ 10^{-16}\ \text{eV/m} \qquad [4]$$

To attain 1 ppm for $(\Delta g/g)$, the energy resolution must be:

$$(\Delta E/E_\gamma) = 10^{-22}\ \text{m}^{-1} \quad \text{at the surface of the earth}$$

for a source-absorber separation of 1 meter.

This is outside the present Mossbauer isotopes resolution. However, there are several isotopes with low energy metastable states[7]. Rh-103 is the most logically choice from a Mossbauer gamma ray energy, isotopic abundance and decay scheme simplicity. The 40 keV transition insures a recoilfree factor of 0.77, and sufficient penetration energy in the absorber. The Ag-109 also has many of the desired characteristics.

Using the Rh-103 parameters, E_γ = 40 keV in equation [4],

$$\Delta E = 4 \times 10^{-18}\ \text{eV/m}$$

The natural linewidth for the 40 keV state is

$$\Gamma = 1.9 \times 10^{-19}\ \text{eV}$$

Or, $\Delta E/\Gamma = 21$ for 1 meter source-absorber separation.

C. Mossbauer Parameters. Most of the Mossbauer parameters can be derived from the nuclear properties. The decay scheme for Rh-103 is shown in fig. 1. The 40 keV transition is E3, from a 7/2+ to ½- state. The 40 keV level nuclear parameters are not known, but have been estimated using deShalit[8] model of a weak coupling core-excitation model. The excited levels are described by the coupling of a single proton to the adjacent double core nucleus. Using these calculations and the measured values,

E_γ = 40 keV

$t_{\frac{1}{2}}$ = 57 m

α_T = 40, X(K) = 0.07 K/(L+N+M) = 0.1

IA = 100%

MG = -0.0883 nm (measured)

MM = 5 nm (calculated)

QM = - 0.20 b (calculated)

$\left|\frac{\Delta R}{R}\right| < 1.2 \times 10^{-3}$ (calculated)

The isomer shift can be estimated from the electrondensity at the nucleus and the change in nuclear radius.

For Rh-103, $|\Psi_s(0)|^2 = 0.49 \times 10^{-26}\ \text{cm}^{-3}$

and $(\Delta E/E) = 1.4 \times 10^{-14}$ for a 5s electron transfer.

*Ranger Engineering Corp.,Fort Worth, Texas,
** NASA, Langly, Virginia.
*** Northwestern State University, Alva, Oklahoma.

The isomer shift does not present a problem in the gravitometer, but line broadening can arise from impurities and crystal defects, which requires a high degree of single crystal source and absorber perfection.

The quadrupole interaction will only effect the 7/2 state, which will split into 4 levels. The magnitude of the quadrupole interaction will depend on the crystal deformations, impurities, dislocations and the Sternheimer Shielding factors;

Or

$$\frac{\partial^2 V}{\partial z^2} = q = q_{latt}(1 - \gamma_\infty) + q_{el}(1-R_o) \qquad [5]$$

for Rh-103, γ_∞ = -21 and R_o = -0.1

The q_{latt} arises from the positive ion cors within the lattice, and q_{el} is due to the non-spherical distribution of the conduction electrons in the immediate vicinity of the nucleus. The quadrupole effect can cause serious line broadening, but by applying a magnetic field the degeneracy can be lifted.

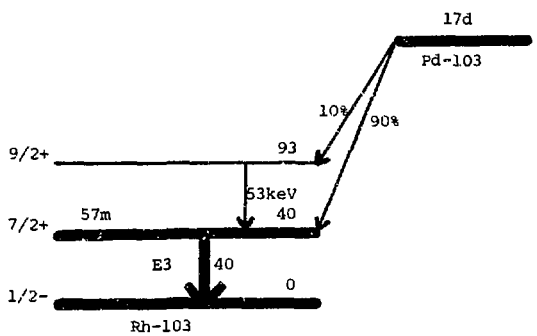

Figure 1. Energy level diagram for the Pd-103 →Rh-103 decay.

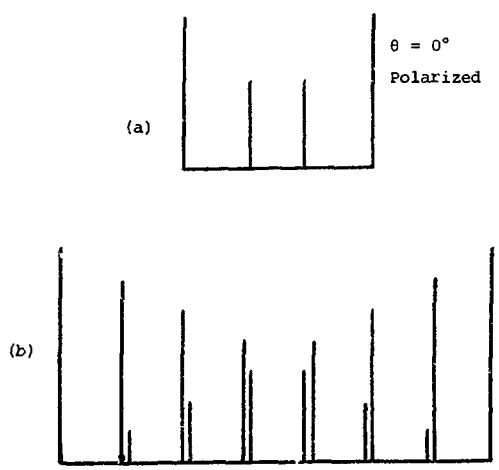

Figure 2. Magnetically split hyperfine spectrum for a). θ=0° polarization and b). unpolarized spectrum, of the 40 keV transition of Rh-103.

Magnetic Hyperfine Splitting. The intensities of the gamma emissions following a nuclear transition can be calculated for unpolarized and magnetically polarized atoms.

In general the intensity of a transition from a ground level $|g_a\rangle$ to an excited level $|e_b\rangle$ due to the absorption of a gamma ray quantum is given by the squared absolute value of matrix elements of unit irreducible tensors between groung level and excited states:

$$I_{ab} = |\langle g_a||\Gamma||e_b\rangle|^2 \qquad [6]$$

The quickest and most elegant evaluation of [6] follows from the Wigner-Eckart theorem, which states that the matrix elements of an irreducible tensor operator Γ for eigenstates of angular momentum depend on the quantum numbers μ_a and μ_b in a way that is completely described by the Clebsch-Gordan coefficients, i.e., the desired element is equal to a constant times the appropriate Clebsch-Gordan coefficient.

The electric multipole radiation associated with the transition $J_a \rightarrow J_b$ is:

$$I_{ab}(\theta,\phi,E) = \sum_{m_a=-J_a}^{J_a} \sum_{m_b=-J_b}^{J_b} P_{m_a} |C(J_a J_b m_a m_b; \ell m|^2 \cdot$$

$$\cdot Z_{\ell,m}(\theta,\phi) \qquad [7]$$

and

$$Z_{\ell,m}(\theta,\phi) = \tfrac{1}{2}\left|1 - \frac{m\,(m+1)}{\ell\,(\ell+1)}\right| |Y_{\ell,m+1}(\theta,\phi)|^2$$

$$+ \tfrac{1}{2}\left|1 \frac{m\,(m-1)}{\ell\,(\ell+1)}\right| |Y_{\ell,m-1}(\theta,\phi)|^2$$

$$+ \frac{m^2}{\ell\,(\ell+1)} |Y_{\ell,m}(\theta,\phi)|^2 \qquad [8]$$

where Y are the spherical harmonics. The Clebsch-Gordan coefficients are given by Rotenberg et. al.(8) and the spherical harmonics by Edmonds (9).

For an unpolarized spectrum, the angular dependance averages out, and the intensities a given by the square of the Clebsch-Gordan coefficients, as shown in figure 2b. When the polarization is θ= 0°, the 14 line spectrum reduces to only 4 lines, as shown in figure 2a. The values of the angular distribution functions for θ = 0° and θ = 90° are:

$Z_{\ell,m}(\theta,\phi)$	θ = 0°	θ = 90°
$Z_{3,3}$	0	105/256π
$Z_{3,2}$	0	70/256π
$Z_{3,1}$	224/256π	7/256π
$Z_{3,0}$	0	84/256π

Magnetic polarization of the source and absorber thus greatly reduces the complexity of the spectrum, and also lifts the quadrupole degeneracy.

Electron-Nuclear Interaction. This dipole interaction between the electrons and nuclear spins,

$$\Delta E(\mu_i,\mu_j) = 2\mu_i\mu_j/d^3 \qquad [9]$$

where d is the lattice spacing. The dipole-dipole interaction can be suppressed by operating at low temperature, or by applying a polarizing magnetic field.

The preparation and isolation of carrier free Pd-103 produced by Rh-103 (d, 2n) Pd-103 reaction has been described by several workers (refs.10,11,12). The procedure used by Gile, et.al, (10) in isolating carrier free Pd-103 from the target element and 41-day Ru-103 reaction, is described below. After bombardment for a predetermined time with 20 MeV deutrons, the 1 gram pure rhodium target was fused with excess potassium acid sulphate and the resulting mass leached with water. Insoluble impurities were separated by centrifugation and the decantate was made 6 N in hydrochloric acid by treatment with 12 N hydrochloric acid and sodium chloride and then 5 milligrams of selenous acid were added to the solution. The resulting solution was treated with excess sulphur dioxide which resulted in precipitation of elemental selenium which carried 99+ percent of Pd-103 from the solution. The precipitate was washed with water, dissolved and reprecipitated. The selenium precipitate was dissolved in concentrated sulphuric acid, transfered to an all-glass distilling flask, 9 N hydrobromic acid added and the mixture distilled at 200°C. The residue contained all of the Pd-103 activity. All these steps can be compleated within a period of 1-2 hours. For the extreme purity required for the (Pd-103 - Rh-103) gravitometer, the source thus produced may have to be subjected to a mass spectrometric separation and single crystal growth.

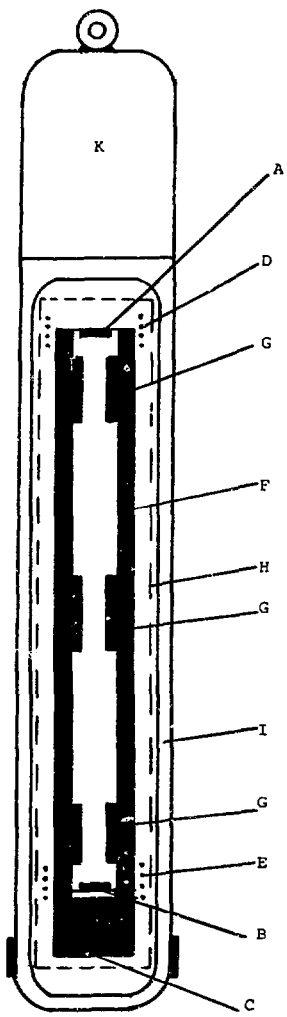

Legend. A- Single crystal Pd-103 source, B- Single crystal Rh absorber, C- Radiation Detector, D- Source magnetic polarization coil, E- Absorber magnetic modulation coil, F- INVAR Source-Absorber separation tube, G- Radiation collimator, H- Magnetic shield, I- Cryogenic enclosure, K- Electronics and cryogenic control section.

Figure 3. Proposed Gravitometer construction.

Preparation of Pd-103 Radioactive Source

There are a number of nuclear reactions that can be used to produce Pd-103 radionuclides. Some of them are summarized in the following table.

Nuclear Reaction	Cross Section
Rh^{103} (p, n) Pd^{103}	(a) (700± 40) mb at E_p = 10 MeV (ref.13) (b) 1100 mb at Ep=12 MeV (ref. 14)
Rh^{103} (d, 2n) Pd^{103}	(a) (58±3) mb at E_d = 14.6 MeV (b) 30±1.5) mb at E_d = 20 MeV (ref.15)

Rh^{103}, which is 100 percent abundant, is commercially available to the 99.999 percent purity level. A typical source preparation calculation based on Rh-103 (p, n) Pd-103 reaction is given below:

Source reaction: Rh-103 (p, n) Pd-103

σ (p, n) at Ep = 12 MeV: 1.1 barns
Assume a 1 gram Rh target.

The bombardment time, using a beam of 100 microamperes, needed to produce 1 curie of Pd-103 is 5½ hours.

Conclusion

The development of a Mossbauer gravitometer is well within the capability of present day technology. The purity and perfection of the source and absorber single crystals is the most important aspect of this development.

This new survey meter will have a maximum diameter of 3.5 inches, making it possible for use in cased boreholes. The absence of mechanically moving parts and the wide range of measurement with magnetic modulation should substantially increase the logging rate.

Acknowledgements

The feasibility study of the Mossbauer Gravitometer was supported by the National Aeronautics and Space Administration under grant NS9 1134. The many helpful discussions with Mr. Marvin Gearhart and Mr. Earl John of Gearhart-Owen Industries, Inc. and Dr. A.H. Jageler of Amoco, Inc. concerning borehole use of the gravitometer is greatly appreciated.

References

1. Pound, R.V., and G.A. Rebka, Jr., Phys. Rev. Letters 4, 337(1960).

2. Singh, Jag J., NASA Technical Memorandum TM X-72703, June, 1975.

3. McCulloh, T.H., U.S. Geol. Survey Circ. 531 (1966).

4. Howell, L.G., K.O. Heintz and A. Barry, Geophysics 31 No.4, 764 (1966).

5. Jageler, A.H., Society of Petroleum Engineers of AIME Paper SPE 5511, September, 1975.

6. Frauenfelder, Hans, The Mossbauer Effect (W.A. Benjamin, Inc., New York, 1962), p. 58.

7. Lederer, C. Michael, Jack M. Hollander and Isadore Perlman, Table of Isotopes (John Wiley & Sons, Inc., New York,1967) 6th ed., p. 241.

8. Rotenberg, M.,N. Metropolis, R. Bivins and J.K. Wooten, Jr., The 3-j and 6-j Symbols(The Technology Press, Massachusettes Institute of Technology, Cambridge, Mass., 1957),p.49.

9. Edmonds, A.R., Angular Momentum in Quantum Mechanics (Princeton University Press, Princeton, New Jersey, 1957), p. 124.

10. Gile J.D.,H.R. Haymond, W.M. Garrison and J.G. Hamilton, J. Chem. Phys. 19, 660(1951).

11. Melnick, M.A. Collected Radiochemical Procedures, LA-1721, 101,(1967).

12. Zoller, W.H., E.S. Macias, M.B. Perkal and W.B. Walters, Nucl. Phys. A-130, 293(1969).

13. Hansen, L.F. and R.D. Albert, Phys. Rev. 128, 297 (1962).

14. Holbrow, C.H. and H.H. Barschall, Nucl. Phys., 42, 264(1963).

15. Betancourt, L. De and S.J. Nassif, Report #IAN-F-2 Instituto de Asuntos Nucleares, Bogota, Columbia, April, 1966.

(cont. from p. 18)

References

1. Gaines, J. L., Kuckuck, R. W., and Ernst, R. D., paper presented at ERDA Symposium on X- and Gamma Ray Sources and Applications, May 19-21, 1976, Ann Arbor, Michigan.

2. Garcia, J. D., Fortner, R. J., and Kavanaugh, T. M., Rev. Mod. Phys. 45 (1973) 111.

3. Reginato, L. L., and Smith, B. H., paper presented at the Particle Accelerator Conference, March 10-12, 1965, Washington, D. C. Also LLL report UCRL-11783, March 2, 1965.

4. Henke, B. L., et. al., Norelco Reporter 14, nos. 3-4 (1967) 112-134.

5. Buck, T. M., Wheatley, G. H., and Feldman, L. C., Surface Science 35 (1973) 345-361.

6. Shima, K., et. al., Japanese Journal of Applied Physics 9 (1970) 1297-1305.

(cont. from p. 258)

3 Haubold, H.-G., Fundamental Aspects of Radiation Damage in Metals, ed. by M.T. Robinson and F.W. Young, U.S.A. ERDA Conf.-751006, 1976

4 Haubold, H.-G.,J. Appl. Cryst. 8 (1975) 175-183

5 Haubold, H.-G., Rep. Kernforschungsanlage Jülich Jül-1090-FF (1974)
Haubold, H.-G., Schilling, W., (1976) to be published

6 Haubold, H.-G., Martinsen, D., to be published

Acknowledgments

I would like to thank Dr. F.W. Young for helpful discussions and carefully reading the manuscript.

(cont. from p. 245)

3.5 Concluding Remarks

The studies reported here clearly demonstrate the potential role of an X-ray fluorescence technique in continuously monitoring the composition of the so-called filler, which is contained in the product emerging from the paper-making machine. Using ^{55}Fe as the excitation source and an X-ray proportional chamber, the monitoring of the level of the filler constituent, TiO_2, is shown to be particularly feasible. Correcting the observed titanium X-ray counting intensities for the effects of change in basis weight, clay content and moisture appears to be feasible, provided independent measurements of these parameters are available on a continuous basis, as is the case in modern plants. Neutron activation analysis proved to be a valuable tool for determining the filler compositions in the experimental samples studied in the present work.

The X-ray fluorescence technique also appears to be feasible for monitoring the levels of $CaCO_3$ present in the finished product, although not when appreciable quantities of TiO_2 are also present. This restriction is owing to the lower fluorescent yield from calcium than from titanium, coupled with the partial overlapping of the fluorescent peaks from the two elements in the present apparatus. Frequently, however, $CaCO_3$ does not appear as a filler constituent along with TiO_2. Correction for variation of basis weight, clay content, and moisture appears feasible for $CaCO_3$ monitoring as for TiO_2.

Acknowledgements

The authors would like to thank Mr. H. Kostalas for technical assistance and Dr. R. Hancock for advice on neutron activation analysis using the SLOWPOKE reactor. We would also like to thank Abitibi Provincial Papers for providing the samples used in this work. This work has been supported in part by the National Research Council of Canada through grants both to the University of Toronto and to Sentrol Systems Limited.One of us (L.A.MacLellan) acknowledges the support of an N.R.C. Industrial Postdoctoral fellowship.

References

1. L. Gottsching, W.F. Hill, and J. Bauer, Papier 26 1, (1972).

2. E.R. Gates and D.F. Booth, Pira Report. TSi20, (1973).

3. B.Y. Cho and O.L. Utt, Instrument Society of America Report 611. 1, (1975), see also the Proceedings of this conference.

4. D. Radage, P. Humphries, and F.A. MacMillan, Instrument Society of America Report IPP 726203. 19, (1972).

5. A. Buchnea, G.E. Cohen, and J.S. Hewitt, Transactions of the American Nuclear Society - Winter Meeting 1975, page 146.

6. J.R. Rhodes, A. Pradzynski, R.D. Sieberg and T. Furata, Applications of Low Energy X-and Gamma Rays edited by Charles A. Ziegler, (Gordon and Breach Publishers; New York, 1971), page 317.

7. W.T. Gartland, and J.F. Cameron, Paper Technology Vol. 11, No. 5. 353, (1970).

(cont. from p. 266)

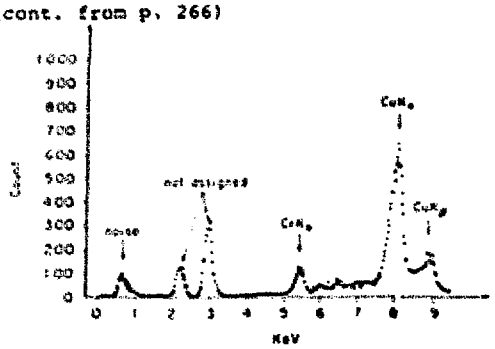

Fig 8 X-ray Fluorescence Spectrum of Cr Doped $LiNbO_3$

Table 1 Yield of Secondary X-ray from Pure Metals (including scattered Primary X-ray)

Atomic number	Metal	CPS
22	Ti	3819
23	V	4449
25	Mn	4436
27	Ni	3999
30	Zn	2750
32	Ge	3162
40	Zr	1974
42	Mo	3604
47	Ag	1849
51	Sb	1766
73	Ta	1185
78	Pt	1313
82	Pb	1937
(SUS27 Alloy)		(7445)

Table 2 Result of Chemical Analysis of sintered Pb Alloy

MnO	0.8%
TiO_2	12 ~ 13%
ZrO_2	15 ~ 20%
PbO	65 ~ 70%
WO_3	Trace

(cont. from p. 67)

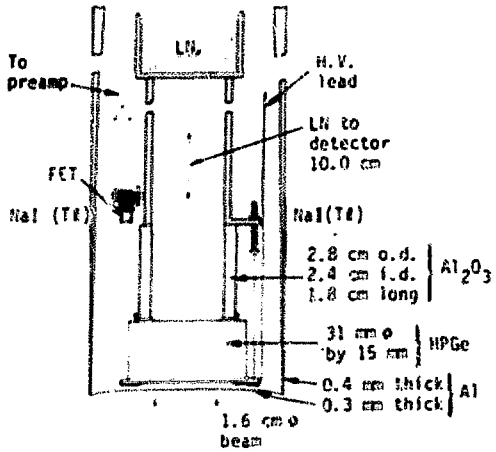

Fig. 2. A schematic drawing of the HPGe cryostat and detector mounting. (See text for details.)

in diameter and has a 14.5-mm-deep intrinsic region. Palladium is used for the p-contact (~0.1 mm) and diffused lithium for the n-contact (~0.05 mm). The detector operates at 2200 V, but is fully depleted at 300 V (~1 × 10^9 impurity atoms/cm^3). The detector is oriented so that collimated gamma rays enter through the p-contact; hence, backscattered photons will pass through the thinner junction.

The detector is mounted against tubular sapphire (Al_2O_3), which serves both as an excellent thermal conductor and as an electrical insulator. The sapphire is positioned against a tubular aluminum cold finger. Indium is used to improve thermal conductivity at each interface. The sapphire and detector are held to the tubular aluminum cold finger by three 0.25-mm-diameter stainless steel wires. Only one is shown in Fig. 2, as they are positioned at 120° intervals around the detector. These wires couple into a 0.75-mm-thick piece of lexan* that extends across the entire face of the detector. The lexan is 1.5 cm thick around the edge of the detector. This low-Z material is used to minimize mass, but it also serves to hold in place a small wire carrying the high voltage to the detector. The signal lead to the input FET is a Cu wire encircling the sapphire and twisted tightly into the indium and sapphire.

The enclosing walls of the aluminum vacuum housing are 0.40 cm thick in the vicinity of the detector, and get gradually thicker (for mechanical strength) away from the detector. The prestressed aluminum end window is 0.30 cm thick and was electron-beam-welded to the housing walls. Thus, mass surrounding the detector has been minimized. Note that no heat shield is employed and that the cold finger and insulator are tubular. It was necessary to adopt this "beam dump" geometry; otherwise the back-scattered gamma-ray distribution (centered about 225 keV) becomes enormous with the excellent Compton continuum suppression that this spectrometer yields.

The split-halves anticoincidence-detector geometry is used. The NaI(Tℓ) detectors, 34 cm in diameter and 17.5 cm thick are optically isolated and integrally mounted in a single housing. Nine 7.6-cm-diameter phototubes view each end. The detector vacuum housing entrance well is 5.0 cm in diameter and 25 cm long, while the gamma-ray-beam entrance well is 1.90 cm in diameter and 9.0 cm long. The much smaller beam entrance reduces the gamma-ray back-scattering solid angle (Θ-max) and allows better suppression in the vicinity of the Compton edges. The NaI(Tℓ) well enclosure walls, designed to reduce mass absorption between the central HPGe detector and the anticoincidence detectors are 0.75-cm-thick aluminum.

Electronics

Figure 3 shows a block diagram of the electronics. The NaI preamplifiers should have excellent overload

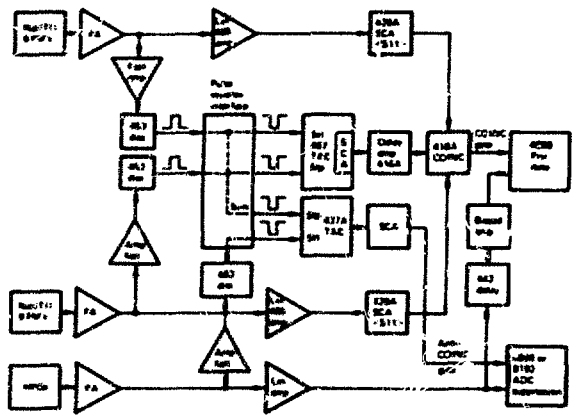

Fig. 3. Electronic circuit used to operate suppression and pair modes simultaneously.

characteristics and very fast recovery times for cosmic ray events. Constant fraction discriminators are used for both NaI and Ge signals. The threshold of the scintillation detector's discriminator should be set as close to noise level as possible, but not in it. The best suppression factor is obtained when the smallest energy interaction in the scintillator is detected. When the system is used as a suppression spectrometer, a signal from either scintillator half in coincidence with a Ge event anticoincidences or rejects that Ge event and stops the TAC. In operation as a pair spectrometer, both scintillator halves must register a 511-keV annihilation quanta. Hence, a "fast-slow" coincidence arrangement is used. A 467TAC fast-coincidence output gates the slow 418A triple-coincidence unit, whose output, in turn, allows acceptance of any Ge event by the analyzer. Note that a biased amplifier is introduced prior to the analyzer to select only that portion of the Ge spectrum above 1.0 MeV. Thus, Compton-suppression and pair data can be recorded simultaneously.

Performance

Figure 4 shows two spectra of Zn-65. The top spectrum is singles data, while the lower data is Compton suppressed. Both spectra were recorded simultaneously. The maximum suppression factor achieved was 25 in the vicinity of 700 keV. This leads to a peak-to-minimum Compton value of 1100 to 1. Zn-65 is a positron emitter; thus the 511-keV peak is normal. Note that the two spectra join at very low energy (~25 keV), corresponding to no suppression or gamma-ray scattering angles less than Θ-min, about 2°30'.

*Reference to a company or product name does not imply approval or recommendation of the product by the University of California or the U.S. Energy Research and Development Administration to the exclusion of others that may be suitable.

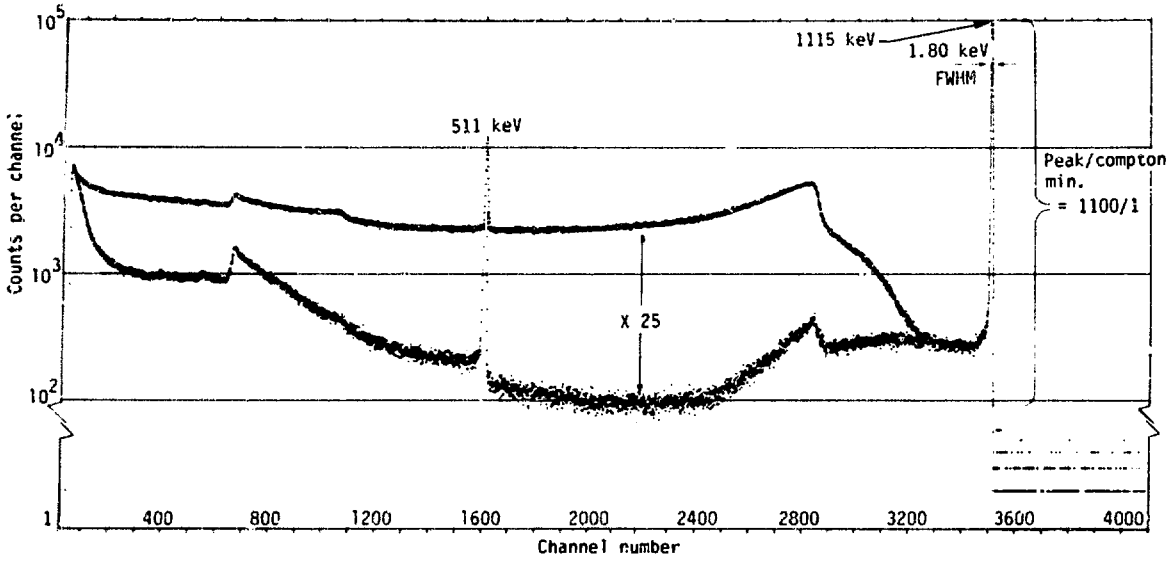

Fig. 4. Compton-suppressed (top) and singles (bottom) spectra of Zn-65.

Figure 5 shows a singles and Compton-suppressed spectrum of Co-60. Here, the two spectra join at about 30 keV for a θ-min corresponding to about 2°20'. Note that the double escape peaks at 151 and 310 keV are suppressed beyond detection. For higher-energy gamma rays, they are not completely eliminated, e.g. the Na-24 2.754-MeV transition. This is easily understood if one considers two annihilation quanta that escape at θ = 0° and 180° respectively, where there is no anticoincidence scintillator. Much less likely, but not zero, is the probability of both 511-keV quanta not interacting at all with either scintillator.

Note the presence of a small 511-keV peak in the suppressed spectrum. This is a result of Co-60 photons interacting via pair production with collimator walls and any mass in the vicinity of the detector. Subsequent to annihilation of the positron, one 511-keV quantum is totally absorbed by the HPGe detector. The large size of the back-scattered gamma ray peak centered about 225 keV is readily apparent. It would have had a much greater area were it not for the "beam dump" geometry used in mounting the detector (see Fig. 2). The gamma-ray peaks show a FWHM of 190 keV, and the peaks are essentially Gaussian. Thus, without significant tailing,

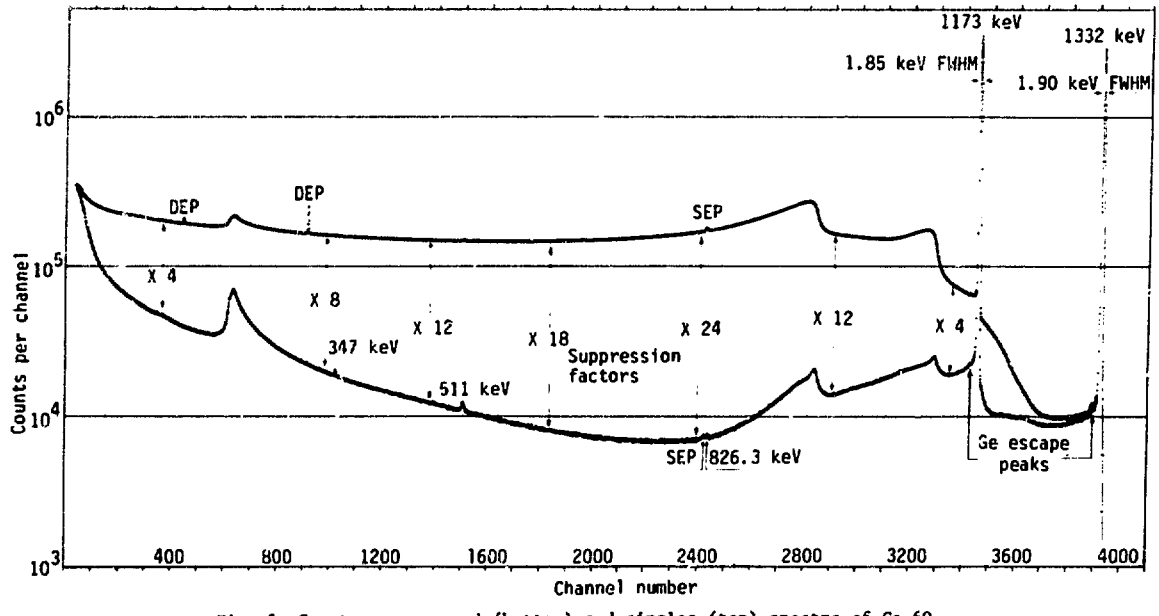

Fig. 5. Compton-suppressed (bottom) and singles (top) spectra of Co-60.

one observes the Ge fluorescent x-ray escape peaks. The excellent peak shape is in part due to collimation of the incoming gamma radiation toward the center of the HPGe detector (Fig. 2), and in part due to the excellent detector material quality, which allows the use of a large overvoltage.

The maximum suppression factor observed so far with this system is 31. It depends sensitively on the NaI(Tℓ) discriminator settings and the condition of the phototubes. With noisy or poorly working phototubes, small light signals will not be detected, and those events will not be rejected. A maximum suppression factor of 24 corresponds to 95.83% rejection, while a factor of 31 corresponds to 96.77%, a difference of less than one percent. In fact, some time after the Fig. 5 data were taken, six noisy and two non-working phototubes were discovered. Also the degree to which the Compton edge "peaks" are suppressed, and the low energy at which the spectra join depend on photomultiplier response and discriminator setting. In data taken earlier, the suppression factors were 25% better than for the data in Fig. 5. As a result, almost no increase was observed to occur in the spectrum towards the low-energy side of the suppressed 1.33-MeV Compton edge, contrary to the increase observed in Fig. 5.

Discussion

The excellent Compton continuum suppression and nearly 4π enclosure of the HPGe detector lead the spectroscopist to consider experiments not otherwise possible. For example, it is nearly impossible to measure quantitatively via beta-spectrum intensities the very weak forbidden beta branches whose endpoint energies lie well within strong allowed beta transitions. However, with significant Compton suppression, it is possible to observe very weak gamma transitions that depopulate levels fed by forbidden beta decay. Raman[3] has succeeded in measuring several such cases (although without suppression). The common radioactivities of Co-60, Zn-65, Cs-134 and Cs-137, and others, all contain possible forbidden beta branches observed via weak gamma-ray-transition-intensity measurements.

Similarly, one can measure weak gamma-ray branches that test various theoretical nuclear predictions. In the quadrupole vibrator model, small inter-particle couplings remove the degeneracy to lead to a triplet of levels (0+, 2+, and 4+) for the two-phonon vibration. Gamma-ray transitions between the 4+ and 2+ levels (the so-called "zero-phonon" transitions) are forbidden according to this model. These weak interband or model-forbidden gamma-ray transitions are generally hidden by the Compton continuum. The degree of forbiddeness could be measured by looking for such transitions. They have been observed[4,5] in a number of nuclei, and the 346-keV transition seen in Fig. 5 is just such a "zero-phonon" transiton in Ni-60. Other examples of weak interband (β- to γ-band) transitions have been observed in the deformed nuclei region.

In the search for states of very high angular momentum via in-beam spectroscopy, Compton suppression will allow the observation of weaker $\Delta I = 2$, no transitions. Thus, those groups who have in the past used Compton-suppression spectrometers should make the small investment required to adapt their old anticoincidence scintillators to fit the modern high-efficiency Ge detectors.

The almost complete 4π enclosure (98.9%) offered by this anticoincidence system combined with the small HPGe detector size makes the system an excellent pair spectrometer. One possible experiment would be the confirmation of the deviation from the experimental-pair-production cross section observed[6] at low energies from the Bethe-Heitler prediction. Another experiment currently under investigation with this system is the search for double-pair production. Quantum electrodynamics predicts a nonvanishing probability for the formation of two electron-positron pairs if $E(\gamma) > 2.044$ MeV. Wilkinson and Alburger[7] were the first to attempt to measure the cross section, but they obtained only an upper limit. More recently, Robertson et al.[8] observed indirect evidence of this process. With the present spectrometer (both SCA's set to pass only 1.022 MeV) and with direct experimental observations possible with both Si and Ge detectors, a cross section for this process can be established, even exclusive of Z dependent cascade first-order processes (see Ref. 7, appendix).

References

1. Camp, D. C., Radioactivity in Nuclear Spectroscopy, eds., J. Hamilton and J. Manthurthil (Gordon & Breach, New York, 1972) Vol. 1, pp. 135-205.
2. Konijn, J., Goudsmit, P., and Lingeman, E., Nucl. Instr. Mon. 199, 83 (1973).
3. Raman, S., and Gove, N. B., Phys. Rev. C 7, 1995 (1973).
4. Camp, D. C., and Van Hise, J. R., Phys. Rev. C (1976) (in press). See also Phys. Rev. Lett. 23, 1248 (1969).
5. Van Hise, J. R., Camp, D. C., and Meyer, R. A., Z. Phys. A274, 383 (1975).
6. Yamazaki, T., and Hollander, J. M., Phys. Rev. 140, 1363 (1965).
7. Wilkinson, D. H., and Alburger, D. E., Phys. Rev. C 5, 719 (1972).
8. Robertson, A., Kennett, T. J., and Prestwich, W. V., Phys. Rev. C 13, 1552 (1976).

REGISTRANTS

Adams, F.
Universitare Instelling
Antwerpen, Belgium

Aeschbach, J.
Tracor Northern
Middleton, Wisc.

Ahmad, I.
Argonne Nat'l Lab
Argonne, IL

Albert, J.
Consultant
New York, NY

Amlauer, K.
Isotope Products Labs.
Burbank, CA

Anderson, C.
Case Western Reserve Univ.
Cleveland, OH

Andrews, F.
Amersham/Searle
Arlington Heights, IL

Anzelon, G.
McClellan Lab. USAF
Sacramento, CA

Armstrong, J.
Argonne Nat'l Lab.
Idaho Falls, ID

Artman, C.
Edsel B. Ford Inst. Med. Res.
Detroit, MI

Artz, B.
Ford Motor Co.
Ann Arbor, MI

Bahn, E.
S. E. Mo. St. Univ.
Cape Girardeau, MO

Beard, G.
Wayne State Univ.
Detroit, MI

Bennish, A.
Univ. of Mich.
Ann Arbor, MI

Beyer, N.
Argonne Nat'l Lab.
Argonne, IL

Bohlen, D.
N. W. Okla. State U.
Alva, OK

Bolin, F.
E. B. Ford Inst. Med. Research
Detroit, MI

Bonner, N.
Lawrence Livermore Lab.
Livermore, CA

Boster, T.
Lawrence Livermore Lab.
Livermore, CA

Bozymowski, J.
G. M. Research
Warren, MI

Brauer, F.
Battelle-Northwest
Richland, WA

Brenner, R.
Argonne Nat'l Lab.
Argonne, IL

Brill, A.
Vanderbilt Univ.
Nashville, TN

Brown, K.
N. W. Oklahoma State U.
Alva, OK

Buchnea, A.
Sentrol Systems Ltd.
Downsview, Ontario

Burns, E.
USAF
Kirtland AFB, NM

Busch, A.
U. S. ERDA
New Brunswick, NJ

Cahill, R.
Illinois Geological Survey
Urbana, IL

Cahill, T.
Univ. of Calif.
Davis, CA

Cameron, J.
Univ. of Wiscosin
Madison, WI

Camp, D.
Lawrence Livermore Lab.
Livermore, CA

Campani, J.
Canberra
Meriden, CT

Campbell, M.
Exxon Nuclear Company, Inc.
Richland, WA

Carlson, R.
Southwest Detroit Hospital
Detroit, MI

Case, F.
ORNL
Oak Ridge, TN

Charatis, G.
KMS Fusion, Inc.
Ann Arbor, MI

Chartrand, M.
Ecole Polytechnique
Montreal, Canada

Chen, Y.
Ohmart Corp.
Cincinnati, OH

Cho, B.
Industrial Nucleonics
Columbus, OH

Chulick, E.
Babcock & Wilcox
Lynchburg, VA

Clayton, W.
Tenn. Valley Authority
Muscle Shoals, AL

Cogburn, C.
Univ. of Arkansas
Fayetteville, AR

Cohen, B.
Univ. of Pittsburgh
Pittsburgh, PA

Colvin, J.
St. Joseph Mercy Hospital
Ann Arbor, MI

Cooper, J.
GRTEC
Oak Ridge, TN

Cronch, S.
Univ. of KY
Lexington, KY

Day, R.
Los Alamos Scientific Lab.
Los Alamos, NM

DeKalb, E.
Ames Laboratory
Ames, IA

Delmastro, A.
Allied Chemical Corp.
Idaho Falls, ID

Dunbar, G.
Amersham/Searle
Arlington Heights, IL

Economou, T.
Univ. of Chicago
Chicago, IL

Elgart, M.
Ford Motor Co.
Dearborn, MI

Eller, E.
Goddard Space FH Cntr/NASA
Greenbelt, MD

Evans, L.
Computer Sciences Corp.
Greenbelt, MD

Ewins, J.
U. of Calif. - LLL
Danville, CA

Fager, J.
Battelle-Northwest
Richland, WA

Farukhi, M.
Harshaw Chemical Co.
Solon, OH

Fleming, T.
Reuter Stokes Inc.
Cleveland, OH

Fletcher, K.
Amersham/Searle
Arlington Heights, IL

Frost, J.
Illinois State Geological Survey
Urbana, IL

Furnas, T.
Molecular Data Corp.
Cleveland Heights, OH

Furuta, T.
Int. Atomic Energy Agency
Vienna, Austria

Gaines, J.
Lawrence Livermore Labs.
Livermore, CA

Gardner, R.
North Carolina State Univ.
Raleigh, NC

Gibbs, A.
E. I. duPont
Aiken, SC

Gilboy, W.
Surrey University UK
Guildford, England

Gillieson, A.
Retired
Ottawa, Ontario

Gleason, G.
ORAU Training Div.
Oak Ridge, TN

Glendenin, L.
Argonne Nat'l Lab.
Argonne, IL

Goss, J.
Measurex Corp.
Cupertino, CA

Griffin, H.
Univ. of Mich.
Ann Arbor, MI

Gunnick, R.
Lawrence Livermore Labs.
Livermore, CA

Haas, F.
Monsanto Research Corp.
Miamisburg, OH

Hadley, J.
Lawrence Livermore Labs.
Livermore, CA

Hanser, F.
Panametrics, Inc.
Waltham, MA

Harget, P.
Allied Chemical Corp.
Morristown, NJ

Hattner, R.
Univ. Calif. San Francisco
San Francisco, CA

Haubold, H.
KFA--JULICH
Juelich, Germany

Hawthorne, A.
NC State Univ.
Raleigh, NC

Heath, R.
Idaho Nat'l Engineering Lab.
Idaho Falls, ID

Helmer, R.
Aerojet Nuclear Company
Idaho Falls, ID

Helmut, L.
Univ. of KY
Lexington, KY

Henderson, L.
Illinois State Geological Survey
Urbana, IL

Henke, B.
Univ. of Hawaii
Honolulu, HI

Herber, R.
Rutgers University
New Brunswick, NJ

Hewitt, J.
Univ. of Toronto
Toronto, Ont. Canada

Hill, R.
General Motors Research
Warren, MI

Himes, R.
Dow Chemical Co.
Midland, MI

Hochel, R.
E. I. duPont
Aiken, SC

Hoffman, R.
Case Western Reserve Univ.
Cleveland, OH

Hoppes, D.
Nat'l Bureau of Standards
Washington, DC

Hurley, R.
Ford Motor Company
Dearborn, MI

Jaklevic J.
Univ. of Calif.
Berkeley, CA

Jenkins, R.
Philips Electronic Instruments
Mt. Vernon, NY

Jones, J.
Phoenix Memorial Lab. U-M
Ann Arbor, MI

Joy, M.
Univ. of Toronto
Toronto, Ontario, Canada

Kamykowski, E.
Grumman Aerospace Corp.
Bethpage, NY

Karin, R.
New England Nuclear Corp.
N. Billerica, MA

Kato, M.
University of Tokyo
Tokyo, Japan

Kaufman, L.
Univ. of Calif.
San Francisco, CA

Kephart, J.
Los Alamos Scientific Lab.
Los Alamos, NM

Kirby, J.
Lawrence Livermore Lab.
Livermore, CA

Knapp, M.
Lawrence Livermore Lab.
Livermore, CA

Knoll, G.
U. of M.
Ann Arbor, MI

Koppel, L.
Lawrence Livermore Lab.
Livermore, CA

Kruse, F.
Owens-Illinois
Toledo, OH

Kuckuck, R.
Lawrence Livermore Lab.
Livermore, CA

Kurtz, T.
Bendix Field Engineering Corp.
Grand Junction, CO

Lange, W.
G. M. Research Labs.
Warren, MI

Larsen, R.
Argonne Nat'l Labs.
Argonne, IL

Law, J.
Longwood College
Farmville, VA

Lazewatsky, J.
M. I. T.
Cambridge, MA

Lehnert, R.
LND Inc.
Oceanside, NY

Leonard, J.
I. E. E. E.
Anaheim, CA

Lindau, I.
Stanford, Univ.
Stanford, CA

Lloyd, W.
Univ. of KY
Lexington, KY

Loveland, W.
Oregon State Univ.
Corvallis, OR

Lowe, D.
Owens-Illinois
Toledo, OH

Lum, H.
U-M
Ann Arbor, MI

Lurie, N.
IRT Corp.
San Diego, CA

Lyons, P.
Los Alamos Scientific Lab.
Los Alamos, NM

McIlroy, J.
U-M
Ann Arbor, MI

McQuaid, J.
Lawrence Livermore Lab.
Livermore, CA

Marlow, K.
Naval Research Lab.
Washington, DC

Martin, M.
ORNL
Oak Ridge, TN

Martinelli, P.
French CEA
Gif-Sur-Yvette, France

Muttarella, S.
AC Spark Plug
Flint, MI

Mazess, R.
Univ. of Wisc. Hospital
Madison, WI

Meyer, R.
Lawrence Livermore Labs.
Livermore, CA

Meyers, T.
U-M
Ann Arbor, MI

Miller, D.
General Electric Co.
Schnectady, NY

Mills, W.
Mobil R & D Corp.
Dallas, TX

Mitchell, T.
Federal Highway Admin.
Reston, VA

Moore, D.
Texas A & M Univ.
College Station, TX

Nardozzi, M.
U. S. Steel Research
Monroeville, PA

Neylan, D.
U. S. Bureau of Mines
College Park, MD

Packer, L.
UTRC
East Hartford, CT

Parker, J.
Los Alamos Scientific Lab.
Los Alamos, NM

Pehl, R.
U. C. Lawrence Berkely Lab.
Berkeley, CA

Pickles, W.
Lawrence Livermore Labs.
Livermore, CA

Piper, D.
E. B. Ford Inst. for Med. Research
Detroit, MI

Polichar, R.
U-M
Ann Arbor, MI

Pradzynski, A.
Univ. of Texas
Austin, TX

Preiss, I.
RPI
Troy, NY

Preuss, L.
Edsel B. Ford Inst. Med. Research
Detroit, MI

Prevo, C.
U. C. Lawrence Livermore Lab.
Livermore, CA

Price, R.
Vanderbilt Univ.
Nashville, TN

Raby, B.
Atomic Energy of Canada, Ltd.
Chalk River, Ontario, Canada

Randtke, P.
E. G. & G. Inc.
Goleta, CA

Renda, G.
Princeton Univ.
Princeton, NJ

Rengan, K.
Eastern Mich. Univ.
Ypsilanti, MI

Richards, A.
U-M
Ann Arbor, MI

Richardson, C.
Bedford Engineering
Bedford, MA

Roche, L.
EDF
Chatou, France

Roder, F.
Meredcom
Fort Belvoir, VA

Rogers, W.
U-M
Ann Arbor, MI

Rose, V.
Univ. of R. I.
Kingston, RI

Rotariu, G.
U. S. ERDA
Washington, DC

Roth, S.
U-M
Ann Arbor, MI

Rothbart, G.
Stanford Univ.
Stanford, CA

Ryge, P.
Princeton Gamma-Tech
Princeton, NJ

Sampson, T.
LASL
Los Alamos, NM

Sandborg, A.
EDAX International, Inc.
Prairie View, IL

Schlosser, P.
Ohio State Univ.
Columbus, OH

Schneid, E.
Grumman Aerospace Corp.
Bethpage, NY

Schneider, R.
Physics International Co.
San Leandro, CA

Seifrid, M.
Ill. State Geo. Survey
Champaign, IL

Sherman, I.
Argonne Nat'l Lab.
Argonne, IL

Short, M.
Ford Motor Co.
Dearborn, MI

Singman, L.
E. G. & G.
Las Vegas, NV

Sparrow, J.
Nat'l Bureau of Standards
Washington, DC

Spaulding, J.
University of Georgia
Athens, GA

Spykerman, J.
Ranger Eng. Corp.
Fort Worth, TX

Stanek, M.
W. S. U.
Detroit, MI

Strauss, M.
Argonne Nat'l Lab.
Argonne, IL

Swierkowski, S.
Lawrence Livermore Lab.
Livermore, CA

Taylor, J.
Atomic Energy of Canada, Ltd.
Chalk River, Ontario, Canada

Taylor, R.
Canberra IND
N. Ridgeville, OH

Taylor, R.
Monsanto Research Corp.
Dayton, OH

Teller, Steen
Isotopcentralen
Copenhagen, Denmark

Thomas, C.
S.U.N.Y.
Buffalo, N.Y.

Tipton, W.
E. G. & G.
Las Vegas, NV

Tominaga, H.
Japan Atomic Energy Research Inst.
Oarai-machi, Ibaraki-ken, Japan

Toohey, R.
Argonne Nat'l Lab.
Argonne, IL

Turcotte, R.
Schlumberger Tech. Corp.
Ridgefield, CT

Tyree, P.
New England Nuclear
N. Billierica, MA

Urrezis, P.
Argonne Nat'l Lab.
Chicago Lawn, IL

Vagelatos, N.
IRT Corp.
San Diego, CA

Vincent, D.
U-M
Ann Arbor, MI

Vintersved, I.
Nat'l Defense Research Inst.
Stockholm, Sweden

Volborth, A.
Univ. of CA
Irvine, CA

Wahl, J.
Schlumberger
Ridgefield, CT

Walker, R.
Kevex Corp.
Indianhead Park, IL

Warner, R.
M. S. U.
East Lansing, MI

Webber, C.
McMaster Univ. Med. Center
Hamilton, Ontario, Canada

West, L.
ORTEC, Inc.
Oak Ridge, TN

Whited, R.
E. G. & G.
Goleta, CA

Wielopolski, L.
N. C. State Univ.
Raleigh, NC

Wiesner, L.

Odenthal, Germany

Williams, J.
U-M
Ann Arbor, MI

Winchester, J.
Florida State Univ.
Tallahasse, FL

Witt, R.
Univ. Wisc. - Madison
Madison, WI

Wogman, N.
Battelle - NW
Richland, WA

Woldseth, R.
Kevex Corp.
Burlingame, CA

Wood, R.
U. S. ERDA
Washington, DC

Woodall, D.
Univ. of Rochester
Rochester, NY

Wysocki, C.
U-M
Ann Arbor, MI

Yule, H.
NUS Corp.
Rockville, MD

Zelenzy, W.
Los Alamos Scientific Lab.
Los Alamos, NM

Zimmer, W.
Atlantic Richfield Hanford Co.
Richland, WA

Zolnay, A.
Ohio State Univ.
Columbus, OH

Zyromski, P.
French CEA
Gif - Sur - Yvette, France

Barker, F.
Bettis Atomic Power Lab.
West Mifflin, PA

*U.S. GOVERNMENT PRINTING OFFICE: 1976-641-358/18